practice guide

NIST recommended

Fractography of Ceramics and Glasses

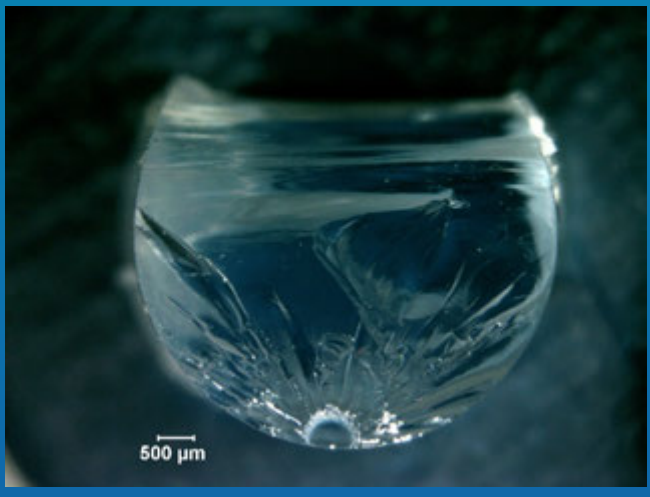

George D. Quinn

This publication is available free of charge from:

http://dx.doi.org/10.6028/NIST.SP.960-16e2

NIST
National Institute of Standards and Technology
U.S. Department of Commerce

Special Publication 960-16e2

NIST Recommended Practice Guide

Special Publication 960-16e2

Fractography of Ceramics and Glasses

George D. Quinn
Materials Measurement Laboratory

This publication is available free of charge from:
http://dx.doi.org/10.6028/NIST.SP.960-16e2

May 2016

U.S. Department of Commerce
Penny Pritzker, Secretary

National Institute of Standards and Technology
Willie May, Under Secretary of Commerce for Standards and Technology and Director

Certain commercial entities, equipment, or materials may be identified in this document in order to describe an experimental procedure or concept adequately. Such identification is not intended to imply recommendation or endorsement by the National Institute of Standards and Technology, nor is it intended to imply that the entities, materials, or equipment are necessarily the best available for the purpose.

National Institute of Standards and Technology
Special Publication 960-16e2
Natl. Inst. Stand. Technol.
Spec. Publ. 960-16e2
640 pages (May 2016)
CODEN: NSPUE2
This publication is free of charge from:
http://dx.doi.org/10.6028/NIST.SP.960-16e2

Preface to the Second Edition

Fractography is a powerful but underutilized tool for the analysis of fractured glasses and ceramics. It is applicable to fractures created under controlled conditions in the laboratory and to component failures in service. Fractography can identify the cause of failure and can even provide quantitative information about the loading conditions.

The goal of this Guide is to make fractographic analysis of brittle materials less an art and more an engineering practice for scientists and engineers. This guide emphasizes practical approaches for problem solving and failure analyses.

Fractographic analysis is to large degree pattern recognition. This Guide includes a wealth of illustrations to aid fractographers in pattern recognition. The Guide also includes an extensive bibliography and a tabulation of published case studies so that the reader can pursue topics of specific interest.

This Guide is a free public service of NIST for the benefit of American industry, and the worldwide ceramic and glass communities. The demand for this book has been very strong since it was first published in 2007. The first print run of 3,000 copies was distributed around the world and the feedback has been very positive. Users say that they appreciate the content, the careful layout and organization, and the wealth of colorful illustrations and examples. This book is often used as a supplement to courses on fractography of ceramics and glasses. I am grateful to the National Institute of Standards and Technology for printing the book on high-quality paper and in color. Although the book is also available electronically, most users prefer the printed form so that it is handy on their desks or laboratories

I became interested in the history of fractography of brittle materials while writing the first edition of this Guide in 2003 to 2007. Chapter 1 lists review articles that I wrote about the history of fractography after the first edition was printed. I learned much while doing these. For example, in the conclusions in his 1942 Journal of Applied Physics paper,[23] Frank Preston made a profound statement about whether pieces from different fractured parts would match, and he also summarized the art of fractographic analysis:

> "From the beginning of time to its end, no two cracked surfaces will fit each other, unless originally they were part of the same piece. Cracks are as distinctive as fingerprints. … Now the important thing about cracks is that they must be propagated. They do not originate all over the final fracture surface, but at one tiny spot, and from thence are propagated out

> to the rest of the area. This fact and the fact that the telltale marks or "fingerprints" of the process are left on the surface, provide the groundwork for the subject of Fracture Diagnosis, which in the last decade has become an important minor branch of physical science."

This guide emphasizes practical approaches for problem solving and failure analyses, but it also distills the state of the art in our "important minor branch of physical science." I get gratification from the free dissemination of all the know-how developed over decades by many conscientious researchers, materials scientists, and engineers. I salute them and have done my best to credit their contributions by liberal use of citations and the extensive bibliographies in this Guide.

This edition is about 15% larger than the first edition. It corrects some of the errors, including the description of vicinal illumination. There are 300 new illustrations; many of which are from my colleagues around the world. All told, there are approximately 1000 illustrations and tables in this second edition. In Chapter 1, Introduction, and Chapter 2, Resources, I added a little about the History of Fractography and the new documentary standards. The fracture mirror size procedures in Appendix D were adopted in an ASTM standard 1678 in 2009, and the text in this Guide has been adjusted accordingly. Chapter 3 on Equipment has updated microscopy techniques, a rapidly evolving field. A major correction was made to the description of "vicinal illumination," which was described erroneously in the first edition. Chapter 4 on Patterns has new material on sketches and drawings, edge chipping, thermal stresses and thermal shock, compression fracture, and laboratory-scale tests on medicinal vials and dental crowns. Chapter 5 on Fracture Surfaces has new information on mechanical fatigue, slow crack growth mechanisms, scarps, glue chips, and a new marking: "step hackle." The term "microstructural hackle" has been refined. Chapter 6, Origins, has 28 additional pages with dozens of new figures, and new information on bubbles, processing and firing flaws, cusps and geometric sharp points. There is a new definition of "Griffith flaw." Chapter 7, Quantitative Analysis, has a number of additions including a figure showing flow lines of stress around bubbles or flaws; new text about "far-field stress;" new text about the accuracy of the Newman Raju stress intensity factors and how to extend them to a/c >1; and Bansal's approximation. Chapter 9, Composites, has new examples of highly-filled resin matrix composite examples from the dental materials field. Strictly speaking, they are not ceramic or glasses, but they behave brittlely and have many of the same fractographic features. There are several new cases studies in Chapter 10, including an AlON coarse-grained IR dome; ceramic dental crowns, and a single crystal sapphire spacecraft refractor. Chapter 11,

Conclusions, has a new paragraph about the revolution in microscopy as well as some thoughts about the fractographer as an expert system. A new beautiful fractograph from Dr. J. Quinn is added to the conclusions.

Acknowledgements

The author derived much inspiration from the late Professor Van Derck Fréchette of Alfred University. Van made many important contributions to the science of fractography of brittle materials, not the least of which was his 1990 seminal book: *Failure Analysis of Brittle Materials*. Van solved many practical, vexing, and spectacular cases and trained hundreds of fractographers over his long and distinguished career.

The author has had a continuing and fruitful collaboration with Professor James Varner at Alfred University. Dr. Varner and the author continue the Van Fréchette legacy by training a new generation of fractographers.

The author thanks Dr. Jeffrey Swab, of the U.S. Army Research Laboratory; Aberdeen, Maryland and Mr. Michael J. Slavin (formerly of ARL) for their help in crafting a framework for fractographic analysis that was used to create the U.S. Army Military Handbook (MIL HDBK) 790 in 1990. This MIL HBDK was the precursor to American Society for Testing and Materials standard (ASTM) practice C 1332 adopted in 1996. This was the first formal standard for fractographic analysis of ceramics and brittle materials in the world. Many of the concepts in this Guide stem from our collaboration on those standards. Dr. Swab and I learned much about how fractographers work from a Versailles Advanced Materials and Standards round robin on ceramic fractography that we organized in 1993-1994.

The author has learned much from discussions with and readings of the prolific writings of Mr. Roy Rice, Prof. Jack Mecholsky, and Dr. Stephen Freiman. They have significantly advanced the state of the art of materials science through their fractographic work. I note with sadness the passing of Mr. Roy Rice in 2011. He was one of the most respected fractographers in the world and from whom I learned much. His books on mechanical properties and microstructure of ceramics and composites are very valuable. Roy gave me many of the single crystal fractographs in Chapter 8 of this Guide.

Mr. Are Tsirk, an enthusiastic knapper who introduced many of us to the fracture of lithics, also succumbed to a long illness in February 2015 within weeks of the publication of his own book on fractures and fractography of

knapping. He gave me some marvelous photos of scarps and parabolic wake hackle images in his final months. We will miss his knapping demonstrations at fractography conferences.

Dr. Roger Morrell of the National Physical Laboratory has been an inspiration, particularly with his astute practical applications of fractography to failure analysis and his own Guide to Fractography.

I also acknowledge the insightful work of Dr. Janet B. Quinn formerly of the American Dental Association, who made her own contributions to the science of brittle materials fractography and sometimes presented challenging fractographic problems to her spouse. About one year after the first edition appeared in 2007, just in time for her own course on Dental Materials Fractography, she suddenly became ill and died. At the time, she was applying fractography to ceramic, glass-ceramic, and composite dental restorations such as crowns and bridges. Janet and her dear friend Dr. Susanne Scherrer of the University of Geneva have taught a new generation of dental materials fractographers around the world how to use fractography effectively.

TABLE OF CONTENTS

Preface

1.	**Introduction**	1-1
2.	**Resources**	2-1
3.	**Tools and Equipment**	3-1
3.1	Low Power Optical Examination and Component Fracture Documentation	3-2
3.2	Photographing the Overall Component: Cameras, Cellphones, and Simple Digital Microscopes	3-7
3.3	Stereo Binocular Microscope	3-11
3.4	Stereoptical Microscope Camera Port and Digital Cameras for Microscopes	3-14
3.5	Digital image Processing and Focus Stacking	3-17
3.6	Discussion Stereomicroscope	3-19
3.7	Digital Microscopes	3-19
3.8	Illumination Sources	3-20
3.9	Coatings	3-26
3.10	Size Measurements	3-30
3.11	Compound Optical Microscope	3-32
3.12	Replication Equipment	3-35
3.13	Scanning Electron Microscope	3-43
3.14	Stereo SEM Imaging	3-56
3.15	Field Emission SEM	3-58
3.16	Environmental SEM	3-59
3.17	Transmission Electron Microscope	3-59
3.18	Atomic Force Microscope (AFM)	3-60
3.19	Optical Profilometer	3-60
3.20	Confocal Scanning Light Microscope	3-62
3.21	Stress Wave and Ultrasonic Fractography	3-64
3.22	High Speed Photography	3-64
3.23	X-ray Topography	3-65
3.24	Dye Penetration and Staining	3-66
3.25	Polariscope	3-70
3.26	Other Equipment	3-71
3.27	Other Resources	3-72
3.28	The Future	3-72

4.	**General examination and fracture patterns**	4-1
4.1	Specimen Reconstruction	4-2
4.2	Crack Branching Patterns	4-3
4.3	Crack Branching Angles	4-6
4.4	Crack Branching Distances	4-9
4.5	Fragmentation Patterns	4-10
4.6	Laboratory Test Fracture Patterns	4-11
4.6.1	Tension strength	4-13
4.6.2	Flexural strength	4-14
4.6.3	Biaxial flexural strength	4-19
4.6.4	Laboratory tests: additional tips	4-22
4.7	Component Fracture Patterns – General	4-22
4.8	T Intersections and Crossing Cracks	4-26
4.9	Invisible cracks	4-28
4.10	Plates and Windows	4-28
4.11	Tempered Windows	4-30
4.12	Thermally Induced Plate and Window Fractures	4-32
4.13	Bottles and Pressure Vessels	4-33
4.14	Torsional Fractures	4-39
4.15	Chipping	4-40
4.16	Laboratory Test Fractures and Component Fractures	4-44
4.17	Controlled Component Fractures	4-44
4.18	Finite Element Analysis	4-46
4.19	Characteristics of Some Common Fracture Modes	4-47
4.19.1	Mechanical overload fracture	4-47
4.19.2	Thermal fracture and thermal shock	4-47
4.19.3	Impact or contact fractures	4-49
4.19.4	Corrosion or oxidation	4-49
4.19.5	Residual stresses	4-49
4.19.6	Time dependent fracture	4-51
4.19.7	Compression fracture	4-51
5.	**Fracture Surface Examination**	5-1
5.1	Introduction	5-1
5.2	Fracture Mirrors, A Fractographer’s Best Friend	5-3
5.2.1	Fracture mirrors in glass	5-3
5.2.2	Fracture mirrors in ceramics	5-16
5.2.3	Fracture mirrors, special cases	5-20
5.3	Hackle	5-31
5.3.1	Coarse hackle	5-31
5.3.2	Wake hackle	5-33
5.3.3	Twist hackle	5-36

5.3.4	Shear hackle	5-42
5.3.5	Corner hackle	5-43
5.3.6	Step hackle	5-43
5.4	Wallner Lines	5-45
5.4.1	Introduction	5-45
5.4.2	Primary Wallner lines	5-47
5.4.3	Secondary Wallner lines	5-50
5.4.4	Tertiary Wallner lines	5-53
5.4.5	Wallner Lambda lines	5-58
5.5	Arrest Lines	5-58
5.6	Scarps	5-61
5.7	Glue Chips	5-63
5.8	Transgranular and Intergranular Fracture	5-66
5.9	Stable Crack Growth	5-69
5.9.1	Slow crack growth (SCG) at ambient temperature	5-69
5.9.2	Stable extension from local residual stress or R-curve effects	5-73
5.9.3	High temperature slow crack growth in ceramics	5-74
5.9.4	High temperature creep fracture	5-77
5.9.5	Mechanical fatigue from cyclic loading	5-81
5.10	Organizing all the Information -Fractographic Montages	5-84
6.	**Origins of Fracture**	
6.1	Origins, Flaws, and Defects	6-1
6.2	The Spatial Distribution of Flaws	6-1
6.3	Are Flaws Intrinsic or Extrinsic?	6-4
6.4	Matching Fracture Halves	6-5
6.5	External Surfaces	6-6
6.6	Volume-Distributed Flaws	6-7
6.6.1	Pores and Bubbles	6-7
6.6.2	Porous regions	6-14
6.6.3	Porous seams	6-14
6.6.4	Agglomerates	6-15
6.6.5	Inclusions	6-17
6.6.6	Compositional inhomogeneities	6-21
6.6.7	Large grains	6-22
6.6.8	Grain boundaries	6-25
6.7	Surface-Distributed Flaws	6-27
6.7.1	Surface voids or pits from processing	6-27
6.7.2	Pits from environmental exposure	6-28
6.7.3	Handling scratches and polishing scratches	6-29
6.7.4	Sharp object impact or contact	6-33
6.7.5	Blunt object impact or contact	6-34

6.7.6	Grinding and machining cracks	6-40
6.7.7	Chips	6-53
6.8	Other Flaws	6-54
6.8.1	Processing and firing cracks in ceramics	6-54
6.8.2	Artificial or controlled flaws, glasses and ceramics	6-59
6.8.3	Other glass origins	6-61
6.9	Fracture Oddities	6-69
6.10	Contaminants	6-71
6.11	Combined or Hybrid Flaws	6-73
6.12	Baseline Microstructure Origins	6-75
6.13	Geometric Sharp points or Cusps	6-76
6.14	Partially-Exposed Flaws	6-77
6.15	Glaze flaws	6-78
6.16	Microfault Pockets	6-80
6.17	Polished Microstructural Sections	6-82
6.18	Flaw Size	6-84
6.19	What to Report	6-84
7.	**Quantitative Analysis**	7-1
7.1	Introduction	7-1
7.2	Stresses from the Extent of Fragmentation	7-2
7.2.1	Annealed parts	7-2
7.2.2	Fragmentation of tempered parts	7-5
7.3	Stresses from the Branching Distances	7-7
7.3.1	Annealed plates and bars	7-7
7.3.2	Tempered plates	7-8
7.4	Stresses from the Mirror Size	7-10
7.4.1	Mirror analysis and constants	7-10
7.4.2	How to measure mirror sizes	7-13
7.5	Fracture Mechanics Analysis of the Flaw Size	7-17
7.5.1	Introduction to fracture mechanics	7-17
7.5.2	The Newman-Raju Y factors for semielliptical surface flaws in bending	7-30
7.5.2.1	The Newman-Raju formulas	7-30
7.5.2.2	Graphical curves for the Newman-Raju formulas	7-35
7.5.2.3	Newman-Raju formulas for deep (a/c > 1) semielliptical surface cracks	7-36
7.5.2.4	Accuracy of the Newman-Raju formulas and alternatives	7-36
7.5.2.5	Bansal's approximation for semielliptical surface flaws	7-37
7.5.3	Irregularly-shaped surface cracks	7-38
7.5.4	Three-dimensional, blunt, and inclined flaws	7-39
7.6	Relationship of K_{Ic} and A	7-40

7.7	Mirror to Flaw Size Ratios	7-41
7.8	Comparing Measured to Calculated Flaw Sizes	7-43
7.9	Crack Velocities from Wallner Line Analysis	7-46
7.10	Slow Crack Growth	7-51
7.11	R- curve Behavior	7-55
7.12	Indentation Mechanics	7-61
7.13	Fractal Analysis	7-65
7.14	Estimation of Residual Stresses	7-68
7.14.1	Introduction	7-68
7.14.2	Estimates of residual stresses from fragmentation	7-68
7.14.3	Estimates of residual stresses from fracture mechanics analysis of flaws	7-68
7.14.4	Estimates of residual stresses from fracture mirror size analysis	7-69
7.14.5	Estimates of residual stresses from indention crack sizes	7-70
7.14.6	Estimates of residual stresses by other means	7-70
7.15	Weibull Analysis	7-71
8.	**Single Crystals**	8-1
8.1	General	8-1
8.2	Preferred Cleavage Planes	8-2
8.3	Fractographic Techniques	8-5
8.4	Fracture Surface Markings	8-8
8.5	Origins	8-21
8.6	Other Sources	8-32
9.	**Ceramic and Glass Composites**	9-1
9.1	Particulate, Whisker, or Self-Reinforced Ceramic Composites	9-1
9.2	Fiber-Reinforced Composites	9-2
9.3	Dental composites	9-6
10.	**Case Studies**	10-1
Case 1	Ruptured Rotor (Ceramic gas turbine rotor)	10-1
Case 2	Busted Barrel (Silicon carbide machine gun liner)	10-7
Case 3	Conflicting Carbide Data (Silicon carbide flaws and slow crack growth)	10-11
Case 4	Vulnerable Vials (Broken medicinal vials)	10-14
Case 5	Damaged Dome (AlON IR dome)	10-16
Case 6	Suffering Setter Plate (Silicon carbide furnace plate)	10-18
Case 7	Ruptured Radomes (Fused silica missile nosecones)	10-20
Case 8	Maligned Machinists (Bend bars made by different shops)	10-23
Case 9	Modeler's Match (Fracture origins in MEMS scale	

SiC micro tensile specimens) 10-25
Case 10 Fractious Fractographers (A fractography round robin) 10-28
Case 11 Perilous Prostheses (Four ceramic dental crowns) 10-30
Case 12 Mangled Margins (Twenty dental crowns) 10-43
Case 13 Ruined Refractors 10-46

11. Conclusions 11-1

Appendix A Bibliography

Appendix B Fractographic Case Studies

Appendix C Fracture Mirror and Branching Constants

Appendix D Guidelines for Measuring Fracture Mirrors

Index

1. Introduction

Why did it break? What was the origin of failure? Did it break as expected or from an unexpected cause? Was there a problem with the material or was the part simply overloaded or misused? Why did this part break and others not? What was the stress at fracture? Was the laboratory strength test successful or was there a misalignment? These are common practical questions and the fractographer can often give straightforward definitive answers.

The curse of brittle materials is that they are prone to catastrophic fracture. Brittle fracture is fracture that takes place with little or no plastic deformation. Nature has partially compensated for this shortcoming by furnishing clear fracture patterns and fracture surface markings that provide a wealth of interpretable information. Indeed, in many respects, fractographic analysis of ceramics and glasses is easier and can produce more quantitative information than the fractographic analysis of metals or polymers.

Figure 1.1 shows broken glass and ceramic rods. Using the techniques described in this Guide, fractographers are able to determine that the rods were broken in bending, from surface flaws, and even determine the fracture stress.

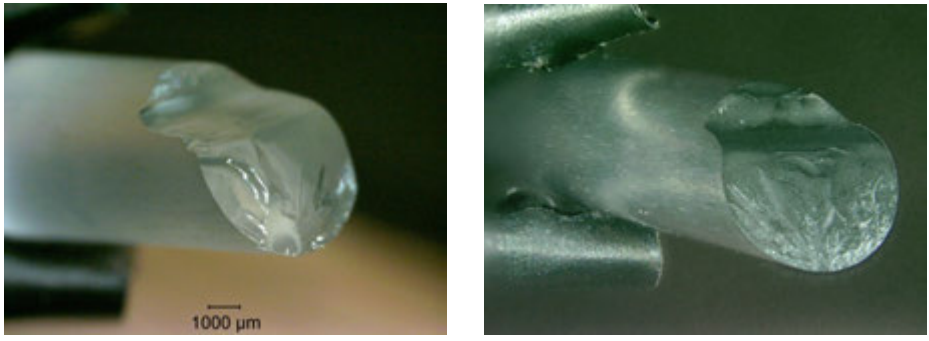

(a) (b)

Figure 1.1 *Fractured glass (a) and ceramic (b) rods.*

This Guide takes a broader view of fractography than merely the examination of the fracture surfaces. The author wrote the definition that is in ASTM standard 1322[1]:

> **fractography,** n – means and methods for characterizing fractured specimens or components

Fréchette[2] also took broad view and described the science of fractography as the study of fragments and their interpretation in terms of material properties and conditions leading to failure.

Examination of the fracture surfaces of broken pieces is an important element of fractographic analysis, but much can be gleaned by first looking at the sizes, shapes, and breakage patterns of the fragments. In some cases, the breakage pattern is all that is necessary and examination of fracture surfaces is unnecessary. For example, even novices can recognize an impact site on an automobile windshield without examining the fracture surfaces. A simple visual examination can tell the observer whether a component fracture was thermally or mechanically driven, whether the stress was large or small, and whether the stresses were uniaxial or multiaxial.

It is surprising how many instances there are in the literature where undue attention was spent on small fracture surface regions that were probably not even in the area of fracture initiation. It behooves one to look at the overall breakage pattern first, before one jumps to a microscopic examination of the fracture surfaces.

Most people recognize that fractography is a valuable tool for failure analysis, but fewer appreciate its value in routine mechanical testing or support of materials processing. Although thousands of ceramic or glass items and test specimens are broken daily, only a tiny fraction is examined fractographically. A wealth of information is lost about the causes of fracture and the nature of the material. The flaw type may be just as important as the fracture stress in a strength test. Rice rued this state of affairs in 1977:[3]

> "The most significant experimental procedure that can aid the understanding of mechanical properties is a study of fracture surfaces, especially to identify fracture origins…. It is indeed amazing the number of mechanical properties studies conducted that were extensively concerned directly or indirectly with the size and character of flaws and microstructure from which failure originated in which no attempt was made to experimentally observe and verify the predicted or implied flaw character."

Some of the reluctance to apply fractographic analysis is that it is unfamiliar to most engineers and scientists. Although there are a few notable exceptions, fractography is not commonly taught in schools and is often learned gradually and autodidactically by experience over many years. Some regard fractographic analysis as a subjective practice that can only be applied by masters. Others deem it as too interpretive. The reality is that what may seem

mysterious to some is in fact objective and quantitative to an experienced fractographer. [a] Interpretation is an essential step, but brittle materials often leave unequivocal markings on fracture surfaces that even a novice can interpret with confidence. The markings are the direct consequence of crack perturbations during propagation. An important element of fractographic analysis is **pattern recognition**. Certain types of fracture leave telltale fracture patterns on the fracture surfaces, or have telltale breakage patterns or fragment shapes. For example, hackle lines radiating from a fracture mirror are features that even novices can identify. These lines lead an observer back to the origin. Other markings may be more subtle and can be overlooked by the casual or inexperienced observer. With a little practice and experience, any material scientist or engineer should be able to analyze brittle fractures and make an interpretation, or at least recognize what pieces should be brought to the attention of a more experienced fractographer. The novice may be tentative at first, but fractography is a cumulative learning experience. The more fractography one does, the easier it becomes.

A good starting place to gain experience is by examining test coupons broken in laboratory conditions. Flexural strength specimens are a common starting point. Pattern recognition skills can be reinforced by seeing multiple examples in a set of specimens. Component failure analysis is often much more difficult, especially if only a single example is available or the fracture occurred under unknown loading conditions.

What are the skills that a fractographer needs? Fractographers ideally should have knowledge of materials science, microscopy, mechanics (stresses and strains), and an aptitude for problem solving and troubleshooting. Puzzle-solving skills can be helpful as well as an ability to be able to sketch or draw as discussed in section 4.7. They should be comfortable with microscopy, since many of the features to be studied are smaller than the unaided eye can discern. Some knowledge of materials science is necessary since strength-limiting flaws and crack propagation behavior are controlled by processing and the microstructure.

Cracks propagate in response to stresses and strains, so fractography often comes quite naturally to mechanical engineers. That is not to say that materials scientists, physicists and geologists do not make good fractographers, but they will have to learn the fundamentals of stress analysis. At a minimum, a

[a] This is reminiscent of Arthur C. Clarke's Third law, which is: "Any sufficiently advanced technology is indistinguishable from magic." *Profiles of the Future: An Inquiry into the Limits of the Possible*, A. C. Clarke, Bantam, 1973.

fractographer should be comfortable with concepts of uniaxial *tensile* stresses (stresses primarily in one direction, such as in a direct tensile strength test specimen), uniaxial *bending* stresses (such as in a beam loaded in bending), and *biaxial* stresses (whereby there are tensile stresses in two different directions such as in a pressurized flat plate or a pressurized bottle). Some important stress configurations are illustrated in Figure 1.2.

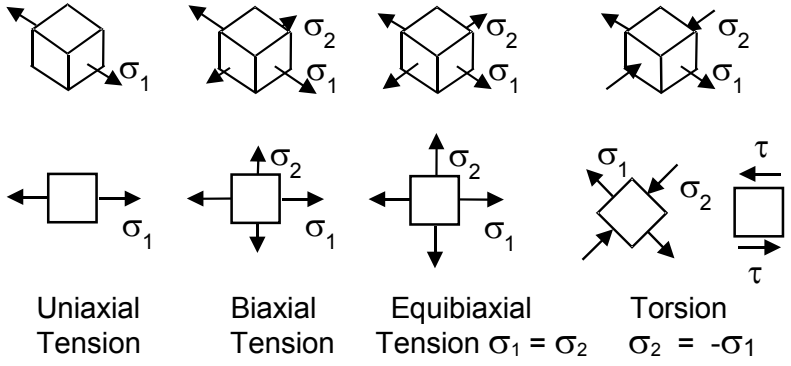

Figure 1.2 *Uniaxial or biaxial stress states may be represented by forces (arrows) acting on the surfaces of tiny differential volume elements. They are shown here as 3-dimensional (top row) or 2-dimensional (bottom row) views. The lengths of the arrows are in proportion to the stress magnitude.* σ_1 *and* σ_2 *are normal stresses and* τ *are shear stresses. In some cases, the stress state is triaxial, and a third stress direction,* σ_3*, may be added to the diagrams above.*

Most fracture problems the reader will encounter will be uniaxial or biaxial stress cases, but there are very important cases (projectile-impacted ceramic or glass armor plates, or localized Hertzian or sharp contact problems) where the stress state is *triaxial;* that is, there are stresses in all three directions, σ_1, σ_2, and σ_3. Some of these are tension stresses that are denoted with a positive sign (e.g., +100 MPa), and some may be compressive stresses, denoted by a minus sign (e.g., -300 MPa). Mechanical engineers are very comfortable with multiaxial stress problems, and can convert the stresses in any arbitrary orientation at a given point to the specific orientation that has the *principal stresses.* (The X-Y-Z axes at any point can be rotated and are reoriented so that the small differential volume element has three normal stresses σ_1, σ_2, and σ_3

and no shear stresses acting on its faces.) Mechanical engineers commonly use a Mohr's circle analysis or finite element analysis to find this orientation and the maximum principal stresses. Maximum principal stresses usually control fracture in ceramics and glasses. Only in specialized cases do shear stresses cause fracture. This is an important difference in how ceramics and glasses break as compared to metals and polymers.

It should also be borne in mind that most parts and laboratory specimens have stress *gradients* and may even have internal *residual stresses*. It is rare that a component has a uniform stress throughout. Simple loading configurations are typically covered in the first chapters of an elementary strength of materials engineering textbook, which may be consulted to gain a basic familiarity with stresses and strains. It is beyond the scope of this Guide to delve into multiaxial stress fracture criteria, but the reader should be aware that what causes fracture in a tensile-loaded ceramic part may be completely different than for a compressively-loaded ceramic part, or for a part with mixed tension and compression stresses. Engineers often use stress diagrams with fracture envelopes to illustrate fracture versus no-fracture boundaries in multiaxial stress problems. Mechanical engineers not versed in ceramic or glass behavior do not appreciate the nuances of multiaxial failure criteria for ceramics and glasses. For example, many finite element modelers who are new to the ceramic field erroneously use the Von Mises (or maximum distortion energy) criterion in their models. While this criterion works quite well for metals, it is completely wrong for ceramics and glasses. Many mechanical engineers are surprised at how different the Poisson's ratios for glasses and ceramics are as compared to those for metals!

There are two special stress conditions that warrant explanation. Mechanical engineers may say that parts are loaded in *plane stress* or *plane strain* conditions. Plane stress refers to a case where there are only two principal stresses, σ_1 and σ_2. The third stress $\sigma_3 = 0$. In other words, all the stresses lie in a flat plane. This is commonly the case with thin parts, such as a thin-walled cylinders or pressurized bottles. The principal stresses are parallel to the surface. In contrast, with thick parts, there can be a σ_3 internal stress. If the part is very thick, lateral thinning strains may be inhibited. The strain through the thickness, $\varepsilon_3 = 0$. There are only two principal strains ε_1 and ε_2 and they are parallel to the surface. This is called the plane strain condition and it is especially important for fracture toughness test specimens. There are stringent requirements on the thickness of metallic fracture toughness specimens to ensure that they are in a plane strain condition. The matter is not important for ceramics and glasses, since the plastic yield zones in ceramics are tiny.

Part of the skill of a fractographer is knowing where to look and how to look. A specimen that breaks into only two pieces may not be too difficult to interpret. Medium to high strength specimens with multiple fractures can initially be confusing, but with a little experience and a few simple precautions, one can find the primary fracture. Component or service failures may be difficult since the loading conditions may be unknown. Key pieces may be missing or the evidence incomplete or contradictory. Multiple crack systems from different causes and events may intersect and confound an interpretation.

The author suspects one reason that fractography is sometimes held with suspicion or is deemed subjective is that some incautious fractographers have jumped to conclusions and reached questionable interpretations. It is unwise to make conclusions based on limited or incomplete evidence. Novices often force fit a fracture scenario to their limited experience base. Some fracture patterns may be difficult to detect or be very subtle and may not be recognized. Good fractographers recognize their strengths and the limitations of their experience base and do not overreach or extrapolate. They should be alert to unusual or new fractographic markings or to failure modes with which they are not familiar and should be ready to search the literature, consult colleagues, or try to create comparable markings in the laboratory. No fractographer is born with a built-in data base of fractographic patterns in the brain, so step-by-step accumulation of experience is necessary. One may consult textbooks, reference articles, and this Guide to help acquire knowledge, but there is no substitute for hands-on direct eyeball and microscopy experience.

There is a wealth of information in the technical literature about fractography of glasses and ceramics, but until the first edition of this book was written in 2007, it was scattered in textbook chapters, in journals, and conference proceedings. Fréchette's 1990 seminal book, *Failure Analysis of Brittle Materials*,[1] was a good starting point for the practical fractography of glasses. This Guide covers fractography of glasses and ceramics and presents practical information for both glasses and ceramics. It also includes an extensive bibliography. There now are formal standard practices in the American Society for Testing and Materials[2] and European Committee for Standardization[4] for fractographic analyses of glasses and ceramics.

Fractography is a tool for the broader topic of failure analysis. Figure 1.3 suggests a simple but apt analogy. The fractographer is called upon to solve a fracture mystery. The detective uses his or her powers of observation to study the scene of the fracture and meticulously collects and preserves the available evidence. The clues are contemplated and weighed against the available background information furnished by witnesses. Comparable cases are

Figure 1.3 *The fractographer as detective.*

considered to determine whether there are similarities and whether there is a pattern. Scientific analysis of the material may be done to verify its quality, composition, and authenticity. Pondering all the information, and keeping an open mind for all possible scenarios, the fractographer detective formulates a hypothesis and checks it against the known facts. The fractographer communicates the findings to the client, management, engineer or processor in a manner that is convincing and fathomable. Sometimes the findings must be presented in formal legal settings. In summary, fractographic analysis is not merely looking at fracture surfaces, but is the integration of knowledge from a variety of sources to solve the puzzle of how fracture occurred (Figure 1.4).

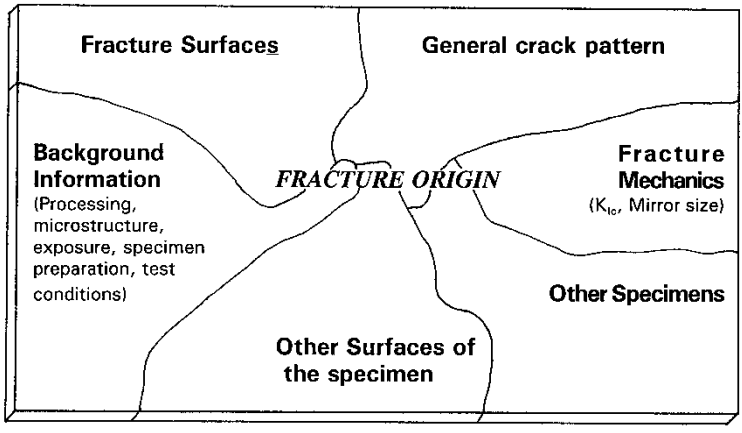

Figure 1.4*. Fractographic analysis is more than examining fracture surfaces.*[5]

One definition of failure analysis is: "A process that is performed in order to determine the causes or factors that have led to an undesired loss of function."[6] Failure may be due to fracture, corrosion, excessive deformation, or wear. Hence, fracture is a subset of a larger class of failure causes. The readers interested in the broader topic of failure analysis in general, including concepts and philosophies about how to conduct an analysis, should refer to the ASM handbook on Failure Analysis and Prevention.[6] That volume has multiple chapters and extensive discussions about failure analysis in general and also has such pragmatic recommendations as: "don't jump to conclusions," "keep an open mind," and "avoid 5-minute best guess analyses."

This is a technical book. It is beyond the scope of this book to delve into issues of litigation, fault, or blame. Readers who are interested in these matters are referred to Chapter 11 "The Expert Witness" in Van Fréchette's book,[2] an article by B. Adams in the second Alfred conference on fractography,[7] an article by C. O. Smith in Volume 11 of the ASM handbook,[8] or a review by Bradt in the third Conference on Fractography of Advanced Ceramics in Slovakia.[9]

A few words about nomenclature are appropriate here. Readers may be surprised that terms for ceramics and glasses are somewhat different than for other materials. For example, "hackle lines" and "lances" refer to steps or lines on the fracture surface running parallel to the direction of crack propagation. "Striae" or "striations" means completely different things to metallurgical fractographers, ceramic and glass fractographers, and glass manufacturers. In this Guide, I have adopted and added to the nomenclature system devised by Professor Van Fréchette since it is descriptive and logical. It was not without controversy when he introduced it formally in 1982 at a conference on fractography.[10] Frechette's concise paper was only three pages long, but was followed by a detailed three page commentary by R. Rice! I have resisted the temptation to devise new and colorful terms, since a proliferation of terms will only lead to confusion. Anne Roulin-Moloney, in the preface of her outstanding book on the fractography of polymers and composites,[11] wrote about the "myriad of weird and wonderful terms to describe the features observed. Some examples are laceration, shish-kebab, cusps, welts, mist, and shards." One cannot help but burst out laughing when one sees some of these terms.

The history of fractography of brittle materials is a fascinating story of microscopy, material science, fracture mechanics, and people. Figure 1, adapted from my review articles,[12,13] chronicles how the field evolved with

contributions from such luminaries as De Freminville, Preston, Griffith, Smekal, Schardin, Weibull, Wallner, Orr, Kerkhof, Shand, Ernsberger, Irwin, Fréchette, Kirchner, Rice, and others.

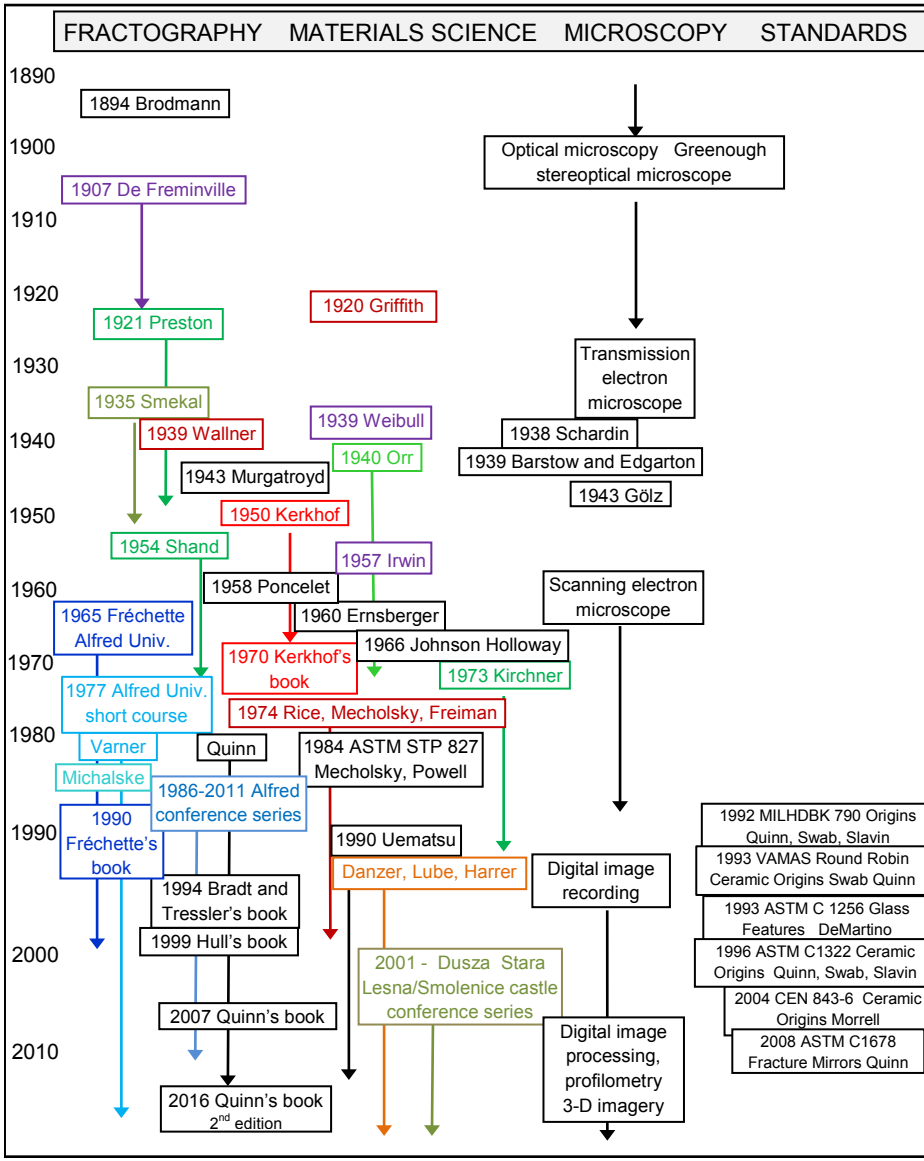

Figure 1.5. *The history of fractography of brittle materials*

At this point it is appropriate to point out a critical aspect of fracture analysis problems. Final fracture often occurs after a chain of events. One event may create a flaw, but then a second or even third event may be necessary to cause fracture. For example, drinking glasses commonly sustain internal impact damage from eating utensils that are carelessly dropped into the glass. Subsequent thermal stresses generated in the dishwasher may cause cracks to extend gradually around the base. If the large crack is not noticed, an unwary user who picks up a liquid filled glass may have an unpleasant surprise. What was the cause of failure in this case: The user pouring a liquid into the glass and lifting it to quench a thirst, the initial impact damage, or the thermal stresses that cause the crack to grow? The answer is all of the above.

Chapter 1 References

1. ASTM C 1322-15, "Standard Practice for Fractography and Characterization of Fracture Origins in Advanced Ceramics," Annual Book of Standards, Vol. 15.01, ASTM Int., West Conshohocken, PA, 2015. (The original version was adopted in 1996.)
2. V. D. Fréchette, "Failure Analysis of Brittle Materials," *Advances in Ceramics,* Vol. 28, American Ceramic Society, Westerville, OH, 1990.
3. R. W. Rice, "Microstructure Dependence of Mechanical Behavior of Ceramics," pp. 199 – 381 in *Treatise on Materials Science and Technology,* Vol. 11, Academic Press, New York, 1977.
4. CEN EN 843-6, "Advanced Technical Ceramics - Monolithic Ceramics – Mechanical Properties of Monolithic Ceramics at Room Temperature – Part 6: Guidance for Fractographic Investigation," European Committee for Standardization, Brussels, 2009.
5. J. J. Swab and G. D. Quinn, "The VAMAS Fractography Round Robin: A Piece of the Fractography Puzzle," pp. 55 -70 in *Fractography of Glasses and Ceramics III,* Ceramic Transactions, Vol. 64, eds., J. R. Varner, V. D. Fréchette, and G. D. Quinn, ACS, Westerville, OH, 1996.
6. *Failure Analysis and Prevention*, ASM Handbook, Vol. 11, American Society for Materials, Materials Park, OH, 2002.
7. P. B. Adams, "Fractography in the Courtroom," pp. 219 – 226 in *Fractography of Glasses and Ceramics, II*, Ceramic Transactions Vol. 17, eds V. D. Fréchette and J. R. Varner, American Ceramic Society, Westerville, OH,1991.
8. C. O. Smith, "Products Liability and Design," pp. 71-78 in Ref. 6.
9. R. C. Bradt, "Fractography, Some Legal Aspects and Challenges," pp. 28 – 42 in *Fractography of Advanced Ceramics, III,* eds., J. Dusza, et al., Transtech Publ., Zurich, 2009.

10. V. D. Fréchette, "Markings on Crack Surfaces of Brittle Materials: A Suggested Unified Nomenclature," pp. 104-109 in *Fractography of Ceramic and Metal Failures,* ASTM STP 827, J.J. Mecholsky, Jr. and S.R. Powell, Jr. eds., American Society for Testing and Materails,1984.
11. A. C. Roulin-Moloney, *Fractography and Failure Mechanisms of Polymers and Composites*, Elsevier, Essex, England, 1989.
12. G. D. Quinn, "A History of the Fractography of Brittle Materials," in *Fractography of Advanced Ceramics, III*, ed. J. Dusza, R. Danzer, R. Morrell and G. Quinn, TransTech Publ., Zurich, 2009. *Key Engineering Materials* Vol. 409 (2009) pp. 1-16.
13. G. D. Quinn, "A History of the Fractography of Glasses and Ceramics," pp. 1 – 56, in *Fractography of Glasses and Ceramics,* Vol. 6, Ceramic Transactions, Vol. 230, eds, J. R. Varner, M. Wightman, American Ceramic Society, Westerville, OH, 2011.

2. Resources

This Guide is designed to be a stand-alone resource. There is a wealth of additional information scattered in books and technical articles that delve into specific topics in more detail.

Appendix A is a bibliography featuring many good publications of special interest to the glass and ceramic communities. The topics include books on fractography, compilations of conference proceedings, overview papers on fractography, reports on fractography round robins, compilations of fracture mechanics stress intensity factors, and papers on microscopy, fracture origin types, fracture mirrors, and fracture mechanics analyses of flaw sizes.

There are two ongoing conference series devoted exclusively to the fractography of glasses and ceramics. One is in the United States and one is in Europe. The conferences have been held at four or five year intervals. The longest running and most famous was begun by Professors Van Derck Fréchette and James Varner in 1986 at Alfred University in New York State. Follow-on conferences were held in 1990, 1995, 2000, 2006, and 2011. The six conference proceedings have excellent information on a range of theoretical and applied problems by leaders in the field. Dr. Jan Dusza of the Institute of Materials Research of the Slovak Academy of Sciences, Košice, Slovakia began a conference series in 2001 that continued in 2004, 2008, and 2013. The next is scheduled for October 2016. Conference proceedings for the first three were published as bound books, but only a selection of papers from the 2013 conference were published in a topical issue of the journal of the European Ceramic Society in 2014.

Appendix B is a unique compilation of case studies that lists a series of publications dealing with specific case studies. These include fracture of windows, bottles, pressure vessels, and various ceramic parts. Some of the cases deal with the mundane and some with the exotic. It is included for the benefit of readers who wish to investigate specific problems.

Appendix C is the most complete tabulation of fracture mirror constants ever compiled for ceramics and glasses. It is an expansion of a similar listing in ASTM C 1322-02a and the first 2007 edition of this Guide.

Each chapter of this Guide also contains a list of references for topics covered in the chapter.

There are now four formal documentary standards pertaining to fractographic analysis of glasses and ceramics:

ASTM C 1256-13, "Standard Practice for Interpreting Glass Fracture Surface Features," ASTM, International, West Conshohocken, PA, originally adopted 1993, current version: 2013.

ASTM C 1322-15, "Standard Practice for Fractography and Characterization of Fracture Origins in Advanced Ceramics," ASTM, International, West Conshohocken, PA, originally adopted in 1996, current version: 2015.

ASTM C 1678-15, "Standard Practice for Fractographic Analysis of Fracture Mirror Sizes in Ceramics and Glasses," ASTM, International, West Conshohocken, PA, originally adopted in 2007, current version: 2015.

EN 843-6, "Advanced Technical Ceramics, Monolithic Ceramics, Part 6: Guidelines for Fractographic Examination," European Committee for Standardization, Brussels, originally adopted, 2004.

3. Tools and Equipment

The most important tools of the fractographers craft are the binocular stereoptical microscope and the scanning electron microscope. The stereoptical microscope affords to the eyes a magnified, naturally-appearing, three-dimensional view of the fracture surface that retains all color and reflectivity information. Fracture origins and flaws in ceramics and glasses can often be detected with the stereoptical microscope, but higher magnifications are often needed to see the flaw more clearly. The scanning electron microscope serves this need and has good depth of field, high magnification capability, and chemical analysis features. Other tools such as hand magnifiers, compound optical microscopes, or even atomic force microscopes play supportive roles.

The "marriage" of the microscope with digital cameras and computers has revolutionized the field. The new technologies have rendered film photography obsolete and are opening up marvelous new capabilities not heretofore available. The shortcomings of conventional compound microscopes (e.g., limited depth of field) or of scanning electron microscopes (e.g., flat-appearing images) can be overcome. Virtual three-dimensional images can be constructed with automatically-rastering optical microscopes or by analysis of multiple scanning electron microscope images taken with slightly different specimen tilts. The pseudo three-dimensional images can be displayed, tilted, and rotated to afford different perspectives. Various quantitative numerical analyses of surface topography (e.g., surface roughness or even fractal dimension analysis) can be performed at almost no extra effort since the surface topography has been recorded digitally.

Simple low-cost software programs are now available that can simply and conveniently overcome the depth of field limitations of virtually any microscope. A series of photos at the same magnification are taken while slightly readjusting the focus in sequential steps. The software interprets the regions that are in focus and stitches these together to create a single image with an infinite depth of field.

In this chapter, traditional and new tools of the trade and are reviewed with an emphasis on their applicability to fractography. Digital cameras are discussed in four sections of this chapter: first in section 3.2 as simple tools for photographing an overall part, then in sections 3.4 and 3.5 as recording devices attached to conventional microscopes, and finally in section 3.7 as components of new digital microscopes which do not even have eyepieces for the viewer to look through.

3.1 Low Power Optical Examination and Component Fracture Documentation

The examination of fractured pieces begins with a visual examination using the unaided eye. Some fractographer prefer to use lint-free gloves when handling fragments, but gloves usually are not necessary. Ceramics and glasses are hard, durable materials and may be cleaned fairly easily.

It may be tempting to rush to a microscopic examination of the fracture surfaces, but study of the general fracture and the overall condition of the component is time well spent. This examination and reconstruction of the specimen may be aided by a simple (1.2X to 1.4X) magnifying glass, whether hand-held or mounted on a stand as shown in Figure 3.1. A stand-mounted lens frees the fractographer's hands for manipulation of the specimen. Larger versions with built-in ring lamps are ideal. A clean, tidy table or bench top is desirable, lest the fractographer inadvertently knock critical fragments onto the floor or against each other, or contaminate or damage the fracture surfaces.

Figure 3.1 *Simple magnifiers.*

Small jeweler's loupes as shown in Figures 3.2 and 3.3 also are handy, particularly in the field. Their working distances range from 50 mm for the low power (5X) loupe, to about 25 mm for a 10X loupe. Some practitioners may be adept at holding a watchmaker's loupe in one eye without using a hand, thereby freeing up both hands. Most fractographers will use one hand to hold

the loupe and the other to hold the examined fragment. Machinist loupes and pocket optical comparators with magnifications up to 20X (two are shown on the right of Figure 3.2) have built-in measuring scales with graduations as fine as 0.1 mm (0.005 in). Rapid measurements of mirror sizes or even fracture origin sizes may be made with these inexpensive tools. Remember, the more powerful the magnification, the smaller the field of view and the shallower the depth of field, so a good general duty loupe or comparator with a 7X or 10X magnification may be perfectly suitable and more versatile than one with a 20X magnification. At these low magnifications, illumination is usually not a problem and ambient light is adequate.

Figure 3.2 *Hand loupes and optical comparators. From the left, 5X and 7X watchmaker loupes; a 20X loupe, a 7X comparator with an internal 20 mm scale marked in 0.1 mm increments, and a 8X to 16X zoom comparator with an 16 mm scale marked in 0.1 mm increments.*

Figure 3.3 *Loupes (5X to 20X) may either be held by the eye or by hand. The part is a single crystal silicon rod.*

Simple holders or clamps may be useful as shown in Figures 3.5 and 3.6, particularly if the fractographer is examining repetitive examples of a particular type specimen or component. It can be exasperating to hold a part in one hand at just the right angle, while holding a magnifier with the second, but then need an extra hand to apply some alcohol with a cotton swab to clean the part. Similarly, the fractographer may wish to jot down some important information as part of a written record.

Figure 3.4 *A jeweler's or hobbyist's head mounted magnifier (2X to 3.5X) can be helpful.*

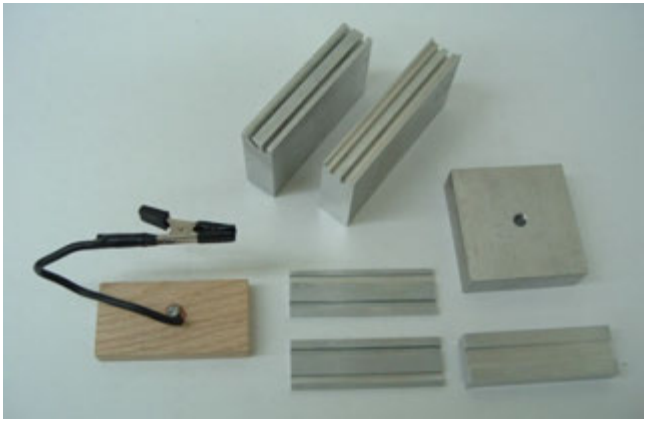

Figure 3.5 *Specimen holders. Clockwise from the lower left are: a bend bar holder made with an alligator clip on a bendable (10 gage electrical) wire with electrical tape wrapped around the teeth to cushion the specimen, two aluminum jigs with slots and grooves for bend bars or tension strength specimens, an aluminum block with hole, and three aluminum holders comparable in size to a glass microscope slide with groves to hold bend bars both on their flats and on edge for chamfer examination.*

Conventional clays should not be used for mounting specimens unless there is no alternative. Clay is a pernicious material that can easily contaminate the fracture surfaces and blend into the fracture features. Natural clays have colors and compositions similar to ceramic products. They are next to impossible to clean off. Their electrostatic surface charge and extremely fine plate-like structure cause them to cling to the fracture surface. Clays often have an oil to keep them plastic that makes things even worse, since the oils can smear over the fracture surfaces even on glasses. Clay often gets on one's hands and then tends to get on everything. More information on clay contamination is in section 6.10.

A completely satisfactory alternative is polymer clay that is available from arts and crafts stores.[a] Some polymer clays can be easily dissolved and cleaned with paint thinner, acetone, and even ethanol. The color in these polymer clays can easily be distinguished on the fracture surfaces. The best colors are deep blues or greens. White or gray should not be used since they cannot be distinguished from many ceramics. Garish colors should not be used, since they are a distraction in photographs.

(a)

(b)

Figure 3.6 *Component or specimen holders. (a) Clockwise from the lower left: a homemade plastic platform mounted on a swivel base; a pivoting wooden holder, a cork ring; a clamp on a stand, an alligator clip on a stand (with electrical tape on the teeth to cushion the specimen), an inverted miniature wood flower pot with a hole, and two wooden candleholders with dolls heads and polymer mounting clay. The doll's head balls can be rotated to obtain optimum illumination angles onto the specimen's surface. (b) shows a polymeric clay that is safe to use and is easily removable.*

[a] One example of a polymeric clay is Sculpey III Polymer, "Oven bake clay" made by Polyform products, Elk Grove, Ill. It is easily dissolved by paint thinner or acetone.

Simple cleaning tools and markers such as shown in Figure 3.7 should be conveniently located at the examination work station. Acetone, ethanol, or methanol with tissues and cotton swab applicators are handy for cleaning. Compressed air from air lines should be used with caution since there may be traces of oil mixed with the air. Water soluble ink pens (with fine tips) are handy for marking the specimen. Ceramic fracture surfaces should never be cleaned with metallic tools or probes. It may be tempting to try to scrape or poke off a contaminant, but metallic tools are abraded by the harder ceramic causing metallic traces to be smeared on the fracture surface. Fractured dental restorations often have plaque on them. The plaque can even be on a fracture surface if it has been exposed to the oral environment for any period of time. An example of what plaque looks like is shown in section 6.10 of this guide, where contaminants are discussed. Plaque can be removed by using an ultrasonic bath with a 16% solution of NaOCl ("bleach") for 8 minutes, then rinsing well with water (courtesy S. Scherrer).

There are two instances where specimens *should be examined before cleaning.* Firstly, staining or discoloration of a flaw may provide important information about the flaw itself. Secondly, fine debris of the material itself on the fracture surface may be a clue that cyclic fatigue has occurred. These are discussed at the very beginning of Chapter 5, Fracture Surface Examination.

Figure 3.7 *Convenient tools and cleaning agents*

3.2 Photographing the Overall Component: Cameras, Cellphones, and Simple Digital Microscopes

It is often prudent to photograph the entire specimen or component. An overall photo provides an essential context for subsequent close up photos. A variety of scales or rulers should be available, which may be set alongside the component in order to show the size or scale. It is prudent to get size markers on the recorded image as soon as possible, otherwise much time can be wasted afterwards deducing or guessing what magnification was used. It is very easy to make mistakes with the size markers added after the fact. Fractographers would do well to follow the example of the archeological community, wherein rulers and meter sticks are ubiquitous features of any formal record of a dig site. In lieu of scales, simple props such as coins or other common objects may be set alongside the component, but perhaps on the side or bottom where they subsequently can be cropped or replaced with marker bars in subsequent reports or publications.

A variety of camera types may be used to photograph an entire component. Digital cameras have become the tool of choice for virtually all such work, but even they are being supplanted by cell phone cameras. Conventional film-based photography (Figure 3.8) has been rendered obsolete for most applications.

(a) (b)

Figure 3.8 *Obsolete conventional film photographic equipment. (a) is a 35 mm single lens reflex camera tripod, and close-up lenses. (b) is a camera stand with instant film (Polaroid) camera, built-in flood lamps and a fiber optic light source for low-angle grazing illumination.*

Modern digital single lens reflex (SLR) cameras and even simple consumer digital cameras with a macro option can be used at very close distances (~100 mm or less) from the object. Digital cameras, either professional high-resolution models or simple consumer versions such as shown in Figure 3.9, have revolutionized fractographic photography. They have auto focus and exposure controls and can capture good images in ambient lighting without a flash. Liquid crystal display (LCD) monitors on the rear of the cameras allow fractographer to see what the lens will capture when the image is snapped. The digital camera instantly displays the captured image. Remedial action can be taken immediately and a new image captured. This is very efficient and led to the rapid obsolescence of film-based photography. Another advantage is that images taken with digital cameras seem to be less sensitive to the illumination source color. Color film often produced odd-colored images if film balanced for outdoors was used indoors with tungsten filament bulbs or fluorescent lamps. Another great advantage of the digital camera is that it needs less light to make a good quality image Ambient illumination usually suffices. Flash lamps used with old film cameras often over- or underexposed an object and created harsh shadows.

Figure 3.9 *Digital camera with macro capability, auto exposure, and auto focus.*

Experience has shown that a digital camera chip with 2 million to 5 million pixels is adequate for most applications. Some publications require no less than 3 megapixel resolution and images must be presented at 120 dots per cm (300 dots per inch). The LCD monitor should be bright and large (at least 40 mm). The camera should have auto focus and auto exposure options and, most importantly, have a macrophotography option for close ups at distances as short as 100 mm. File storage format should include a Joint Photographic Experts Group (JPEG) or Tagged Image File Format (TIFF) option. Sometimes Bitmap (BMP) format files are used with Microsoft Windows operating system computers. Some professionals prefer the raw image format (RAW), which is

image data with very little processing or compression. Image compression is important for the various formats.

JPEG images have an option that they may be saved with variable amounts of compression, but users should record images with little or no compression. A copy of the image can be made at a later time with some compression to reduce the file size so that electronic documents or presentations with many images do not become unwieldy. JPEG files are as much as $1/5^{th}$ to $1/10^{th}$ the size of an uncompressed TIFF file, with very little or no loss of detail. JPEG is available only for true color or grayscale images. JPEG reduces the number of bits in the image by eliminating repetitive image data or image data that is hard to see. The software may allow various compression levels and the higher the level of compression, the lower the quality of the image. JPEG may compress more than other methods and the results may not be fully reversible. At higher compression ratios (> 20:1 or a 50% setting), JPEG can degrade the quality of the image. A JPEG file is automatically uncompressed when it is opened.

TIFF is either an uncompressed format or a LZW (Lempel-Ziv-Welch) compressed format. LZW compression translates common patterns in an image into short codes and is best at preserving all the image data and achieving good compression. It doesn't achieve the high compression ratios that JPEG does. LZW is available for monochrome, grayscale, palette, and true color images.

The RAW format is used by manufacturers to contain the raw (minimally processed) data from the image sensor in a digital camera. RAW file formats are proprietary and can differ greatly from one manufacturer to another and sometimes between cameras made by one manufacturer. RAW files are normally only used when additional computer processing is intended. The proprietary nature of RAW files poses severe problems that fractographers should keep in mind. Photographers will find their older images inaccessible, as future software versions lose support for older cameras and entire camera brands and RAW format subtypes may disappear!

The author typically saves and presents his images in JPEG format with no compression. Virtually all the photographic images in this Guide were saved in the JPEG format. Line art and graphs were saved in LZW compressed TIF files.

The digital camera should be capable of easily transferring images to a computer, either through a cable to a USB or FireWire port on the computer or via a docking port. Common consumer digital cameras that have these features

now cost less than one hundred dollars. More elaborate single lens reflex (SLR) digital cameras have more options, more versatile lenses, and higher resolutions. Some may have extremely high resolutions, but it should be borne in mind that the stored image file sizes may be very large. SLR cameras should be ordered with close up lenses as an option.

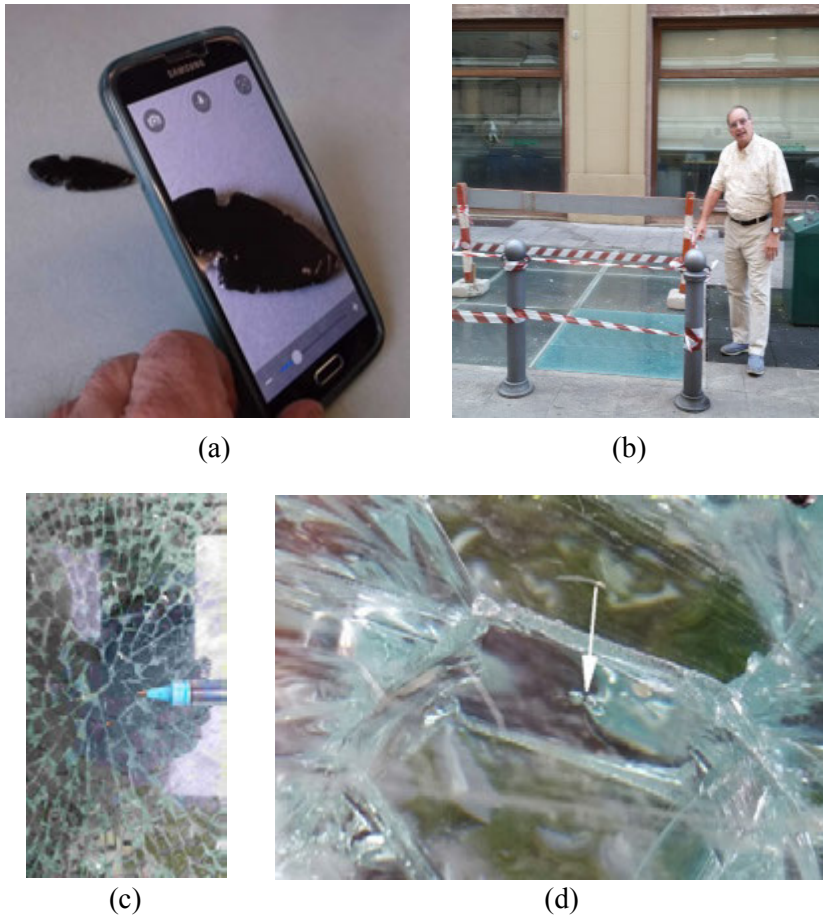

(a) (b)

(c) (d)

Figure 3.10 *Cell phones can be used for fractographic analysis (a) shows an obsidian arrowhead as viewed at 2X magnification in a cell phone; (b) a street photo near Santo Stefano Basilica in Bologna, Italy in 2014; (c) a close-up of the tempered glass fracture pattern, and (d) the close-up at 5X of the internal inclusion origin (arrow). The author was on his hands and knees for (d), which was shot at 5X about 60 mm above and aiming through the glass at an angle.*

Built-in cell phone cameras have surprisingly high resolutions as shown in Figure 3.10. Some models can be adapted with free applications ("apps") that enable the phone to be used in a magnifier mode. As this was being written in 2015, the author uses a cell phone with 110 mm sized bright digital screen and autofocus with a 5X magnification capability. It can be used as close as 60 mm from an object. Some cell phone manufacturers have clip-on close-up lenses and simple holder-stand accessories that can reach even greater magnifications. Users can construct their own little stands to hold the camera steady when taking close-up images (e.g., some are shown on the Internet). The author has also been surprised in some of the courses on fractography that he teaches when students used cell phones to take images through one eyepiece of a stereoptical microscope.

Digital camera photography has eliminated many of the color problems associated (e.g., sensitivity to incandescent bulb temperature) with older film technology. In some cases, the best results can be obtained by photographing the component outdoors with ambient lighting on a neutral-colored background, such as a white or gray poster board. The author often photographs specimens on the window sill of his office on a white poster board base. An additional white cardboard is placed vertically as a reflector on the inside of the room to reflect some external light to back-fill the lighting on the specimen.

3.3 Stereo Binocular Microscope

More powerful magnification will be needed in most cases to observe small fracture origins or markings on the fracture surfaces. The fractographer's single most valuable tool is the stereoptical binocular microscope or stereomicroscope as shown in Figure 3.11. Basic binocular stereomicroscopes have magnification ranges to the eyes of about 8X to 32X or 10X to 40X, but these limit one's view of a small fracture origin flaw and greater magnifications are needed. Upper magnifications of 100X or as high as 300X are available with many stereomicroscopes and are better for fractographic analysis. On the other hand, having a small magnification at the lowest limit (e.g., 5X) facilitates taking an overall picture of a small component. Hence, a stereoptical microscope with a broad zoom range (e.g., range of 10, 16, or even 20 power) is very advantageous. *A 50/50 beam splitter (half the light is sent to the eyes and half is sent to a camera) in the stereo binocular microscope is very desirable since it allows one to look through the eyepieces at the same time an image is sent to the camera.* The alternative, a lever which diverts light either to the eyes or to the camera, is cumbersome and less desirable. It can be exasperating to use.

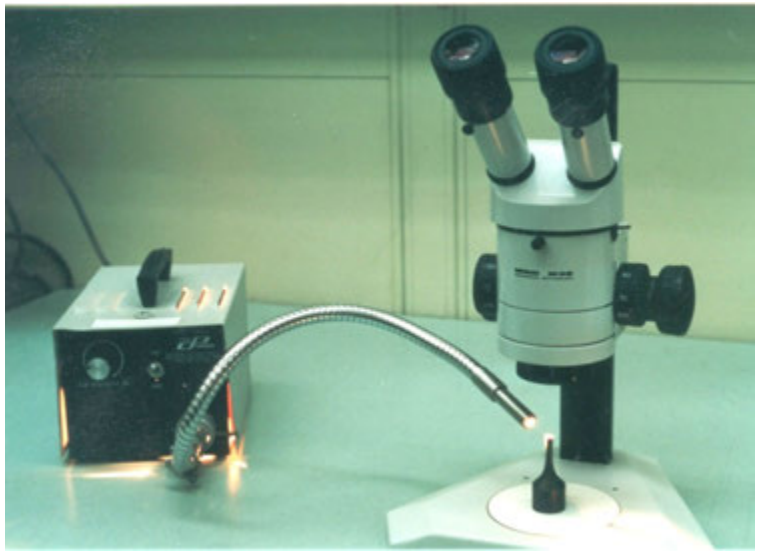

Figure 3.11 *Stereo binocular microscope with a fiber optical light source for directional illumination. This is an indispensable tool for the ceramic and glass fractographer. "Low-angle, grazing illumination" is illustrated in the picture. In other cases, a ring light mounted on the objective lens of the microscope may be suitable. This particular microscope has interchangeable 0.63X, 1.0X and 2.0X objective lenses, a body zoom magnification range of .65X to 4X, and 25X eyepieces for an overall magnification range of 10X to 200X . The moderately tall (300 mm) mounting post enables specimens up to 150 mm tall to be placed under the microscope.*

The stereomicroscope is designed such that each eyepiece views the object from a slightly different angle, thereby creating two different images. The brain interprets these as a three-dimensional view. The stereomicroscope is in reality two separate microscopes. Older rudimentary Greenough design stereoscopes had two completely different optical paths, one for each eye. They had very limited capabilities. Most contemporary stereomicroscopes use a common objective lens and then two internal optical light paths in the body up to the eyepieces. Parfocality, whereby the object remains in focus while the magnification is changed, is a very advantageous feature of the microscope. Follow the manufacturer's guidelines to set the eyepieces for Parfocality.

Stereomicroscopes present an image that is right side up and is laterally correct. The images are therefore easy to correlate to a specimen held in the hands or on the stage. The long working distance from the objective lens and the good

depth of field make it possible to clearly see surface features despite the inherent roughness or curvatures of fracture surfaces. Some stereomicroscopes also have diaphragm apertures that can be stopped down to enhance the depth of field. Many stereomicroscopes are modular and easily modified or expanded.

The total magnification of a stereomicroscope is the product of the magnifycations of the objective lens, the body, and the eyepieces. There often are different objective lenses (0.5X to 2.0X) that screw into the bottom of the microscope. Low power 0.5X or 0.63X lenses are useful for examining or photographing an entire test specimen or viewing large areas of the fracture surface. Higher power lenses (1.6X or 2.0X) may be screwed in for close-up examination. It may come as a surprise that the objective lenses have such low magnifying power, but a large diameter lens is needed to create the two optical views at slightly different viewing angles. The low power also means that the working distance from the objective lens to the object is very large, on the order of 20 mm to 200 mm. This is a very important and desirable feature for the examination of irregular components. One advantage of the long working distance is that illumination sources such as fiber optic gooseneck light guides can be brought into close proximity to the work piece and the angle can be adjusted with plenty of room as shown in Figure 3.11. A good fractographic examination set up should have both a low power objective lens (0.5X or 0.63X) and a high power lens (1.6X or 2.0X). An intermediate power lens (1.0X) may also be handy. Objective lenses can cost anywhere from $ 400 to $ 4,000 each. The more expensive lenses have better sharpness at greater magnifications and have less chromatic aberration.

Basic student-model stereoptical microscopes have a limited magnification range. They have little or no capability for expansion (e.g., addition of different objective lenses or camera ports) and have very limited working distances. They are not a wise investment for the serious fractographer. Nevertheless, when such a microscope is the only one available, it is possible to use a cell phone to take an image through one eyepiece.

Much of the magnification occurs in the body of the stereomicroscope. Most bodies have multiple magnifications either through the use of discrete lenses that can be rotated into the optical path, or better, through stepless-zoom magnification. Modern stereomicroscopes have been vastly improved over earlier generation models that may have only had a 2X or 4X zoom range. Modern bodies can steplessly zoom over a 10X, 16X, or even 20X range while keeping the object in focus. *A very desirable feature is discrete click stops on the zoom knob corresponding to specific magnifications.* This feature is critical

for size measurement purposes, either by the use of a graduated reticule in the eyepiece, or by a camera mounted on the microscope.

Final magnification is provided by the wide field eyepieces that are usually 10X, 16X, or 25X. Stereomicroscopes may be used either with or without eyeglasses. The distance between the eyepiece tubes usually can be adjusted for the interpupilary distance. Eyepieces may have rubber boots that attach to the eyepieces for screening out stray light coming into the eyes. These can be removed or slid out of the way for eyeglass wearers. Typical overall magnifications can range from as low as 5X to as high as 200X. Some modern stereomicroscopes can achieve as much as 300X to 400X magnification with 16X or 20X body magnifications and 1.6X objectives.

The stereoptical microscope should be mounted on a tall mounting post so that large objects can be placed on the stage. Often it is necessary to mount long specimens end on so that the fracture surface is viewed directly. Figure 3.11 shows a model with about a 300 mm post that allows specimens as large as 100 mm to 150 mm tall to be placed on the stage.

It is also advisable to have one or both eyepieces adjustable, so that the operator can focus each eyepiece independently. One reticule should have a cross hair, which is valuable if one wishes to show a colleague a particular feature, or the stereomicroscope will be used for size measurement in conjunction with a traversing stage as will be described below. If no independent measurement system is incorporated, then a built-in graduated reticule should be mounted in one of the eyepieces. The reticule readings will have to be calibrated at various magnifications.

A very valuable but expensive optional feature is a tilting eyepiece head that may be adjusted up or down so that the viewer does not have to extend or bend his or her neck to see through the eyepieces, or to have to move a chair or stool up or down. A tilt head can cost between $ 3,000 and $ 4,000.

3.4 Stereoptical Microscope Camera Port and Digital Cameras for Microscopes

Stereomicroscopes may be equipped with a camera port for a video or digital camera. The port will be in line with either the left or right optical paths. The camera cannot record or display both images that the eyes see and the brain interprets as a three-dimensional image. The camera commonly will be mounted on the camera port through a C-mount or an F-mount that must be chosen with care. It must fit the camera port's diameter, but also have with an

appropriate internal lens to match the image size to the camera chip size. Some microscope bodies have a lever switch that directs the light to *either* the eyepiece or to the camera. This is extremely inconvenient. A much better scheme is a beam splitter that directs 50 % of the light to the eyepiece and 50 % to the camera so that the image can be viewed at the same time it is projected onto a monitor.

Instant film cameras are now obsolete. They were supplanted first by video cameras, but now almost exclusively by digital cameras connected to a computer. Video cameras which had fast image capture capabilities had to be used with frame grabbers to snap an image. They had very low 640 x 480 or 768 x 500 picture element resolutions so that many images per second could be taken. They have been rendered obsolete as digital cameras became more capable, less expensive, faster even with low light, and easier to use.

Digital cameras designed to be attached to microscopes can show "live" images at up to 10 to 20 fames/sec with nominally reduced resolutions-on the computer monitor. Once the object is framed and focused, a higher quality image can be acquired or "snapped." A small piece of white paper is often handy, since it can be momentarily placed in the field of view and the camera color-balanced by pressing a camera software button. A fast "live" image mode makes focusing on a computer monitor very efficient. Fractographers should avoid systems with slow refresh rates since focusing is exasperating as one makes a slight focus adjustment, and then has to wait a few seconds to see the effect on a monitor. A digital camera chip with 2 million to 5 million pixels is adequate for most applications. The most common image formats in 2015 are JPEG, TIFF and sometimes BMP as discussed in section 3.2. Image compression should be minimized or not used at all when capturing and saving images. Sometimes excessive emphasis is placed on having large pixel counts in digital cameras. There is no harm in having digital cameras with larger pixel counts, but storing and handling very large files might become cumbersome, especially if the images are embedded in documents. Refresh rates on "live" images may also be slowed down. Nearly all the microscope images in this Guide were captured with a CCD (charge-coupled device) digital camera having a 11.8 mm x 8.9 mm RGB color mosaic chip having 2 megapixels (1600 x 1200) and saved as 24 bit color jpg files. The price of these cameras is cost effective and resolutions of 3 megapixels or more are common at prices less than $ 4,000 as this Guide was written. CCD chip cameras are commonly used but CMOS (complementary metal oxide semiconductor) chip cameras are also becoming more popular. (A microscope digital camera specialist or salesman can be consulted for the advantages and disadvantages of each.)

The camera input can be fed to free software provided with the digital camera as part of a complete package, or to a separate image processing software package. In the past there inevitably were compatibility problems with software and cameras and all the usual annoying nuances of computer programs. Contemporary digital cameras and software packages are much more user friendly. Nevertheless, it probably is best to have digital cameras and their software installed by a camera or microscope company representative who has experience trouble shooting installation and compatibility problems.

The simpler the software the better! The author has used digital software packages that are excessively complicated, in large part since they were written with lots of options and clever additions for experts. They are slow and cumbersome, and have so many menus and submenus that they are a nuisance to use. (Users should beware of salespersons who are eager to sell expensive software packages that the user does not really need.) A lot of time is lost in training students and new users.

A very important attribute of a digital camera is the ease which a magnification marker bar can be added to an image. Some digital cameras come with free software that allows not only the usual image adjustments (brightness, contrast, sharpness, cropping, etc.) and file-saving options, but annotations and arrows as well. This is important, and the fractographer can mark a feature on an image immediately and not have to use a secondary software package back in his or her office. Even more importantly, it is crucial to be able to put a magnification – size marker bar onto an image. *The fractographer should get into the habit of doing this immediately.* It can be confusing afterwards to know just what magnification a photo was taken with, and an erroneous marker bar might be put on. One option is to save a file with an image name that includes the magnification, e.g., "specimen 6 side view at 32X.jpg". If a microscope has a variety of lenses and body magnifications, then calibration factors for each combination will have to be established in the software. Usually this is not too difficult, and once these values are set, they can be retrieved automatically by the software afterwards. The author uses a scheme whereby the camera software has a list of files with all possible lens magnification combinations, with file names that are easy to understand, e.g., "1.6X obj 4X body" which is short for: "1.6 X objective lens, 4X body magnification." The author routinely needs only 5 to 10 seconds to put an accurate magnification marker bar on his digital images. The author has gone to fractography laboratories around the world and has been pleasantly surprised that others have used simple schemes like this, and it is possible to start using the microscope with little or no confusion.

3.5 Digital Image Processing and Focus Stacking

Digital image technology has revolutionized techniques for processing images. Brightness, contrast, sharpness, and gamma adjustments can easily be made to captured images. Complex discussions about the gamma adjustment and luminance of pixels can be found on the internet or in software packages, but can be confusing to newcomers. Simply put, gamma settings adjust the brightness of the pixels that are between the limits of the very bright and very dark regions in an image. In other words, a gamma adjustment does not alter the bright or dark regions, but everything in between.

Inexpensive commercial software now overcomes the depth of field limitations of common microscopes. A series of ten to twenty JPEG or TIFF digital images of an object are taken by an ordinary digital camera with the focus adjusted slightly between each photo. Only a portion of the object is in focus in each image. The software evaluates each image, assesses which portions are in focus, and then constructs a composite final image with all elements in focus in just a few seconds. This is called "focus stacking" or "Z-axis stacking." It does not matter whether the images are from a camera mounted on a tripod, an optical microscope, or a scanning electron microscope. Figures 3.12 and 3.13 show examples. Even if the images shift slightly after refocusing in a stereoptical microscope, the software compensates for the shifts. The practical ramifications of this technology is that infinite depths of field are achievable with all microscopes, dramatically enhancing the versatility of all microscopes.

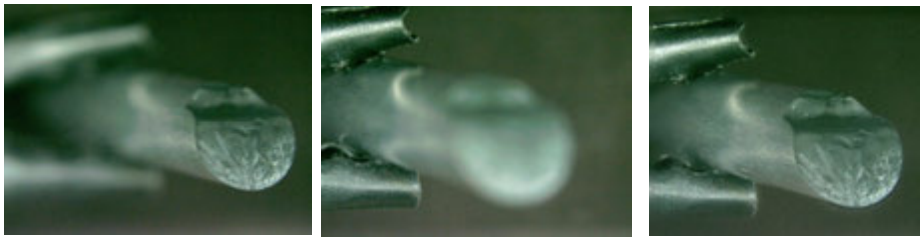

(a) (b) (c)

Figure 3.12 *A silicon nitride 6 mm diameter rod broken in flexure (801 MPa). (a) and (b) show stereoptical microscope digital images. Even though the microscope has great depth of field, the cantilever curl and holder are out of focus in (a). (b) shows the holder in focus. (c) shows the digitally reconstructed composite image from 15 separate images.*

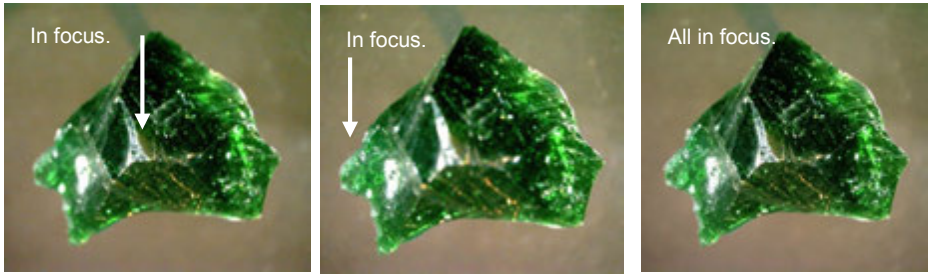

(a) (b) (c)

Figure 3.13 *A 25 mm glass fragment. (a) and (b) show typical images made by a stereoptical microscope at low magnification. Although the microscope has excellent depth of field, portions of the fragment are out of focus in each view. (c) shows the digitally reconstructed image made from 16 separate images focused from the top to bottom of the fragment. The digital reconstruction took less than 1 minute.*

Figure 3.14 *A discussion stereoptical microscope that allows two observers to simultaneously view an object. Note the very tall post (800 mm) on which the microscope body is mounted. The entire assembly can be moved up or down as required to facilitate examination of very large or very small specimens. Beam splitters in the optical path enable simultaneous viewing through the eyepieces at the same time the digital camera views the object.*

3.6 Discussion Stereomicroscope

Figure 3.14 shows a "discussion stereoptical microscope" that enables two observers to simultaneously see the image. A beam splitter diverts half of the light to the auxiliary viewing station. The configuration shown is a side-by-side model which is preferred for most fractographic analysis. Discussion microscopes often have a built in moveable pointer that can be seen by both observers. Discussion microscopes are extremely valuable for training new fractographers or for showing features to clients or colleagues. The auxiliary viewing station should also have adjustable eyepieces so that the secondary observer can adjust the focus to match the focus of the primary observer. A camera port can be included with another beam splitter so that the image can be projected onto a monitor at the same time it is viewed through the eyepieces.

3.7 Digital Microscopes

Simple digital microscopes, also known as USB microscopes, connect directly to an ordinary computer. They do not have eyepieces to look through. Everything is projected onto a computer monitor. They are a new technology

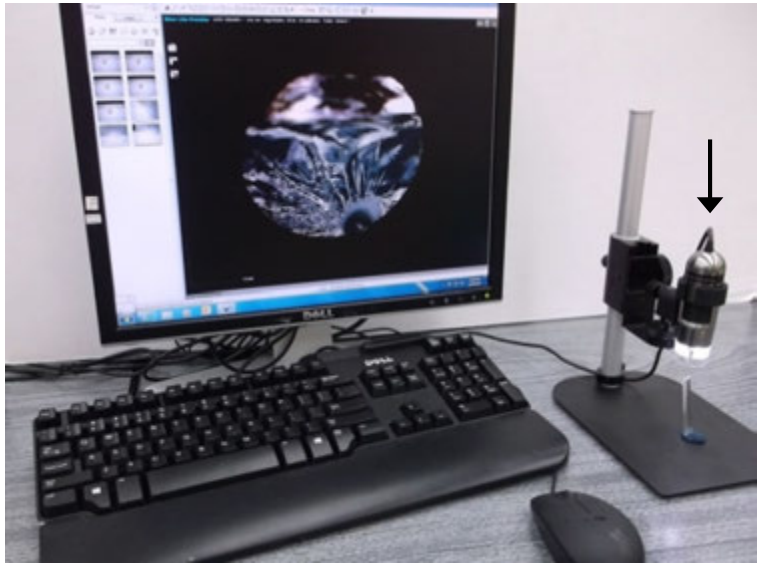

Figure 3.15 *Digital microscopes are a new tool for the fractographer. This simple digital microscope (arrow) is mounted in a stand on the right. It is focused on the fracture surface of a broken glass rod. The monitor and computer (not shown) are separate components*

that is becoming increasingly common. They can range from inexpensive low-power, hand-held models to elaborate, high-power, expensive models mounted on a rigid platform with full Z-axis control and digital image stitching capabilities. Figure 3.15 shows a mid-priced model (~$ 1,000 plus $130 for the stand) with variable magnifications from 20X to 250X and corresponding working distances of 48 mm to 2 mm. It may be difficult to obtain sharp, focused images with the simpler models that are hand held, so a stand is advisable. The digital microscope is not parfocal. As the magnification is changed, the image must be completely refocused and the working distance is changed significantly. This is a nuisance. Another limitation is illumination, which is usually provided by built-in light-emitting diodes surrounding the lens. This limits their ability to highlight or even discern critical fracture surface features. For example, shadowing, or low-angle grazing illumination, which is essential for ceramic examination and fracture mirror examination, cannot be done. A separate light source is recommended.

At the other end of the spectrum are high-end digital microscopes mounted on very rigid fames and bases and which may have built-in vibration dampers. They may have fully-motorized positioning stages and automated Z-axis focusing and even have motorized tilting heads. Camera and stage controls are via joysticks, electronic knobs, or even touch-screen monitor manipulation. These systems can automatically conduct Z-axis focus stacking analysis and, combined with the stage control, can generate quantitative three dimensional profiles of the fracture surface. The virtual three-dimensional image can be displayed on the monitor and rotated and viewed from different perspectives. Despite this extraordinary versatility, the illumination systems with such microscopes (usually a ring of LEDs) are very limited. Many of the techniques described in this Guide require fully-independent illumination control. It is recommended that independent illumination sources such as shown in the next section be acquired for use with such high-end digital microscopes. The working distances between the lens and the piece should be large enough that independent light can be directed onto the specimen at variable angles.

3.8 Illumination Sources

Figure 3.16 shows some options for specimen illumination. Bright light sources are advisable to facilitate the examination of dark ceramics and the use of high magnifications. The most common illumination source for fracto-graphic analysis is a ring light that clamps to the objective lens. The author rarely uses it. It provides uniform lighting, but may not be effective in

Figure 3.16 *Illumination sources for use with a stereomicroscope. Clockwise from the middle left: a ring light intended to be clamped to the objective lens, a ring dark light illuminator on an adjustable stand, a line light source on a stand, and a transmitted light platform.*

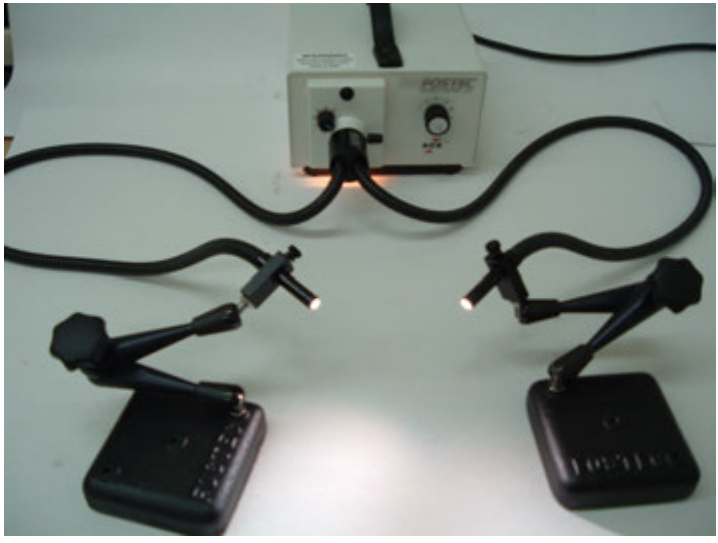

Figure 3.17 *Dual gooseneck fiber optic light guides allow flexibility in directional illumination.*

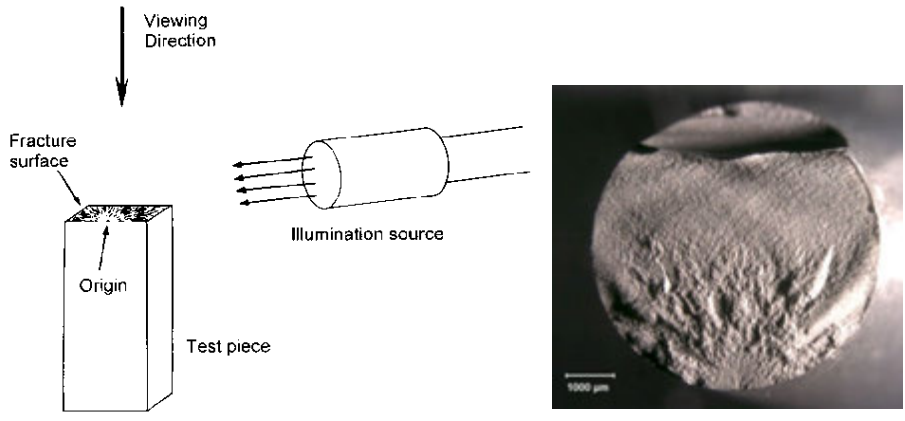

Figure 3.18 *Low-angle grazing illumination (a) is effective in highlighting fracture surface topography as shown in (b), which is the fracture surface of a ceramic rod broken in flexure.*

highlighting ridges or valleys. Directional illumination can be achieved with one or more fiber optic gooseneck light guides that direct an intense light beam onto the fracture surface at an angle. Dual gooseneck guides from a single light source as shown in Figure 3.17 are convenient so that one guide may be used for illuminating the key features while the second can be used as filler.

Low-angle grazing illumination is very effective for accentuating peaks and valleys on fracture surfaces as shown in Figure 3.18. The ability to adjust the angle of the illumination source is critical. Easily-adjustable holders are a great time saver.

This is one major revision in this 2nd edition of this Guide as compared to the first edition. Low-angle grazing illumination was erroneously termed "vicinal illumination" in the first edition. Vicinal illumination is different.

"Vicinal illumination," illustrated in Figures 3.19 and 3.20, is helpful in detecting cracks that may be difficult to see by other means in a translucent material. A bright light illuminates an area near to ("in the vicinity"), but not directly on the area to be studied. Light is scattered sideways in the translucent material. If the light encounters a crack, much of the light is reflected. Only some is transmitted across the crack. This creates a sharp delineation between light and dark areas that highlights the crack.

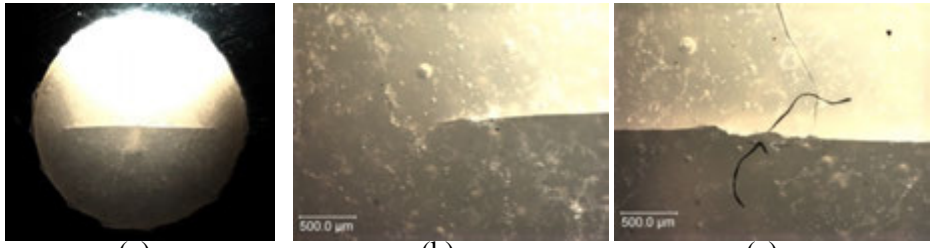

(a) (b) (c)

Figure 3.19 *Vicinal illumination of a PEG dental resin with amorphous calcium phosphate filler. The disk specimen (a) broke in a biaxial strength test, but there was insufficient stored elastic energy to fully break the specimen. (b) is a close-up of one crack tip, and (c) is a close-up of the tensile surface at the fracture origin. The flaw is a trapped hair or fiber. This was confirmed by examination of the fracture surfaces once the specimen was snapped in half by hand.*

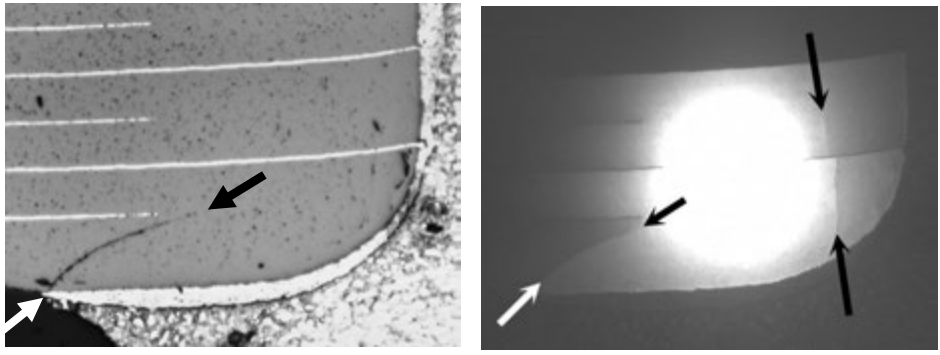

(a) (b)

Figure 3.20 *Bright field reflected light (a) and vicinal illumination (b) of a multilayer ceramic capacitor. Both images are at the same magnification. Only one crack is apparent in (a). Vicinal illumination revealed the second crack on the right in (b). These are from a compound optical microscope. The aperture was stopped down for the image in (b). (Courtesy of S. Hull, NASA, Goddard Research Center.)*

Dark field illuminators such as shown in Figure 3.21 may also be handy. The dark field illuminator is similar to a normal ring light, but the light is directed sideways from the ring towards an object in the middle. It is in essence low-angle grazing illumination from all directions. This sideways illumination accentuates subtle surface features and scratches.

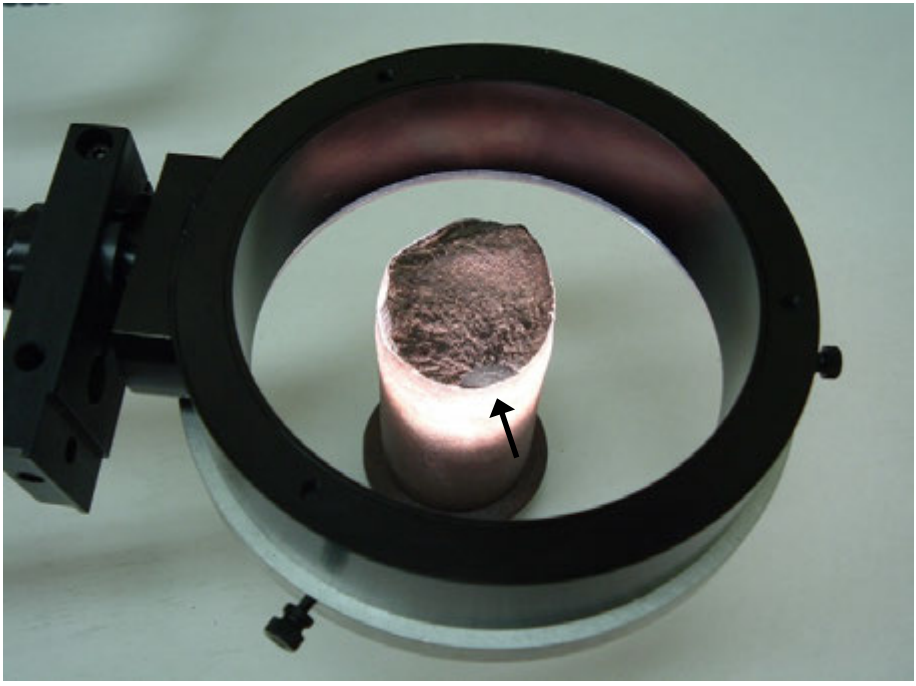

Figure 3.21 *Dark field illumination of the fracture surface of a fractured steel railroad coupler pin. The arrow points to a fatigue crack.*

Some stereomicroscopes have a light source in the base for transmitted illumination that is useful for glasses and transparent ceramics. Illuminated bases as shown in Figure 3.22 may also be used.

Some translucent or transparent specimens may be illuminated by "transillumination." The fiber optic light source is directed through the material from one side. Usually the side surface nearest the light guide will be washed out, but internal features and subtle fracture surface features may stand out elsewhere on the fracture surface. Figure 4.1 in the next chapter shows examples.

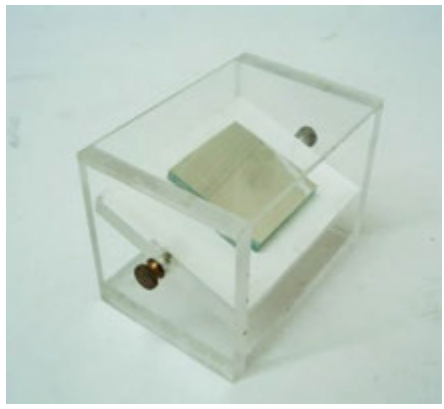

(a) (b)

Figure 3.22 *Transmitted light can be from an illuminator plate as shown in (a) or in (b), an improvised stage made of Plexiglas, and white paper or a mirror for transmitted illumination. A fiber optic light source can be directed onto the tiltable inclined plane so that light is reflected up through a specimen mounted on the top. (Thanks to Dr. D. Shechtman for suggesting this to the author.)*

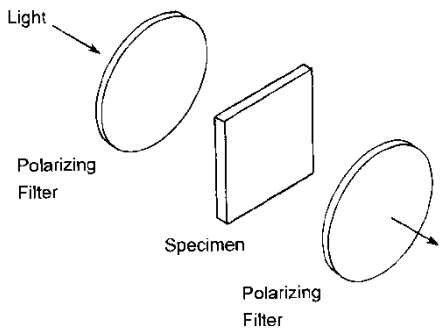

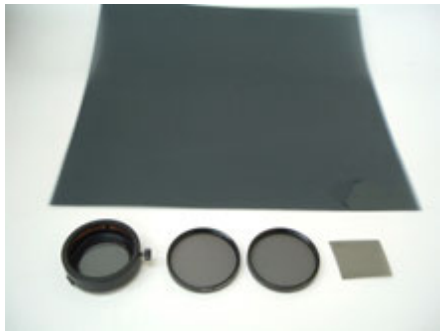

Figure 3.23 *Crossed polarizing filters or plastic sheets. Polarizers can either be dedicated accessories for the stereoscope, or can be improvised from ordinary single lens camera lens attachments or sheets of plastic polarizing film.*

Polarizers (Figure 3.23) may be valuable for examining transparent materials. They may reveal residual strains in glasses or twins in single crystals. One polarizing filter may be placed between the transmission light source and the specimen and an analyzer (another polarizing filter) attached to the objective lens. The analyzer can be rotated as required to achieve the desired color or brightness differences. Polariscopes are discussed in section 3.25 below.

3.9 Coatings

Coatings may be applied to specimens that have poor reflectivity or which are translucent and scatter light from beneath the surface, thereby washing out the surface detail. A thin layer of gold or platinum may be sputtered onto the specimen surface in a small vacuum chamber. Such equipment is commonly used to prepare a specimen for scanning electron microscope examination, but the coating may enhance optical examinations as well. Figure 3.24 shows an example.

Gold and platinum coatings may be removed without harm to most ceramic specimens by soaking the pieces for about 1 minute in "aqua regia." This is a combination of 1 part by volume of nitric acid and 3 to 4 parts hydrochloric acid. This is a hazardous combination and appropriate precautions must be taken (e.g., gloves and eye protection). Only mix the amount to be used in a cleaning session. *Never store it, since it releases gasses that build up pressure in a sealed container.* The specimens should be rinsed in water afterwards. When disposing of used aqua regia, water should not be added to the acid mix. Instead, the acid mix should be carefully poured into a large container of water or a sink with ample flowing water.

Aqua regia can cause harm to a specimen if the specimen contains anything metallic, such as a metallic-inclusion fracture origin. The author once had a highly-filled resin matrix dental composite bend bar that had some trapped contamination covering the origin during the initial SEM examination. The original gold coating had to be removed, the specimen recleaned and recoated for a second SEM examination. The fracture origin was a calcium rich inclusion. The aqua regia not only removed the gold coating, but it also reacted with the fracture origin forming calcium chloride. The EDX analysis during the second SEM session showed chlorine at the origin, which was puzzling until the author remembered the aqua regia cleaning step and realized that the HCl had reacted with the flaw.

(a)

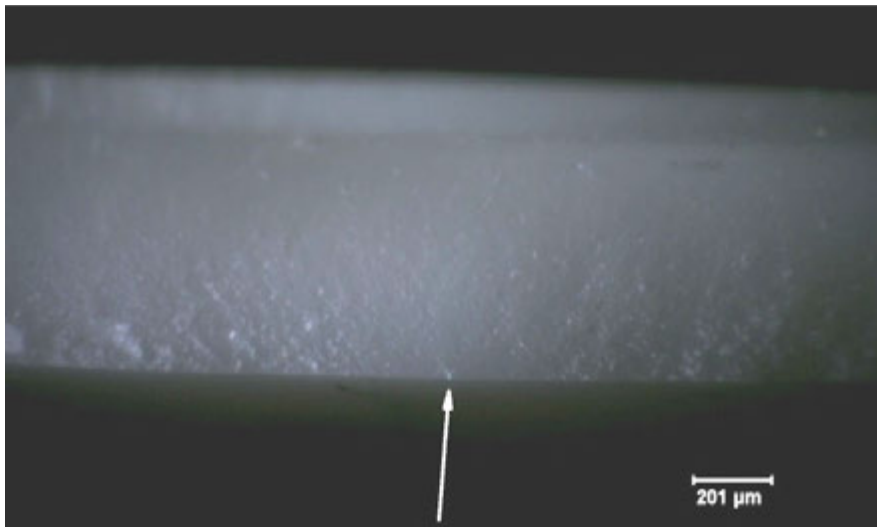

(b)

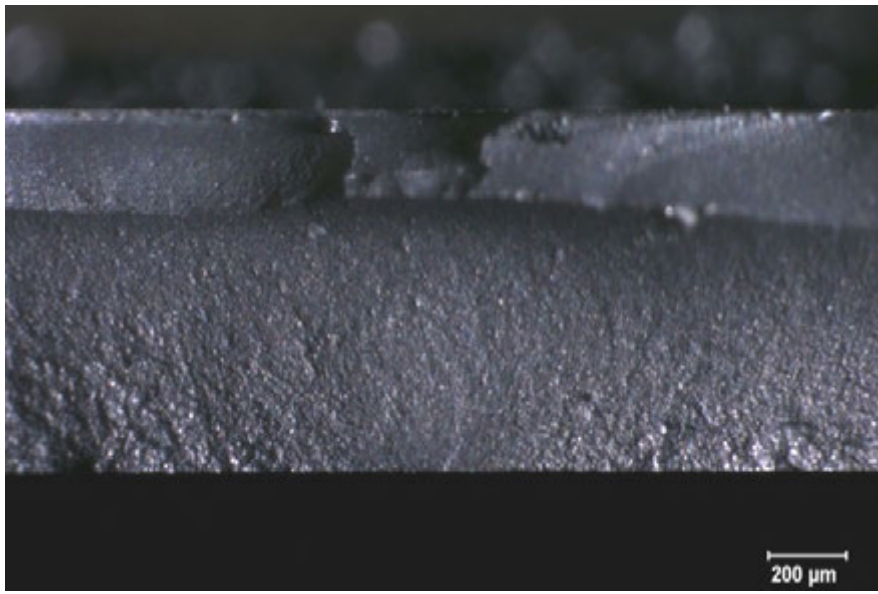

Figure 3.24 *Two views of a fractured yttria-stabilized tetragonal zirconia disk with reflected light illumination. (a) shows the uncoated fracture surface and (b), the same region after a thin gold coating was applied.*

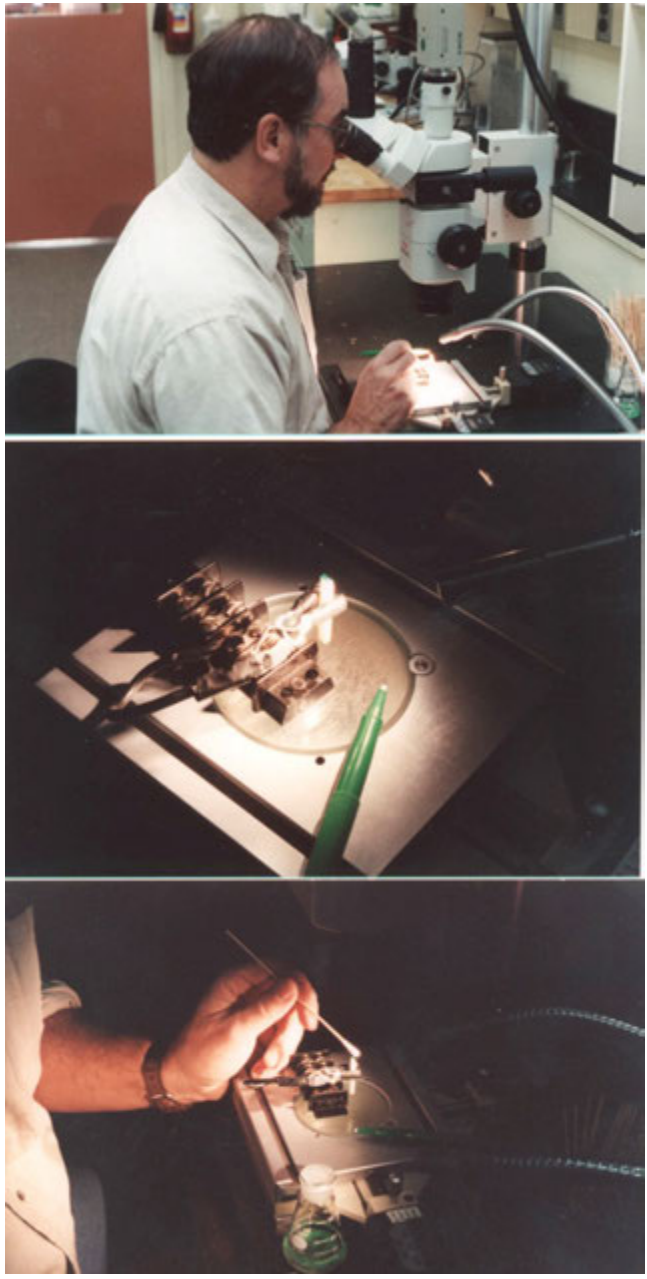

Figure 3.25 *A simple but effective coating technique for white ceramics is to stain the surface with a green felt tip pen. The staining can be watched in real time through the microscope. The green stain can be easily removed with ethanol alcohol on a cotton swab applicator and the process repeated.*

A simple expedient that works very well for many white or gray ceramics is a common felt tip pen as shown in Figures 3.25 and 3.26. Green felt tip pens work the best, partly because the eye is most sensitive to green wavelengths, but probably also due to the character of the green dye. [b] The dyes can easily be removed with ethanol within a few seconds or minutes and the process repeated in a matter of seconds. Most of the dye will come off, but some may penetrate into crack branches or undercuts in the fracture surface and may be more persistent. If the green dye is allowed to sit for longer periods of time, it can be removed by soaking the part for 1 to 2 minutes in a 30% solution of H_2O_2 (hydrogen peroxide). Note this is a much greater concentration than is use for topical cleaning of wounds. Gloves and eye protection should be used. Additional dye and staining techniques are discussed in section 3.24 later in this chapter.

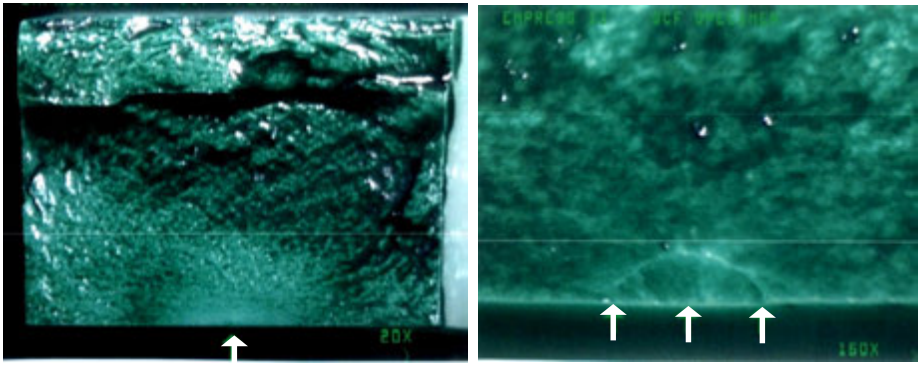

(a) (b)

Figure 3.26 *An example of green dye staining on a dental glass ceramic bend bar. (a) shows the entire fracture surface illustrating how the stain drains into valleys and accentuates hackle lines and ridges and how easily the fracture mirror region stands out (arrow). The bottom view shows the fracture origin: a surface crack (arrows) made by Knoop indentation for a fracture toughness measurement. The pictures were medium resolution video prints and the thin horizontal line is an artifact from a defect in the print head.*

[b] Papermate Flair, 1.1 mm, Sanford Corporation, Division of Newell, Rubbermaid.

3.10 Size Measurements

Sizes may be measured by means of a graduated reticule in a microscope eyepiece. The graduations must be calibrated by means of a stage micrometer such as shown in Figure 3.27. Users should be cautious about the accuracy of stage micrometers. Some are rudimentary and only meant to furnish an approximate magnification for photography and can be as much as several percent in error. Others may be very accurate. If a stereomicroscope has a zoom capability, it is best that the body have discrete click steps or detents so that precise magnifications can be calibrated and recorded at the discrete steps.

(a)

(b)

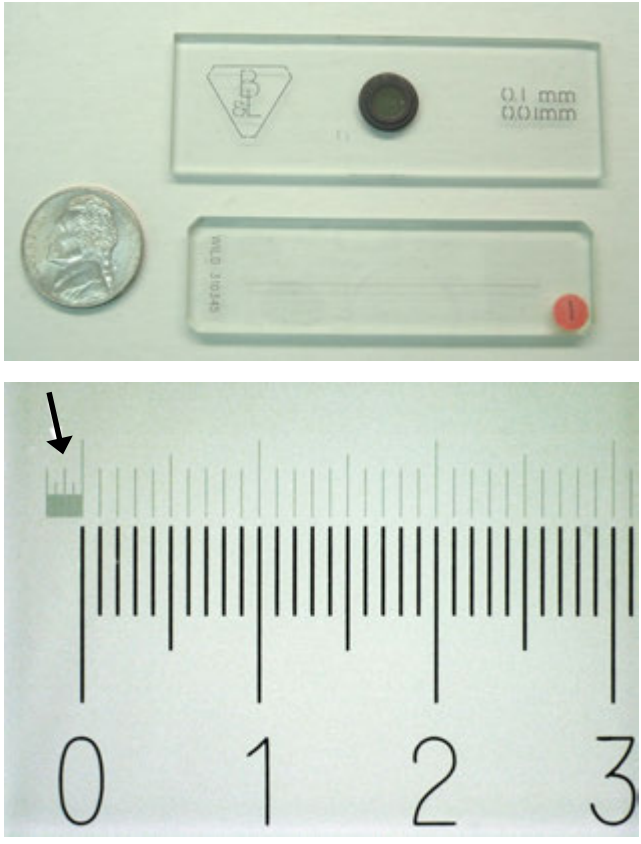

Figure 3.27 *Two stage micrometers (a). A close-up of the bottom one is in (b). The numbers show 1 mm spacings. The thin lines on the top right are 100 μm apart. The thin lines on the top left (arrow) are 10 μm apart. This model was accurate to an amazing 0.01 %.*

A powerful accessory to a microscope is a traversing X-Y stage with micrometer positioning heads such as shown in Figure 3.28. This accessory is especially valuable for precisely aligning a specimen in the field of view, particularly when photographing an image. (A lot of time can be lost when nudging a specimen around with one's hands.) The micrometer heads, in conjunction with a crosshair in one eyepiece, also facilitate accurate size measurements of features. One advantage of such a system is that if the fracture surface is viewed directly from above through both eyepieces, and the fracture plane is horizontal, then the micrometer-measured sizes need not be corrected for foreshortening, as long as the surface being examined is parallel to the X-Y stage.

If size measurements are made on recorded images, care must be taken to ensure that the camera axis is near to perpendicular to the fracture surface plane. Cameras mounted on a stereomicroscope view the fracture surface at an small angle to the fracture surface, so its view may be foreshortened. The specimen may have to be tilted a few degrees to obtain a true view of the size of the fracture surface. So, for example, one can tilt a bend bar sideways a little bit until the camera does not "see" the sides of the bend bar.

An additional advantage for the X-Y stage measurement is that the size readings are independent of the magnification used to view the specimen. In contrast, images captured by the camera must be calibrated for the exact magnification.

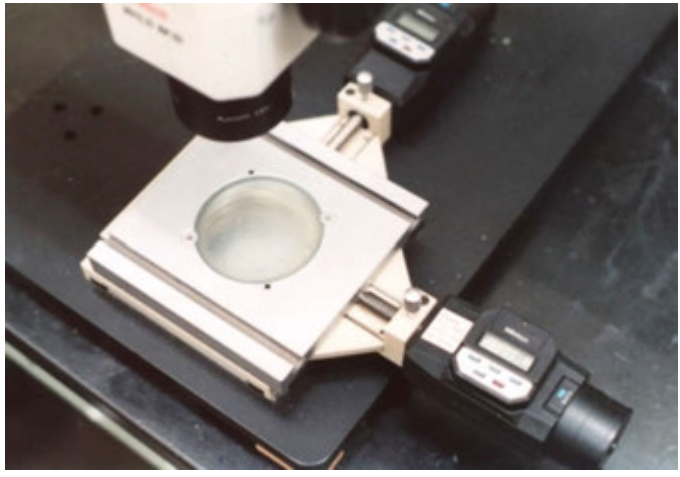

Figure 3.28 *A X-Y traversing stage with digital micrometer heads is very convenient for positioning a piece and making accurate size readings.*

One drawback to the traversing stage is that it takes up vertical space and hence the microscope body must be moved up higher and possibly may limit the working range under the objective if the microscope is mounted on a short post. As noted above, stereomicroscopes for fractographic examination should be mounted on tall posts for maximum versatility.

3.11 Compound Optical Microscope

Compound optical microscopes such as shown in Figures 3.29 and 3.30 may be used for fractographic analysis, but are less versatile than stereo-microscopes. Compound microscopes are best suited for small specimens with relatively flat surfaces. They magnify much more (up to 1600X) than a stereomicroscope, but three-dimensional topographical effects are lost. Virtually all work is now done with air lenses. Oil immersion lenses are no longer needed.

Objective lenses from 5X to 100X may be used in the lens turret, but in practice the limited depth of field makes it difficult to see a fracture surface in focus at larger magnifications. Only portions of a fracture surface may be in focus even at lower magnifications. Working distances are also very small, and care must be taken not to contact the objective lens with a specimen. Long focal length objectives are ideal. These have greater working distances, but at the cost of some loss of light collecting power and resolution. The author uses a compound microscope with long focal length lenses. The 100X objective has a 1.3 mm clearance and 0.8 numerical aperture. Some 100X lenses are available with working distances as long at 13 mm, but these have lower numerical apertures (0.5 to 0.6) and thus less resolving capability. The clearance between a stage and the objective lenses may also preclude examination of large fractured pieces. Low-angle grazing illumination is difficult to achieve with compound microscopes, especially at greater magnifications.

Dark field illumination may be effective for examining cleavage planes in single crystals. Direct reflected light illumination may be too bright or wash out details due to the mirror-like reflection from a cleaved crystal surface. Dark field illumination blocks the central portion of the illumination light coming through an objective, allowing only oblique rays in a ring to strike the specimen. Only light that is scattered by features on the fracture surface is reflected back up into the objective for the viewer to see. Fracture surfaces appear as small bright lines and spots against a dark background. Dark field can highlight subtle cleavage steps and make the symmetry of a fracture mirror more evident.

Figure 3.29 *Compound reflected light microscope. Although the microscope has twin eyepieces, they both view the same image collected by the objective lens. Overall magnifications can be as much as 1000X, but the working distances and the depths of field are very small. Only relatively flat specimens may be examined.*

Figure 3.30 *A research compound microscope with a digital camera and computer. Linear encoders with a 1 micrometer resolution are attached to the traversing X-Y stage and facilitate rapid size measurements. The instant film camera on the top was a common accessory in the 1970s to 1990s, but has been rendered obsolete by digital cameras such as the one marked by the arrow. A fractured glass rod mounted on blue polymeric clay is on the stage. The fracture mirror can be viewed through the eyepieces at the same time it is projected on the monitor.*

Compound microscopes are useful for measuring very small features, such as tiny fracture mirrors in optical fibers or other strong test specimens. Compound microscopes can also be used in transmitted illumination mode. These microscopes are also optimal for measuring fracture mirror sizes in glasses.

Compound microscopes may be very useful for examining fine detail in replicas. Thin polymer replicas of curved surfaces may be flattened by taping the ends of a replica on a glass microscope slide, or the replica may be placed between two glass slides so that the curved surface can be flattened and examined at high magnification in either transmitted or reflected light.

Compound microscopes are essential for examining polished specimens for microstructural analysis, a useful adjunct to the fractographic analysis.

3.12 Replication Equipment

Replicas of fracture surfaces may be valuable in some instances. Some fractured parts may be so large or unwieldy that it may be difficult to position them under an optical microscope. In other instances, the fractured part may be a critical piece of evidence that cannot be removed to the fractography laboratory. Replicas can also be an important backup source of critical fracture surface information if the component is lost or damaged. They can be valuable teaching aids in a course on fractography since every student gets to examine the same object with the same features!

In some cases, fracture surface features may actually be easier to observe on the replica than on the original surface. In many transparent or translucent ceramics such as porcelains or coarse grain ceramics, light scattering from below the surface can obscure the fracture surface details. For example, subtle wake hackle lines behind pores may be easier to see on replicas. Curved surfaces can be made more amenable to high magnification examination, since a replica can be flattened. Since some replicas are a negative of the fracture surface, depressed features such as pores or cracks are converted to raised features on the replica that sometimes are more easily imaged in the scanning electron microscope.

There are a variety of materials that may be used to make a replica as shown in Figures 3.31 to 3.35. Two excellent summary papers with practical tips are by Varner.[1,2] The replica must be made without the introduction of artifacts. The replica material must also not damage the original material nor chemically react with it!

Figure 3.31 *Thin cellulose acetate replica tape, acetone, applicator, and bend bar specimens. These are used to make reversed (negative) replicas.*

There are two types of replicas: "positive replicas" and "negative (or reversed) replicas." Some replica materials are laid over a fracture surface then removed after they dry sufficiently to retain the critical surface features. The material preserves a mirror image of the fracture markings: what was left is now right, and so forth. This is a "reversed replica" or a "negative." Other replicas may be made in multiple steps to create a "positive replica." So for example, a silicone impression or mold may be made around an object, and then pulled off the fracture surface. An epoxy resin is then cast into the mold and allowed to dry. The mold is removed, and now the epoxy represents a positive replica (i.e., a clone) of the original part. The dental materials community has a good line of products suitable for making mold impressions of teeth and these materials are suitable for general fractographic applications as well, as discussed by Scherrer *et al*. [3] Fréchette also describes replication techniques in his book.[4]

Cellulose acetate tapes or films (such as used in transmission electron microscopy) are convenient replica materials that may be made at room temperature as shown in Figure 3.31. The specimen surface should be clean. A short strip of 0.13 mm to 0.25 mm thick tape is cut from the sheet or roll and then moistened on one side with acetone. Thick tapes or films may be

(a)

(b)

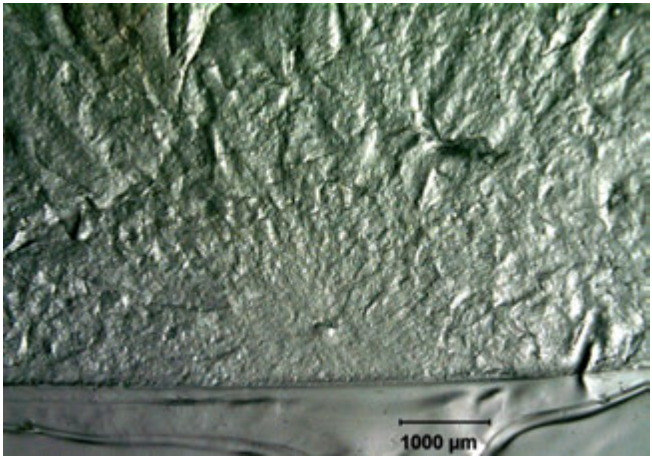

(c)

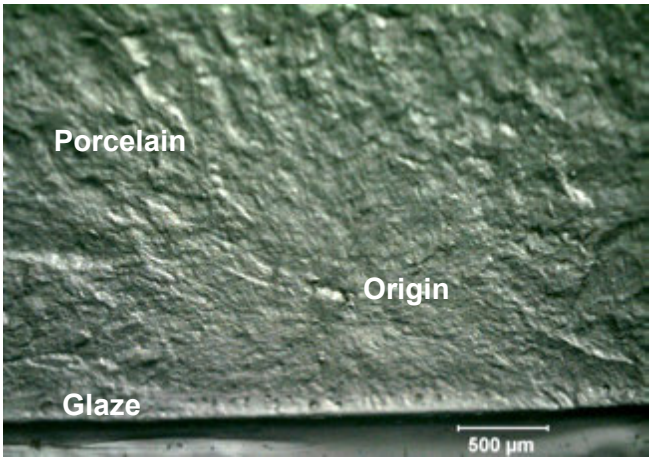

Figure 3.32 *Cellulose acetate replica of a fracture surface of a porcelain electrical insulator. (a) shows the replica taped to a glass microscope slide. (b) and (c) show close-ups of the replica which reveals the fracture mirror and an inclusion flaw.*

immersed in acetone for 10 s to 15 s, whereas thin tape may be wetted by a few drops from an eye drop applicator. The specimen surface may also be wetted by acetone, although that step is not always necessary. The tacky film or tape is applied to one side of the fracture surface and then is gradually brought into contact with the remainder. The replica material should be applied so as not to entrap any air. Pressure is applied to the replica for 15 s up to two or three minutes as required, taking care to not slide or shift the replica material. A small pad (or if the specimen is small enough, a finger or thumb) may be used to apply the pressure. If a finger is used, a folded tissue or small pad between the finger and the tape should be used so that one's fingerprints do not get superimposed on the back side of the replica tape! The pressure is carefully removed without disturbing the replica which remains in contact with the fracture surface for 10 min to 15 min more drying time. The replica is peeled from the fracture surface (or it may pop off) and may be trimmed with scissors or mounted on a glass microscope slide such as shown in Figure 3.32.

Cellulose acetate replicas may be viewed with reflected or transmitted illumination in an optical microscope. An interesting advantage of a replica over an original surface is that even if the original surface is curved, the replica can be flattened out and examined in a compound optical microscope at greater magnifications (in either reflected or transmitted light mode) than if the replica were only examined with a stereoptical microscope. Gold or carbon coatings can be sputtered onto negative replicas to enhance viewing in reflected light or to prepare the replica for SEM examination.

Since "reversed" replicas like the cellulose acetate tapes are flipped versions of the fracture surface, it is prudent to label them clearly as to their location on the component, lest the fractographer confuse top-bottom, or left-right orientations. Special care should be taken to avoid artifacts in the replicas such as trapped air pockets, tears, or handling artifacts. Replicas should be kept clean and carefully stored in containers.

If it is possible to warm a specimen, then negative replicas made with the thermoplastic compound polyvinyl chloride (PVC) (180°C) or, alternatively, silicon elastomers may also be used (100°C).[4] If PVC is used, the specimen is heated and the PVC applied with a Teflon rod.

Positive replicas may be made with filled silicone rubbers, unfilled (transparent silicone rubber, and polyvinylsiloxane (PVS).[1,2,3] The latter material is commonly used in dentistry to make impressions in patient's mouths as shown in Figures 3.33 and 3.34. Extraction of a damaged dental crown from the mouth typically requires its destruction. Therefore it is prudent to make a

(a)

(b)

Figure 3.33 *Dental replica equipment. (a) shows a typical PVS applicator gun which has interchangeable tips and compounds. (b) shows Dr. S. Scherrer demonstrating the technique in a dental materials fractography class.*

replica before the crown is extracted as discussed by Scherrer *et al* [3] and shown in Figure 3.34. Sometimes just one PVS compound is adequate, but in other cases it is optimal to use two PVS compounds. The first is a very fluid PVS that can retain very fine detail (e.g., Ultra-Light Body) when applied to the fractured part. Once it sets, a second PVS that is a fast setter is applied over the first layer. It is used to build up a larger, more handleable mold.

Once the mold has set, an epoxy resin may be poured into it. One interesting advantage of this procedure is that the mold can be reused to make multiple epoxy replicas. They are useful as teaching aids since every student examines the same object with the same features. Gold or carbon coatings can be sputtered onto positive replicas to enhance viewing in reflected light or to prepare the replica for SEM examination.

Sections on replication techniques are in both the Visual Examination and Light Microscopy and the Transmission Electron Microscopy (TEM) chapters in the ASM Handbook on Fractography.[5]

In general, some practice is needed to create successful replicas with good detail and without artifacts. Before a critical component is replicated, it is prudent to practice with the materials to optimize one's procedure.

(a) Top view of the fractured all-ceramic crown (first upper left molar) in the patient's mouth. The broken crown is cleaned with alcohol on a cotton swab.

(b) The crown is water spray rinsed and air dried.

(c) A light body precision impression material is injected around the fracture surface.

(d) The whole crown is covered with more impression material.

(e) The mold is removed.

(f) A positive replica is cast with epoxy resin. It is then gold coated for SEM examination.

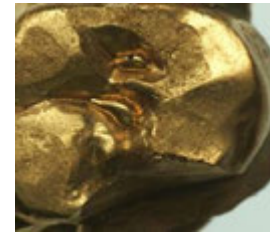

Figure 3.34 *Steps in the preparation of a dental replica that is a positive duplicate of a fractured crown. Photos a-d were taken in the patient's mouth. Figure 6.80 has additional views of this fractured alumina crown. (Photos and technique courtesy of S. Scherrer, Univ. Geneva)*

(a)

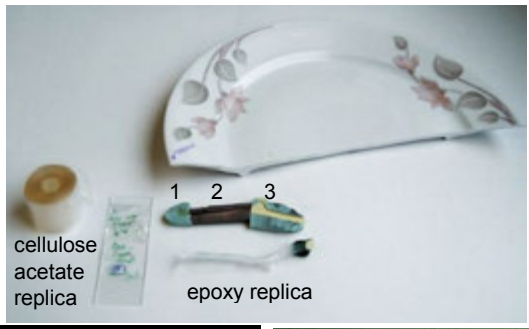

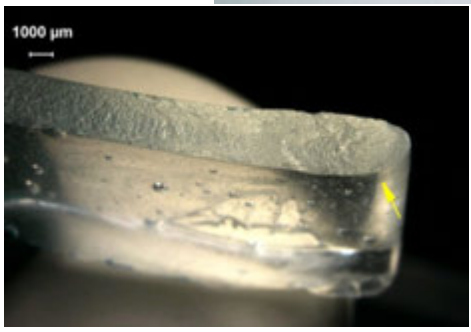

(b)

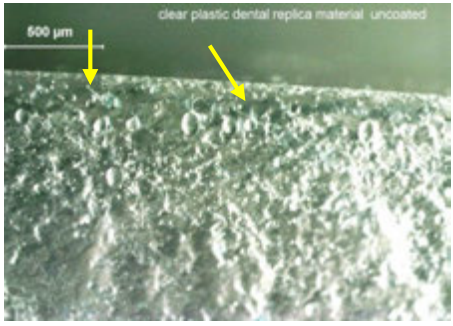

(c)

(d)

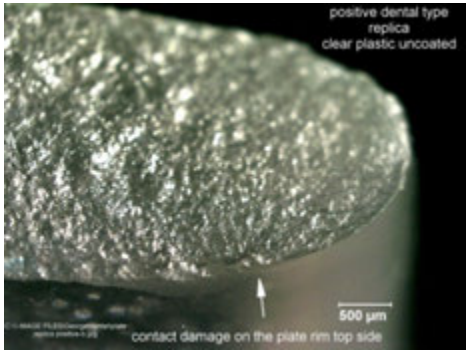

Figure 3.35 *Replicas of a broken whiteware plate. (a) shows both a cellulose acetate tape replica on the left, and a dental PVS mold and epoxy positive replica on the right. The PVS mold was cut into 3 pieces (labeled 1,2,3) and the middle one gold coated. (b) shows the cast epoxy resin positive from the plate rim area. (c) shows a close-up of the epoxy replica. Telltale small wake hackle lines (described in chapter 5) are seen in the glaze (arrows). These little "weathervanes" are more easily seen in the glaze than in the whiteware body and they help direct one's attention back to an origin area shown in (d) . Coarse hackle lines (chapter 5) lead back to the origin site, a contact damage crack on the rim marked by the arrow. Coating the clear epoxy with a thin gold coat would have made the markings even easier to interpret.*

Figure 3.36 *A conventional scanning electron microscope.*

3.13 Scanning Electron Microscope

Despite the versatility of optical microscopy, there inevitably will be cases where the fracture initiating flaw is too small to be clearly discerned and the scanning electron microscope (SEM) is required (Figure 3.36). The SEM is a complementary tool to the optical microscope. They "see things" differently. It is best to examine specimens with the optical microscope first, since much valuable information such as color, reflectivity, and internal flaws in translucent or transparent materials cannot be detected by the SEM. Nevertheless, the SEM is a versatile tool that can view large portions of a specimen at low magnifications and yet instantly zoom in for high-resolution close-ups of regions of interest. It can also provide compositional information. The practical limits of magnification for fractographic analysis are of the order of 10X to 20,000X.

Modern SEMs are not difficult to use and materials scientists and engineers can perform their own routine examinations without the need of an expert operator. The advent of commercial SEMs and transmission electron microscopes in the 1960s led to a quantum jump in the quality of fractography of ceramics and glasses. Researchers and engineers could finally see and characterize the strength-limiting flaws that previously were too small to be clearly discerned with optical microscopy. It is fair to say that the SEM opened up a whole new

world of possibilities for fractographers, processors, and mechanical testers and led to many major advances in materials science and engineering.[c]

The SEM uses electrons as a signal source and, since the probe size can be made smaller than the wavelength of light, smaller features can be resolved and much greater magnifications achieved. A vacuum is necessary to remove gas that would interfere with the electron beam. The SEM has superb depth of field over a broad magnification range. For a working distance of 20 mm, the depth of field may be 0.4 mm at 100X or 40 μm at 1000X and 4 μm at 10,000X.[6] Sometimes the SEM is preferred for this reason at even low magnifications (100X to 500X) that are well within the range of optical microscopes. On the other hand, SEM images often look flat and tend to de-emphasize large surface topography changes. The SEM image can also be deceptive and it may be confusing to interpret whether a feature projects above the surface or is a depression below the surface. Stereo SEM viewing, described below, can help solve this dilemma. A great advantage of the SEM is that compositional analysis can also be done using accessories that detect X-rays emitted from the fracture surface.

Specimens must fit into the vacuum chamber and are usually cut and mounted on a small aluminum stub that will be placed into the SEM as shown in Figure 3.37. The SEM should have a large opening to accommodate broken fragments and test specimens without having to cut or trim them to small sizes. The stage has external controls that permit the specimen to be positioned in X, Y, and Z directions, rotated, and tilted. The size of the chamber and the mount station, plus the clearance to the electron optics all put limits on the size of specimens than can be examined. A good SEM for fractography has a large chamber, a large entry port, and can pump down with a minimum of difficulty.

Specimens on an aluminum stub are shown in Figure 3.37(b) and 3.38. It is convenient to cut the specimens so that they will sit square and facing upward. Irregular specimens can be propped up by small metallic pieces. It is best to cut multiple specimens to have similar lengths to minimize refocusing time when viewing in the SEM. A small laboratory cut off wheel with a thin diamond wafering saw is also handy for cutting long specimens into manageable lengths for the SEM. The specimens should be cut so that the fracture surface is approximately perpendicular to the incident beam in order to avoid distortions from foreshortening. Once in the SEM, the specimen

[c] The coincidental advent of modern fracture mechanics in the late 1950s, described in chapter 7, also led to major breakthroughs in the study of ceramics and glasses.

(a)

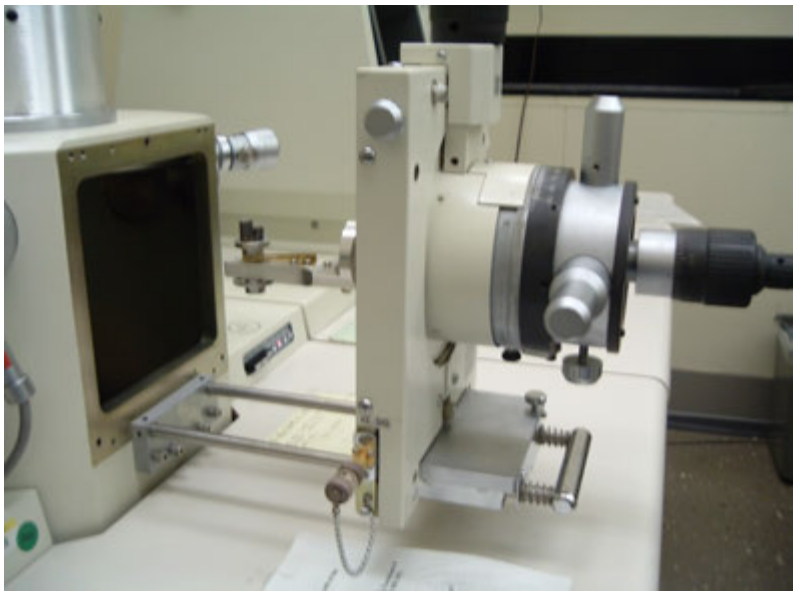

(b)

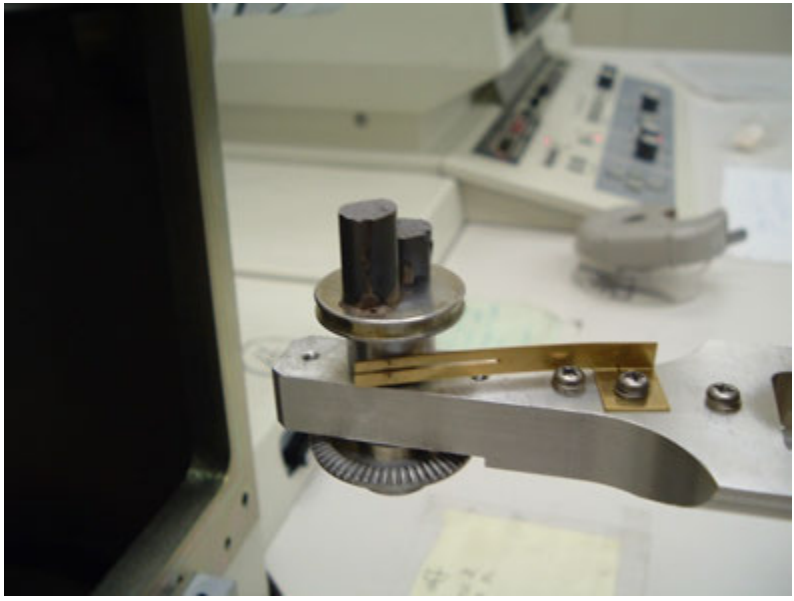

Figure 3.37 *(a) shows an open SEM vacuum chamber showing the specimen station on the left and the positioning controls on the right, outside of the chamber. (b) shows a close up of the two fracture specimens on their stub on the examination mount. Both fragments had to be cut from longer pieces to fit in the chamber. This model has a large opening and the stage can accommodate specimens as tall as 25 mm.*

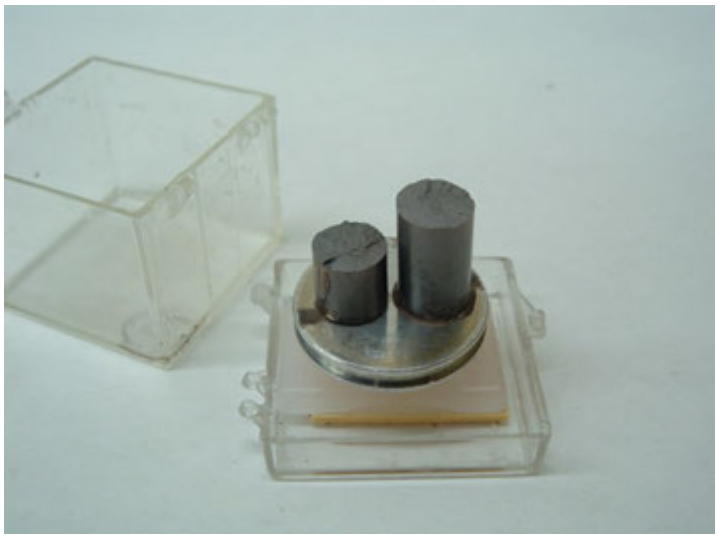

Figure 3.38 *Two matching fracture halves of a broken round tension specimen on a stub in a protective plastic box. Silver paint was used to attach the specimens to the stub. Ideally, the halves should have been cut to similar lengths to save time refocusing in the SEM.*

Figure 3.39 *SEM specimen preparation tools. Clockwise from the top left are two SEM length calibration standards, two silver paint bottles, a double-sided conductive adhesive tape roll, two sheets of double-sided conductive adhesive disks, and an assortment of aluminum stubs.*

can be tilted to enhance the emissions and signal responses if necessary.

Figure 3.39 shows some common accessories and tools for SEM examination. The specimens must be cleaned carefully of greases, dust, or debris. It can be exasperating to find a tiny piece of dust right on top of the origin site when the specimen is in the chamber. Soaking the specimen in a small beaker of acetone in an ultrasonic bath for a minute or so is often effective. After removal, a gentle blast of compressed air can eliminate any acetone residue. Sometimes it may be sufficient to swipe the fracture surface with a cotton swab soaked in acetone. Small trays or plastic boxes are convenient for holding the specimens and protecting them from contamination prior to examination. Special containers are available for mounting stubs. The best procedure is to keep the specimens as clean as possible from the moment the fragments are recovered.

There must be a good electrical contact between the specimen and the stub. The specimen can be affixed to the stub by silver paint or by conductive carbon double-sided sticky tape. If multiple specimens are placed on a stub, it *is a good idea to make a hand drawn sketch or map to show which specimen is where on the stub,* lest the viewer become confused when viewing the array in the SEM. Furthermore *all the specimens should be oriented in a similar way*. For example, if a series of bend bar fracture surfaces are being examined, they all should have their tensile surfaces facing the same way. Otherwise, much time can be lost getting oriented or searching the wrong areas during the SEM session. A set of optical photos of the fracture surface can be handy when the specimens are examined in the SEM.

The next step for most SEM examinations is to apply a thin 5 nm to 40 nm conductive gold, gold-palladium, or carbon coating by means of a sputter coater shown in Figure 3.40 or a thermal evaporator. The former is preferred for rough surfaces. The coatings are needed for ceramics and glasses in order to eliminate surface charge build up from the electron bombardment. For most applications, the coating does not interfere with the image. A coating is not needed for conductive ceramics or for examinations with low accelerating voltages (1 keV to 5 keV). Low accelerating voltage examinations may have a diminished resolution, however. Carbon coatings are used if X-ray information of lighter atomic weight elements is desired. Coating with gold or carbon is a simple procedure that only takes a few minutes. Sometimes a gold coating may be applied to facilitate some *optical microscopy* that is scattered back up through a fracture surface in translucent or transparent specimens (see Section 3.9, page 3-26). The sputter coater will preferentially coat from one direction, and sometimes it is advantageous to position the specimen and the stub at an angle so that shadow coating will occur on the surface. Slight charging on

Figure 3.40 *A gold sputter coater used to apply conductive coating. It is helpful for both optical and scanning electron microscopy.*

some edges of the fracture surface may enhance the image by promoting contrast. Coating along the specimen sides may be incomplete, so sometimes it is wise to add a thin silver paint line along the specimen sides from the fracture surface to the stub. Of course, the silver paint should be kept well away from the fracture origin or any features of interest on the fracture surface. The conductive coating step may be omitted for some modern SEMs that operate at low accelerating voltages and low vacuums as described in a later section on environmental SEMs. Additional details and tips on coatings for SEM examination may be found in the paper by Healy and Mecholsky.[7]

The SEM can be operated in several modes. A focused beam of high-energy electrons (typically 1 keV to 30 keV) is rastered over a rectangular portion of the specimen. Some electrons interact with the specimen surface and some penetrate into the volume. Figure 3.41 shows that the interaction volume is larger than the size of the incident beam, which may be as small as 10 nm diameter.[8] The three most important signals are secondary electrons, backscattered electrons, and X-rays. Secondary electrons reveal the surface topography. Backscattered electrons give a combination of the topography and atomic number and crystallographic information. X-rays reveal compositional information.

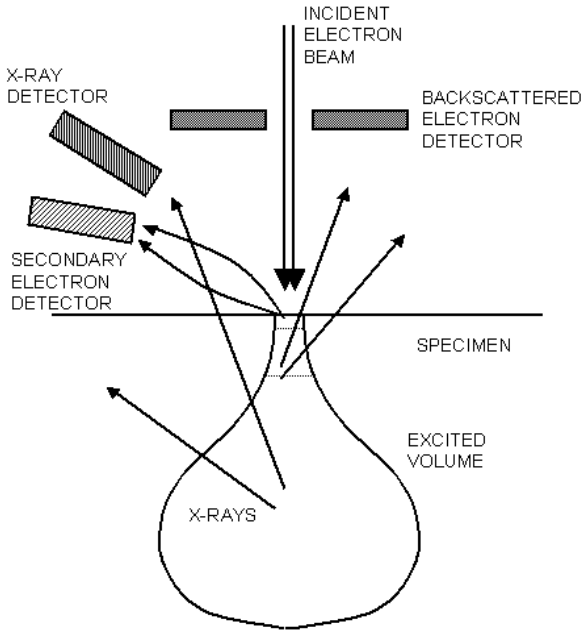

Figure 3.41 *The electron beam interacts with the specimen surface and volume creating emissions that may be analyzed. Signals are generated in all directions, but they come from different depths of the material. The beam is rastered over the surface and an image is sequentially formed.*

The initial working distance can be adjusted to enhance the field of view and the depth of field. Long working distances allow a lower minimum magnification which is sometimes helpful in initial orientation or in photographing the whole part or as much as possible. A longer working distance also allows the specimen to be tilted more. On the other hand, longer working distances reduce resolution and may reduce X-ray signal acquisition. Image clarity is also affected by specimen tilt. As noted above, having the surface perpendicular to the incident beam minimizes foreshortening, but secondary electron and X-ray collection can be maximized by tilting the specimen towards the detectors.

Initial inspections on older SEMs with a cathode ray tube (CRT) display often are typically with 500 line scans, but when a image is recorded on film, a higher resolution CRT with 2000 or more line scans is used. The raster of the beam on the specimen is synchronized with that of the electron beam that rasters across the display CRT. Modern SEMs with digital monitors also have differences in resolution between “live image” displays and captured images.

The secondary electron mode of operation provides the best spatial resolution and produces a surface topographical image. Secondary electrons are low energy electrons (10 eV to 50 eV) primarily produced from the material close to the surface. Since they are low energy, a positively charged detector off to one side can capture the emitted electrons for the image. These electrons may even follow a curved trajectory from the surface to the detector. Edge charging can be a problem with very rough surfaces or those with sharp corners and cracks, in which case gamma adjustments to the image may help. Gamma adjustments can suppress bright areas and enhance dark areas. For some edge charging cases, backscattered imaging may be preferred.

Backscattered electrons are higher energy electrons (5 keV to 40 keV), up to the energy of the incident beam and are emitted from a larger volume than the secondary electrons. The backscattered electrons travel in straight lines and are registered by a different detector that may have to be slid into proximity with the fracture surface. They often have a central hole for the incident electron beam. Backscattered electrons include both topographical and compositional responses. Detectors can be split ring or four quadrant (or more) versions and, by turning different elements on or off in the detector, it is possible to emphasize topographical or compositional information. Backscattered electron imaging is effective in detecting phase distributions in heterogeneous or composite microstructures and also aberrant features such as inclusions or second phase concentrations. Such information is often completely missed by secondary electron imaging.

Figures 3.42 through 3.45 show matching secondary electron and backscattered electron images of fracture origins. Figure 3.42 shows how the backscatter mode can even help highlight a controlled semi-elliptical flaw made by a Knoop indenter.

X-ray emissions provide valuable information about the elemental composition. This energy-dispersive spectroscopy by X-ray analysis (EDS or EDX) is especially useful for detecting and characterizing inclusions, second phase variations, or compositional inhomogeneities, which all may act as strength-limiting flaws. The analysis is over a region of the order of size of a few micrometers, but penetrates into the interior 1 μm to 2 μm. With most SEMs and with coated surfaces, elements from sodium (Z = 11) or heavier can be detected simultaneously. Lighter elements such as boron or carbon are not readily detected. A better resolution of the lighter elements is obtained with very thin gold or carbon coatings, or even uncoated specimens with low accelerating voltage. Newer detectors and vacuum-tight polymer windows

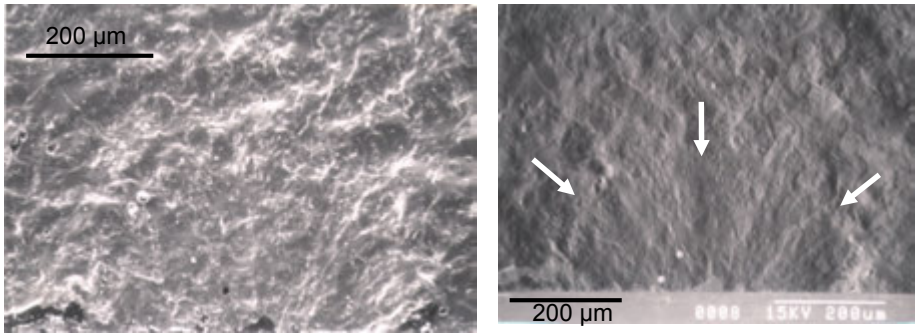

(a) (b)

Figure 3.42 *Comparative secondary electron (a) and backscattered electron (b) images of the fracture surface of a Knoop semi-elliptical precrack in a silicon nitride fracture toughness test specimen. The edge charging in (a) emphasizes certain features, but (b) shows that the flattening effect of the backscattering mode tends to better reveal the overall crack (arrows).*

(a)

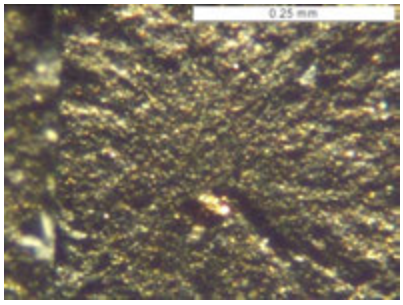

(b)

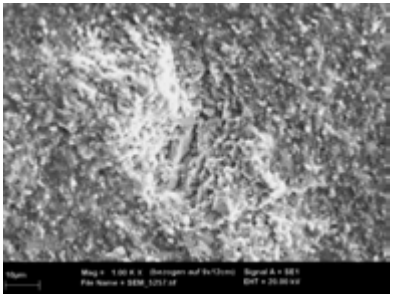

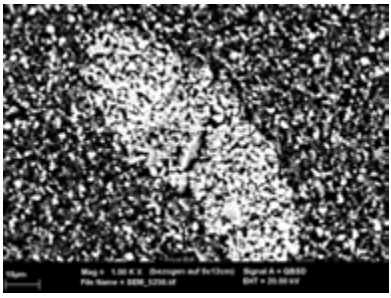

(c)

Figure 3.43 *Backscattered mode electron scanning electron microscopy is effective in showing compositional difference of fracture origins flaws relative to the background. (a) is an optical image of a silicon nitride with 30 mass % TiN bend bar illustrating the origin has a gold color (722 MPa). (b) is an SEM secondary electron image of the origin. (c) is a backscattered electron image of the flaw. This origin may be termed either a TiN agglomerate or a compositional inhomogeneity. (Courtesy J. Kübler, EMPA).*

(a)

(b)

(c)

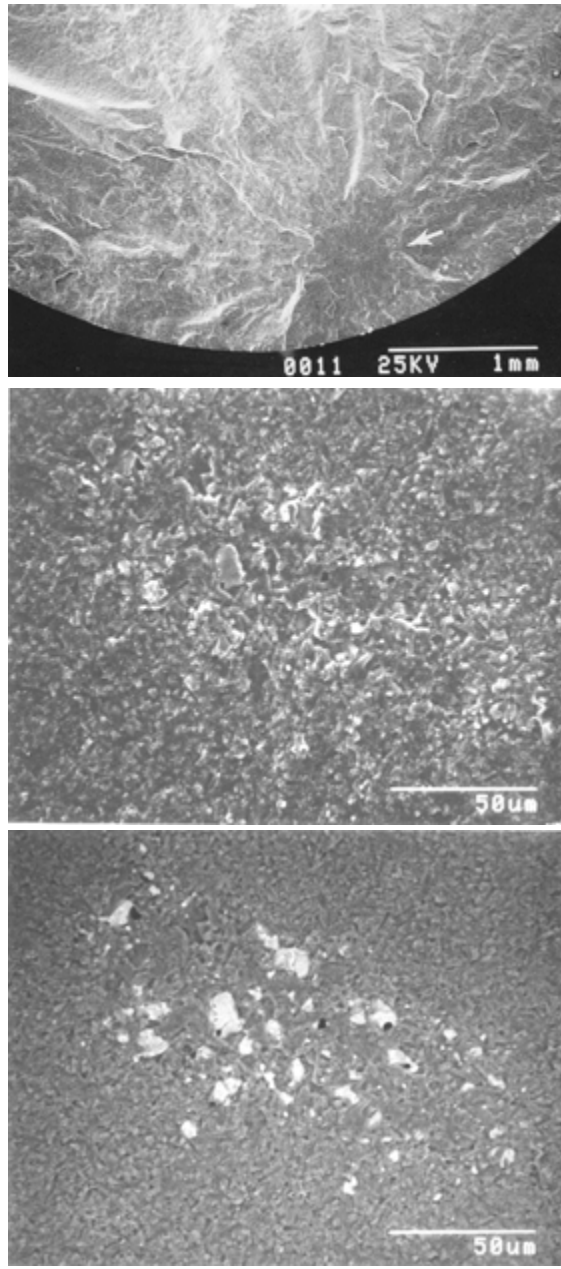

Figure 3.44 *A cluster of iron particles acting as an origin in a silicon nitride rod broken in flexure. The origin is below the surface. The stress at the origin was 682 MPa. (a) and (b) show secondary electron images and (c) is the backscattered image at the same magnification as (b).*

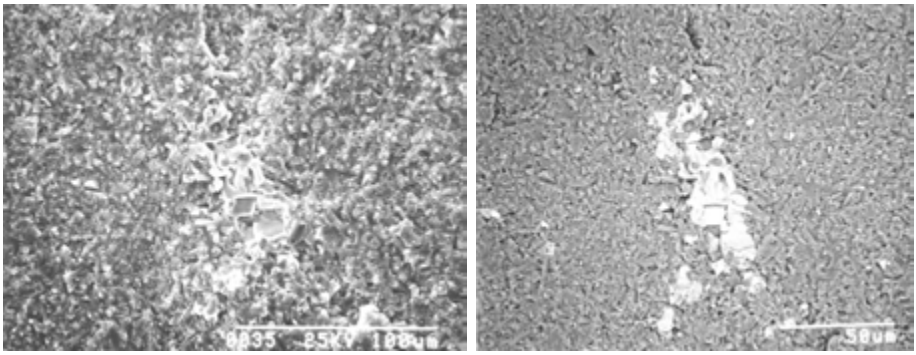

(a) (b)

(c)

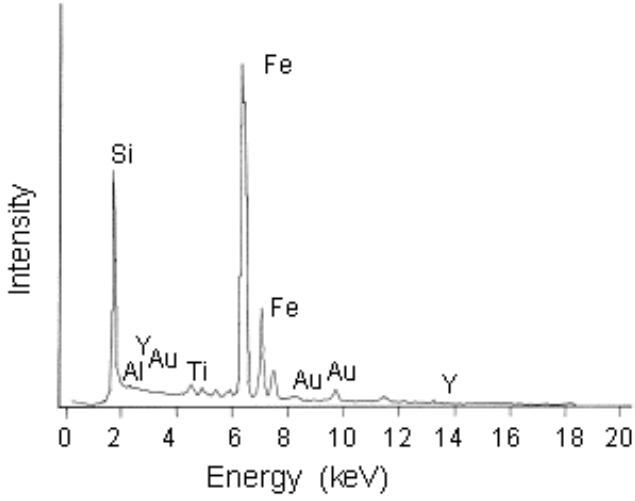

Figure 3.45 *An iron inclusion in a silicon nitride rod (684 MPa). Matching secondary electron (a) and backscattered electron images (b). (c) is the EDX pattern of the inclusion revealing it is iron.*

allow lighter elements including boron, carbon, nitrogen and fluorine to be detected with modern equipment.[9]

An X-ray scan may require several minutes as the electron beam illuminates the surface and the detector accumulates a sufficient signal of a range of emitted X-rays. A typical scan appears as shown in Figure 3.45c where signal intensity is plotted versus X-ray energy or wavelength. The specimen response is compared to known characteristic wavelengths of the various elements to identify which elements are present. A common procedure is to scan the critical feature, then rescan a different area away from the feature and compare the patterns. The accelerating voltages should be high enough to activate emissions from the elements. This should be 1.5 times the threshold energy of the element. So for example, to detect copper which has Kα X-rays of 8.0 keV, it is best to use an accelerating voltage of 12 keV or greater. Otherwise if the voltage is too low, then the X-rays will not be emitted or detected, even if copper is present.[10] Similarly, for zirconium, which has Kα X-rays of 15.7 keV, it is best to use an accelerating voltage of 25 keV or greater.

X-ray compositional maps, tailored to a particular element, may be made of the region being examined. The areas that contain the element in question emit X-rays and create bright spots on the map, whereas regions without the element appear dark. Digital image maps may be constructed with false colors representing areas of similar composition.

Figures 3.45a,b shows matching secondary electron and backscattered electron images of an inclusion in a silicon nitride tension specimen. Figure 3.45(c) shows the EDX analysis from a close-up view of the inclusion. In this case the iron peak stands out prominently. At other times, the inclusion peaks may appear only as a small fraction of the intensity of the primary constituent (Si in this case) due to the averaging effect of the area being imaged. Several peaks at different energies and intensities characterize each element and sometimes these will overlap with peaks from other elements, which can confuse the interpretation. Gold or palladium peaks from the coating may also be present. EDX analysis is usually semi quantitative, and even under the most ideal conditions, the mass fraction concentration is only precise and accurate to ± 1 %.[11] The minimum concentrations that can be detected are 0.5 to 1.0 mass fraction % under ideal conditions, but more typically is several mass fraction % or more.

Electron backscatter diffraction (EBSD) is a valuable tool for studying microstructures and can discern the variation of crystallographic orientation of individual grains, but it requires a flat specimen surface. An example is shown

Figure 3.46 *Electron backscatter diffraction map of the flat exterior surface of a tungsten carbide/11 mass % cobalt fracture toughness test specimen. The black crack has propagated through the microstructure. Individual grains with different crystallographic orientations are shown in color. Crack propagation was under static loading and was mixed inter- and transgranular, with the latter through the grains on* $[10\bar{1}0]$ *slip planes. (Image courtesy of R. Morrell and K. Mingard, NPL)*

in Figure 3.46[12] which images the exterior surface of a fracture toughness test specimen. A focused electron beam is scanned across a crystalline material and at each point an electron diffraction pattern is created and analyzed. At the present time EBSD is not amenable to analysis of rough fracture surfaces.

Magnifications displayed on the SEM monitor (e.g., 1000X) may not be accurate. Brooks and McGill state that accuracies of 5 % are typical.[11] The superimposed micrometer bars on the photos or images are usually better than a nominal magnification, but are not necessarily exact either. If quantitative measurements are made with the SEM, then care should be taken to ensure the fracture surface is not foreshortened. An SEM length calibration standard such as shown in Figure 3.47 should be used to check the magnifications. Some older SEMs have magnifications that vary across the field of view and which are not the same vertically and horizontally.

A paper by Healey and Mecholsky on SEM techniques and their application to brittle materials is very instructive.[7] An excellent, detailed article on the use of the SEM for fractography is by Brooks and McGill.[11]

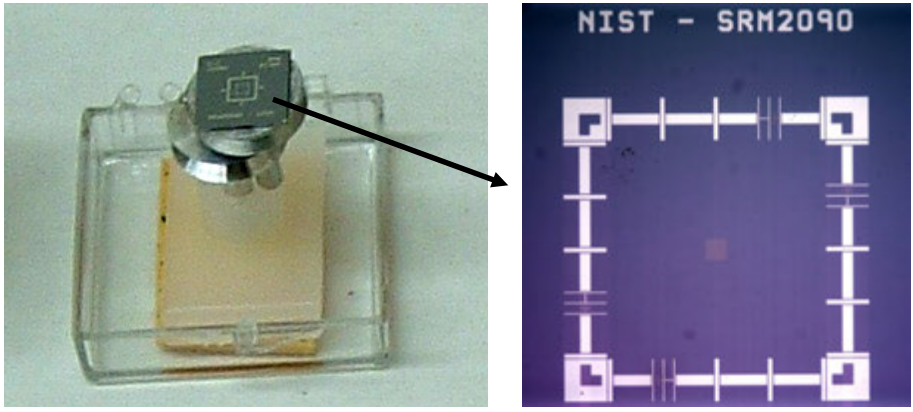

Figure 3.47 *A NIST Standard Reference Material SEM length calibration standard. Finely spaced reference lines are located at intervals along the sides of the box on the right close up view.*

3.14 Stereo SEM Imaging

The SEM takes pictures that make the surface look flat and do not show the topography clearly. A much better sense of the full topography can be revealed by the simple process of taking matching stereo photographs. Two photos of the same area are taken, but with the specimen tilted 5° to 15° in the SEM chamber between shots. A minor adjustment to the brightness and contrast may be necessary for the second photo, but is not essential. Some people are able to hold the two images in front of their eyes and focus the left eye on the left photo and the right eye on the right photo. The distance between the photos is adjusted and the eyes are "relaxed." The brain merges the images and interprets them as a single three-dimensional view. Most people find it easier to put the images under a stereoscope, which is a stereo viewing optical device as shown in Figure 3.48. The fractographer looks into two eyepieces and the photos are spaced apart and adjusted slightly back and forth until the three-dimensional effect is achieved. It may take a little practice to get the two images to register, but the usual trick is to focus each eye on an identical feature or spot in the two photos. Initially the two eyes will discern the spot as two separate images, but by carefully sliding one or the other photos around, the spots can be made to merge. At that instant the three-dimensional effect should be detected since each eye will be viewing the same surface, but from different perspectives. This may take a little practice, but the viewer helps make it easy for most people. One curious effect is that the perception of what

features are up or down may change depending upon which photo is on the left and which is on the right. It may be necessary to swap the photos to get the correct rendition. The orientation of the photos may have to be turned 90° as well in order to match the tilt angle used in the SEM.

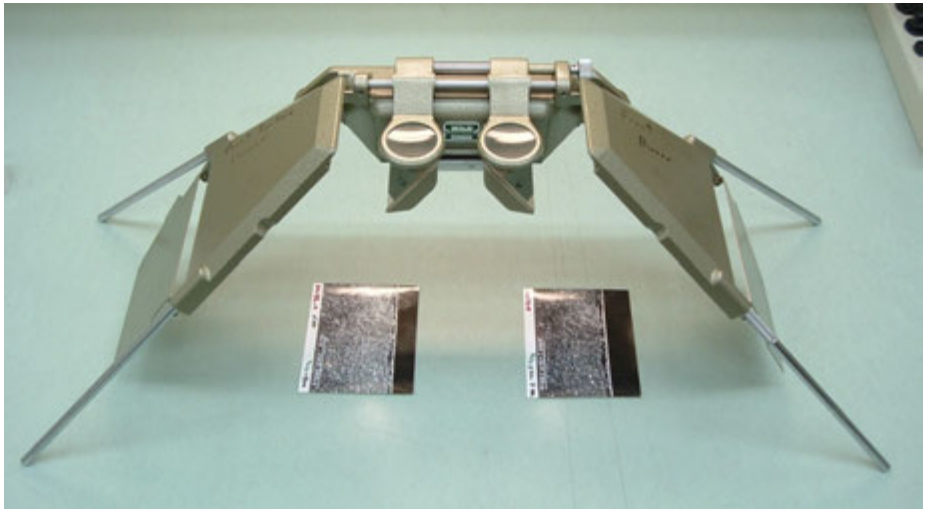

Figure 3.48 *Stereoscope. The two photos are placed under the viewer and the viewer looks into the two eyepieces. The photos are moved around slightly until they appear as one image in three dimensions.*

Some modern SEMs can digitally capture the pair or of tilted images, or even three images at different tilts. Image analysis software can then interpret the multiple images and constructs a pseudo three-dimensional rendition that is displayed on a monitor. The computer image can be rotated or displayed from different vantage points and height profiles through various sections can be displayed. Quantitative analysis may be done by a procedure known as stereophotogrammetry. A few applications to ceramics so far were hampered by contrast limitations[13] or lack of computing power,[14] but the latter problem probably is less of a concern now.

3.15 Field Emission SEM

Field emission scanning electron microscopes (FESEM) offer dramatic increases in magnifications (600,000X) compared to the SEM and improved resolutions down to 1 nm (Figure 3.49). They rival the resolution and contrast of many transmission electron microscopes. The field emission cathode replaces conventional tungsten cathodes on the common SEM. A smaller probe beam is used. Accelerating voltages are lower and conductive coatings are not needed in many cases. Energy dispersive X-ray spectroscopy (EDX) can be applied to smaller regions than in a conventional SEM. The FESEM is used much the same way that a conventional SEM is used for fractographic analyses. One problem with such microscopes is that the working distances and the pre-evacuation chambers are very small and it may not be possible to get large pieces into the microscope. The author used such a FESEM to take Figures 6.69 and 8.21 which show origin flaws in single crystal silicon as small as 200 nm, possibly the smallest fracture origin flaws ever detected.[15]

Figure 3.49 *A field emission scanning electron microscope*

3.16 Environmental SEM

The environmental scanning electron microscope (ESEM) is designed to operate either in a high or low vacuum unlike conventional scanning electron microscopes, which require a high vacuum. The environmental SEM can operate with environments having water vapor or other gases. A specimen coating is not needed, as static charges do not develop on the specimen since the gasses ionize and can neutralize excess electron charge build up on the specimen. Magnifications up to 100,000 are possible, but resolutions are less than that from a conventional SEM. One advantage of the ESEM is that dynamic processes such as corrosion or chemical reactions can be studied by time-lapse imaging. The ESEM is primarily used for biological materials or with materials when it is undesirable to apply a coating.

3.17 Transmission Electron Microscope

The transmission electron microscope (TEM) is capable of extraordinarily high magnifications and high resolutions (< 0.1 nm). It is limited to specimens about 0.5 μm or less in thickness, however. The TEM can reveal critical microstructural details. Prior to the advent of modern scanning electron microscopy, TEM was applied to replicas of fracture surfaces in order to study the fracture morphology. Today, the TEM is not used for routine fractographic analysis, but is a critical tool for research projects studying the effect of microstructure on properties. It can reveal crucial information about defect densities in grains, grain boundary sliding and cavitation, twin formation, damage accumulation, phase changes, fracture mode (intergranular or trans-granular), and grain boundary phases and their thickness. TEM specimens are cut from the bulk and then electrochemically or ion milled to very thin foils that are transparent to electrons. Alternatively, carbon replicas may be made for examination. Since the TEM examines only tiny portions of the material, it is almost never used to find and characterize fracture origins or classical fracture surface markings.

3.18 Atomic Force Microscope (AFM)

The AFM is a powerful microscope that uses a tiny tip (radius about 2 nm to 20 nm) at the end of a cantilever to probe the surface. The tip is brought into close proximity to the sample surface and either gently contacts the surface or taps it while the tip is oscillated close to the cantilever's resonant frequency. The probe is held at a fixed location in the X-Y plane and the surface to be examined is rastered in the X-Y plane. The Z-deflection of the cantilever is magnified by a laser beam that reflects off the cantilever into a position sensitive photo detector or interferometer. A computer records the X-Y and Z displacements and a three-dimensional image of the surface can be constructed. The AFM is capable of extremely fine resolution (10 pm) and does not require any special specimen preparation or testing environment, but the specimen must be very nearly flat and has to be mounted flat on a holder. The AFM is most frequently used in microelectronic and biological studies. It has been applied to the study of fatigue crack markings in metals and fracture mirror roughness measurements in glasses. There are limitations to the AFM. The scanned area is usually quite small, depending upon the resolution it can be as small as 1 μm square to as large as 150 μm square. The vertical surface features can only be a few micrometers in size. Acquisition times may be long. Color and reflectivity information are lost. Therefore the AFM is almost never used to search for fracture origins or other telltale fracture markings, but instead is used for very close up, high-resolution examination of surface roughness detail or coating evaluations. Hull used it to study the nature of mist and hackle lines in brittle epoxies.[6]

3.19 Optical Profilometer

Optical profilometers are designed to make non-contact three-dimensional surface roughness measurements from 0.1 nm to several millimeters. The sub nanometer resolution for an optical system with white light illumination source (halogen bulb) may seem surprising, but interferometry allows the small height variations to be resolved. Optical profilometers either translate the specimen vertically or, if the specimen is tilted slightly, laterally in front of an interferometer. Reflected light from the specimen and a reference surface are combined to form fringes that are projected onto a digital camera. Height variations are denoted by color and contrast differences in a computer generated image as shown in Figure 3.50. One advantage of the optical interferometer is that precise height and roughness variations are quantitatively recorded and can be interpreted by the program software.

(a)

(b)

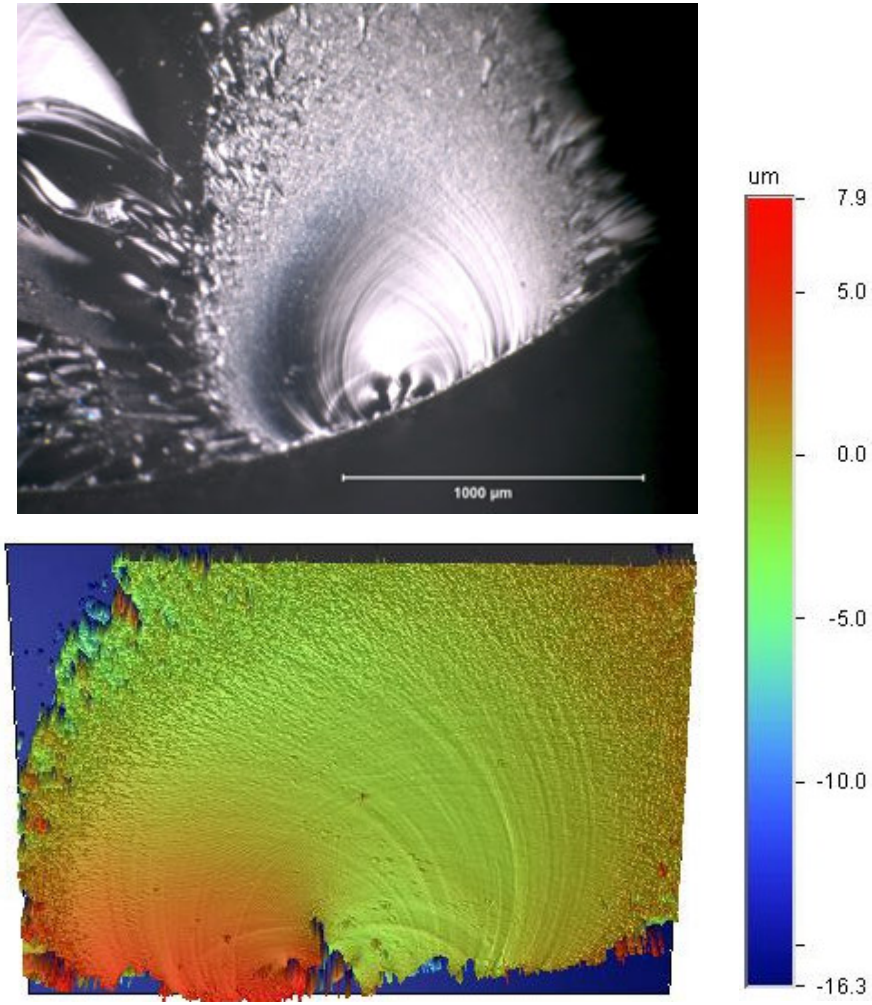

Figure 3.50 *Matching (a) optical microscope and (b) lateral scanning optical profilometer images of a fracture mirror in a ground glass rod. (b) shows an area 1.0 mm tall x 1.3 mm wide. The colors correspond to the scale range shown on the right (+7.9 µm to -16.3 µm). Wallner lines and mirror mist are readily detected and displayed. The origin is a surface crack from a scratch. (b is courtesy of R. Gates)*

3.20 Confocal Scanning Light Microscope

This is a variant of an optical microscope. Rather than broadly illuminate a fracture surface, a point source of light (often from a laser) is scanned over the surface and reflected into the microscope through a pinhole aperture. A lens with a large numerical aperture is used and on uneven surfaces only a small portion of the surface will be in focus. A photo-multiplier tube records the strong return signal from the in-focus regions. Optical slices of in-focus surface are registered and recorded by a computer as the focus is finely adjusted. The final product is a computer generated three-dimensional topographic map of the specimen surface, often in false color corresponding to the surface heights. Figure 3.51 shows an example for a glass fracture mirror. Resolutions are of the order of 0.25 μm or greater. The primary virtue of the confocal microscope is that in-focus images can be collected that would not otherwise be possible due to the limited depth of field of the light microscope. Quantitative information about height differentials can also be recorded. Confocal microscopes usually have longer image acquisition times than common optical microscopes with cameras, although some contemporary models can acquire and display images in as fast as $1/30^{th}$ s which is suitable for video rate imaging. A full topographical characterization can require 10 s or more.

Some fracture surfaces are difficult to view with a confocal microscope. Carbon and graphite surfaces reflect very little light back up to the lens. Single crystals can act as specular mirrors and reflect light away from the lens. Diffuse reflection may be enhanced by application of a coating in such cases.

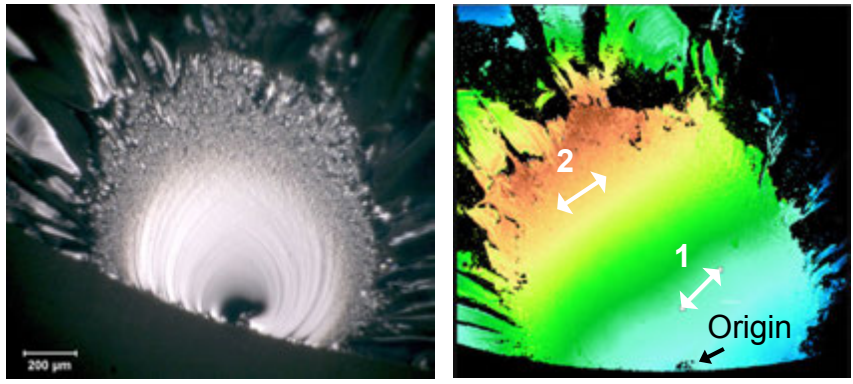

(a) (b)

(c)

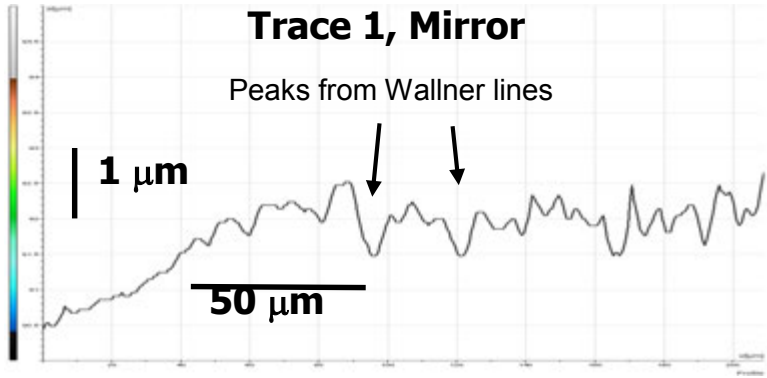

(d)

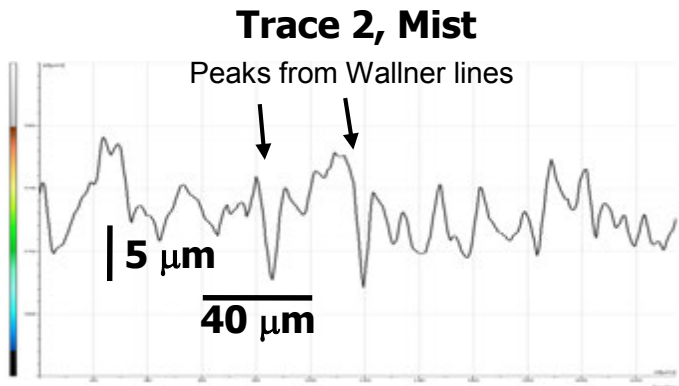

Figure 3.51 *Matching stereoptical (a) and confocal microscope (b) images of a glass rod fracture mirror. Height profiles for tracks 1 and 2 are shown in (c) and (d). The major peaks are from Wallner lines. The minor peaks show the inherent roughness in the mirror and mist regions. (b) and traces are courtesy of J. López-Cepero Borrego and A. Ramirez de Arellano Lopez, Univ. Seville.)*

3.21 Stress Wave and Ultrasonic Fractography

Ultrasonic or stress wave fractography is an effective fractographic tool in the laboratory that was pioneered by Kerkhof.[16,17] A transducer attached to the specimen creates continuous elastic waves at a specific frequency. The elastic waves create ripples on the fracture surface as shown in Figure 3.52. Local crack velocity can be simply calculated on the basis of the spacing between the lines and the frequency of the pulses. Richter and Kerhof [17] used 5 MHz lead zirconate titanate transducers to measure cracks running at terminal velocities in glass. Their review article has a wealth of additional details about this method and many fascinating examples of its use. Additional examples of their work are in section 5.4.4 on tertiary Wallner lines.

Tsirk improvised[18] with a simple hand-held woodworking palm sander that vibrated in a circular motion at 11,000 rpm (183 Hz) and was able to create makings on the fracture surfaces of obsidian pieces that he was knapping. Figures 5.48 d - f in chapter 5 show his images.

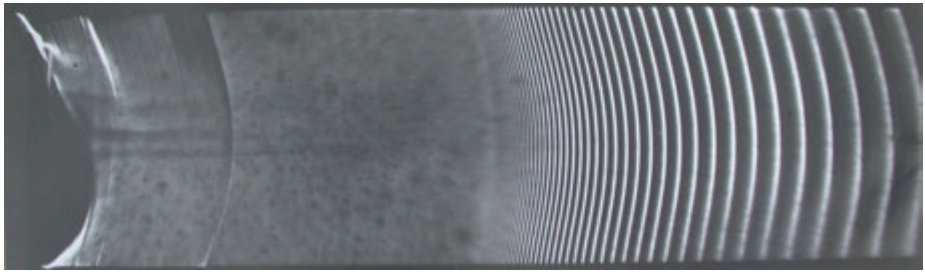

Figure 3.52 *Fracture in a glass plate. Fracture originated at the left and accelerated to the right as attested to by the increased spacing between the timing ripples. (Courtesy H. Richter)*

3.22 High Speed Photography

Studies of impact fractures have benefited from high speed photographic techniques. Field's review is good starting point.[19] The first extensive use of high-speed photography to study fracture in glasses was by Schardin and colleagues.[20] In 1937, Schardin and Struth used a multiple spark camera to observe that the terminal velocity of cracks in soda lime glass was about 1500 m/s.

3.23 X-Ray Topography

X-ray topography is a specialized technique for single crystals.[21,22] An X-ray beam illuminates the test specimen and images formed using the diffracted beams are recorded. The image from an ideal crystal is completely homogeneous, but imperfections that distort or "strain" the crystal lattice produce image contrast. Often the defects themselves are not visible. It is the disturbances to the lattices that are revealed, and these are often magnified in size relative to the defect size. X-ray topographs will reveal dislocations, stacking faults, inclusions, and surface damage. Since diffracted X-rays form the image, interpretation is not always straightforward. Figure 3.53 shows examples of X-ray topographs. They reveal handling damage on and below the polished surfaces of a sapphire hemispherical domes and which were not visible with the optical or scanning electron microscopes.

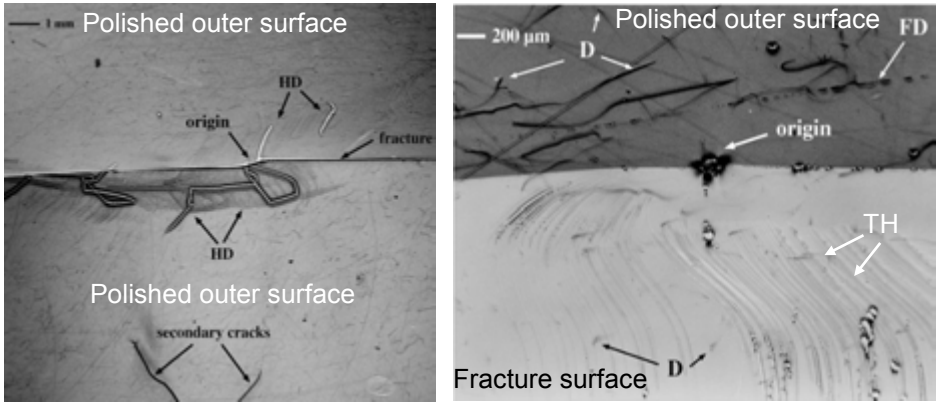

(a) (b)

Figure 3.53 *X-ray topographs of a fractured sapphire hemispherical dome. (a) shows the outer polished surfaces of the matching fracture halves. The broken halves were carefully realigned for this image. It reveals handling damage (HD) cracks not readily visible to the optical or scanning electron microscopes. (b) shows a close up of one piece tilted to show both the fracture surface and outer polished surface. Twist hackle – cleavage step lines (TH), dislocations (D), and fabrication damage (FD) are apparent. (Courtesy D. Black).*

3.24 Dye Penetration and Staining

Dye penetration is a staple of nondestructive testing, but it also has value for fractographic analysis. It is commonly used to search for hidden cracks in a ceramic part prior to usage or after exposure to some loading or environmental conditions. Simple staining with common dyes such as the felt tip pens shown in section 3.9 can aid post-fracture interpretation in porous or coarse-grained materials that are otherwise very difficult to interpret. The dye can be applied to the fractured parts. For example, Figure 3.54 shows a portion of a fractured porcelain toilet tank. Simple staining revealed tiny incomplete crack branches that gave a clear indication of the direction of crack propagation. Figure 4-30 shows thermal shock cracks highlighted by red dye.

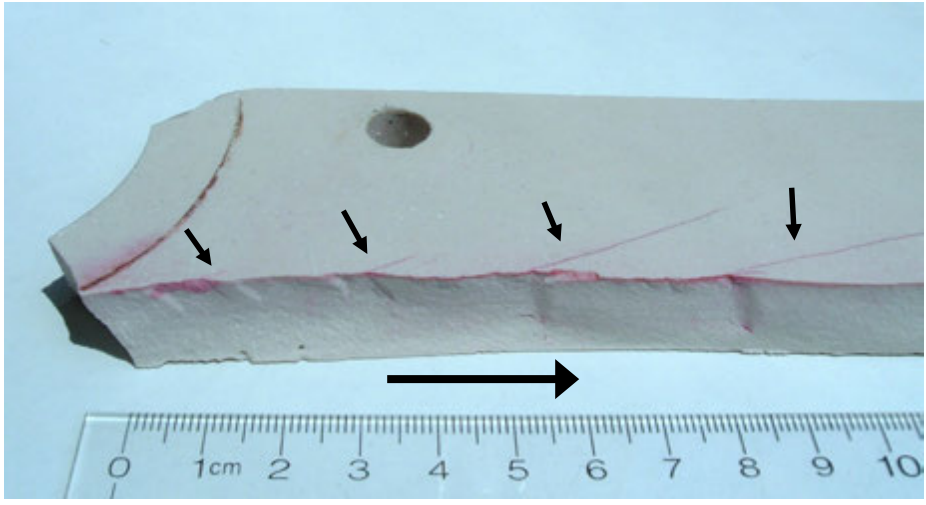

Figure 3.54 *Fractured porcelain part with dye penetration by a common felt-tip pen. The dye reveals crack branching patterns (small arrows) and thus the direction of crack propagation (large arrow).*

Dye penetration is sometimes used with ceramics to try to penetrate grinding induced cracks, but these are often very small and tight, making penetration problematic. Examinations of the fracture surfaces are done after fracture to ascertain whether the dye has penetrated beneath the ground surface. Dye "bleeding" can be a problem if the dye migrates into the fracture surface either during the fracture event or afterwards.

Simple colored staining dyes or felt tip pens may be used with white ceramics. Level 4 ultrahigh sensitivity fluorescent dyes are used with dark ceramics. Ultrahigh penetrating fluorescent dyes are needed to get into the tiny cracks. Special precleaning and soaking steps sometimes are necessary to facilitate dye penetration. Sometimes it may even be necessary to heat or vacuum treat a part to eliminate adsorbed gasses on the crack faces prior to dye penetration. After penetration, ultraviolet or "black lamp" illumination (Figure 3.55) is used to excite the dye such that it fluoresces and can be seen by the eye. Parts may be examined under a stereoscope, but the images are dim since the amount of light emitted is very slight. It is difficult or impossible to photograph features under these conditions. Compound optical microscopes, on the other hand, may be used with intense xenon light sources and fluorescent filters so that images may be captured as shown in Figure 3.56. The photo shows an image made on an older generation instant developing film that was exposed for several minutes. Digital cameras would have made a better recorded image. Figure 3.57 shows a C contact damage crack in a large notched silicon nitride ball prior to and after a controlled fracture.[23] Fischer et al.[24] have used fluorescent dyes on flaws in dental ceramics.

Figure 3.55 *Fluorescent dye penetration equipment. Two double torsion specimens are shown. The white one is an alumina, the black one, a silicon nitride.*

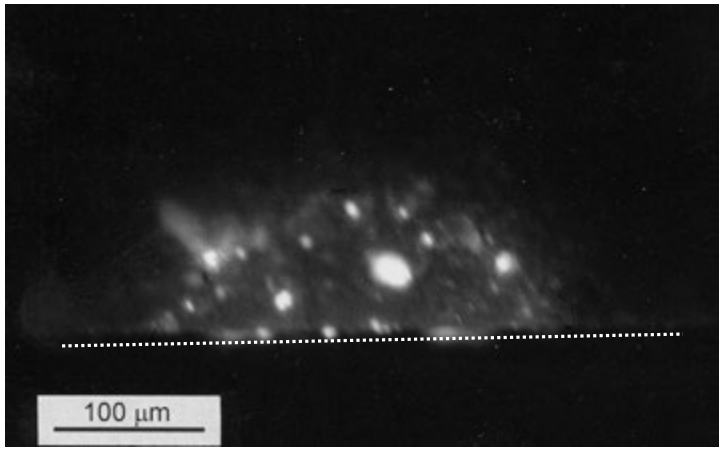

Figure 3.56 *Fracture surface of a silicon nitride specimen with a Knoop semielliptical surface crack that was penetrated by a fluorescent dye prior to fracture. The dashed line is the specimen bottom surface. This photo was made with a compound microscope with xenon bulb illumination and a fluorescence filter at a nominal 200 X magnification. The dim blurred image is typical for the weakly-emitting dye penetrant. This photo was made with old style instant-developing film that was exposed for several minutes.*

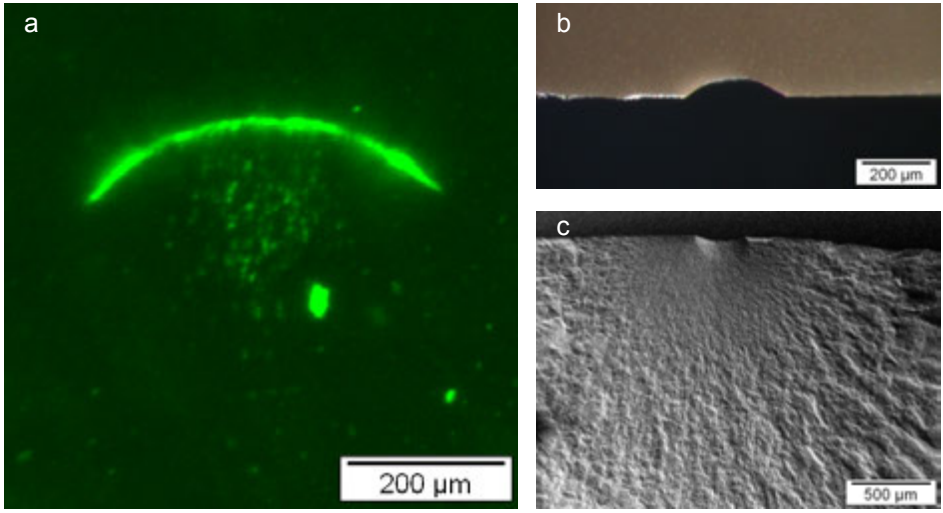

Figure 3.57 *C contact damage crack in a silicon nitride ball. (a) shows the outer surface and the crack highlighted by fluorescent dye penetrant. (b) shows one half of the notched ball after it was broken. (c) shows the fracture surface. (Courtesy T. Lube and R. Danzer, Mountain University Leoben).*

Machining cracks are small and tight, and difficult to dye penetrate. Part of the problem with them is that there usually is a thin zone (of the order of only a few micrometers) on the surface that is in residual compression. It clamps the cracks tight at the surface. Mizuno et al.[25] devised a clever procedure to use a metallic solution with $Pd(NO_3)_2$ impregnation in a vacuum. The solution normally would not penetrate the as-ground surfaces, but this was overcome by two methods. One was to polish off the surface compression layer. The alternative method was to apply a small amount of bending to open up the cracks for penetration on the tensile surface. The palladium-penetrated cracks were evident on the fracture surfaces when viewed by SEM, presumably in the backscattered mode. Kanematsu used this methodology but with an electron micro probe to study machining cracks by using cold-isostatic pressing to infiltrate the dye. [26,27,28,] He further used plasma etching to highlight the surface and subsurface damage around grinding damage and indentations.[27,29] Figure 3.58 from reference 28 shows matching SEM images and palladium maps for three different specimens ground with a 100 grit, 75% concentration, resin-bonded diamond wheel.

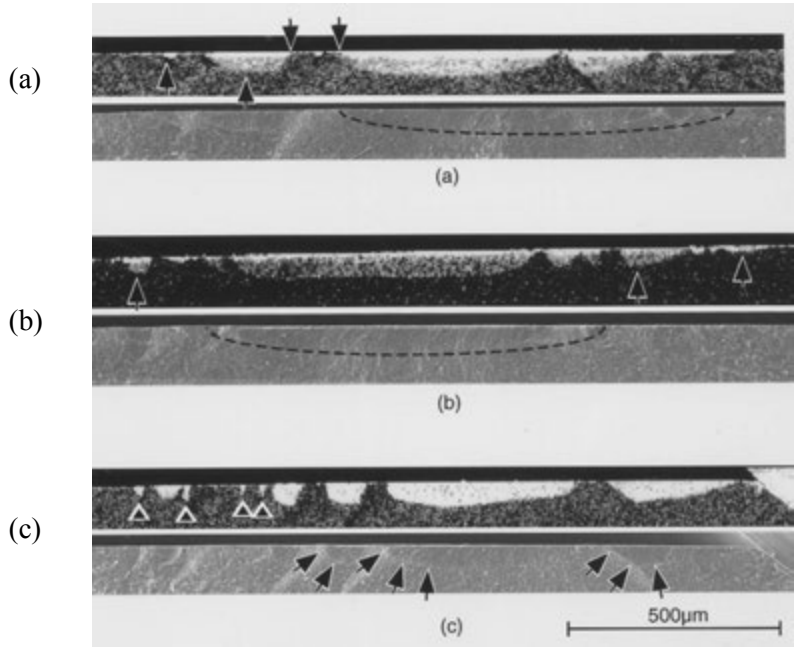

Figure 3.58 *Grinding cracks in silicon nitride revealed by palladium nitrate solution impregnation. These are paired views of fracture surfaces for three different specimens. The first image in a pair is a palladium map. The second is a conventional backscattered SEM image at the same magnification. (Courtesy of W. Kanematsu).*

The Nagaoka University of Technology in Japan has done fine work with novel dye penetration methods to investigate three-dimensional structures and flaws in powdered compacts and fired ceramic structures. For example, Professors Uematsu and Tanaka and students have used potassium iodide and iodine in diluted water missed with a saturated boric acid solutions to study the uniformity and lack of uniformity in pressed compacts.[30,31]

3.25 Polariscope

As discussed in section 3.7 on lighting, transparent objects may be viewed through crossed polarizers. A dedicated polariscope such as shown in Figure 3.59 may be used to examine large objects such as bottles or plates held between the rear polarizer and illumination source and the front polarizer (or eyepieces).

In photoelastic materials the existence of residual stresses may be revealed by light and dark patterns or color bands. Glasses and plastics are photoelastic. The method is based on the property of birefringence, whereby a light ray passing through the material has two refractive indices. Many crystals are birefringent, but plastics and glasses become birefringent when stressed. The strains in the body cause the horizontally- and vertically-polarized light waves

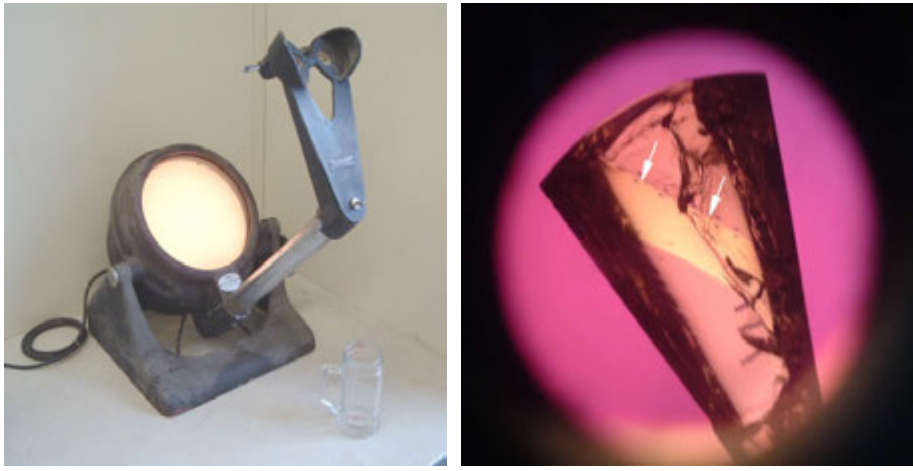

Figure 3.59 (*a) shows an old but still very useful polariscope. (b) shows a twin band (arrows) in a complex single crystal sapphire part. The photo was taken by a simple digital consumer camera held up to the eyepiece*.

to travel at different velocities through the stressed material in the directions of the maximum principal stresses. Photoelastic analysis is usually applied to two-dimensional X-Y problems, such as plates or bottles and vials. The stresses that are revealed are those that are in the X-Y plane of the structure and not those that may exist through the thickness. If the stress optical coefficient for the material is known, then quantitative stress estimates may be made. Highly stressed parts will have a sequence of alternating light and dark bands, or "fringes," that can be counted and used with the stress-optic law to estimate the stresses. One thing a fractographer should keep in mind is that once a part breaks, the internal strains can be relieved to some extent, and the stress distribution will be different than that in the unbroken part.

Polariscopes are also valuable with single crystals. Twins may be revealed as shown in Figure 3.59b.

3.26 Other Equipment

A common scanner such as shown in Figure 3.60a is handy for converting print images to digital JPEG or TIFF files.

Figure 3.60b shows a simple ultrasonic cleaner that is helpful for cleaning small specimens prior to SEM examination. The specimens may be placed into small beakers with a solvent such as acetone and then placed into the sonic cleaner bath which is partially filled with water. Methyl alcohol is effective in removing finger prints. A few minutes vibration is usually sufficient to remove common contaminants and cutting debris.

Figure 3.60 *Other useful equipment for a fractography laboratory. Digital scanner (a) and ultrasonic cleaning bath (b).*

Simple cutoff or wafering machines (Figure 3.61) are handy for cutting large specimens to sizes that can be mounted in optical or scanning electron microscopes. Cutting should be done wet to flush debris away and to minimize heating of the specimen.

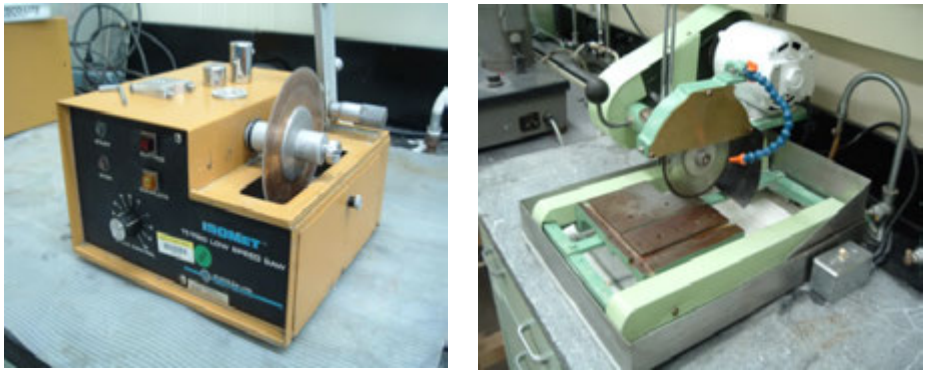

Figure 3.61 *Wafering and cut off wheel machines.*

3.27 Other Resources

The ASM Handbooks Volume 11 on Failure Analysis and Prevention and Volume 12 on Fractography have articles on fractographic equipment.[5,32] Appendix A of this Guide lists additional sources of information.

3.28 The Future

The merger of the microscope with digital cameras and computers will continue and virtual imaging with computer-generated topographical images will become commonplace. Despite all the advantages of the new tools and advanced technologies, they will never replace direct optical imaging. The stereoptical microscope will always be a primary tool since it is easy to use and retains color and reflectivity information and can capture internal reflections. Most of the new digital technologies emphasize topographic detail to the exclusion of all else. Very often a key feature will be fleetingly observed through the microscope eyepieces during the rotation of a specimen or the angle of lighting.

New computer software and digital camera technologies will enhance the capabilities of the conventional compound optical microscope so that it

partially replaces the scanning electron microscope. The latter is most commonly used at 200X to 1000X for fractographic work, since this is all the magnification that is ordinarily needed to find and record 5 μm to 100 μm size flaws. These magnifications are well within the reach of enhanced compound optical microscopes with digital cameras and Z-axis image stacking. On the other hand, the chemical (energy dispersive x-ray analysis) and structural analysis (electron diffraction) capabilities of the SEM will ensure it is a staple of the fractographers tool box for many years to come.

Microanalytical techniques in the SEM will continue to improve. Spatial variations in microstructure can have a strong influence on crack propagation. We tend to envision a microstructure as uniform with all the grains being randomly oriented. Variations in composition, grain orientations, and second phase distributions can have a profound influence on local properties and local crack propagation. Electron backscatter diffraction is limited at the present to very flat surfaces, but imagine how our eyes will be opened if it or some other technology can be applied to fracture surfaces.

Perhaps one of the greatest current limitations of the art of image storage and display is that it is all two-dimensional. Fracture surfaces are by their very nature three-dimensional, so something is lost when an image of a fracture surface is captured and stored in a computer's memory. This is partially solved by new image analysis computer programs used in conjunction with multiple SEM images (taken with different tilts) or optical microscopes with Z-axis rastering such that a computer generated model or depiction of the surface can be displayed. Such virtual images can be color enhanced and can be tilted, rotated, or viewed from different angles. Yet, they are all displayed on two-dimensional computer monitors.

One can imagine the future fractographer donning special eyepieces or a visor that enable him or her to traverse over or "fly over" a virtual fracture surface. These will certainly have considerable novelty value, but one wonders whether they will lead to better diagnoses than those made by an experienced observer looking through a simple stereoptical microscope. It is very common for the fractographer, while wiggling and tilting a fracture surface under a stereoptical microscope, to detect a fleeting reflection or stray subtle fracture line, which upon further examination unlocks the secret of a particular problem. Will future computer software and image analysis programs ever match this skill?

Perhaps the great breakthrough will occur when technology is invented that can capture genuine three-dimensional images that retain full color, reflectivity, and internal reflection information *and display* them with full fidelity in three

dimensions. The author can personally attest to the hours of desperate struggle to acquire the best two-dimensional image to capture a critical detail, only to feel despair when showing the image later and realizing that it "just doesn't show what the eyes saw."

Chapter 3 References

1. J. R. Varner, "Using Replicas in Fractography of Glasses and Ceramics – Advantages and Pitfalls," pp. 299- 307 in *Fractography of Glasses and Ceramics, VI,* eds. J.R. Varner and M. Wightman, Ceramic Transactions, Vol. 230, Wiley, Hoboken, NJ, 2012.
2. J. R. Varner, "Replicas as a Technique for Examining Fracture Surfaces of Ceramics," pp. 107-112 in *Fractography of Advanced Ceramics, III,* eds. J. Dusza *et al*., Transtech Publ. Zurich, 2009.
3. S. S. Scherrer, J. B. Quinn, G. D. Quinn, H. W. Anselm Wiskott, "Fractographic Ceramic Failure Analysis Using the Replica Technique," *Dental Materials*, **23** [11] (2007) 1397-1404.
4. V. D. Fréchette, *Failure Analysis of Brittle Materials*, Advances in Ceramics, Vol. 28, American Ceramic Society, Westerville, OH, 1990.
5. *Fractography,* Vol. 12, ASM Handbook, ASM Int., Materials Park, OH, 1987.
6. D. Hull, *Fractography, Observing, Measuring and Interpreting Fracture Surface Topography*, Cambridge University Press, Cambridge, 1999.
7. J. T. Healy, and J. J. Mecholsky, Jr., "Scanning Electron Microscopy Techniques and Their Application to Failure Analysis of Brittle Materials," pp. 157–181 in *Fractography of Ceramic and Metal Failures, ASTM STP 827*, ASTM, West Conshohocken, PA,1984.
8. B. L. Gabriel, "Scanning Electron Microscopy," pp. 166 – 178 in *Fractography,* Vol. 12, ASM Handbook, ASM Int., Materials Park, OH, 1987.
9. S. Burgess, X. Li, and J. Holland, "High Resolution Energy Dispersive X-ray Spectrometry in the SEM and the Detection of Light Elements Including Lithium," *Microscopy and Analysis*, May 2013, pp. S8-S13.
10. L. S. Chumbley and L. D. Hanke, "Scanning Electron Microscopy," pp. 516 – 526 in *Failure Analysis and Prevention,* Vol. 11, ASM Handbook, ASM Int., Materials Park, OH, 2002.
11. C. R. Brooks and B. L. McGill, "The Application of Scanning Electron Microscopy to Fractography," *Mater. Charact.,* **33** (1994) 195-243.
12. K.P. Mingard, H. G. Jones, M. G. Gee, B. Roebuck, J. W. Nunn, "In situ Observation of Crack Growth in a WC-Co Hardmetal and Characterization of Crack Growth Morphologies by EBSD," *Int. J. Refr. Met. Hard Mater*., **36** (2013) 136-142.
13. H. U. Marschall, R. Danzer, and R. Pippan, "Three-Dimensional Analysis of Decorated Ceramic Fracture Surfaces by Automatic Stereophoto-grammetry," *J. Am. Ceram. Soc*., **83** [1] (2000) 223 – 225.
14. T. D. Fletcher, J. J. Petrovic, and J. E. Hack, "Quantitative Fractography of SiC Whisker-Si_3N_4 Matrix Composites," *J. Mat. Sci.,* **26** (1991) 4491 – 4498.

15. G. D. Quinn, "Fractographic Analysis of Miniature Theta Specimens," *Ceram. Eng. Sci. Proc.*, **29** [3] (2008) 189 – 199.
16. F. Kerkhof, "Bestimmung der Maximalen Bruchgeschwindigkeit Verschiedener Gläser Nach Der Ultraschalmethode," *Glasstechn. Bericht*, **35** (1955) 267 - 272.
17. H. G. Richter and F. Kerkhof, "Stress Wave Fractography," pp. 75 – 109 in *Fractography of Glass*, eds., R. C. Bradt and R. E. Tressler, Plenum, NY, 1994.
18. A. Tsirk, *Fractures in Knapping*, Archaeopress, Oxford, UK, 2014.
19. J. E. Field, "High-Speed Photography," *Contemp. Phys*., **24** [5] (1983) 439 – 459.
20. H. Schardin and W. Struth, "Neuere Ergibnisse der Funken-kinemographie," *Zeitschrift Tech. Phys.,* **18** (1937) 474 - 477.
21. D. R. Black and G. G. Long, *X-Ray Topography*, NIST Recommended Practice Guide, NIST Special Publication 960-10, April 2004.
22. D. Black and G. D. Quinn, "X-ray Topography for Fractography of Ceramic Single Crystals," *J. Fail. Anal. Prev.,* **6** [3] (2006) 69 -76.
23. T. Lube, S. Witschnig, P. Supancic, R. Danzer, and O. Schöppl, "The Notched Ball Test – Characterization of Surface Defects and Their Influence on Strength," pp. 225 – 234 in *Fractography of Glasses and Ceramics, VI,* eds. J.R. Varner and M. Wightman, Ceramic Transactions, Vol. 230, Wiley, Hoboken, NJ, 2012.
24. H. Fischer, F. Karaca, and R. Marx, "Detection of Microscopic Cracks in Dental Ceramic Materials by Fluorescent Penetrant Method," *J. Biomed. Mater. Res.*, **61** [1] (2002) 153-158.
25. S. Mizuno, N. Kobayashi, and K. Miyata, "Analysis of Sintered Silicon Nitride Grinding Damage," SAE Technical Paper 930163, March 1-5, 1993, SAE Int., Warrendale, PA, 1993.
26. W. Kanematsu, M. Sando, L. K. Ives, R. Marinenko, and G. D. Quinn, "Determination of Machining Crack Geometry by Dye Penetration Technique," *J. Am. Ceram. Soc*., **84** [4] (2001) 795-800.
27. W. Kanematsu, "Visualization of Subsurface Damage in Silicon Nitride from Grinding by a Plasma Etching and Dye Impregnation Method," *J. Am. Ceram. Soc.,* **89** [8] (2006) 2564-2570.
28. W. Kanematsu and L. K. Ives, "Propagation Behavior of Machining Cracks in Delayed Fracture," *J. Am. Ceram. Soc*., **87** [3] (2004) 500-503.
29. W. Kanematsu, T. Miyajima, and M. Sando, "Visualization of Knoop Indentation Damage of Silicon Nitride by Plasma Etching," *J. Am. Ceram. Soc.*, **84** [10] (2001) 2427-2429.
30. Z. Kato, S. Tanaka, N. Uchida, and K. Uematsu, "A Novel Method to Investigate the Non-uniformity of the Internal Structure of Granule Compacts," in *Key Engineering Materials, Vols. 206-213, Proc. 7th Eur. Cer. Soc.*, (2002) pp. 341 – 344, Trans Tech Publ., Zurich, Switzerland.
31. Y. Saito, S. Tanaka, N. Uchida, and K. Uematsu, "Direct Observation of Three-Dimensional Structure in Powder Compact," in *Key Engineering Materials, Vols. 206-213, Proceedings of the 7th Eur. Cer. Soc.,* (2002) pp. 657 – 660, Trans Tech Publ., Zurich, Switzerland.
32. *Failure Analysis and Prevention,* Vol. 11, ASM Handbook, ASM Int., Materials Park, OH, 2002.

4. GENERAL EXAMINATION AND FRACTURE PATTERNS

Analysis begins with a simple visual examination of the broken pieces. The general patterns of crack extension and branching not only point the way back to a fracture origin, but also provide information about the cause of fracture, the energy of fracture, and the stress state. The majority of brittle fractures start at one origin and radiate outward. Severe thermal stresses or impact loadings can create multiple origin sites. Sometimes once one primary fracture occurs, large fragments remain that are still under load, and they can have secondary fractures.

Fréchette defined the fracture origin as: "that flaw (discontinuity) from which cracking begins."[1] A slightly broader definition considers that the fracture origin is both a location and a flaw:

***fracture origin**: the source from which brittle fracture begins.*

Even if the primary objective is to find the fracture origin, the overall breakage pattern should be examined first. Most of this chapter is concerned with breakage patterns in general. Examination of the fracture surfaces is covered in Chapter 5. An experienced fractographer may simultaneously examine the general breakage pattern and the fracture surfaces. Chapter 6 covers the types of fracture origins that one might find.

Breakage may be sudden, unstable, and catastrophic as in a laboratory strength test or a dropped glass. Alternatively, it may be in stages as in a fractured dental crown restoration, or a crack growing in an automobile windshield.

Most but not all origins in glass are from surface- or edge-located origins. Ceramics fracture from volume, surface, or edge sources. The fracture origin is the site that had the worst combination of tensile stress and flaw severity. The latter is determined by the flaw size, shape, and thermoelastic or chemical interactions with the matrix. A large flaw may not necessarily trigger fracture, especially if it is located in a portion of a part that has low stress or it is very blunt such as a spherical pore. The severity of a flaw and whether local stresses are sufficient to trigger fracture are covered by principles of fracture mechanics presented in Chapter 7. This chapter begins with some generic breakage patterns and shows some common examples, both for laboratory tested specimens and component fractures. The end of the chapter has some general observations about fractures caused by mechanical overload, impact or contact, thermal, corrosion or oxidation, and some observations on how residual stresses may affect fracture patterns.

4.1 Specimen Reconstruction

The general examination often begins with specimen reassembly. Ideally all fragments are available. Even if the pieces with the origin are lost, valuable information can be gleaned from the fragments. With some experience and with a familiar breakage pattern, irrelevant shards or ordinary secondary fracture fragments may be ignored. At this point the fractographer should take care not to introduce contamination to the fragments and especially the fracture surfaces.

Sometimes an experienced fractographer is able to look at fragments of a familiar component or test specimen type and be able to immediately find the piece with the fracture origin. For example, experienced fractographers are able to sift through a bucket of tempered glass fragments and find the origin pieces on the basis of their telltale morphology.

A common concern is whether it is safe to put the pieces together. This step is discouraged when conducting analysis of polymer or metal fractures. In contrast, ceramic and glasses are hard and durable materials. The pieces usually fit perfectly together. It is acceptable to fit pieces together gently, taking care to avoid abrasion or chipping. Single crystals and glasses are more sensitive to chipping than polycrystalline ceramics and must be handled more carefully.

Simple adhesive tapes may be used to temporarily hold pieces together. Apply the tape sparingly and only on an external surfaces and not between fracture surfaces. Small strips of masking tape may be used judiciously, but it should be borne in mind there is a risk of contamination. Whatever tape is used, it should be a type that is easily removable. Keep in mind that a reassembled body held together by tape strips may be unwieldy.

In complex cases with multiple fragments, it may even be necessary to glue fragments together. Glues should be used sparingly and preferably in a tack-bonding mode away from candidate fracture origin regions. Avoid getting glue on the fracture surfaces. The overall assembly will fit better if there is no build up or misfits from glue joints between fracture planes. Simple cheap nitrocellulose air-drying cements[a] are suitable and set fast. They can easily be removed by peeling off with a fingernail or razor knife or by dissolving with common solvents. In special cases it may be necessary to use a strong cement to glue the pieces together on their fracture surfaces. Cyanoacrylate ester

[a] Duco cement or Scotch “All purpose adhesive, Super strength”.

("super") glues may be used since they can set with very thin bonds such that cumulative misfits are held to a minimum. Such glues can be removed by soaking in acetone or nail polish remover. *In any case, glues should be used sparingly and every precaution taken to prevent them from coming into contact with fracture origin areas*.

During reconstruction it may be helpful to mark the pieces with a number or letter scheme in order to expedite the examination and to minimize specimen–to-specimen refitting exercises. Judicious marking with a pencil or fine tip felt tip marker pens are effective, but care should be taken to avoid contaminating the fracture surfaces or the fracture origin. Felt tip pen markings can usually be removed with alcohol or acetone.

During the initial examination it may be advantageous to try *transillumination* on white and translucent ceramics. Transillumination, whereby the part is illuminated from behind or from the side, may reveal internal cracks, flaws, and microstructural irregularities not detected by examination of the outer surface. Figure 4.1 shows three examples.

4.2 Crack Branching Patterns

Crack branching and radiating patterns may be interpreted before the fracture surfaces are examined. Much of the fractographer's craft is in the observation and interpretation of these patterns. Crack branch patterns can lead back to an origin and also tell much about the stress state and stress magnitude. A simple example is a glass biaxial strength test specimen shown in Figure 4.2. The radiating pattern is intuitive and leads the observer back the origin which is in the disk middle. Sometimes multiple fractures can be simultaneously triggered. Examples are severe thermal shock fractures, or mid-body fractures on each side of an impacted bottle. Secondary origins are often present in components that initially break from one origin, but then the fragments themselves fracture.

The first general rule is the:

Law of Normal Crack Propagation*: a crack propagates normal to the direction of the maximum local principal tension stress.*

The word "normal" means "perpendicular." As the crack propagates, minor perturbations in the direction of local principal tension can modify the plane of cracking. These minor perturbations can create telltale markings such as Wallner lines or hackle on the fracture surface as described in Chapter 5. Internal stresses or inhomogeneities can also cause crack local deviations.

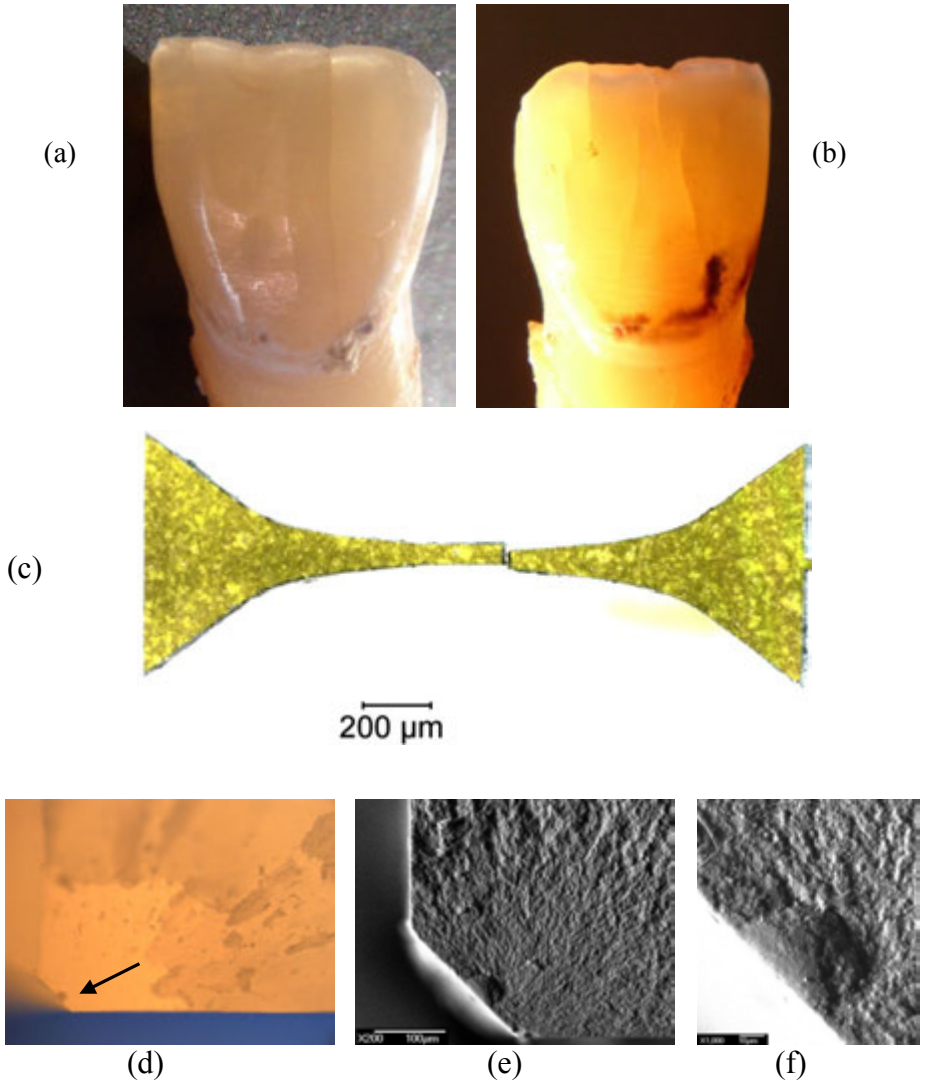

Figure 4.1 *Transillumination. (a) and (b) are an extracted human tooth from an approximately 80 year old patient. Transillumination from the side shows internal enamel cracks. (courtesy S. Scherrer) (c) shows transmitted (through) illumination of a chemical vapor deposited SiC micro tensile specimen. Very coarse grains acted as light pipes through the body. Relatively pure SiCs are green. (d) – (f) show an aluminum-rich inclusion origin, in a highly-filled resin-matrix dental composite. (d) is a trans-illumination view with light from below. Although the fracture surface features are blurred by the material's translucency, the origin flaw stands out at the chamfered corner. The SEM images (e) and (f) show the inclusion.*

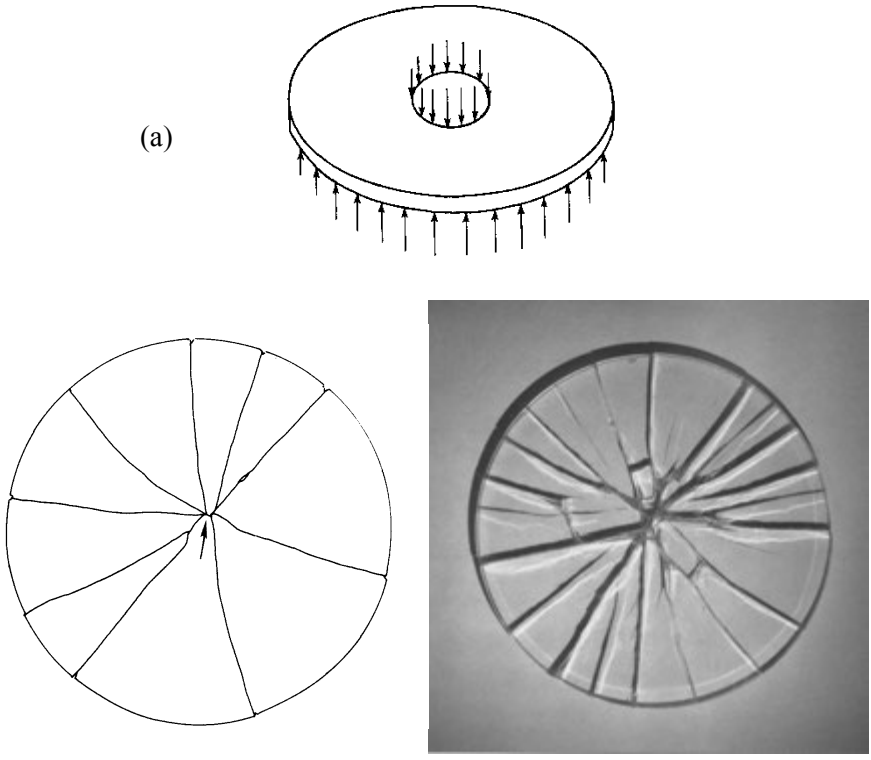

Figure 4.2 *Fracture patterns in a moderately-strong glass disk tested in ring-on-ring biaxial strength test. (a) shows the test arrangement, (b) shows a schematic of a fracture pattern. The arrow marks the origin. (c) shows an example in a BK-7 borosilicate crown glass disk.*

Once fracture has commenced, the propagating crack can fork or branch into multiple propagating cracks. These may be at non-normal angles to the far-field stress direction. Nevertheless, the initial fracture starts out as a single radiating crack that separates the part into two pieces. Often the search for the fracture origin entails studying the branching patterns and tracing them back to the region of first fracture where the two pieces with the origin join across a flat surface as shown in the center of Figure 4.2b.

Branching may not occur at all if the failure stresses are low, or if they drop off in the direction of crack propagation, or if the opening up of the crack makes a specimen more compliant such that the stresses are relieved.

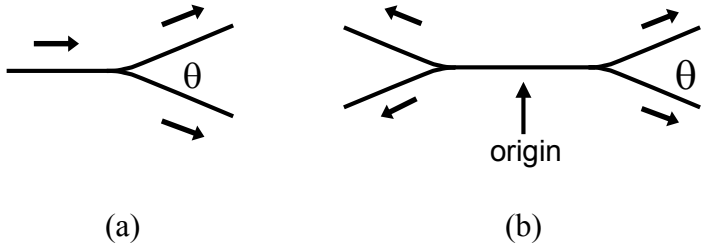

Figure 4.3 *Crack branching indicates the direction of crack propagation.*

4.3 Crack Branching Angles

Cracks which have reached their terminal velocity (normally about 50 % to 60 % of the shear wave velocity) may split into two cracks with an acute angle between them as shown in Figure 4.3a. Fréchette[1] terms this *velocity branching, velocity forking, or velocity bifurcation.* Branching patterns are a valuable aid in diagnosing the direction of crack propagation. For example, a pair of branches in opposite directions typically brackets the origin as shown in Figure 4.3b.

Another very useful pattern is that the angle of forking varies with the stress state as shown in Figure 4.4. The trend shown by the solid line was reported by Preston in 1935 for the fracture of glass articles.[2] Uniaxially-stressed parts, such as direct tension strength or bend bar specimens, fork at about 45°. Equibiaxially-stressed parts, such as a uniformly-loaded thick window that has an origin near the center, fork at as much as 180°. Pressurized bottles, which have circumferential hoop stresses that are double the axial stresses, fork at about 90°. Torsion fractures, wherein the ratio of the principal stresses is negative (one stress is tensile, the other is compressive as shown in Fig. 1.2), have very small forking angles. Preston said that the angles were very consistent and varied by only a few degrees, but other investigators have observed much greater variability.

It now appears that systematic variations can occur due to component shape, the exact loading configuration, the stress level, and possibly the material properties. For example, the 180° branching angle for equibiaxial tension ("drum skin tension") reported by Preston occurs for pressure loaded, thick windows that fracture at high loads. Shinkai[3] shows such a fracture (his Figure 22a) in a 1.7 m x 0.9 m x 6 mm building window. On the other hand, most laboratory scale disk specimens tested with ring-on-ring equibiaxial

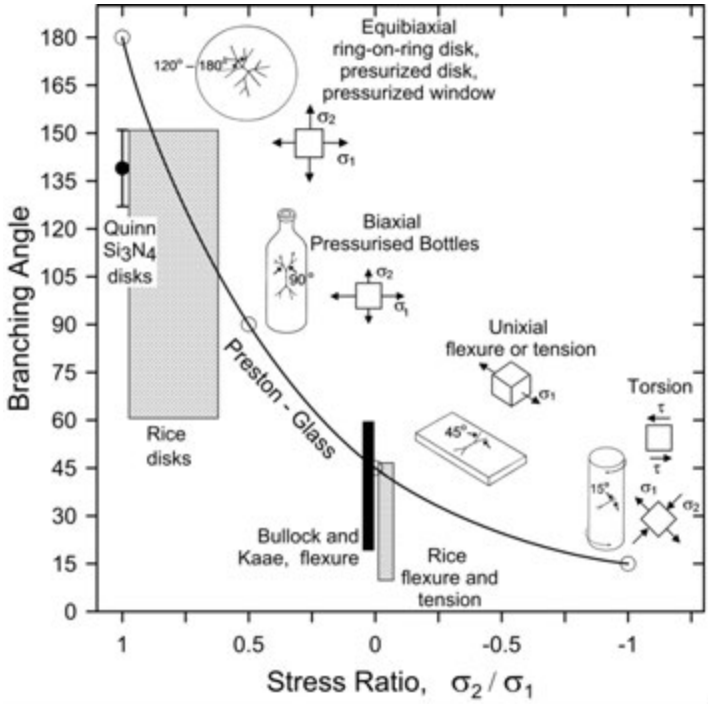

Figure 4.4 *Branching angle versus stress state. The solid line is the trend for glass shown by Preston.[2] The shaded bands show Rice's data[4] ranges for several ceramics and Bullock and Kaae's range for a glassy carbon.[5] The author's data for silicon nitride ring-on-ring disks are also shown.[6]*

loading (Figure 4.2) have smaller angles from 120° to 155° and only approach 180° if the specimen is very strong and has much stored elastic energy at fracture. Laboratory scale specimen data by Rice[4] on a range of ceramic materials, Bullock and Kaae[5] on glassy carbon, and the author on silicon nitride,[6] tend to confirm Preston's general trend, but with smaller angles. Most of Bullock and Kaae's uniaxial angles were 30°. The exact biaxial stress ratio for Rice's data for his thermally-shocked and ring-on-ring loaded disks is unclear and therefore is shown as a band in Figure 4.4. Some of the fractures were outside the inner loading ring where the hoop and radial stresses were not the same and thus $\sigma_2/\sigma_1 < 1$. Some of his data was for ball-on-ring loaded specimens which were also not equibiaxial unless fracture began at the exact center. It is also unclear how he defined his angles. They may have been the angle between any two crack segments or the included angle between the two crack segments that were the furthest apart. Based on Figure 12 of his paper, it may have been the former. Nevertheless, Rice made a number of useful

observations about the details of branching angle. A number of measurements were made and the standard deviations indicated there was some variability in branch angles even in uniaxially-loaded specimens. In some instances, the branching angle depended somewhat on whether the crack split into two branches or into three, including an extension of the original crack. He also noted that even along a given branch the angle did not necessarily stay constant. If a branch started out at an unusually low angle, it tended to curve to increase the angle. The converse was also observed.

Rice suggested that branching patterns tend to split the broken component into regions of approximately similar area.[4] This implies that the cracks partition the component into pieces with comparable areas and strain energies, a reasonable supposition. Bullock and Kaae also noted that the branching angles diminished with progressive branching.[5]

Unfortunately there is no consensus on how to measure branching angles. Both Preston and Fréchette recommended that the angle be measured close to the point of forking, but it may be more appropriate to measure the angle once it has stabilized. Close inspection shows that a branch starts at a shallow angle and then increases to its stable configuration as shown in Figures 4.5 and 4.6. Preston's original sketch (Ref. 2, his Figure 2) for the equibiaxial disk pattern in fact shows such a gradual curvature at the origin and the angle reached 180^{o} only after a small extension. J. Quinn used magnification to study branch angles in biaxially stressed glass disks and also observed angles that started small, but then stabilized at a larger angle.[7] She observed that there was a stress magnitude dependence of the final angle: highly stressed disks had angles that approached the 180 degree limit, whereas lower stressed disks had smaller final angles. Rice evidently measured the angles after they had been fully developed. Branching angles often vary within a broken part, usually due to spatial variations of the stresses. So for example, in a ring-on-ring loaded disk the stresses are equal in the middle circle, but the radial and hoop stresses drop off at different rates outside the inner circle out to the rim. Furthermore, as cracks progressively branch they may begin to interact with other branching cracks. Hence, it is common for an initial branch angle to be large in the middle near an origin in a biaxially stressed disk, but the subsequent branch angles diminish out towards the rim.

So although there are discrepancies in the reported data, and the optimum manner of measuring the angles is unresolved, branching angles provide at least a *qualitative* indication of the stress state. There may be material property or component shape effects. This may be a good topic for a graduate thesis.

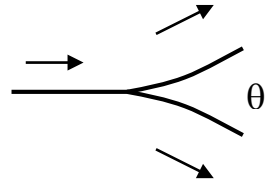

Figure 4.5 *Close up of the branching point.*

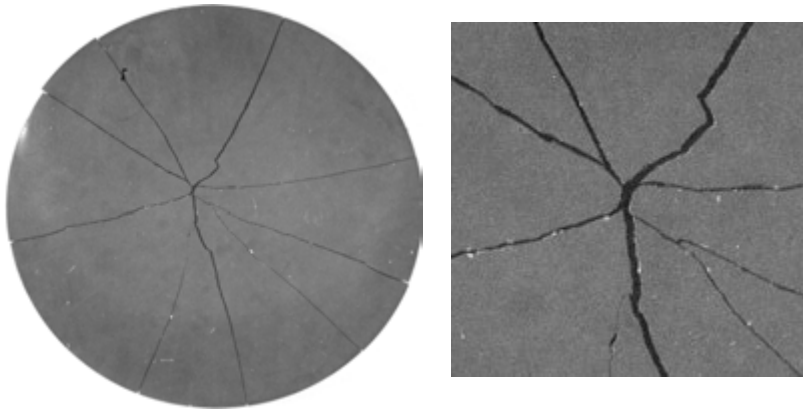

(a) (b)

Figure 4.6 *Fracture pattern in a 44.5 mm silicon nitride ring-on-ring (10 mm x 40 mm) equibiaxial strength test disk. The stress at fracture in the inner ring was 447 MPa. The branching is curved near the origin. Successive secondary branching occurs over short distances. (b) is a close up of the origin area showing that the initial branch angles are 140^o and 145^o. Additional branching is minimized as the crack propagated into lower stress areas away from the disk center.*

4.4 Crack Branching Distances

The distance a propagating crack travels before branching is directly related to the stresses and stored energy in the component. The greater the stored energy, the shorter the distance to branching. If the crack travels through a region of constant stress, the empirical relationship is:

$$\sigma\sqrt{R_b} = A_b \tag{4.1}$$

where σ is the stress, R_b is the branching distance (radius), and A_b is a material constant called the fracture branching constant. A table of branching constants is in Appendix C. Additional details about equation 4.1 and A_b, including the latter's similarity to fracture toughness, are discussed in chapter 7 on Quantitative Analysis. There is some evidence that A_b may not be a material constant[8,9] and may depend upon geometry and stress state.

4.5 Fragmentation Patterns

A general qualitative assessment about the stresses in a part can be made from the number of fragments. Quantitative analysis is discussed in Chapter 7. Low stress, low energy fractures create minimal branching and hence few fragments. High energy fractures cause extensive fragmentation. The extent of fragmentation depends upon the stress state throughout the body and the total energy available for fracture. A small pebble or BB gun shot creates only localized damage in a window, but a hurled brick will cause window bending in addition to localized impact damage. Sometimes a general observation about fragmentation patterns is sufficient for a diagnosis. For example, if a fracture occurs at an unexpectedly low stress the fractographer might suspect and search for a gross material, handling, or impact flaw that has weakened a part. Many thermal breaks are low energy fractures. High local or transient stresses may precipitate initial crack propagation, but the stress levels may be low in most other portions of a part. Low energy fractures often have few or no telltale markings on the fracture surfaces, as discussed in the next chapter.

Processing cracks that occur on firing also generate minimal fragmentation. That is because the cracks are so large that they significantly weaken the part. Differential shrinkage or out-gassing often create local stresses that can initiate a crack in the green state or during final firing, but the stresses may relax as the crack opens. Such cracks are often rough, twisted, and winding. Their internal fracture surfaces may have telltale thermal rounding or discoloration from being exposed during processing. Section 6.8.1 in the chapter on Origins has examples of large processing and firing cracks.

Moderate-stress failures create more fragments that can be reassembled so that branching patterns can be interpreted. There may be more fracture surface markings.

On the other end of the spectrum, high-energy fracture may be so virulent and create so many fragments that reconstruction may be impractical. Critical pieces may be lost. That is not to say fractographic analysis is hopeless. Sometimes telltale pieces that contain the origin can be culled out of a mass of

fragments and the critical information gleaned while the majority of pieces are ignored. Analysis of the fracture surfaces can reveal whether fracture was caused by tension or bending, as will be discussed in the next chapter.

Uneven stress states may be manifested in many ways. For example, Fréchette[1] showed an example of a tempered, high-powered lamp that cracked spontaneously as a result of heating in-service. In the fracture origin area, the fragments were large, attesting to a low to moderate stress level. Elsewhere in the lamp, extensive fragmentation and dicing typical of tempered glass was observed. Fréchette concluded that the intense heating in service caused the middle of the lamp to lose its temper and weaken such that it was more susceptible to fracture from thermal stresses.

Although similar techniques are applied to analyze laboratory-generated fractures and component service fractures, it is convenient to treat them separately in the following paragraphs. Even if one is primarily interested in component analysis, the experience gained with laboratory fractures can help.

4.6 Laboratory Test Fracture Patterns

In the laboratory the cause of fracture is known. Fractographic analysis may be done to identify strength-limiting flaws or to study crack microstructure interactions. It also may be done to verify that the test was done correctly and that the fixtures and specimen were aligned properly. It also may be done to gain valuable experience in examining fracture patterns in a particular material that can help with component failure analysis.

A simple precaution should be taken before the testing commences: *Shielding or buffering material should be placed around the specimens to catch all the fragments and to minimize secondary fractures and impact damage.* Cotton or tissue buffering and paper shields can be placed around the test specimens. In some instances the specimens may be partially taped before the test so that the pieces remain attached to the tape after fracture. This must be done judiciously and in no instance should tape interfere with the load application. Tape should never be on the tensile stressed surfaces. Biaxial ring-on-ring loaded disks may be taped on the compression side of the specimen with a tape circle inside the loading ring and a tape annulus outside the inner loading ring. The portion of the surface in direct contact with the loading ring should not be taped.

Specimens should be premarked with orientation or location marks. This preliminary step can dramatically aid post fracture analysis. For example, the

orientation of round specimens tested in tension should be marked to ascertain whether fracture occurs preferentially from one side or another. Similarly, flexural strength specimens should always have the loading points marked on the side once the specimen has been inserted and preloaded in the bend fixtures. The marks will help ascertain whether breakages occur at the load pins. Sometimes a grid may be marked on a specimen to help with reconstruction. This may help with biaxial disks loaded in flexure, but again, any such markings should be on the compression side of the specimen.

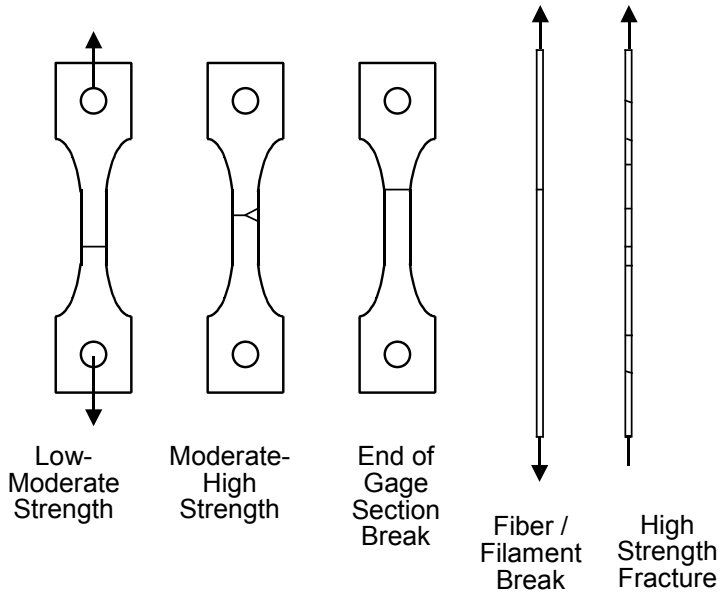

Figure 4.7 *Tension specimen and fiber fractures.*

4.6.1 Tension strength

This category includes machined specimens with grip holes or shoulders, glass optical fibers pulled in tension, or long tubes or rods that are pulled apart. Direct tension is conceptually one of the simplest loading configurations, but in practice it can be tricky to achieve. Slight loading misalignments or test specimen irregularities can create superimposed bending stresses. Breakage patterns in properly aligned specimens are usually quite simple as shown in Figure 4.7. Fractures initiate and run perpendicularly to the loading axis until and if they branch. Moderate-to-high strength specimens may branch with the telltale 30^{o} to 45^{o} angle as discussed in section 4.3. Fractures at a nonperpendicular angle to the loading direction (or with compression curls as discussed in the next section) should be cause for concern and suggest misalignments in the load train. It is especially important to ascertain whether fracture origins are located on the specimen surface, in the interior, or at an edge as will be discussed in the next chapter. Breakages in a group of test specimens should be randomly distributed within the gage section. An occasional break near the end of the gage section is probably not too serious, but if all specimens break from the end, then the tester should review the test specimen design. The stress concentration at the end of the gage section, the fixture and grip alignments, and the machining of the blend junction at the end of the gage section should be checked.

High strength fibers have the added complication that secondary fractures are common. After initial fracture, the intense stored elastic energy in the fiber releases, sending stress waves through each broken portion. Reverberations and fiber whipping cause additional breakages. Fragmentation may be so thorough that it may be impractical to find a primary fracture. Testing in oil or coating the fibers with grease may minimize the whipping and secondary breakage, at the risk of contaminating the primary fracture and altering the environmental sensitivity of fiber strengths.

4.6.2 Flexural strength

Flexural strength testing with rod or bar specimens is often done in lieu of direct tension testing. Flexure is much easier to do. Specimens and testing equipment cost considerably less. A drawback is that much less volume and area are exposed to the full tensile stresses. Hence, flexural strengths are typically greater than direct tension test strengths. Reference 10 is a review of flexural strength testing of ceramics. For our purpose here, it is convenient to briefly review the stress state as shown in Figure 4.8. The bending loading creates a stress distribution such that the maximum tensile stress is on the bottom as shown in (b) and (c). The stresses diminish into the interior until they are zero in the middle, at the "neutral axis." The tensile stresses are balanced by compression stresses on the opposite side. The maximum stress exists only directly opposite the middle loading point in three-point loading and diminishes linearly with distance from the middle loading point to the outer support points. In four-point flexure, the maximum stress occurs over a larger region between the two inner loading points.

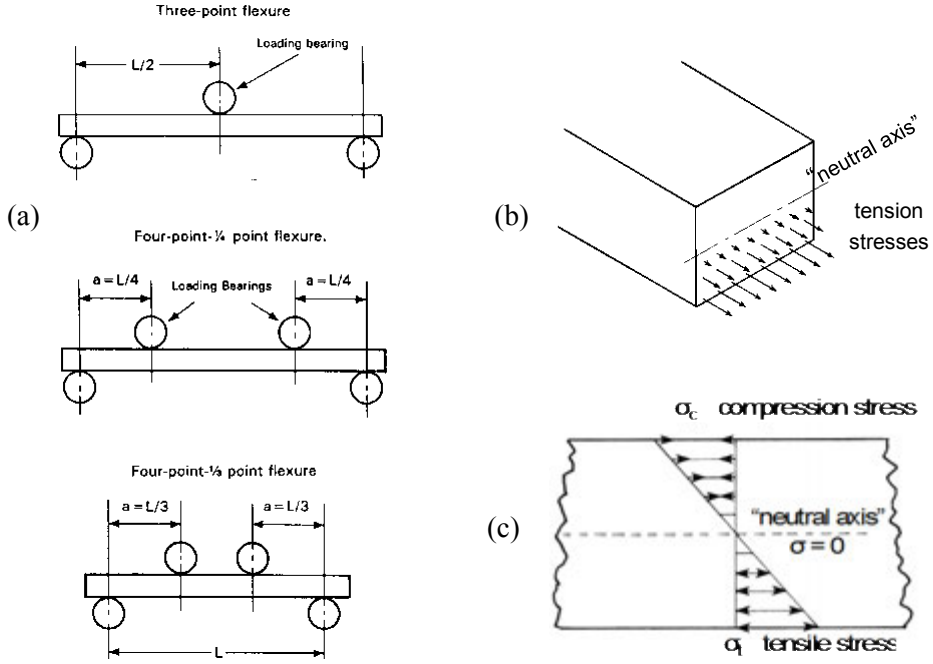

Figure 4.8 *Three- and four-point flexure test configurations are shown in (a). The stress distribution on a cross section is illustrated in (b) and (c).*

A very telltale feature of bend fractures is the *compression curl*, also known as the *cantilever curl*, shown in Figures 4.9 and 4.10. Once the crack has propagated from the tensile half of the specimen into the compression side, it slows down and changes direction. In stronger specimens the crack can branch, creating a double curl. The existence of a compression curl is an important sign that the specimen either was loaded primarily in bending or had a strong

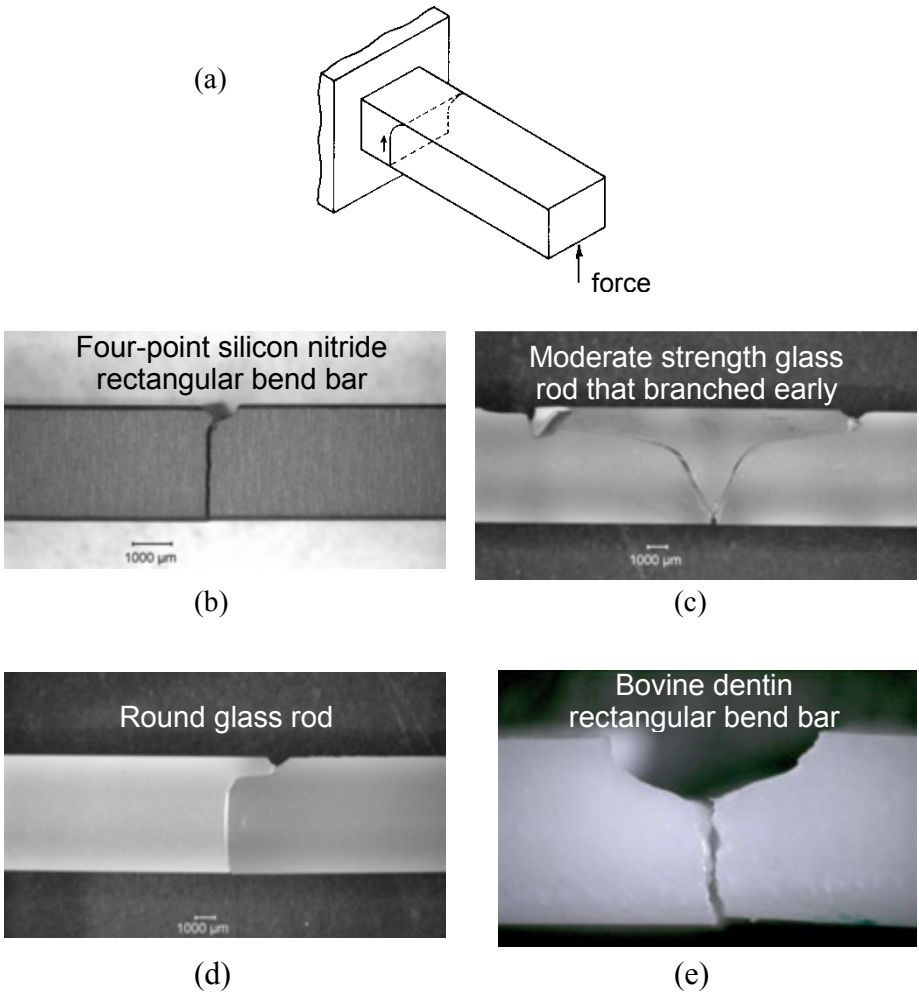

Figure 4.9 *Compression or cantilever curls are a telltale feature of flexural fractures. (b) – (e) show side views of four-point flexure specimens. In each case shown, the tension surface is on the bottom and the compression surface is on top.*

bending component. Compression curls are not normally present in direct tension specimens, unless they were badly misaligned such that some bending was superimposed on the gage section. The origin of fracture on a fracture surface is directly opposite the compression curl. The presence or absence of compression curls may be important for interpreting not only test specimens, but component fractures as well. Thermal fractures usually do not have compression curls. Tsirk argued in his book[11] that in simply supported beams as shown here in Figure 4.9a, the curl tends to run back towards the support. He argued this is due to shear stresses and that the maximum principle stresses steers the crack in that direction. To verify this, I tested fourteen glass rods supported in a vice with cushioned grips, by tapping with a small mallet hammer on the rod ends as shown in Figure 4.9. The rods had a small score mark on the tensile surface near the support to weaken them. If the score mark was within the contact area of the grips, the curl came out toward the applied force. If the score was right at the end of the cushioned support, the curl went back into the grips. If the score was just outside the gripped area, the curl went back to the grips, but sometimes came outward towards the force as shown in Figure 4.9. The angle of the force was a critical parameter, and if the force were angled slightly away from the vice, the curl came outward toward the force. I concluded that the direction of the curl varied with the location of the origin and the precise angle of the force.

Kolsky,[12] using very high speed photography in glass, showed that the compression curl in beams in bending is formed late in a fracture sequence, often due to elastic wave reverberations interacting with the slowly moving crack in its final stages of breakthrough. This may seem counter-intuitive since the fracture surface shows that fracture very quickly reaches terminal velocity (if a fracture mirror and hackle form as discussed in the next chapter), but cracks may in fact slow down very rapidly once they get to the compressively-loaded half of the beam. Furthermore, Kolsky showed that the local stress state around the crack is dramatically altered during the fracture event. It is very much a dynamic situation. Most of this is of secondary importance, however. The key point here is quite simple: a compression curl indicates a part was loaded in bending.

Figure 4.10 shows a variety of fracture patterns in bend bars. Low strength fractures are often the easiest to interpret since the specimen breaks into only two or three pieces. Often a small “T” shaped piece will be opposite the origin, but this fragment can be ignored since it never has the origin on it. The origin is below the “T” fragment on the two matching pieces nearer to the tensile stressed surface. Sometimes it is handy to keep the “T” fragments to confirm the other fragments do fit together.

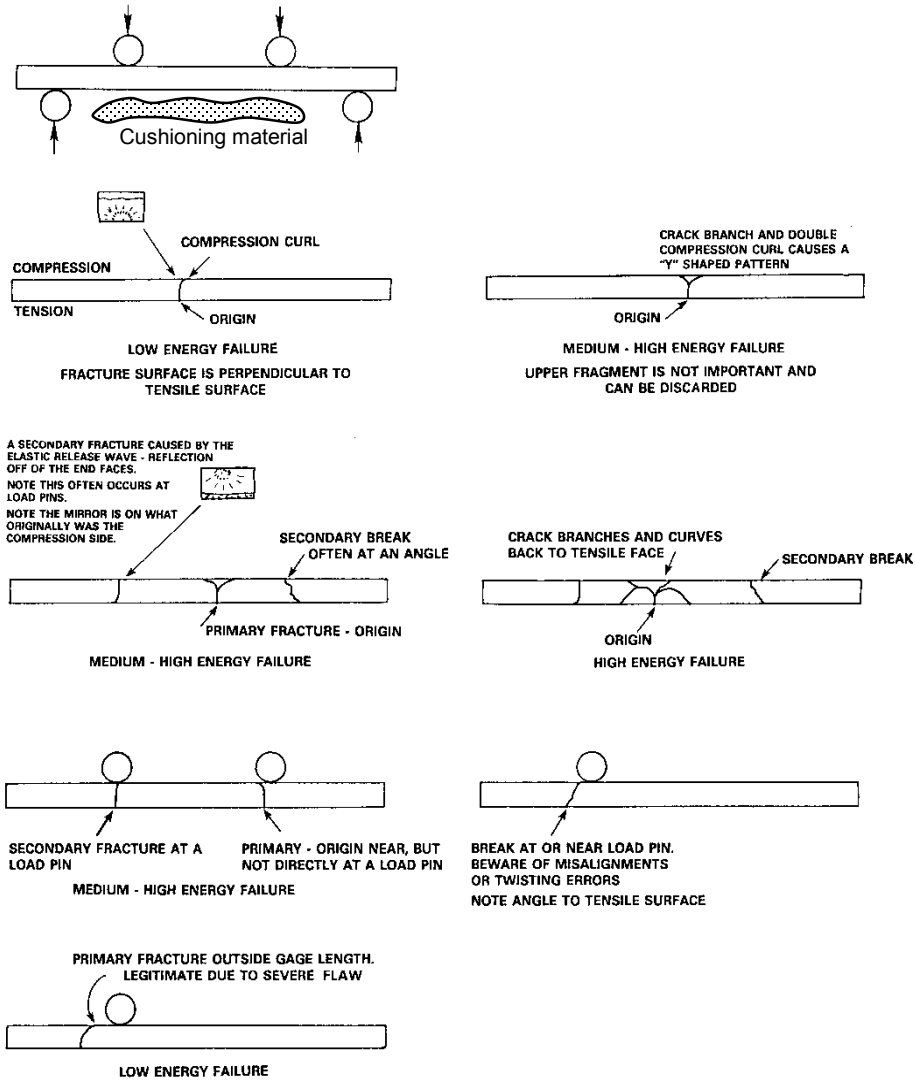

Figure 4.10 *Fracture patterns in four-point flexure specimens. Cushioning material under the specimens minimizes damage to the fracture surface edge.*

Higher strength bars have two or more fractures and it must be deduced which was primary. Secondary fractures are caused by reverberations and stress reflections after the first fracture has occurred.[12,13] Secondary breaks frequently occur at the loading points. If there are two fractures and one is

located at an inner loading point and the other is in the inner gage section, the latter is probably the primary fracture with the first origin. If the two breaks are close to the two inner loading points, then the exact locations on the tensile surface should be examined closely. Often one fracture will be right under a loading point, whereas the other may be close, but not right at the loading point. The latter is usually the primary fracture. If both are exactly under the two inner points, it may be difficult to deduce which was first. There is also the possibility the specimen might have been loaded unevenly causing stress concentrations at both sites. If this occurs for more than a few specimens in a set, then the fixture should be checked as well as the specimen's parallelism.

Properly aligned specimens and fixtures almost always cause a perpendicular primary fracture in the middle gage section. Secondary fractures are often but not always at a slight non-perpendicular angle to the specimen axis. Misaligned specimens or fixtures can cause twisted crack planes as shown in Figure 4.11 and described in Ref. 14.

An unusually large flaw outside the gage section can trigger a fracture with crack plane tilted towards an inner loading pin. Specimens with such low strength fractures usually do not have secondary breaks. *Fractures outside the inner gage section in properly aligned specimens and fixtures are usually completely valid and a warning that unusually large flaws are present.* They should not be cavalierly dismissed as invalid tests.

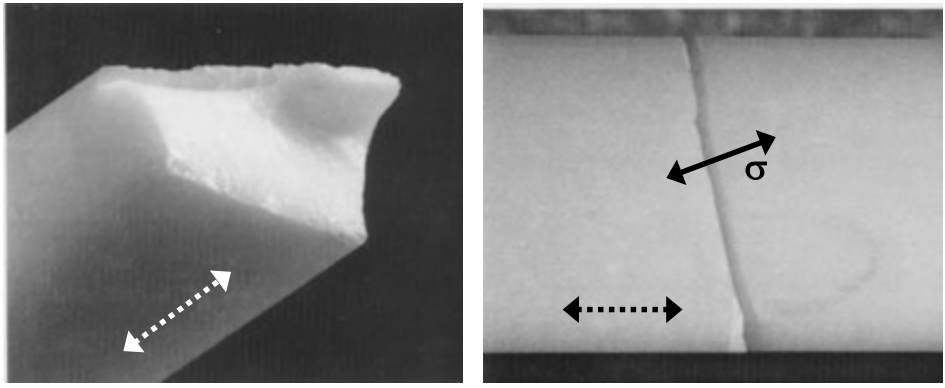

(a) (b)

Figure 4.11 *A twisted fracture surface in a misaligned alumina bend bar in a fixture that did not articulate properly. (a) shows the fracture surface, and (b) the tensile surface of both halves. The principal stress direction (solid black arrow) was 14 degrees off the expected direction (dotted arrows). Twisted or angled fracture planes should prompt the tester to check the fixture articulation and specimen alignment procedures.*

4.6.3 Biaxial flexural strength

Plates or disks may be tested in biaxial tension by a variety of methods including: pressure on-ring, ring-on-ring, piston-on-ring, ball-on-ring, and ball-on-three balls.

Pressure-on-ring loading (whereby a specimen is supported on a ring and is loaded by a uniform pressure on the opposite surface) has the virtue that a large area is stressed biaxially. There are no loading point or stress concentration problems with the inner loaded area. Ring-on-ring loading, which is more commonly done since it is simpler to do, creates an Equibiaxially- stressed region in the inner circle. Pressure-on-ring and ring-on-ring are best used with specimens that have flat and parallel surfaces for even contact with the loading and support fixture rings. Figure 4.12 shows fracture patterns in ring-on-ring specimens.

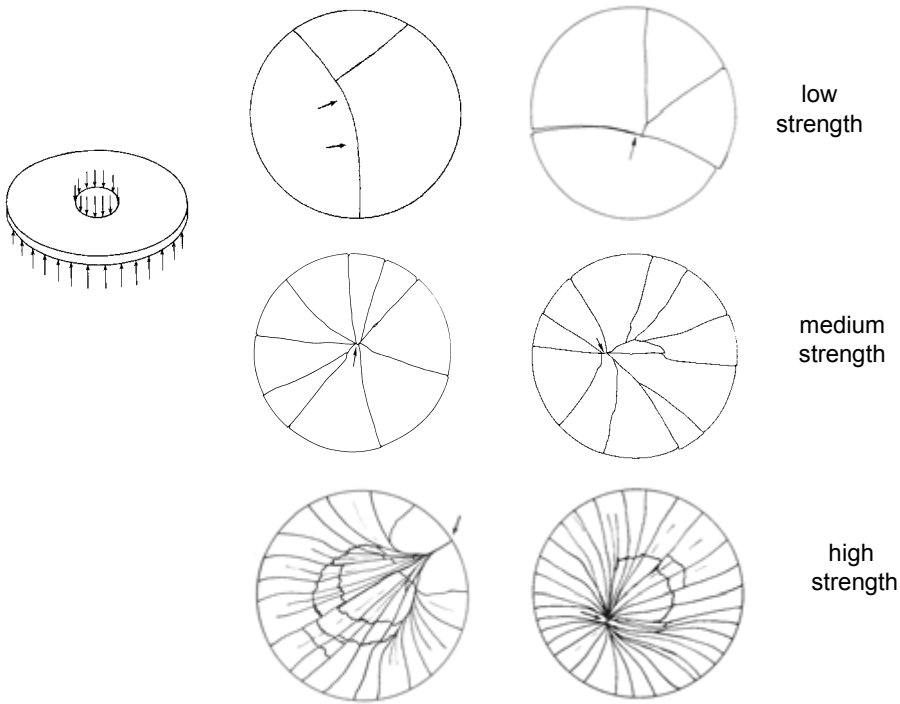

Figure 4.12 *Fragmentation patterns in ring-on-ring loaded specimens. The small arrows mark likely origin areas. In low strength parts, after the first break has occurred, the larger remnant may still bear load from the inner loading ring, and it in turn will break in bending. In moderate to high strength disks, secondary circumferential cracking occurs near the inner loading ring.*

The single ball loading schemes have the drawback that only a tiny spot directly under the loading point experiences the maximum stress. The concentrated forces of the ball distort the stress field in the vicinity. Fracture almost always starts directly below the loading ball.

The ball-on-three balls or piston-on-three balls schemes are better suited for uneven specimens, but the stress state is not very symmetric. Cracks often align themselves to run between the supporting balls. *Excessively thick test specimens should not be used, since breaking forces are so high that contact cone cracks can be initiated by the middle loading ball*. These disturb the stress state and, in the worst case, the cone cracks will propagate through the specimen thickness and reach the tensile side and cause unintended fracture. This is an invalid test.

A common misperception about ring-on-ring testing is that the edge condition is unimportant, since the maximum stresses are within the inner loading circle. This notion is only partly correct. Figure 4.13 shows one of several fractured BK-7 borosilicate crown glass specimens that were part of a large set of specimens intended to generate a comprehensive design and reliability database. The overall fracture pattern showed the origin was on the rim. Fracture surface examination confirmed that outer rim grinding cracks caused fracture. Stress analyses for ring-on-ring specimens (e.g., Fessler and Fricker[15] or Salem and Powers[16]) show that the maximum hoop and radial stresses are in the inner circle. The radial stresses gradually diminish to zero out at the rim. *Hoop stresses also diminish, but are finite at the rim and depend upon the specimen dimensions, the fixture sizes, and Poisson's ratio.* In the case of the disk shown in the Figure, the hoop stresses were as large as 48 % of the maximum stresses in the middle. It was not surprising that with a highly-polished tensile surface, the disk fractured from grinding flaws on the rim. In this testing episode, the problem was detected early after only six disks had been tested. The remaining disks were reground and HF acid etched to diminish the severity of the grinding cracks. Subsequent fracture testing was successful and almost always initiated fracture from the central disk region. If this precaution had not been taken and the remaining disks tested to fracture, the database would have been nearly worthless. The point here is that fractography is a valuable aid to mechanical property testing.

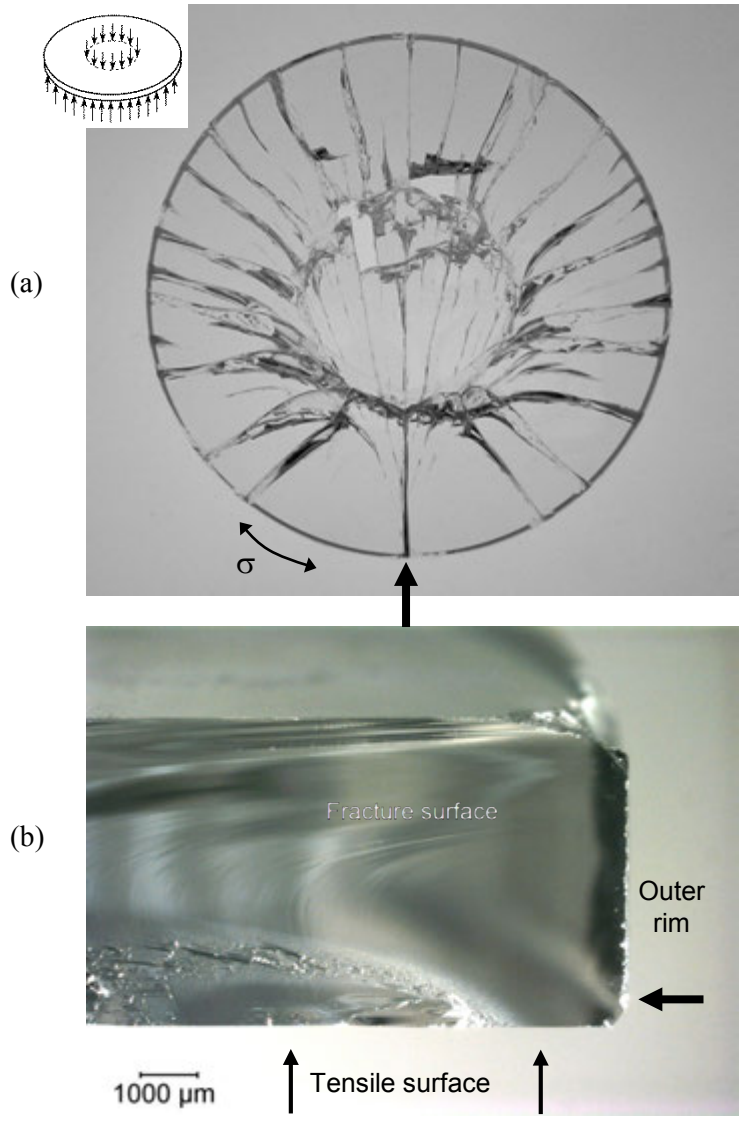

Figure 4.13 *A fractured glass ring-on-ring tested disk. (a) shows the overall breakage pattern. Fracture started on the rim (large arrow) in response to the uniaxial hoop stress σ (small arrows), propagated towards the middle, and branched in response due to the greater biaxial stresses in the middle. (b) shows the fracture surface. The origin is a grinding crack on the outer rim (large arrow).*

4.6.4 Laboratory test specimen analysis: additional tips

It is often helpful to look at contact marks or scuff marks where the specimen was loaded, whether it was in tension, uniaxial or biaxial bending. Such surface marks are one type of *witness marks:*

Witness marks: *marks on a specimen surface that attest to contact with a foreign body.*

In this manner it may be possible to ascertain whether loading was in fact uniform or not. Contact marks in a bend specimen may also help with the interpretation of whether a break occurred directly opposite a loading pin.

Test specimens are often broken in batches of ten, thirty, or more. Which specimens should be examined first? The pragmatic answer is that the weakest ones should be examined first, since they are the easiest to interpret. The experience gained from these easy specimens facilitates examination of the more complex fractured specimens, since the fractographer will be better prepared to recognize primary fractures and distinguish them from secondary breaks.

4.7 Component Fracture Patterns – General

Component fractures have the complication that the state of stress or the cause of failure may be unknown. The general fragmentation pattern can provide powerful clues. The fractographer first should obtain whatever ancillary information is possible about the component. What exactly was the material? What were the circumstances of the fracture? Was it an isolated case or part of a series? Had some change been made to the material or the loading conditions? Was there a noise (e.g., shattering sounds or water hammer)? Were there other parts or evidence found with the fractured material (impact debris)? Was there a witness? Is the witness honest? Does the witness have a good memory? Background information such as this may be crucial for the broader failure analysis. Nevertheless, the fractographer must keep an open mind, and let the pieces tell their story.

A wise precaution is to retrieve as many pieces as possible. In some instances where there is an obvious pattern, the fractographer can cull out important fragments. On the other hand, if other people have the fragments, you *cannot expect them to know* which are the important pieces. They should retrieve all pieces. If remnants are in a mount or assembly, then they should not be

retrieved or extracted until after the fractographer has had an opportunity to examine them in situ. Of course, this may not always be practical, but the fractographer should make an effort to see the fracture scene and fragments in as close to in situ state as possible. At the minimum, photographs of the overall fracture pattern and close-ups as necessary should be taken. Figures 4.14 illustrate some of these recommendations for a practical failure problem. This window fracture also illustrates how witness marks or traces of the impactor material aided the interpretation.

Figure 4.14 *Dr. J. Quinn with a window fracture problem at NIST. Evidence collected at the scene included foreign material attached to the impact site as shown in (c). The crack patterns indicated impact from the exterior. That, plus the height of the impact above the ground, the tuft of fur, the time of the year (November, the rutting season) and similar occurrences elsewhere suggested the cause of failure shown in (d). The deer saw its reflection in the window and attacked it!*

The impulse is to jump directly to an examination of the fracture surfaces to find an origin. While there may be no harm in this (and it is human nature for most fractographers to take this step), there is one extra step that is prudent to take immediately, especially if a moderate or great amount of time will be spent in specimen reconstruction or the part will be involved in serious failure analysis or litigation:

The entire component or part should be photographed or sketched.

There are several reasons why it is wise to capture an image of a whole structure or sketch it at an early stage. There are obvious instances, for technical or legal purposes, why a permanent record is required. It is best to make the record as soon as possible, lest pieces be lost, misplaced, or mangled in handling. An early record is essential if pieces need be cut up for microscopic examination. If the pattern of fracture is complex and an origin location not obvious, the fractographer may have to examine many pieces in order to track the cracking pattern back to the origin. A sketch or photo that can be marked up aids this process. Figure 4.15 shows an example of a broken component and an accompanying sketch with work notes.

An overall sketch or photo will help the analyst show other fractographers, engineers, managers, or clients the overall context of the fracture origin or fracture pattern. Is the fracture from the same location as other parts, is the pattern of breakage the same, or has a new failure mode been triggered? Much time and accuracy may be lost in orally explaining or drawing sketches from memory the fracture patterns days or weeks later. A handy overall photo of the part can save time and reassure others that the correct fracture origin photos indeed have been taken. A ruler, magnification marker, or a common object such as a coin should be placed next to the component when a photo is taken. Many close-up images of fracture features in the technical literature are unconvincing or may in fact have nothing to do with a bona fide fracture origin.

If many examples of a particular part are to be studied, then a sketch or photo of an *unbroken* part may be useful as a blank onto which fracture patterns may be sketched or drawn.

There is another very important and overlooked reason why a fractographer ought to make sketches. In the very process of drawing a line, the fractographer must think: “where exactly is that line, exactly what does it mean, and which way does it go?” Why did it start here and not there? The fractographer must contemplate and interpret what has happened as the sketch

(a)

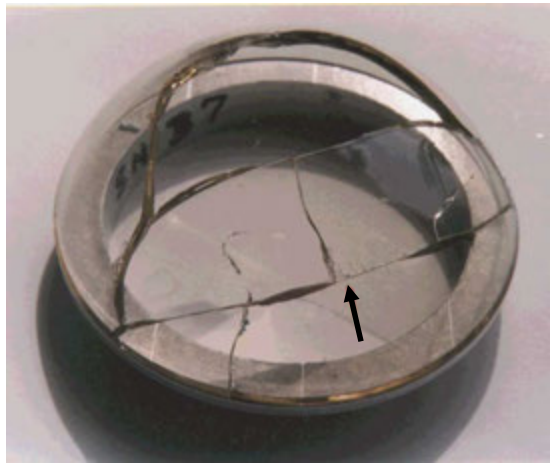

(b)

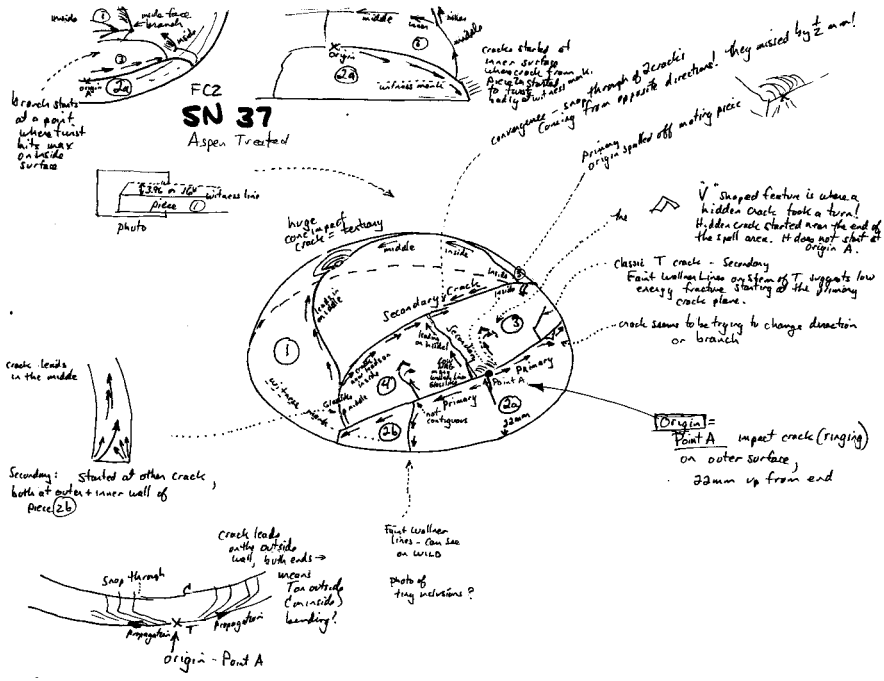

Figure 4.15 *A fractured single crystal sapphire hemispherical dome that broke in a high temperature, high Mach wind tunnel. The crack progression along individual pieces was used to back track to the origin (arrow). The sketch (b) helped integrate and keep track of the information from examination of the individual pieces. The origin is marked by the arrow in (a) and is labeled "origin" in (b). Figure 8.19 shows the actual origin flaw which was a tiny particle impact site. Thermal stresses then caused the dome fracture.*

is being made. This is an important step in an interpretation and diagnosis of fracture. My colleague Professor James Varner at Alfred University put the matter rather succinctly: "One can take a photo without thinking, but one cannot make a drawing without thinking." One study noted that students who took a museum tour had more difficulty remembering the objects if they only photographed them, rather than if they looked at the objects without taking a photo. Indeed, the popular author David Macauley, who has written a series of well-illustrated books such as Cathedral,[17] or City,[18] has said that when he creates his drawings he must contemplate how the structures were designed, what materials were used, and how they were assembled. Leonardo da Vinci's drawings underscore the depth of his knowledge about objects both natural and manmade and how they worked.

Some common fracture patterns are shown in the following examples. The reader is referred to the bibliography for more information. Fractographers who are dealing with specific component failures are strongly advised to search the literature for prior examples and documentation of similar fracture patterns. Appendix B of this guide is a compilation of fractographic case studies.

4.8 T Intersections and Crossing Cracks

Intersecting cracks may pose interpretation problems in component fracture analysis. A fractographer may initially be confused by the multitude of intersecting cracks. Which came first? Which way was the crack going? With a little experience and applying the process of deduction, it usually is not too difficult to answer these questions. Figure 4.16 offers some guidance.

Crack branching creates patterns shown in (a). The branch angle depends upon the stress state as shown previously in section 4.3. Even with biaxial loading and branch angles near 180°, a close examination of the branching point will show which way the crack was moving as it split. Hence the determination of the crack propagation direction is easy. Intersecting cracks as shown in (b) are also easy to interpret. The first crack passes through the plate undisturbed. The second crack approaches and is stopped at the intersection since it is unable to traverse the previously cleaved material. Intersections are commonly at 90° since the second crack moves at right angles to tensile stresses and tensile stresses cannot be carried across the previously cleaved crack. Examination of the fracture surfaces (to be discussed in the next chapter) will also corroborate the interpretation, since the fracture surface of the first crack is planar and undisturbed though the intersection. Wallner lines and hackle lines for the first crack plane are continuous and connected on each side of the intersection.

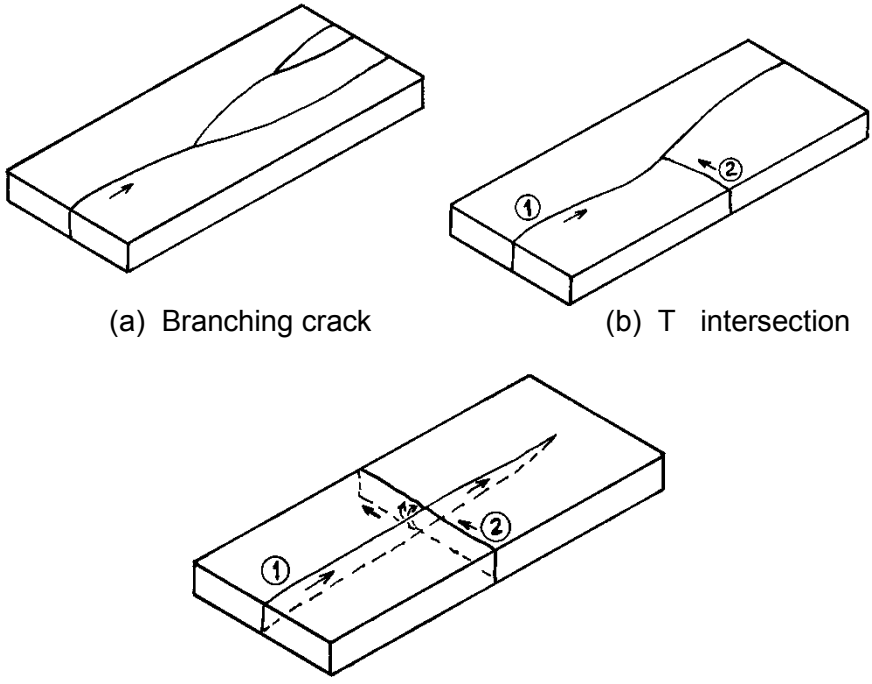

Figure 4.16 *Intersecting cracks. (a) shows common crack branching, which can be distinguished by the gradual forking. (b) shows a T intersection. The numerals indicate the first and second cracks. (c) shows a crossing crack, which may occur if the first crack does not completely cleave the part.*

The scenario shown in Figure 4.16c is less common, but occurs in cases where an initial crack does not completely cleave the plate. This can easily occur with bending fractures wherein the crack leads on one side that is in tension, but does not necessarily go all the way through on the compression side. The window in Figure 4.14b has examples. In such cases, the remnant ligament of unbroken material provides a path for a crossing crack to traverse the first crack. The key feature to look for is a disturbance in the fracture surface features. The fracture surface markings (Wallner lines and hackle) on the first plane are continuous on either side of the intersection. On the other hand, the second crack has a pronounced change in the markings on its crack plane, often a jog, or a hook around and up to complete the fracture just on the other side of the first crack. Sometimes two cracks seem to cross exactly over each other at exactly 90^{o}, but a very close inspection of the exact intersection will show that one (the second crack) has a slight offset or step where it intersects the other.

4.9 Invisible Cracks

Incomplete fractures sometimes create cracks that are difficult or impossible to see. The interfacial separations may be less than the wavelengths of light and the cracks are not visible even under a microscope. The cracks may even be partially healed. Interfacial adhesion may be due to hydrogen bonding from water molecules adsorbed onto the fresh surfaces following the initial crack opening.[19,20,21,22] The healing can occur even in inert environments and vacuum, and indeed, the literature shows that dangling ruptured silicate bonds do link back up. When a crack is created but closes quickly, as in the case of a window impact, pockets of air may be trapped between the crack faces. These pockets may be visible if light is reflected off the glass-air interface. Sometimes the light is refracted creating elusive but colorful reflections that are visible only at certain angles. (This is one reason why it is wise to rotate and shift a piece while inspecting it, or to move around it if the piece is stationary.) "Chill check" cracks, described in section 6.8.3 and shown in Figure 6.57, are tiny cracks formed by transient, very-localized thermal shock. They can be very difficult to see. Sometimes crack segments will *appear* to be isolated and not connected to other cracks or to an origin, but they are in fact connected by invisible segments. Fréchette[1] described a case wherein an invisible long crack in an intravenous bottle went unnoticed in a hospital, leading to a fatality.

4.10 Plates and Windows

Plates and windows can exhibit a wide variety of fracture patterns. Some common modes are shown in Figure 4.17. An excellent article on the fracture of flat glass is by Shinkai, reference 3. His article shows subtle variations in the fracture patterns depending upon whether the plate edges are freely supported or are built in. Variations also occur with plate thickness. The extent of residual stress in tempered glass plates may also be estimated from the size of the diced fragments as will be discussed in 7.2.2. Heat strengthened glasses also have compressive residual stresses such that the glass is twice as strong as an annealed plate, but the pieces do not dice into small fragments. Heat strengthened pieces break into triangular shards like annealed plates.

Blunt objects may create a cone crack that penetrates partially or completely through the plate. Such a flaw may or may not necessarily constitute a failure, since the plate is essentially intact. At higher velocities, radial cracks may be generated from the impact site. Radial cracks also may be triggered by impact of sharp objects.

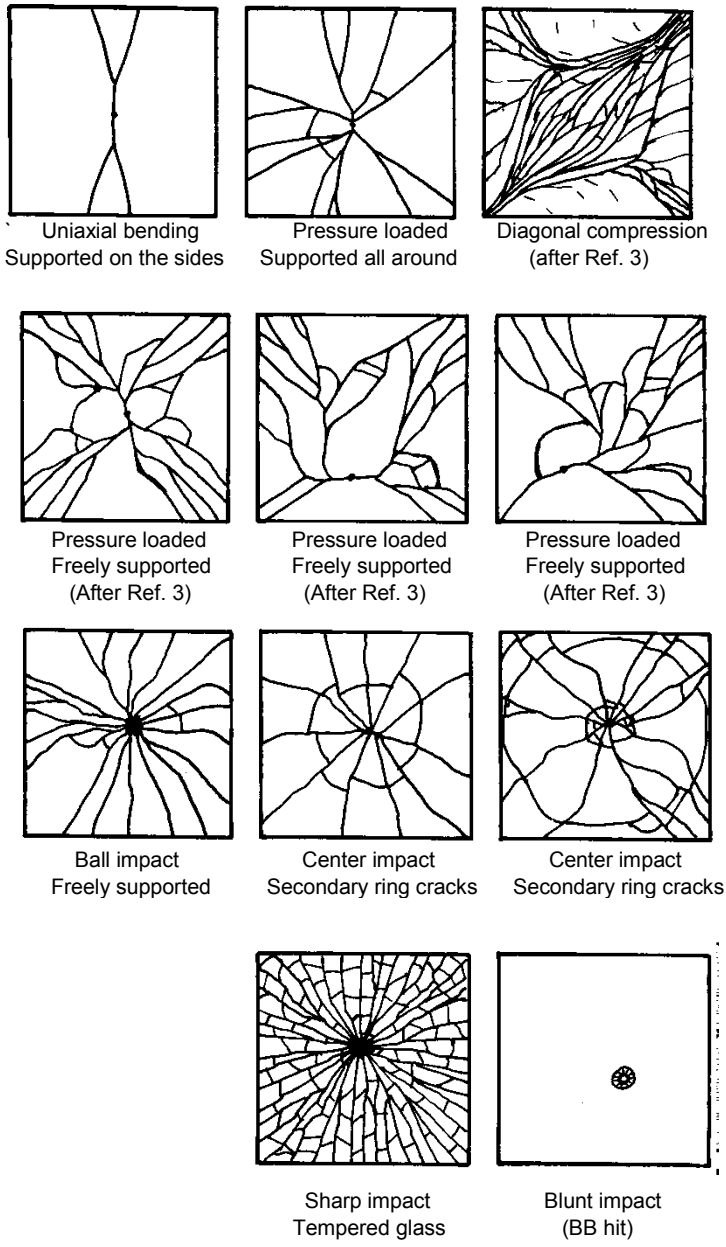

Figure 4.17 *Plate and window fracture patterns. Figure 4.14b shows an example of a center impact plate with secondary ring cracks*

In other cases, the bending forces from the impact may cause the crack (once it is away from the immediate impact site) to run on the opposite side of the plate from the direction of impact. At even higher velocities, many radial cracks fan outward from the impact site. The continued loading of the plate causes the radially-fractured segments to bend inward, causing them to break in bending leading to circumferential secondary cracking. In these secondary fractures, the maximum tension is on the impacted side of the plate. These rings around the impact often have offsets at the radial cracks, confirming that the radial cracks occurred first. Figures 4.14b and 4.17 show examples. Sometimes a secondary ring crack may step across a radial crack if the latter has not completely severed the plate. Very blunt objects may not necessarily create cracking at the impact side. Bending forces can create tension opposite the impact side and can trigger crack growth from flaws on the opposite side. In some instances, the very blunt object can generate bending forces in the plate that triggers a crack from a flaw at the plate edge. A crack runs to the impact site, and then radiates and branches repeatedly outward. In analyzing such fracture sequences, it is often very useful to combine the overall crack pattern analysis with an examination of the fracture surfaces, as described in the next chapter. The fracture surface examination reveals whether the crack was running uniformly through the thickness or was leading on the inside or outside plate surfaces. The latter information can establish whether the plate was in bending, and if so, which side was in tension.

4.11 Tempered Windows

Tempered glasses fracture into many small fragments. Occasionally such fractures are triggered by internal flaws such as nickel sulfide inclusions (discussed in Chapter 6). More commonly, the fracture is triggered by impact or sharp contact loading on the surface. If the loading is sufficient, it drives a surface crack through the surface compression temper zone and into the interior tensile stresses. Once this occurs, the plate will spontaneously fracture into many small fragments, since the internal stresses are more than sufficient to cause propagation and branching. Often the diced glass remains in place and does not fall apart. Figure 3-10 showed an example of a street skylight. The origins can often be deduced from the branch crack patterns as shown in Figures 3-10 and 4.18. Close examination of the origin area often reveals that in moderate impact or loading cases, the crack branching creates matching symmetrical hexagonal shaped pieces at the origin as shown in Figures 3-10 and 4.18c. Indeed, as will be discussed in section 7.3.2 and Figure 7.6, the first branch distances may be used to estimate the temper stress. An excellent article on the fracture of tempered flat glass is by Shinkai, reference 3. Shinkai states that some higher energy impacts may not have the two telltale fragments

at the origins, and may instead have cone cracks that penetrate from the surface.

Finding the origin fragments may seem hopeless for extensively fractured tempered plates if the fragments have fallen out of a frame, but the hexagonal (or pentagonal or heptagonal) fragments are distinctive and can be found by simply sifting through the rubble. With persistence and a little luck, the patient fractographer may be rewarded. Professor J. Varner has singled out origin pieces from a bucket full of swept up fragments. In some instances, tempered plates do not break up into uniform fragments. The existence of atypical fragments is often a sign that the temper was non-uniform either by design (e.g., Shinkai, Ref. 3, p. 288) or not (e.g., Fréchette, Ref. 1, case 10.18), or relieved by high temperature exposure (e.g., Fréchette, Ref. 1, case 10.22).

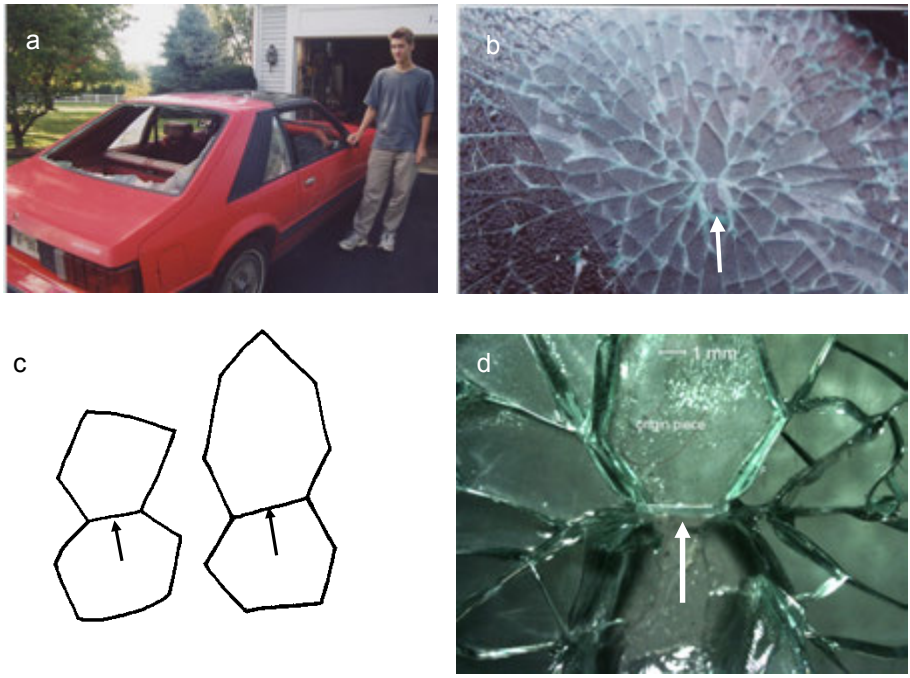

Figure 4.18 *Tempered glass fractures in the author's son's car. Flying debris from a tornado in College Park, Maryland in September, 2001 caused the impact fractures (a, b, d). The arrows show the actual origin in one window and (c) shows some variations of shape of typical matching origin pieces. The fracture surface of the origin piece is shown in Figure 5.19b*

4.12 Thermally Induced Plate and Window Fractures

A center-heated plate is one which is heated in the middle while the rim is cooler. Differential strains put the middle of the plate into compression and the rim into tension. The plates fracture as shown in Figures 4.19 and 4.20. The crack starts from an edge origin in tension and initially propagates at 90° to the edge, but then changes to a meandering wavy pattern as it approaches the initially biaxial compression stressed middle portions of the plate. The waves are often periodic as shown in (b). The waviness is an example of Hopf

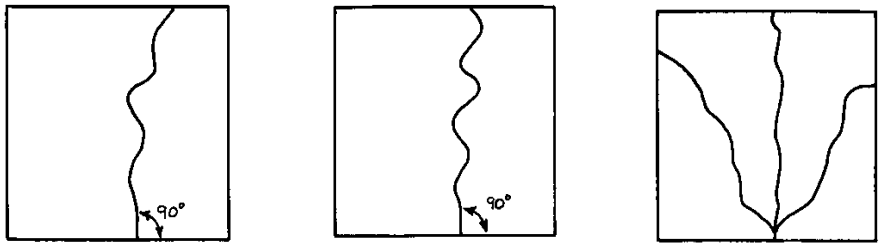

(a) (b) (c)

Figure 4.19 *Fractures in center-heated plates. (a) and (b) are low stress fractures (less than 10 MPa {1,500 psi} in glass), and (c) is a higher stress fracture such that branching occurred.*

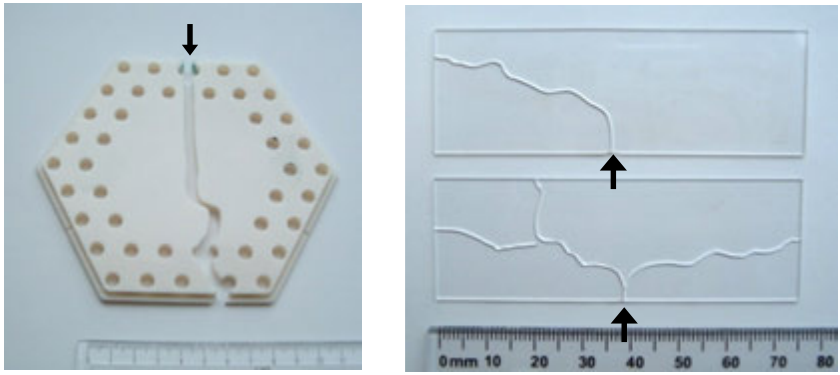

(a) (b)

Figure 4.20 *Thermal fractures with origin marked by arrows. (a) shows an alumina furnace baffle plate. Fracture started from grinding cracks associated with a hole. (b) shows glass slides broken by simply heating them on a hot plate.*

bifurcation problem that can occur in nonlinear systems.[23,24] Figure 4.20 shows a thermal failure in an alumina plate. Case 6 in Chapter 10 shows another example in a SiC furnace plate. Fréchette[1] noted that meandering cracks are not proof of thermal stresses and they can also form in impact cases in the final stages of breakup.

Thermal stress fractures often have localized tensile stresses that start fracture, but diminish away from the origin site. Branching may be minimal and the fracture surfaces may be relatively featureless and flat in regions away from the origin. Wallner lines or hackle lines (discussed in the next chapter) are rare. On the other hand, there may be multiple arrest lines attesting to stepwise propagation of the crack. Scarps may be present on the initial parts of the fracture surface if the part was thermally shocked by a cooler fluid.

The relatively featureless fracture surfaces mean that the crack is moving slowly when the wavy pattern forms. The crack alters the stress distribution and it in turn alters the crack path. This nonlinear interaction causes the crack to curve back and forth.

4.13 Bottles and Pressure Vessels

Bottles and pressure vessels are susceptible to a variety of failure scenarios. Figure 4.21 shows some common modes, but this illustration is by no means complete. The reader is referred to the excellent review article by Kepple and Wasylyk[25] for a more detailed presentation with more illustrations. Preston's article[26] in 1939 was an outstanding early contribution. Kepple and Wasylyk cite earlier work by F. W. Preston from the 1930s and 1940s in their review. Fréchette[1] also illustrated a number of interesting glass bottle fractures.

Fractures from internally-pressurized bottles (e.g., carbonated beverages, Fig. 4.21 a-c, have vertical initial cracks since hoop tensile stresses are double the axial stresses (as discussed in detail below). Fractures usually initiate on the outside wall and branch in a symmetrical pattern about the vertical axis. The number of branches is proportional to the stress in the glass. Fractures start on the outside wall since larger flaws are more apt to be present there, but as the crack propagates it will extend to the interior and then lead slightly on the internal surface, since the stress is slightly higher there. Secondary breaks from bending have crack fronts that strongly lead on the *inside* surface. Pressure fractures from the base will also have extensive forking as shown in Figure 4.21d.

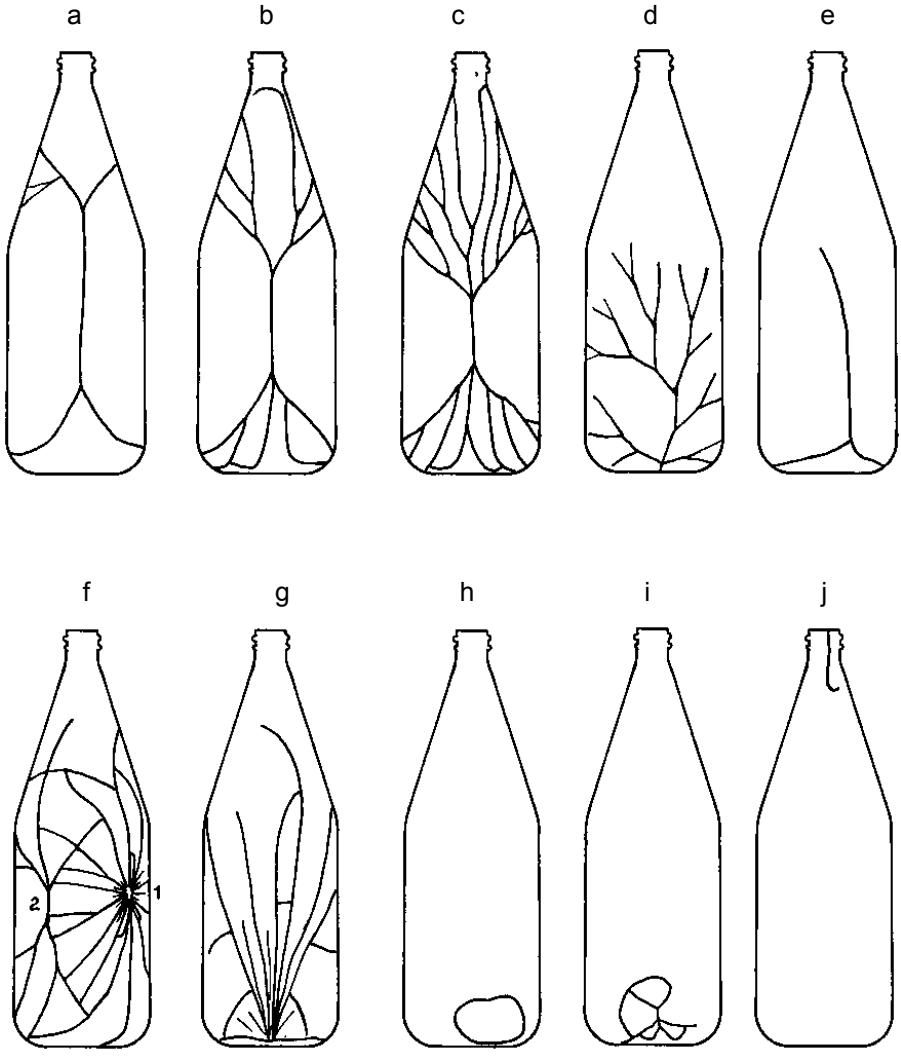

Figure 4.21 *Bottle fracture patterns. (a-c) sidewall fractures due to internal pressure at progressively greater pressures; (d) internal pressure fracture starting from the base; (e) is a thermal fracture from sudden cooling of the base; (f) is an impact fracture on the right side (labeled 1) with a hinge fracture on the side (labeled 2); (g-i) show water hammer fractures and (j) shows a fracture from diametral rim clamping.*

Thermal fractures have very little or no branching as shown in Figure 4.21e. Sudden temperature differentials can occur in a variety of different ways. Tensile stresses are generated when a portion of the body is suddenly cooled and attempts to shrink. The warm portions resist the contraction and put the cooler portions into tension. The temperature gradients can be either through the thickness or from one part of the body to another. Exposure of a hot vessel to a cold liquid often leads to thermal shock fracture. Fracture often starts and runs around the base and may extend up into the sidewall. Fréchette[1] and Kepple and Wasylyk[25] cover more thermal stress fractures of glass containers. Additional information about thermal fractures is in section 4.19.2 later in this chapter.

Sometimes impact damage sites may be found around the base, either on the inside or the outside. Impact damage sites on the inside of drinking glasses or beer mugs are often due to careless dropping of eating utensils into the glasses.

External impact fractures on the side walls often have a starburst pattern at the impact site as shown in Figure 4.21f and 4.22. The principal crack system does not necessarily start at the impact site, however. The force of impact can cause the sidewall of the vessel to flex outwards creating a bending stress in the side of the vessel. This can trigger so-called "hinge fractures" 45° to the side of the impact site. Wallner lines indicate that fracture starts on the outside surface of the hinge fracture sites. A network of cracks from the impact site can start on either the inside or outside of the impact site, depending upon the sharpness of the impactor. The impact site may create the initial fractures, but in many cases the hinge origins fracture first. They then send a *leader crack* over to the impact site that triggers or exacerbates the fragmentation at the original impact site. Figure 4.22 shows an example of this in a glass tube.

Filled glass containers dropped on their side trigger fracture from origins on the inside surface.

Water hammer is a phenomenon that can cause vessel fractures as shown in Figures 4.21g-i. The sudden arrest of a liquid in motion or a surge of liquid that collapses a void in a partially-filled vessel can create transient intense internal localized pressures. Figure 4.21g shows a base fracture initiated by water hammer when a filled bottle was dropped. There may be a high concentration of cracks at the origin, but little branching afterwards since the stresses were focused at the base. Collapse of a void can occur in vacuum-sealed or incompletely-filled vessels. Base fractures shown in Figures 4.21h,i can result. Vessel necks are vulnerable to many forms of damage from chipping

due to capping-clamping stresses. Figure 4.21j shows a crack triggered by diametral clamping around the rim.

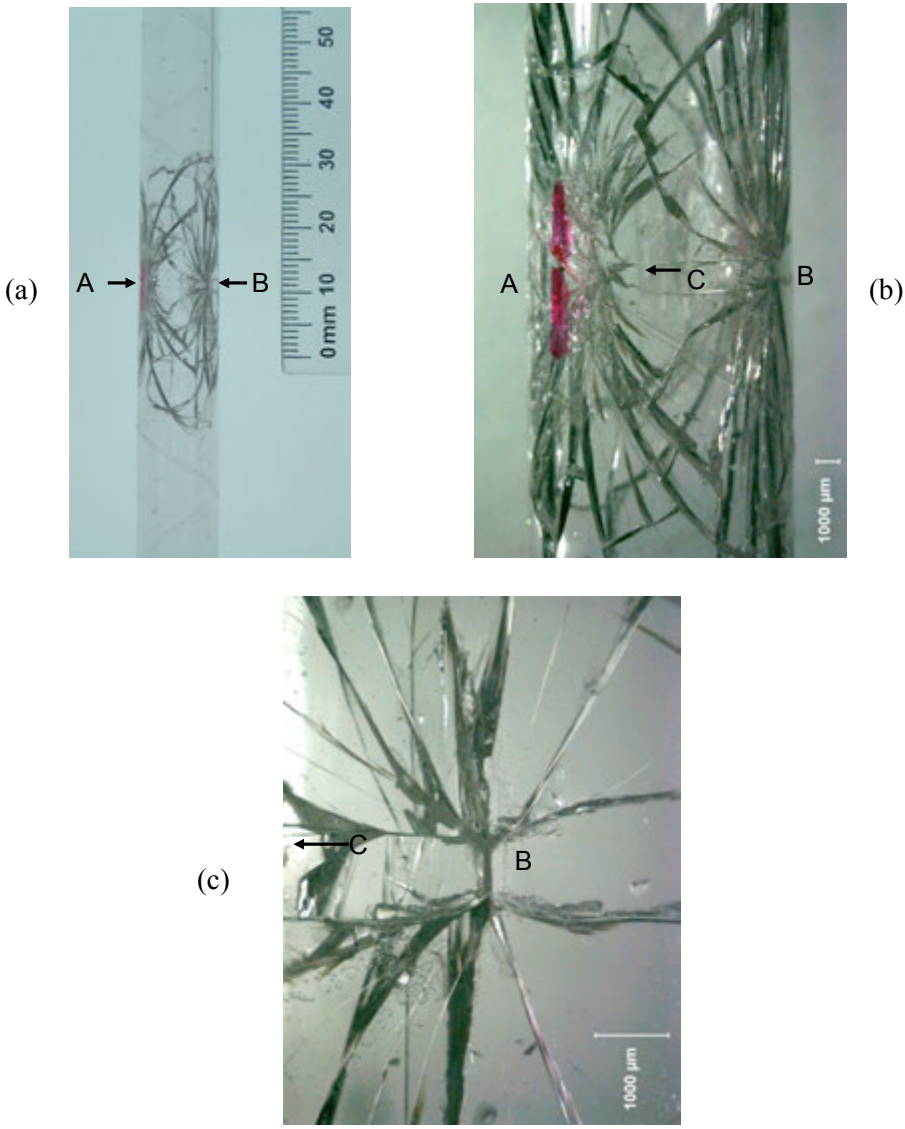

Figure 4.22 *Small glass tube loaded diametrally at opposing points A (only the front is shown). Fracture started at the side hinge point B which generated an array of radiating cracks. One of these is the "leader crack" C (arrows in b and c) which went to the loading site A where it branched repeatedly and fanned out yet again. (Tube courtesy of W. Haller.)*

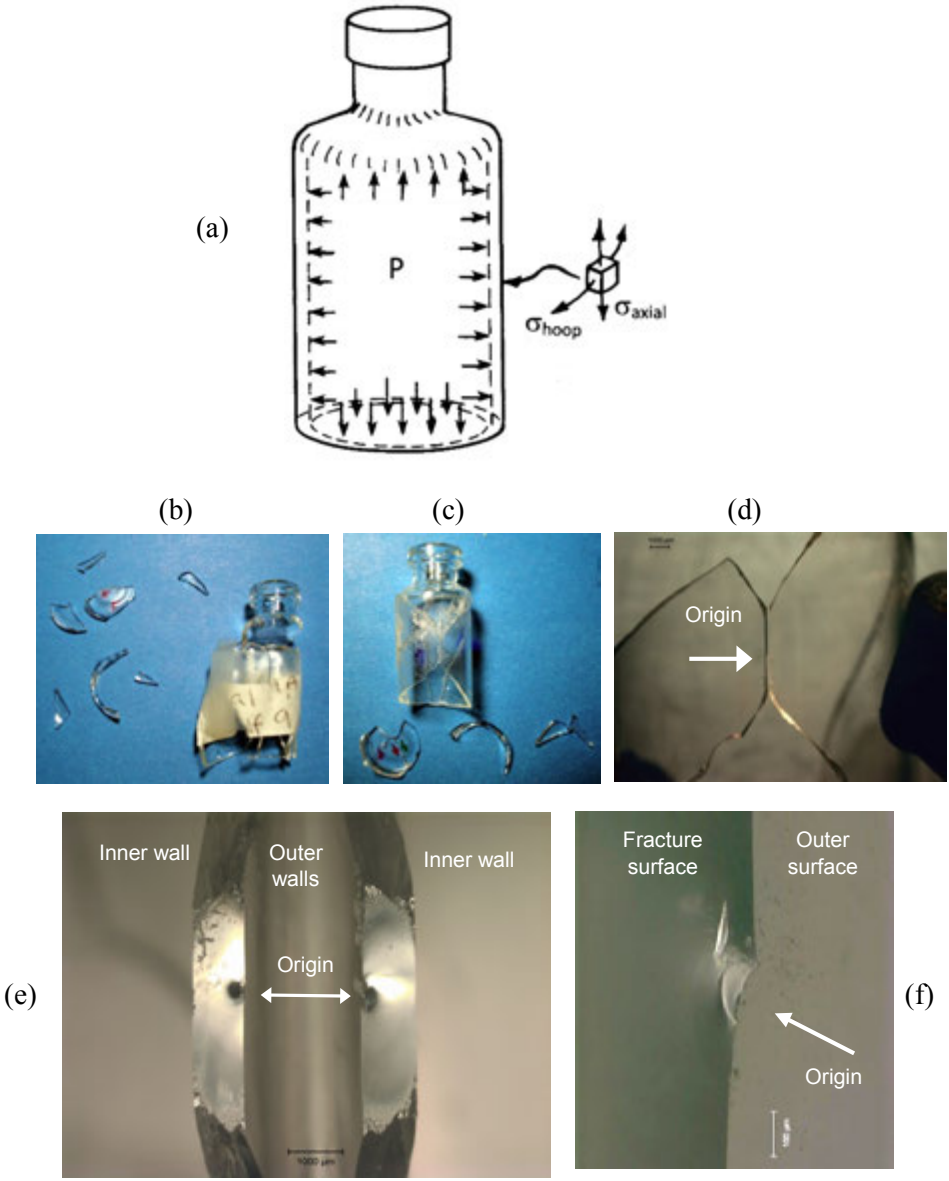

Figure 4.23 *Pressurized thin-walled vessels. (a) shows that the side walls are stressed in biaxial tension. Hoop stress is double the axial stress and therefore the first fracture is usually vertical as shown in the medicinal vial shown in (b)–(f). (e) shows the matching fracture surfaces at the origin. There is a distinct fracture mirror centered on the origin. (f) shows the origin was an arc shaped crack in the outer wall, a clear indication of blunt contact damage.*

As noted above, fractures from internally-pressurized bottles (e.g., carbonated beverages, Fig. 4.21 a-c, or medicinal vials Fig. 4.23) usually have vertical initial cracks since hoop tensile stresses are double the axial stresses, irrespective of the pressure. This is a good opportunity to show a stress analysis of a simple structure.

Imagine making a vertical cut through the middle of the bottle with height *L*, radius *r,* and wall thickness *t,* under pressure P. This is a common practice for mechanical engineers to do when they construct "free body diagrams" to analyze stress problems. A part is cut in an imaginary sense. The external forces and moments acting on one half of the component are balanced with internal stresses in the walls. For the bottle, the forces from the sideways expanding pressures that act on the arc of the inside surface are balanced against the constraining forces in the side walls. These are the sum of the hoop stresses in the two side walls that have cross-sectional area 2*Lt*:

$$\int_{-\pi/2}^{\pi/2} P\cos\theta r d\theta L = 2rLP = 2Lt\sigma_{hoop} \tag{4.2}$$

$$\sigma_{hoop} = \frac{Pr}{t} \tag{4.3}$$

For the axial stress (vertical direction), imagine splitting the vessel in a horizontal plane midway along its height. The force created by the sum of the pressures on the bottom circular surface of area πr^2 is balanced by the sum of the vertical axial stresses in the vessel side walls which have a total cross sectional area of $2\pi rt$:

$$P\pi r^2 = 2\pi rt\sigma_{axial} \tag{4.4}$$

$$\sigma_{axial} = \frac{Pr}{2t} \tag{4.5}$$

Hence:

$$\sigma_{hoop} = 2\sigma_{axial} \tag{4.6}$$

This solution is for thin-walled vessels where it may be assumed there is negligible stress gradient through the wall thickness. Engineering textbooks should be consulted for thick–walled vessels since there will be a stress gradient through the wall thickness.

4.14 Torsional Fractures

Torsional loadings such as shown in Figure 4.24 produce twisted fracture surfaces at an angle to the part length. Torsional stresses usually do not induce a special failure mode in ceramics or glasses. Fracture starts at a flaw and the crack propagates normal to the plane of maximum tensile stress, which is aligned at 45° to the shear stress direction. In other words, the shear stress (τ) state is equivalent to one in which a material element is pulled in tension (σ_1) in one direction and compressed laterally (σ_2) as shown in Figure 4.24a. Fracture primarily occurs due to σ_1 tensile stress and fracture propagates perpendicular to σ_1. Many parts that fail in torsional loading also have some bending as well. Fracture surfaces often have ample twist hackle markings as discussed later in section 5.3.3. Figure 4.11 shows an example of a fracture in a bend bar that had superimposed bending and torsional stresses. Figure 5.31 shows the fracture surface of a glass rod with mixed tension and torsional loading.

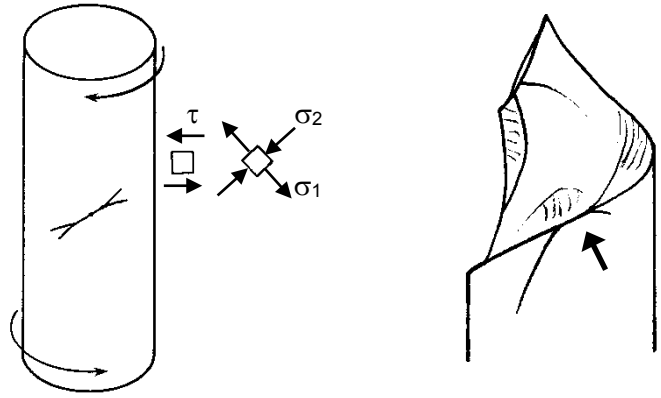

Figure 4.24 *Torsional loading causes fractures at an angle to the longitudinal axis of a part. The shear stresses are τ. These generate equivalent principal stresses σ_1 in tension and σ_2 in compression as shown in (a). Fracture occurs perpendicular to σ_1. (b) shows a schematic of a glass rod fractured in torsion (after Michalske, ref. 27). The origin is at the arrow. Note how branching occurs to either side of the origin, but that only one branch in each case continues, giving rise to the curved fracture surface.*

4.15 Chipping

Concentrated loads near an edge can chip off a portion of the body. Figure 4.25 shows some examples. Chipping can either be a primary mode of fracture, or it can be a secondary nuisance. For example, it is one of the leading causes of failure of all-ceramic dental restorations such as crowns or bridges, and hardmetal (e.g., tungsten carbide) or ceramic cutting tools. On the other hand, it may be a nuisance if there is so much chipping that it interferes with interpretation of a fracture from some other cause. Thus, it is important to be careful when fitting pieces together during an initial examination.

The force to cause fracture depends upon the shape of the object that applies the contacting force, the distance from the edge, the angle of the applied force P, the angle of the edge, and the material's fracture toughness. In general, the greater the distance away from an edge, the greater the force that is necessary to create a chip. Modern use of this test for engineering materials was started in 1986 at the National Physical Laboratory in United Kingdom by Almond and McCormick.[28] A remarkable finding was that the shape of the chip was invariant with material. Edge chipping is a field of growing attention, and there is a growing literature on it. Quite interestingly, Charles de Freminville's seminal 1907 treatise on fracture of brittle materials included excellent illustrations (Fig. 5) of edge chips in glass.[29] Several papers on edge chipping were given in a session at the 2000 Alfred Conference on Fractography of Ceramics and Glasses.[30] Edge chipping also has been a topic in the lithic fracture literature and flint knappers have a good practical knowledge on the topic (e.g., Refs. 11, 31).

The exact force-distance trend depends upon the type of indenter (sharp or blunt). In a laboratory setting, sharp diamond indenters (Rockwell, Vickers, Knoop) or sharp conical tools are used, but in practice any contact type loading can create a chip at an edge. Lab-scale indenters initiate cracks around the contact site which then grow to form a chip. On the other hand, some loadings with blunt contactors near an edge cause a pre-existing crack to propagate parallel to the specimen side and to form a long flake. The top of the flake, where the force is applied, is called the "platform" in the lithics literature. The fracture mechanics of chip formation and how long slender flakes may be formed by stable crack extension are fascinating.[31,32] The long slender flakes can be used as cutting tools. Cotterell makes the case that the ability to form such long slender stone tools was a critical step in the evolution of mankind.[31]

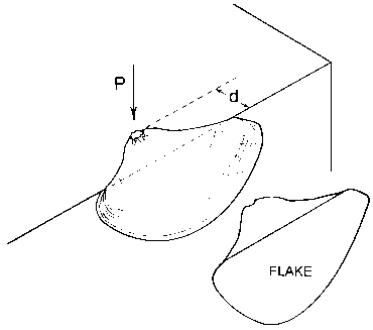

(a)

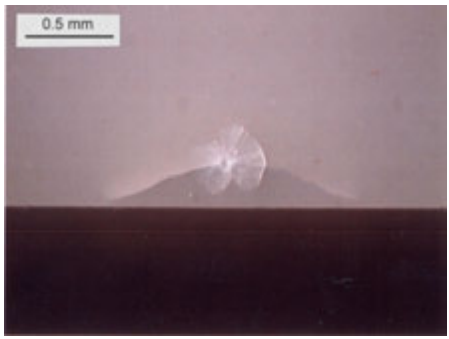

(b)

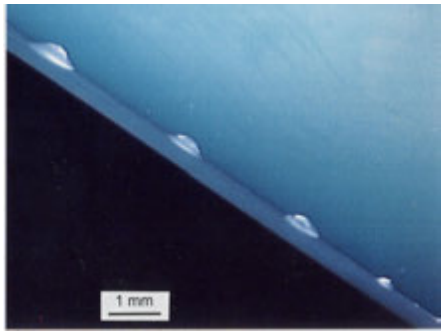

(c)

(d)

(e)

(f)

Figure 4.25 *Examples of chip fractures. (a) is a schematic that shows how a chip is formed and the telltale shape. (b) shows a top view of a chip that is just about to pop off a lithium disilicate foundation dental glass-ceramic. The loading point is obvious. (c) shows a row of edge chips created in porcelain under controlled conditions in the laboratory. (d) is a close-up. (e) and (f) show edge chips in an ancient Roman (circa 300 AD) 22 cm square x 3.4 cm thick hypocaust stone from Trier, Germany. (b,c,d, courtesy J. Quinn)*

The shape of chips varies with the angle of the applied load as shown in Figure 4.26.[33] This has practical significance, since the shape of the chip can tell a fractographer the direction of the force that caused the chip. Since the first edition of this book was written, I have followed up on the edge chipping work of my departed spouse Dr. Janet Quinn. We have published a number of papers on edge chipping of dental ceramic and composite restorative materials and structural engineering ceramics and we have a new quantitative model.[34,35,36] Early work emphasized a linear relationship between force and distance the

(a)

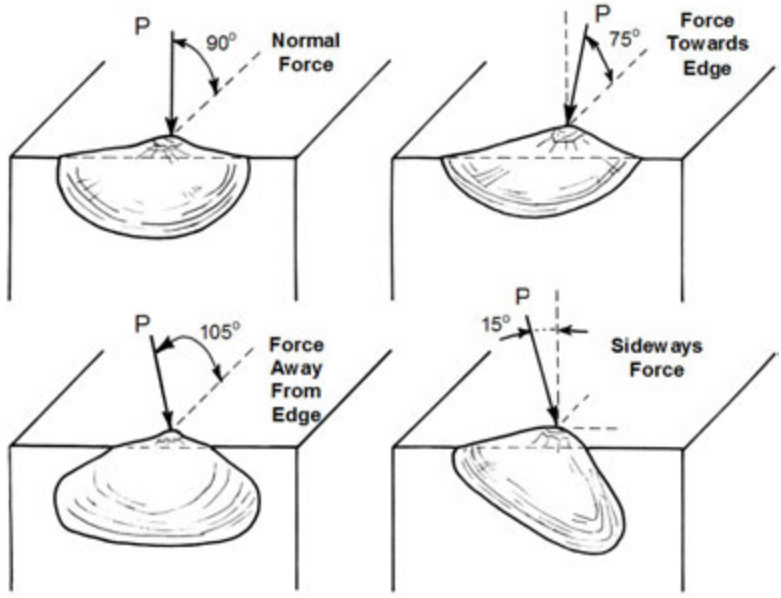

(b)

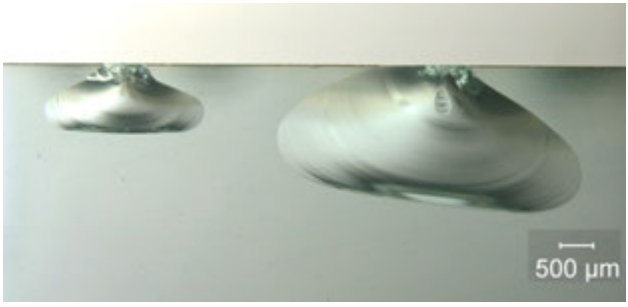

Figure 4.26 *The angle of the applied load affects the shape of edge chips. (a) is a schematic that shows the patterns and (b) shows front views of two chips in glass (at different loads and distances from the edge) made by a conical indenter tool angled away from the edge at 105°. (after J. Quinn and R. Mohan, Ref. 33).*

force is applied away from the edge, but new results indicate nonlinear trends can result from the partitioning of indenter energy into competing deformation and fracture modes in the material. Figures 4.27 and 4.28 show some of the new chips.

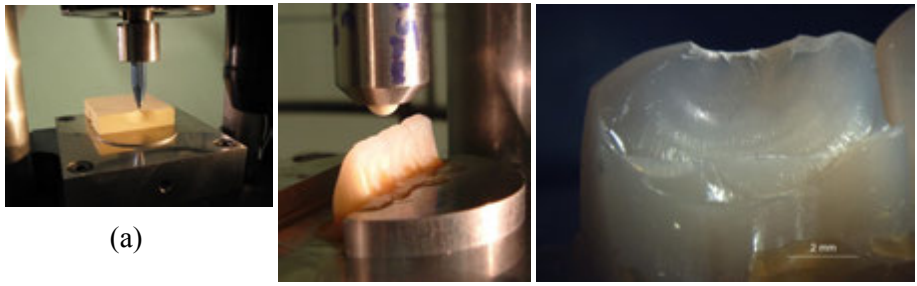

(a) (b) (c)

Figure 4.27 *Edge chipping. (a) shows the test machine with a 120º sharp diamond scriber making a chip in a dental stone material. (b) and (c) show a ceramic ball indenter chipping brittle denture material tooth specimens.*

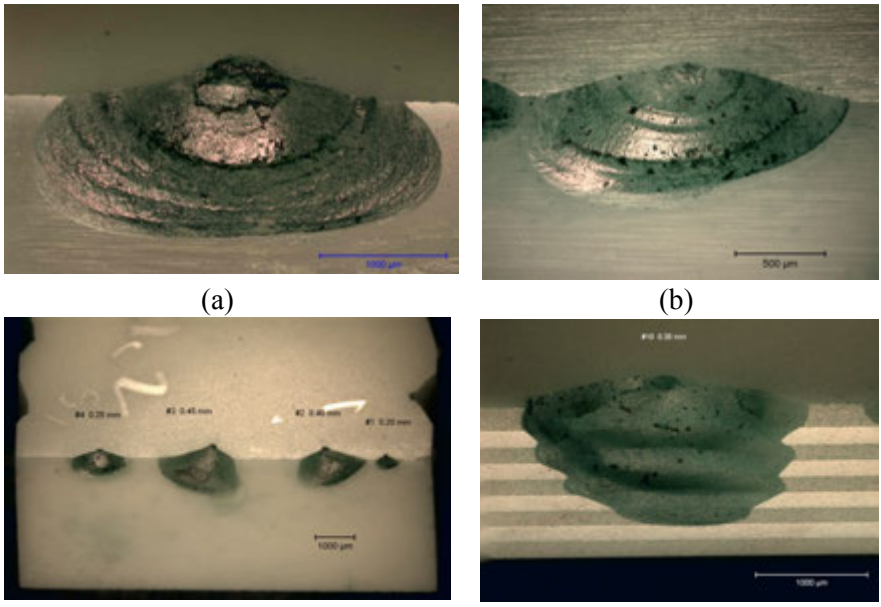

(a) (b)

(c) (d)

Figure 4.28 *Edge chips formed in (a) dental lithium disilicate glass ceramic; (b) dental 3Y-TZP zirconia; (c) dense alumina; and (d) laminated alumina/alumina-zirconia ceramic. The chips were stained with a green felt tip pen to make the fracture surfaces easier to see in these translucent materials.*

Edge chips are very common as *secondary fractures* on broken ceramic or glass fragments. As secondary fractures, they may have had nothing to do with the original cause of fracture. They easily occur if fragments bump into each other or impact other objects during breakage or subsequent handling. If there is any doubt as to whether an edge chip is a secondary or a primary fracture, compare the matching fracture halves. If the chip is only on one half, then it is a secondary fracture. It is quite common, especially with glasses, to have one fracture half rub against the edge of the matching fracture half, causing chips in the latter. Undesirable secondary fracture chips can occur in bend bar strength specimens and other test coupons if the pieces fly around and impact the fixtures after the first break. Often the tensile edge of a bend bar will hit first, and the genuine fracture origin may be chipped off! Soft cushioning material should be placed in the fixtures under the bars as discussed in section 4.6. Some additional means to prevent the fragments from flying about should also be used (e.g., cotton or rolled paper or tape pieces).

4.16 Laboratory Test Fractures and Component Fractures

Examination of laboratory test coupon fracture surfaces can often aid interpretation of component failures. It is not unusual to be confronted with only one or two component fractures. The fracture surface markings may be unfamiliar and common fracture markings such as hackle lines or cantilever curls may be hard to recognize. A few broken bend bars, tension specimens, or fracture toughness specimens of the same material may be invaluable in such cases. The fractographer can study the crack propagation behavior and markings for these familiar configurations.

The author used this approach to aid the interpreting of broken large (≈1 m) sintered porous fused-silica missile radomes in the mid-1980s. This is Case 7 discussed in Chapter 10. Only a few broken components were available and an initial examination of the weak material with its rough fracture surfaces was unsuccessful. Examination of bend bar and double torsion fracture toughness specimens gave the author more experience in interpreting crack propagation directions. Optimum examination conditions for detecting hackle and Wallner lines were discovered. This know-how was then applied to the full size components, with the result that fracture surfaces which initially confounded the author became tractable on the reexamination. The origins were found.

4.17 Controlled Component Fractures

Sometimes one must resort to controlled laboratory fractures of components themselves in order to simulate expected or actual fracture modes. Morrell et

al.[37] and Richter[38] have documented two superb examples of this approach for ceramic hip joint balls. Morrell et al.[37] supplemented their component testing with biaxial disk and bend bar fracture testing.

An excellent recent analysis of 27 *in vivo* (in the patient's mouth) all-ceramic dental crown fractures was recently described by Øilo et al.[39] Crowns are shell-like ceramic restorations which are cemented onto a tooth that is too damaged for repair by amalgam or composite fillings. The crowns were a dense alumina, primarily from one source. Most of the clinical fractures split the crowns vertically into two or more pieces such as shown in Figure 4.29. Laboratory testing (*in vitro)* of 30 model crowns of the same material system was done using three different loading schemes. One of the loading schemes, occlusal (top surface) loading of the crowns with a large 30 mm diameter ball pressing on a 3 mm thick rubber disk (to distribute the load and prevent localized contact damage) generated nearly identical fracture patterns as in *in vivo* fractures. Fractographic analysis of both the model and clinical

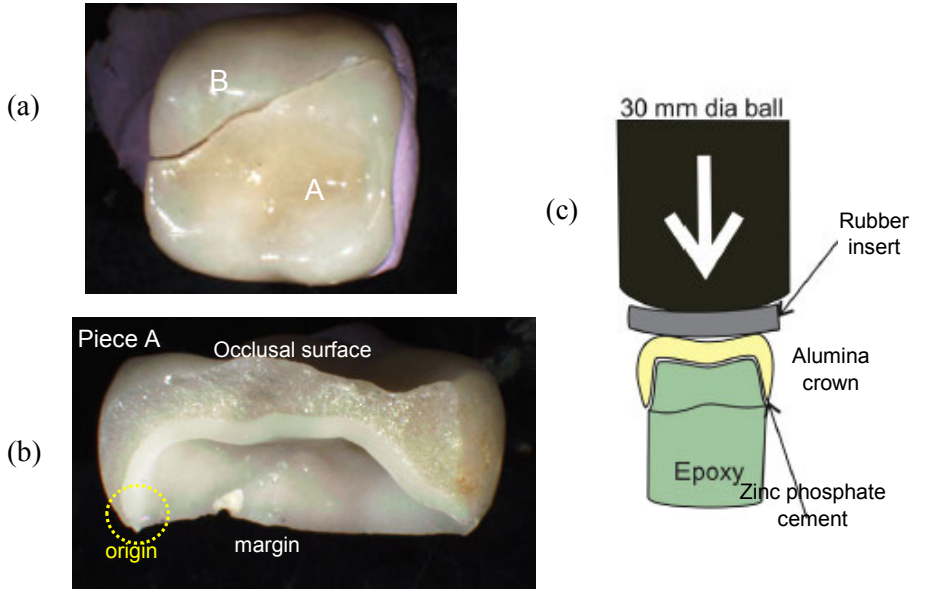

Figure 4.29 *Alumina molar crown (clinical 33) which fractured after 6 years in the patient's mouth. (a) shows an occlusal surface (top) view. (b) shows a side view and the fracture surface of piece A. Careful examination showed the origin was on the margin on the left, and the fracture ran up through the crown and to the other side, splitting it in half. (c) shows the laboratory test set up which produced nearly identical fracture patterns. The epoxy base simulated the dentin of the reduced human tooth. (courtesy M. Øilo)*

fractures confirmed that the occlusal loading generated internal expansion of the shell-like crown, creating high hoop stresses along the margins (the open end of the crown that is in contact with the gum line). Subsequent work verified that the clinically-fractured pieces had excessive faults (chips, cracks, irregularities) at much too sharp (~0.1 mm) margins. Figure 6.70 is one example, and several more are shown in Case 12 in Chapter 10. The combination of the faults with the hoop stresses led to premature splitting fractures.

Another dental example, but on an actual human tooth, was by Dr. J. Quinn.[40] She mimicked a fracture of an upper right canine tooth that broke at the root several days after the patient had heart surgery. It was thought that blunt force damage during intubation by an anesthesiologist had caused damage that led to the fracture. Fractographic analysis showed that fracture started from the lingual (tongue) side and caused a curved fracture plane from cantilever loading. Dr. Quinn obtained a comparable tooth from an extraction (from another patient) and loaded it in cantilever loading in a laboratory setting. It broke in an almost identical manner. This, plus tooth decay in the original tooth, evidence of step wise crack growth, and evidence of bruxism, showed the tooth was damaged before the surgery. The anesthesiologist was not at fault. Nevertheless, it was recommended that mouth guards (commonly used by bruxers when sleeping) ought to be used during intubation for surgery as well.

4.18 Finite Element Analysis

Stress solutions may be straightforward for simple shapes and loadings, but many components have complex shapes and asymmetrical loadings. Closed-form solutions for the stress state may not be available. Finite element analysis (FEA) is a valuable tool for such problems. FEA models partition a body into small elements and uses computer analysis to obtain the stresses and strains in each using the theory of elasticity. In principle, the entire stress distribution in a body can be analyzed, provided that the loading conditions are accurately simulated. Software for FEA is becoming increasingly easy to use, but some skill is needed in setting up the problem, applying a good mesh, and identifying the correct boundary conditions. Richter utilized FEA results to help interpret the ceramic hip ball fractures.[38]

FEA analysis can be a case of "garbage in and garbage out." Modelers may be so enamored of the models with their assumed loading conditions and anticipated fracture modes that they are unreceptive to obvious evidence that a component is not fracturing "the way it is supposed to break." A good

modeler should be flexible and not afraid to modify or adapt the simulation based on the fractographic findings. Reference 41 reviews several case studies and compared model predictions to actual fracture modes.

4.19 Characteristics of Some Common Fracture Modes

4.19.1 Mechanical overload fracture

This chapter has illustrated only a sampling of mechanical fractures. The general breakage patterns can sometimes lead one directly back to an origin site, but often it is necessary to examine the fracture surfaces to interpret the directions of crack propagation as shown in Chapter 5. Once a fracture pattern is recognized and an origin site identified, the next step is to assess whether the flaw is intrinsic to the manufacture of the part (as in a pore or inclusion), or from surface finishing, or from handling, contact or impact damage, or environmental attack (e.g., corrosion, oxidation, or erosion). Origins are covered in chapter 6.

4.19.2 Thermal fracture and thermal shock

Thermal stresses are created by differential strains created when portions of the body try to stretch or contract, but are constrained by other portions of the body at different temperatures. Thermal stresses may either be steady state (invariant with time) or time dependent. Gradual or linear spatial temperature gradients usually do not generate thermal stresses. Two types of thermal stress cases occur: (a) components with stresses arising from overall temperature gradients between portions of the body, and (b), surface and interior stresses caused by through-thickness temperature gradients.

The center-heated plate problem discussed in section 4.12 is a classic case of (a). The differential expansion of the middle regions of the structure relative to the rim creates uniaxial hoop type tensile stresses at the rim that trigger fracture from an edge origin. The crack initially propagates perpendicularly to the edge, but then slows down and meanders in the interior biaxial compression stress field. The interior stresses are of insufficient magnitude to cause crack branching. The fracture surface markings (discussed in the next chapter) may be sharp and clear near the origin but then fade away to a very smooth featureless appearance as the crack slows down in the interior. Case 6 in Chapter 10 is an example of a center heated plate fracture in a silicon carbide furnace part. Center-cooled plates have the opposite stress state: tension in the interior and compression at the rim. Fracture is less likely to occur since the edge, which is likely to have the more serious flaws, is in compression.

Thermal stresses and strains occur during transient cool down or heat up events. Sudden temperature changes are called "thermal shock." Thermal shock can cause strains between portions of a body or through-thickness stresses. Ceramics and glasses are most susceptible to sudden cool down thermal stresses, since tensile stresses are created at the surface. The surface layer of the part cools quickly and tries to contract, but the hotter interior portion prevents the contraction thereby creating tensile strains and stresses in the outer layer. Compressive stresses are generated in the interior. Suddenly cooling the surface with a fluid such as water can generate substantial tensile stresses and fracture since the fluid promotes rapid heat transfer from the surface. Some procedures, such as laboratory quenching of hot bend bars into water, create sharp stress gradients with a biaxial stress state at the surface. This leads to the formation of a two-dimensional network of surface cracks that may not necessarily penetrate completely into the interior. Examples are shown in Figure 4-30. Shao et al. [42] showed some images showing how cracking patterns in alumina plates changed with increasing temperature shock. At low shock, a few looping cracks formed. With greater shock, a dense cellular structure formed. With the maximum shock, a cellular structure with enveloping larger cracks appeared.

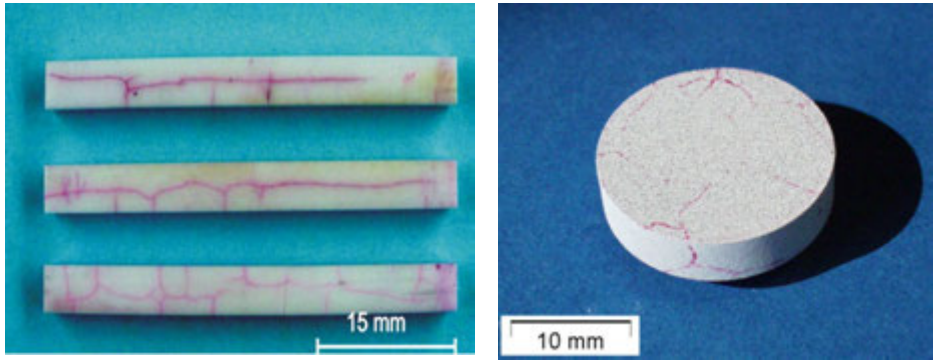

(a) (b)

Figure 4.30 *Thermal shock cooldown cracks in alumina bend bars (a), and a disk (b). The cracks are highlighted by red dye penetrant. (courtesy of R. Danzer and T. Lube, Mountain Univ. Leoben)*

Very-localized thermal fractures from contact of a component surface with a cooler contacting object can create "chill checks" that are very localized tiny cracks (Figure 6.57). These do not penetrate far or very deep since thermal strains are very localized. The cracks are susceptible to extension leading to fracture by subsequent events or loadings.

4.19.3 Impact or contact fractures

Impacts may create localized damage sites that can become the origin of fracture if the impactor is small or sharp, but can also cause fracture by imposing bending stresses on a structure such that fracture initiates on the side opposite the impact site or elsewhere in the body. Section 4.13 shows both scenarios. Sharp and blunt impacting objects create different types of localized damage origins as shown in sections 6.7.4 and 6.7.5. When an impact or contact fracture is suspected, the surface should be carefully examined for "witness marks" as discussed in section 4.6.4.

4.19.4 Corrosion or oxidation

Oxidation and corrosion can weaken a part and leave it susceptible to fracture. Telltale surface reactions are often readily apparent on the surface in the form of numerous pits, discoloration, and surface scale. Sometimes the damage is confined to small localized pits, bubbles, or blisters as shown in Figure 6.26. In some difficult to interpret cases, the reactions are localized along grain boundaries and can only be discerned with the SEM. Chemical analysis can show cation migration to or from a reaction site. It can also indicate contamination or reaction with the environment or furnace linings or insulation. Richerson[43] shows several examples of corrosion-oxidation damaged silicon nitrides.

4.19.5 Residual stresses

Residual stresses can arise from many sources. They can be intentional as in tempered or heat-strengthened glass or unintentional as in ceramics sintered in furnaces with thermal gradients. Residual stresses can exist at different scales within a structure. It is convenient to differentiate these as: *bulk, through the thickness, localized, or microstructural residual stresses.*

There may be bulk residual stresses in a part whereby one portion or side is straining against other portions due to differential contractions during cooling. They can even cause spontaneous fractures in the absence of externally applied stresses. For example, there are reported cases of improperly-sintered porcelain toilets that fractured spontaneously leading to catastrophic house flooding. Residual stresses may also exist through the thickness of a part, as in heat-strengthened or tempered glass plates. Residual stresses may be very localized, such as around a sharp impact or contact damage site (e.g., a sharp particle impact site or Vickers indentation). Shallow residual stresses are also common

on machined and ground surfaces. They typically are compressive within a few micrometers of the outer surface and change to tensile further beneath the surface. As such they can affect origins located on the surface. Finally, residual stresses may exist at a microstructural level, such as at the grain boundaries between grains or between two phases in polycrystalline materials, or between an inclusion and the matrix. The inclusion may have very different thermal contraction or elastic properties than the matrix. Thus, it is simplistic to say: "the piece had residual stresses." One must be more specific and recognize that there may be multiple types of residual stress in a part. Furthermore, the existence of a residual stress may not necessarily be harmful. Some are compressive and some are tensile. Where an origin is located and the type of residual stress it is exposed to are important factors to consider. Crack propagation and branching may be dramatically affected as a crack moves from one type of stress field into another (e.g., compressive to tensile). Residual stresses may be highly variable within a part. Reference 44 is an interesting new paper on the variability of residual stresses in air-jet tempered glass plates. Reference 45 has other examples of nonuniformly-tempered glass including one illustration of a large automobile windshield. Uneven fragmentation and crack patterns are telltale signs of nonuniform tempering.

The fractographer may be tipped off to the existence of residual stresses by the overall fracture patterns as shown in this chapter. A sudden change in crack propagation direction may be another sign. They can also be indicated by abrupt, seemingly spontaneous fractures when a component is being cut or machined. They may also be signaled by Wallner line markings on the fracture surfaces as shown in the next chapter. Distortions in the size and shape of a fracture mirror can be evidence of residual stresses. Analysis of flaw sizes can also be used to estimate residual stresses as shown in section 7.14.

Fréchette described a case of boron carbide blanks fracturing during machining.[46] Fractographic analysis showed that the fracture started at the root of the machine cut and then spread rapidly along the centerline of the slabs and then outward to the free surfaces. This indicated the interior was in tension and the outer portions were in compression. The firing schedule was reviewed and it was learned that the part was allowed to free cool between 1950 ^{o}C to 1800 ^{o}C followed by very gradual cooling thereafter. The free cooling occurred in a range where creep was possible which could have set up a final stress state not unlike tempered glass. Afterwards, no matter how carefully the slicing was done, once it reached the tensile interior stresses the part fractured. The problem was simply remedied by changing the cool down rate through the creep regime to minimize differential strains during the cool down, thereby eliminating the source of the residual stresses.

4.19.6 Time-dependent fracture

Delayed fracture can occur due to slow crack growth from preexistent flaws. The loading conditions and stresses may initially be insufficient to cause breakage, but a flaw may slowly grow when it is under load until it reaches a critical condition and then triggers breakage. The rate of crack growth is very sensitive to the stresses and stress intensities acting on a flaw, and growth can be very slow or rather fast. For constant stress, cracks accelerate with time in accordance with fracture mechanics analyses shown in section 7.10. There may be little or no warning of the imminent failure since the extent the crack grows to become critical may be very small. Sometimes the slow crack growth leaves telltale markings on a fracture surface as shown in section 5.9.

4.19.7 Compression fracture

Genuine compression fractures are rare. The compression strength of ceramics and glasses is ten or more times greater than the tensile strength. Unless special precautions are taken in testing many specimens actually break from tensile stresses and not from genuine compression. Tensile stresses can arise from even slight misalignments or elastic property mismatches, and the tensile stresses will cause fracture.[47,48,49,50] Specimen design is critical. End splitting can occur if the compliance of the loading anvils creates sideways stresses at the ends of the specimen. Right circular cylindrical specimens are especially

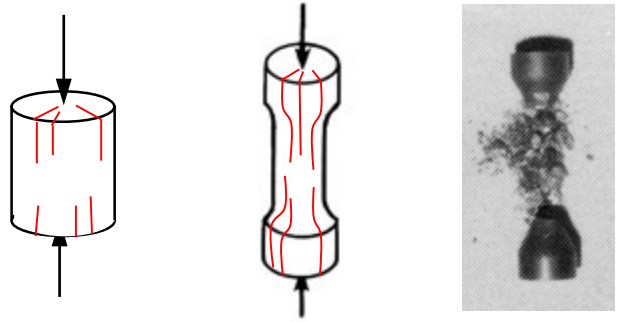

(a) (b) (c)

Figure 4.31 *Compression strength specimens. Cylindrical specimens (a), are very susceptible to end splitting shown by the red cracks. Dumbbell specimens (b) are also susceptible to end splitting if the loading anvils are not carefully chosen or are misaligned. (c) shows a valid compression fracture whereby the gage section is pulverized but the end caps are intact. (c is courtesy C. Tracy).*

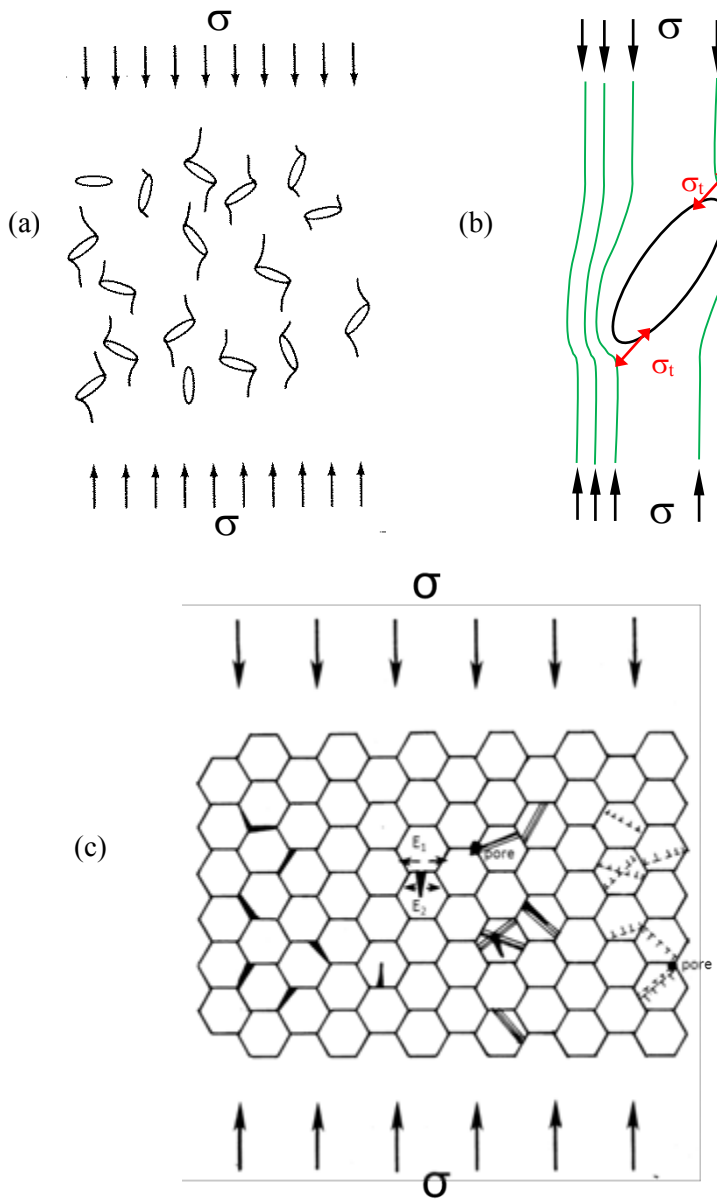

Figure 4.32 *Mechanisms of compression fracture. (a) shows microcracks ("wing cracks") that form from preexisting flaws such as pores. (b) is a close-up of the flow lines of stress around an inclined semielliptical pore. Localized tensile stress occurs at the flaw ends. (c) shows a simulated microstructure with hexagonal grains. Microcracks can be generated at grain boundaries (left), or from elastic property mismatch at grain boundaries (middle), or from twinning or dislocation activity within grains (middle and right side).*

prone to these problems, and often fractures occur due to end splitting as shown in Figure 4.31a. Such results are invalid. Dumbbell tapered specimens are preferred, as shown in Figure 4.31b,c. A properly-tested specimen fracture is shown in Fig 4.31c. The extraordinary fragmentation of the gage section is notable. There is no point in looking for a single fracture origin. The goal of a fractographic analysis is more to verify that a test was done correctly, and to identify the mechanism of compression fracture as described in the next paragraphs.

The primary mechanisms of compression fracture are shown in Figure 4.32. One mechanism shown in (a) and (b) involves preexisting flaws.[51,52] Although the overall stress state is compression, the flow lines of stress cannot pass through an open flaw such as an inclined pore. They bend around the obstacle and create localized, sideways tensile stresses at the pore ends. (Shear stresses exist across the flaw and at its ends, but they can be resolved to localized tensile stresses as shown in Figure 4-32b.) Microcracks initiate, then grow stably and alter the flow lines of stress such that the local tensile stresses gradually rotate to a horizontal orientation. The microcracks propagate and align themselves parallel to the compression loading axis and eventually stop as shown in Figure 4.32a. These cracks are often called "wing cracks." New microcracks initiate at other pores with different orientations and sizes. As loading continues, the structure becomes saturated with a high density of microcracks. Final fracture occurs with a sudden dramatic collapse and "explosion" of the specimen. Enormous stored elastic energies are released in the form of pulverization, kinetic energy of the fragments, sound waves and reverberations, and even triboluminescent light emission. The key point here is that compression strength is not controlled by a single large flaw. It is controlled by the flaw density and size distribution. Pores are used in the explanation above, but other flaws (e.g., inclusions) can induce the same response if the elastic properties of the flaw do not match the matrix or there are localized residual stresses around the flaws.

Figure 4-32c shows several alternative modes of fracture that do not necessarily require initial flaws. Microcracks can be generated in a microstructure by several mechanisms.[53,54] Grain boundary microcracks (on the left in Figure 4-32c) can be initiated due to elastic property mismatches between the adjoining grains that have different orientations. The elastic moduli and crystal constants can be dramatically different on different orientations, especially in non-cubic materials. Furthermore, strong residual stresses can exist along grain boundaries due to differential shrinkage between adjoining grains with different orientations. The middle of Figure 4-32c shows two grains with different orientations and moduli and, as vertical force is applied, the lateral strains can

be very different, causing the nucleation of wedging cracks in one or the other grain. On the right of the Figure 4-32c, twins or dislocations within grains can initiate microcracks. Usually there are not enough independent slip systems active at low temperatures to lead to generalized plasticity, but the very large compression stresses can create sufficient dislocation activity and buildups to form microcracks within grains or at grain boundaries.

Chapter 4 References

1. V. D. Fréchette, *Failure Analysis of Brittle Materials*, Advances in Ceramics, Vol. 28, American Ceramic Society, Westerville, OH 1990.
2. F. W. Preston, "The Angle of Forking of Glass Cracks as an Indicator of the Stress System," *J. Am. Ceram. Soc.,* **18** [6] (1935) 175 - 176.
3. N. Shinkai, "The Fracture and Fractography of Flat Glass," pp. 253 – 297 in *Fractography of Glass*, eds. R. C. Bradt and R. E. Tressler, Plenum Press, NY, 1994.
4. R. W. Rice, "Ceramic Fracture Features, Observations, Mechanism and Uses," pp. 5 – 103 in *Fractography of Ceramic and Metal Failures,* Special Technical Publication 827, American Society for Testing and Materials, West Conshohocken, PA, 1984.
5. R. E. Bullock and J. L. Kaae, "Size Effect on the Strength of Glassy Carbon," *J. Mat. Sci.,* **14** (1979) 920 – 930.
6. G. D. Quinn and G. Wirth, "Multiaxial Strength and Stress Rupture of Hot Pressed Silicon Nitride," *J. Eur. Ceram. Soc*., **6** (1990) 169 - 177.
7. J. B. Quinn, "Extrapolation of Fracture Mirror and Crack-Branch Sizes to Large Dimensions in Biaxial Strength Tests of Glass," *J. Am. Ceram. Soc*., **82** [8] (1999) 2126 – 2132.
8. D. Shetty, A Rosenfield, and W. Duckworth, "Crack Branching in Ceramic Disks Subjected to Biaxial Flexure," *Comm. Amer. Ceram. Soc.,* Jan. 1983, C10-C12.
9. D. Hull, "Influence of Stress Intensity and Crack Speed on the Fracture Surface Topography: Mirror to Mist to Macroscopic Bifurcation," *J. Mat. Sci.*, **31** (1996) 4483 – 4492.
10. G. D. Quinn and R. Morrell, "Design Data for Engineering Ceramics: A Review of the Flexure Test," *J. Am. Ceram. Soc*., **74** [9] (1991) 2037 - 2066.
11. A. Tsirk, *Fractures in Knapping*, Archeopress, Oxford, United Kingdom, 2014, page 171, Figure 11.3.
12. H. Kolsky, "The Waves Generated by Brittle Fracture in Glass," *Trans. Soc. Rheology*, **20** [3] (1976) 441 – 454.
13. J. Miklowitz, "Elastic Waves Created During Tensile Fracture, The Phenomenon of a Second Fracture," *J. Appl. Mech.,* Mar. 1953, 122 – 130.
14. G. D. Quinn, "Twisting and Friction Errors in Flexure Testing," *Ceram. Eng. Sci. Proc*., **13** [7-8] (1992) 319-330.
15. H. Fessler and D. C. Fricker, "A Theoretical Analysis of the Ring-on-Ring Loading Disk Test," *J. Am. Ceram. Soc.,* **67** [9] (1984) 582 – 588.

16. J. A. Salem and L. Powers, "Guidelines for the Testing of Plates," *Ceram. Eng. Sci. Proc.,* **24** [4] (2003) 357-364.
17. D. Maccauley, *Cathedral: The Story of Its Construction*, Houghton Mifflin, New York, 1981.
18. D. Maccauley, *City: A Story of Roman Planning and Construction,* Houghton Mifflin, New York, 1974.
19. D. G. Holloway, "The Fracture Behavior of Glass," *Glass Technol.,* **27** [4] (1986) 120 -133.
20. T. A. Michalske and E. R. Fuller, Jr., "Closure and Repropagation of Healed Cracks in Silicate Glasses," *J. Am. Ceram. Soc*., **68** [11] (1985) 586-590.
21. S. M. Wiederhorn and P. R. Townsend, "Crack Healing in Glass," *J. Am. Ceram. Soc*., **53** [9] (1970) 486 – 490.
22. B. Stavrinidis and D. G. Holloway, "Crack Healing in Glass," *Phys. Chem. Glasses,* **24** [1] (1983) 19-25.
23. A. Yuse and M. Sano, "Instabilities of Quasi-static Crack Patterns in Quenched Glass Plates," *Physica D,* **108** (1997) 365-378.
24. A. Yuse and M. Sano, "Transition Between Crack Patterns in Quenched Glass Plates," *Nature,* **362**, 25 March 1993, 329-331.
25. J. B. Kepple and J. S. Wasylak, "Fracture of Glass Containers," pp. 207 – 252 in *Fractography of Glass,* ed. R. C. Bradt and R. E. Tressler, Plenum, NY, 1994.
26. F. W. Preston, "Bottle Breakage – Causes and Types of Fractures," *Bull. Am. Ceram. Soc*., **18** [2] (1939) 35 -60.
27. T. A. Michalske, "Quantitative Fracture Surface Analysis," pp. 652 – 662 in *Engineered Materials Handbook Ceramics and Glasses, Volume 4*, ed. S. Schneider, ASM Int., Metals Park, OH 1991.
28. E. A. Almond and N. J. McCormick, "Constant-Geometry Edge-Flaking of Brittle Materials," *Nature*, **321** [6065] (1986) 53-55.
29. Ch De Freminville, "Caractères Des Vibrations Accompagnant Le Choc Dé L'Examen Des Cassures," *Review de Mettalugie*, **4** (1907) 833-884.
30. *Fractography of Glasses and Ceramics IV*, eds. J. R. Varner and G. D. Quinn, *Ceramic Transactions*, Vol. 122, Amer. Ceram. Society, Westerville, OH, 2001.
31. B. Cotterall, *Fracture and Life,* Imperial College Press, London, 2010.
32. M. D. Thouless, A. G. Evans, M. F. Ashby, and J. W. Hutchinson, "The Edge Cracking and Spalling of Brittle Plates," *Acta Metall*., **35** [6] (1987) 1333-1341.
33. J. B. Quinn and R. Mohan, "Geometry of Edge Chips Formed at Different Angles," *Ceram. Eng. Sci. Proc.,* **26** [2] (2005) 85 – 92.
34. G. D. Quinn and J. B. Quinn, "A New Analysis of the Edge Chipping Resistance of Brittle Materials," *Ceram. Eng. Sci. Proc.*, **35** [1] (2015) 209 -224.
35. G. D. Quinn, A. A. Giuseppetti, and K. H. Hoffman, "Chipping Fracture Resistance of Dental CAD/CAM Restorative Materials: Part 1, Procedures and Results," *Dent. Mater.*, **30** (2014) e99 – e111.
36. G. D. Quinn, A. A. Giuseppetti, and K. H. Hoffman, "Chipping Fracture Resistance of Dental CAD/CAM Restorative Materials: Part 2, Phenomenological Model and the Effect of Indenter Type," *Dent. Mater.*, **30** (2014) e112 - e123.

37. R. Morrell, L. Byrne, and M. Murray, "Fractography of Ceramic Femoral Heads," pp. 253 – 266 in *Fractography of Glasses and Ceramics IV,* eds. J. Varner and G. D. Quinn, Cer. Trans., Vol. 122, Amer. Ceram. Society, Westerville, OH, 2001.
38. H. Richter, "Fractography of Bioceramics," pp. 157 - 180 in *Fractography of Advanced Ceramics*, ed. J. Dusza, Key Engineering Materials, Vol. 223 (2003), Trans Tech Publ., Switzerland.
39. M. Øilo, A. K. Kvam, J. E. Tibballs, and N. Gjerdet, "Clinically Relevant Fracture Testing of All-Ceramic Crowns," *Dent. Mater.*, **29** (2013) 815-823.
40. J. B. Quinn, L. W. Schultheis, and G. E. Schumacher, "Failure Analysis of a Broken Tooth," *J. Fail. Anal. Prev.*, **4** [1] (2004) 41-46
41. G. D. Quinn, "Design and Reliability of Ceramics, Do Modelers, Designers and Fractographers See the Same World?" *Ceram. Eng. Sci. Proc*., **26** [2] (2005) 239 – 252.
42. Y. Shao, X. Xu, S. Meng, G. Bai, C. Jiang, and F. Song, "Crack Patterns in Ceramic Plates after Quenching," *J. Am. Ceram. Soc*., **93** [10] (2010) 3006 – 3008.
43. D. W. Richerson, Chapter 16 in *Modern Ceramic Engineering, 2nd edition,* Marcel Decker, NY, 1992.
44. J. Anton, A. Errapart, M. Paemurru, D. Lochegnies, S. Hödemann, and H. Aben, "On the Inhomogeneity of Residual Stresses in Tempered Glass Panels," *Estonian J. Engineering*, **18** [1] (2012) 3-11.
45. K. Blank, "Some Practical Aspects of Thermally Strengthened Glass," pp. 485 – 499 in *Strength of Inorganic Glass*, ed. C. Kurkjian, Plenum, NY, 1985.
46. V. D. Fréchette, "Fractography and Quality Assurance of Glass and Ceramics," pp. 227 - 236 in *Quality Assurance in Ceramic Industries*, eds. V. D. Fréchette, L. D. Pye, and D. E. Rase, Plenum, NY, 1978.
47. A. Rudnick, C. W. Marschall, W. H. Duckworth, and B. R. Enrick. "The Evaluation and Interpretation of Mechanical Properties of Brittle Materials," U.S. Air Force Materials Laboratory Technical Report, AFML TR 67-316, April 1968.
48. C. A. Tracy, "A Compression Test for High Strength Ceramics," *J. Test. and Eval.,* **15** [1] (1987) 14-19.
49. W. Dunlay, C. Tracy, P. Perrone, "A Proposed Uniaxial Compression Test for High Strength Ceramics," MTL TR 89-89, US Army Materials Technology Laboratory, Watertown, Mass., 1989.
50. G. Sines and M. Adams, "Compression Testing of Ceramics," pp. 403-434 in *Fracture Mechanics of Ceramics, Vol. 3,* eds. R.C. Bradt et al., Plenum, 1978.
51. M. Adams and G. Sines, "Crack Extension from Flaws in a Brittle Material Subjected to Compression," *Tectonophysics,* **49** (1978) 97-118.
52. F.M. Ernsberger, "Tensile and Compressive Strength of Pristine Glasses by an Oblate Bubble Technique," *Phys. Chem. Glasses,* **10** (6) 1969 pp. 240-245.
53. J. Lankford, "Compressive Strength and Microplasticity in Polycrystalline Alumina," *J. Mat. Sci*., **12** (1977) 791 – 796.
54. R. W. Rice, "The Compressive Strength of Ceramics," pp 195 – 229 in *Ceramics in Severe Environments*, eds. W. W. Kriegel and H. Palmour III, Plenum, NY, 1971.

5. Fracture Surface Examination

5.1 Introduction

Fracture surfaces have a wealth of information that may help determine the cause of fracture and even the fracture origin itself. The fracture surfaces should have an initial examination to look for any signs of contamination, and they should be cleaned as discussed in section 3.1 if necessary. There are two important cases where it may be wise to *examine fracture surfaces before cleaning*. First, surface contaminants may provide clues about the fracture event and may not be merely contamination picked up afterwards from handling. Figure 10.26e in Chapter 10 is a good example where discoloration at the origin was an important clue to understanding the initial flaw in a broken dental crown. Second, fine debris on a fracture surface may be a clue that cyclic fatigue may have occurred, if the debris is crushed material that was dislodged from the microstructure. This is covered in section 5.9 on page 5-84.

The origin may range from a type and location anticipated by the fractographer (as in a broken bend bar) to an unexpected type from an unexpected location or cause (as in a broken component). With familiar laboratory strength test specimens, the fractographer may proceed directly to the primary fracture surface and quickly locate the origin area. Usually the fractographer seeks a fracture mirror, a key feature centered on the origin. Figure 5.1 shows two examples. The origins are often very small and magnification by a microscope is necessary. Stereoptical microscopes are ideal for initial fracture surface examinations. Sometimes this examination may be all that is needed for a full characterization of the origin. In other instances, the flaw at the origin is so small that scanning electron microscopy is needed.

Unexpected failure modes or component fractures require more time to study. The crack propagation markings on fracture surfaces allow one to evaluate the state of stress, the crack velocities, and interpret crack propagation paths back to an origin. In instances where an origin is not obvious, it may be necessary to study many fragments and carefully determine the local direction of crack propagation. Stereoptical microscopes are ideal for this initial fracture surface examination. Wallner lines and hackle markings are helpful indicators of the direction of crack propagation (dcp) in each piece. It is helpful to mark which way the crack was running in a fragment. This can be repeated for other fragments and then the pieces reassembled so that the lines of crack propagation can be tracked back to an origin site. Even very complex fractures may be interpreted if the fractographer is patient and systematic.

The greater the stress in the part at fracture, the more the stored energy, and the richer the fracture markings. Weak parts with low stored energy are often difficult to interpret. The part breaks into two pieces with relatively featureless fracture surfaces. Very porous or coarse-grained materials also can mask fracture surface fractographic markings. On the other hand, very strong

(a)

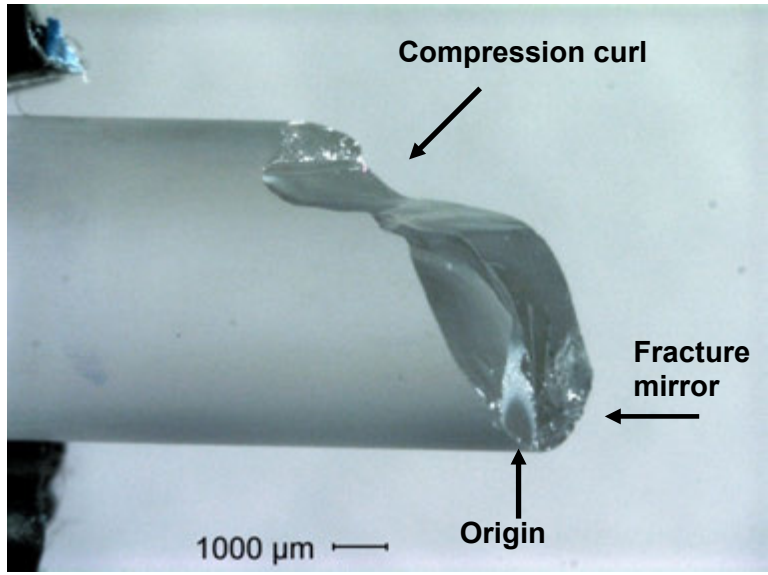

(b)

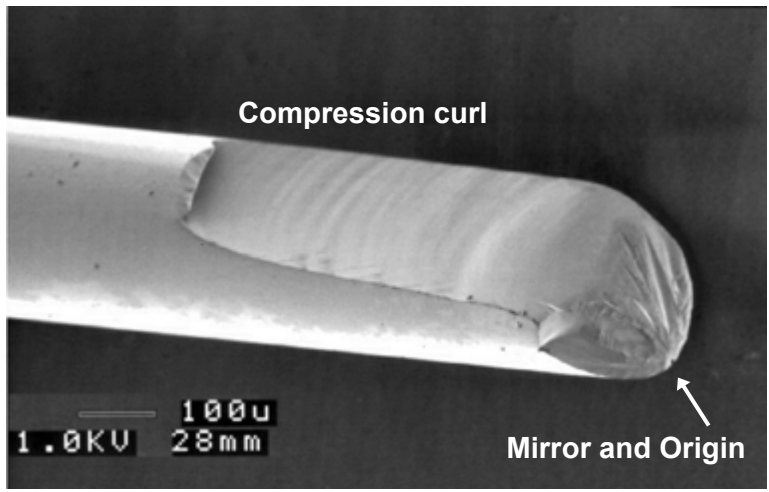

Figure 5.1 *Classic fracture patterns. (a) shows* a low-power stereoptical microscope image of a *fused silica rod fractured in bending at 88.5 MPa (12.8 ksi) (b) shows an SEM image of a chalcogenide fiber fractured in bending at 368 MPa (53.4 ksi). (b is courtesy of J. Quinn and V. Nguyen)*

components such as some glass optical fibers may have so much stored elastic energy at fracture that excessive fragmentation occurs and the origin cannot be found.

The nomenclature of fracture markings is varied. For example, “twist hackle” is also referred to as “river delta” lines. The Guide adopts the nomenclature system devised by Fréchette.[1] His system is practical, logical, and designed to be easily remembered. Some of the definitions in the next sections are from Fréchette and many are new.

“Conchoidal fracture” and “cleavage fracture” are terms commonly used in the geological community. Cleavage fractures are smooth and planar fractures such as those on preferred breakage planes in single crystals. Conchoidal fractures do not follow natural planes of separation and often are curved, in a manner reminiscent of curved seashells. Conchoidal is derived from the Greek word for a mussel shell. Glass and many ceramic fractures are conchoidal. “Joint” is a common term in the geological community and means a fracture surface. Joints are defined as a fracture or crack in a rock mass along which no appreciable movement has occurred. “Parting” is another geological term describing flat fractures in a mineral, but is not necessarily along preferred cleavage planes. Parting is sometimes associated with twinning.

5.2 Fracture Mirrors, A Fractographer’s Best Friend

5.2.1 Fracture mirrors in glass

Fracture mirrors: *Relatively smooth regions surrounding and centered on the fracture origin.* (ASTM C 1322 and C 1145)

Once a fractographer finds a mirror, he is reasonably sure that the fracture origin has been found. Figures 5.1 to 5.3 show mirrors in glass. They are telltale features that can be recognized by even novice fractographers. In strong specimens they are approximately circular or semicircular in shape, but significant deviations may occur as discussed later. Usually there is only one mirror corresponding to a single fracture origin, but there are exceptions that are discussed later in this chapter. There won’t always be a fracture mirror and, if the fractographer cannot find one, he or she should not worry. More about this will be covered later in this chapter, but for now let us take a closer look at the fractographer’s best friend.

The fracture mirror is the region where a crack radiates outwards from a flaw at

(a)

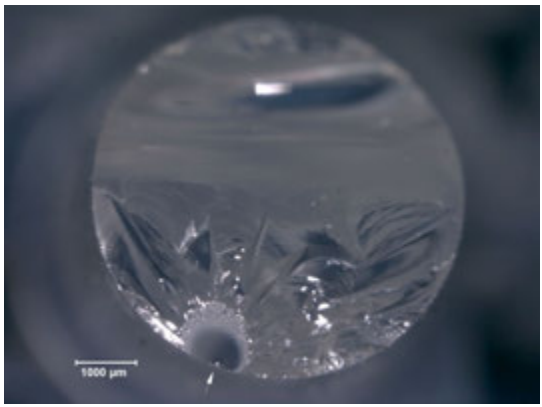

(b)

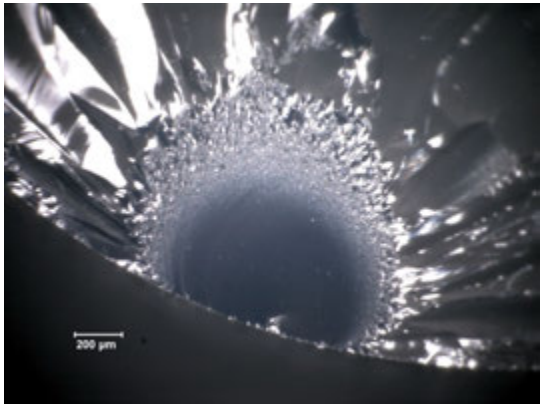

(c)

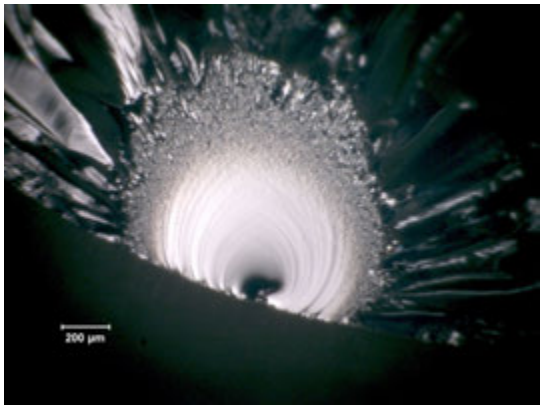

Figure 5.2 *Three views of a fracture mirror in fused silica glass rod broken in bending at a high stress level (96.2 MPa, 13.9 ksi). (a) shows the entire fracture surface. (b) is a close-up of the mirror, and (c) is the same region but with the illumination adjusted. Maximum tension was at bottom center in view (a). The mirror is asymmetric due to the bending stress field.*

(a)

(b)

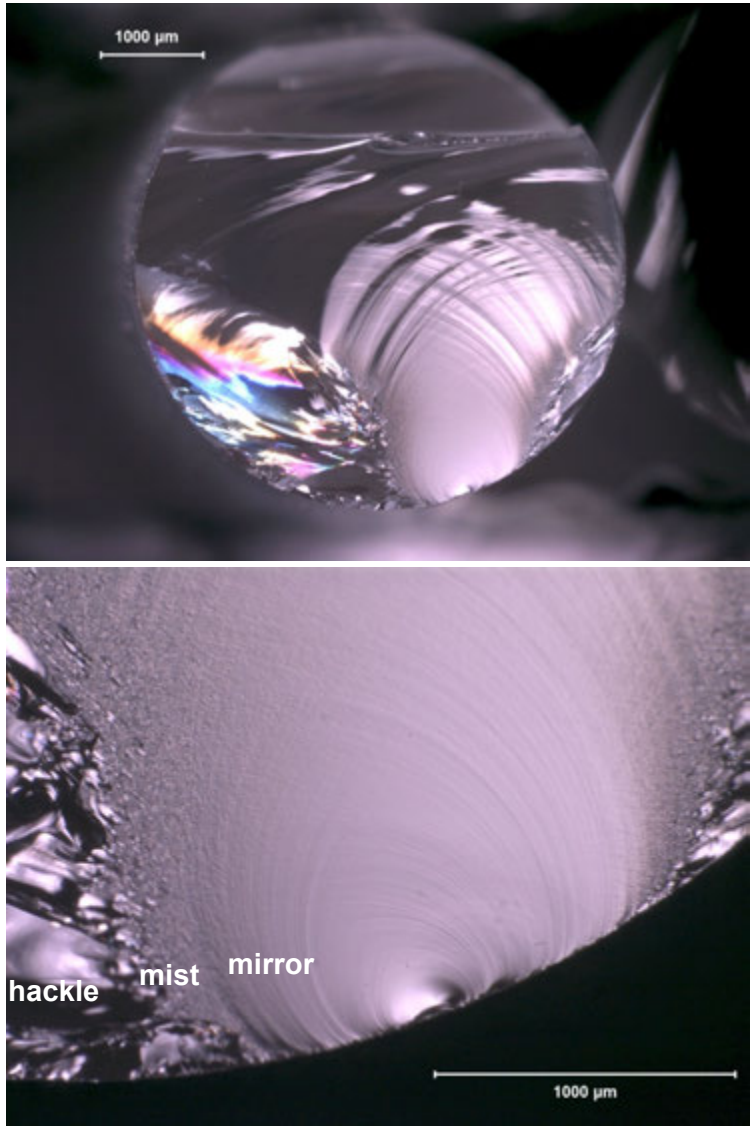

Figure 5.3 *Two views of a fracture mirror in a moderate strength (76.2 MPa, 11.0 ksi) fused silica glass rod broken in bending. The mirror is incomplete since it was large relative to the cross section size. The advancing crack propagated into a decreasing stress field in the interior and did not have sufficient energy to form the mist and hackle in a complete circle. If this rod had been loaded in direct tension instead of bending, the mirror would have been fully formed and semicircular. The incomplete mirror in the direction of the interior is a telltale sign of bending.*

the fracture origin. The crack accelerates from near zero velocity to terminal velocity within the mirror region. Using ultrasonic stress wave fractography on soda lime silica specimens, Richter and Kerkhof[2] and Field[3] showed that a crack accelerates to between one-half to the full terminal velocity (≈ 1500 m/s) by the time the mirror-mist markings formed. This remarkable acceleration over a very short distance occurs in microseconds. Smekal[4] arrived at the same conclusion from his analysis of the Wallner lines (described later in this chapter) inside fracture mirrors.

The terminal velocity in glasses ranges from 700 m/s to 2500 m/s depending upon composition and elastic properties. Terminal velocities are greater for ceramics. Table 5.1 lists some values. The terminal velocity is about 0.5 to 0.6 times the Raleigh surface wave velocity in an elastic body, or about 0.38 times the longitudinal (dilatational) stress wave velocity. The Raleigh wave velocity is less than the longitudinal wave velocity, $v_l = \sqrt{E/\rho}$, where E is the elastic modulus and ρ is the density. The terminal velocity of the crack is limited by the speed that elastic energy is transferred to the crack tip. In principle, the crack can travel as fast as the Raleigh wave speed, but in practice the local deviations of the crack front that create mist and hackle limit the crack speed. Some atypical shock loading cases can drive a crack faster than the normal terminal velocity provided that the crack does not develop mist, hackle, or branching. Maximum crack velocities in single crystals whereby mist and hackle formation are suppressed can reach a greater fraction of the Raleigh wave speed than glass and polycrystalline ceramics. In some ballistic impact conditions, a *damage wave* of cracking in glass can proceed at velocities 80 % to 90 % of the *longitudinal* wave speed.[5,7] High speed photography revealed that individual crack segments traveled no more than the conventional terminal velocity of 1480 m/s, but that secondary cracks nucleated right behind the shock wave.

If the stresses acting on the advancing crack decrease, the crack can decelerate and even stop. This is not unusual in thermal shock cases where stress gradients can be large.

The term mirror came in to being as a result of early optical microscopy of glasses wherein the mirror region was so smooth that it reflected light like a mirror. From my research into the history of fractography of brittle materials, it appears that Brodmann[6] first used the word "*mirror*" in 1894. Figure 5.2c shows a bright mirror region. (The illumination in this figure also accentuates the faint curved Wallner lines within the mirror, about which more shall be said later in this chapter.) In polycrystalline ceramics or composites, the qualifier

Material	Maximum Crack Velocity (m/s)	Ref.
Soda lime glass	1510	8
Soda lime glass	1580	3
Soda lime glass	1540	12
Soda lime glass	1600	9
Soda lime glass	1500	11
Soda lime glass	1460	7
Various flint glasses	750 - 1400	8
Heavy flint glasses	700 - 1095	9
Mirror glass	1520	9
Borosilicate crown glass (BK-7)	1677	9
Borosilicate crown glass (BK-7)	1800	4
Fused silica	2100	4
Fused silica	2500	11
Fused silica	2155	8
Reaction bonded Si_3N_4 (AME)	2950	10
Hot pressed Si_3N_4 (HS 130)	3500	10
KCl, single crystal	700	3
LiF, single crystal	1700	3
MgO, polycrystalline (85% dense, 15 μm)	1800	9
MgO, single crystal, cleavage {100}	5100	3
Diamond, cleavage {111}	7200	3
Al_2O_3, single crystal sapphire, cleavage on $\{10\bar{1}0\}$	4500	3
Al_2O_3, polycrystalline (Lucalox 15 μm)	2000	10
Tungsten	2200	3
Tool Steel	1700	10
Resin Plastic	420	8
PMMA	770	10

Table 5.1 *Terminal crack velocities from Field (3), Smekal (4), Winkler et al. (7), Schardin et al. (8), Kerkhof (9), Congleton and Denton (10), Chaudhri (11), and Barstow and Edgarton (12)*

"relatively," as in "relatively smooth," must be used, since there is an inherent microstructural roughness even in the area immediately around the origin flaw.

The underlying principal that accounts for the micro and macro branching has been attributed to the crack reaching a critical velocity,[13] a critical energy level,[14] a critical stress intensity,[15,16,17,18] or a critical strain intensity.[19] A velocity criterion for crack branching was discounted by data shown by Congleton and Petch.[16] Richter and Kerkhof,[2] Field,[3] and Döll[20] used ultrasonic fractography to show that cracks approached terminal velocity before the formation of the mist boundary and there was no pronounced change in velocity when the mirror formed. Kirchner et al.[17,18] showed convincing evidence that a stress intensity criterion accounts for the mirror sizes and

shapes. Congleton and Petch[16] demonstrated that a stress intensity criterion controlled branching. They also showed that the Johnson and Holloway energy criterion[14] was related to the stress intensity criterion. Tsai and Mecholsky[21] have pointed out that for isotropic materials it is difficult to distinguish between the energy, stress intensity, or strain intensity criteria since they are all related. This topic will be discussed again in Chapter 7 on Quantitative Analysis and in Appendix D on Guidelines for How to Measure Fracture Mirrors.

Careful electron microscopy and atomic force microscopy now have shown that the formation of the mirror is a gradual progression of very localized crack path deviations from the main plane. Figures 5.4 a-e show superb transmission electron microscope images of various regions in a glass fracture mirror collected by Beauchamp.[22,23] Poncelet[24] showed comparable images in 1958, but Gölz may have been the earliest with extraordinary electron microscope photos published in 1943.[25] Rounded ridges that are elongated in the direction of crack propagation gradually coarsen in amplitude. At some point, they develop slight hackle steps where over running and under running fingerlike crack segments link. This point, where nano-micro scale hackle lines begin to form, could be an important transition point. Close examination of Beauchamp's Figure 5.4 b shows they are not present inside the mirror, but they are just visible in his Figure 5.4c near the mirror-mist boundary.

Attempts to correlate the mirror boundaries with surface roughness parameters have had only limited success, as discussed in more detail in Appendix D. Hull[26] pointed out that different surface roughness characterization devices such as atomic force microscopes (AFMs), mechanical profilometers, and laser optical profilometers all have different advantages, disadvantages, sensitivities, and scanning zone sizes. AFMs can measure tiny regions with very high sensitivities, but may miss large hackle steps in a mist or hackle zone. These latter features can dramatically alter the average or root mean square roughness. Mist and hackle regions may have different roughness at different scales. Hull discusses these various scales of roughness in some detail in his book.[26]

The mirror markings can be explained with reference to Figures 5.2, 5.3b, and 5.4. The explanation below closely follows Fréchette's[1] general discussion as well as Beauchamp's[22] convincing analysis. As the crack accelerates away from the origin, micro portions of the crack front begin to twist slightly or tilt up and down out of the main fracture plane. These local deviations occur as consequence of the stress field in front of a fast crack having maxima that are out of plane, unlike the case for a static or slowly moving crack.[13] The momentary tilting or twisting does not persist for very long since crack plane

(a)

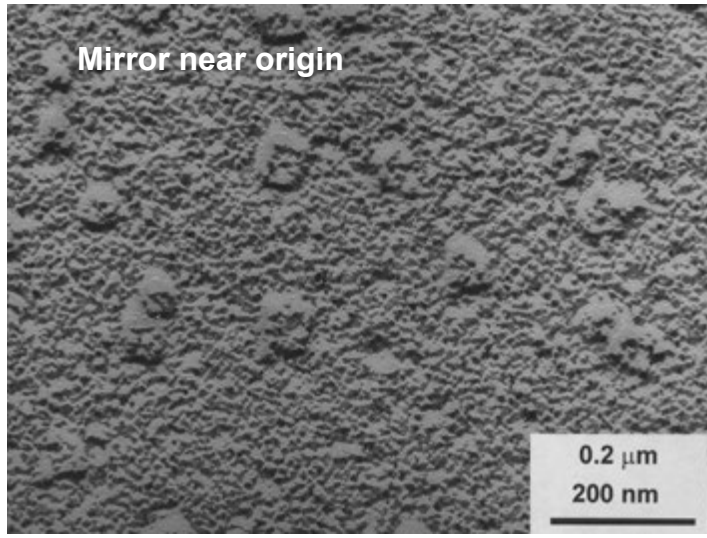

(b)

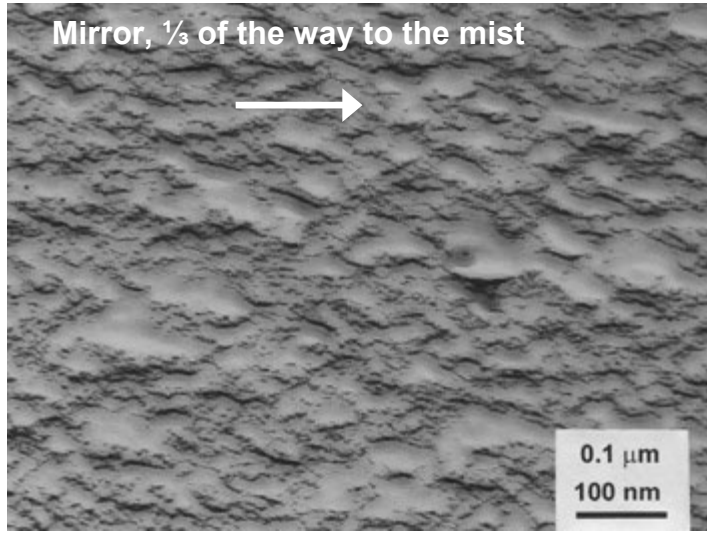

Figure 5.4 *Transmission electron microscope pictures from parts of the fracture mirror in a lightly tempered soda lime glass sheet. (courtesy E. Beauchamp, refs. 22,23) (a) is in the smooth mirror area near the critical flaw. The tiny black dots are an artifact of the specimen preparation, but the larger (50 nm) round bumps are genuine. (b) is in the mirror region about 1/3rd of the way to the mirror/mist boundary. The arrow shows the direction of crack propagation (dcp). The ridges and valleys are elongated in the direction of crack propagation, but they are too small to be detected optically.*

(c)

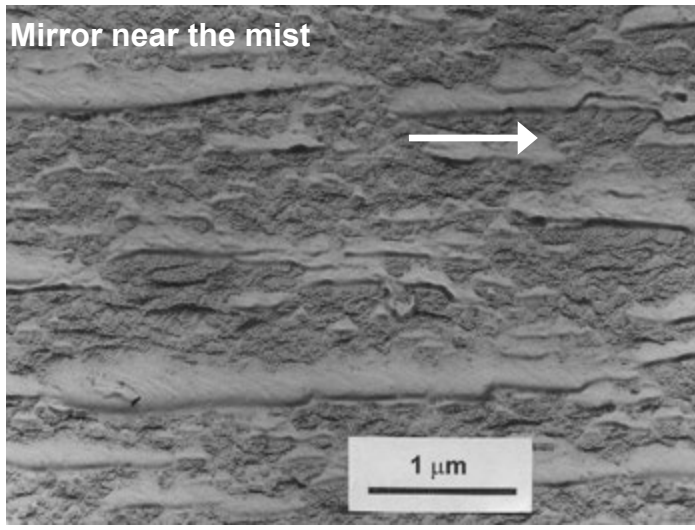

(d)

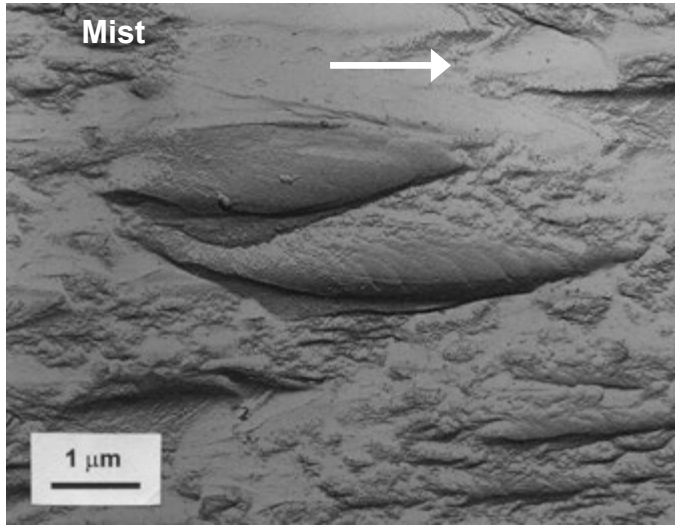

Figure 5.4 continued *(c) is a region still inside mirror but close to the mist boundary. The ridges are longer and wider. (d) is in the mist, just beyond the mirror/mist boundary. The features are similar to the prior figure, except that they are now large enough to be detected optically. Close examination of (c) and (d) reveals faint but distinct twist hackle lines in some of the large features, attesting to some localized lateral crack growth.*

(e)

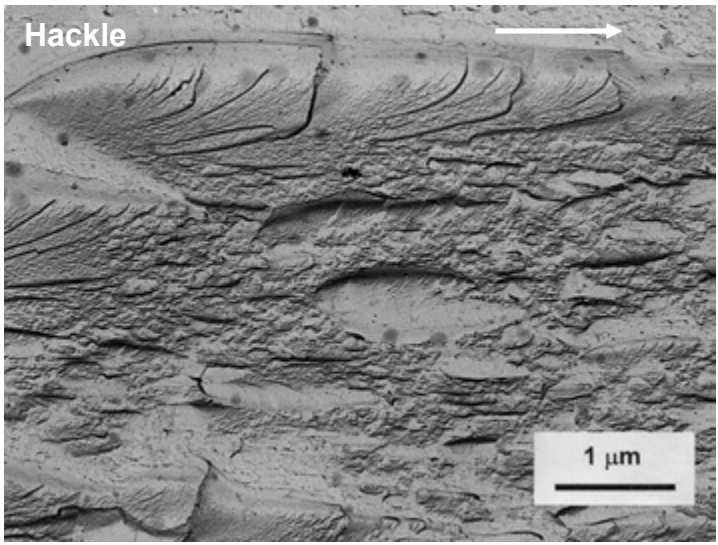

Figure 5.4 continued *(e) shows features in the hackle zone. The features are now larger than 10 μm, but are similar in character to those in the mist and mirror zones.*

deviations are restricted by the energetic cost of creating additional crack surface. The slight tilt or twist variations in crack plane quickly rejoin the main propagating crack plane. These tiny local crack perturbations exist well within the mirror region, but are too small to be optically discernable. As the crack advances, they eventually become large enough to be just discernable with the optical microscope as the "mist" zone surrounding the origin (Figure 5.4d). The mist has a slight frosty appearance such as when water condenses on a reflecting mirror. As the crack continues to advance, the local perturbations increase and begin to oscillate and form larger tongue-like segments that may deviate from the average fracture plane to the degree that micro steps are generated running parallel to the direction of crack propagation. (Some have described the out-of-plane perturbations as "fingers.") The perturbations gradually coarsen such that the tongue-like elements can overcut other portions of the crack front thereby generating large "velocity hackle" lines that run parallel to the direction of crack propagation. Beauchamp[22,23] pointed out that many of these features are similar in character from within the mirror out to the hackle zone. They differ only in scale. The transitions between the regions are gradual and are usually described as not abrupt. One intriguing observation by Beauchamp[22] was that tilted or twisted hackle segments that relink with the main crack plane may generate elastic pulses and Wallner lines (described later in this chapter) that could trigger additional hackle along the crack front. This

could be the impetus to form a band of hackle along the crack front and hence the mist-hackle boundary.

In summary, although the process of roughening through the boundaries has often been described as gradual, there are two potential transition points. The mirror–mist boundary may be a transition where nano-micro steps form between ridges that are tens of nanometers tall. The mist-hackle transition boundary may be where a band of microhackle forms that is triggered by self-generated or external elastic pulses (Wallner lines).

Fréchette[1] defined hackle and mist hackle. This Guide adopts his definition for the former, but makes a slight modification to the latter:

Hackle: *A line on the surface running in the local direction of cracking, separating parallel, but noncoplanar portions of the crack surface. (Ref.1, Fréchette)*

Mist hackle*: Markings on the surface of an accelerating crack close to its effective terminal velocity, observable first as a misty appearance and with increasing velocity revealing a fibrous texture, elongated in the direction of cracking.*

It is implied in these definitions that hackle lines are physical steps on the fracture surface, as opposed to undulations. Mist is fairly obvious in glasses, but is difficult or impossible to discern in ceramics due to the microstructure. Fréchette's definition of mist hackle originally also included the words "and coarsening up to the stage at which the crack bifurcates" which suggests it encompassed all mirror markings including hackle right up to the point of crack branching. It seems reasonable to distinguish the mist region from hackle region for practical reasons that will become evident when ceramic mirrors are discussed below. Therefore this Guide adds the following term:

Velocity hackle*: Hackle markings formed on the surface of the crack close to its terminal velocity, observable as discrete elongated steps aligned in the direction of cracking.*

Mirrors are very important since they not only draw attention to the fracture origin, but their size may be used to estimate the stress in the part at the moment of fracture. For a long time it was common practice to interpret the mirror as having distinct boundaries between the mirror and mist and between the mist and hackle. Extensive empirical work showed that the relationship between the mirror size and the stress at the instant of fracture is:

$$\sigma \sqrt{R} = A \qquad (5\text{-}1)$$

where σ is the tensile stress at the origin at the instant of fracture, R is the mirror radius, and A is a constant, known as the "mirror constant" and is considered by many to be a material property constant. It has units of stress√length, which are the same units as stress intensity which is discussed in detail in section 7.5.1. The mirror radius may either be the mirror-mist boundary or the mist-hackle boundary for glasses. There are different A's for each boundary. For polycrystalline ceramics there usually is simply a single mirror-hackle boundary. Equation 5-1 is discussed in more detail in Chapter 7, Quantitative Analysis and in Appendix D (where guidance is given on how to actually make the measurement), but for the moment we need only consider some general ramifications.

This simple relationship has tremendous practical value. It can be used to estimate the fracture stress. It is not necessary to have a-priori information about the how the part was loaded. The smaller the mirror, the larger is the stress at the origin site. A small mirror is proof that the part was strong and had a small strength-limiting flaw. Conversely, large mirrors mean the failure stress was lower and implies a large defect. In some instances, a part may be so weak that the mirror size is larger than the part cross-section and hence the mirror markings are not visible. That, in and of itself, is valuable information. The existence of a mirror boundary implies that the part was stressed to a moderate or high level. Alternately, very strong parts (e.g., pristine optical fibers) may have such high strengths that mirrors are so small as to be not practically measurable with optical microscopes or the mirror may not even be found due to excessive fragmentation.

Mist and hackle are sometimes triggered earlier than they would otherwise form by material flaws or microstructural features. Figures 5.5a-c shows examples. Strong Wallner lines, described later in this chapter, may also trigger mist formation in fracture mirrors such as shown in Figures 5.6. Figures 5.2 and 5.3 shown earlier also hint at this possibility. Beauchamp has described cases like these where perturbations of the crack front can trigger early mist and hackle[27] and long, persistent "hackle streaks."

Surface irregularities often cause a fracture mirror centered on a surface origin to depart from a semicircular shape and turn slightly inward towards an origin as shown in Figures 5.2 and 5.3.

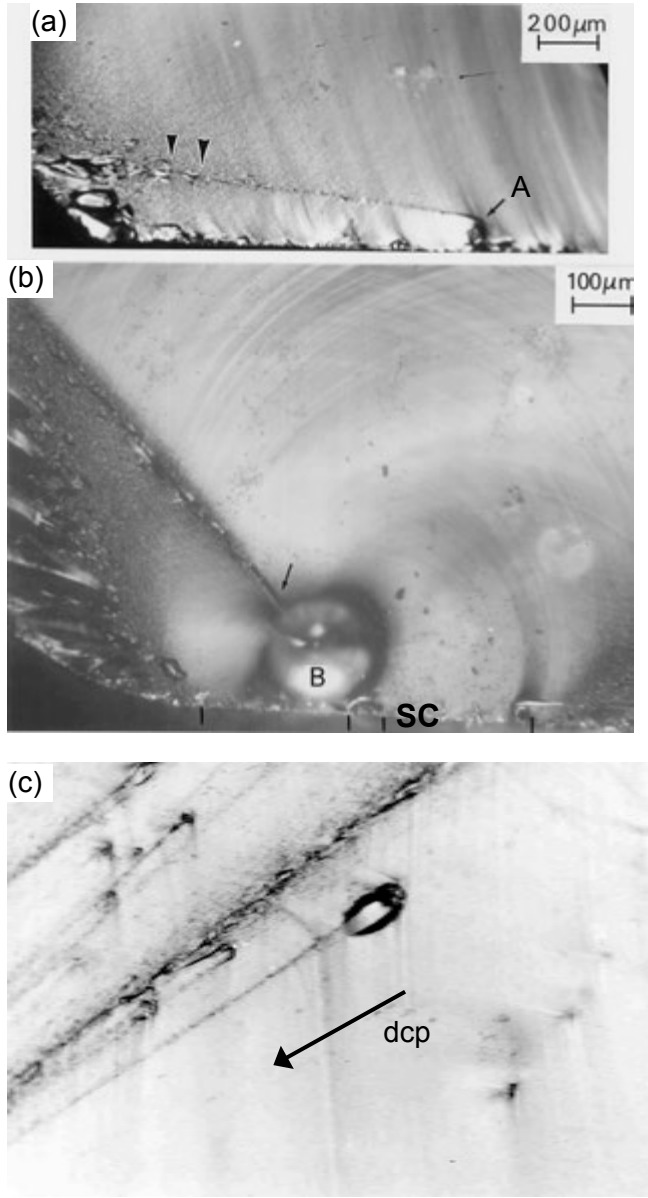

Figure 5.5 *Early mist and hackle streaks associated with defects. (a) shows mist and hackle triggered by a surface crack at site "A" in a soda lime glass specimen at 65 MPa. The origin was well to the right, beyond the photo edge. (b) shows early mist and hackle triggered by a large bubble "B" in a 70 MPa strength specimen. The origin is a surface crack "SC." (c) shows mist behind inclusions in obsidian. Gull wings (described later in this chapter) are also evident. (a and b courtesy R. Rice, c is courtesy A. Tsirk.)*

(a)

(b)

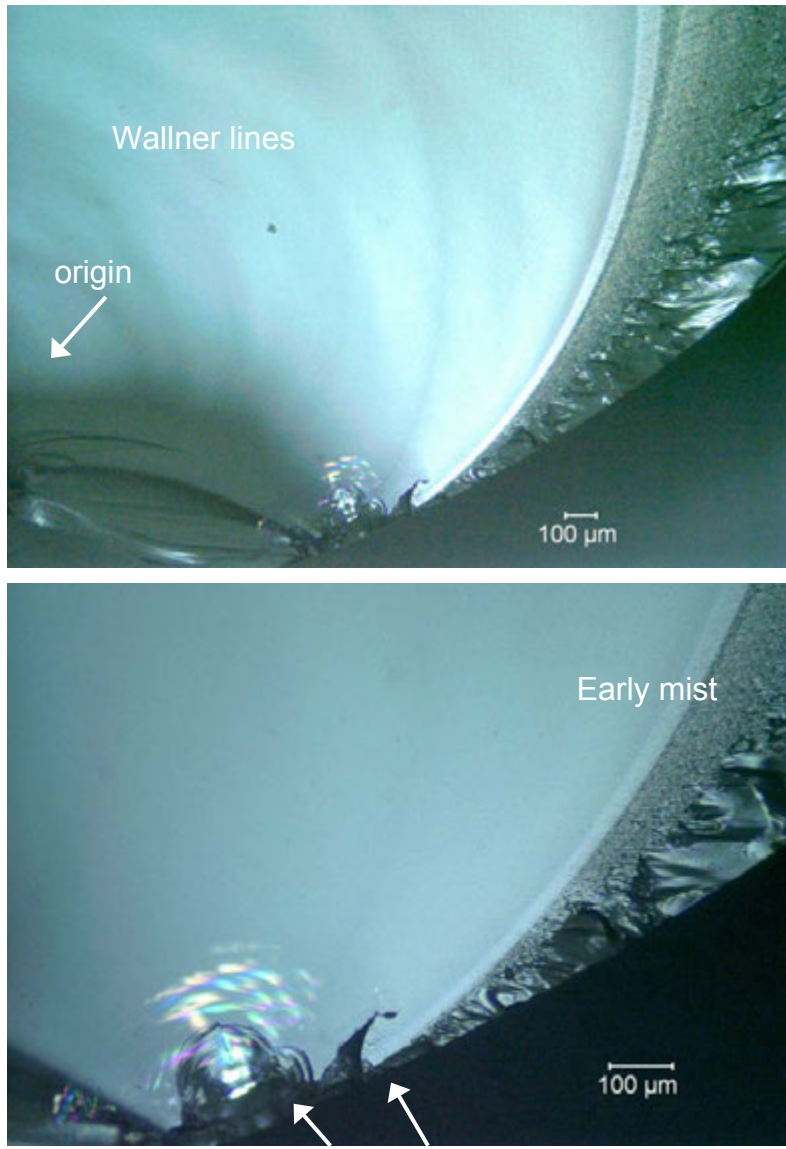

Figure 5.6 *Early mist and hackle. (a) and the enlargement (b) show an example of early formation of mist. The Wallner lines in (a) suggest the origin is off to the left in the image. The crack radiating outwards encounters other cracks in the surface shown by the arrows in (b). A strong primary Wallner line is generated and it triggers mist earlier than normal during mirror formation.*

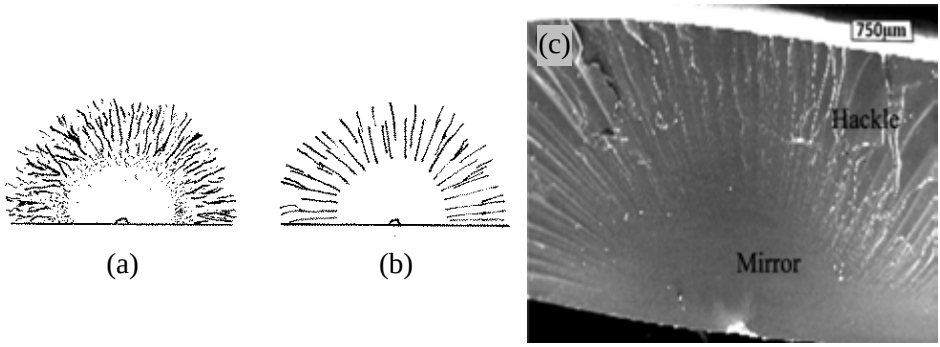

Figure 5.7 *Mixed-mode loading creates fracture mirrors without mist but with a systematic array of "lance hackle." (a) shows a normal mirror from pure opening mode I loading. (b) and (c) show mirrors from mixed opening/shear modes I/II, (c is courtesy J. Mecholsky).*

Gopalakrishnan and Mecholsky et al.[28,29] showed that mist does not form around glass fracture mirrors if the loading has some in-plane shear (Mode II loading) acting on the crack at the same time it is under opening Mode I loading (see chapter 7). Hackle markings are very distinct in such cases as shown in Figure 5.7. The boundary is comprised of "lances" or "lance hackle" that are very similar to twist hackle. These steps on the fracture surface probably all go up (or go down) systematically as one goes around the crack front periphery, unlike the case of Mode I loading, where hackle steps are random or alternating up and down out of the fracture surface. The size of the mirror is not altered by the mixed-mode loading. The mirror/mist boundary for pure Mode I loading and the onset of lances in mixed Mode I/II loadings are comparable in size. The practical significance of this difference in appearance is that if a glass fracture mirror is comprised of lances with no mist, then the loading was not pure tension, Mode I, but mixed mode with some shear. Sommer[30] has shown similar fracture surfaces with lance hackle and no mist in glass rods loaded in combined tension and torsion (i.e., mixed Mode I and Mode III loading).

5.2.2 Fracture mirrors in ceramics

The microstructure and polycrystalline nature of most ceramics obscures most of the fine details of fracture mirrors. Figures 5.8 - 5.10 show some variants of mirrors in ceramics. Mist is usually not recognizable. Sometimes coarse microstructural elements or flaws in a mirror may trigger early hackle lines within the mirror, prior to the onset of the generalized velocity hackle that

forms the mirror boundary. The mode of crack propagation, whether it is trans- or intergranular, also affects the mirror markings. Transgranular fracture is a mode whereby the crack propagates directly through grains on cleavage planes, whereas intergranular fracture is a mode whereby the crack takes paths along grain boundaries between grains. These modes will be discussed later in section 5.8. Mirrors may be easier to see in materials that start out with transgranular fracture, but then develop increasing fractions of intergranular fracture. On the other hand, it may be more difficult to define mirrors when the fracture mode is intergranular from the origin right through the entire mirror. For these reasons it is appropriate to add the qualifier "relatively" as in relatively smooth when describing the mirror region since there is an inherent roughness from the microstructure even in the area immediately surrounding the origin. Rice observed that mirrors are more detectable in strong specimens and are less clear in weak specimens.[31] Mirrors may not be detectable in coarse grained materials or those with more than 10 % porosity. Mist can only be detected in fine-grained ceramics or those that fracture transgranularly.[32]

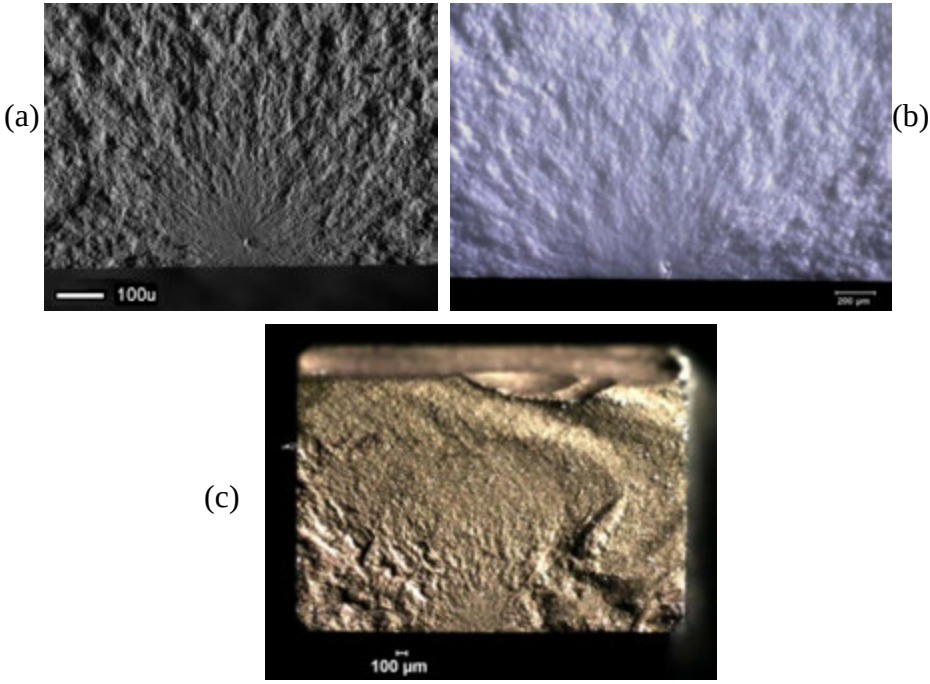

Figure 5.8 *Fracture mirrors in ceramics. (a) is a SEM image of a strong bend bar (1024 MPa) of Y-tetragonal zirconia polycrystal (Y-TZP) for dental crowns. (courtesy J. Quinn) (b) is a stereoptical microscope of another Y-TZP bend bar (486 MPa) for an engine application. (c) is a stereoptical image of a silicon nitride bend bar (487 MPa).*

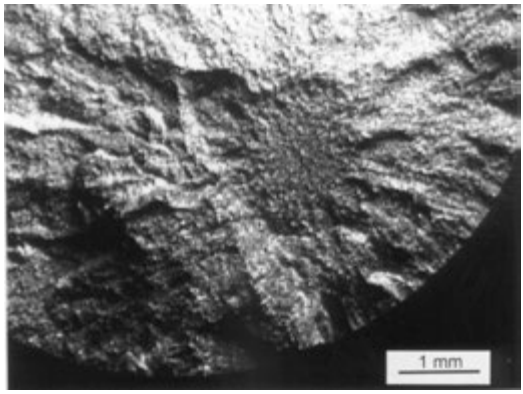

(a)

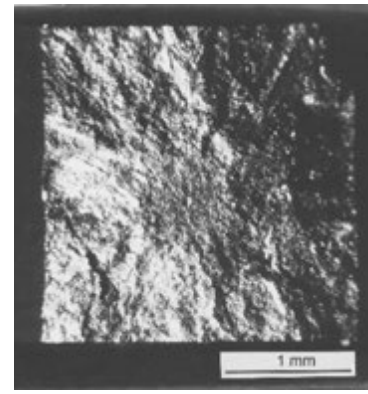

(b)

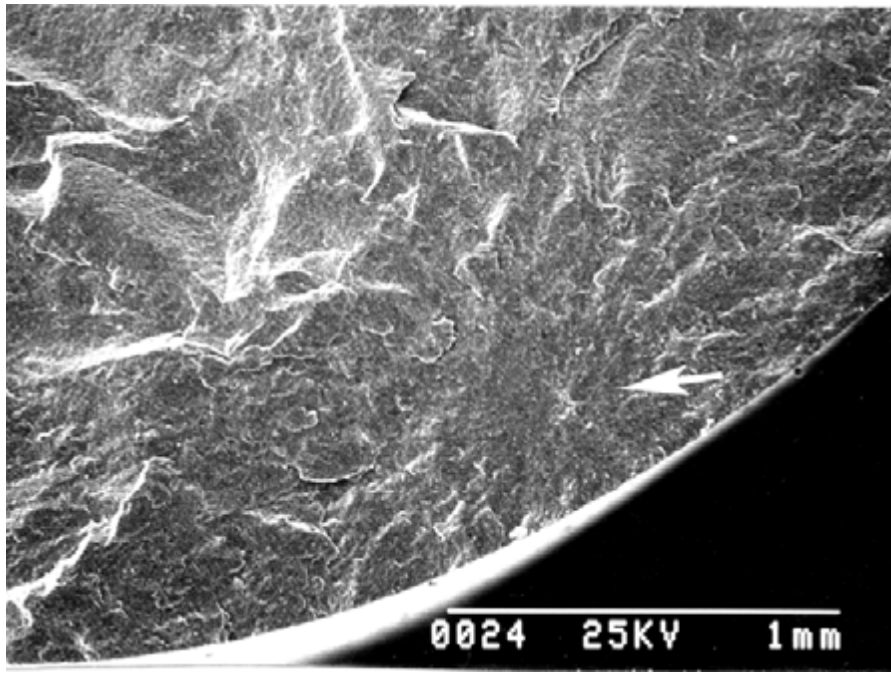

(c)

Figure 5.9 *Fracture mirrors in ceramics. (a) is a hot-pressed silicon carbide tensile specimen (371 MPa). (b) is a silicon carbide tension specimen and (c) is a silicon nitride rod broken in flexure. Many beams and rods broken in flexure have internal flaw origins if the specimens are ground carefully.*

(a)

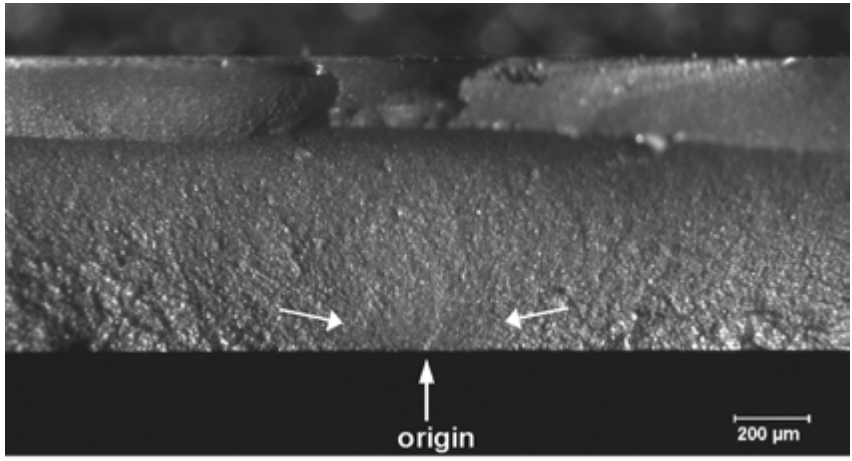

(b)

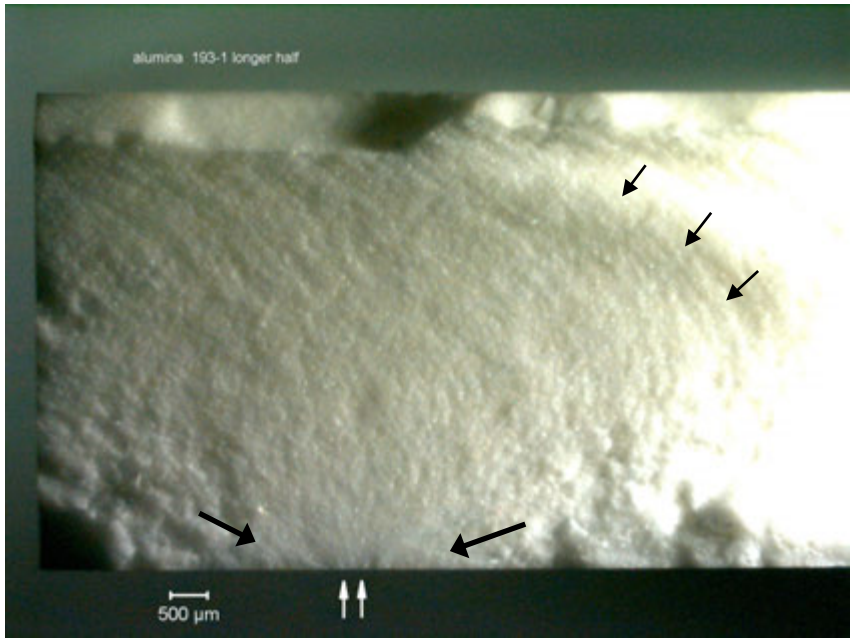

Figure 5.10 *Examples of incomplete ceramic mirrors due to bending stress fields. (a) shows an optical image of a gold-coated biaxial Y-TZP zirconia disk. The arrows mark the origin and the mirror. (b) is an alumina bend bar with low-angle grazing illumination to reveal the mirror in this stereoptical microscope image of this translucent material. The small white arrows mark the origin (a grinding crack) and the large black arrows mark the mirror. The small black arrows mark one of many coarse, arced Wallner lines.*

5.2.3 Fracture mirrors, special cases

Multiple fracture mirrors
In many cases, only one origin is activated, and there is only one fracture mirror. The crack propagates and reaches terminal velocity after only a short extension and in a period of microseconds. In rare instances, two virtually identical flaws may be triggered simultaneously in a laboratory strength test such as shown in Figure 5.11.

Sometimes there will be multiple simultaneously-activated origins in a component or test specimen due to severe loadings such as laser heating or thermal shock by water quenching.[33] Another example is a side-impacted bottle as shown in Figure 4.21f whereby the impact causes the sidewalls of the vessels to flex outwards. The bending stresses activate "hinge fractures" to either side of the impact site. When there are multiple origins, each generates a crack system and the fractographer must deduce the sequence of events that causes them. Sometimes, once one origin starts a crack system, the component stresses are redistributed and a second origin is then activated. The burst gas turbine rotor Case 1 in chapter 10 is an example.

Secondary fractures can occur due to a variety of causes. Elastic wave reverberations after an initial fracture can cause secondary fractures. These complicate the interpretation of high strength four-point bend specimens and it can be difficult to determine which one was the primary fracture as shown in Figure 4.10. An observation that a fracture mirror is on what once was the *compressively*-loaded surface in a bend bar is proof the break was secondary. If there are two fracture planes with mirrors on the tensile side in the inner gage section, the larger mirror may be the primary break and the smaller mirror may be secondary due to stress reverberations that momentarily created a greater local stress.

Concentric mirrors have been reported by Ramulu et al.[34] and correspond to a crack front that is alternately decelerating and accelerating. Such markings also occur in high-strength tensile specimens when a crack branches repeatedly. At each branch, the crack slows down somewhat, then accelerates back to near terminal velocity and branches again.

Steps or jogs in a mirror
In some cases there may be a pronounced step or jog starting at the origin. This usually occurs when the critical flaw is irregular, three-dimensional, or inclined at an angle to the principal stress. Crack extension from the irregular flaw may occur on slightly-offset, parallel planes and thereby create a step or jog which

(a)

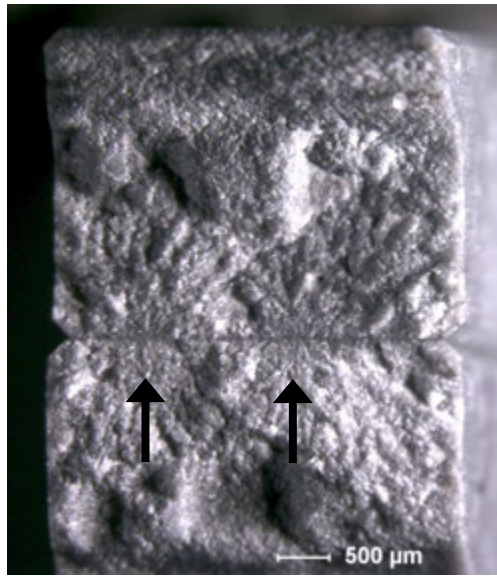

(b)

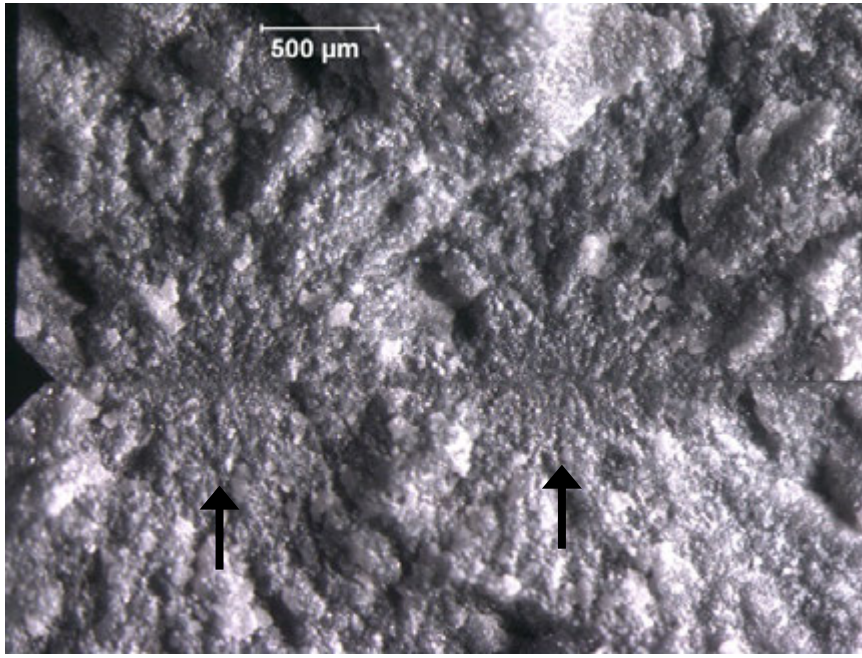

Figure 5.11 *Multiple mirrors from grinding damage in a silicon nitride bend bar. (b) is a close-up of (a). Grinding damage caused fracture in these examples and the origins in each mirror were nearly identical. (Ref. 35)*

(a)

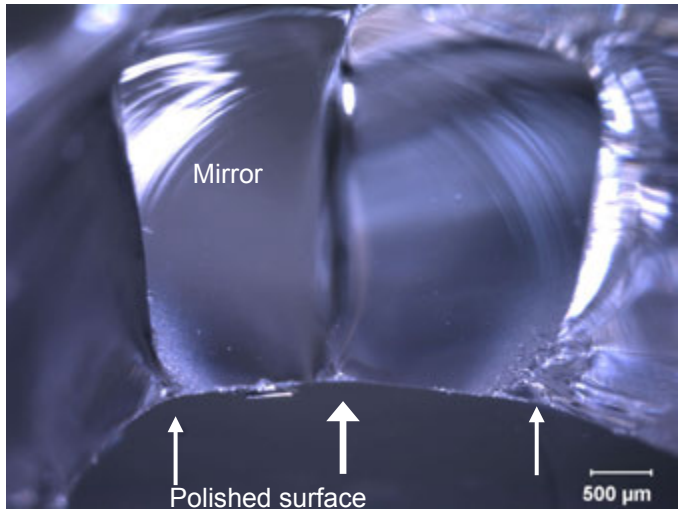

(b)

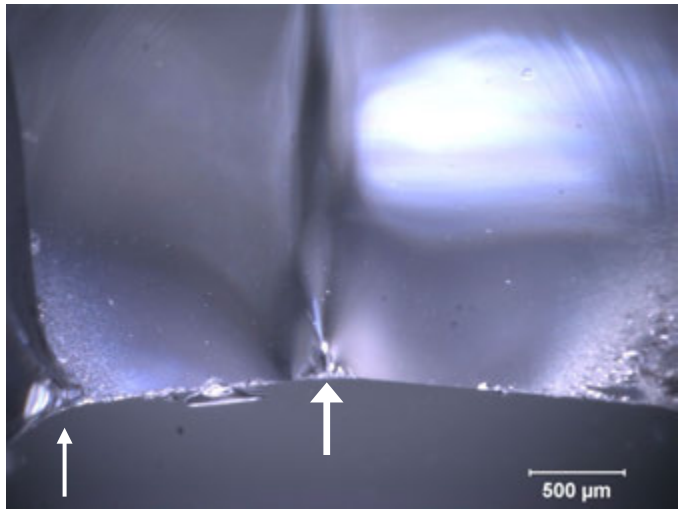

Figure 5.12 *Bent mirror in a BK-7 borosilicate crown glass ring-on-ring disk strength specimen. The origin was a Vickers indentation flaw (large white arrows) with multiple radial and median cracks. (a) and the close-up (b) show the fracture surface with the specimen tilted back to show the outer polished surface where the indentation (white arrows) started fracture. Fracture started from Vickers indentation radial cracks oriented in different directions. A hackle line extends from the origin straight up through the mirror. Notice how main crack branching occurs (small white arrows) soon after the mirror boundaries formed in this equibiaxial-loaded specimen. Notice also that the branching angle initially is small then flares out to its final configuration.*

may persist up into the mirror or even further. These steps are one type of "hackle" as described later in section 5.3. They usually point back to the origin and are an additional aid to locating the origin flaw.

Curved or bent mirrors
Cracks propagate perpendicular to the maximum principal tension stress, but some parts may have maximum stresses that are invariant with orientation. Equibiaxial stressed ring-on-ring test coupons (Figure 4.2) are an example. Curved or wavy fracture mirrors may occur in equibiaxial-loading cases. Figure 5.12 shows an example of a bent mirror.

Non circular mirrors
Mirror shape distortions may reveal important information about flaws or the stress distributions in a part. Mirrors that are not circular or semicircular indicate stress gradients, residual stresses, or elongated flaws at the origin.

Parts with mirrors centered on an interior origin in part are usually circular. Oblong or elliptical mirrors in the interior are less common. Figure 5.9 shows three internal fracture origins and mirrors in ceramic test specimens. In one case (Figure 5.9c), the part was tested in flexure, but the mirror was relatively small and showed no obvious distortion or elongation.

On the other hand, parts with surface origins often have flared or elongated mirrors, especially if the part was stressed in flexure. The bending loading mode usually creates a stress gradient with a maximum tension at the surface, zero stress at the middle ("the neutral axis"), and compression on the opposite surface as shown in Figure 4.18. As the crack accelerates from the surface origin, it traverses through a diminishing stress field towards the interior. This slows down the crack and elongates the mirror shape towards the interior as shown in Figures 5.10, 5.13, and 5.14. It can even eliminate the mirror markings altogether if the mirror is large relative to the specimen cross-section size. The stress gradient does not affect the markings along the tensile surface. There often is a small cusp on either side of the mirror pointing back to the origin in glasses. The cusp is accounted for by fracture mechanics considerations. (A crack that connects to a free surface experiences a slightly greater stress intensity factor right at the surface.) The small cusp is inconsequential for most analysis, except when fracture mirror sizes are measured as discussed in chapter 7 and Appendix D.

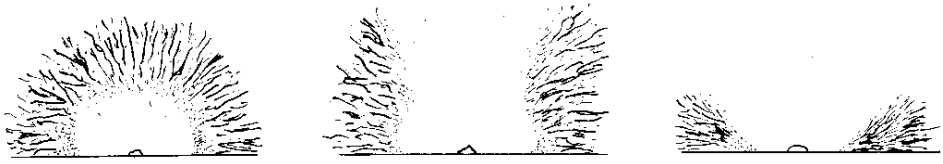

(a) (b) (c)

Figure 5.13 *Mirror shapes around surface origins. (a) is common for tension specimens, or flexure specimens or plates in bending if the mirror is small relative to the thickness. (b) and (c) show mirrors that are incomplete into the interior. This occurs when the mirror is large in a part loaded in bending.*

Figure 5.14 *Fracture mirrors in four glass rods broken in flexure. The maximum tensile stress was on the bottom in each case. Fracture mirrors on the rod sides had pronounced flair or were incomplete due to the stress gradient.*

The elongations in Figures 5.13 and 5.14 are common. Flexural stress gradients always cause elongations towards the interior. On the other hand, there are several important cases whereby elongations along the outer surface of the part occur as shown in Figure 5.15**.** Elongated flaws may generate elongated mirrors and sometimes even mirrors with side protuberances. Figure 5.16 shows two possible scenarios for the formation of such elongated mirrors. Machining/grinding cracks and polishing scratches cause such markings.[35,36] Figures 5.17 and 5.18 show examples.

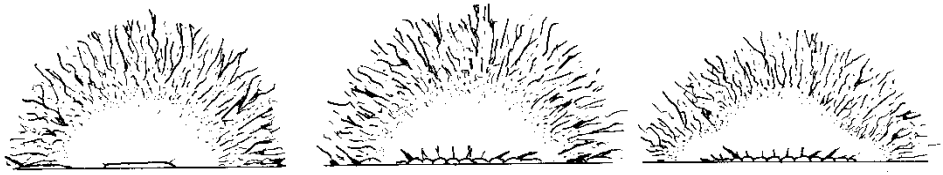

Figure 5.15 *Mirror elongations along the surface can occur if the origin is a scratch or a long parallel grinding crack. (a) shows a single elongated crack at the origin, (b) shows a grinding zipper crack (see section 6.7.6), and (c) shows a zipper crack that generated lobes on the sides of the mirror.*

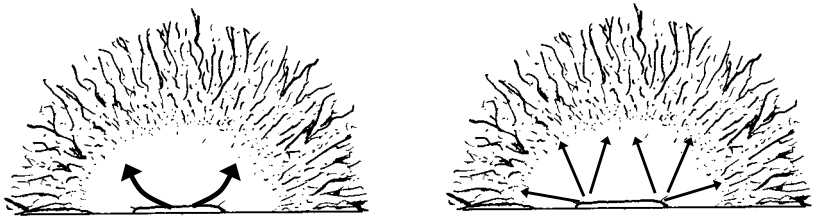

Figure 5.16 *Two scenarios that could account for mirror elongations along the surface from long flaws. (a) shows how a crack could unzip or propagate quickly along the surface. (b) shows that criticality could be reached at several points on the flaw periphery and fracture commences accordingly.*

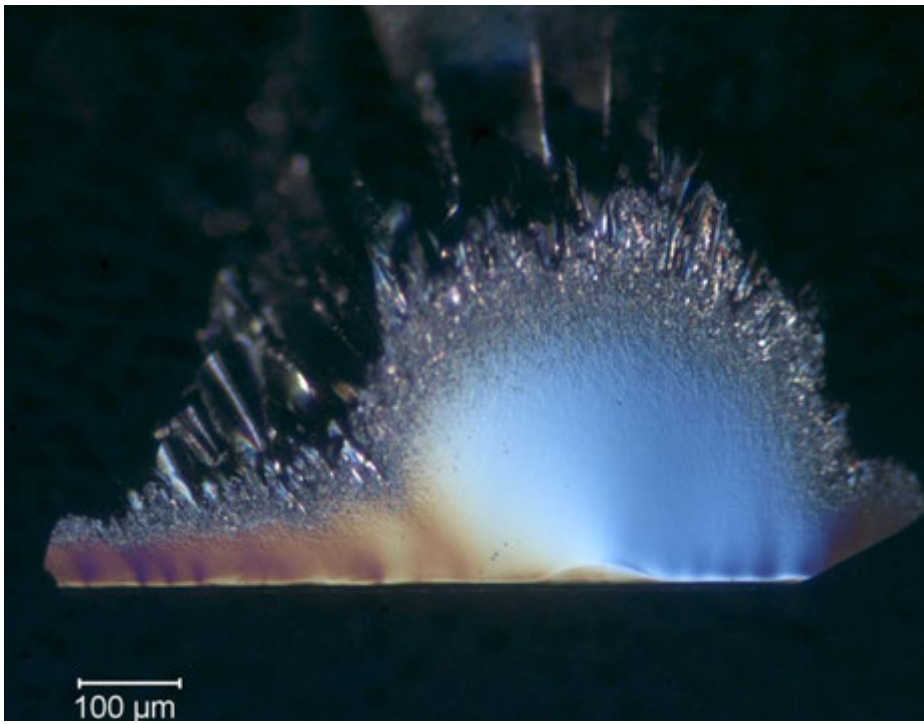

Figure 5.17 *Elongated mirror in a fully-annealed BK-7 borosilicate crown glass ring-on-ring disk strength specimen tested in inert conditions (dry nitrogen). (146 MPa, 21.2 ksi). The origin was a 7.3 µm deep long crack presumably from a scratch in the polished surface although all surface traces of the offending scratch had been eliminated by the final polishing. An SEM image of the origin flaw is shown in Figures 6.28 a,b and 7.22 a,b,c. In this optical photo the initial flaw appears as a thin white band on the bottom. Notice the slightly deeper penetration of the flaw in the middle of the mirror suggesting that it grew to criticality here first. The crack then fanned out to form the elongated non-circular mirror, but also unzipped along the surface to the left and right. The shadow bands extending up from the flaw are Wallner lines generated by minor flaw perturbations extending up into the mirror. Differential interference contrast image from a reflected-light compound microscope.*

(a)

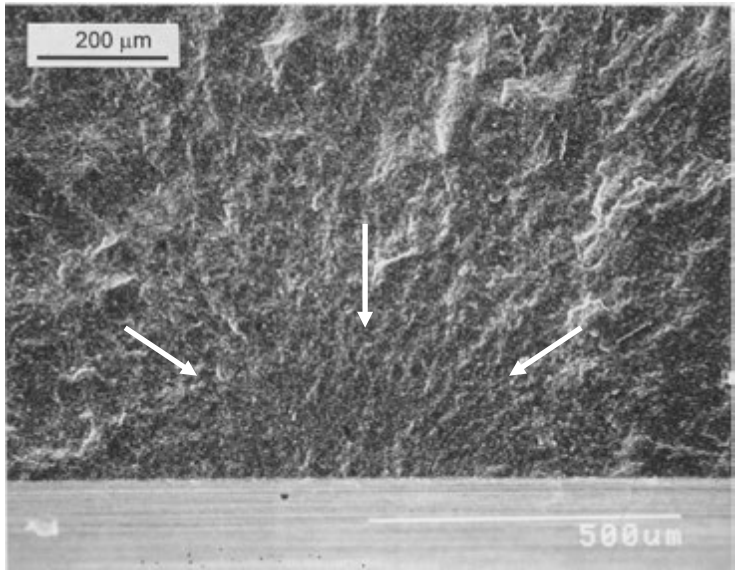

(b)

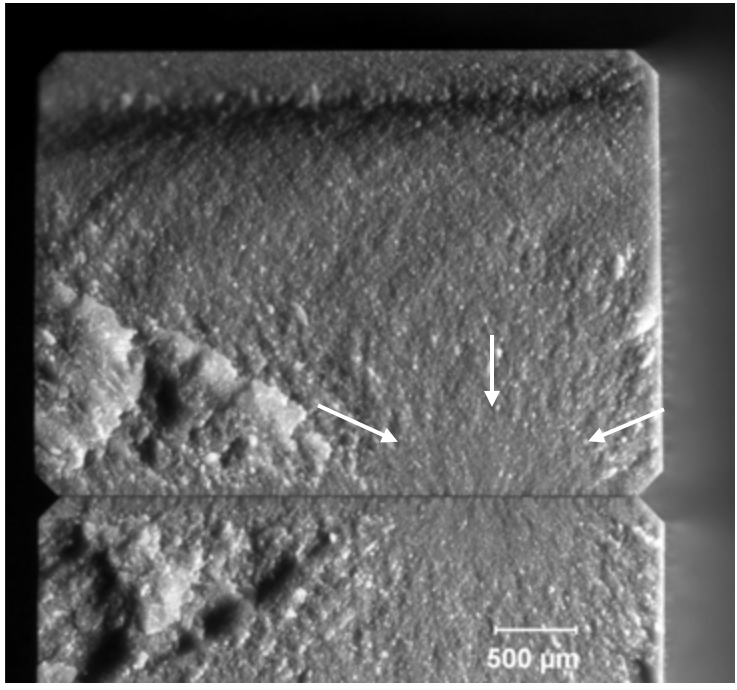

Figure 5.18 *Sideways-elongated mirrors from grinding flaws in ceramic bend bars. (a) "zipper machining crack" (section 6.7.6) in sintered reaction bonded silicon nitride. (542 MPa) (b) zipper crack in sintered silicon nitride. (432 MPa)*

Residual surface stresses may also alter mirror shapes. The shape distortion depends upon the magnitude, sign, and depth of the residual stresses. Figure 5.19 shows a typical parabolic residual stress distribution in glass from thermal tempering.[37] Stresses are strongly compressive at the surface, decrease to zero about 21% of the thickness in from each surface (assuming the two surfaces are cooled at the same rates), and change to tensile in the interior. The compressive stress at the surface is twice the magnitude of the interior tensile stress. Figure 5.20 shows mirrors in a heat-strengthened glass consumerwares. For a surface origin, the compressive surface residual stresses suppress mirror boundary markings along the outer surface. Compensating residual internal tensile stresses shorten the mirror dimensions into the interior. A more detailed discussion of discussion of mirror shapes in tempered plates is in Appendix D and Figure D.8 in particular. Diced pieces from fully-tempered glass show mist and velocity hackle in the interior in Figure 5.21.

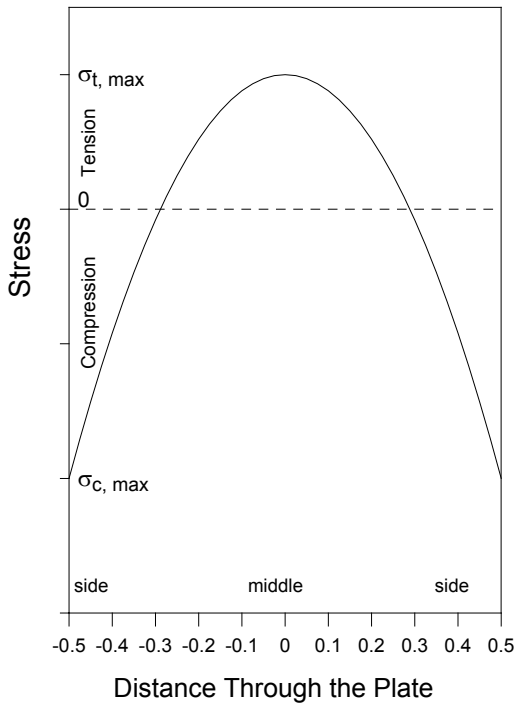

Figure 5.19 *Residual stresses in thermally-tempered glass pieces.*

(a)

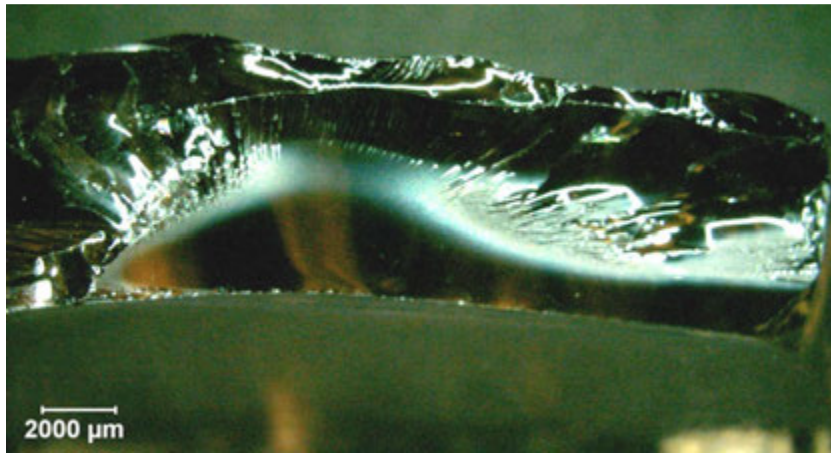

(b)

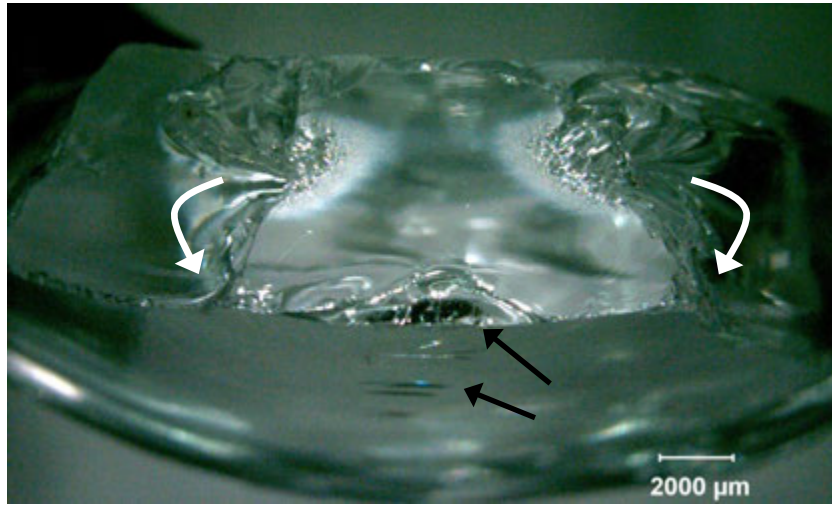

Figure 5.20 *Residual stresses alter the mirror shape. These images show thermally-strengthened glass consumerwares. The piece in (a) shows a complete suppression of mirror boundary markings along the lower right surface, but they are present to the left of the origin. This indicates the piece was thermally-strengthened with emphasis to protect the rim. The mirror is well-developed into the depth since residual tensile stresses there help form the mist and hackle. (b) shows a piece with mirror markings into the interior, but not along the bottom surface. The crack branched from the mirror sides in the interior of the piece then hooked back around to sever the fragment as shown by the arrows. The origin is one or a series of chatter cracks (black arrows) from contact damage on the outer surface.*

(a)

(b)

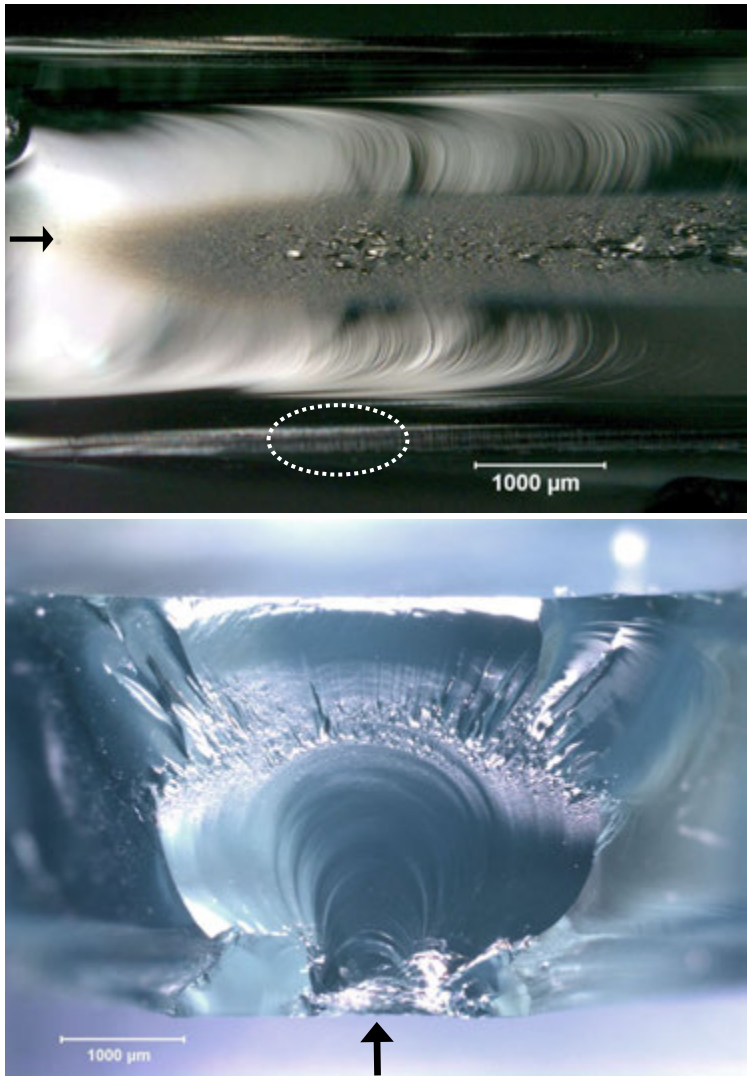

Figure 5.21 *Mist and velocity hackle in tempered glass. These photos are of the same auto window pieces in Figures 4.18b and d. (a) shows the crack reached terminal velocity in the interior where the tensile stresses were greatest. The black arrow shows the direction of crack propagation and the onset of mist. Each diced piece usually has this pattern since cracks slow at a branch then accelerate to terminal velocity again. Crack propagation was retarded at the outer surfaces due to the compression. Final breakage through to the surface has vertical twist hackle (white dashed ring). The arc shaped lines are secondary Wallner lines described later in this chapter. (b) shows the exact single impact origin (arrow) and mirror for the window.*

5.3 Hackle

In addition to the mist hackle and velocity hackle (described on page 5-12 in the mirror section), that are self-initiated by the crack at terminal velocity, there are other types of hackle that are very useful for ascertaining the direction of crack propagation. These markings enable the fractographer to trace crack propagation back to an origin. Hackle lines are sometimes called "lances" and less commonly "striations," but this latter term is not recommended. Hackle can be generated from irregularities in the origin flaw. A good example is "*grinding crack hackle"* shown in section 6.7.6 in the chapter on origins.

5.3.1 Coarse microstructural hackle

Coarse microstructural hackle: *Large broad hackle lines that form from non-specific sources, but most likely variations in the microstructure.*

Ceramics often develop coarse hackle even in the absence of mirrors or other well-defined fracture surface markings. They occur in low-strength or porous ceramics and often are the only marking on a fracture surface that indicate the direction of crack propagation. The microstructure or some geometric irregularity causes portions of the crack to advance on non-coplanar regions separated by rounded ridges as opposed to sharp steps. Figures 5.22 and 5.23 show examples. "Fine microstructural hackle" is described on page 5-36.

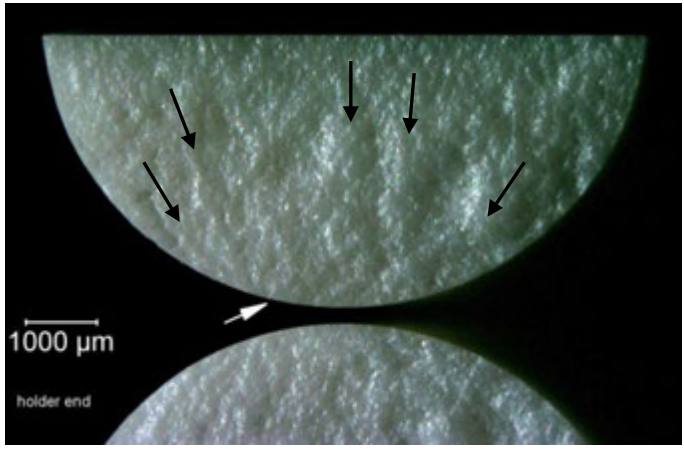

Figure 5.22 *Coarse microstructural hackle. Matching fracture surface halves of a split cylinder flexural strength specimen of a coarse-grained (50 µm to 80 µm) Mg partially-stabilized zirconia. It has a very rough clumpy fracture surface. Low-angle grazing illumination shows the coarse hackle lines (black arrows) radiating from the origin region (white arrow).*

(a)

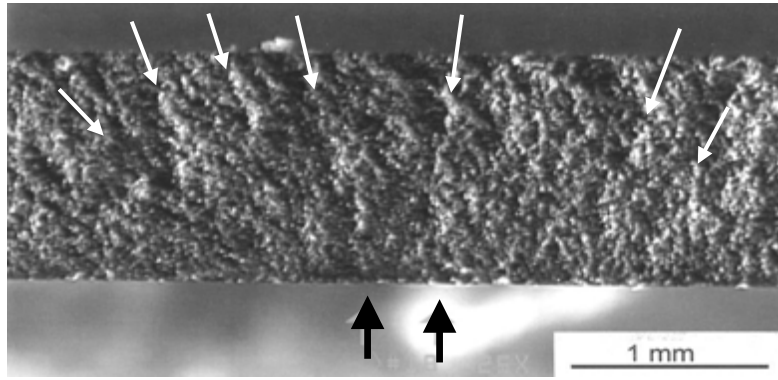

(b)

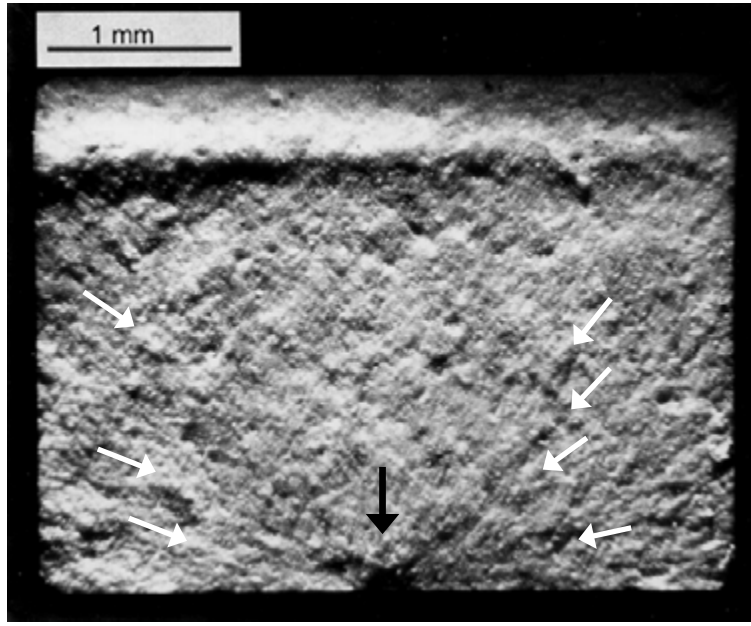

Figure 5.23 *Coarse microstructural hackle. (a) is a broken O-ring specimen of a ceramic membrane material. (b) is a silicon nitride bend bar with a Knoop indentation flaw on the bottom middle (black arrow). Coarse microstructural hackle lines (white arrows) guide the observer back to the origins. The only other fractographic feature observable is the compression curl in (b). Both specimens are so weak that fracture mirrors are larger than the cross sections.*

5.3.2 Wake hackle

Wake hackle: *A hackle mark extending from a singularity at the crack front in the direction of cracking.*

When an advancing crack encounters an elastic singularity such as an inclusion or a pore, the crack front may split at the object and sweep past it on both sides. The two fronts often pass the obstacle on slightly different planes and create a step or "tail" between them. The tail may fade away quickly or persist for long distances. These markings are very recognizable and may either be large or very small. They serve as miniature "weather vanes" which tell the direction of local crack propagation. Figures 5.24 – 5.26 show examples.

Wake hackle in *glazes or veneers* often is the only recognizable fracture surface feature in kitchenware, electrical insulators, and some dental ceramics. The core ceramic materials in these instances are often coarse-grained, porous, or weak, and few fracture surface markings are evident. Sometimes in even the most difficult materials, tiny porosity will aid the fractographer by serving as a source of wake hackle. A superb example was shown by Ko, reference 38.

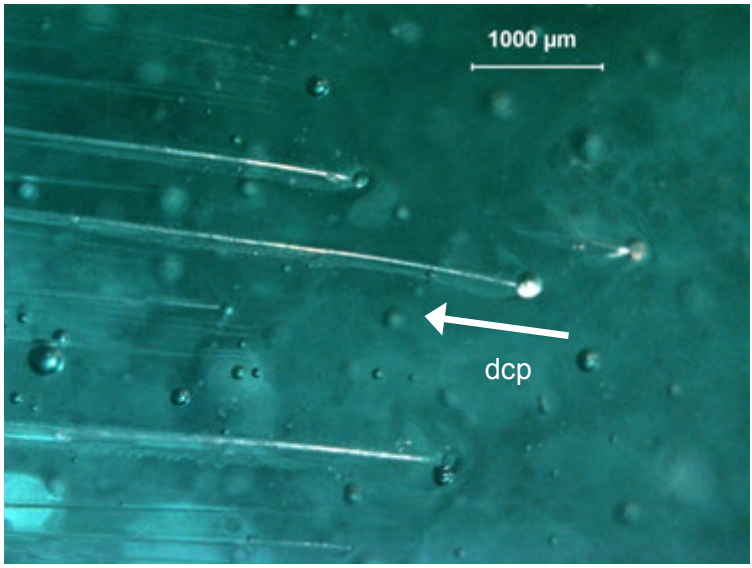

Figure 5.24 *Wake hackle, the fractographers "weather vane" for crack propagation. This shows wake hackle from bubbles in glass. The direction of crack propagation (dcp) is shown by the arrow. Many bubbles are beneath the surface in this view.*

(a)

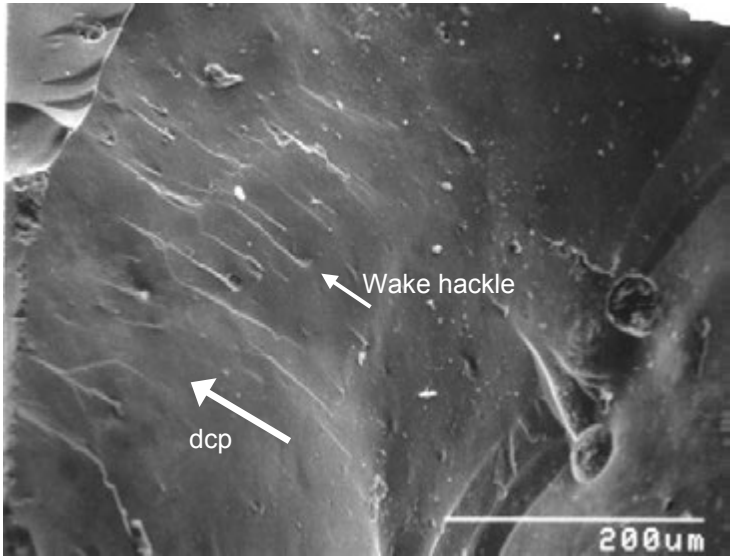

(b)

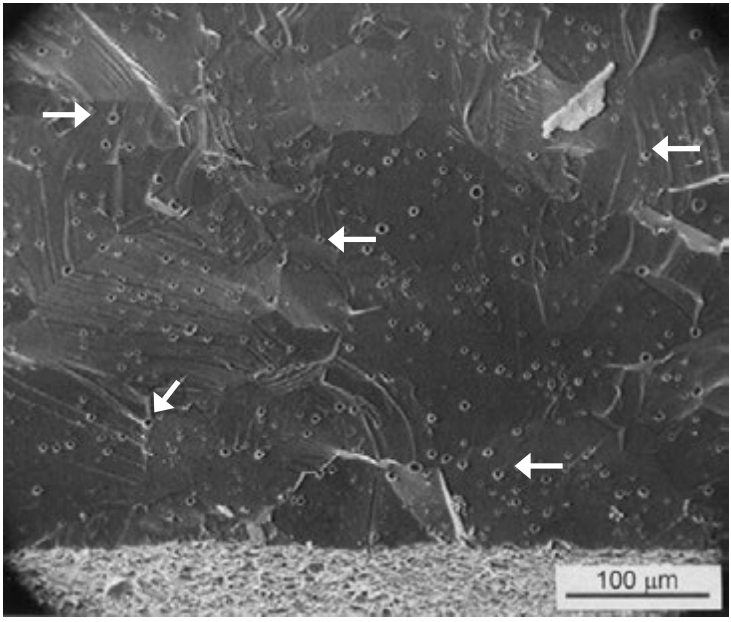

Figure 5.25 *Wake hackle. (a) shows an array of wake hackle from pores in an Empress II dental crown veneer. The direction of crack propagation is marked by the arrow. Notice that some hackle is triggered even though the crack did not cleave the pore (small white arrow). (b) shows an example of transgranular fracture from a large grain origin in polycrystalline AlON. Wake hackle was triggered by grain boundaries and tiny pores (small arrows).*

(a)

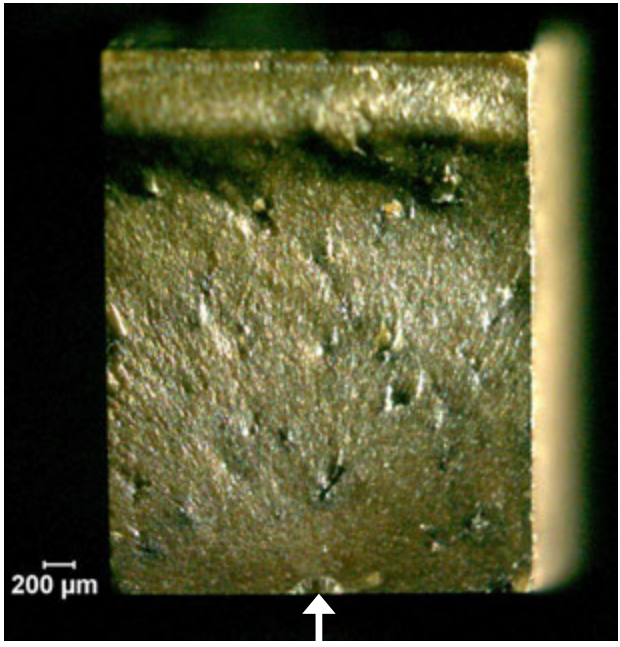

(b)

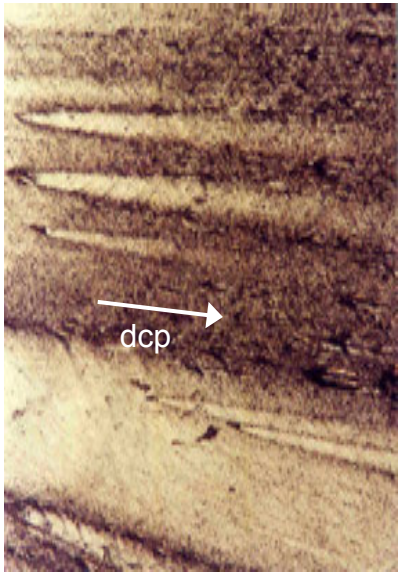

(c)

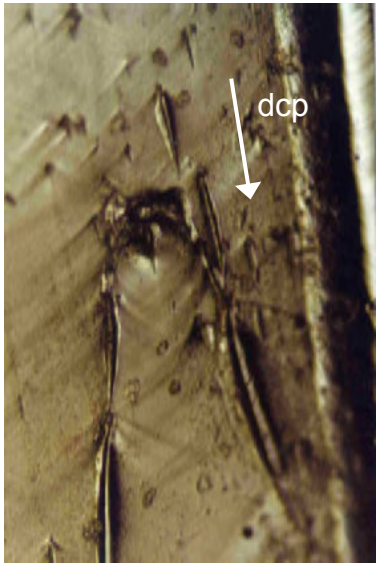

Figure 5.26 *Wake hackle (a) shows wake hackle from inclusions in a lead zirconium titanate bend bar. They point back to the origin on the bottom. The tensile surface is on the bottom and a compression curl is on the top. The origin is a semielliptical surface crack (arrow) generated by a Knoop indentation. (b) and (c) show parabolic double wake hackle tails triggered by inclusions in obsidian glass. (b,c courtesy A. Tsirk)*

Irregularities such as pores or inclusions are not the only sources of wake hackle in ceramics. Grain boundaries and local crack path redirection as a crack propagates from one grain to another with a different crystallographic orientation, or local-density or other microstructural variations all can trigger "fine microstructural hackle:"

Fine microstructural hackle: *Small hackle lines of the order of size of the microstructure that occur as a crack interacts with the local microstructure.*

Sometimes meticulous observations of within-grain cleavage, micro-wake hackle, and micro-twist hackle lines can allow one to backtrack to an origin.

Kerkhof and Sommer used ultrasonic fractography to show that a crack accelerates in the immediate vicinity of a hole in glass, but then is retarded as the crack runs past the hole.[39] Figure 5.45d later in this chapter shows an example.

5.3.3 Twist hackle

Twist hackle: *Hackle that separates portions of the crack surface, each of which has rotated from the original crack plane in response to a lateral rotation or twist in the axis of principal tension. (Fréchette, Ref 1.)*

Twist hackle are very telltale markings as illustrated in Figures 5.27 and 5.28. They are also known as delta patterns, river deltas, river patterns, lances, and sometimes even in the geological community as striations. (Striations in this instance are not to be confused with fatigue striations, a well-known metallurgical fracture surface marking). The roughly parallel segments point in the direction of *local* crack propagation. Twist hackle can be generated by the primary crack as it travels directly through the body, especially as it goes around corners or geometric irregularities, or when stress conditions changed.

Twist hackle can also occur from final breakage between local crack segments, or through to the side of a specimen that had had strong thermal or stress gradients. Twist hackle shows the *local* direction of crack propagation. Plates in bending often have curved cracks that run quickly on the tension side, but do not quite break through to the opposite surface. The crack later snaps through to the opposite surface leaving twist hackle markings as shown in Figure 5.29a. Double torsion fracture mechanics specimens often have such markings. Figures 5.21a and 28b show a similar circumstance whereby final breakthrough of tempered glass has twist hackle near both outer surfaces.

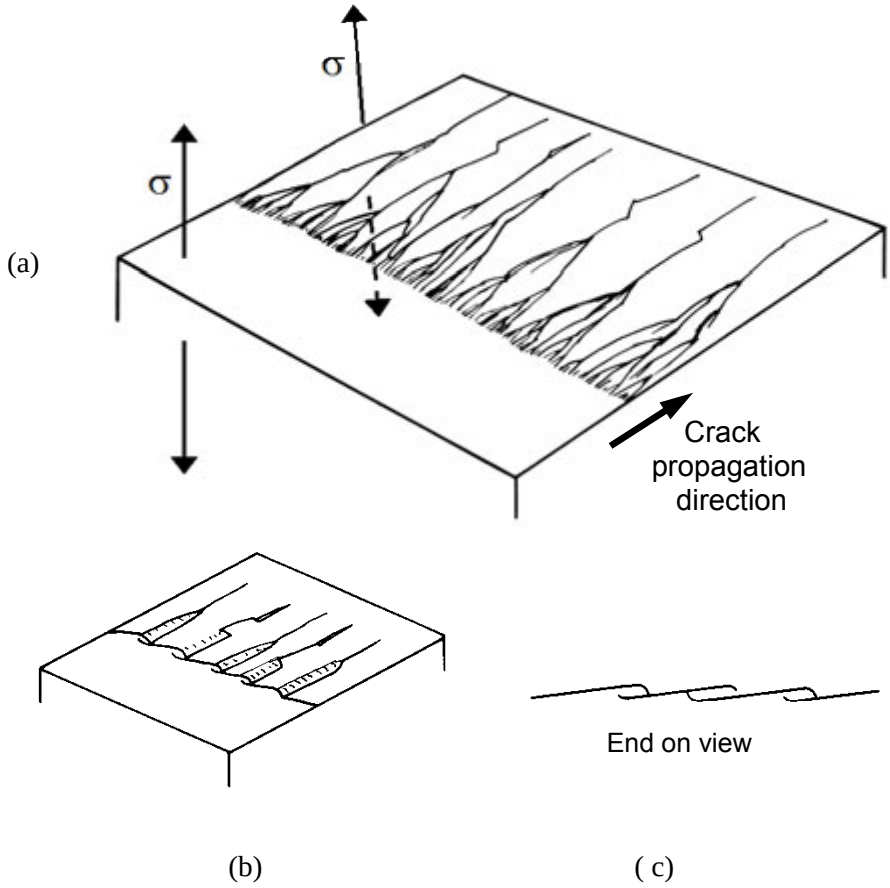

Figure 5.27 *Twist hackle. (a) shows how twist hackle is formed. A crack propagating from left to right runs perpendicular to the initial stress field as shown on the left. The axis of principal stress then tilts as shown on the top middle. The crack is unable to rotate all at once in response to the new stress direction, so it breaks into small, unconnected segments. The steps are "hackle lines" or "lances." Lateral breakthroughs occur between the micro segments as shown in (b) and (c). Note in (c) how the micro segments can link either by a top segment breaking though to a bottom segment or vice versa. On any given lance, the link up can alternate between either segment creating a barbed appearance. Sometimes an incomplete segment can breakthrough long after the main fracture has occurred, generating faint tinkling sounds and creating very sharp needle like fragments that fall free from the fracture surface. The small hackle lines gradually merge into coarser hackle lines, and so on, until the new crack plane is aligned perpendicular to the new tensile stress axis. Usually crack propagation is in the direction of fine to coarse hackle.*

(a)

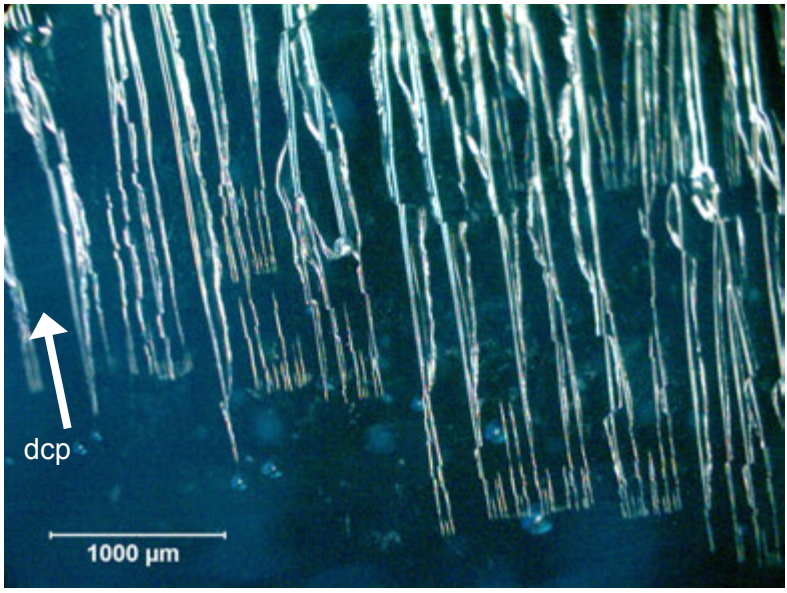

(b)

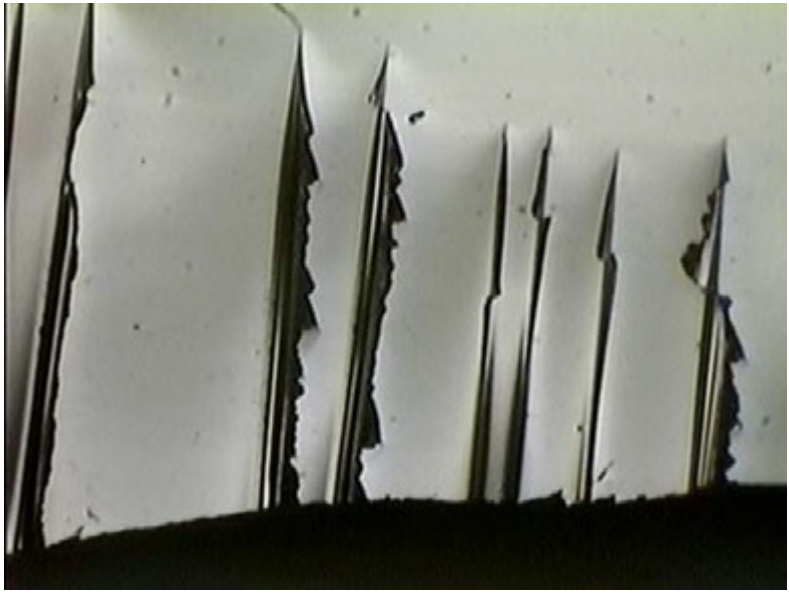

Figure 5.28 *Twist hackle. (a) and (b) show close-ups of twist hackle in glass. The crack was running in the direction of the arrow in (a). (b courtesy J. Varner)*

(a)

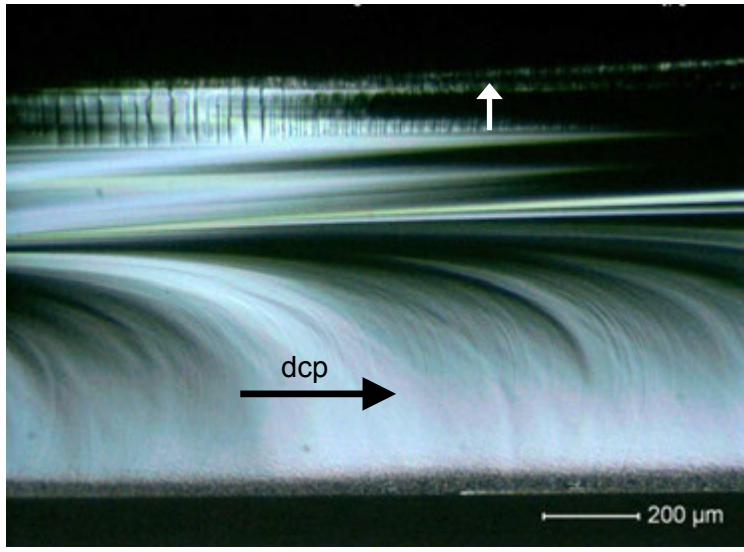

(b)

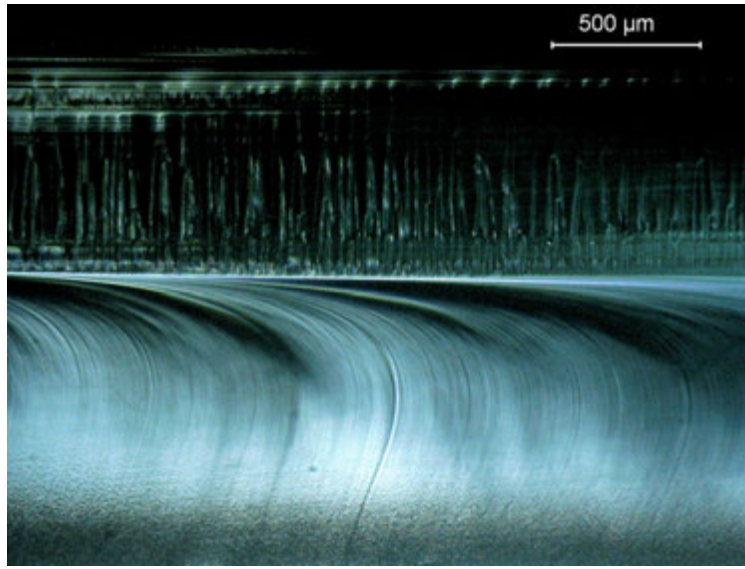

Figure 5.29 *Twist hackle. (a) shows a glass microscope slide that was broken in bending with a little superimposed torsion. The main crack fracture from left to right, leading on the bottom surface as attested to by the profusion of mist and secondary Wallner lines and an occasional primary Wallner line (described in the next section). Final break-through to the top surface (white arrow) created the twist hackle along the top. (b) shows a similar pattern but with a tempered glass fragment.*

(a)

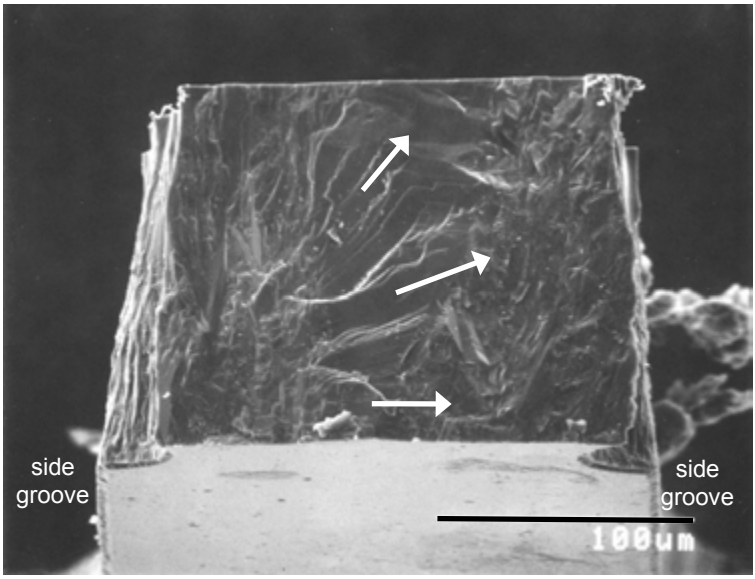

(b)

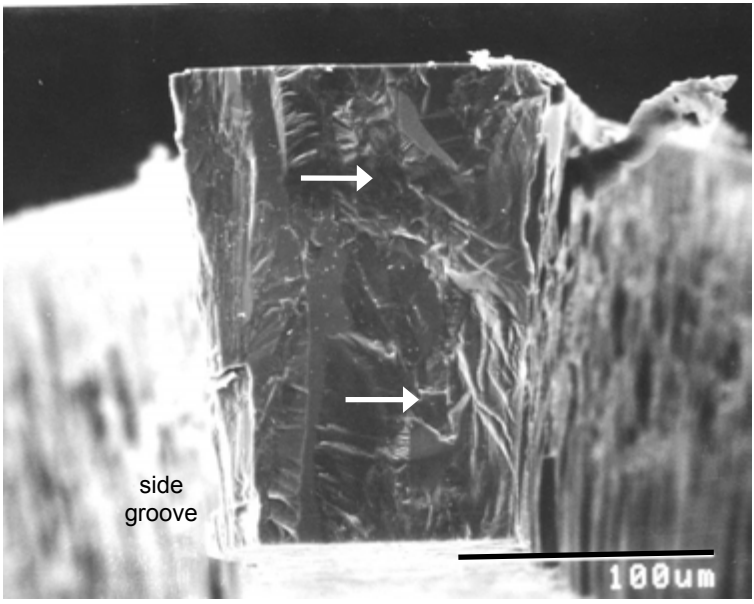

Figure 5.30 *Twist hackle in grains. (a) and (b) show fracture surfaces of chemical vapor deposition (CVD) silicon carbide micro-tensile specimens. CVD materials often have coarse, columnar grains. Such grains run from top to bottom in this view. Twist hackle in these grains in both images show that fracture propagated from left to right as shown by the arrows. Fracture occurred from cracks located at the bottom of the grooves on the left side in both cases.*

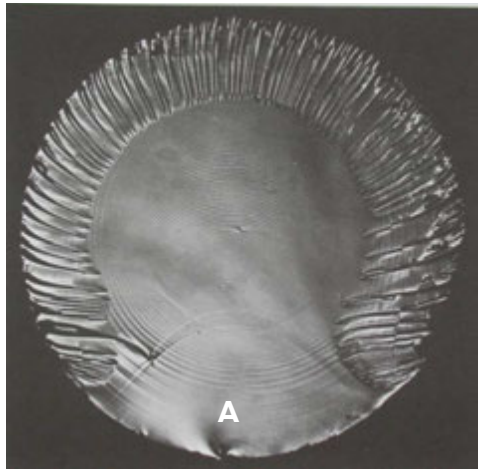

Figure 5.31 *Twist hackle around the circumference of a 15 mm diameter glass rod broken in tension (induced by lateral fluid pressure compression around the periphery while the rod ends were free) with some superimposed torsion. The wavy lines are tertiary Wallner lines (described in the next section) created by ultrasonic fractography. Fracture started at the bottom at point A and progressed into the rod interior. Final breakthrough to the outer surface generated the twist hackle. (Sommer, ref. 30, Kerkhof and Sommer, ref. 39, and Richter and Kerkhof, ref. 2.)*

In polycrystalline ceramics, twist hackle markings within coarse grains can serve as very helpful markers. They are local indications of crack propagation and it is often possible to track a propagating crack back to an origin by reading the local "weather vanes." Figure 5.30 shows examples. The fractographer may be surprised to see that twist hackle line within separate grains may not all line up the same way. It is quite common for cracks to take detours through the microstructure in response to local conditions.

Sommer[30] analyzed the formation conditions of twist hackle and concluded that in glasses a stress redirection of 3.3^{o} is needed to initiate the twist hackle. Beauchamp[27] observed hackle with only 1^{o} of twist. Torsional stresses superimposed on tension stresses can create twist hackle markings as shown in Figure 5.31 which shows a rod loaded in mixed mode I, opening mode, and mode III, out-of-plane shear, as described in section 7.1. An interesting paper[40] reported on how a continuum phase-field approach could be used to model twist hackle formation and propagation. Very small initial perturbations along the initial crack front would form parallel "daughter crack segments" that gradually coalesce, as the main crack plane rotated.

5.3.4 Shear hackle

Shear hackle: *A particular form of twist hackle that occurs in the lazy loops generated in the latter stages of fracture of a hollow specimen. (Fréchette, Ref 1.)*

This definition may seem peculiar, but once the fractographer has seen an example such as Figure 5.32, it becomes clear what Fréchette had in mind.[1] He said: "Far from the fracture origin, it is common to see the crack turn through 90^o and develop a cupped surface, inclined at 45^o to the free surface, from whose centerline a spray of twist hackle emerges. It has little significance in reconstructing a failure event in industry, but it is useful in problems of rock fractures."

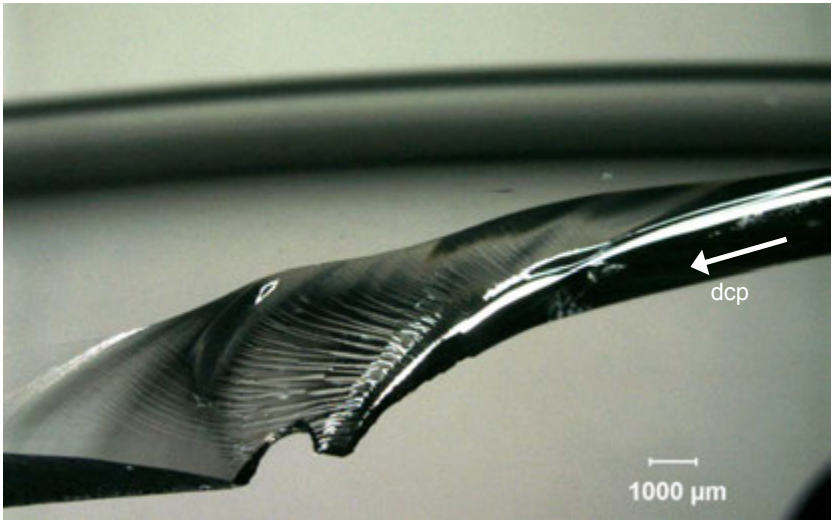

Figure 5.32 *Shear hackle in a glass plate. The crack was perpendicular to the glass surface and was slowing as it moved in the direction of the white arrow. It then turned 90^o parallel to the surface and finally broke through to the surface at about 45^o, producing the spectacular fan-shaped shear hackle. Shear hackle is a variant of twist hackle.*

5.3.5 Corner hackle

Corner hackle: *A fan like array of hackle lines created when a crack curves in a plate or goes around a corner of a component.*

Figure 5.33 shows two examples. The fan like array spreads outwards in the direction of crack propagation.

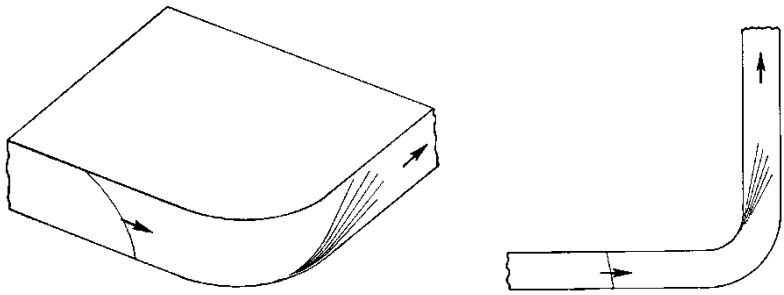

(a) (b)

Figure 5.33 *Two types of corner hackle. (a) shows a fan like pattern that occurs when a crack that is leading on the bottom surface turns to another direction. (b) shows a fan-like pattern that occurs when a crack goes around a corner of a container or vessel.*

5.3.6 Step hackle

Step hackle: *A type of twist hackle in the form of a single line that is an arc shaped line on a fracture surface of a plate broken in bending and twisting.*

Step hackle is a line that is a step on the fracture surface such as shown in Figure 5.34. The line is parallel to the local direction of crack propagation. Unlike most twist hackle, it is an isolated line. The arc curvature of a step hackle line is opposite to the curvature of arrest lines or Wallner lines that may exist on the same fracture surface as shown in Figures 5.34b and c. The fracture surface is usually tilted or curved and not perpendicular to the plate outer surfaces (end-on view Figure 5.34a.). The step can initiate by itself if the tilt is strong enough, or may be triggered by other features such as bubbles, inclusions or mist. Step hackle is shown here for glasses, but can occur as "*cleavage step hackle*" as described in Chapter 8 on single crystals.

(a)

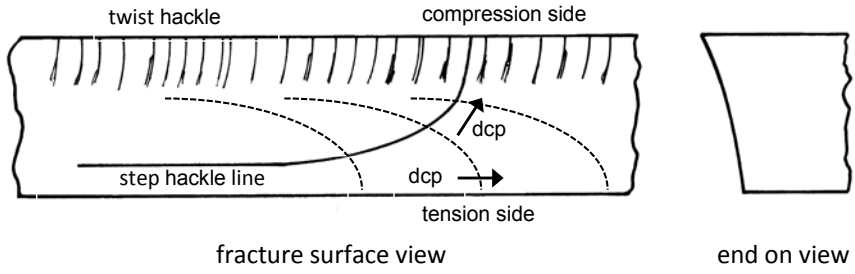

(b)

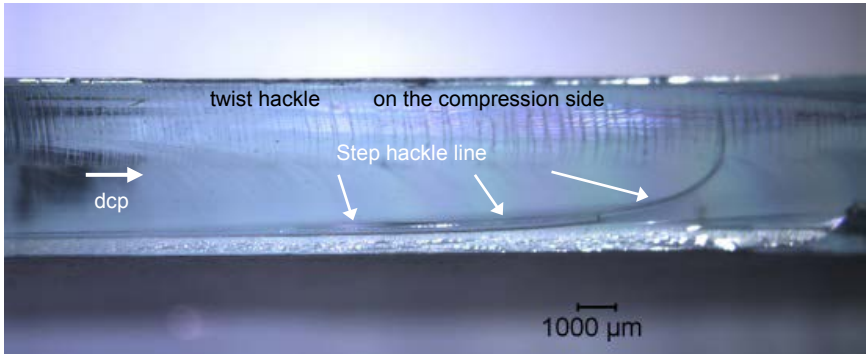

(c)

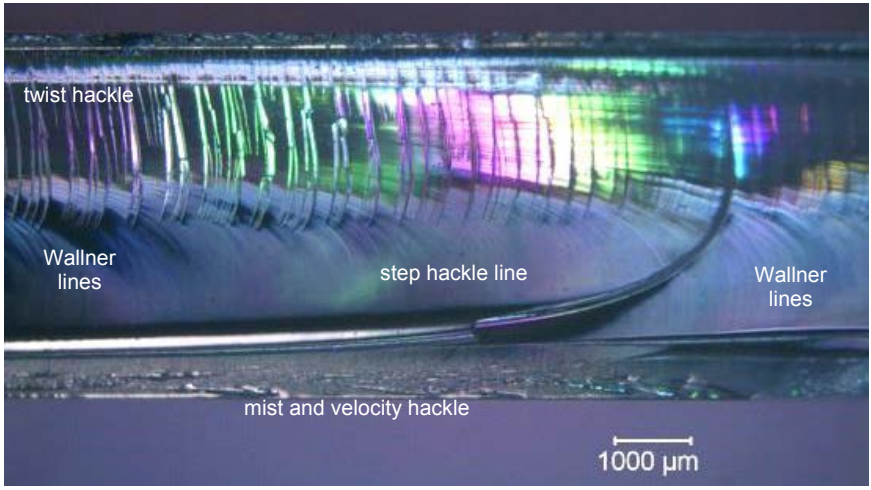

Figure 5.34 *Step hackle schematic (a). (b) and (c) show a piece of a large (1.5 m by 0.75 m) glass mirror that fell off a wall in the author's home. The mirror broke into over 100 pieces. Many fragments had evidence of bending and twisting. Notice the opposite arcs of the step hackle line and the Wallner lines (thin dashed lines in a).*

5.4 Wallner Lines

5.4.1 Introduction

Wallner line: *A rib shaped mark with a wavelike contour caused by a temporary excursion of the crack front out of plane in response to a tilt in the axis of principal tension. It may also form from passage of the crack front through a region with a locally shifted stress field, as at an inclusion, pore, or surface discontinuity. (adapted from Fréchette, Ref. 1)*

Also known as "ripples" or "rib marks," Wallner lines were named for Helmut Wallner who first explained how they formed in 1939.[41] He showed beautiful images (similar to Figures 5.2 and 5.3 of this Guide) of fracture mirrors in flexurally tested glass rods with the lines within the mirrors. He presented a splendid sketch showing how an expanding crack front was overtaken by an expanding elastic wave. The Wallner line is the locus of the intersection of the elastic wave and the crack front. The elastic wave momentarily causes the crack to ripple out of plane like a wave on a pond surface. The shape of the line depends upon the respective shapes and speeds of the elastic wave and the crack front, as well as the direction the wave approaches the crack front. Wallner lines are invaluable in determining the direction of crack propagation. As will be shown, they usually do not have the exact same shape as the crack front, but they are usually curved (bowed) in the direction of crack propagation. They are best understood by the examples that follow.

Wallner lines are very shallow hillocks on a fracture surface. They look like a thin shadow band and they tend to shift slightly as illumination is adjusted. This is in marked contrast to crack arrest lines that are sharp and do not appear to move as light is adjusted. Wallner lines are very easy to see on fracture surfaces once the lighting is adjusted, but they are very difficult to see on the scanning electron microscope, since they produce almost no contrast and are very shallow.

There are several types of Wallner lines depending upon the source of the elastic wave. Fréchette[1] thoughtfully categorized these as primary, secondary, and tertiary. This Guide follows his scheme and adopts his definitions. His figures showing the evolution of the loci are instructive, but have been revised and expanded into separate illustrations in this Guide to make them easier for the beginner to understand. Keep in mind that a crack front through a plate may be straight or have different shapes according the stress state as shown in Figure 5.35.

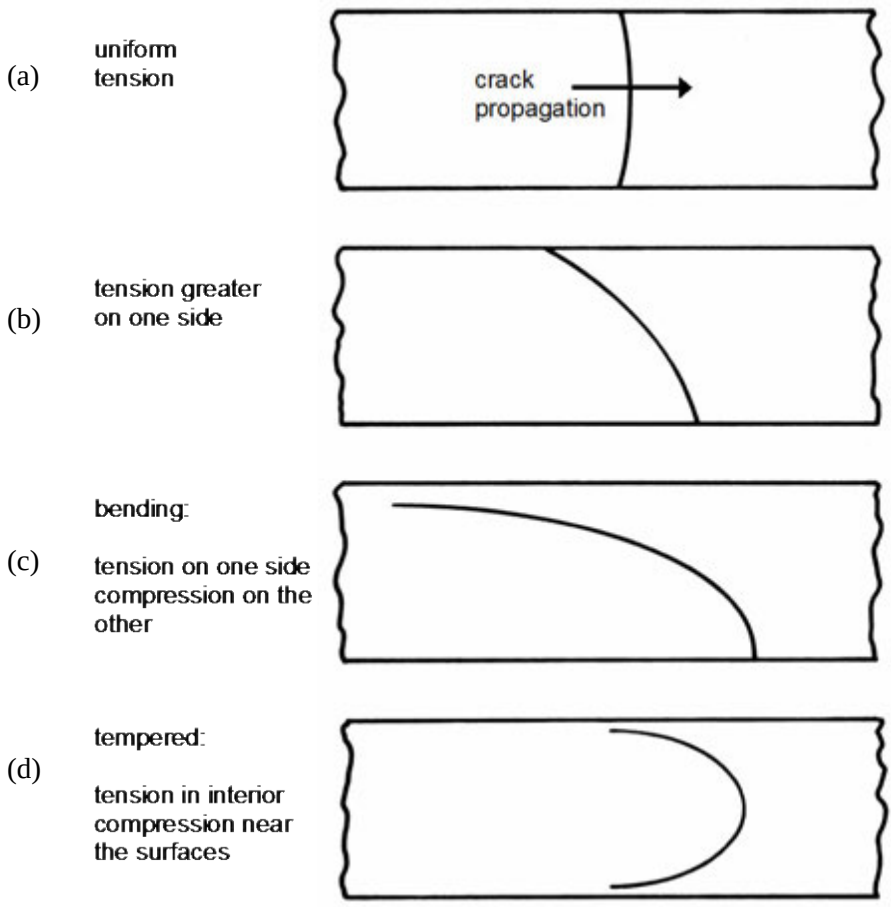

Figure 5.35 *Crack front variations due to stress distributions through the thickness. (a) shows a crack front in a uniform tensile loaded plate. (b) a plate with greater tensile stress on the bottom. (c) a plate in bending such that the bottom is in tension and the top in compression. (d) a tempered plate with tensile stresses in the interior and compressive stresses at the surface.*

5.4.2 Primary Wallner lines

Primary Wallner line: *A Wallner line formed by an elastic pulse generated by some portion of the crack front with a singularity in the specimen such as a discontinuity at the free surface or within the specimen, or with any localized stress field or elastic discontinuity. (Adapted from Fréchette, ref. 1)*

Primary Wallner lines commonly are generated by surface blemishes and irregularities such as scratches, pits, or edge chips. Figure 5.36 shows an example and Figure 5.37 illustrates how they are formed. If a Wallner line is seen to emerge from such a surface blemish, it is evidence that the surface fault was present at the instant the crack ran by. Alternatively, if a large blemish or chip is on a glass fracture surface, but there is no Wallner line from it, the blemish occurred afterwards and was not initially on the piece.

Unless the crack is moving very slowly (and the elastic wave traverses the entire crack front very quickly), primary Wallner lines do not show the exact crack front profile. Nevertheless, they are curved in the same direction and can help the fractographer deduce which way a curved crack was running. It is fairly easy to show that straight crack fronts generate straight Wallner lines, but they will tilt at a different angle than the original crack front depending upon the crack velocity.

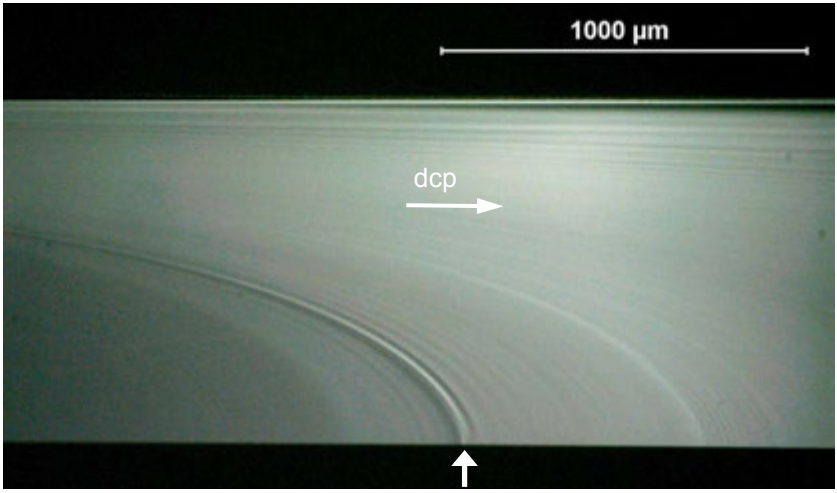

Figure 5.36 *Primary Wallner line in a glass slide broken in bending. A simple scratch on the surface (arrow) triggered the strong Wallner line as the crack ran from left to right. Other tiny faults triggered fainter primary Wallner lines.*

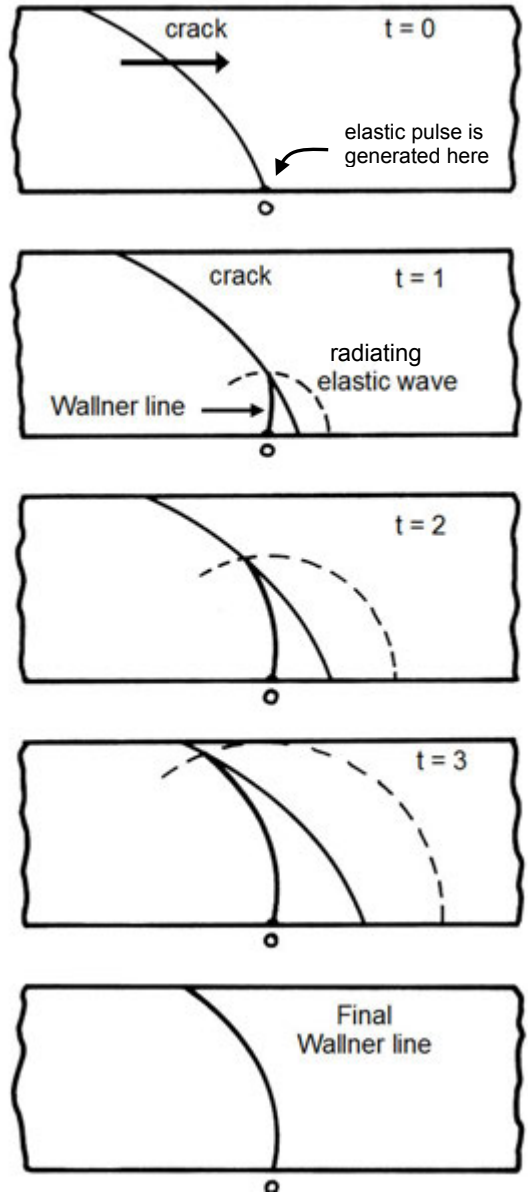

Figure 5.37 *Primary Wallner lines. This schematic series shows the progressive advance of the crack at successive time intervals. The elastic wave that forms the Wallner line (thick line) is generated when the advancing crack hits a surface irregularity "O". The crack leads on the bottom surface, but is moving at constant velocity in this example.*

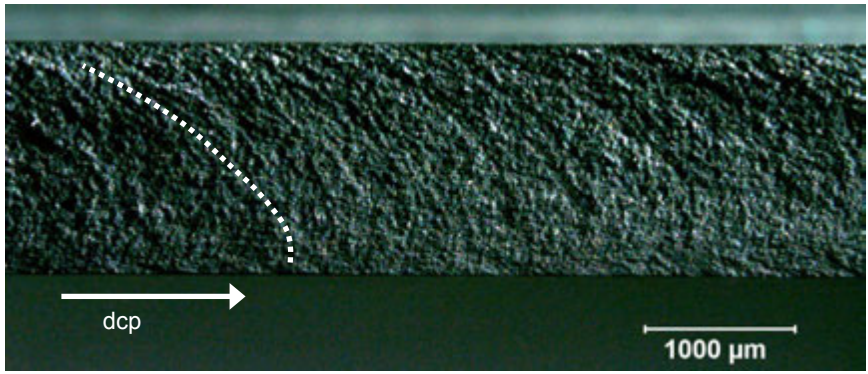

Figure 5.38 *Wallner lines are more difficult to see in polycrystalline ceramics. Low-angle grazing illumination is effective. This is an optical image of a silicon nitride double torsion fracture toughness specimen. The crack was running in the direction of the white arrow. The double torsion configuration bends a specimen so that the bottom is in tension and the top in compression. The cracks lead on the bottom surface. Primary Wallner lines formed with arcs shown by the white dashed curve. See also Figure 5.10b.*

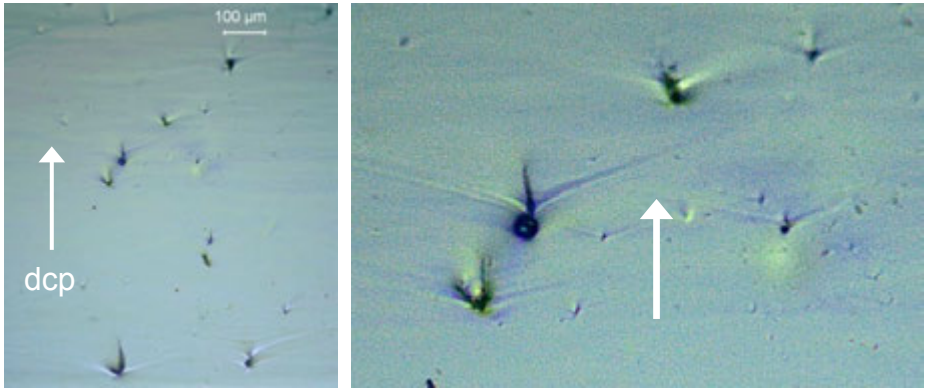

(a) (b)

Figure 5.39 *Gull wings are a variant of primary Wallner lines. (b) is a close-up of (a). Most of these pores also have wake hackle as well. These images are from obsidian with crack propagation from bottom to top as shown by the arrows. The wing angles can be used to measure crack velocity (section 7.9). (specimen courtesy A. Tsirk)*

Wallner lines are less easy to see in ceramics. Figures 5.10b and 5.38 show examples. In porous, granular, or coarse-grained ceramics, large broad ridges that are Wallner lines may be the only recognizable marking on the fracture surface. If so, the ridge may have been caused by microstructural irregularities or surface flaws on one side of the origin or to a geometric irregularity (e.g., an inside corner in a formed-ware, or a ridge on a plate).

Figure 5.39 shows "gull wings," a variant of primary Wallner lines. They are usually formed by a stress pulse created as the crack encounters pores, inclusions, or other irregularities. There even are instances where they may be triggered by secondary fracturing behind the primary crack front, and hence will be detached from obvious irregularities.[42]

5.4.3 Secondary Wallner lines

Secondary Wallner line: *A Wallner line generated by an elastic pulse released by a discontinuity in the progress of the crack front, typically one of the rough details which arise as the crack approaches its effective terminal velocity. (After Fréchette, Ref 1.)*

Unlike the primary Wallner lines that form as a result of a crack encountering an external feature, secondary Wallner lines occur from features the crack generates itself. Mist and hackle are disturbances created by crack running at or near terminal velocity. The mist and hackle generate copious secondary Wallner lines. Figure 5.40 shows their formation sequence and Figure 5.41 shows examples. It is very common for both primary and secondary Wallner lines to be present. They can be distinguished by their different curvatures. Secondary Wallner lines are more hooked (like a fish hook) than primary Wallner lines. As was the case with primary Wallner lines, secondary Wallner lines do not show the exact crack front profile. Even so, it is helpful to deduce from their curvature which way a crack was running.

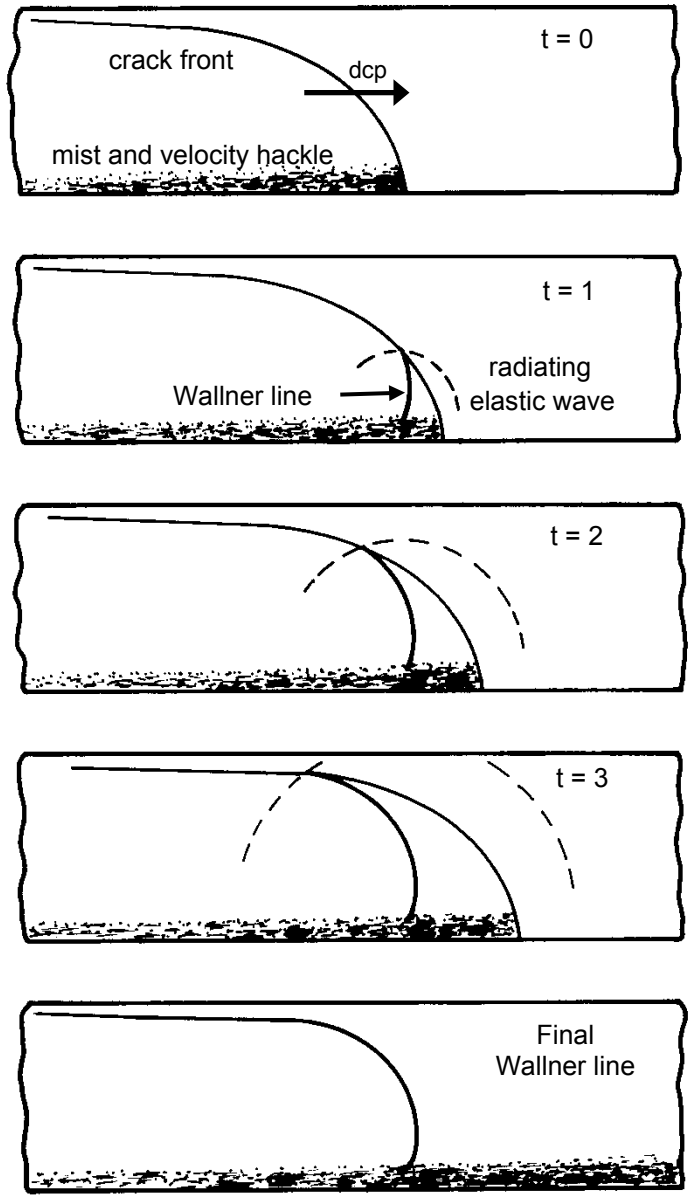

Figure 5.40 *Secondary Wallner lines are formed by the crack itself. This schematic series shows the progressive advance of the crack and the elastic pulse that forms the secondary Wallner line (dark line) in a plate with a stress gradient. Notice the hook final shape, a consequence of the stress gradient caused by the variation in the crack velocity from a maximum on the bottom to close to zero at the top.*

(a)

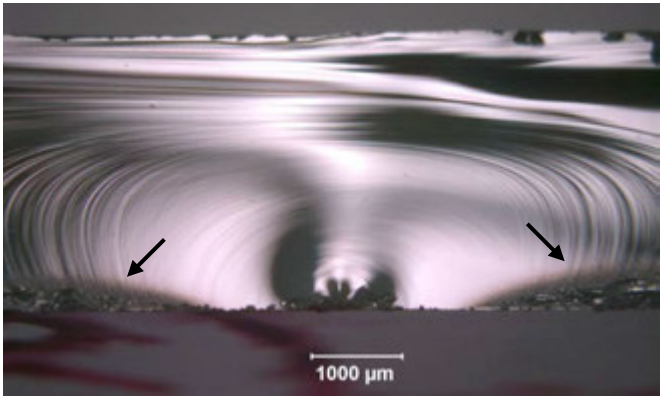

(b)

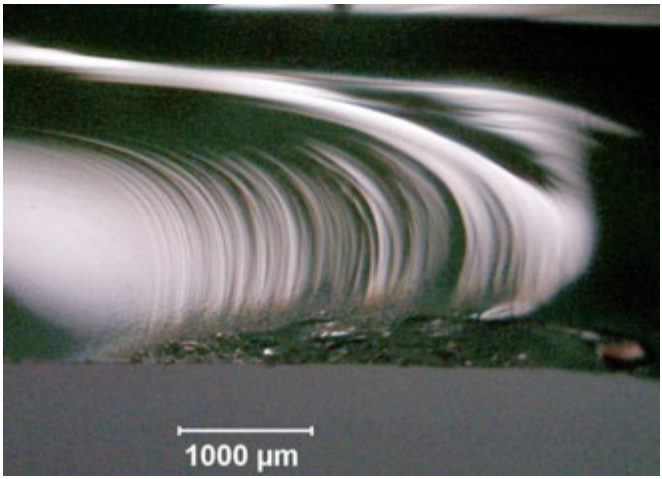

(c)

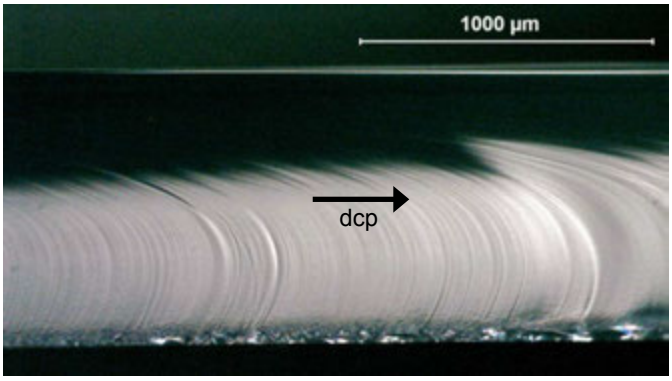

Figure 5.41 *Examples of secondary Wallner lines in glass microscope slides. (a) and (b) show Wallner lines from the sides of a mirror. (b) is a close-up of the right side of (a). Mist and hackle triggered the secondary Wallner lines. There also are fainter primary Wallner lines inside the mirror. Notice their different arcs. (c) is a slide broken in bending.*

5.4.4 Tertiary Wallner lines

Tertiary Wallner lines: *Wallner lines caused by elastic pulses generated from outside the crack front. (Fréchette, Ref. 1)*

Vibration or shock from a source other than the crack itself can create waves that intersect with and cause momentary deviations in the crack front. Depending upon the source of the elastic pulse relative to the crack plane, the interaction may generate Wallner lines that may be very close to the shape of the crack front, or it may produce an arc formed by a progression of intersections as in the examples shown above. For example, if the crack is moving relatively slowly, the fast elastic wave will overtake all portions of the crack front nearly simultaneously, producing a Wallner line "snapshot" of the crack front.

If the pulse source is located at a site normal to the fracture plane, the pulse may reach all portions of the crack front simultaneously also producing a

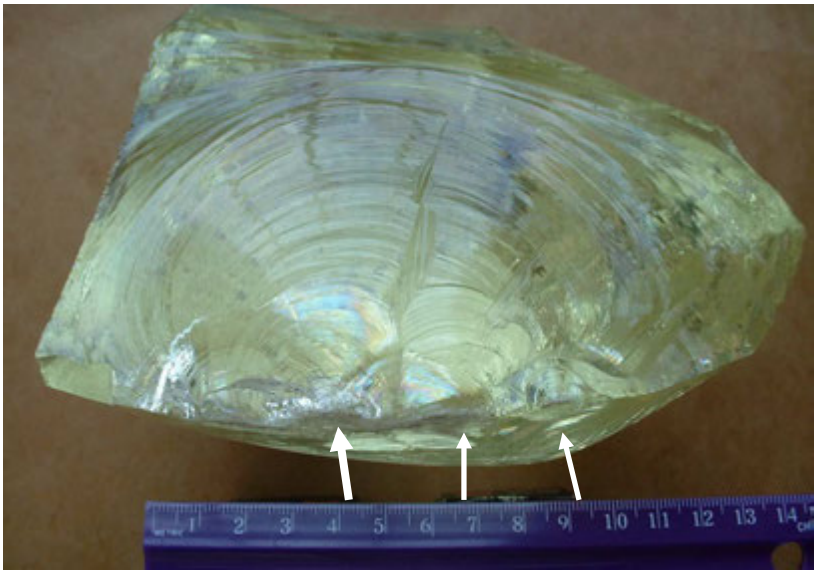

Figure 5.42 *Tertiary Wallner lines in a large chunk of glass that was hammered into pieces. There are multiple impact sites marked by arrows, the most prominent of which is marked by the larger white arrow. Notice how the tertiary Wallner lines are concentric about the impact sites. This was one of Professor Fréchette's demonstration pieces.*

"snapshot" of the crack front. The impacted glass shown in Figure 5.42 is a good example. Notice how the tertiary Wallner lines are *concentric* about the impact sites. The impact site not only generated the cracks, but the elastic pulses as well. (In contrast note how the primary and secondary Wallner lines in Figures 5.3 and 5.41a *cross over each other on top of the origin*.) Impact typically results in a ringing within the specimen that may be short lived, but will be long enough to endure for the period a crack traverses through a body.

On the other hand, a sudden stress relief may create a brief vibration when a crack pops in or propagates. This may be accompanied by an audible snap, but only generates faint elastic pulses so that only a few tertiary Wallner lines form near the origin. Fréchette[1] noted that window panes that are cracked by thermal stresses may have only a few tertiary Wallner lines near the origin and are featureless elsewhere.

A schematic case of a pulse overtaking a crack from the rear is shown in Figure 5.43. The reader is reminded that Wallner lines do not always create a "snapshot" of the crack front shape. Tertiary Wallner lines are not always formed by pulses arriving from a source so conveniently located as in test pieces studied with ultrasonic fractography. They may come from any direction including from sources that are out of the crack plane.

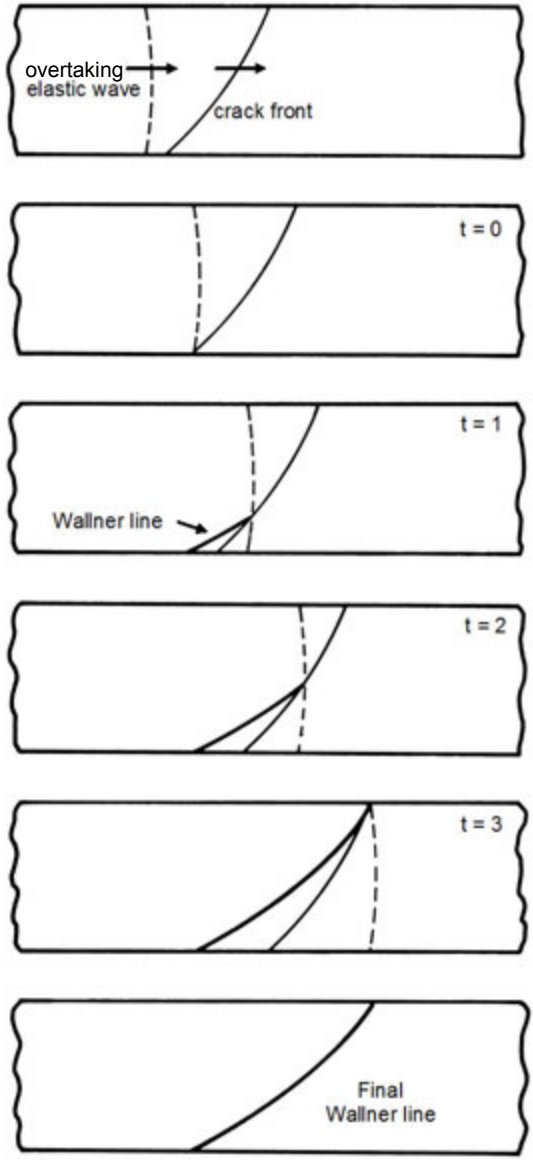

Figure 5.43 *Schematic showing the stages of formation of a tertiary Wallner line for a curved crack front overtaken by an elastic wave from behind the crack. The Wallner line has a similar concavity as the crack front, but the loci are different.*

Ultrasonic or stress wave fractography,[2,6] previously mentioned in section 3.21, deliberately creates elastic waves to make tertiary Wallner lines on the running crack. Figures 5.44 and 5.45 show some examples from Richter and Kerkhof's work.[2] Local crack velocity can be simply calculated on the basis of the spacing between the lines and the frequency of the pulses. They were able to measure cracks running at terminal velocities in glass with 5 MHz lead zirconium titanate transducers. Their review article[2] has many fascinating examples of the application of this method to study crack front profiles and velocities.

(a)

(b)

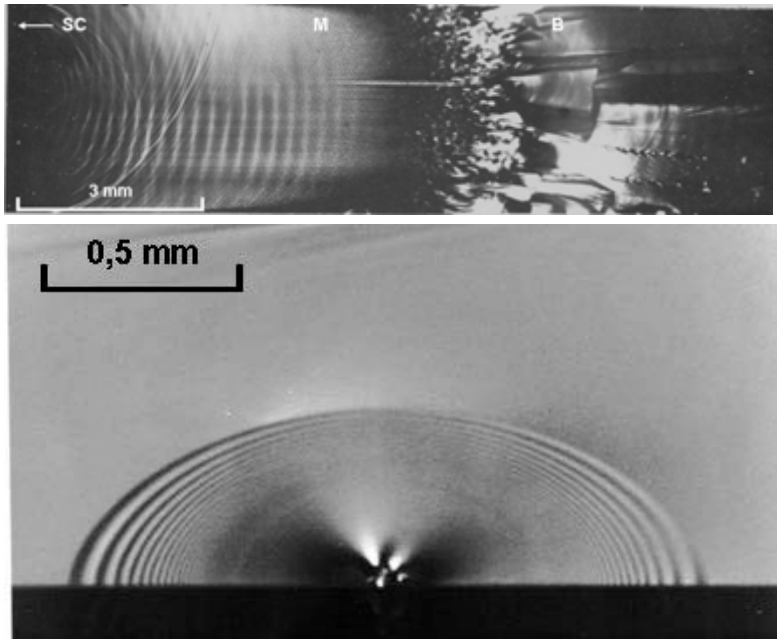

Figure 5.44 ***T****ertiary Wallner lines from ultrasonic fractography. A transducer created elastic pulses that made "snapshots" of the crack fronts as they propagated through glass test specimens. (a) is a notched tension specimen loaded to fracture. The crack started at "SC" and ran to the right forming mist at M, and branching at B. The crack reached a terminal velocity of 1540 m/s, two waves to the right of the letters SC, well before the mist formed. (b) shows an accelerating crack that grew from an indentation flaw in a bend bar. The ellipse shapes are in perfect accordance with fracture mechanics predictions as discussed in section 7.5.2. These two images show how these Wallner lines are wave-like undulations on the fracture surface, unlike the sharp arrest lines in Fig. 5.47c. (a + b courtesy, H. Richter)*

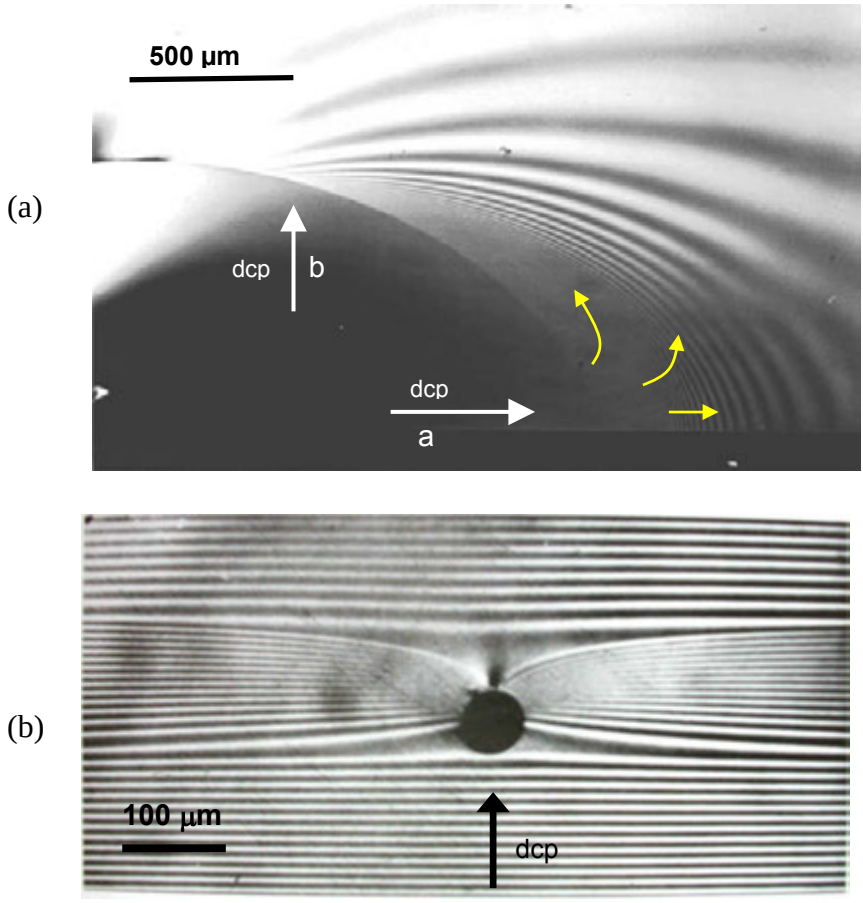

Figure 5.45 *Tertiary Wallner lines examples from ultrasonic fractography.* *(a) shows a surface crack in a bend bar that went unstable from one side when growing by slow crack growth in water. The bending stress field caused the crack to grow faster along the surface (arrow a) than into the depth (arrow b). The crack went unstable on the right side (yellow arrows) and then rapidly fanned out and around the still slowly-advancing main crack. See also Figure 5.56. (d) shows a crack front approaching a capillary tube void at 60 m/s. The arrow shows the crack propagation direction. The crack locally accelerated to 60 m/s as it approached the void, but then slowed down to 20 m/s as it passed around it, and then jumped at a faster velocity after passing around the void. (Ref. 2, photos courtesy of H. Richter)*

5.4.5 Wallner lambda lines

Elastic waves can reflect off free surfaces creating a lambda shaped line on the fracture surface as shown in Figure 5.46. These are typically formed by primary or secondary Wallner lines. Crack velocity can be calculated from the spacing of the Wallner lines as discussed in section 7.9 and Figure 7.31.

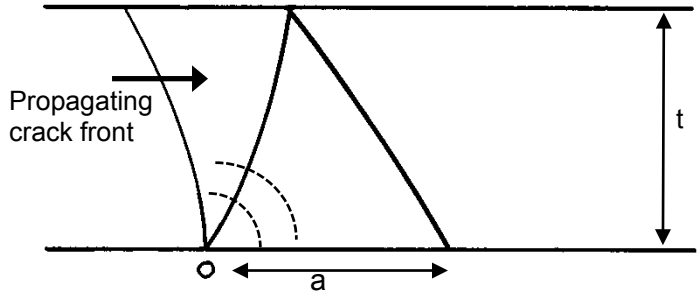

Figure 5.46 *Wallner lambda line mark. The schematic shows the advancing crack (thinner line) encountering a discontinuity at point O. An elastic pulse creates a radiating elastic wave. The intersection of the wave and the advancing crack front creates a primary Wallner line that runs upward to the top surface. When the elastic wave reflects from the opposite surface, the Wallner line continues back downward.*

5.5 Arrest Lines

Arrest Line: *A sharp line on the fracture surface defining the crack front shape of an arrested, or momentarily-hesitated crack. Resumed crack propagation occurs under a more or less altered stress configuration.*

This is an adaptation of Fréchette's original definition.[1] His definition included the words "rib mark" as in "rib shaped," but this author has seen straight arrest lines in thermally-stressed plates, so a more general definition seems in order. The words "momentarily-hesitated" are also added to Fréchette's definition since it is not necessary for the crack to come to a complete halt. Fréchette also explained this in his book. The arrest line occurs because the crack repropagation is on a slightly different plane, usually in response to a slight change in the axis of principle tension.

Arrest lines are different than Wallner lines in two key respects: arrest lines are sharp, and, unlike most Wallner profiles, arrest lines show the crack front profile at an instant in time. Sometimes, if the crack repropagation occurs in a slightly different direction, twist hackle lines will form that lead away from the arrest line.

Michalske showed that cracks that arrested after slow crack growth sometimes require extra loading to repropagate after aging.[43] The crack tip blunts slightly during the aging, and the crack has to resharpen before repropagation. This process occurs with slight variations along the crack front so that when the crack repropagates there are slight humps and valleys along the crack front and tiny hackle lines leading away from the arrest line.

Concentric arrest lines in ceramics and glasses sometimes bear a resemblance to classical mechanical-fatigue markings in metals, but they are not the same. Classical mechanical fatigue in metals is iterative crack extension by cyclic loading. Repeated loading on a crack causes damage nucleation, accumulation, and stepwise growth in metals. This leaves periodic, spaced striation lines on the fracture surface. This mechanism is not operative in most fine-grained equiaxed-microstructure ceramics and glasses. Section 5.9.5 below has more on mechanical fatigue.

(a)

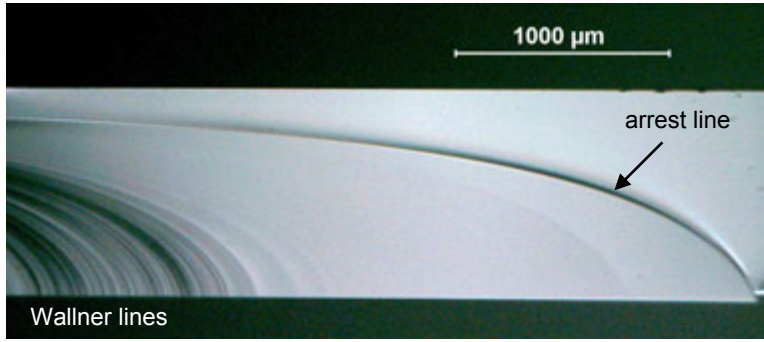

(b)

(c)

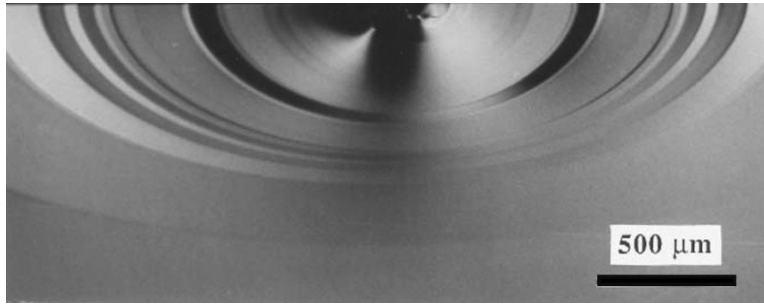

Figure 5.47 *Crack arrest line examples. (a) shows a glass microscope slide broken in bending and the arrest line is on the right (arrow). The lines to the left are primary Wallner lines. Wallner lines are not as sharp as arrest lines. (b) shows an arrest line in a glass slide that broke from thermal stresses.* ***(c)*** *shows concentric arrest lines from repeated cyclic loading of a glass plate in bending. Compare the sharp lines in this photo to the wavy tertiary Wallner lines in Figure 5.44b. (c is courtesy D. Green and is the same as Fig. 5.66).*

5.6 Scarps

Scarps shown in Figure 5.48 are subtle curved lines on a fracture surface caused by interaction of a propagating crack and a liquid or a reactive environment. The liquid can act to retard a crack front or can cause it to accelerate, sometimes in a discontinuous fashion. The scarps mark sudden transitions in crack velocities that can occur due to interactions of the crack with liquid. They usually correspond to transitions in the crack tip environment, including changing from wet to dry, dry to wet, humid air to dry air, etc. They even can occur in totally wet environments if the crack accelerates so fast that the viscous liquid cannot keep pace and instead cavitates behind the crack tip. Scarps are usually only detected in glasses and single crystals. Scarps could exist in polycrystalline ceramics, but the inherent roughness from the microstructure masks their presence.

The *practical significance* of scarps is that they are evidence that fracture occurred in the presence of a fluid, most commonly water. They also can help confirm the local direction of crack propagation.

Fréchette has identified several types of scarps and accounted for their formation.[1] Scarps can vary from as simple as a single faint line across the fracture surface perpendicular to the direction of crack propagation (cavitation scarp), to a complex network of curves such as shown in Figure 5.48. Figure 5.48b of a scarp in single crystal sapphire is, to the best of my knowledge, the only documented example of a scarp in a ceramic material.

Fréchette called some of these “Sierra scarps” if they are pointed in the direction of crack propagation as shown here as Figure 5.48c (and also in Frechette’s book, Figures 2.28 and 2.29) due to their similarity to his favorite mountain range. They form when water (in the form of spaced fingerlets as in a Taylor instability) overtakes a decelerating dry crack, causing local advances forward by the crack front.

“Cavitation scarps” occur when an accelerating crack causes void formation or cavitation in the water between the fracture surfaces that is trying to keep up with the crack tip. Once cavitation occurs the crack outruns the fluid water and a scarp line is left behind. The faint vertical lines within the scarps in Figure 5.48d have been described as “subcavitation hackle” by Michalske and Fréchette, who describe it as a microhackle precursor to complete cavitation.[1,44] The faint lines have alternatively been described as “streaks” by Beauchamp, since they may not in fact be steps, but slight perturbations in the crack plane.

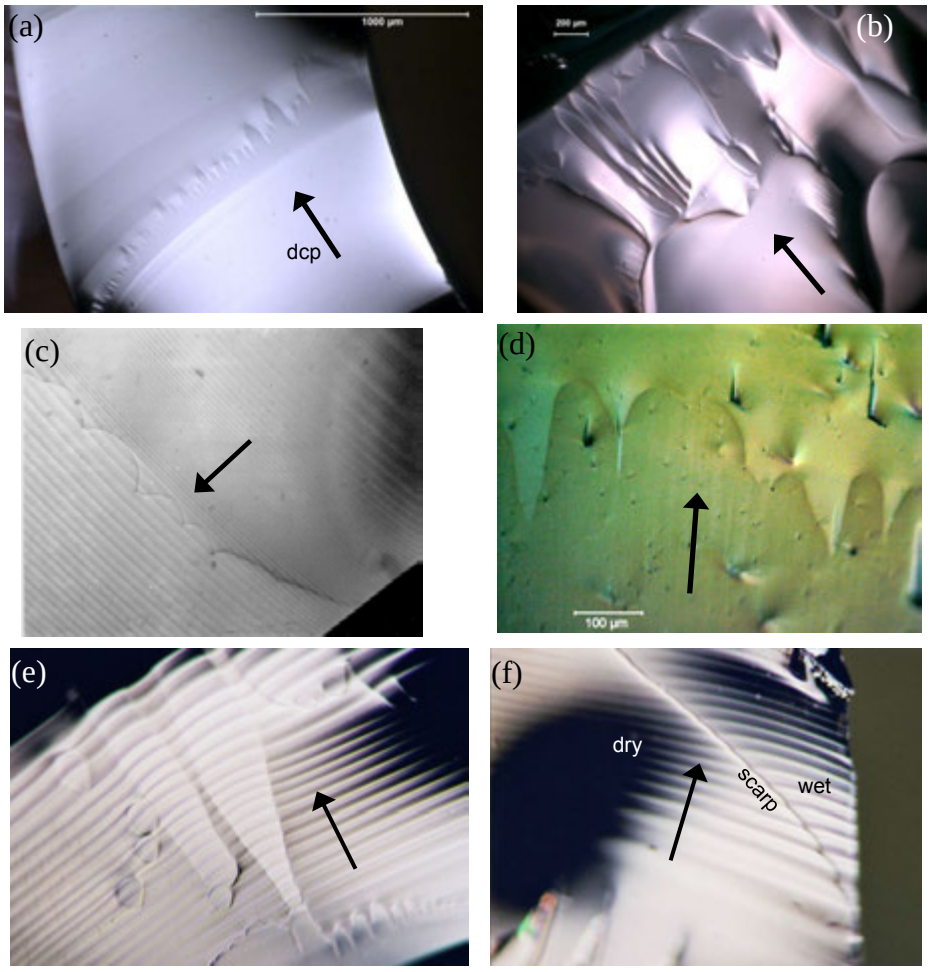

Figure 5.48 *Examples of scarps. The arrows show the direction of crack propagation. (a) is a fractured glass medicinal vial. The liquid was the medicine within the vial. (b) is from a single crystal sapphire hemispherical dome broken by water quench thermal shock. This differential interference contrast optical photo shows the scarps have variability in height. (c) shows Sierra scarps in glass caused by water "fingerlets" overtaking the advancing crack (courtesy E. Beauchamp) (d) - (f) are obsidian flakes formed by knapping. (courtesy A. Tsirk) The faint vertical lines within the scarps in (d) are either "streaks" or "subcavitation hackle," a precursor to complete cavitation. The parallel bands in (c), (e) and (f) are tertiary Wallner lines intentionally introduced by vibrations from an engraver (c), or a hand palm sander (e,f) to study the crack velocities. In (f) water that was available from the right side facilitated crack advance causing the scarp.*

Scarps are very subtle and can be very difficult to see. They are easily overlooked. They are best seen in an optical microscope with the specimen tilted to create a mirror-like reflection from the fracture surface. The specimen or the lighting must be tilted back and forth until one catches just the right reflection. They usually exist in only a portion of the specimen and usually where the crack is moving at a slow to moderate speed.

Tsirk[45,46] has studied a variety of scarps in knapped obsidian arrowheads and knives formed by pressure flaking. Some of the scarps were generated in antiquity when they chipped during usage. Tsirk has postulated that the shape of scarps may depend upon the nature of the fluid and possibly the viscosity. Scarps that have been observed associated with blood are different from those formed with water or saliva.[45,46] The reader is referred to Fréchette's book[1] and References 43-46,47,48 for details on scarps.

5.7 Glue Chips

Glue chipping is a process used by artists to create surface decorations on glass. Figure 5.49 illustrates the geometries. Figures 5.50 and 5.51 show examples. Glue is coated onto a lightly-abraded glass surface. The plate is warmed causing the glue to contract. Shallow cracks enter the glass at the edge of the glue at about 45 degrees then run parallel to the surface. The glue is peeled away removing scalloped chips in the glass. Fréchette noted that the chips formed by this artistic process closely resemble flaws generated in glasses in architectural and structural applications.[49]

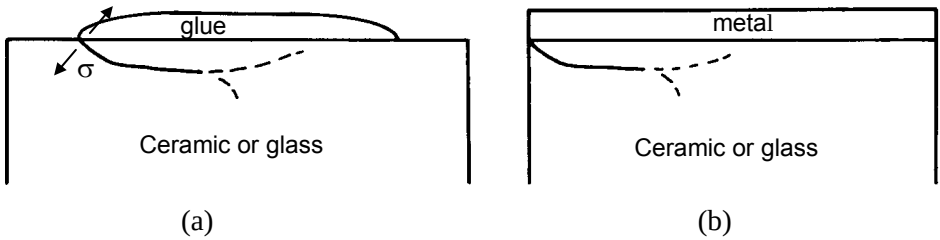

Figure 5.49 *Glue chipping cracks. (a) show a side view with glue applied to the surface of the glass of ceramic. Contraction of the glue causes a crack to enter the ceramic or glass at about 45^o to the surface. (b) shows a comparable geometry with a metal bonded to a ceramic or glass. If the metal contracts more than the ceramic, edge cracks can be created.*

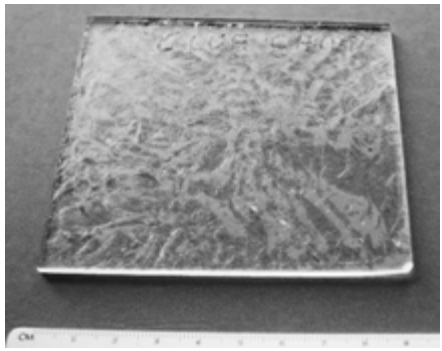

(a)

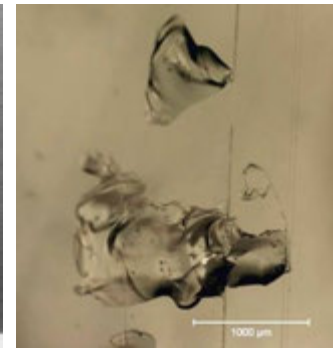

(b)

(c)

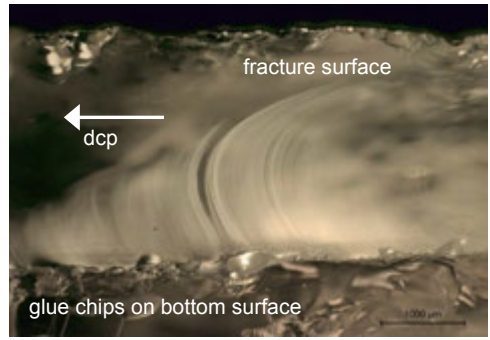

(d)

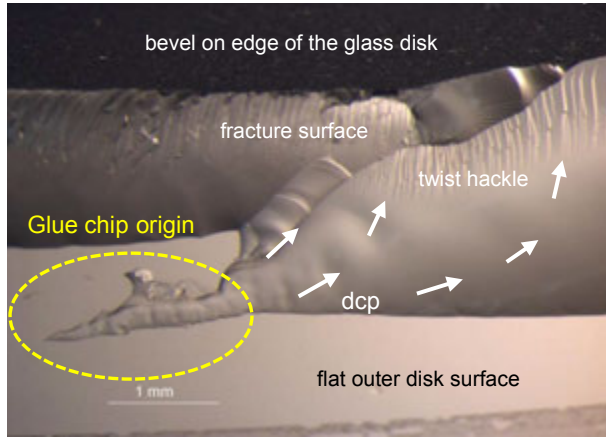

Figure 5.50 *Examples of glass glue chips. (a) shows an Alfred University demo plate covered with glue chips. (b) is a close-up of isolated glue chips on the surface. (c) shows a side view of a broken plate that shows glue chips on the bottom that affect crack propagation. (d) shows large glass disk that fractured from a glue chip caused by an epoxy bond to a metal part.*

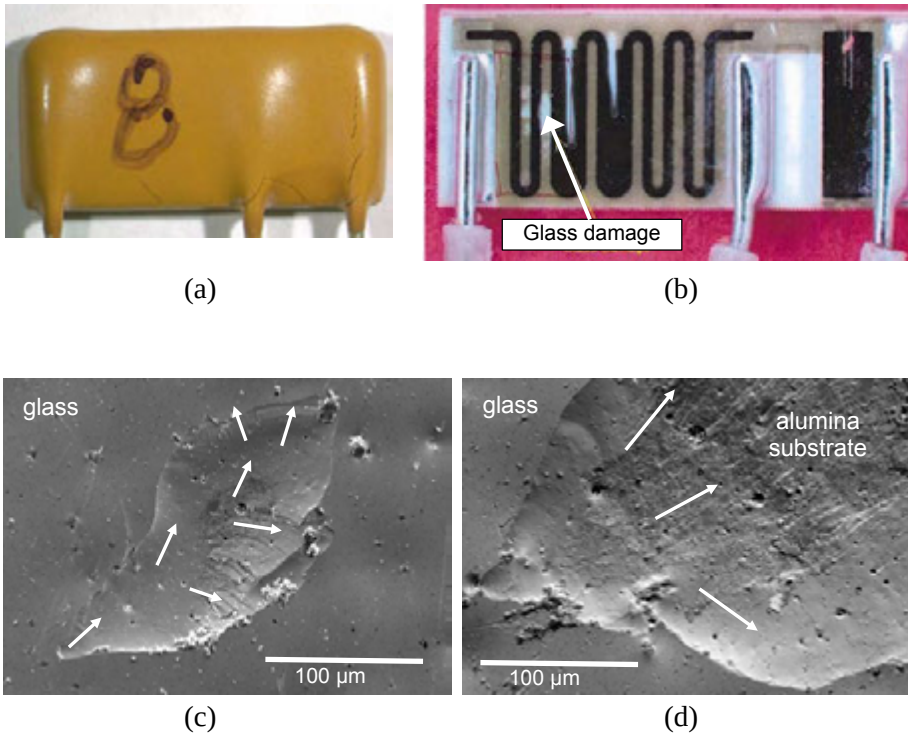

Figure 5.51 *Glue chipping damage in a thick-film resistor that cracked during thermal cycling. (a) shows the component in its epoxy encapsulant. (b) shows the exposed electrical circuitry. Scallop cracks (white-colored reflective patches) formed in an inner glass encapsulating layer. (c) and (d) show two glue chips in the glass. The arrows show the direction of crack propagation. (all photos and interpretation courtesy R. Tandon and S. Monroe)*

The conventional wisdom in many joining problems is to choose a metal or other material that contracts more than the ceramic or glass. During cool down from the elevated temperature joining process, the ceramic or glass is put into residual compression. This indeed is what happens, *except right at the edge of the joint* where a localized tensile stress can introduce cracks in the ceramic or glass as shown in Figure 5.49. If the cracks remain shallow and come back to the surface joint, they are harmless. Alternately, if they remain in the ceramic or glass interior, where subsequent tensile loadings activate them, or they tilt down away from the joint, they can cause severe strength degradation. Glue chips, when exposed so as to reveal their fracture surfaces, have ample twist hackle, arrest lines, and tertiary Wallner lines.

Glue chips were the origins of fracture in spectacular failures of very large windows in the John Hancock skyscraper in Boston in the early to mid-1970s.[49] The windows were 25 mm – 32 mm (1 inch to 1.25 inch) double-glazed glass panels with two 6.35 mm (0.25 inch) thick individual panels bonded with a lead spacer between them. A copper coating was flame sprayed to the inside rims of the glass panels. The glass panels were then soldered to the square lead spacer around the rim. Differential contraction of the lead versus the glass created incomplete glue chips in cold weather. (A silver reflective coating on the inside of the outer glass panel may also have been a factor.) Subsequent mechanical and thermal loadings caused the cracks to propagate, and the windows eventually fractured. The author and his future spouse, who were undergraduate students at Northeastern University, looked at the building in the 1970s as we came out of engineering classes. At any time, hundreds of glass panels were replaced temporarily by plywood sheets. Eventually, all the windows in the skyscraper were replaced. The above interpretation of the cause of the John Hancock window failures is based on my private communications with Prof. Fréchette, Mr. Leighton Orr, and information in Reference 49.

Frechette[49] reported a second instance where glue chipping cracks caused tempered float glass spandrels to fracture in a high-rise building. In this instance, the actual cause was spots of copper metal from weld spatter. The high shrinkage of the metal droplets on cooling caused glue chip type cracks.

5.8 Transgranular and Intergranular Fracture

In addition to finding the fracture origin, in polycrystalline ceramics it is often important to observe whether crack propagation is transgranular and cleaves through grains or is intergranular whereby the crack runs around the grains along grain boundaries. It is usually necessary to have scanning electron micrographs of the fracture surface for this characterization. Figures 5.52 and 5.53 show examples. Sometimes the word *intra*granular is used inter-changeably with transgranular, but the former word is not recommended, since it is so similar to *intergranular* that it often creates confusion.

Material scientists are concerned with the mode of propagation since it provides information about how cracks interact with the microstructure. Intergranular fracture may indicate weak boundary strength. It may be a manifestation of between-grain stresses due to elastic or thermal anisotropies, especially in non-cubic ceramics. Mixed inter- and transgranular fracture modes are common. It is customary to make approximations or estimates of

the fraction of inter- and transgranular fracture and to show an illustration. There is clearly some interpretation involved and what may be a 50 % to 50 % mix for one observer might be reported as a 40 % to 60 % mix by another.

(a)

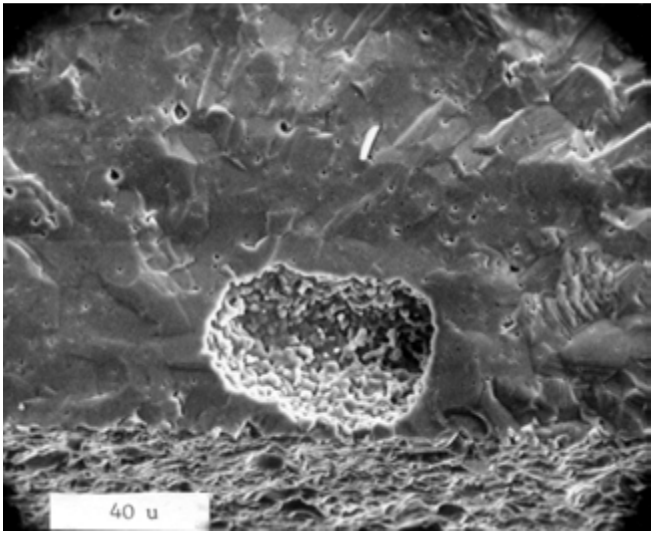

(b)

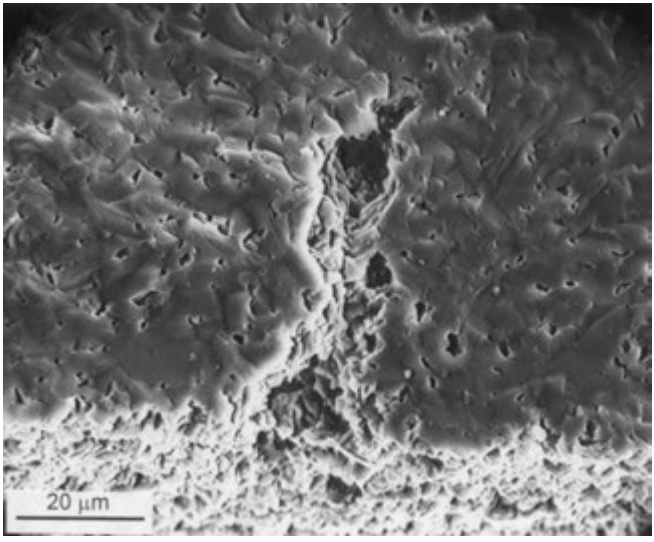

Figure 5.52 *Transgranular fracture examples around fracture origins. (a) is aluminum-oxynitride. Notice the wake hackle triggered by the grain boundaries and some small pores. (b) is a sintered alpha silicon carbide.*

(a)

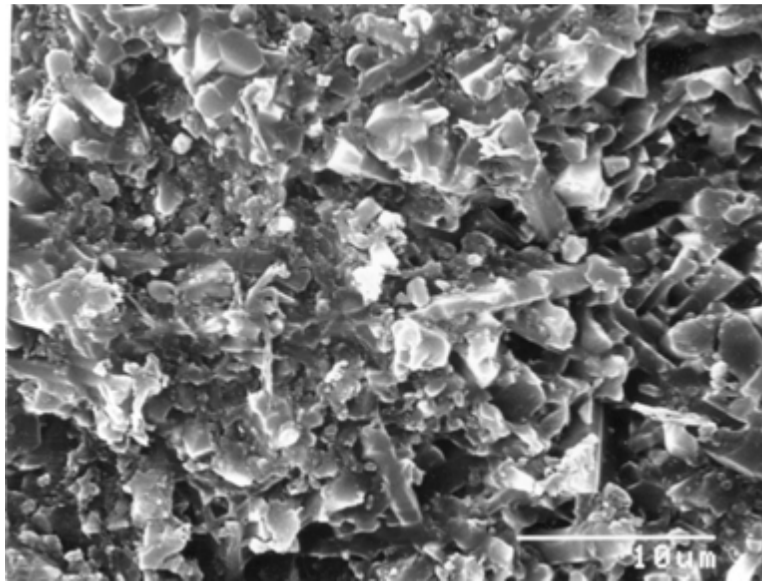

(b)

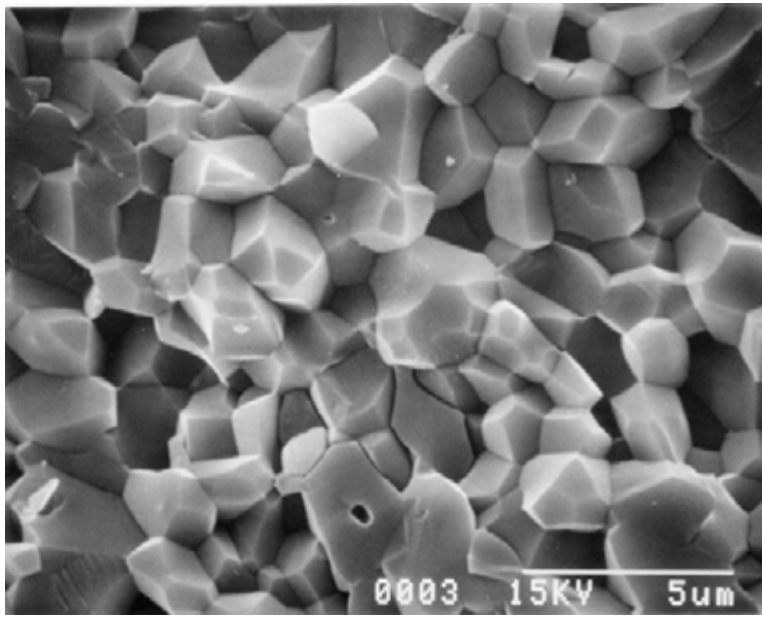

Figure 5.53 *Examples of intergranular fracture surfaces. (a) is an elongated grain silicon nitride. (b) is a 99.9 % sintered alumina.*

Fracture mirrors in polycrystalline ceramics may initially have transgranular fracture but change to mixed trans- and intergranular fracture as the crack radiates outwards.[32]

Slow crack growth or environmentally-assisted crack growth usually occurs intergranularly. Grain boundaries are weaker than matrix grains and secondary phases or glasses often are distributed along the grain boundaries. There are exceptions, however.

Transgranular fracture though grains often generates twist hackle and/or cleavage steps within the grains as the crack twists and turns to follow preferred cleavage planes within the microcrystals. These markings can be interpreted to evaluate the local direction of crack propagation.

5.9 Stable Crack Growth

5.9.1 Slow crack growth (SCG) at ambient temperature

Many glasses, oxide ceramics, and nonoxide ceramics with an oxide sintering aid are susceptible to environmentally-assisted slow crack growth (SCG). The expression "slow crack growth" usually is used in the context of stable crack extension due to combined effects of stress and environment. (It is also commonly used to describe high temperature stable crack extension as described later in section 5.9.3.) Water, either in liquid or as a vapor, is the most common reactive species that causes slow crack growth, although other small polar molecules such as hydrazine (N_2H_4), ammonia (NH_3), and methanol (CH_3OH) can enhance crack growth in silicates.[50,51] Ceramics such as alumina and magnesium fluoride are also susceptible to environmentally-enhanced crack growth. Acetonitrile (CH_3CN) can attack magnesium fluoridate, but not alumina or silica.[50,51] Slow crack growth requires both a stress to open the crack faces and a reactive species to chemically react with the strained atomic bonds at the crack tip. Hence, it is sometime called "stress corrosion cracking." Figure 5.54 illustrates the leading theory for how environmentally-assisted slow crack growth occurs in glasses. Slow crack growth can lead to weakening and/or time dependent fracture. Slow crack growth is also sometimes called "static fatigue" if the loading is steady or constant. If the stable crack growth occurs while loading increases at a constant rate, as in common strength tests, it is sometimes referred to as "dynamic fatigue."

All glasses are susceptible to slow crack growth. Many other ceramics are too, particularly if they are bonded by a glassy boundary phase, no matter how thin. Covalently-bonded ceramics are not susceptible to SCG at room temper-

ature, unless there is an oxide boundary phase. Section 7.10 has more qualitative information about the mechanics of slow crack growth and Table 7.2 lists materials that are or are not susceptible.

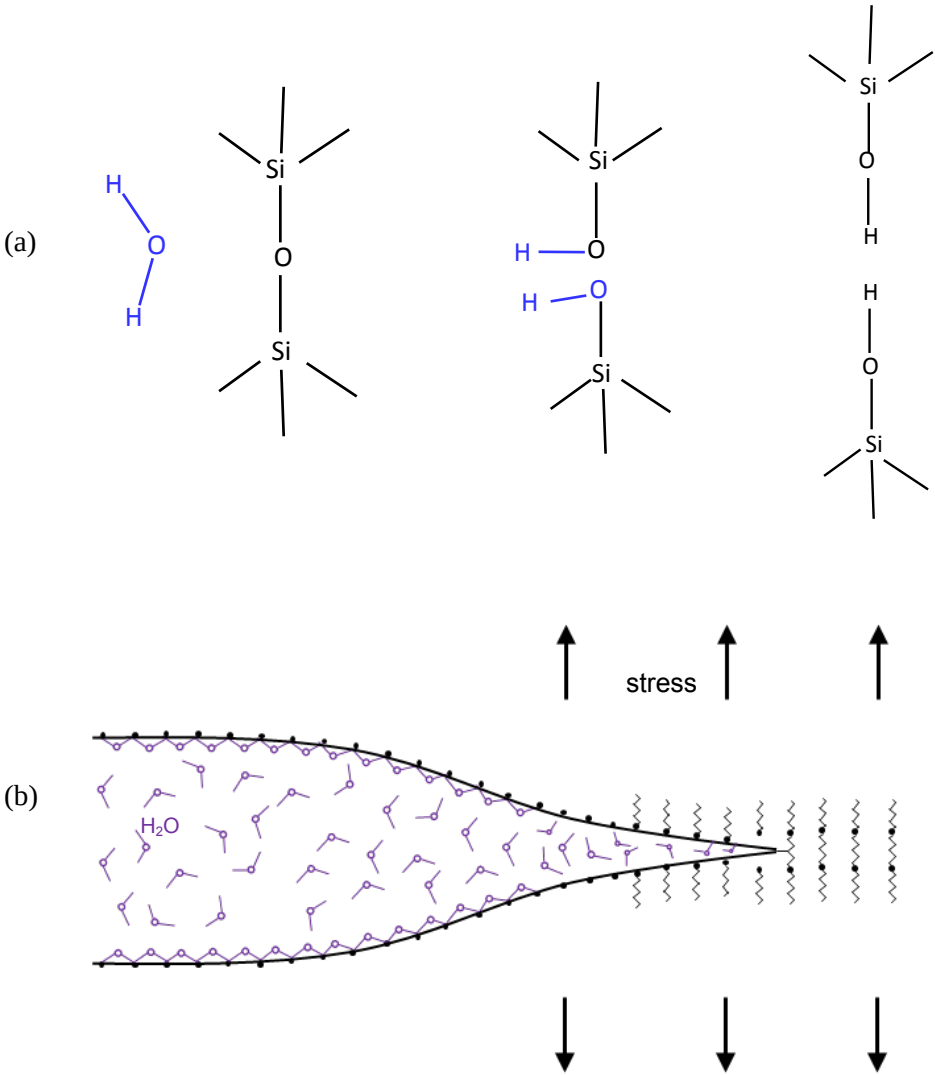

Figure 5.54 *Stress corrosion cracking can cause slow crack growth in glasses. The polar water molecule, either in liquid or gaseous form, attacks strained silicate bonds. (after Michalske and Freiman[50] and Michalske, Bunker, and Freiman[51])*

Sometimes it is possible to detect evidence of the stable crack extension. Slow crack growth is usually intergranular in polycrystalline ceramics. If the fast, unstable fracture mode is transgranular or mixed, then the difference in propagation morphology may be detectable as a SCG "halo" on a fracture surface as shown in Figure 5.55.

Slow crack growth halo: *A region or band around a flaw in a ceramic caused by stable crack extension. The band is caused by changes in the mode of crack propagation.*

SCG halos can often be detected with both optical and SEM microscopy as shown in Figure 5.55 for the case of a high-purity alumina.[52] Usually the intergranular zone appears darker when viewed with an optical microscope since the rougher fracture surface scatters light in different directions. In contrast, the slow crack growth zone looks lighter in the electron microscope possibly due to slight charging effects on edges of the intergranularly-fractured grains. Mecholsky[53] showed superb pictures of intergranular slow crack growth (from constant stress-to-fracture tests, "static fatigue") versus transgranular fast fracture in magnesium fluoride. Morrell presented a case of a fractured alumina hip ball with an unusual circular intergranular zone of slow crack growth that appeared shiny in the optical microscope.[54]

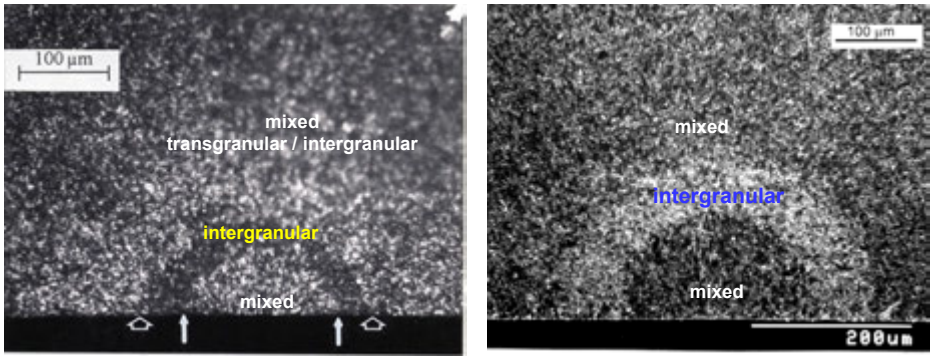

(a) (b)

Figure 5.55 *Knoop semicircular flaws in two specimens with SCG "halos" in a sintered 99.9 % alumina. (a) is an optical image of a 29 N indentation flaw (Courtesy J. Swab), and (b) is a SEM image of a 49 N flaw. The precracks are mixed transgranular-intergranular. The halo is mostly intergranular. The fast fracture is mixed transgranular-intergranular. The crack growth occurred in only a few seconds during an ordinary strength test. Notice that the rougher intergranular surface appears dark in the optical photo since it scatters light, whereas it appears light-colored in the SEM.*

(a)

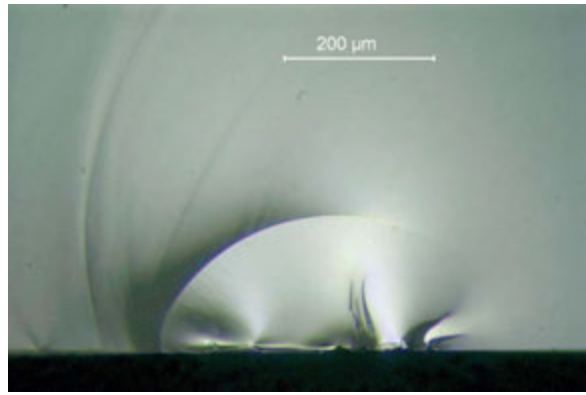

(b)

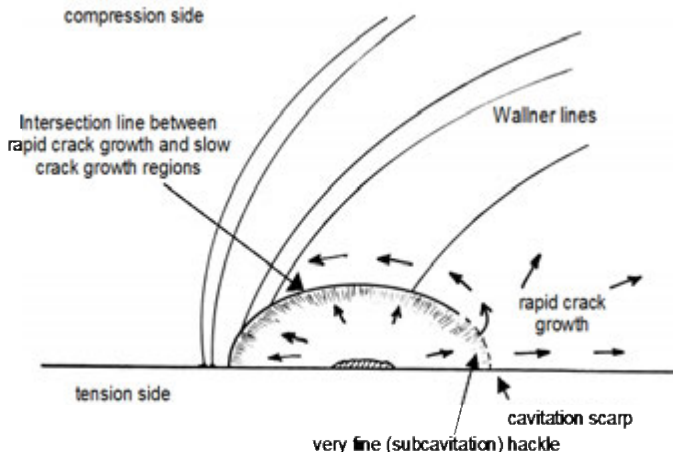

Figure 5.56 *Slow crack growth in glasses sometimes leaves a partial semielliptical line that approximates the critical crack size. (a) shows an example for a glass disk tested in ring-on-ring biaxial flexure in water. The original flaw was an 8 μm to 10 μm deep crack from a polishing scratch. It grew approximately 20 times deeper in the bending stress field before it went unstable along the right side. Only a very faint cavitation scarp exists at that position, but a more distinct line forms around the crack front periphery as the unstable crack wraps around it. (b) shows a schematic of this sequence. See also Figure 5.45a.*

The usual remedies to eliminate SCG in laboratory strength testing are to test either at a very fast loading rate or in an inert atmosphere. The SCG halos disappear when testing is done in inert atmosphere.[52]

In glasses a subtle partial elliptical line that sometimes appears on the fracture surface provides a strong clue that SCG has enlarged a flaw as shown in Figures 5.45a and 5.56.[55,56] The part elliptical line is a slight step that forms as a result of the intersection of the unstable crack that wraps around the portion of the crack that has not gone unstable.

5.9.2 Stable extension from local residual stress or R-curve effects

Stable crack extension can occur, even in the absence of environmental effects, if a flaw has a strong local residual tensile stresses. Indentation crack flaws made by either Vickers or Knoop indentation are good examples. Damage zones underneath the indentation can provide the tensile stresses that are the driving force for crack extension. As the crack extends away from damage zone and the crack periphery gets larger, the effect of the tensile stresses diminish and the crack slows down and arrests in the absence of externally-applied stresses. Alternatively, in fast fracture tests where the specimen is loaded to fracture, there can be momentary stable crack extension of the flaw prior to rupture. Figure 5.57 shows an example of stable crack extension at room temperature due to local residual stresses in a hot-pressed silicon nitride.

Rising R-curves, which will be discussed in more detail in chapter 7, can also lead to stable crack extension at room temperature. There is only a small fractographic literature on this effect, in part due to the fact that the amount of stable crack extension prior to a flaw going unstable is often very small. (Stable crack extension from local residual stresses or due to R-curve effects is usually not termed “slow crack growth” in the literature.)

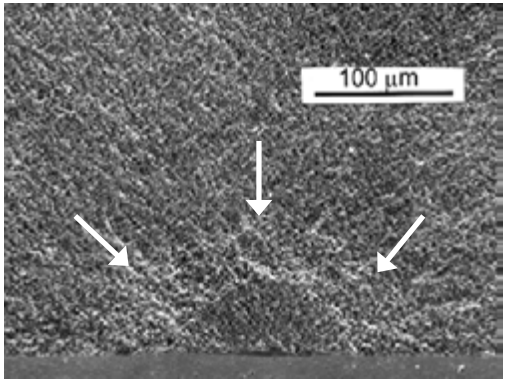

Figure 5.57 *Knoop flaw (dark semiellipse) in silicon nitride showing stable crack extension (white arrows). The local residual stresses underneath the indentation provided the impetus for the extension. Traces of the very shallow, elongated Knoop indentation can be seen on the bottom surface.*

5.9.3 High-temperature slow crack growth in ceramics

At elevated temperatures, increased atom mobility and decreases in boundary phase viscosity can lead to intergranular crack growth. This also can cause weakening or time dependent fracture. The environment may or may not play a role in slow crack growth. Figures 5.58 and 5.59 show flaws that have been altered as a result of slow crack growth. The slow crack growth zones are usually rougher than the normal fast fracture surface and are usually easy to detect due to the topography difference in the SEM or by a topography or reflectivity difference in an optical microscope. Oxidation of the material in a slow crack zone often causes a color or reflectivity difference that is also easy to detect in an optical microscope. The slow crack growth zones can be very small and may enlarge a flaw just enough to cause it to reach criticality. Alternatively, at lower stresses they may have extensive crack growth zones that can cover as much as one half of a fracture surface as show in Figure 5.60. In such cases, it often is impossible to locate the initial flaw from which the crack growth occurred.

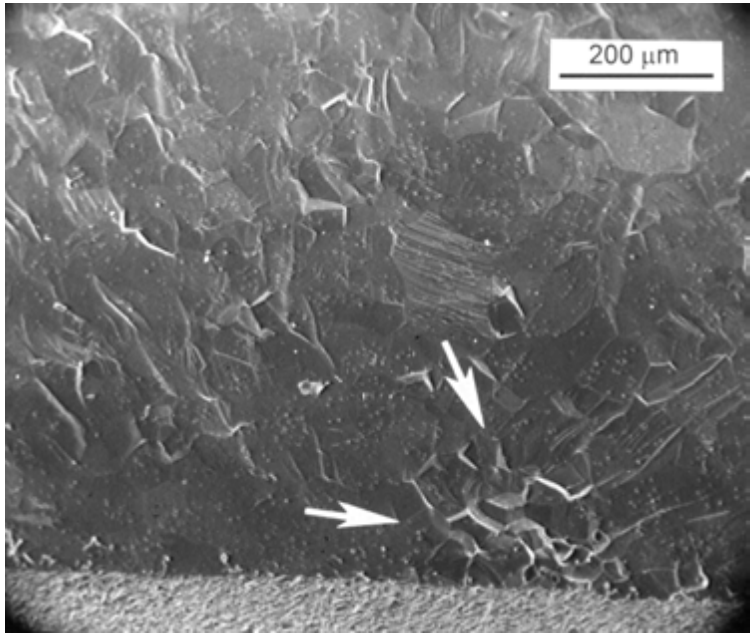

Figure 5.58 *Intergranular slow crack growth in a pure AlON at elevated temperature. The slow crack growth zone (arrows) formed in the short time that was needed to break the specimen in a strength test. (1200^{o} C, 155 MPa, 22.5 ksi)*

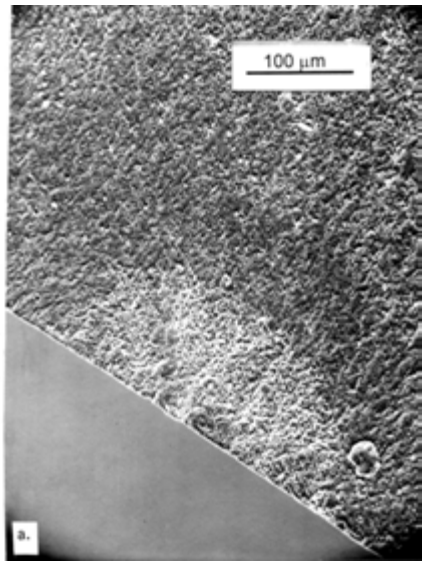

(a)

(b)

(c)

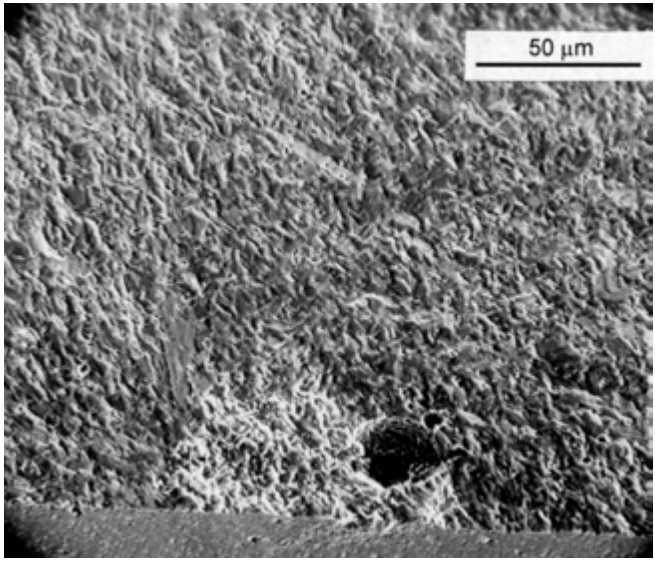

Figure 5.59 *Elevated-temperature slow crack growth in sintered alpha SiC tested in stress rupture at 1400 °C in air (a). The close-up (b) shows the boundary between the intergranular SCG and the transgranular fast fracture zones. (c) shows another alpha SiC specimen wherein the slow crack growth appears to have originated near a pore.*

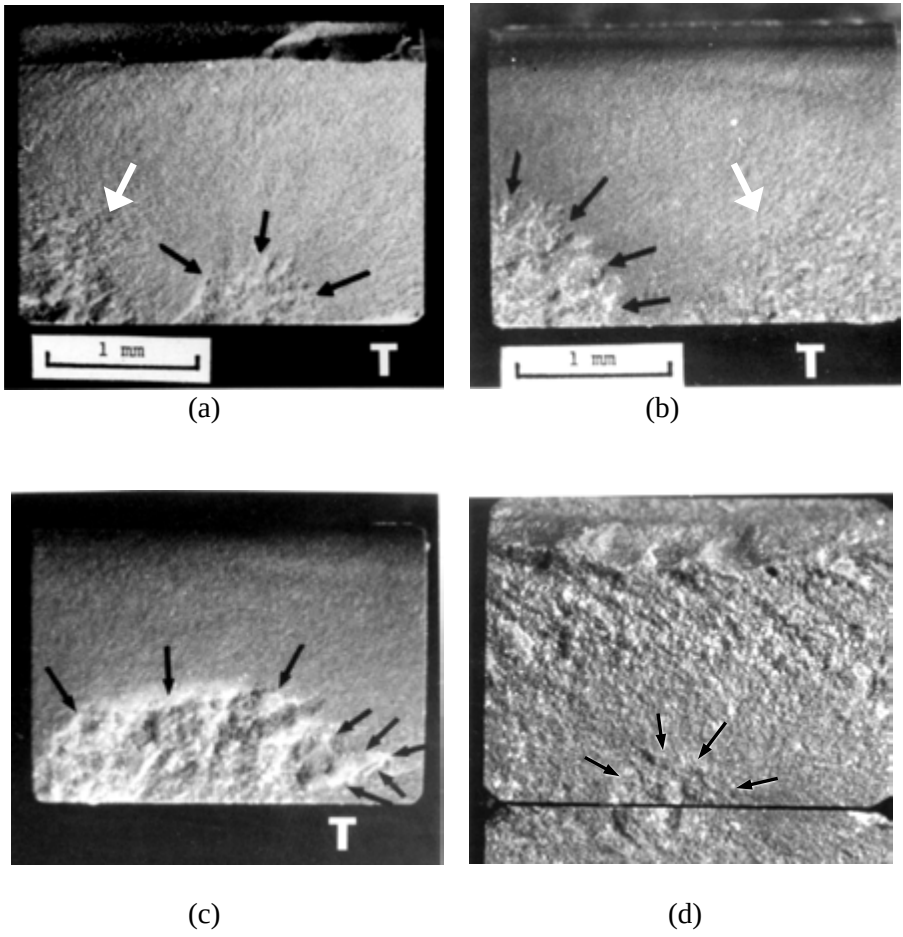

(a) (b)

(c) (d)

Figure 5.60 *Elevated-temperature slow crack growth zones in hot-pressed silicon nitride. These four bend specimens were tested at 1200 °C in air. The black arrows mark the intergranular crack growth zones, which appear lighter since they have oxidized somewhat, unlike the final fracture regions. Notice the roughness of mirror-like hackle on the left side of (a) and the right of (b) as marked by the white arrows. At low magnification, this roughness could be confused with a slow crack growth zone, but closer examination shows it has directional lines typical of hackle.*

5.9.4 High-temperature creep fracture

Creep can cause fracture at higher temperatures and lower stresses. There is so much boundary phase ductility that sharp flaws are blunted. Fracture is due to the nucleation and growth of cavities, microcrack formation, and their coalescence. Creep fracture surfaces often look like the slow crack growth zones shown above, but with growth zones that extend across a major fraction of the fracture surface. Final rupture frequently occurs from creep crack zones connected to specimen corners. Tensile surfaces often reveal extensive tortuous microcrack patterns. A key difference between slow crack growth and creep fractures is that the former can occur with negligible bulk deformation, whereas the latter inevitably have significant permanent deformations with strains of 1% or more. Figure 5.61 shows several examples.

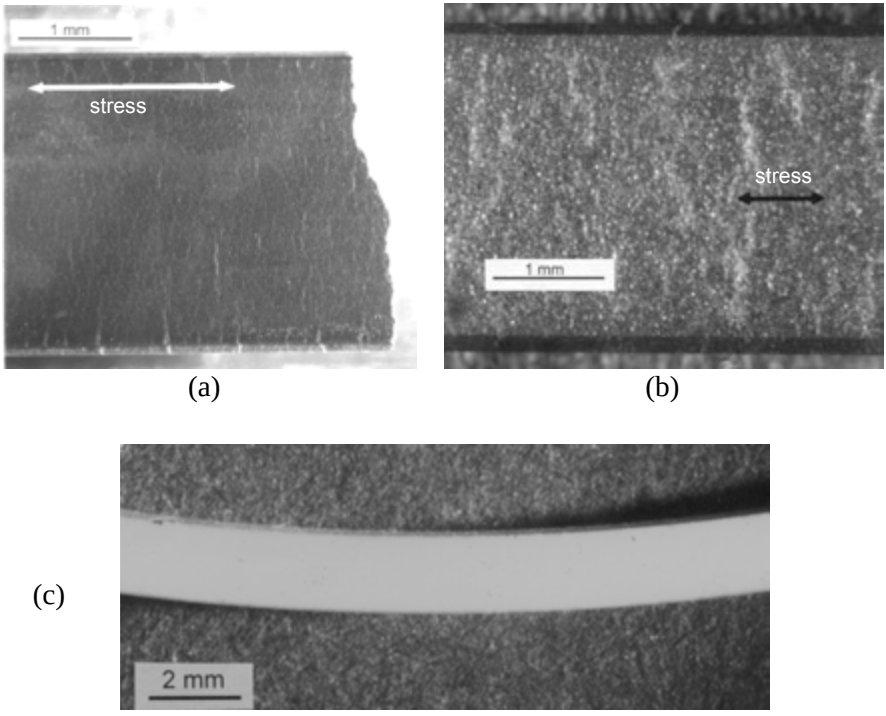

(a) (b)

(c)

Figure 5.61 *Bend specimens tested under creep fracture conditions. (a) shows the tensile surface of a hot-pressed silicon nitride specimen. Notice the extraordinarily rough fracture surface on the right side of (a). (b) shows the tensile surface of a siliconized silicon carbide specimen. Note that the microcracking is perpendicular to the axis of tensile stresses (double arrow). (c) shows a side view of a bend bar tested in creep fracture conditions.*

Figure 5.62 illustrates the differences between slow crack growth and creep fracture. Glassy boundary phases such as shown in Figure 5.63 usually account for both processes.

Slow crack growth occurs from preexistent flaws that grow until they reach a critical condition. Fracture toughness at elevated temperature is often greater than at room temperature due to the onset of limited plasticity. Hence, critical flaw sizes can actually be much larger at elevated temperature than at room temperature. Specimens that fail from slow crack growth have negligible (< 0.2 %) permanent strain.

Creep fracture on the other hand usually does not involve the initial flaws. It blunts them. Voids and microcracks are nucleated, then coalesce, and then grow leading to rupture. Creep fracture specimens have considerable permanent strain at fracture. Failure is more a matter of accumulation of damage. The intergranular crack growth zone on creep fractured bend bars often extends over 33 % or more of the fracture surface.

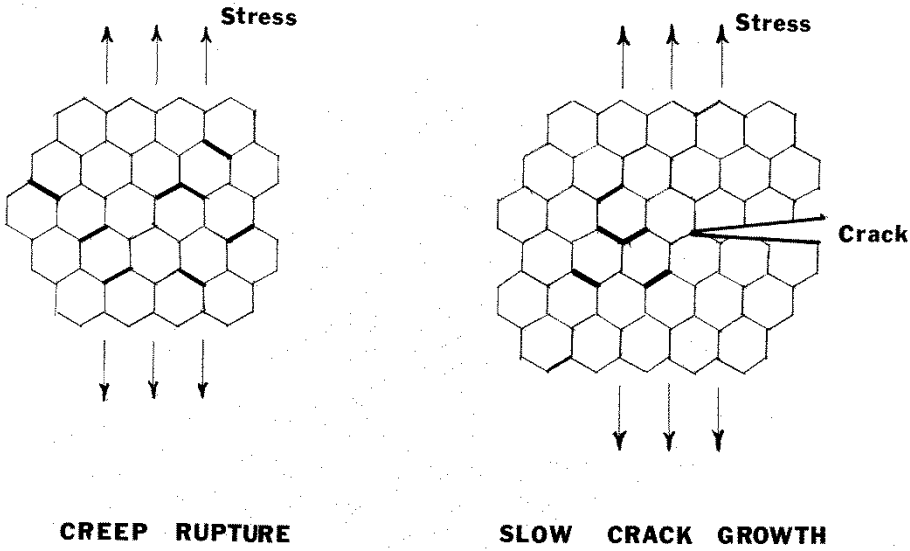

Figure 5.62 *Creep fracture and slow crack growth usually are intergranular at high temperature. In creep fracture (a), cavitation and microcrack nucleation occur throughout the body. In slow crack growth (b), the processes are confined to the crack tip region.*

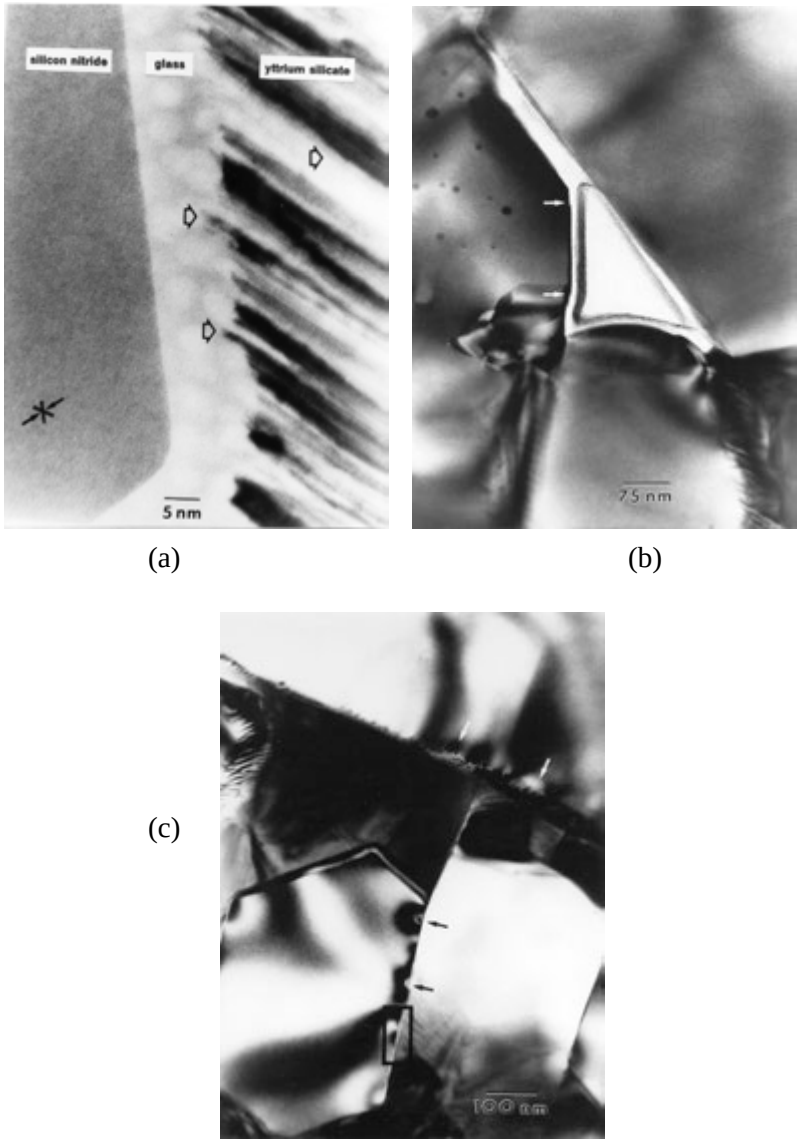

Figure 5.63 *Transmission electron microscopy images show the glassy boundary phase that often is the source of intergranular slow crack growth and creep crack growth. (a) shows the boundary phase which has partially devitrified in a silicon nitride with a yttrium aluminosilicate glass sintering aid. There still is a thin glassy layer that led to SCG and creep fracture. (b) shows a creep cavity opening up at a triple-grain junction. (c) shows strain sworls (black arrows) from grain boundary sliding. (Ref. 57, Photos courtesy W. Braue).*

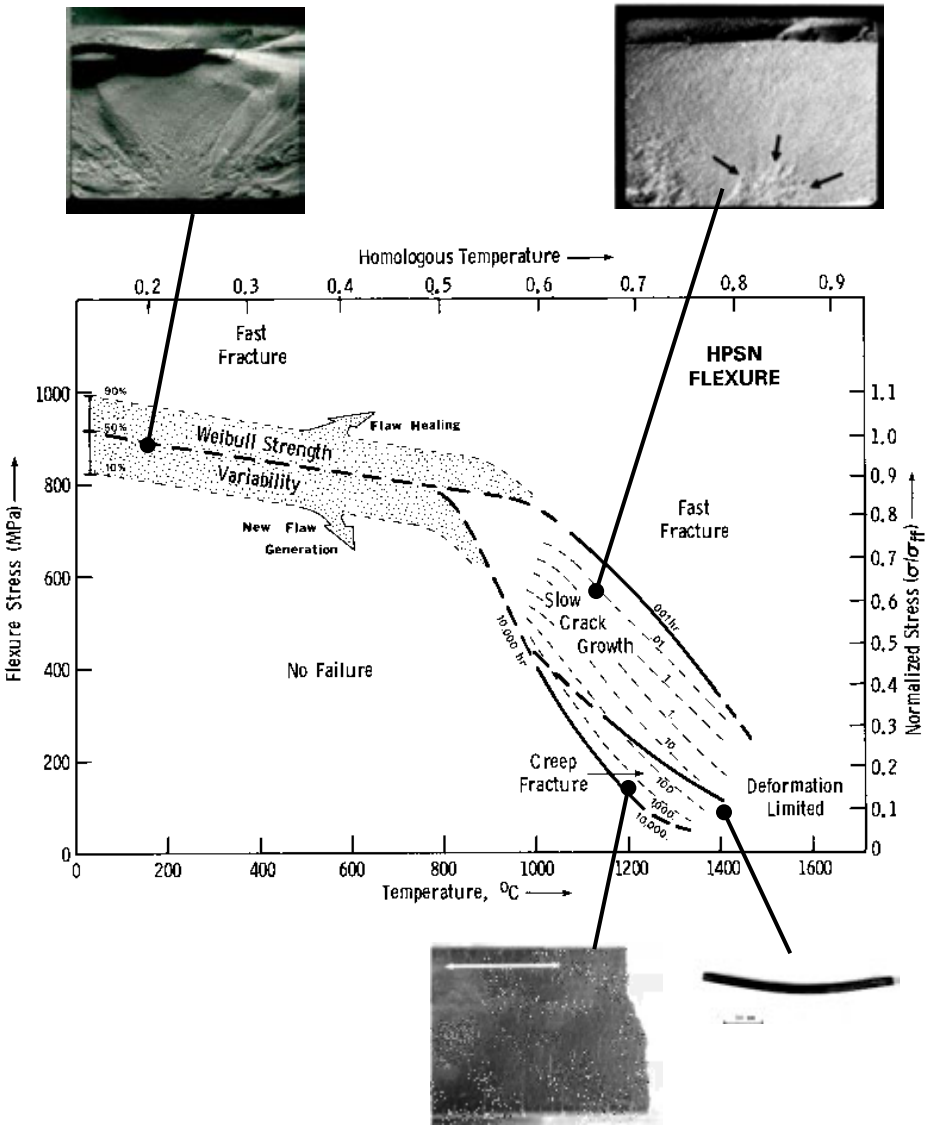

Figure 5.64 *Fracture mechanism map for hot-pressed silicon nitride from Reference 58. This map is for flexurally-loaded specimens.*

Figure 5.64 is a fracture mechanism map that puts these pheneomena into context.[58] It is for a commercial silicon nitride hot-pressed with about 1 mass % magnesium oxide. The sintering aid reacted with silica on the surface of the starting powders and formed a very thin silicate boundary phase glass. Depending upon the stress and temperature, flexural specimens fractured from any one of several mechanisms. At low temperature, material and grinding flaws controlled strength. At moderate temperatures in an oxidizing environment, flaws either remained unchanged and controled strength, or they healed or blunted causing some strengthening. On the other hand, oxidation sometimes created pit flaws that weakened the body. At 1000°C and greater, integranular slow crack growth caused flaw growth and eventual fracture in times shown in hours on the dashed lines. At low stresses and high temperature, creep fracture controlled lifetime.

5.9.5 Mechanical fatigue from cyclic loading

Fine-grained ceramics and glasses are usually not susceptible to classical mechanical fatigue, in the sense of stepwise stable crack growth from accumulated mechanical damage from repeated loading and unloading. Figure 5.65 shows classical metal fatigue markings that are called “fatigue crack striations.” It is exceedingly rare to see genuine fatigue bands like this on ceramic fracture surfaces. In metals, each band-arc line may correspond to a number of loading cycles during which a damage process may occur, leading to one crack jump forward and then arrest, with the process repeating with additional cycling.

With ceramics and glasses, if lines like these are observed, they are more likely to be simple arrest lines from iterative loading such as shown in Figure 5.66 which is from Reference 59. The lines are visible due to slight variations in the crack plane between loading cycles. Incremental crack growth during cyclic loadings might be simply due to the accumulated effect of the slow crack growth phenomena described in section 5.9.1. Evans showed another good example in glass in Reference 60.

The fracture surfaces of laboratory coupons (e.g., tension or bend bar specimens), even if they do fracture from fatigue cycling, will often not show such markings. The initial flaws grow a small amount before they go unstable because fatigue often occurs only for specimens that are loaded near the fast fracture strength.

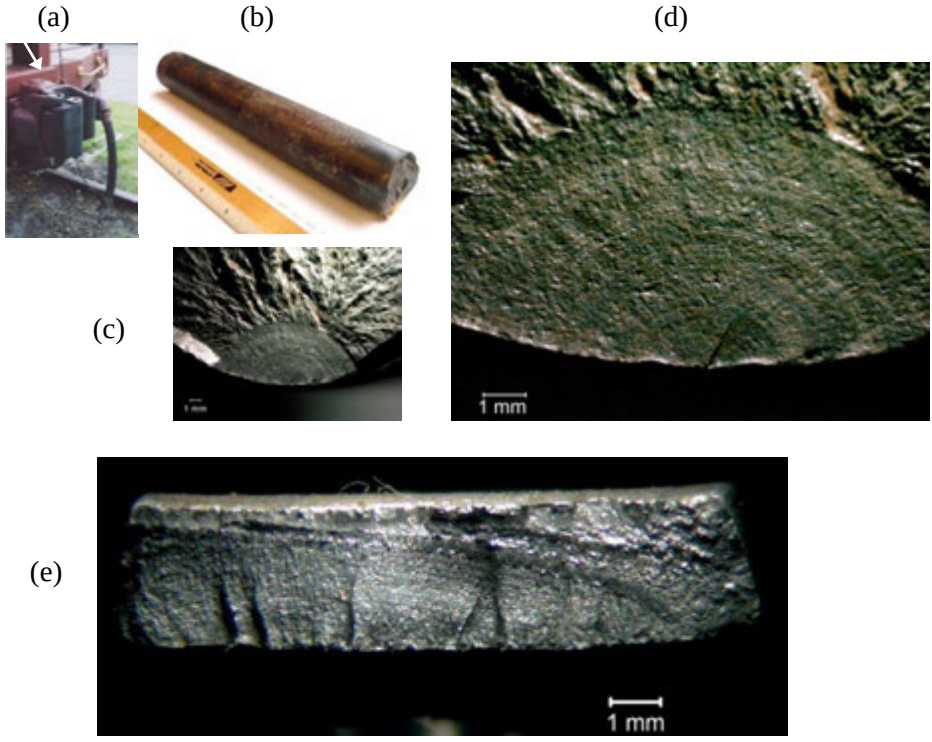

Figure 5.65 *Classic metal fatigue striations in (a-d,) a steel railroad coupler pin (see also Fig. 3.21), and (e) an aluminum bicycle bracket. An arc line does not necessarily correspond to one loading cycle.*

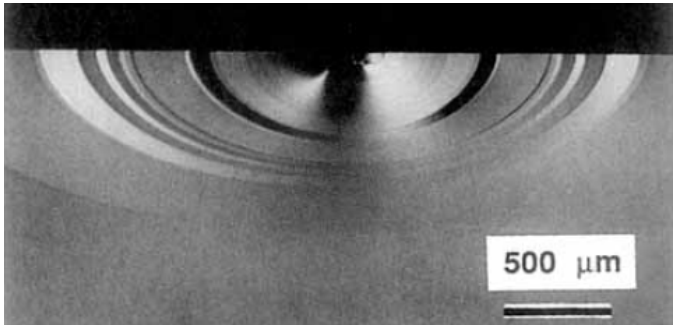

Figure 5.66 *Concentric arrest lines in a plate of soda lime silica that was cyclically loaded in flexure. The lines are due to slight variations in the crack growth planes on each loading cycle. (courtesy of D. Green, Penn State University, same as Figure 5.47c)*

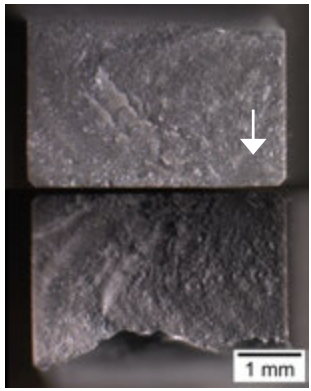

(a)

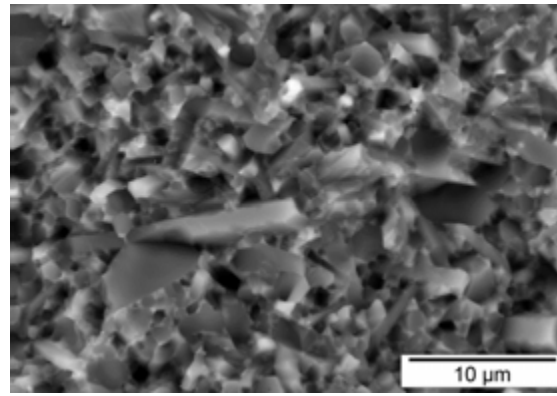

(b)

(c)

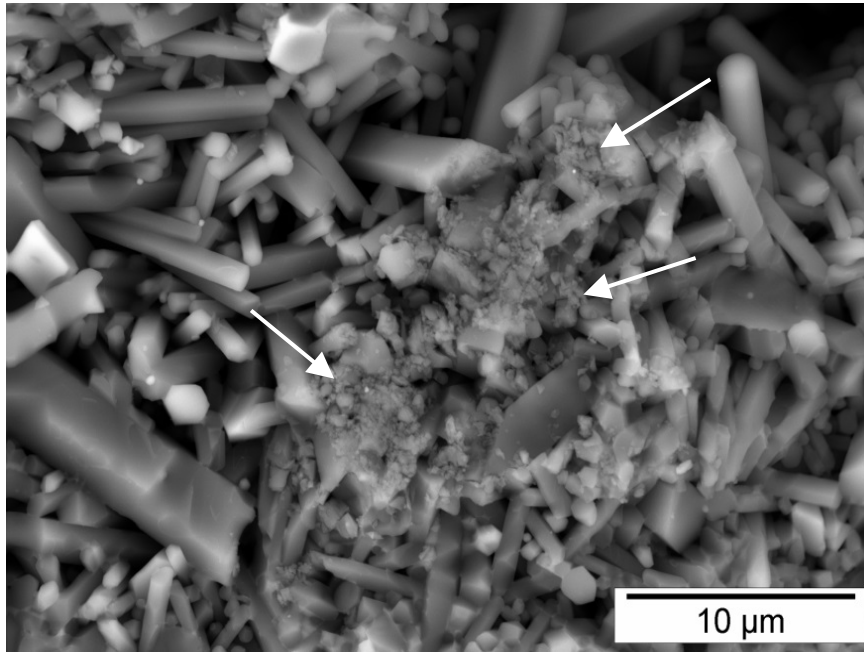

Figure 5.67 *Bend bar that was tested to fracture in cyclic fatigue loading. The material was a yttria and alumina additive sintered silicon nitride with an elongated grain structure for enhanced fracture toughness. (a) shows the bend bar fracture surfaces with the origin marked by the arrow. (b) shows a typical fast fracture portion of the fracture surface. (c) shows the origin region and fine debris (arrows) created by fatigue cycling. (courtesy T. Lube and R. Danzer)*

On the other hand, polycrystalline ceramics having coarse-grained or elongated-grain microstructures and anisotropic properties may be susceptible to fatigue crack growth. This is a curious tradeoff: the enhanced fracture toughness of an elongated-microstructure ceramic may be offset to some degree by sensitivity to mechanical fatigue. Unfortunately, the microstructures creates rough fracture surfaces such that it is difficult or impossible to discern evidence of progressive crack extension.

One subtle, but effective sign of genuine fatigue damage cyclic, is *small debris particles* on the fracture surfaces of polycrystalline ceramics such as shown in Figure 5.67, which are from Reference 61. The debris is small and detectable only in the SEM. The backscatter mode may help detect such debris. The fine debris can occur if the loading entails cyclic *tension and compression,* (e.g., the R factor, which is the ratio of the maximum stress to the minimum stress, is negative.) Dislodged or fractured grains near the crack tip may be crushed between the crack faces if the crack faces go into compression. The debris may or may not be present if the crack is loaded in cyclic tension-tension (e.g., the R factor is zero or positive). One suspects that too zealous a cleaning of a fracture surfaces beforehand might be harmful! On the other hand, it is possible that the crushing may help the debris adhere to the fracture surface and a light cleaning will not necessarily remove it.

5.10 Organizing all the Information – Fractographic Montages

Some component fracture analyses are complex, and an origin site may not be immediately obvious. In such cases, the entire fracture surface may be examined with the goal of observing the local directions of crack propagation. Wake hackle, gull wings, Wallner lines or arrest lines as described in this chapter provide such clues. A map of the overall fracture surface can be constructed in the form of a large montage, around which key local closeup photos of the crack propagation directions can be marked. Little arrows labeled "dcp" can then be put on the overall image. The localized direction of crack propagation can be "backtracked" to an origin site that might not have been immediately obvious. A good example is Figure 5.68 for an alumina dental crown which split into two pieces in a patient's mouth. It was a relatively low energy fracture that created only two pieces. The core ceramic microstructure was not easy to interpret, but there were enough markings in it and the outer veneer porcelain layer that it became obvious that fracture started at a margin.

Ko also showed marvelous montage examples for an alumina that broke from fatigue loading.[37] There were many tiny wake hackle lines from microporosity in an otherwise rough fracture surface that he used to back track to the origin.

A fracture map like this also has great value in communicating a failure analysis. It illustrates how much work has gone into an anlysis, and it can also provide context. It can be much more effective in convincing a client or reader than merely showing a handful of closeup photos and relying on the client to trust the fractograpgher's judgement.

Montages may also be used to integrate fractographic information with mechanical property test data such as a Weibull graph as shown in Section 6.19 and Figure 6.78.

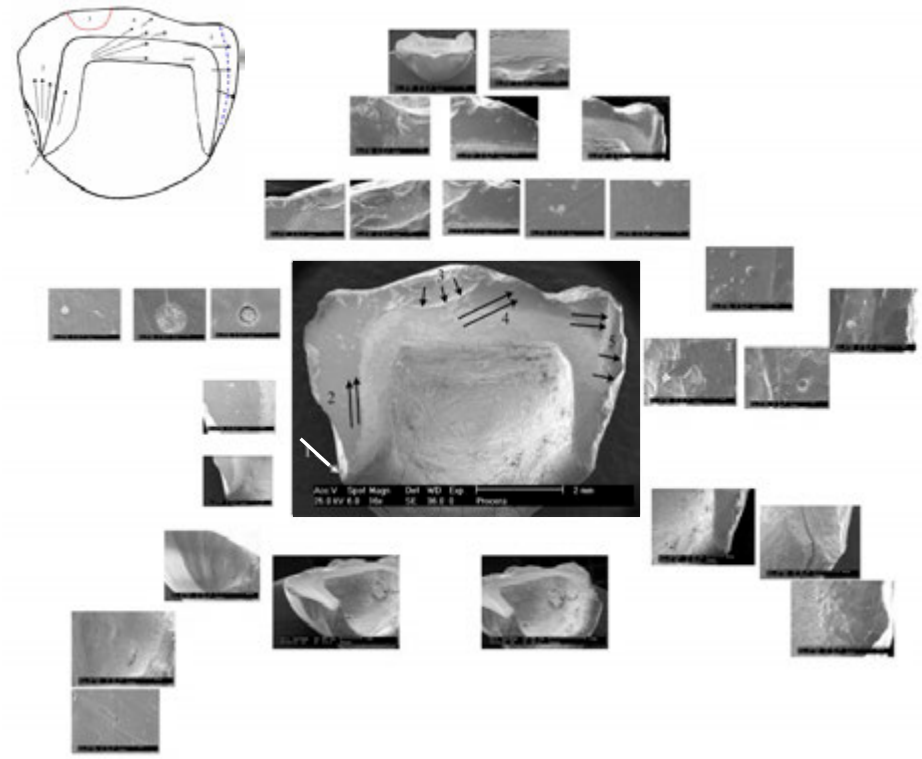

Figure 5.68 *A fractographic map - montage that integrates a lot of local information into a global interpretation. The photos are too small here to see the important details. The montage shows the concept. The local photos are organized in a systematic manner around the overall image that provides context and location information. The white arrow marks the fracture origin. Notice the sketch in the top left. Closeup photos and the actual fracture origin are presented as Figures 10.26 and 10.27 at the end of this book as the Procera alumina molar crown, one of the examples in Chapter 10. (SEM photos and the montage courtesy of S. Scherrer)*

Chapter 5 References

1. V. D. Fréchette, *Failure Analysis of Brittle Materials*, Advances in Ceramics, Vol. 28, American Ceramic Society, Westerville, OH, 1990.
2. H. G. Richter and F. Kerkhof, "Stress Wave Fractography," pp. 75 – 109 in *Fractography of Glass*, eds., R. C. Bradt and R. E. Tressler, Plenum, NY, 1994.
3. J. E. Field, "Brittle Fracture: Its Study and Application," *Contemporary Physics*, **12** [1] (1971) 1 - 31.
4. A. Smekal, "Procedures for the Measurement of Fracture Propagation Velocities on Fracture Surfaces," *Glastechn. Ber*., **23** [3] (1950) 57 – 67.
5. U. Hornemann, H. Rothenhäuser, H. Senf, J. F. Kalthoff, and S. Winkler, "Experimental Investigation of Wave and Fracture Propagation in Glass Slabs Loaded by Steel Cylinders at High Impact Velocities, pp. 291 – 298, in Int. Phys. Conf. Series No. 70, *3rd Conference on Mechanical Properties at High Rates of Strain*, Oxford, The Institute of Physics, London, 1984.
6. C. Brodmann, *Nachrichten von der Gessellschaft der Wissenschaften zu Göttingen, Mathematisch-Physikalische Klasse*, **1** (1894) 44-58.
7. S. Winkler, H. Senf, and H. Rothenhäusler, "High Velocity Fracture Investigation in Alumina," pp. 165 – 183 in *Fractography of Glasses and Ceramics, Advances in Ceramics*, Vol. 22, eds., J. Varner, and V. Fréchette, American Ceramic Society, Westerville, OH, 1988.
8. H. Schardin, L. Mücke, and W. Struth, "Bruchgescwindigkeit von Gläsern," *Glastechn. Ber*., **141** [5] May 1954, 19 -147. Also available translated into English in *Glass Industry*, **36** [3] (1955) 133 – 168.
9. F. Kerkhof, "Bestimmung der Maximalen Bruchgeschwindigkeit Verschiedener Gläser nach der Ultraschall-Methode," *Glastechn. Ber.*, **35** [6](1962) 267 – 272.
10. J. Congleton and B. K. Denton, "Dynamic Fracture Toughness Experiment," Final Technical Report, University of Newcastle on Tyne to U. S. Army European Research Office, July, 1975.
11. M. M. Chaudhri, "High-Speed Photographic Investigations of the Dynamic Localized Loading of Some Oxide Glasses," pp. 87 – 113 in *Strength of Inorganic Glass*, Plenum, NY, 1985.
12. F. E. Barstow and H. E. Edgarton, "Glass Fracture Velocity," *J. Am. Ceram. Soc.*, **22** [9] (1939) 302 – 307.
13. E. H. Yoffe, "The Moving Griffith Crack," *Phil. Mag.*, **42** (1951) 739 – 750.
14. J. W. Johnson and D. G. Holloway, "On the Shape and Size of the Fracture Zones on Glass Fracture Surfaces," *Phil Mag.*, **14** (1966) 731 - 743.
15. A. B. J. Clark and G. R. Irwin, "Crack-Propagation Behaviors," *Exp. Mech.*, **6** (1966) 321 – 330.
16. J. Congleton and N. J. Petch, "Crack-Branching," *Phil. Mag.*, **16** (1967) 749 – 760.
17. H. P. Kirchner and J. W. Kirchner, "Fracture Mechanics of Fracture Mirrors," *J. Am. Ceram. Soc.*, **62** [3-4] (1979) 198 – 202.
18 H. P. Kirchner and J. C. Conway, "Criteria for Crack Branching in Cylindrical Rods: I, Tension, and II, Flexure, " *J. Amer. Ceram. Soc.*, **70** [6] (1987) 413 – 425.

19 H. P. Kirchner, "Brittleness Dependence of Crack Branching in Ceramics," *J. Am. Ceram. Soc.,* **69** [4] (1986) 339 – 342.
20 W. Doll, "Investigations of the Crack Branching Energy," *Int. J. Fract.,* **11** (1975) 184 – 186.
21. Y. L. Tsai and J. J. Mecholsky, Jr., "Fracture Mechanics Description of Fracture Mirrors Formation in Single Crystals," *Int. J. Fract.,* **57** (1992) 167 – 182.
22. E. K. Beauchamp, "Mechanisms of Hackle Formation and Crack Branching," pp. 409 – 446 in *Fractography of Glasses and Ceramics III*, eds., J. Varner V. D. Fréchette, and G. D. Quinn, Ceramic Transactions, Vol. 64, American Ceramic Society, Westerville, OH, 1996.
23. E. K. Beauchamp, "Fracture Branching and Dicing in Stressed Glass," Sandia Laboratories Research Report, SC-RR-70-766, Jan., 1971.
24. E. F. Poncelet, "The Markings on Fracture Surfaces," *J. Soc. Glass Technol*., **42** (1958) 279T – 288T.
25. E. Gölz, "Übermikroskopische Feinstructuren an Glassbruchflächen," (Ultramicroscopic Fine Structures on Glass Fracture Surfaces), *Zeitschrift Physik,* **120** (1943) 773 – 777.
26. D. Hull, Chapter 5, in *Fractography, Observing, Measuring and Interpreting Fracture Surface Topography*, Cambridge Univ. Press., Cambridge, 1999.
27. E. K. Beauchamp, "Crack Front Stability and Hackle Formation in High Velocity Glass Fracture," *J. Amer. Ceram. Soc*., **78** [3] (1995) 689-697.
28. K. Gopalakrishnan and J. J. Mecholsky, Jr., "Quantitative Fractography of Mixed-Mode Fracture in Soda Lime Silica Glass," *J. Am. Ceram. Soc.,* **95** [11] (2012) 3622-3627.
29. K. Gopalakrishnan and J. J. Mecholsky, Jr., "Quantitative Fractography of Mixed-Mode Fracture in an R-curve Materials," *J. Mat. Sci.,* **48** (2013) 7081 – 7087.
30. E. Sommer, "Formation of Fracture 'Lances' in Glass," *Eng. Fract. Mech.,* **1** (1969) 539 - 546.
31. R. W. Rice, "Fracture Topography of Ceramics," pp. 439 – 472 in *Surface Interfaces of Glasses and Ceramics*, eds., V. Fréchette, W. LaCourse, V. L. Burlick, Plenum, NY, 1973.
32. R. W. Rice, "The Difference in Mirror-to-Flaw Size Ratios Between Dense Glasses and Polycrystals," *J. Am. Ceram. Soc*., **62** [9-10] (1979) 533 – 535.
33. D. Lewis, III and J. R. Spann, "Fracture Features at Internal Fracture Origins in a Commercial Glass Ceramic," *Comm. Am. Ceram. Soc.,* Oct. 1982, C-173 – C-174.
34. M. Ramulu, R. C. Bradt, A. S. Kobayashi, and K. H. Yang, "A Dynamic Fracture Mechanics Interpretation of Multiple Mist Regions on Soda-Lime-Silicate Glass Fracture Features," pp. 215 – 227 in *Fractography of Glasses and Ceramics, Advances in Ceramics*, Vol. 22, J. Varner, and V. Fréchette, eds., American Ceramic Society, Westerville, OH, 1988.
35. G. D. Quinn, L. K, Ives, and S. Jahanmir, "On the Fractographic Analysis of Machining Cracks in Ground Ceramics: A Case Study on Silicon Nitride," Special Publication 996, NIST, Gaithersburg, MD, May, 2003.

36. G. D. Quinn, L. K, Ives, and S. Jahanmir, "On the Nature of Machining Cracks in Ground Ceramics: Part I: SRBSN Strengths and Fractographic Analysis," *Mach. Sci. Technol.*, **9** (2005) 169 - 210.
37. J. Barsom, "Fracture of Tempered Glass," *J. Am. Ceram. Soc.* **51** [2] (1968) 75 – 78.
38. H. Ko, "Fracture Behavior of Sintered Alumina Under Rotary Bending and Static Fatigue," pp. 15 – 29 in *Fracture Mechanics of Ceramics 12*, eds. R. C. Bradt, D. P. H. Hasselman, D. Munz, M. Sakai, V. Ya Shevchenko, Plenum, NY, 1996.
39. F. Kerkhoff and E. Sommer, "Das Bild der Bruchfläche (von Gläsern)," in *Handbuch der Mikroscopie der Technik, Vol. IV, Mikroskopie der Silicate*, Umschau Verlag, Frankfurt am Main, Germany, 1964.
40. A. J. Pons and A. Karma, "Helical Crack-Front Instability in Mixed-mode Fracture," *Nature*, 464 (4 March 2010) 85 - 89
41. H. Wallner, "Line Structures on Fracture Surfaces," *Zeitschrift fur Physik*, **114** (1939) 368 – 378.
42. A. Tsirk, "Formation and Utility of a Class of Anomalous Wallner Lines on Obsidian," pp. 57 -69 in *Fractography of Glasses and Ceramics*, Advances in Ceramics, Vol. 22, eds., J. Varner, and V. Fréchette, American Ceramic Society, Westerville, OH, 1988.
43. T. A. Michalske, "Fractography of Stress Corrosion Cracking in Glass," pp. 111 – 142 in *Fractography of Glass*, eds., R. C. Bradt and R. E. Tressler, Plenum, NY, 1994.
44. T. A. Michalske and V. D. Fréchette, "Dynamic Effects of Liquids on Crack Growth Leading to Catastrophic Failure in Glass," *J. Am. Ceram. Soc.*, **63** [11-12] (1980) 603 – 609.
45. A. Tsirk, "An Exploration of Liquid-Induced Fracture Markings," pp. 87 – 101 in *Fractography of Glasses and Ceramics, IV, Ceramic Transactions*, Vol. 122, eds., J. Varner, and G. D. Quinn, American Ceramic Society, Westerville, OH, 2001.
46. A. Tsirk, *Fractures in Knapping*, Archaeopress, Oxford, UK, 2014.
47. V. D. Fréchette, "Markings Associated with the Presence of H_2O During Cracking," pp. 71 – 76 in *Fractography of Glasses and Ceramics*, Advances in Ceramics, Vol. 22, eds., J. Varner, and V. Fréchette, American Ceramic Society, Westerville, OH, 1988.
48. T. A. Michalske, J. R. Varner, and V. D. Fréchette, "Growth of Cracks Partly Filled With Water," pp. 639 – 649 in *Fracture Mechanics of Ceramics, Vol. 4*, eds. R. C. Bradt, D. P. H. Hasselman, and F. F. Lange, Plenum, NY, 1978.
49. V. D. Fréchette and M. Donovan, "Some Effects of The "Glue-Chipping" Process on Strength," pp. 407 –411 in *Fractography of Glasses and Ceramics, II, Ceramic Transactions*, Vol. 17, eds., V. Fréchette, and J. Varner, American Ceramic Society, Westerville, OH, 1988.
50. T. A. Michalske and S. W. Freiman, "A Molecular Mechanism for Stress Corrosion in Vitreous Silica," *J. Amer. Ceram. Soc.*, **66** [4] (1983) 284-288.
51. T. A Michalske, B. C. Bunker, and S. W. Freiman, "Stress Corrosion of Ionic and Mixed Ionic/Covalent Solids," *J. Amer. Ceram. Soc.*, **69** [10] (1986) 721 – 724.

52. J. J. Swab and G. D. Quinn, "Effect of Precrack 'Halos' on K_{Ic} Determined by the Surface Crack in Flexure Method," *J. Am. Ceram. Soc*., **81** [9] (1998) 2261 - 2268.
53. J. J. Mecholsky, Jr., "Intergranular Slow Crack Growth in MgF_2," *J. Am. Ceram. Soc.,* **64** [9] (1981) 563-566.
54. R. Morrell, "Dealing with Component Failures," pp. 353 -368 in *Fractography of Glasses and Ceramics V*, eds., J. R. Varner, G.D. Quinn, M. Wightman, Ceramic Transactions, Vol. 199, American Ceramic Society, Westerville, OH, 2007.
55. T. A. Michalske, "Fractography of Slow Fracture in Glass," pp. 121 – 136 in *Fractography of Ceramic and Metal Failures*, ASTM Special Technical Publication 827, eds., J. J. Mecholsky, Jr. and S. R. Powell, Jr., ASTM, West Conshohocken, PA, 1984.
56. T. A. Michalske, V. D. Fréchette, and R. Hudson, "Dynamic Effects of Liquids on Surface Crack Extension in Glass," pp. 1091 – 1097 in *Advances in Fracture Research*, Vol. 2, ed., D. Francis, Pergamon, NY, 1981.
57. G. D. Quinn and W. R. Braue, "Fracture Mechanism Maps for Advanced Structural Ceramics, Part 2, Sintered Silicon Nitride," *J. Mat. Sci.,* **25** (1990) 4377 – 4392.
58. G. D. Quinn, "Fracture Mechanism Maps for Advanced Structural Ceramics, Part I, Methodology and Hot-Pressed Silicon Nitride," *J. Mat. Sci*, **25** (1990) 4361 - 4376.
59. P. J. Dwivedi and D. J. Green, "Determination of Subcritical Crack Growth Parameters by In Situ Observation of Indentation Cracks," *J. Amer. Ceram. Soc.*, **78** [8] (1995) 2122-2128.
60. A. G. Evans, "Engineering Property Requirements for High Performance Ceramics," *Mat. Sci. and Eng.*, **71** (1985) 3 – 21.
61. T. Lube, I Khader , A. Kailer, U. Degenhardt, and K. Berroth, "Ermüdungsbruch in Siliziumnitrid," *Prakt. Met. Sonderband*, **46** (2014) 353-358.

6. Origins of Fracture

6.1 Origins, Flaws, and Defects

The origin is not only a location, but also an object. In the parlance of the engineer or scientist, the irregularities that initiate fracture are termed flaws or defects. The fractographer should use the terms "defect" and "flaw" with discretion. Scientists and engineers understand that virtually all brittle materials are imperfect and contain irregularities that can behave as flaws, but nontechnical people may misunderstand these terms. That the material contains flaws or defects does not necessarily mean that the material has been prepared improperly or is somehow faulty. Conversely, there are instances where defects or flaws do indicate defective material. The author usually avoids using the word "defect" because of its similarity to the word "defective." "Flaw" seems a little less severe and sounds to many as a more technical term. If there is any doubt, then the fractographer may fall back upon the most innocuous term: "fracture origin." Ceramists, engineers, and researchers occasionally use the term "Griffith flaw:"

Griffith flaw: *A hypothetical sharp crack, usually envisioned as a tiny, slender, elliptically-shaped flaw, that intensifies stress at sharp tips.*

Griffith flaws and fracture mechanics are discussed in chapter 7.

There are hundreds if not thousands of papers on flaws in ceramics and glasses. Only a handful are cited in this chapter, but many other key papers and books are listed in Appendix A, in the sections: "Origins in Ceramics" and "Origins in Glass." The contributions of Mr. R. Rice, Prof. K. Uematsu, and Dr. F. Lange are particularly valuable. Starting in the 1990, Profs. Keizo Uematsu and Satoshi Tanaka at Nagaoka University did fine work to characterize flaws in ceramics, starting from the earliest processing stages and monitoring flaw evolution during subsequent processing. They confirmed the link between the flaw size and the strength distributions. This topic is discussed further in Weibull Analysis section 7.15 of this Guide.

6.2 The Spatial Distribution of Flaws

Flaws are either *surface*- or *volume-distributed*. For example, inclusions are almost always volume-distributed. Grinding cracks are inherently surface-distributed. Some flaws may even be edge-distributed. The distinction is important for understanding how flaws originated and whether they are from processing or from subsequent handling, finishing, or service damage. The distinction is also crucial for brittle material design engineers who often must

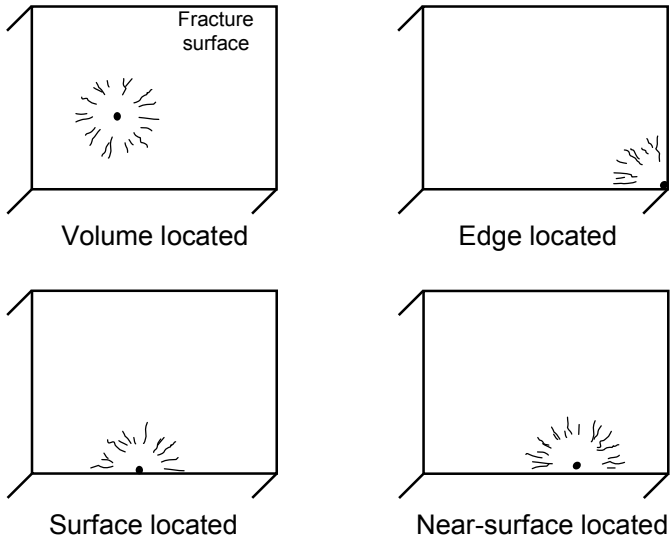

Figure 6.1 *Schematics that show the four possible locations of a volume-distributed flaw.*

scale the strengths of laboratory test data to predict component strengths via the Weibull theory.[1,2,3,4,5] Strength scaling and reliability predictions may be dramatically different for area and volume scaling. Glasses usually, but not always, break from surface-distributed flaws. Ceramics can fracture from surface or internal flaws.

One aspect about the spatial distribution of flaws needs clarification as shown in Figure 6.1. A single *volume-distributed* flaw may be *located* in the volume (in the bulk), at the surface, near the surface, or at an edge. For example, an inclusion originally may have been in the interior of a ceramic plate, but when a test bar was cut out, the inclusion ended up on the surface of the test bar.

Surface-distributed flaws can only exist at the surface or at an edge. While the above statements may seem obvious, there are two reasons to keep the distinction clear. Firstly, if a flaw is found at a surface location, it does not necessarily mean it is a surface type flaw. It could be a volume type flaw located at the surface. Some causal analysts simply look at the locations of the fracture origins. If they are located at the surface they simply interpret the origin as a surface type flaw. This is often wrong, particularly if the test data set is from bend bars or biaxially-loaded plates. It is a common misunderstanding that these two configurations always break from surface flaws.

Origins indeed are often located at the surface of these bending configurations, but if reasonable precautions are taken to control the grinding damage, then they are quite likely to break from volume-distributed flaws. The following pages show many such examples. Secondly, even if the data are not intended for design, a common mistake is to assume that all surface-located flaws are machining damage.

Thus, the fractographer should be careful when answering questions like: "What were the origins?" A cavalier answer such as "surface flaws" does not convey enough information. The answer should be more specific such as: "volume-distributed inclusions located at the surface," or "volume–type flaws located at or near the surface," or "surface-distributed grinding cracks."

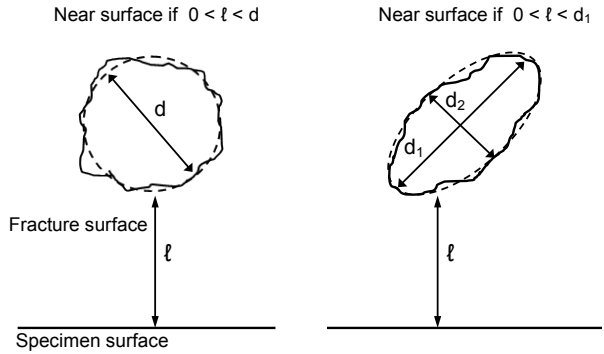

Figure 6.2 *Near surface (NS) origins are no deeper (ℓ) than the flaw diameter or major axis length.*

One might ask at what point is a volume type flaw "near surface." A review of the fracture mechanics stress intensity shape factors for flaws located at various distances in proximity to a surface suggests the criterion shown in Figure 6.2. At distances closer than one diameter, the stress intensity shape factor for such flaws increase by more than a few percent. Sometimes the characterization of location is important for service-performance issues or fracture mechanics analyses of the flaws. For example, some near-surface located origins may be more susceptible to time-dependent crack growth than equivalent volume-located origins. A classic example of this for time-dependent fractures in sintered silicon carbide is Case Study 3 in Chapter 10 of this Guide. Pores located at or near the surface behaved differently than identical pores located in the bulk. Near-surface-located origins may also be likely to link up with surface machining or impact damage, or to extend subcritically to the surface prior to catastrophic fracture.

6.3 Are Flaws Intrinsic or Extrinsic?

The irregularities that act as fracture origins in advanced ceramics can develop during or after fabrication of the material. Large irregularities (relative to the average size of the base microstructure) such as pores, agglomerates, and inclusions are typically introduced during processing. Some might deem inclusions and other irregularities as extrinsic flaws in a material, but to the extent that they occur naturally during fabrication and cannot be avoided, they could be considered intrinsic. For example, if a material customarily has a ball milling step in the process, and mill fragments flake off and become inclusions in every batch, then these may be considered intrinsic. Other origins can be introduced after processing as a result of machining, handling, impact, wear, oxidation, and corrosion. These usually can be considered extrinsic origins. However, machining damage may be considered either extrinsic or intrinsic. It is intrinsic to the manufacture to the extent that machining is a natural consequence of producing a finished specimen or component. In any case, the differentiation between intrinsic and extrinsic is often of no practical concern and it is pointless to argue the distinction.

Wherever possible, the origin should be characterized by what it is rather than a description of how it appears, since the latter may depend upon the mode of viewing. Descriptions such as the origin was a "white spot" should be avoided. It may be white in an optical microscope, but it most likely will not in a SEM (Figure 6.3). Sometimes descriptive terms may be used, but as qualifiers to the true flaw identity, e.g., "pores that appear white when viewed optically."

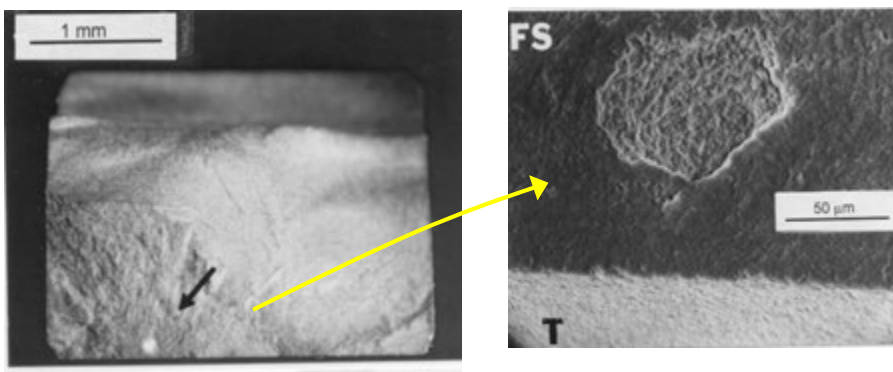

(a) (b)

Figure 6.3 *Wherever possible, describe flaws by what they are, not how they appear. (a) shows a white spot at the origin in a reaction-bonded silicon nitride bend bar. The SEM image of the origin in (b) shows the origin is a pore. FS denotes fracture surface and T denotes tensile surface.*

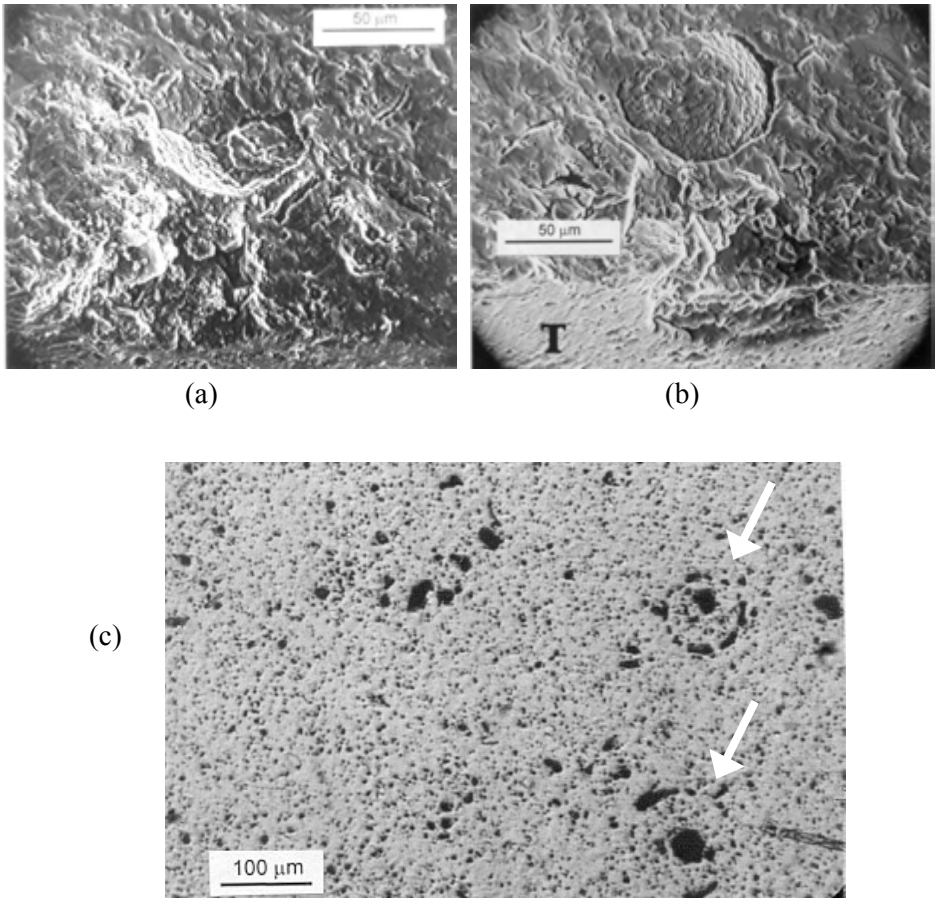

(a) (b)

(c)

Figure 6.4 *Fracture origin in a sintered alpha silicon carbide flexure specimen. (a) suggests the origin is a pore, but (b), which shows the mating half, shows it is an agglomerate. (c) shows a polished microstructural section for this material that reveals the agglomerates (arrows).*

6.4 Matching Fracture Halves

Both halves of the fracture surface should be examined whenever possible, since each contains information about the fracture origin. For example, Figure 6.4 illustrates a case wherein an agglomerate was strength limiting. If only the (a) half was examined, the fractographer may have erroneously interpreted the flaw as a pore.

6.5 External Surfaces

If an origin is located at the surface, it is wise to examine the exterior surface by tilting the specimen back or by directly looking at the exterior surfaces for clues as to the flaw type as shown in Figure 6-5. A common question is: "Was it a scratch or a grinding flaw?" If the surface-trace lines up with the striations that show the grinding direction as in Figure 6.5a, it is likely a grinding fault. If the fault has a different axis, as in Figure 6.5b, then it is a scratch. Section 6.7.3 later in this chapter has more on scratches.

(a)

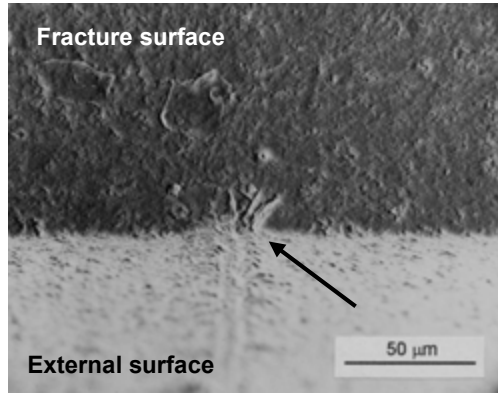

(b)

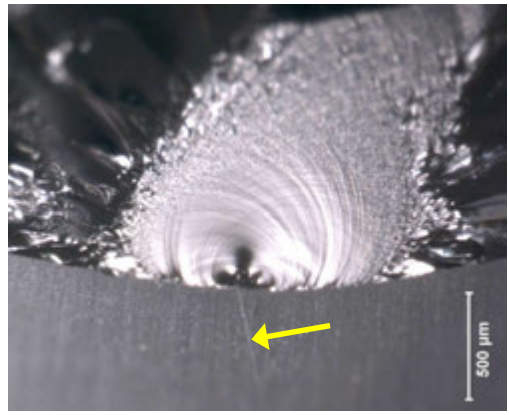

Figure 6.5 *The exterior surface should be checked if the flaw is located on the surface. (a) shows an irregular, deep grinding flaw with a distinctly different ground-surface trace at the origin in a reaction-bonded silicon nitride component. It is very likely that a large "renegade" abrasive grit in the grinding wheel caused this damage. (b) shows the fracture origin of a fused silica rod broken in flexure. This tilted-back view shows a scratch on the surface (arrow) coincident with the origin.*

6.6 Volume-Distributed Flaws

6.6.1 Pores and bubbles

Pores are one of the easiest flaws to find and identify. In ceramics they are often equiaxed, but can easily assume a myriad of odd shapes as shown in Figure 6.6. Pores are volume-distributed flaws that are discrete cavities. For more information about pores as origins, see Rice's article, Reference 6.

Pores in glass or porcelain are often very smooth and round, and may contain trapped gas. As such they may be called "bubbles." Their effect upon strength is very different. Since they are very smooth, they usually act as simple stress concentrators and not as sharp flaws. This distinction is important as discussed in detail in Chapter 7. A material may have large *internal* pores that are relatively harmless, and they may not necessarily act as fracture origins. On the other hand, they can be extremely deleterious *if they contact an exterior surface* or *each other,* as illustrated in Figure 6.7. Bubbles that are close to an outer surface are also prone to interact with grinding or machining damage that can link with the bubble, turning an otherwise harmless bubble into an extremely serious flaw. A good example of this was shown as Figure 5.5 in the previous chapter. Figures 6.8 and 6.9 show other examples of bubble origins. Reference 7 has more information about the feldspathic porcelain strengths and bubble/pore fracture origins. This dichotomy in behavior poses a dilemma to design engineers working with flaw sizes and Weibull statistics. A volume-distributed bubble can be either harmless or a dominant flaw depending upon where it is located in a piece.

Pore-bubbles in ceramics or glass ceramics, can act as strength-limiting flaws even if they are located in the interior. It is often suggested (but rarely shown) that rim cracks a few grain diameters long extend from the bubble surface into the ceramic. These are a "Rings of Saturn" type flaw (e.g., Figure 7.26c) and fracture mechanics solutions for the stress intensity factors may be found in the literature. It is not likely that the actual flaws around the periphery of a real pore will be so idealized, however. Figures 6.10a,b show a fascinating example by Lewis[8] of a large (100 μm diameter) internal bubble fracture origin (Figure 6.10) in a cordierite glass ceramic bend bar. The spherical bubble was probably smooth in the parent glass, but roughened during crystallization. Bernthaler[9] used polymeric spheres in alumina to create spherical fracture origin flaws in an alumina such as shown in Figure 6.10c.

Bubbles in glasses and porcelains can be very helpful to fractographers, since they are a good source of wake hackle lines on fracture surfaces that show the direction of crack propagation.

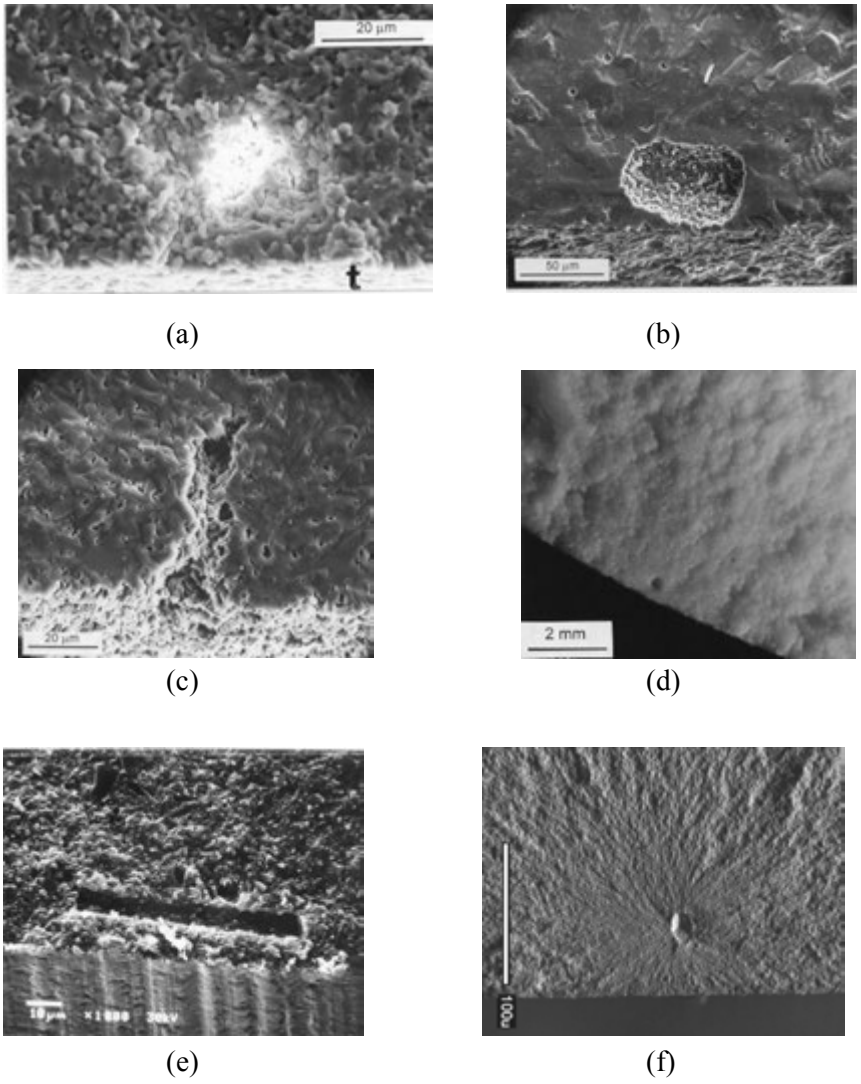

(a) (b)

(c) (d)

(e) (f)

Figure 6.6 Examples of pore fracture origins in ceramics. (a) shows a SEM image of a pore in a 99.9% alumina bend bar. Electron charging created the bright spot. (b) shows a pore in an aluminum oxynitride bend bar that is within 5 μm of the surface. This is a "near surface" location example. The transgranular fracture near the pore helps the pore stand out very clearly. (c) is an irregular pore in a sintered alpha silicon carbide bend bar. (d) is a pore in a porcelain electrical insulator (courtesy J. Taylor and R. Rice). (e) is a cylindrical pore in a silicon nitride probably from a fiber or hair burn out. (f) is a pore in a yttria-stabilized tetragonal zirconia polycrystal (3Y-TZP) (f is courtesy J. Quinn).

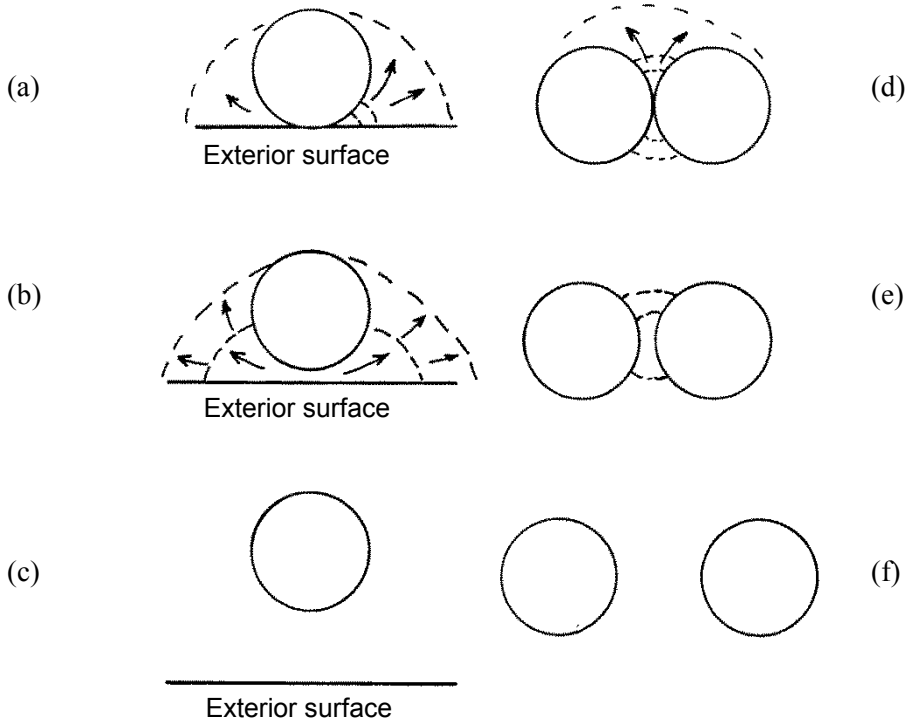

(g)

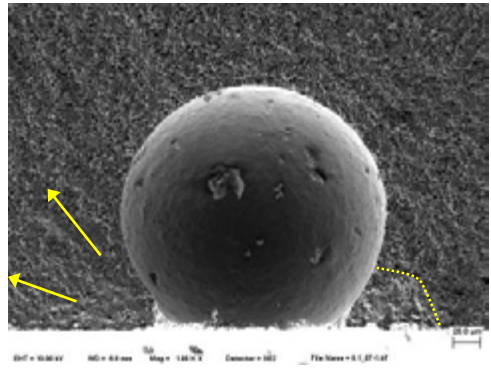

Figure 6.7 *Bubbles are smooth pores and may be relatively harmless or extremely deleterious depending upon location. (a) shows a bubble just "kissing" the exterior surface, creating very sharp cusps from which cracks will likely pop in and grow. (b) shows a near-surface bubble which can easily link up with grinding or other surface damage. (c) shows an interior bubble that is relatively harmless. Similar behavior can occur with two bubbles in proximity to each other. (d) and (e) are likely to form a strength-controlling flaw, whereas configuration (f) is relatively harmless. (g) is an example of (a) in alumina. (courtesy T. Bernthaler)*

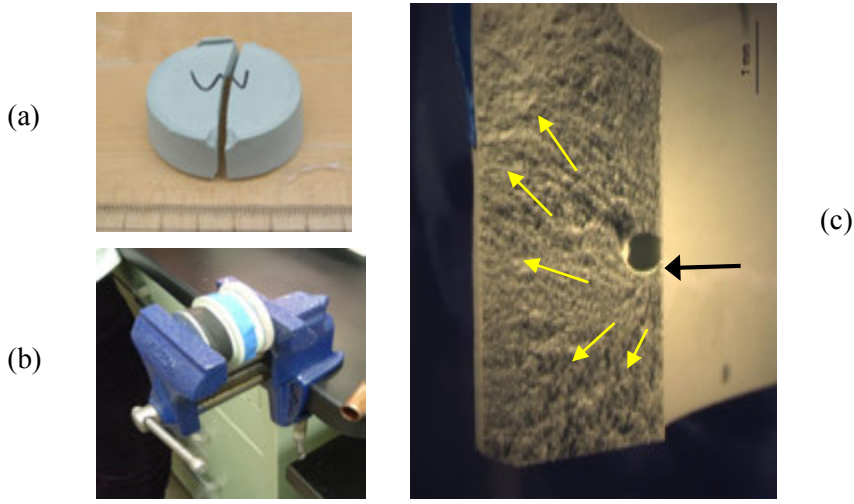

Figure 6.8 *Bubble origin in a mock-up of a dental crown. Dental stone is cast into a cup shape that is loaded in a vise with an inner rubber stopper. When the vise is tightened, the stopper expands and the "crown" splits in half. Blue tape holds the fragments together. Hoop tensile stresses in the wall triggered fracture from a bubble touching the inner surface (c). Grazing illumination accentuates hackle lines. Fracture started from the cusp marked with a black arrow. These mock-up crowns simulate real crown fractures.*

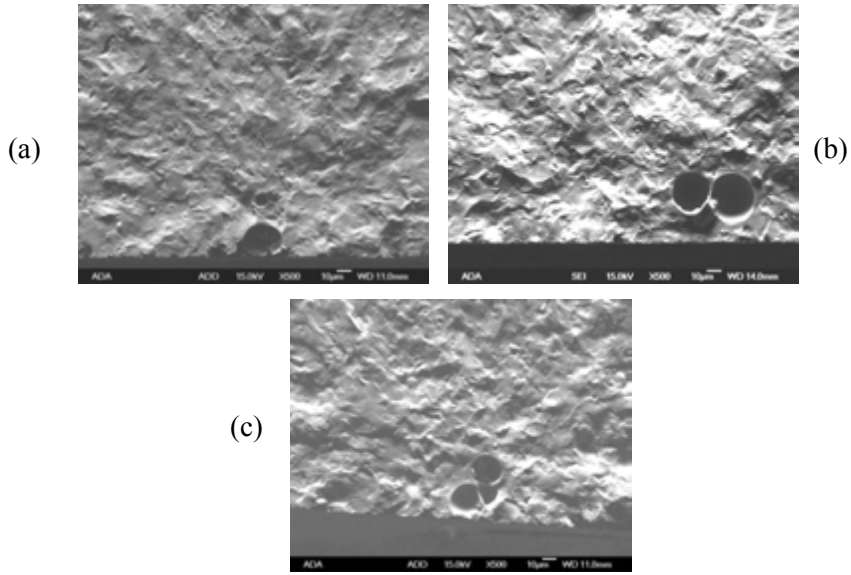

Figure 6.9 *Strength-limiting flaws in Vita Mark 2 feldspathic dental porcelain bend bars. The strengths were: (a)120 MPa, (b)119 MPa, (c) 115 MPa.*

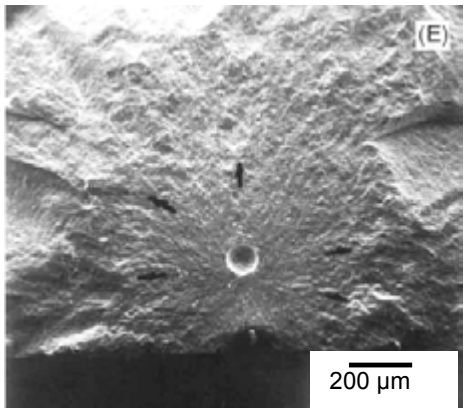

(a)

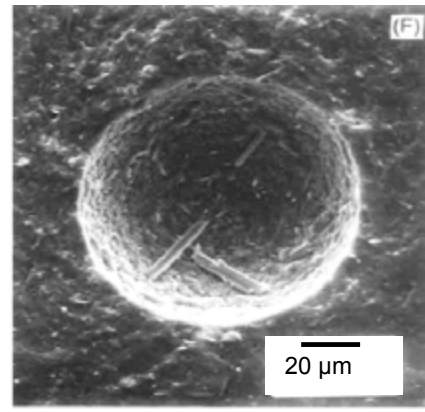

(b)

(c)

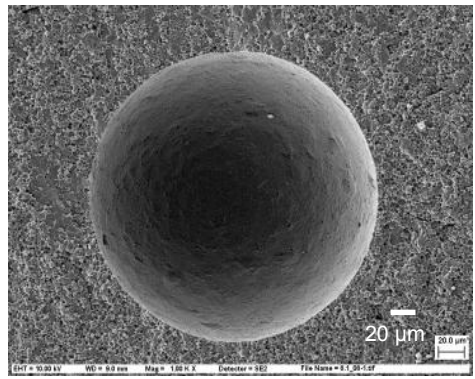

Figure 6.10 *Internal pore-bubbles in ceramics and glass ceramics. (a) and (b) show an internal spherical pore fracture origin in a cordierite glass ceramic bend bar (315 MPa). The pore was from a bubble in the original glass. The material crystalized around the bubble during the ceraming step. The arrows mark the hackle boundary of the fracture mirror. (courtesy D. Lewis, III) (c) shows a large internal seeded-pore origin in alumina. (courtesy T. Bernthaler)*

Pores may often be very irregular and jagged. One way these may occur is by the formation of pressing defects when preparing the green body. Spray-dry powder agglomerates may not be eliminated during final pressureless sintering. Figure 6.11 shows examples. Hot pressing or hot isopressing would likely eliminate such flaws. These flaws are sometimes called: “pressing flaws” or “blank pressing flaws.”

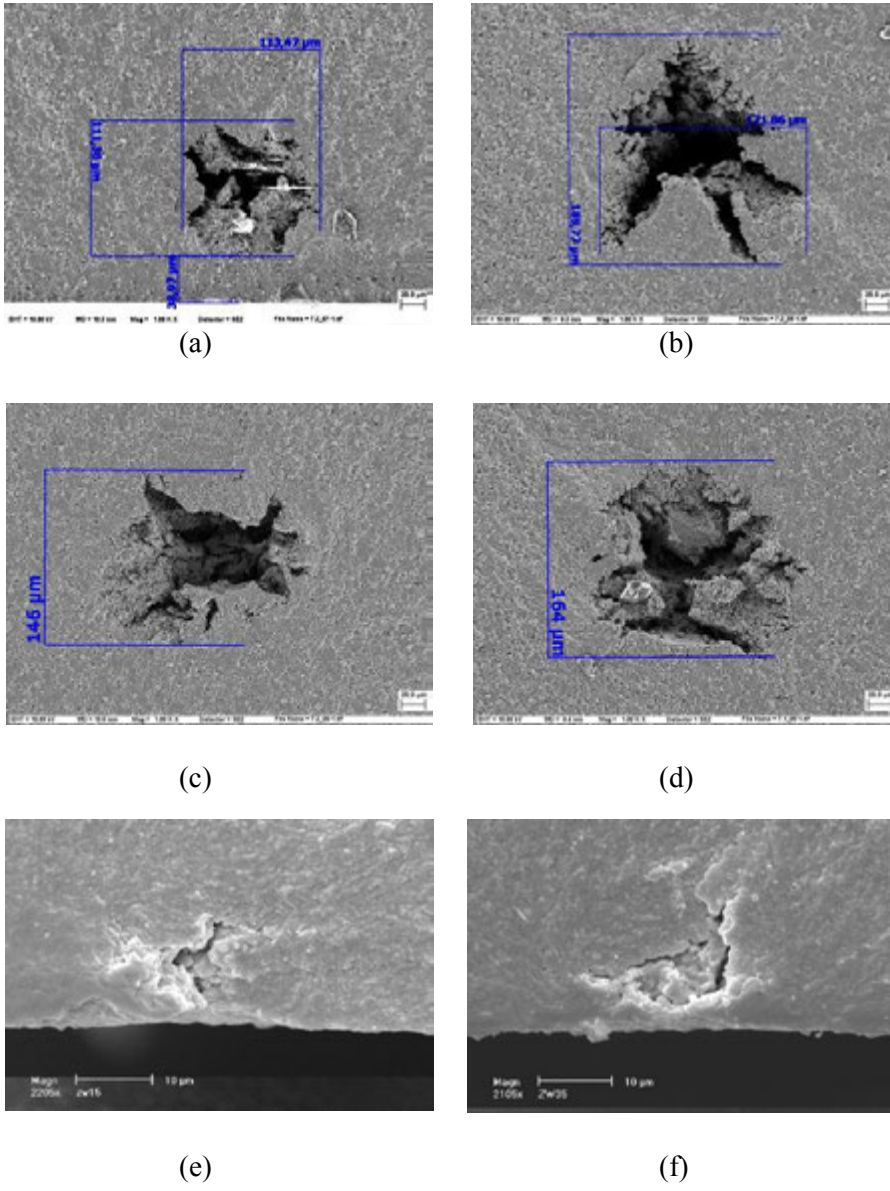

Figure 6.11 *Irregular pore origins. (a) through (d) were formed during cold pressing of alumina spray-dried powders. (courtesy T. Bernthaler). (e) and (f) are in a sintered 3Y TZP zirconia, (courtesy S. Scherrer).*

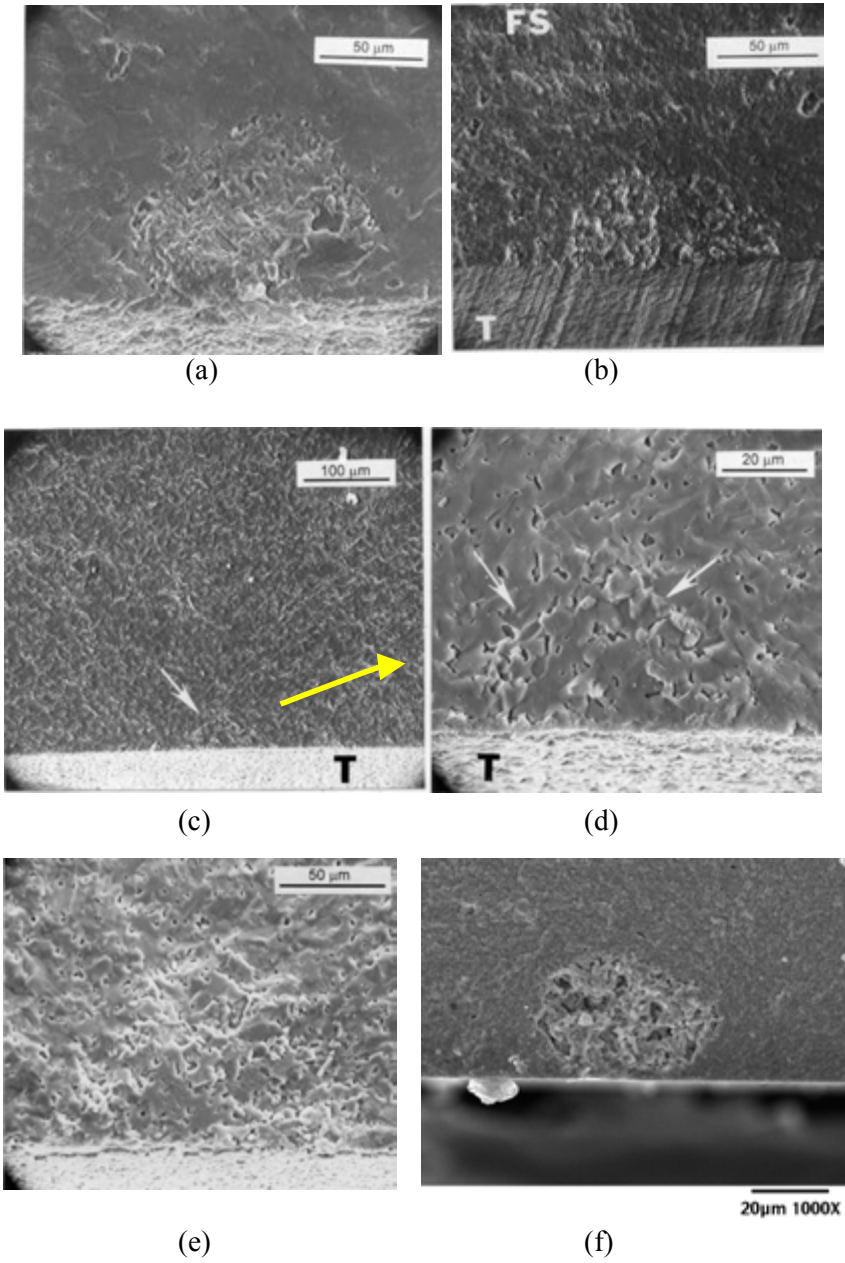

Figure 6.12 *Examples of porous region fracture origins in ceramics. (a) is in sintered aluminum oxynitride. (b) is in a reaction-bonded silicon nitride. (c) and (d) are both from one sintered alpha silicon carbide bend bar, (e) is also from a sintered silicon carbide. (f) is a common type found in tetragonal zirconia polycrystals (3Y-TZP).*

6.6.2 Porous regions

Porous regions are volume-distributed flaws that are three-dimensional zones of porosity or microporosity regions. Examples are shown in Figure 6.12. These can be obvious or very subtle. SEM microscopy is usually needed to identify these flaws. Optical microscopy may not be effective since the color and contrast at the origin match the surrounding material.

6.6.3 Porous seams

Porous seams are similar to porous regions, but are more planar or two-dimensional. Examples are shown in Figure 6.13. If the material separated completely between these seams, the flaw might be more aptly described as a processing crack, as described below in section 6.8.1.

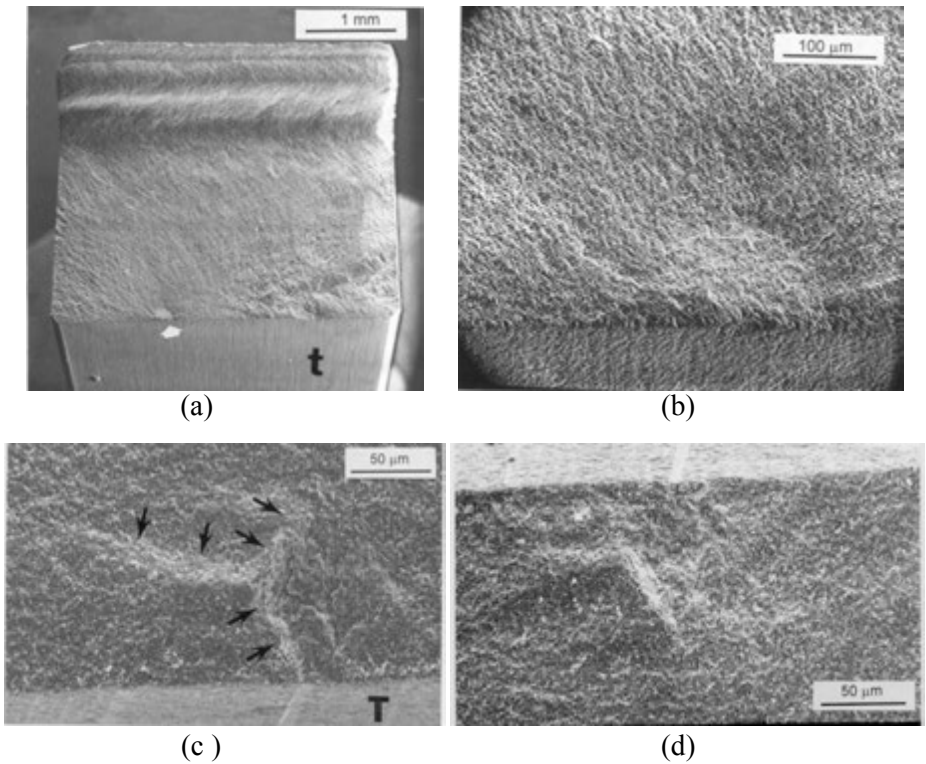

Figure 6.13 *Examples of porous seam fracture origins. (a) and (b) show the origin in a fine-grained sintered 99.9% alumina. (c) and (d) show the origin in matching halves of another fine-grained sintered 99.9 % alumina bend bar.*

6.6.4 Agglomerates

Agglomerates are volume-distributed flaws that are a cluster of grains, particles, platelets, or whiskers or a combination thereof. They are a common flaw in ceramics made with powders that are prepared by spray drying. Spray dry agglomerates are often hollow. Agglomerates often sinter away from the matrix, creating a shell like void around the agglomerate. Since the composition is identical to the matrix, the color and reflectivity of this flaw are identical to the matrix. If agglomerates are suspected, examine more of the fracture surface for similar spherical or ring like features, since if there is one, there usually are many. Examples are shown in Figures 6.4 and 6.14.

Lange *et al*.[10,11,12] wrote an excellent set of articles about agglomerates as fracture origins in alumina/zirconia composites.

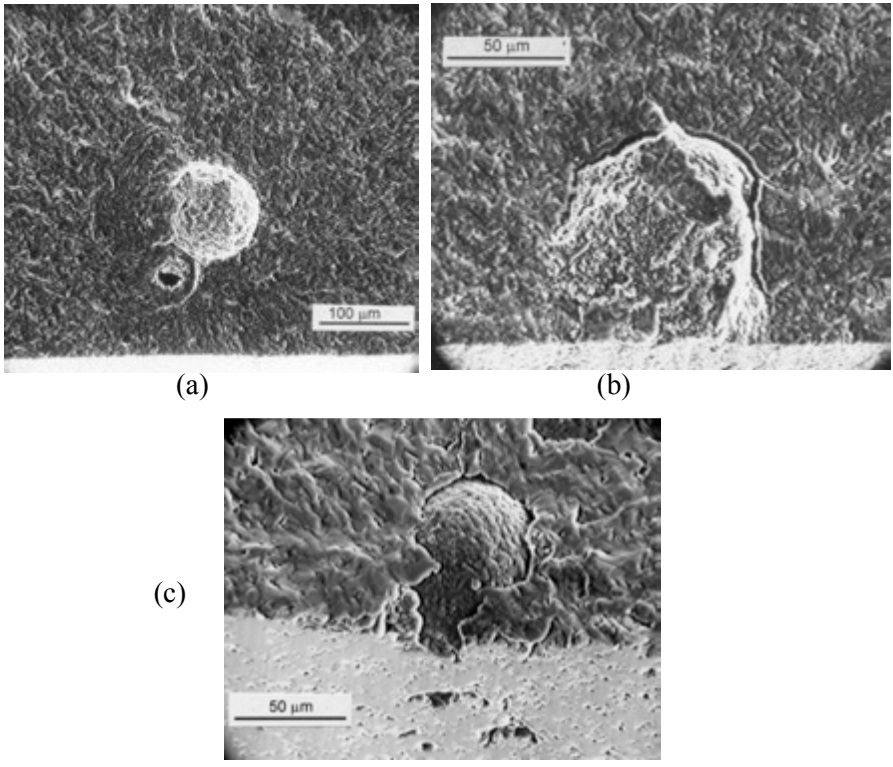

(a) (b)

(c)

Figure 6.14 *Examples of agglomerate fracture origins. (a – c) show spray dry agglomerate fracture origins in sintered alpha silicon carbide. Agglomerates often sinter away from the matrix leaving a void-like crack.*

Up to this point, agglomerates have been considered as discrete, isolated flaws. On the other hand, they may be pervasive and may make up the entire microstructure of a body that has not been fully-densified. Green bodies made up of dry-pressed, spray-dried particles can be sintered or hot-pressed to full density. If not, then the microstructure may comprise particles with incomplete bonding and inter-particle porosity such as shown in Figure 6-15. Polished microstructural sections may reveal the incomplete bonding, which may be subtle. It may be very difficult to discern this on a fracture surface, but it may be seen with optical microscopy if the lighting is carefully adjusted as shown in Figure 6-15c. Gee and Morrell[19] showed similar features in dry-pressed, spray-dried β-alumina. Hangl[13] showed good images for an industrial grade zinc oxide for a varistor application.

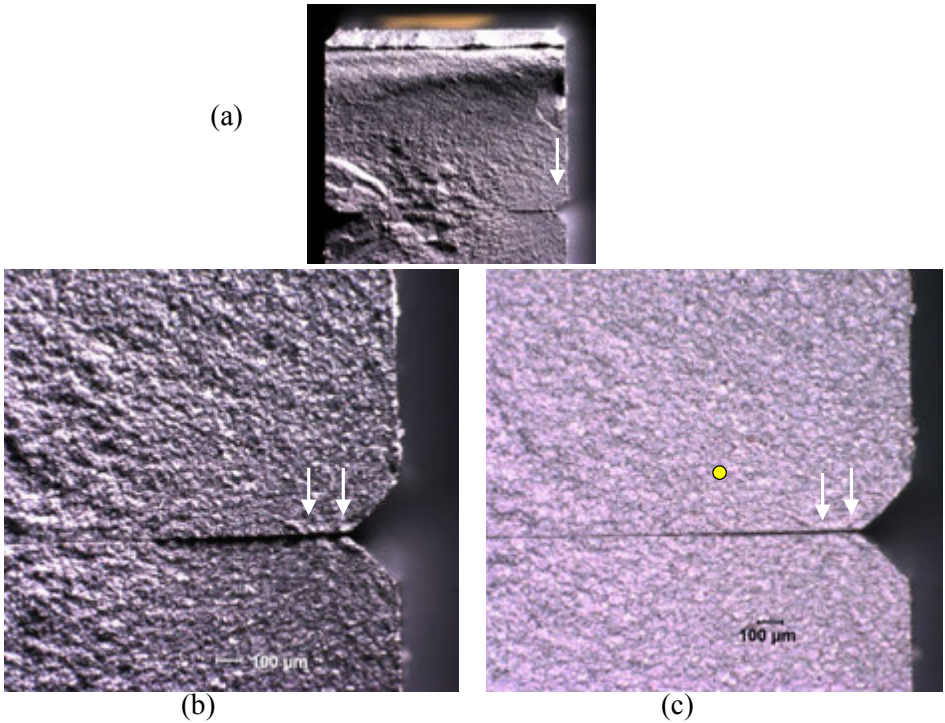

Figure 6.15 *Incomplete densification can lead to interparticle porosity throughout a body. This example shows fracture surface of a reaction-bonded silicon nitride bend bar. The fracture origin was grinding cracking and is marked by the large white arrows. Although this material had low fracture toughness, the grinding cracks penetrated only one granule deep, since the intergranular porosity impeded further extension. The spherical granules are revealed by careful lighting in (c). The small yellow circle shows their size.*

6.6.5 Inclusions

Inclusions are also volume-distributed flaws that are a foreign body with a composition different than the normal composition of the glass or ceramic. They are often easy to detect due to color or reflectivity differences compared to the matrix. Sometimes they are round and equiaxed, other times they are odd shaped or fragmented. Figures 6.16 and 6.17 shows some examples.

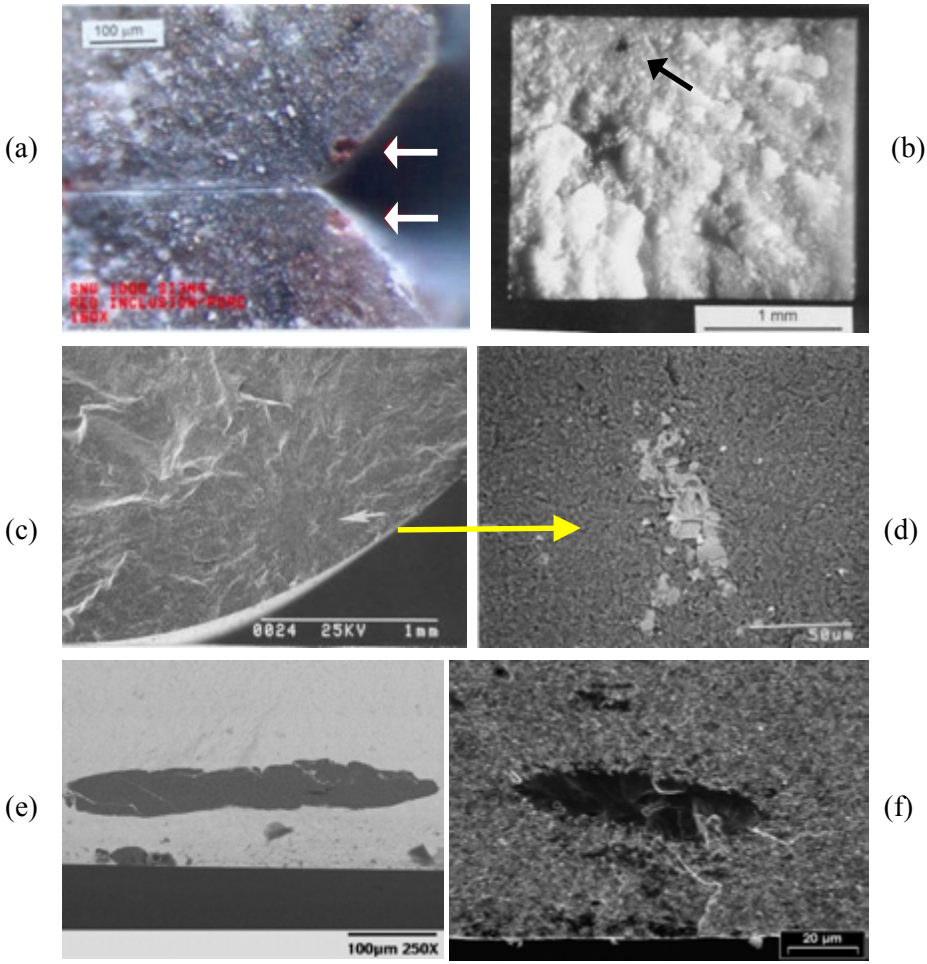

Figure 6.16 *Examples of inclusion origins. (a) is a red iron inclusion in sintered silicon nitride bend bar at an edge chamfer. (b) is an inclusion in a silicon nitride tension specimen. (c) and (d) are an iron inclusion in a silicon nitride. (e) is an alumina inclusion in a 3Y-TZP zirconia biaxial disk specimen (courtesy J. Eichler), and (f) is a vanadium inclusion in a binderless tungsten carbide bend bar. (courtesy J. Swab)*

The nickel sulfide inclusion shown in Figure 6.17a is a particularly deleterious flaw in tempered glasses, since it can undergo a spontaneously phase transformation at room temperature with an attendant volume expansion of several percent. If the inclusion is located in the interior, where it is exposed to tensile residual stresses, it can cause spontaneous catastrophic breakage at any time with no warning. Several cases are listed in Appendix B.

The tungsten inclusion shown in Figure 6.17c and d is also unusually deleterious. The tungsten impurity, from tungsten carbide ball milling media, can form very brittle tungsten silicides that lower the fracture toughness around and in the flaw.[14]

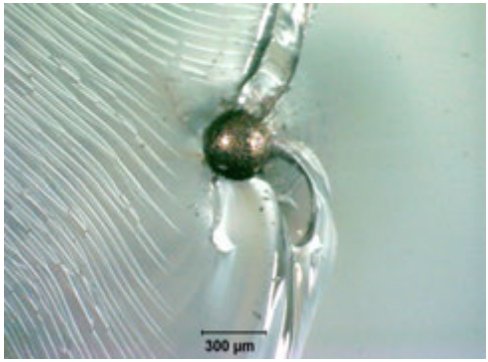

(a)

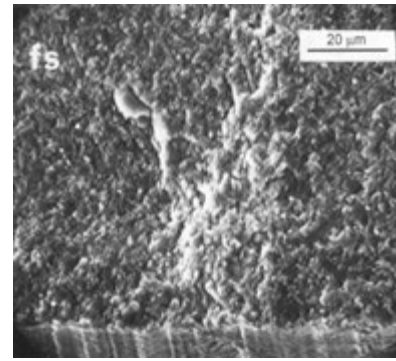

(b)

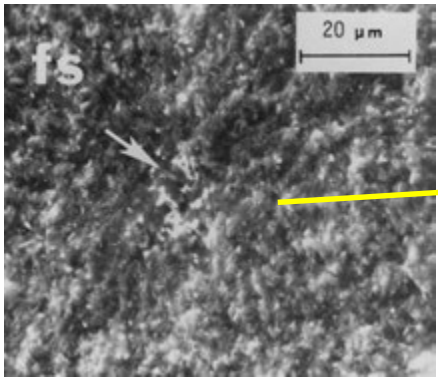

(c)

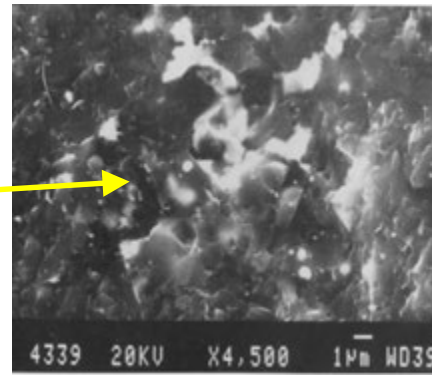

(d)

Figure 6.17 *Examples of inclusion origins. (a) is nickel sulfide in tempered glass plate that spontaneously fractured. (b) is an irregular iron and chrome inclusion in a sintered SiAlON bend bar. (c) and (d) are views of a tungsten inclusion in a hot-pressed silicon nitride bend bar.*

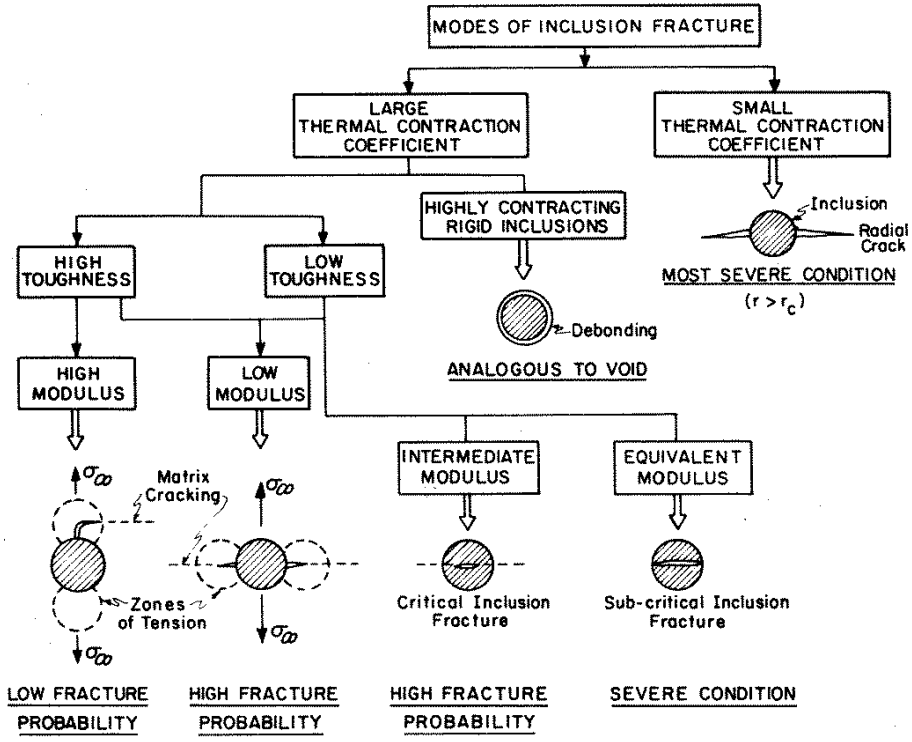

Figure 6.18 *The mismatch in properties between an inclusion and a matrix determine how severe an inclusion will be. From Evans, ref. 15.*

Not all inclusions behave the same. Their effect depends upon whether their elastic and thermal properties match or mismatch those of the matrix.[15] Inclusions can cause cracking in the matrix, may crack themselves, or may detach and pull away from the matrix creating a void like flaw. Figure 6.18 from a paper by Evans[15] illustrates the possibilities.

Inclusions can also control strength in highly-filled resin-matrix dental restorative materials such as shown in Figures 6.19 and 4.1d-f. Trans-illumination can be effective in finding them in such translucent materials.

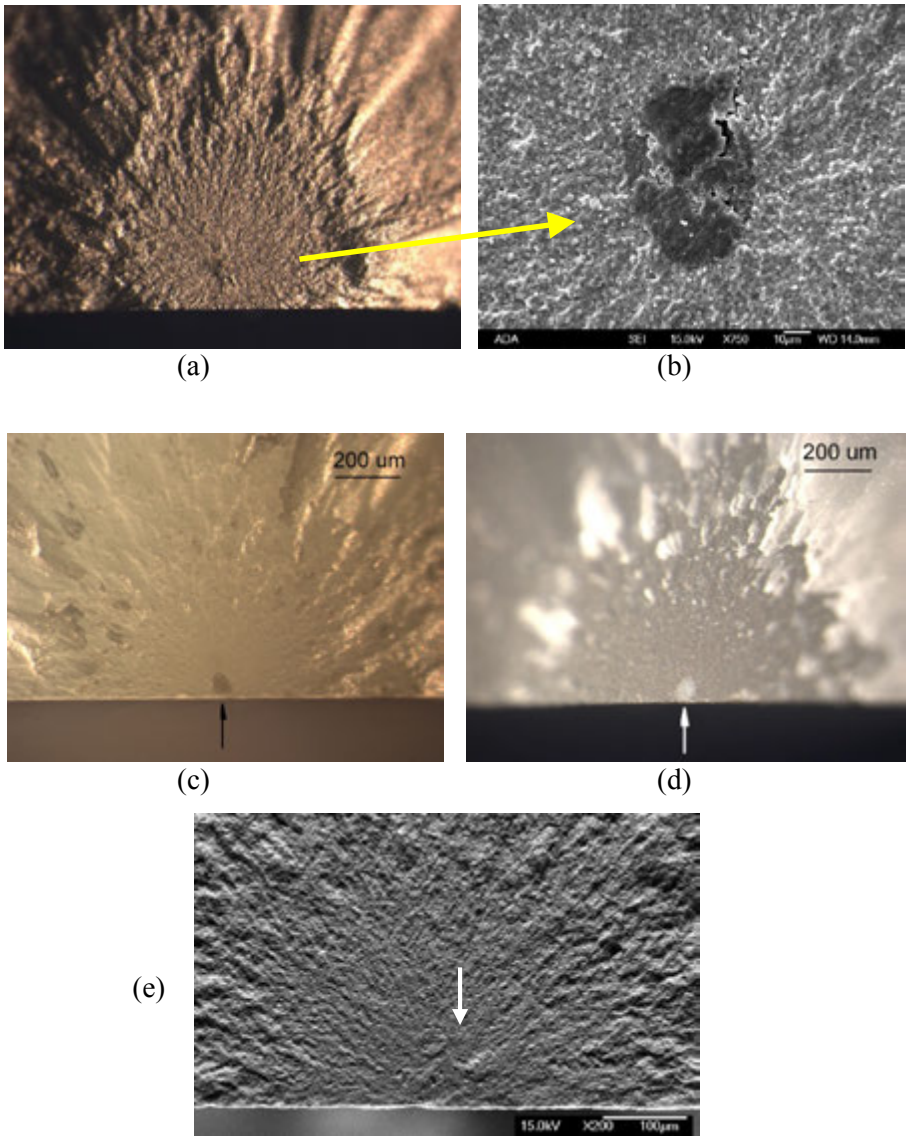

Figure 6.19 *Examples of inclusion origins in a highly-filled resin-matrix dental composite (Paradigm MZ 100) (a) and (b) show a calcium rich inclusion. (c) – (e) show the same aluminum inclusion with: transillumination (c), conventional reflected light (d), and in the SEM (e).*

6.6.6 Compositional inhomogeneities

These are microstructural irregularities related to the nonuniform distribution of the primary constituents, an additive, or a second phase. They may have a color or reflectivity difference compared to the matrix. Sometimes they are pockets of glass in a ceramic. Examples are shown in Figure 6.20 and 6.21.

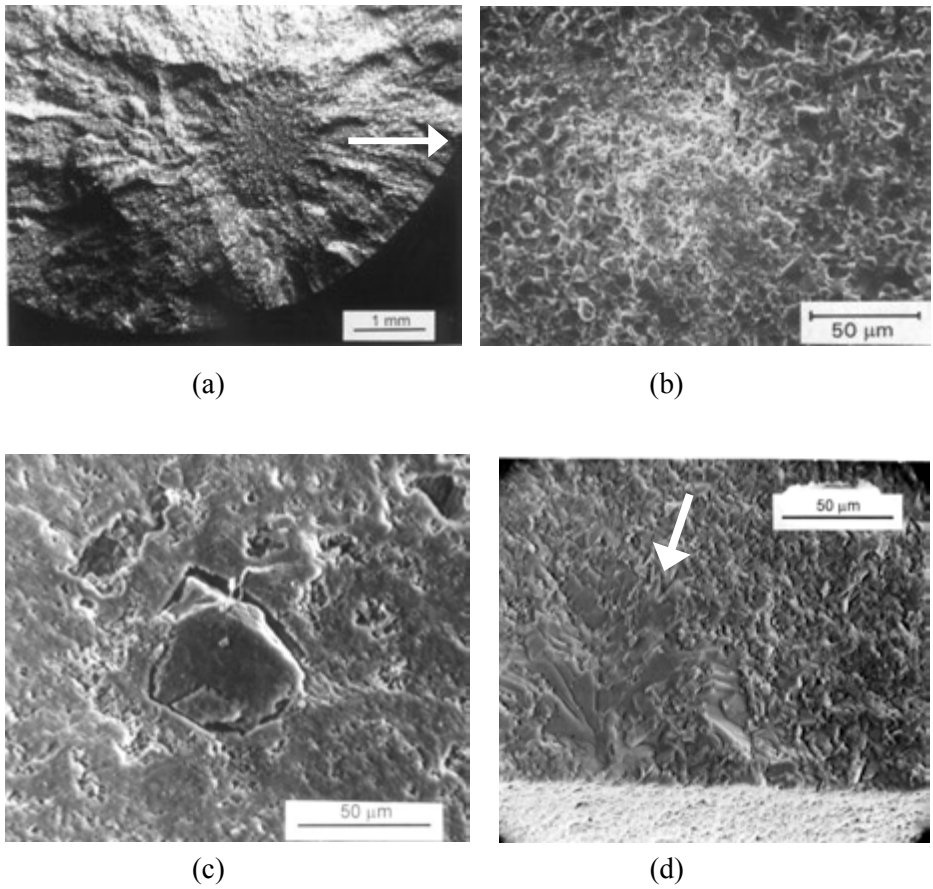

Figure 6.20 *Examples of compositional inhomogeneity fracture origins. (a) and (b) show an example of an aluminum rich zone in a hot-pressed silicon carbide. Aluminum is an element in the sintering aid. (c) shows an unreacted silicon globule that pulled away from the matrix in a reaction-bonded silicon nitride. (d) shows a silicon lake in a siliconized silicon carbide.*

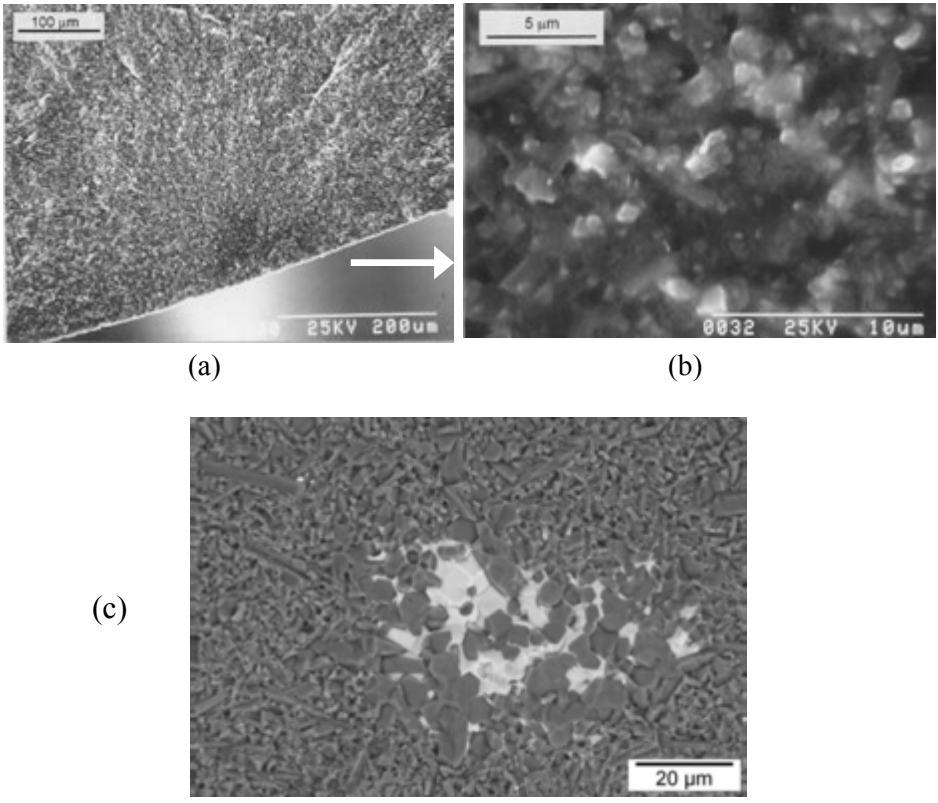

Figure 6.21 *Examples of compositional inhomogeneity fracture origins. (a) and (b) are an example of a local excess of sintering aid in a sintered reaction-bonded silicon nitride. (c) is a yttria-alumina agglomerate in a silicon nitride bend bar. (c is courtesy T. Lube and R. Danzer)*

6.6.7 Large grains

Large grains can occur due to local exaggerated grain growth. They may form due to a slight compositional or density variations during sintering. The compositional variability can be from an impurity or a sintering aid. Large grains can be a single or a cluster of grains having a size significantly greater than the range of the normal grain size distribution. They can often be seen with the optical microscope due to a difference in reflectivity compared to the matrix. Examples are in Figure 6.22. Rice's book[16] on grain size and mechanical properties of ceramics has a good discussion of large grains as fracture origins on pages 13 – 16.

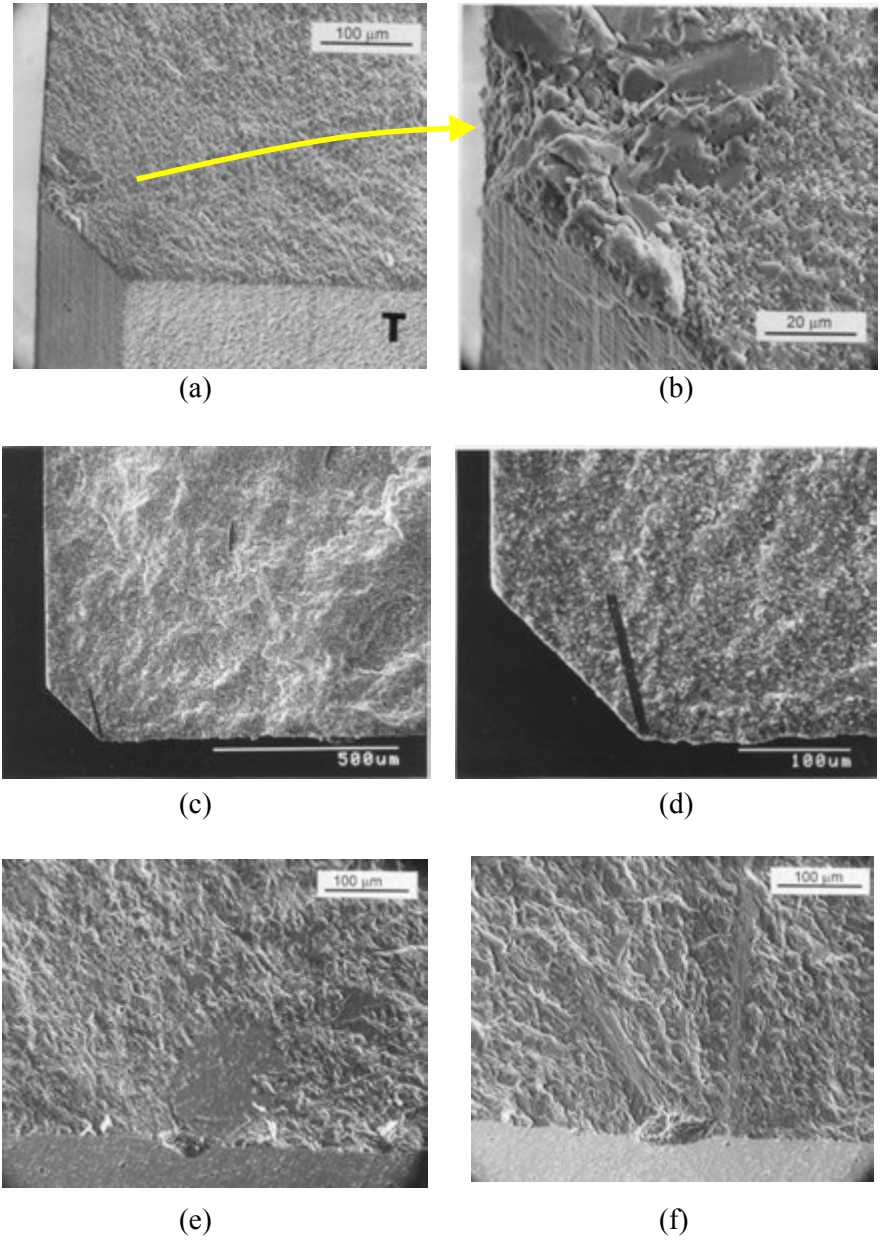

Figure 6.22 *Examples of large grain fracture origins. (a,b) show a cluster of large grains at a chamfer in a 99.9% alumina bend bar. (c,d) show an oversized grain in a silicon nitride. The material had small interlocking elongated grains intended to enhance fracture toughness. Notice how these are legitimate material flaws, and the chamfer preparation was completely satisfactory. (e, f) show examples of acicular large grains in sintered alpha silicon carbide.*

Large quartz grains can act as strength-limiting flaws in porcelains. Quartz has several polymorphs and displacive transformations during cooldown from processing temperatures can cause cracking around and within the large quartz grains as shown in Figure 6.23. This is referred to as the β - α quartz inversion. If the quartz grains are much larger than the normal microstructure, they may stand out clearly on a fracture surface. If the quartz grains are similar in size to the normal microstructure, then the origin flaw may blend into the rough fracture surface and be difficult to discern. Good examples have been shown by Gee and Morrell, [17] Carlstrom and Carlsson,[18] Southan[19] (who had superb high-quality glossy color-prints), and Banda and Messer.[20]

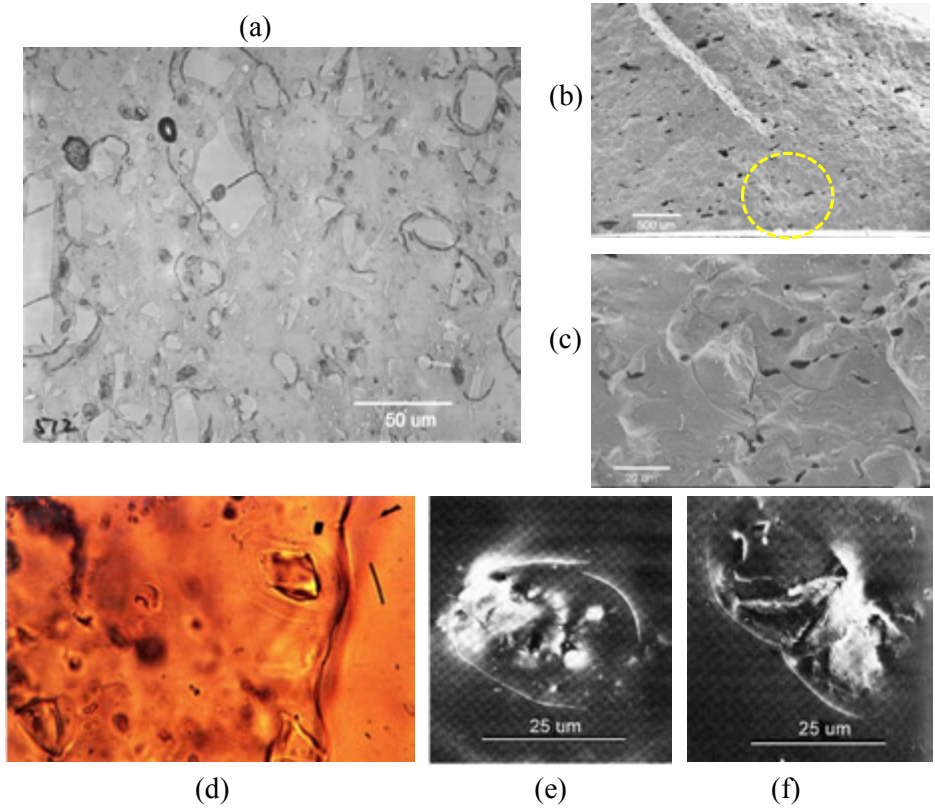

Figure 6.23 *Cracking around and through quartz grains. (a)-(c) are from a porcelain mortar that was broken and are courtesy R. Morrell. (a) shows a polished and etched microstructural view. (b) shows an SEM image of one fracture origin (circled). (c) is a close-up SEM image showing microcracking around quartz particles. (d) – (f) are from porcelain dental crowns, courtesy of D. Southan.[19] The thin-section polarized-light color image (d) reveals a reaction zone and microcracking around the quartz grains.*

6.6.8 Grain boundaries

Grain boundaries may be vulnerable areas and, if the grain size is large enough, the boundaries can act as strength limiting flaws. Such flaws are very difficult to unequivocally identify as origins since the fracture path may be intergranular and follow other grain boundaries thereby creating a very rough fracture surface. There are many papers on the effect of grain boundary cracking upon strength, but few actually show a grain boundary origin. Davidge and Tappin[21] showed grain boundary origins in alumina.

Sometimes the grain boundary cracking occurs from internal strains set up from differential contractions in anisotropic, noncubic ceramic grains. In other cases, impurities or sintering aids can gravitate to grain boundaries and weaken them. For example, Salem[22] found tiny alumina particles at grain boundaries of coarse-grained $MgAl_2O_4$ cubic spinel transparent plates. These so weakened the material that jagged crack paths formed and debris separated from the material upon fast fracture. Fracture origins were either large grains or the grain boundaries in disk strength specimen. Swab et al.[23] also studied a coarse-grained spinel which had irregular crack surfaces and even had granular debris generated during fracture. Lithium and fluoride from the sintering aid concentrated at the grain boundaries and dramatically weakened the material.[23] I examined one large (40 cm square) plate made of this material and there was so much grain boundary cracking that green dye used to stain the fracture surface bled profusely into the bulk. Grains literately fell out of the fracture surface while I was doing this.

Coarse-grained (50 μm to 70 μm) magnesia partially-stabilized zirconia typically fails from grain boundary cracks as shown in Figure 6.24. Microstructural analysis of polished specimens is essential for the diagnosis in such cases. Gee and Morrell[17] showed another good example in a partially-stabilized zirconia.

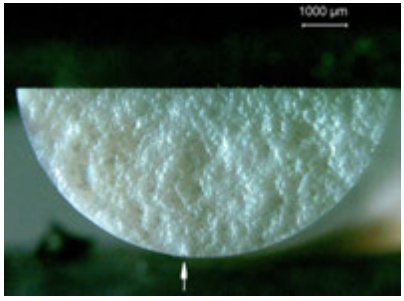

(a)

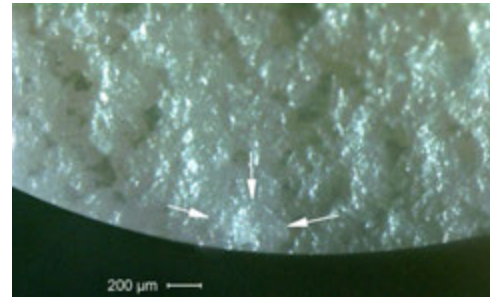

(b)

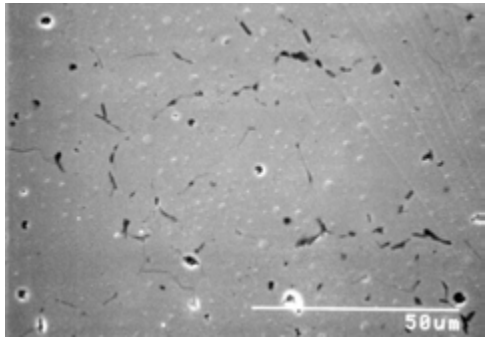

(c)

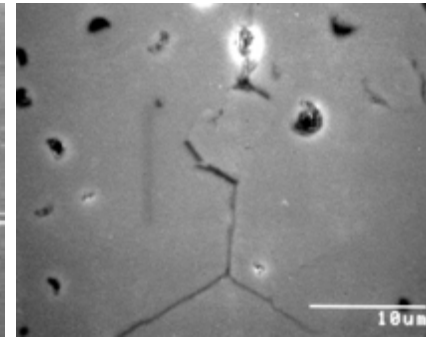

(d)

(e)

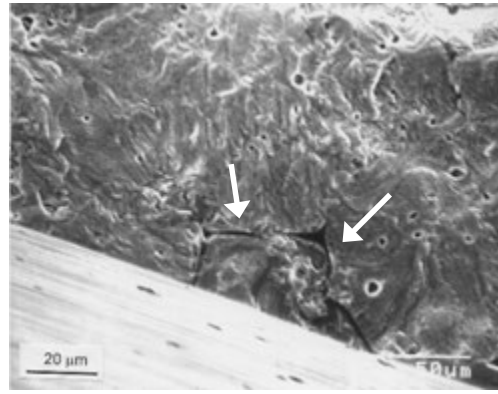

Figure 6.24 *Grain boundaries may be flaws in coarse-grained materials such as Mg partially stabilized zirconia (50 µm to 70 µm grain size). (a) and (b) show optical images of the rough fracture surface of a split rod flexural strength specimen. The rough surface is due in part to weak grain boundaries. (c) and (d) show SEM images of a polished surface revealing the gaps and cracks along the grain boundaries. (e) shows a grain boundary fracture origin. Tiny wake hackle from several small pores radiate away from the origin.*

6.7 Surface-Distributed Flaws

6.7.1 Surface voids or pits from processing

Surface voids are cavities on the surface of a component created by a reaction with the *processing* environment. They are similar to pores, except that they only arise on the surface. Surface voids can be in a reaction layer from hot-isostatic pressing with a glass encapsulation cladding or from trapped outgassing bubbles. Examples are shown in Figure 6.25.

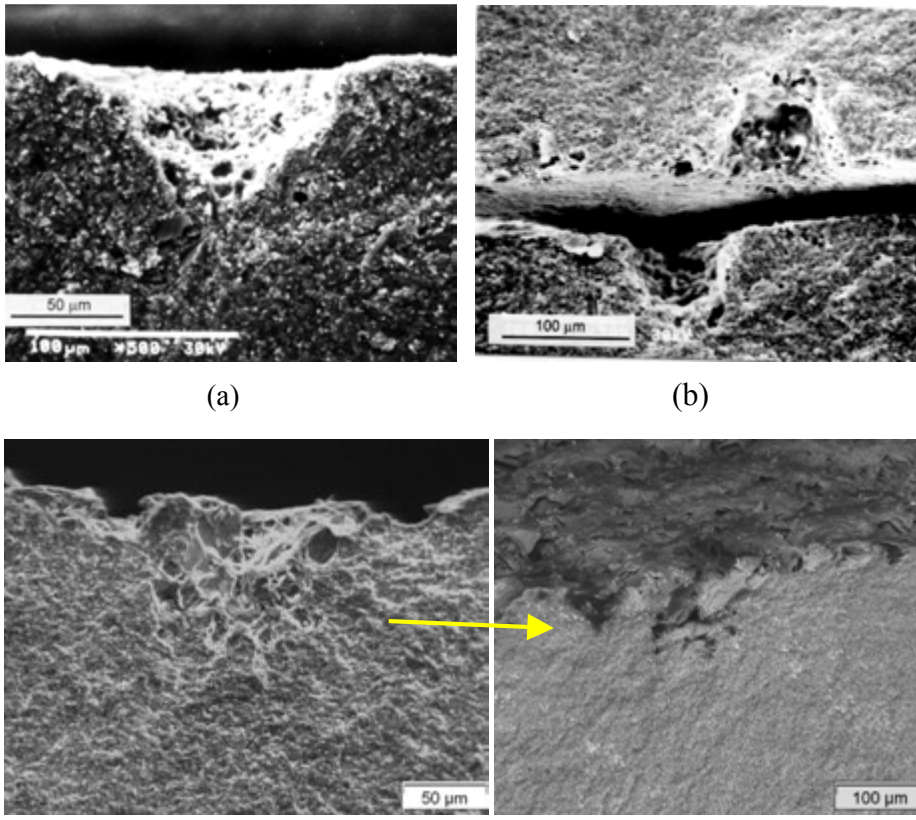

(a) (b)

(c) (d)

Figure 6.25 *Examples of surface void fracture origins. (a) and (b) are in as-fired bend bars of injection-molded sintered silicon nitride. (c) and (d) show a surface void in an as-fired silicon nitride component with yttria and alumina sintering aids. (d) is tilted so that the outer surface is visible. EDX analysis showed an excess concentration of aluminum at the site, so the flaw also has characteristics of a compositional inhomogeneity. (a, b are courtesy A. Pasto; c,d are courtesy T. Lube, W. Harrer, and R. Danzer).*

6.7.2 Pits from environmental exposure

Pits are surface cavities that may form as a result of a reaction between a ceramic or glass and the *usage* environment. Corrosion or oxidation can create pits. Examples are shown in Figure 6.26. Richerson[24] shows several good examples of oxidation and corrosion pits in silicon nitride. Pits have chemistry or structural differences that make them distinguishable from pores or surface voids. Sometimes the damage can be confined to grain boundaries and the flawed regions can be difficult to discern on a fracture surface.

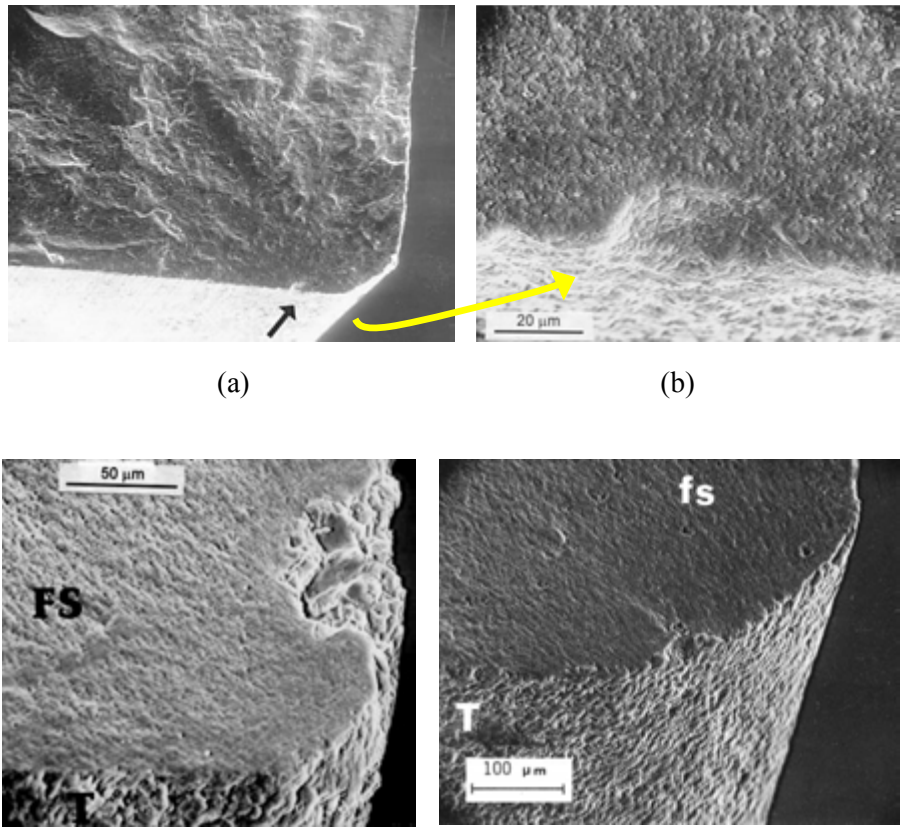

Figure 6.26 *Examples of pit fracture origins. (a) – (c) are in oxidized hot-pressed silicon nitride. (b) is a close-up of (a). (d) is a reaction-bonded silicon nitride.*

6.7.3 Handling scratches and polishing scratches

Handling damage may be scratches, chips, cracks, or other flaws due to handling or impact. Examples are shown in Figures 6.27, 6.28, 6.29, and 6.5b earlier in this chapter. Scratch damage varies widely depending upon the material, the sharpness or bluntness, the speed, depth of cut, and force of the scratching device or abrasive. At low force, a simple groove may be created that is smooth with mostly plastic deformation and minimal cracking. At higher forces and with more abusive tools and conditions, grooves with severe cracking may be generated. The cracking will be of several types: a crack that penetrates beneath the groove and follows the direction of the scratch, a series of shorter jagged cracks that jut out to either side of the scratch, and sometimes lateral cracks that are parallel to the surface and cause material to spall off. The depth of the cracking can be much greater (ten times or more) than the visible groove. Scratches that occur after fabrication and finishing are usually easy to identify. They are usually isolated and stand out on a surface, provided that the fractographer is careful to illuminate the part from different directions. Figure 6.5b and 6.27 show examples. It is easy to overlook a scratch on a surface if the lighting is not optimal. If scratches are suspected, then it is wise to rotate the part under the illumination or move the illumination around while watching through a microscope. A quick momentary reflection may be the first sign a fractographer gets of a scratch. Scratches may also be overlooked on the SEM since they have very low contrast. If the tensile stresses are oriented at an angle to the axis of the scratch, then only be a small portion of the scratch may trigger a fracture as shown in Figure 6.27. The origin will be seen as an irregular crack on the fracture surface. These cracks may be so irregular as to confuse a fractographer who may mischaracterize the origin or arbitrarily assume it is machining damage. This is a good example of how, if a surface-located flaw controls strength, the fractographer should look at the exterior surface for other clues.

In other cases with biaxially-loaded parts, such as pressurized vessels or plates, or laboratory ring-on-ring strength tests, there will always be a tensile stress available that is oriented perpendicular to the scratch axis. Figure 6.28 shows examples. In these cases the fracture follows the scratch for a distance. These can be tricky to diagnose if the fracture follows the entire length of the scratch, since the scratch trace on the outer surface may be overlooked or hard to see on the exact fracture edge, even if the pieces are put back together. On the other hand, fractures often veer off from the scratch axis, since the irregular jagged cracks that protrude off to the side of the scratch can redirect the main fracture.

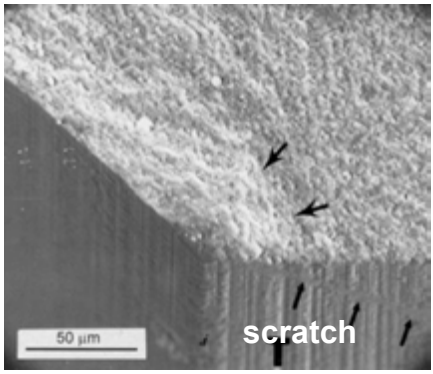

(a)

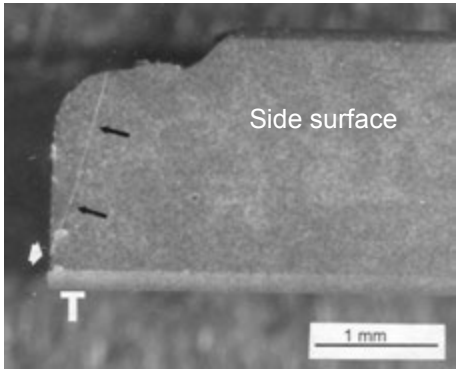

(b)

(c)

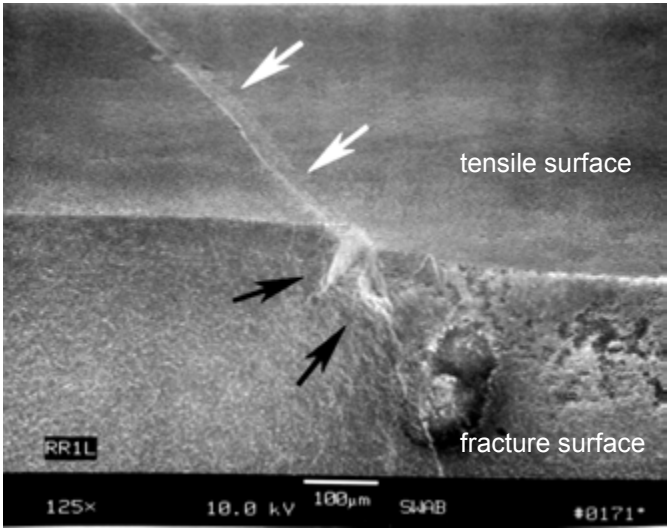

Figure 6.27 *Examples of scratch origins with the scratch at an angle to the tensile stress. The cracks penetrate much deeper than the scratch groove depth. Scratches can create damage that may be mistaken for grinding cracks, so it is wise to look at the orientation of the scratch relative to the grinding striations. Scratches will be at irregular angles and are often isolated. (a) is in a SiAlON bend bar with a scratch near the chamfer. (b) is a side view of a reaction-bonded silicon nitride bend bar. Scratches often require illumination at just the right angle to be seen. (c) shows a scratch on an alumina bend bar surface (white arrows) and the continuation of it into the interior that acted as the fracture origin in a bend bar (black arrows) (c is courtesy J. Swab).*

It is not uncommon with polished surfaces, to find a scratch-created flaw at the fracture origin, but all grooves or exterior surface traces are gone. Additional polishing after the scratch flaw was created removed all the surface traces. Figure 6.28 shows examples.

Scratch/dig specifications are used with visual inspections of the outer surfaces of glass or transparent ceramic materials. The older MIL-PRF-13830B (1997) scratch specification is based on a visual comparison to reference pieces. The number is sometimes connected to the width of the scratch surface trace, but the literature and web sites are contradictory about the actual values. A #40 scratch sometimes is listed as a 4 μm wide scratch and in other cases as a 40 μm wide scratch. The dig specification is more consistent, and is the diameter of a spot such as is caused by grinding, impact, or contact damage (see 6.7.4 and 6.7.5 below). Unfortunately, the outer surface features often have no correlation to the extent and size of cracks that may, or may not, lie underneath.

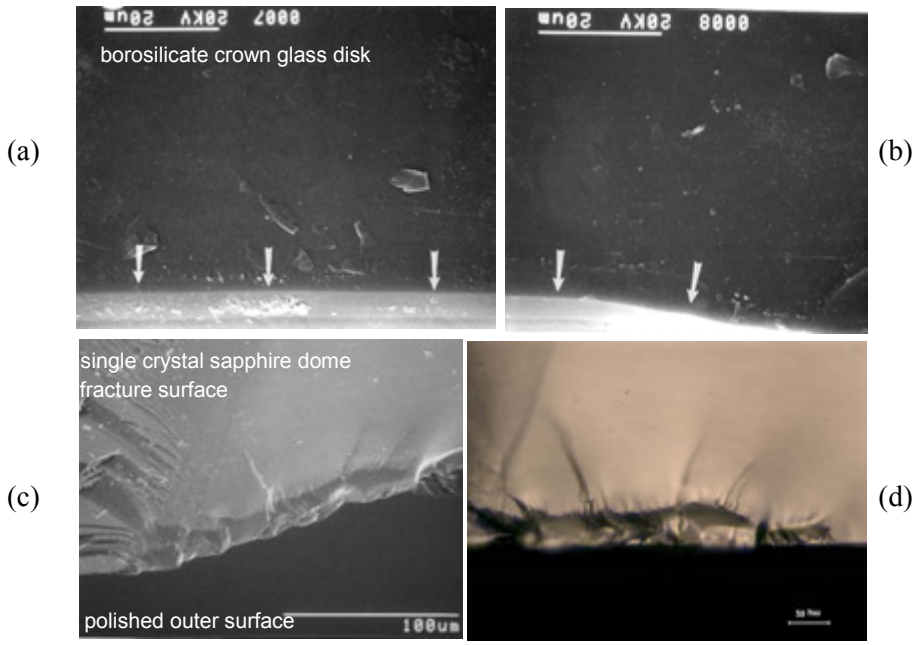

Figure 6.28 *Two examples of scratch crack fracture origins with the tensile stress normal to the scratch. (a) and (b) show the origin in a polished BK-7 borosilicate crown glass disk broken in ring-on-ring flexure. The origin is a very long, but smooth 7.3 μm deep crack. Figure 5.15 shows the fracture mirror. (c) and (d) show matching SEM and optical images of an origin in a sapphire dome that broke in a high-temperature wind tunnel test rig. There were no traces of the scratches on the outer polished surface in either case.*

When scratches are suspected, it is usually a good idea to look for other scratches elsewhere on the exterior surface of the part. Figure 6.29 shows an example where scratches controlled strength in an engine part.

Occasionally a fractographer is called upon to examine an *intact* part and assess where a line on the surface is a crack or a scratch. The former may be very serious and may prompt a part to be replaced, whereas the later could be a simple cosmetic irregularity. How does one decide? In my experience, scratches usually have jagged edges when viewed with a 5 to 10 power hand loupe and strong lighting. They also will not allow water or alcohol to penetrate. Cracks, on the other hand, have very-sharp, narrow edges on the surface. If water or alcohol is applied, the surface may dry quickly, but the crack will stay wet a while longer. If the material is transparent, one can shine a strong flashlight or laser pointer through the part side and look for reflections from the interior of the crack. Sometimes cracks may be invisible, however, as discussed on page 4-48.

(a)

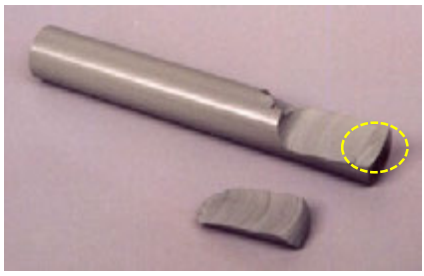

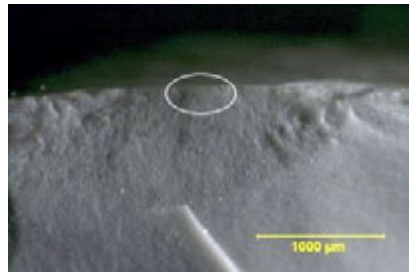

(b)

(c)

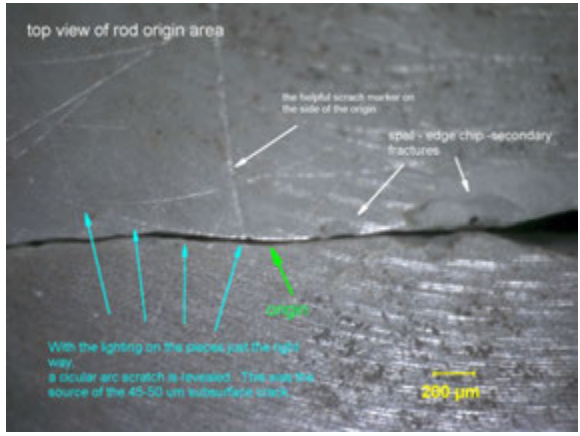

Figure 6.29 *A fractured silicon nitride pin. Examination of the fracture surface (b) alone might lead one to conclude that machining damage was the origin flaw, but closer examination of the outer surface (c) shows it actually was a scratch. Notice how the origin flaw has the same arc as the scratch.*

6.7.4 Sharp object impact or contact

Figure 6.30 shows examples of origins created by impact or contact of a sharp object. Median and radial cracks may penetrate deeply beneath the impact site, which is often heavily damaged with small fragments missing. Vickers indentations are often used to mimic such flaws. Witness marks on the exterior surface may give clues as to the nature of the impactor. The exterior surface should be examined for other nearby impacts. Fréchette[39] describes sharp contact site damage as "pecks." "Digs" are visually-detected contact damage sites in glasses and optical ceramics. Specifications for the allowable dig diameter may have some utility, but as the figures in this Guide show, and as discussed in the previous section (page 6-31), the surface damage size may or may not correlate with the size of the cracking beneath the surface.

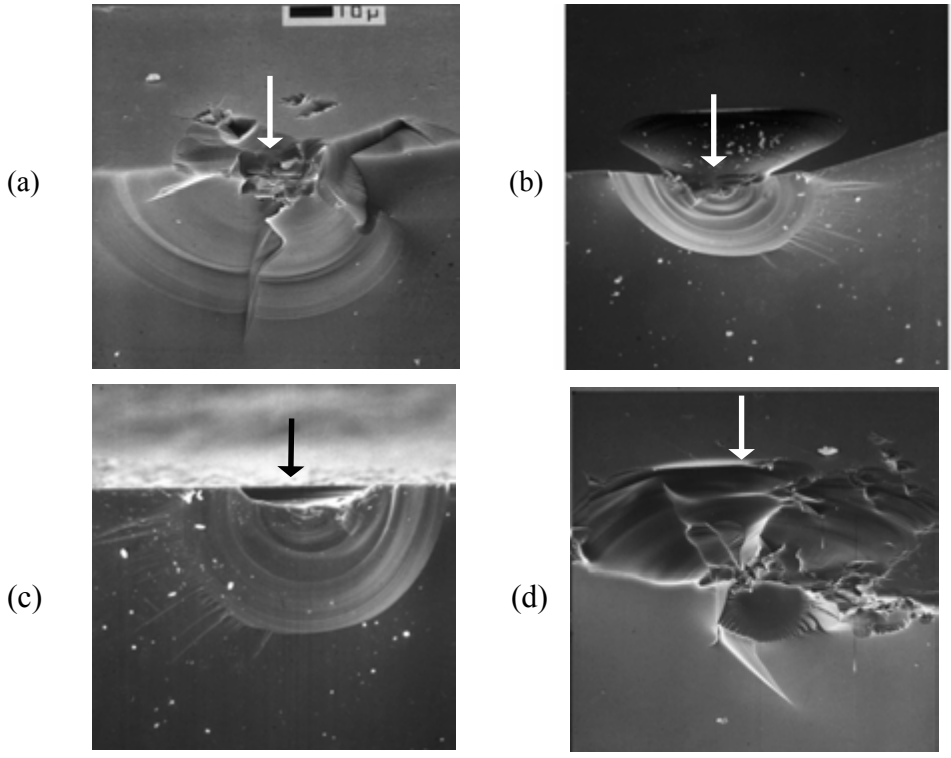

Figure 6.30 *Examles of sharp particle imact origin. in glass. The direction of impact is shown by the arrows. All of the impacts have created penetrating median – radial cracks. (b) and (d) have pronounced lateral cracks as well. In each case the impact site has been pulverized or crushed, unlike blunt impact sites.(a-d courtesy J. Varner).*

6.7.5 Blunt object impact or contact

Blunt impacts or blunt contact loadings produce round Hertzian cone cracks as illustrated in Figure 6.31. These may be complete or partial rings as shown in Figures 3.57 (a C-crack in a ball bearing), and 6.32, 6.33 – 6.35. The cone crack initiates as a ring just outside the footprint of the two contacting bodies as shown in Figure 6.31a. The size of the contact area depends upon the load, geometries, and elastic properties of the two materials. A simple rule of thumb is that the contacting object is almost always several times larger than the observed ring size on the contacting surface as shown in Figure 6.31. Of course, if the blunt object penetrates through the plate and makes a large hole, then the impactor may be comparable in size to the hole. When contact damage is detected, the exterior surface should be examined for witness marks at the contact site, as well as other nearby impacts.

Blunt contact cracks often leave little trace on an outer surface. A pretest inspection for "digs" may not find contact damage cracks. The contact cracks might be revealed prior to fracture by very careful examination with adjustment of lighting angles. After fracture, they are easier to detect since they leave *a small telltale arc* on the fracture surface plane at the origin site.

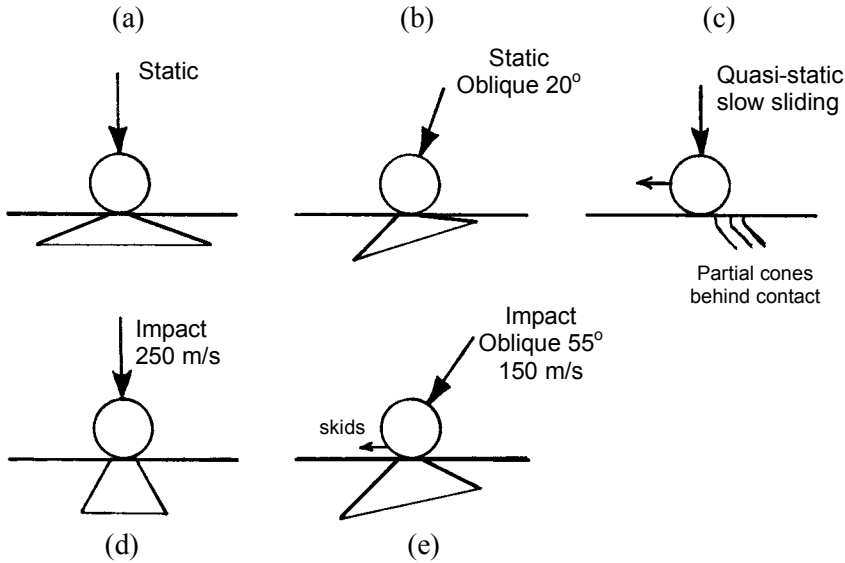

Figure 6.31 *Blunt contact or blunt impact cone crack profiles. These are side views. Notice the blunt impactor is larger than the size of the contact circle and first ring to form at the impact site.*

Ring cracks initially pop in normal to the surface but then turn and propagate into the depth with an included angle of 125° to 135° for quasi static loading[1] in glasses as shown in Figure 6.31a. The included cone angle decreases markedly with increasing impact velocity as shown in Figure 6.31d. It may be possible to estimate the projectile velocity from the included cone angle.[25,26,27] For example, at 250 m/s, 0.8 mm to 1 mm diameter steel balls created 60° to 80° cone cracks in glass[25] and 70° to 90° cracks in silicon carbide.[27] During quasi static or impact loadings, as load increases the footprint area may expand and generate multiple concentric ring and cone cracks. Kirchner and Gruver[28] have described interesting variations of cone cracks from impact, whereby cracks can nucleate on one side, then branch, and then even spiral around the contact site.

If a ball that is loaded perpendicular to the surface is slid over the surface at quasi static rates, the cone axis tilts such that the rear of the cone dips down deeper, and the front portion of the cone disappears (Figure 6.31c).[29] Partial cone cracks are the result. This is not surprising since the forward motion of the ball creates an additional tensile stress behind the ball, but adds compressive stresses ahead of the ball.

Conditions are different if the contactor is loaded (or strikes at) at non-perpendicular angles. Full cones form, but they tilt so that the backside approaches the surface while the front side penetrates deeper into the surface as shown in Figures 6.31b,e.[30]

Most blunt contact loadings produce a cone crack that penetrates partially or completely through a plate or body as shown in Figure 4.17. These may not cause component breakage and may merely be a cosmetic fault unless the structure is intended to seal the environment. Subsequent loading in tension or flexure may cause new crack extension from the cone crack as shown in Figures 6.32 (d) and (e). Many structures such as dental crowns may have numerous harmless cone cracks in the veneers. They are only revealed when a fracture that commenced elsewhere passes through the cone (Figure 6.32f).

Impacts at moderate or high energy create radial cracks and bending stresses that can propagate cracks far beyond the impact site and any cone cracks, thereby causing component fracture. Figure 6.34b shows an example.

A common, serious flaw in ceramic balls and ball bearings is a so called “C crack” such as shown previously on page 3.68 in section 3.24 on fluorescent

[1] Stationary or with slow motion.

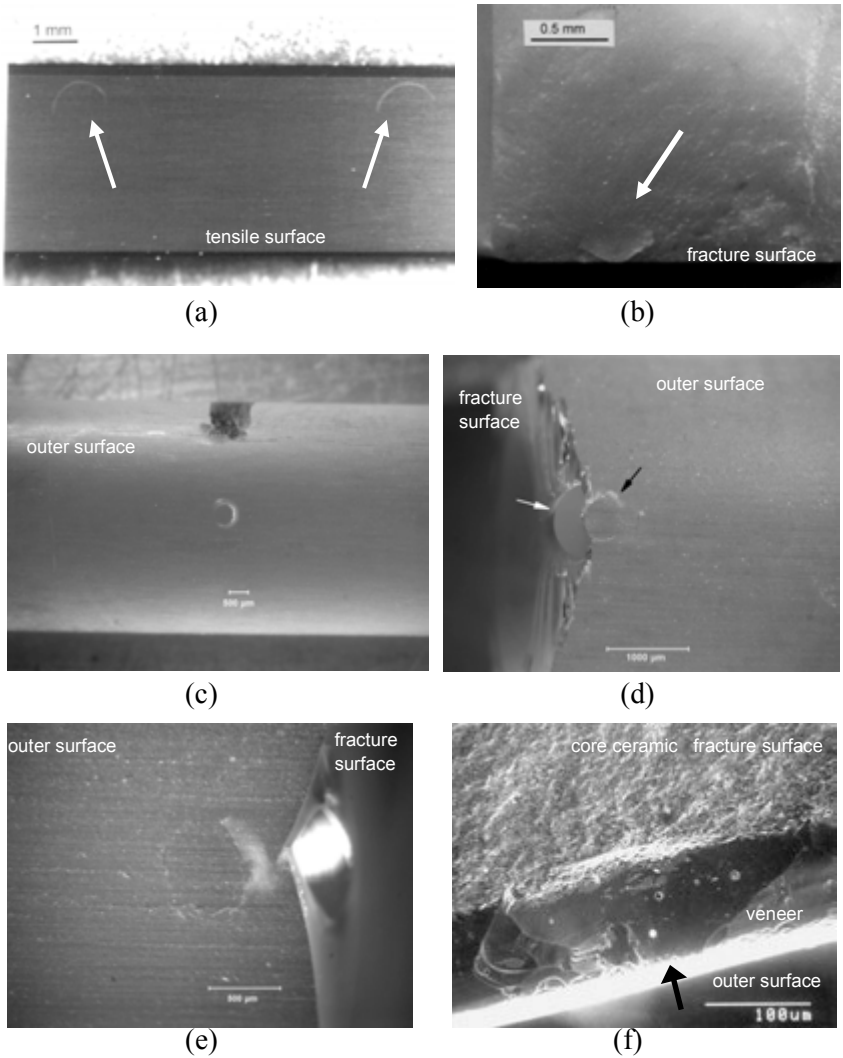

Figure 6.32 *Examples of blunt impact or contact crack damage fracture origins. (a) shows the tensile surface of a silicon nitride bend bar with partial crack rings that were created by a ball-tipped micrometer. Such rings were fracture origins in some other bend bars. (b) is a cone crack fracture origin from a blunt contact or impact on a rectangular bend bar. (c) shows a blunt contact crack from a loading roller on a cylindrical rod glass flexure specimen. Notice that the ring is incomplete. The cone crack can act as a strength-controlling flaw if loaded in tension as shown in (d) and (e). (f) shows a cone crack in a dental bilayer crown. The cone crack, which initiated from contact on the veneer layer, was harmless. Fracture initiated elsewhere and a crack simply passed though the cone crack.*

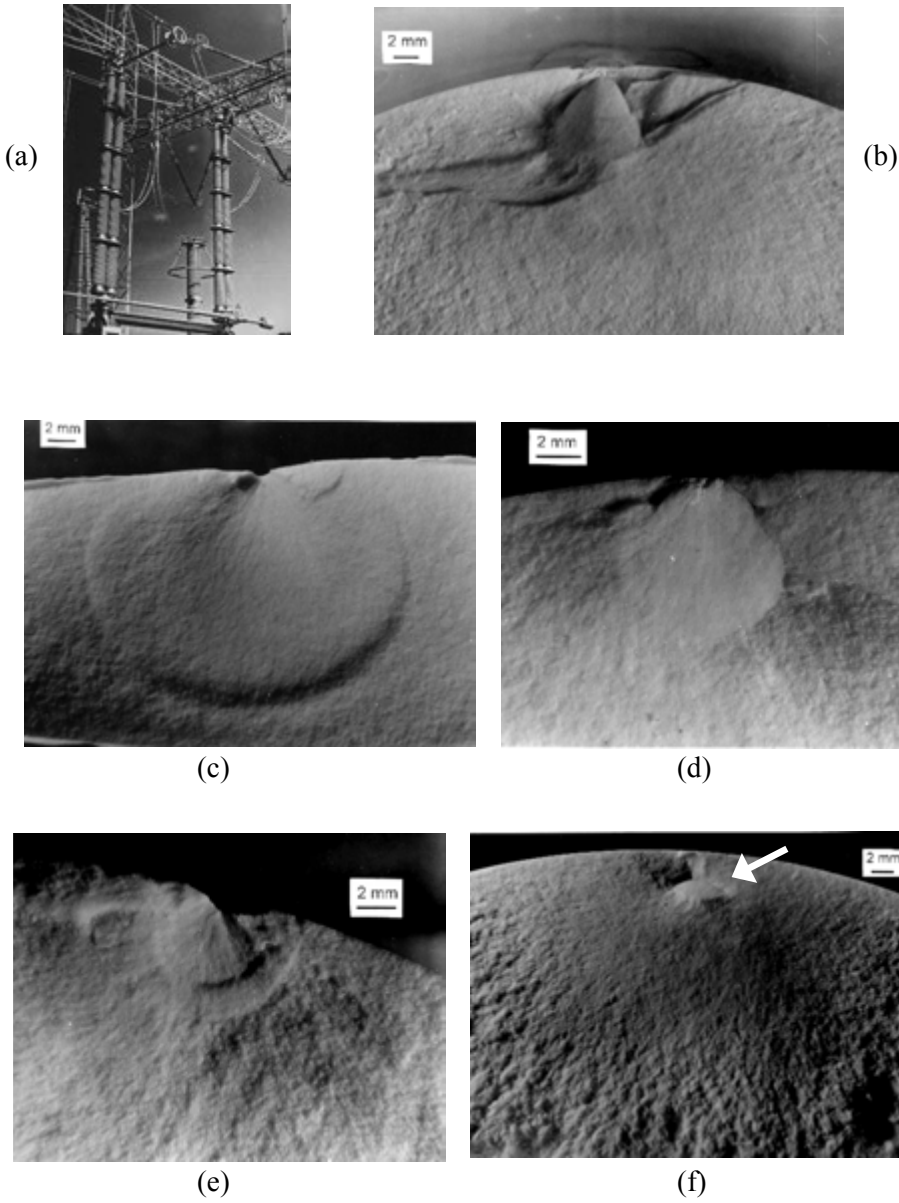

Figure 6.33 *Blunt impact origins in electrical insulator porcelains. (a) shows the installed insulators. (b) and (c) are blunt impact damage from "BB" gun projectiles. (d) is damage from a sling shot projectile. (e) and (f) are impact origins from contact with support structures. Note the partially exposed cone in (f) (arrow). (Photos courtesy of J. J. Taylor and R. W. Rice)*

(a)

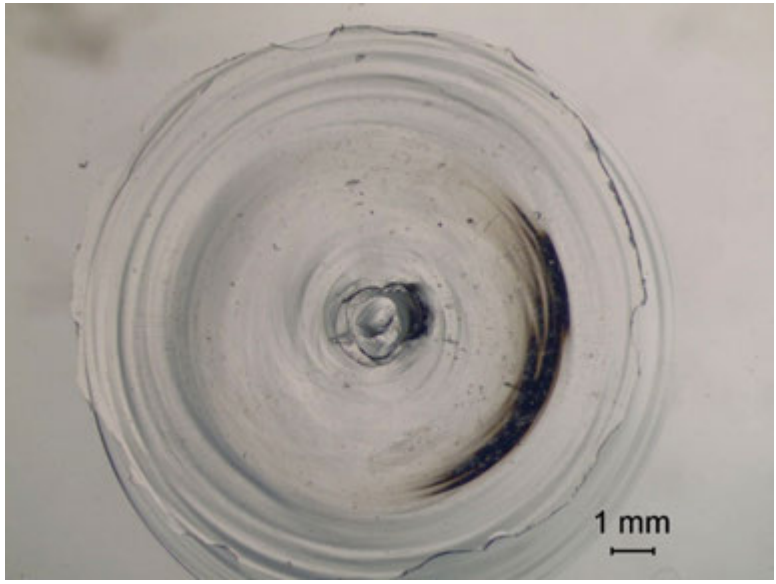

(b)

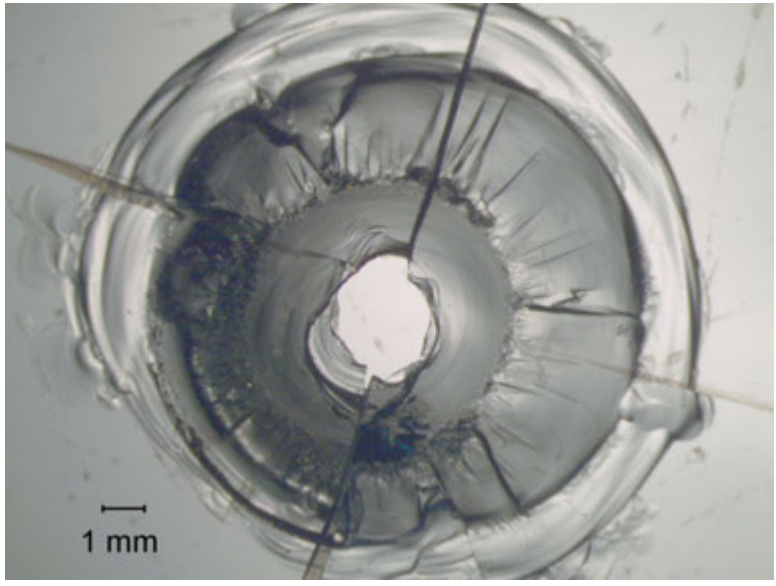

Figure 6.34 *Blunt impact origins in glass plates. (a) shows a mild – moderate impact with cone cracks. The plate did not break into pieces. (b) is a severe impact that was sufficient to create cone and radial cracks. The latter caused plate fracture. (Specimens courtesy of J. Varner and V. Fréchette, Alfred University)*

dye penetration. It was a partial cone crack. They are often formed by ceramic balls impacting each other! Manufacturers wisely started to package ceramic balls more carefully once the problem was recognized.

Blunt-contact cracks can also be a problem in the glass container and pharmaceutical industries. Figure 6.35 shows examples. Case 4 in Chapter 10 has another example of contact damage cracking in a medicinal vial. Figure 4-23 on page 4-37 shows another good example in a medicinal vial.

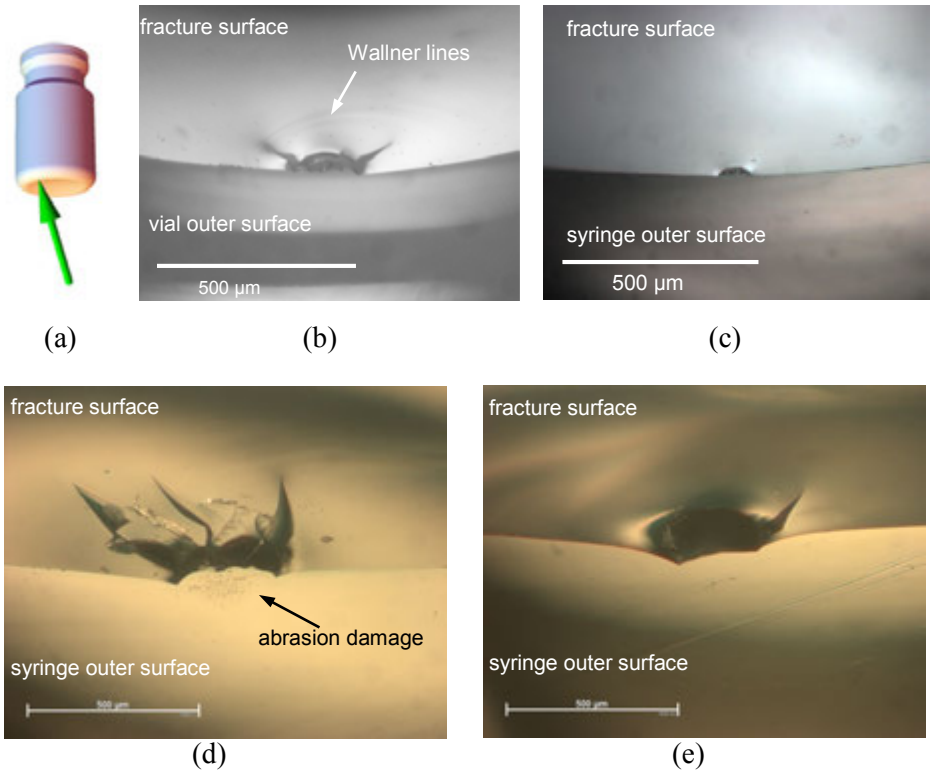

Figure 6.35 Blunt contact damage in pharmaceutical glass. (a) and (b) are a vial. The pictorial (a) schematic shows a possible impact direction and is a useful aid for explaining a fracture event. (c) - (d) are three glass syringes. When arc-shaped contact cracks propagate to fracture, they often have hackle lines that emanate from the flaw. Notice how these tilt in opposite directions on the flaw sides indicating that fracture radiated outwards. Such hackle at an origin site suggests "eyelashes." Notice the witness mark of abrasion damage in (d). (Photos courtesy of F. Maurer)

6.7.6 Grinding and machining cracks

Grinding or cutting introduces damage to the surface. The damage can be controlled, usually by using progressively finer grinding and polishing steps to remove damage introduced by prior steps. Edges are particularly susceptible to damage and can easily be cracked or chipped. Bevels, chamfers, and rounding are effective treatments for the latter. They are commonly applied to biaxial disks and bend bars and are carefully aligned circumferentially or lengthwise lest the beveling introduce more cracks.

Surface grinding procedures use grinding wheels as shown in Figure 6.36. The grinding process entails material removal, often by means of microcrack and microchip formation. By its very nature, cracking is introduced into the surface. Initial grinding is done with coarse-grit wheels and modest depths of cut in order to facilitate material removal. Intermediate- and final-stage grinding is done with finer-grit wheels and smaller depths of cut to reach final part dimensions and surface finish requirements, but also to remove prior damage while introducing a minimum amount of new damage.

Fractographers realize that there often is no correlation between the strength of a part and the final surface finish. The reason is simple. Grinding induced cracks penetrate far deeper (10 to 20 times) below the surface than the surface undulations and striations. Sometimes the crack depths are proportional to the depth of the surface grooves, and the surface finish may correlate to strength. On the other hand, strength may be controlled by deep grinding cracks from earlier steps that are not removed in the final finishing phase which may produce a very fine outer surface finish. The following case illustrates the point. The author ordered a batch of conventional alumina bend bars to be cut and ground out of a billet by a new machine shop. The shop was instructed to surface grind longitudinally and not use their preferred Blanchard grinding process that creates random swirl marks and attendant cracking. The shop ignored the instructions and Blanchard ground the bend bars and then lapped them to a beautiful finish. The strength of the bars was quite low, however. They fractured from severe, randomly-oriented grinding cracks introduced by the Blanchard process. The final lapping did not go deep enough to remove the prior damage.

Figure 6.36, an adaptation of a figure by Rice and Mecholsky,[31] illustrates some key aspects of machining flaws. Parallel cracks oriented in the direction of grinding are longer and are the same depth or deeper than the orthogonal cracks. Thus, the parallel cracks are more deleterious to strength.

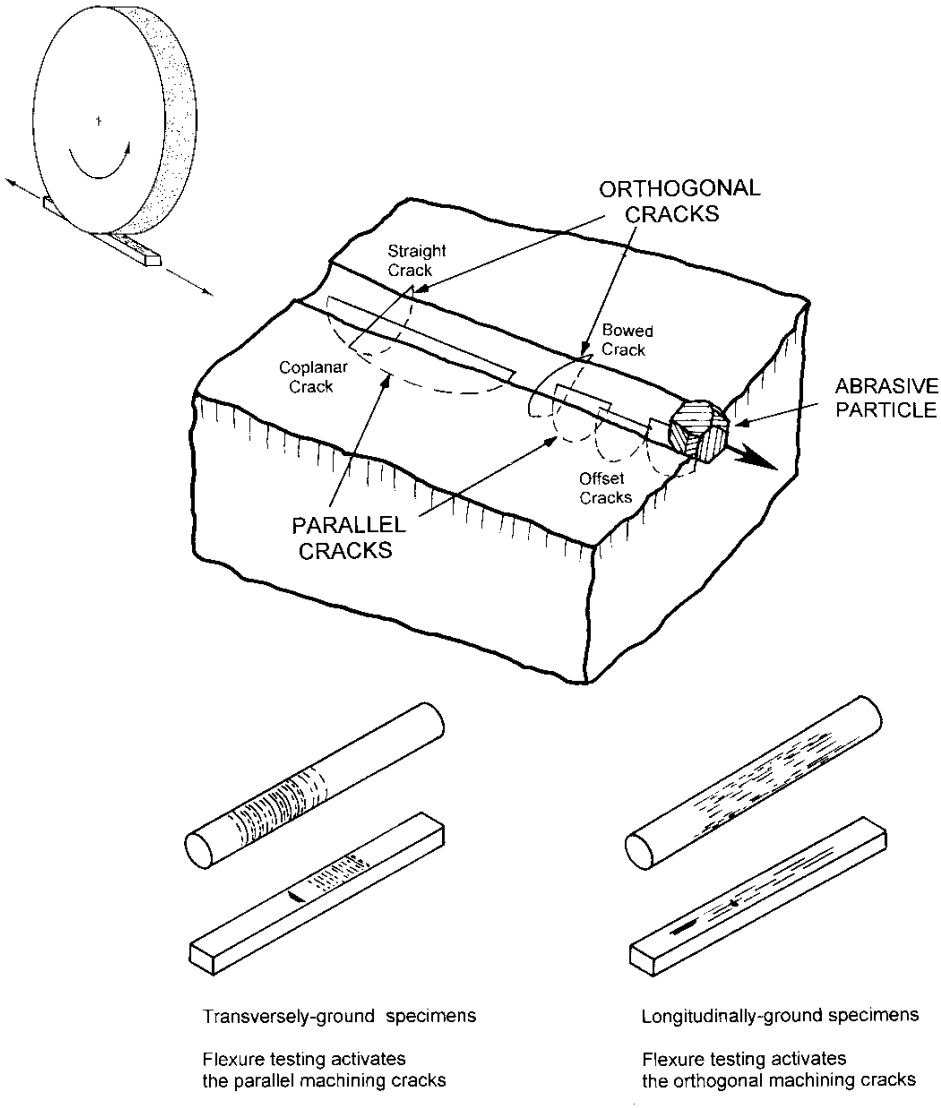

Figure 6.36 *Surface grinding (insert) creates grinding grooves (striations) and subsurface cracking. The cracking includes long deep "coplanar parallel cracks" or "offset parallel cracks" aligned with the striations in the direction of abrasive motion. Orthogonal cracks form at right angles to the striation and may be bowed in the direction of abrasive motion. Lateral cracks or spalls that are roughly parallel to the surface may also form (not shown). The axis of grinding is often chosen to align the worst cracking damage (parallel cracks) with a specimen axis as shown on the bottom right.*

The differences between the orthogonal and parallel cracks give rise to strength dependence with orientation (if grinding cracks are the controlling flaws). Only one striation groove is shown in the schematic and it should be remembered that the ground surface actually contains a complex overlapping network of such cracks and grooves.

With some experience it is not too difficult to find parallel grinding crack flaws in dense materials, such as glass, single crystals, and either very coarse-grained or extremely fine-grained ceramics. Detection of grinding cracks in porous, heterogeneous, or mid grain-sized materials is very difficult, however, since the machining crack blends in to the background microstructure. This is especially true for the short orthogonal cracks. They are hard to find in nearly all materials. Figure 6.37 shows some examples of orthogonal cracks, which sometimes are described in the literature as "longitudinal-grinding flaws." (That expression means: "the flaws that are created by longitudinal grinding" with respect to the specimen's long axis.) Additional examples are shown in some of the papers by Rice and Mecholsky listed in the Bibliography, Appendix A.

Parallel machining cracks are much easier to detect and often can be found with routine optical microscopy, but only if low-angle grazing illumination is used. Figure 6.38 shows examples. Figure 6.39 shows a schematic of these parallel flaws and their telltale signs. Figure 6.40 shows how "V" machining cracks form in ground round parts. Several of these grinding crack flaws exhibit another form of hackle on fracture surfaces:

Grinding crack hackle: *Hackle formed on the fracture surface originating from irregularities and steps in grinding cracks.*

Grinding crack hackle is sometime also known as "shark's teeth." The size of grinding cracks, and hence their effect on strength, depends upon material properties such as hardness, elastic modulus, and fracture resistance or fracture toughness. It also depends on the grinding wheel and machine conditions such as abrasive type, grit size and concentration, depth of cut, wheel speed, grinding forces and machine horsepower. The crack size also depends upon the material's grain size. Deep grinding cracks can form in very coarse-grained ceramics since the single crystal fracture toughness is less than the polycrystalline fracture toughness. It is beyond the scope of this guide to delve into this topic other than to say that abrasive grit size is the dominant parameter that controls crack size for typical surface grinding procedures. Figure 6.40 shows the effect of grit size upon parallel crack depth in a commercial silicon nitride.[32]

(a)

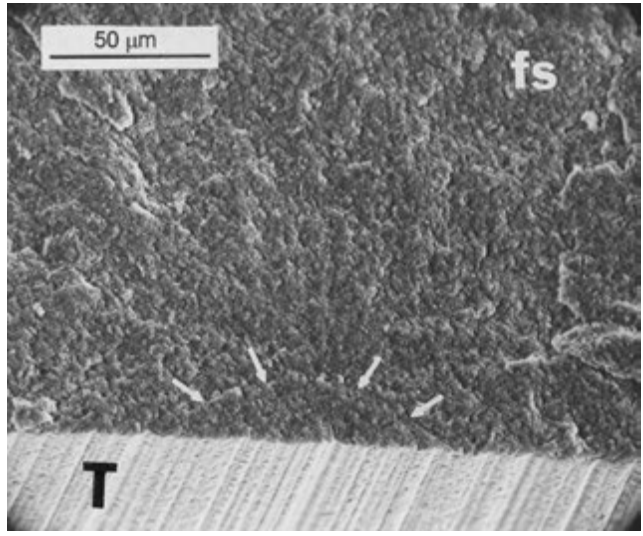

(b)

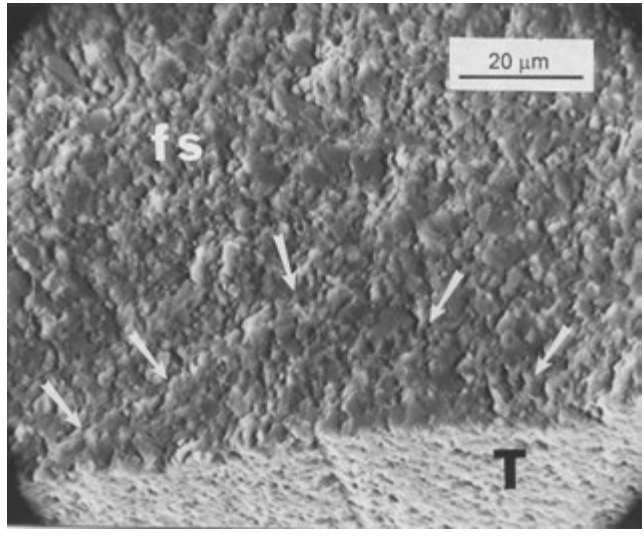

Figure 6.37 *Orthogonal grinding cracks as seen in some very fine-grained ceramics. (a) shows a crack in a hot-pressed silicon nitride bend bar. (b) shows a crack in a hot-pressed silicon carbide. The bars have been tilted back in the SEM to reveal parts of the ground surface "T" which was in tension. "fs" means fracture surface. The specimens were ground longitudinally with respect to the specimen's long axis. Slightly larger than normal striations are evident on the ground surface in each case. The orthogonal cracks are hard to find even with the SEM, since they tend to blend in with the microstructure.*

(a)

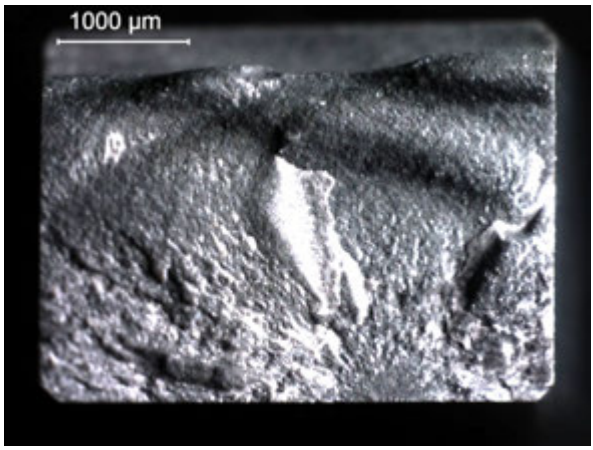

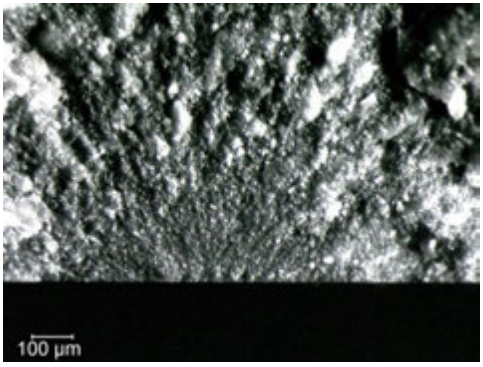

(b)

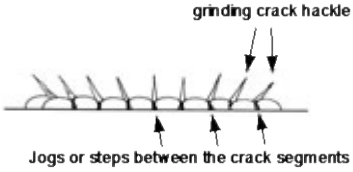

(c)

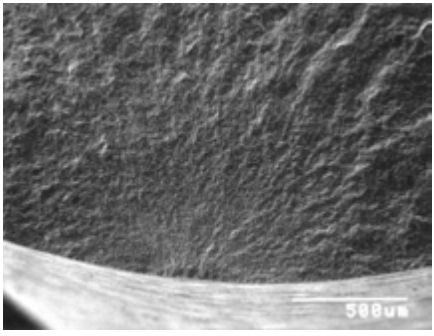

(d)

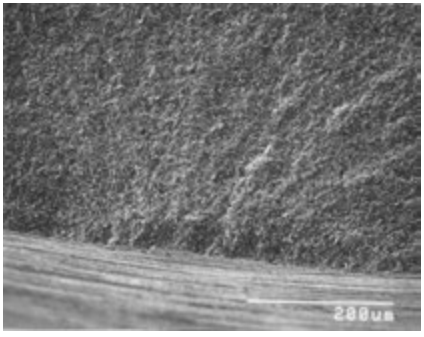

(e)

Figure 6.38 *Examples of parallel grinding cracks. (a) and (b) show optical images of a "zipper crack" in a sintered silicon nitride bend bar. (d) and (e) show SEM images of a crack in a silicon nitride rod.*

(f)

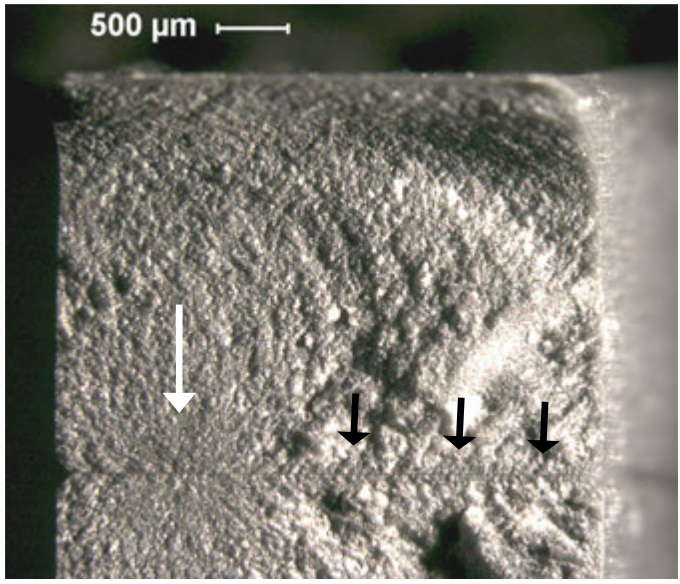

(g)

Figure 6.38 (cont'd) *Examples of parallel grinding cracks. (f) shows back-to-back halves of a silicon nitride bend bar with coarse grinding (150 grit) cracks. A zipper crack is at the origin (large white arrow). The small black arrows show that there also is a machining crack "skin zone" along the entire surface. (g) is an alumina bend bar with low-angle grazing illumination from the side revealing a zipper crack.*

(a) elongated “coplanar parallel crack”
(or coplanar linked semi-elliptical cracks).
A deep striation may or may not necessarily be present.
The fracture mirror may be elongated along the outer specimen surface.

(b) elongated “coplanar parallel crack”
linked with a natural flaw.
A step in the fracture origin emanates from the material flaw.

(c) “zipper crack”
This is a series of short semi elliptical cracks, which have linked. A series of short tails, or “machining crack hackle,” emanate from the links or overlaps of the flaws and extend up into the fracture mirror. These tails may be tilted to the left or right and help confirm that fracture originated in the central region of the set. The short tails are telltale features of slightly misaligned or overlapping transverse machining cracks (or a scratch) and are often easier to see with an optical microscope with low angle lighting than with a scanning electron microscope. The fracture mirror may be elongated along the specimen outer surface or it may have one or two prominent side lobes. This origin type is common in transversely-ground rectangular flexure specimens or scratched biaxial disk specimens.

(d) coarse “zipper crack”
This is made up of a series of irregular, less coplanar semi- elliptical cracks. Larger tails than in (c) are created. In severe cases, the tail may extend all the way to the mirror boundary. The fracture mirror may be elongated. This origin is common in transversely ground or scratched specimens and the markings are sometimes termed “shark’s teeth.”

(e) “V machining crack”
The crack intersects the fracture surface at an angle. Only a portion of the machining crack or crack series is exposed. A pronounced step occurs in the fracture mirror. One or two (shown) tails extend well up into the fracture mirror. The machining direction is not quite perpendicular to the specimen length and uniaxial stress axis due to grinding wheel cross feed. This origin is common in cylindrical specimens prepared by centerless or cylindrical transverse grinding wherein the wheel and work piece displace axially relative to each other.

(f) “coarse grinding parallel crack”
The origin is a deep machining crack that extends along the entire surface. The origin is often bumpy since the origin is comprised of offset parallel cracks. Thin bands of uniform depth extend along the specimen surface on either side of the fracture mirror. The bands have the same depth as the grinding cracks. Short tails, or “machining crack hackle” which may be in the thin bands are tilted away from the origin. This origin type is common in coarse ground surfaces.

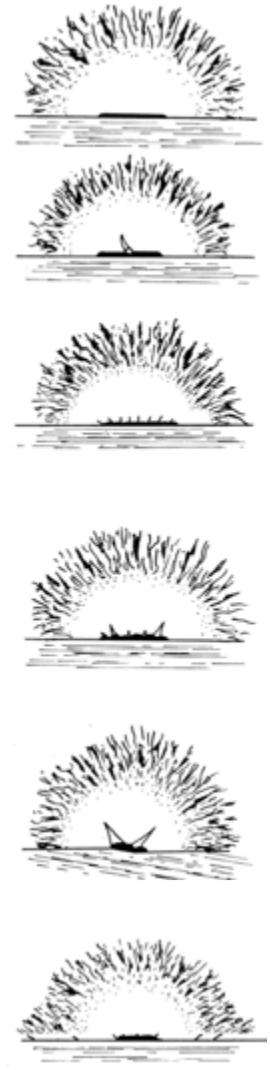

Figure 6.39 *Schematics of telltale features of parallel machining cracks. These origins are common in biaxial disks, pressure-loaded plates, and transversely-ground flexural or tension strength specimens. Low-angle grazing illumination facilitates their detection with optical microscopy. Some have elongated mirors along the surface, an important telltale sign.*

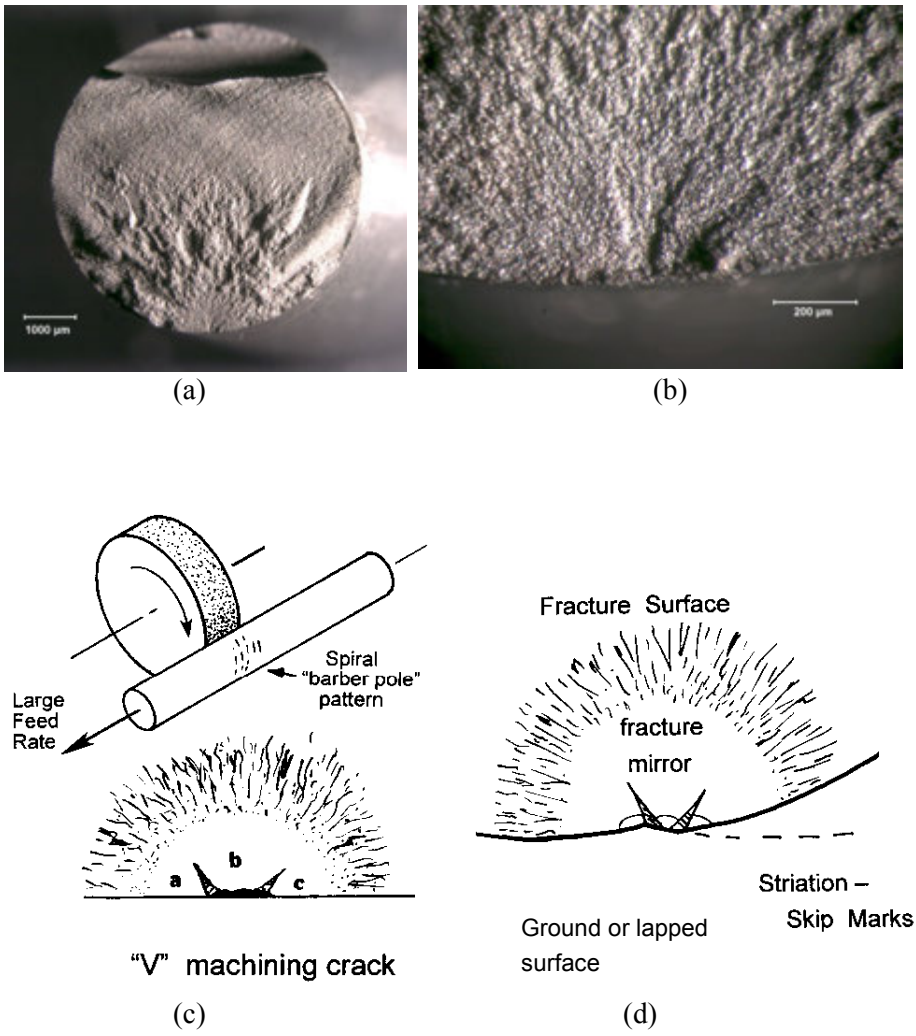

Figure 6.40 *Round parts may have "V" machining cracks formed from small parallel crack segments a, b, c on different planes as shown in (a) and (b) for a silicon nitride rod. The steps between the individual crack segments form two or more telltale hackle lines, which extend up into a mirror. Examination of the ground surface shows striations (grinding grooves) that have a small angle relative to the rod axis. V crack flaws are easy to see even at very low magnification with low-angle grazing illumination.*

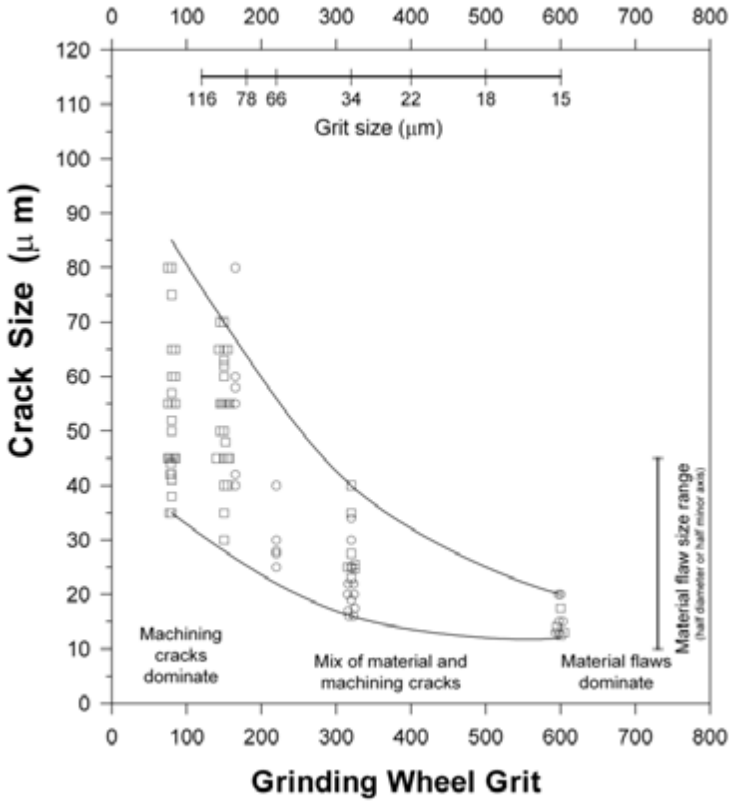

Figure 6.41 *The depth of grinding cracks as a function of grinding wheel grit in a silicon nitride. The notes show the strength-controlling flaws. Ref. 32*

The *average* grit size may not necessarily be the controlling parameter. Instances of *renegade abrasive grits* in a grinding wheel that caused atypical damage have been reported.[32] Figure 6.5a earlier in this chapter and Figure 6.42 below show an example of damage from a renegade grit in a silicon nitride. Calculations based on the wheel and table speeds and the specimen and wheel diameters confirm that a single grit can cause such long striations. Striation here means a grinding groove.

Although it is widely believed that materials with rising R-curves form smaller grinding cracks than materials with flat R-curves, there is evidence that just the opposite is true.[33] Materials with rising R-curves are more difficult to grind, but for a given wheel speed and depth of cut, greater grinding forces are generated to overcome the removal resistance. The greater forces cause cracks to penetrate deeper than in materials with low fracture toughness or flat R-curves that cut or grind more freely.

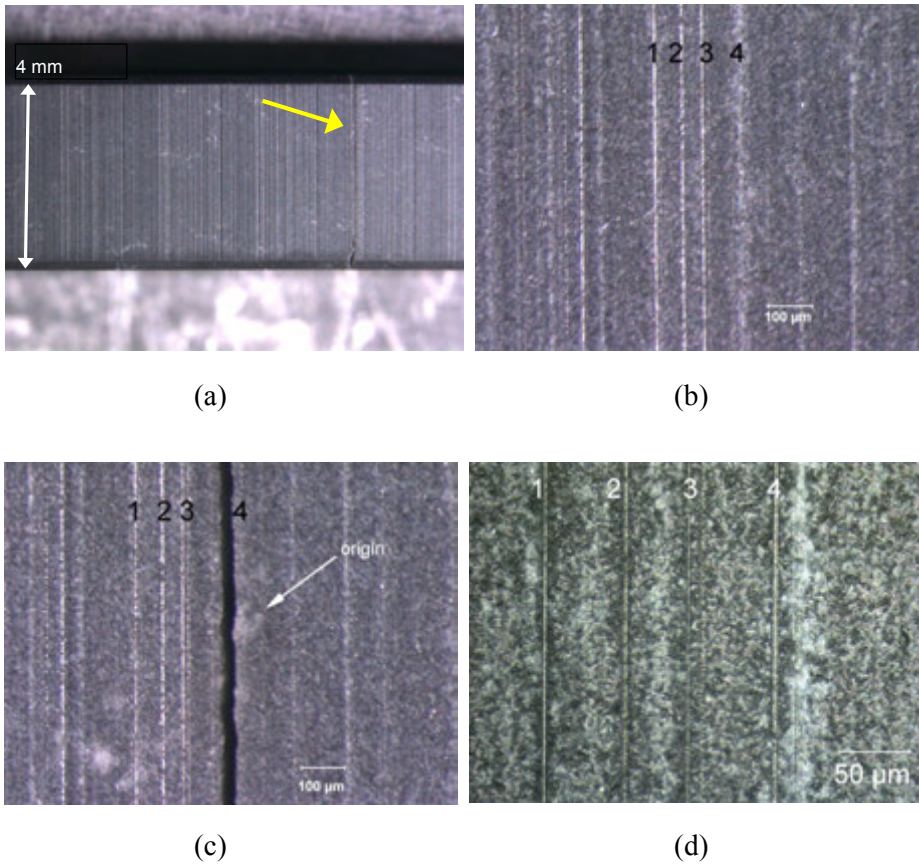

Figure 6.42 *Evidence of "renegade- grit" damage in a 150 grit transversely-ground 4 mm wide silicon nitride bend bar. (a) shows the tensile surface and the plane of fracture marked by the arrow. (b) shows a pattern of four repeating striations that existed periodically (every 2 mm) along the bar length. Every bend bar in the set broke from one of the #4 striations such as shown in (c). (d) is a close-up in this slightly-translucent material, illustrating that considerable subsurface grinding damage occurred beneath striation #4. Figure 6.38e shows a typical fracture surface for this set and shows the damage associated with striation #4.*

Machining cracks often link up with each other or with other materials flaws as shown in Figure 6.43. We tend to focus only on the ones that we see on a fracture surface, and it should be borne in mind that the surface actually contains a complex network of cracks as shown in Figure 6.44.

Figure 6.43 *Machining cracks can link with each other or with material flaws.*

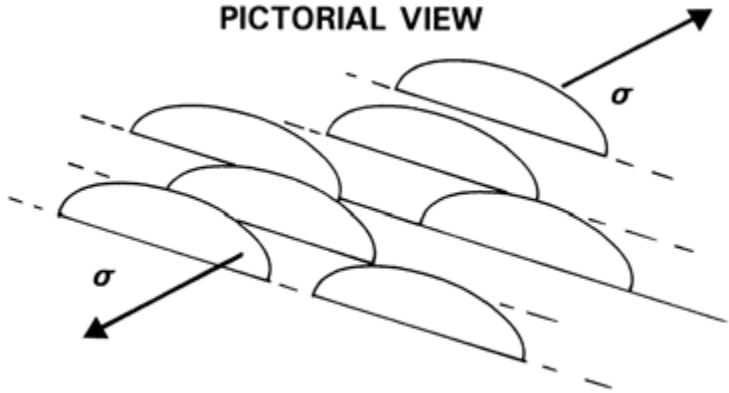

Figure 6.44 *Ground surfaces contain a dense network of machining cracks. This simplified schematic does not show cracks running parallel to the stress axis or lateral cracks parallel to the surface.*

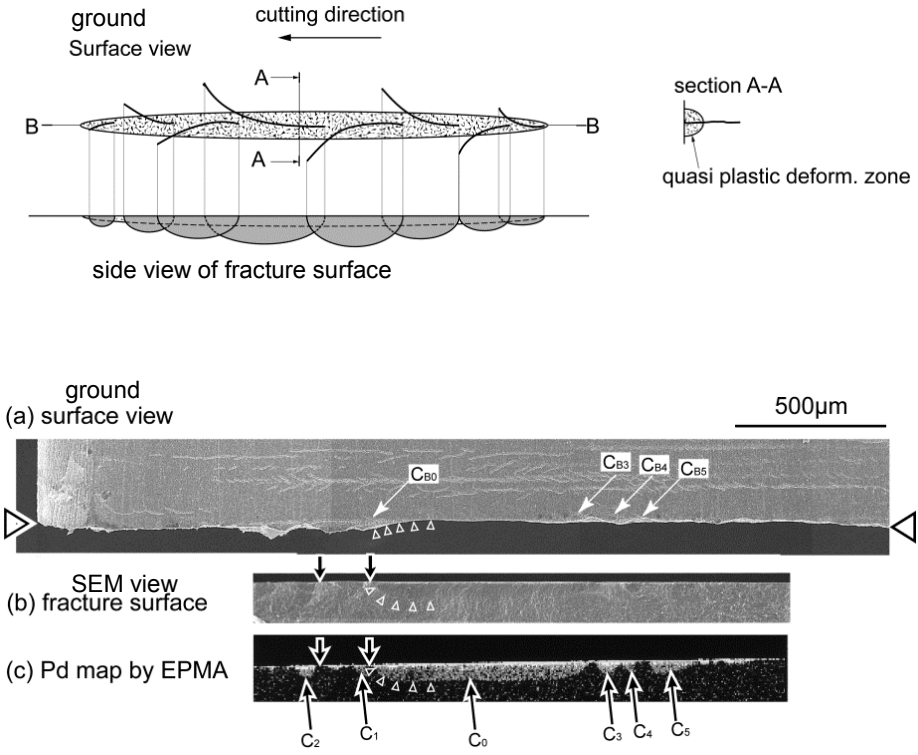

Figure 6.45 *A different pattern of grinding damage termed "herringbone crack pattern" discovered by Kanematsu, Ref. 34. Figure 3.58 shows additional examples. (images courtesy W. Kanematsu)*

Kanematsu[34] identified a "herringbone pattern" of grinding cracks in silicon nitride that has a completely different morphology those shown previously in this chapter. Figure 6.45 shows the cracking is made up of long, closely-spaced (but not touching) parallel cracks that curve off in the direction of abrasive motion. Indeed Figure 3.58 in chapter 3, which showed his innovative dye penetration technique applied to machining cracks illustrated, has several of these. These grinding cracks were in a fine-grained dense silicon nitride ground with 100 grit, 75 concentration resin bonded diamond wheels.

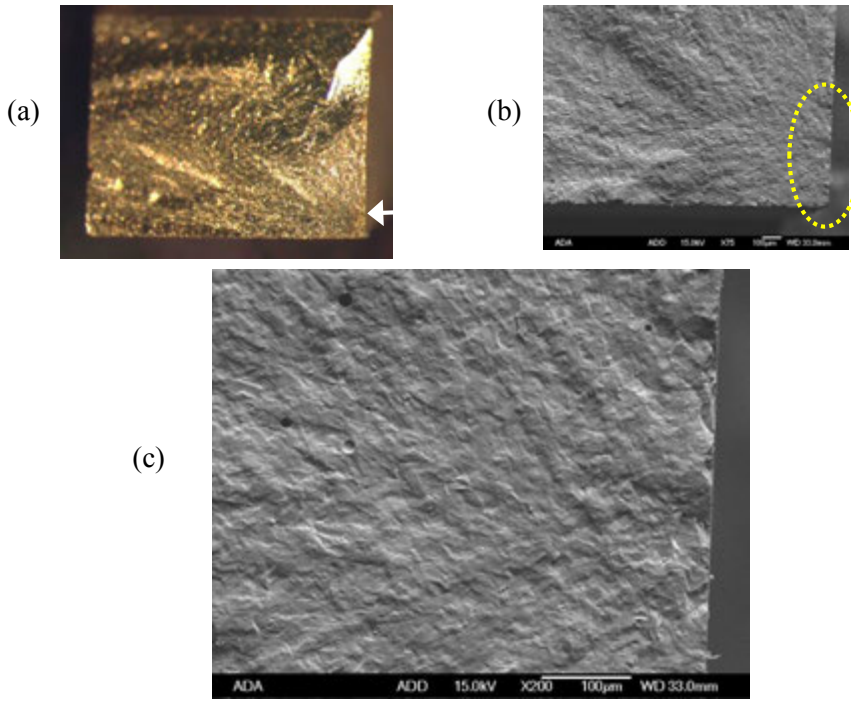

Figure 6.46 *Fracture surface of a feldspathic porcelain bend bar. (a) shows the entire surface of the 3 mm x 4 mm bar with a gold coating. The origin is on the right side wall (arrow). (b) and (c) show SEM images of the damage along the right side wall. Notice the slightly greater roughness of the fracture surface along the right side as compared to the fracture mirror centered on it.*

Figure 6.46 shows an interesting example of parallel grinding damage on the *side wall* of a dental porcelain bend bar. Five of twenty-six test bars broke from such side wall damage.[7] This is unusual since bend bars typically have the four main surfaces ground the same way.

Careful examination of the exterior surfaces of the porcelain bars revealed that the bottom tensile surface had been polished adequately to minimize residual grinding damage. The tensile surface probably had been initially ground in a longitudinal direction. The side walls on the other hand had residual grinding damage from transverse grinding. Although the side walls were also polished, it was not done deep enough and the damage was not completely removed. Most porcelains have a rough fracture surface due to the microstructure, and such distinct fracture mirrors and grinding damage may be obscured. This particular porcelain, Vita Mark 2, is an exception due to its fine-grain size.

6.7.7 Chips

Blunt or sharp impacts or contact loadings near an edge can chip off a piece as shown in Chapter 4. The chip can in turn become a strength limiting flaw on subsequent loadings. Figure 6.47 shows examples.

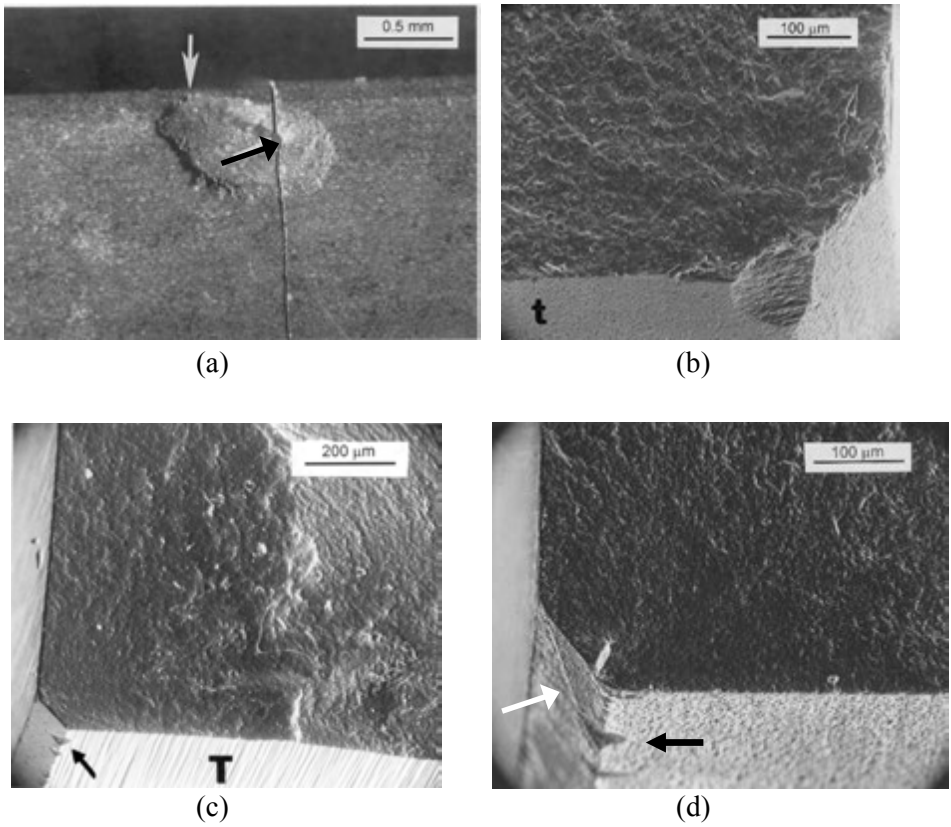

Figure 6.47 *Examples of chips that acted as origins. (a) is an edge chip that acted as the flaw in a bend bar. This view shows the reassembled halves from the side. The top arrow shows the impact point that first created the chip. When broken in flexure, the fracture initiation site was found to be at the small black arrow. Notice the continuity of the chip shape on each side of the final fracture. This confirms that the chip was in the bar to begin with, and was not a secondary fracture. (b) is an edge chip in a sintered silicon carbide bend bar chamfer. (c) and (d) show chips on bend bar chamfers in hot-pressed silicon nitride. Close examination of the chamfers revealed that the grinding was not done longitudinally, but at an angle causing the chips. Notice the striation marked by the white arrow on the chamfer in (d).*

6.8 Other Flaws

6.8.1 Processing and firing cracks in ceramics

Cracks that form in the green state or during firing are quite variable and troublesome. Firing stresses can be very irregular, may be transient, and may depend upon thermal gradients in the kiln or furnace. Firing or shrinkage crack examples are shown in Figures 6.48 - 6.52.

Cracks that *meander, are segmented, and/or are granular on the fracture surface* may have formed in the green state or during firing. Since the body is not fully dense, the fracture surfaces are very granular and do not have the characteristic fracture surface markings. Close examination of interior crack surfaces may reveal thermal rounding of the particles and grains.

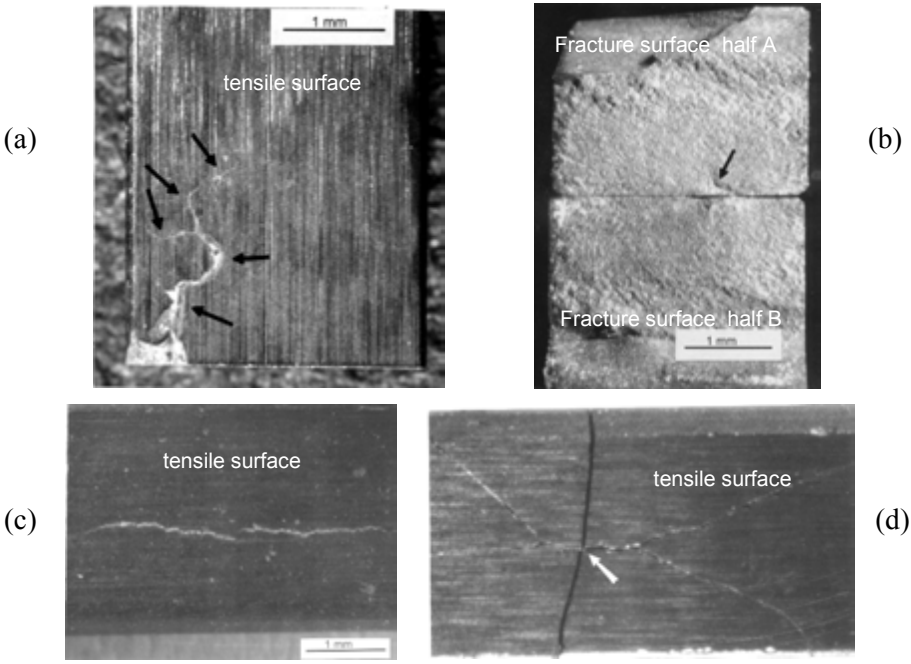

Figure 6.48 *Examples of processing cracks. (a) shows the tensile surface and (b) the fracture surface of two different silicon nitride bend bars which had an unstable boundary phase associated with yttrium silicates. (c) shows a bend bar that had a moderate strength despite a huge processing crack running perpendicular to the tensile axis. The origin was at the arrow. (d) shows another example of a firing crack in a bend bar. The origin is marked by the arrow.*

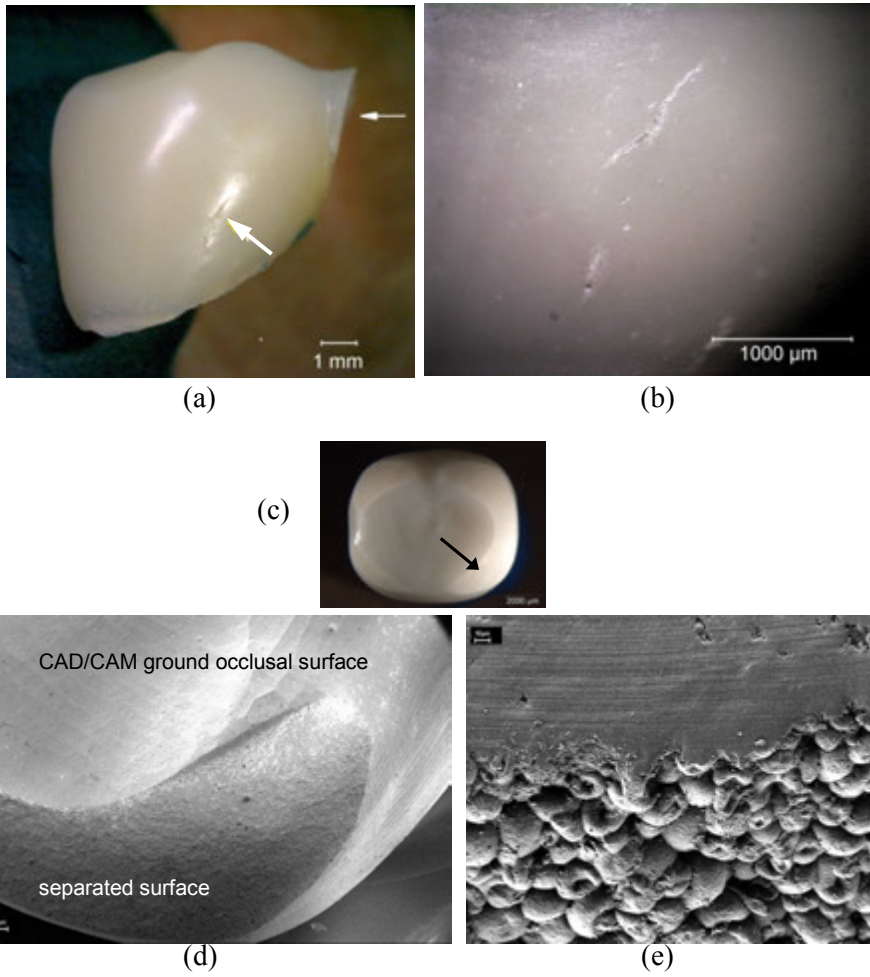

Figure 6.49 *Processing cracks in dental ceramics. (a) and (b) show one tooth of a three-unit alumina dental bridge. (a) shows a frontal (buccal) view of the end unit which fractured at the narrow connection to the next unit (small white arrow). A sintering crack is evident on the face of the crown (large white arrow). It did not cause fracture in this instance because it was in a low stress area. (b) shows a close-up of the processing cracks. (c) – (e) show a broken zirconia crown. A large piece has separated off a cusp on the crown top (occlusal) surface (c) and (d). The apparent "fracture surface" is in fact a huge processing crack. Portions of the crown separated during firing and what is seen are exposed spray-dry agglomerates. The manufacturer claimed the fracture was due to patient overload or faulty installation by the dentist. This was wrong, since the CAD/CAM blank had the processing crack in it. (c - e are courtesy Dr. S. Scherrer and the ETH, the University of Zurich.)*

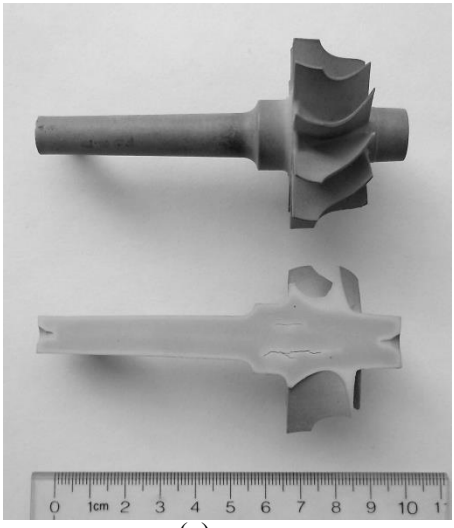

(a)

(b)

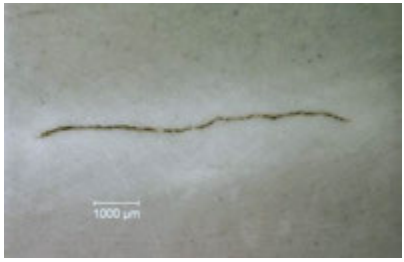

(c)

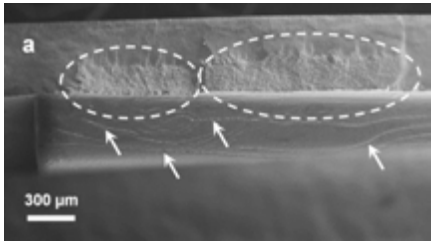

(d)

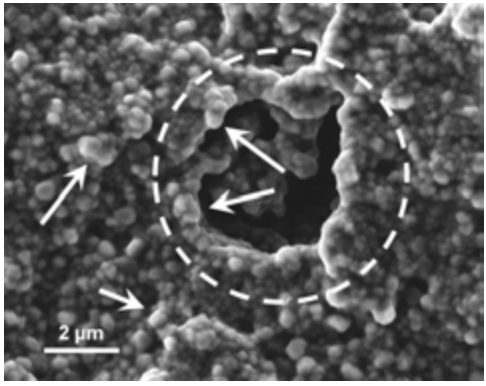

(e)

Figure 6.50 *A prototype Ford silicon nitride automotive turbocharger rotor (a). The material is a reaction-bonded form of silicon nitride and was formed by injection molding. The lower view in (a) shows the interior after sectioning with a diamond cutoff wheel. The close-up views in (b) and (c) show how differential shrinkage during firing caused cracks to form in the thickest portion of the part. Notice the lighter-colored areas of low density that envelop the cracks. (d) and (e) are of a zirconia watch bracelet. (d) is a close-up from inside the processing crack that shows rounded zirconia grains and porosity. (d, e are courtesy J. Kübler)*

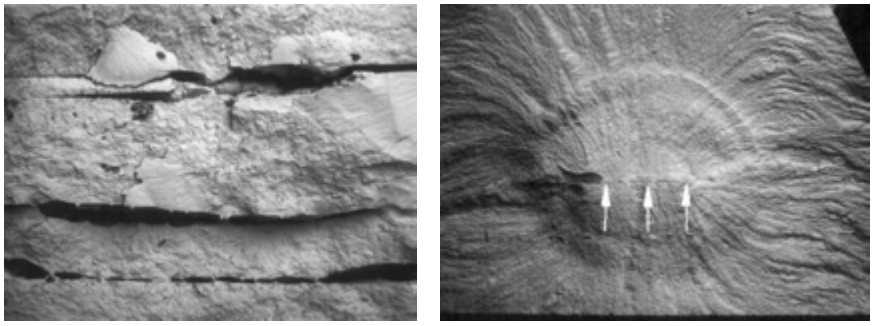

(a) (b)

Figure 6.51 *Delaminations revealed on the fracture surfaces of two tape-cast PZT bend bars. (a) has severe delamination between tape cast layers. (b) was processed much better but still had a very small horizontal delamination (arrows). The curved lines are arrest lines on the fracture surface. (courtesy C. Wu.)*

Delaminations are a particular type of processing crack that are generally planar cracks within a material that arise from separation during green body forming, especially from mold or press release operations. They can also occur between bonded layers of dissimilar material or joints. Delaminations often occur in layered or tape cast structures such as the two lead zirconium titanate (PZT) examples shown in Figure 6.51 from reference 35. Diagnosis and remedial action for processing cracks usually requires close consultation with the processor to review the details of the fabrication and any steps that could lead to differential shrinkage, outgassing, or phase changes. Processing cracks and their effect on overall breakage and fragmentation are also covered in section 4.5.

On the other hand, cracks that are sharp and planar (not rough and granular) may have *popped in during or after cool down from the firing temperatures*. Such cracks may have fracture surface markings such as hackle or arrest lines. The microstructure will look fully dense with no roughness or rounding. Figure 6.52 shows such an example. Sometimes these are termed "thermal cracks."

Varner and Fréchette[36] identified *dunt cracks* in whitewares. These are cracks that from during cool down when quartz particles undergo a sharp change in volume (due to the β - α phase change) when matrix glass is viscoelastic. The dunt crack appears as an atypically shiny transgranular fracture.

(a)

(b)

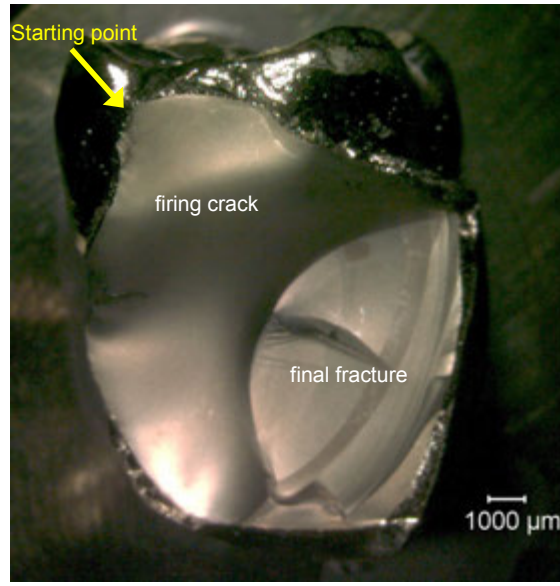

(c)

Figure 6.52. *A sharp firing crack in a dental prosthesis. This is a large single piece zirconia five-unit "telescoping denture," a single-piece insert for a patient with substantial tooth and jaw bone loss. Two implants held it in place at the left end and the fourth tooth in this view. The cantilevered fifth molar tooth broke off after only three months. (a) shows the four surviving units and (b) shows the end tooth that broke off. (c) shows the same piece with a gold coating to make optical examination easier. The origin of the final fracture was the large firing crack that propagated almost two-thirds through the massive zirconia cross section. This sharp, smooth and probably very-tight crack was unnoticed during fabrication and installation in the patient. It started from irregularities in the veneer and core area marked by the yellow arrows. Final fracture occurred on a different plane and in stages as attested to by multiple arrest lines. One normally does not expect fracture in such a massive zirconia piece, but the cantilever loading on the end piece which had an enormous initial crack caused it to break. (courtesy M. Karl, U. Lohbauer, J. R. Kelly) References 37 and 38.*

6.8.2 Artificial or controlled flaws, glasses and ceramics

Sometimes it is advantageous to deliberately create strength-controlling flaws. This is often done in fracture mechanics studies to create a controlled starting crack and then load it to fracture in order to evaluate the material's fracture resistance. Cracks made for fracture mechanics tests are typically called "precracks." Artificial flaws are sometimes made by fractographers to help get acquainted with fracture markings on a new or difficult material. Usually a microhardness testing machine with a Knoop or Vickers indenter is used to make the controlled flaw in a bend bar or disk specimen. The indentation not only makes a crack, but significant residual stresses as well. The residual stress damage zone extends three to five times the indentation depth beneath the surface. The best remedy to deal with the residual stresses is to polish or hand-grind the residual stress damage zone off, leaving behind a stress-free semielliptical surface crack.

The Knoop indenter produces a much more controlled "cleaner" crack than the Vickers indenter. The Knoop indentation procedure for creating controlled flaws is described in more detail in section 7.12. When used to measure fracture toughness with bars in bending, the method is known as the surface crack in flexure (SCF) method. Figures 3.26, 3.56, 5.23, 5.55, 5.57, and 6.53 show examples of Knoop surface flaws that were fracture origins in bend bars.

The Vickers indenter creates a complex "messy" three-dimensional network of median, radial, and lateral cracks. There is much shear faulting and densification as well. Most fracture mechanics experts prefer simple, straight cracks for testing purposes.

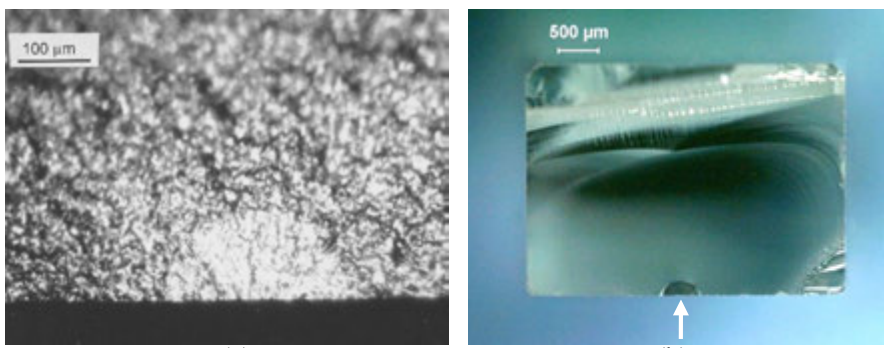

(a) (b)

Figure 6.53 *Examples of nice, clean Knoop indentation flaws. (a) shows a precrack in a sintered alpha silicon carbide bend bar. (b) shows a BK-7 borosilicate crown glass bend bar. (c)-(h) are on the next page*

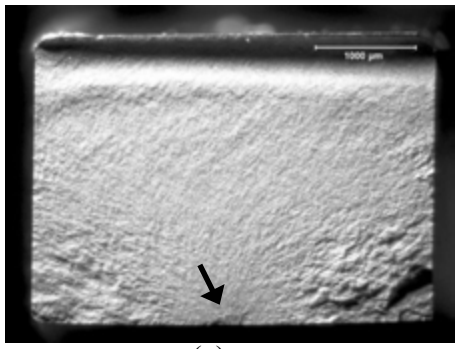

(c)

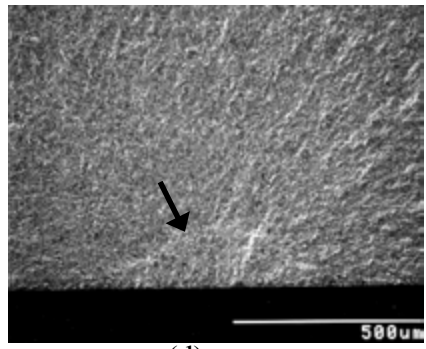

(d)

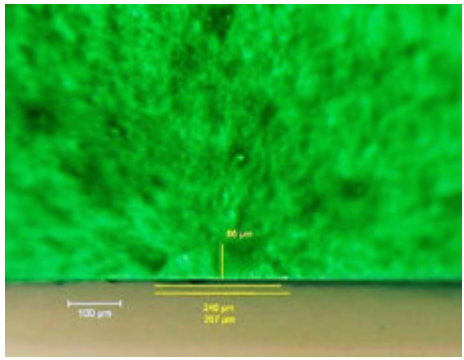

(e)

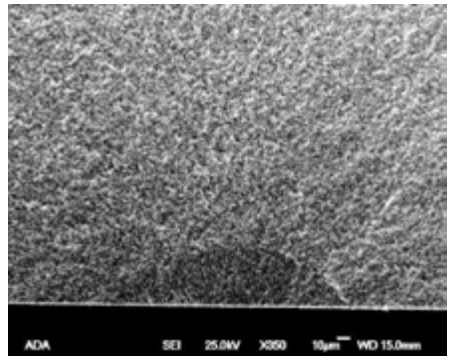

(f)

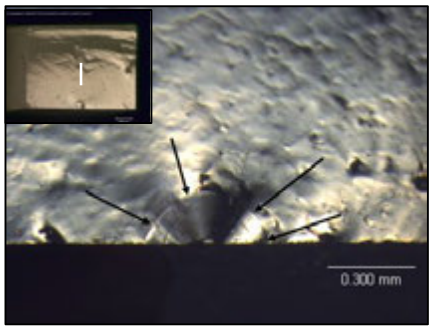

(g)

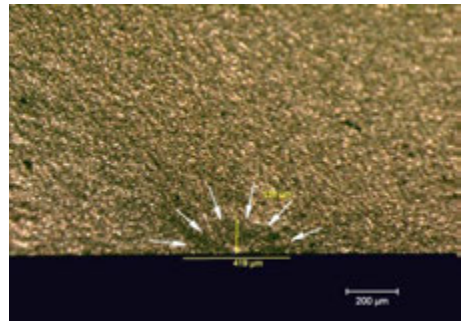

(h)

Figure 6.53 *continued. (c) and (d) are optical and SEM images of cracks in a sintered reaction-bonded silicon nitride. (e)and (f) are an e.max CAD dental lithium dislicate glass ceramic with optical green dye(e) and SEM (f) images of the same crack. (g) is a dental porcelain designed to be fused to zirconia, and (h) is a Vita Enamic ceramic network, resin-infiltrated composite.*

6.8.3 Other Glass Origins

Examples of glass origins have been shown previously in this chapter: nickel sulfide inclusion in Figure 6.17a, scratches in Figures 6.5b, polishing-grinding cracks in Figure 6.28a,b, impact and contact cracks in Figure 6.30, 6.32 and 6.35, and artificial flaws in Figure 6.53. Other flaw types that are common in glasses are shown below. Varner[39] and Fréchette[40] have described the character of flaws in glass.

Flaws from the melt may come in several forms. These flaws are inclusions, pores, or compositional inhomogeneities, but have been given more specific names by the glass community.[39,40,41,42,43] *Devitrification inclusions* or *devitrification stones* (Figure 6.54) can form if the glass crystallizes. *Stones* are grains of unreacted raw material or refractory material broken off the tank or pot walls. Devitrification stones and stones have completely different chemistries and causes, so they should not be confused. Gas bubble origins are termed *blisters* if large, and *seeds* if small. *Striae* are streaks of inhomogeneous, transparent glass. Their refractive index is different than the glass bulk. Very intense striae are termed *cords* and may appear as ropes or strands such as shown in Figure 6.56.

Figure 6.54 *Unusually large (≈ 1 cm) glass devitrification inclusions with a blossom-like structure as well as smaller seed bubbles. (Specimen courtesy of J. Varner and V. Fréchette*)

(a)

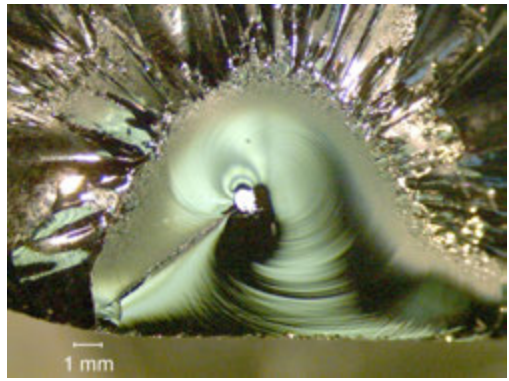

(b)

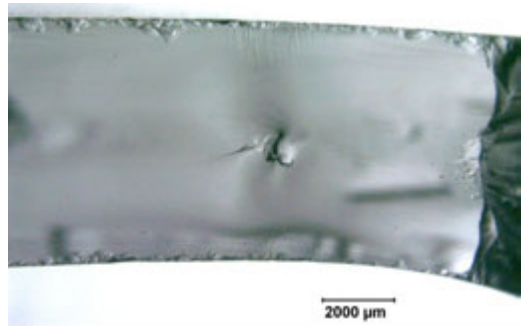

(c)

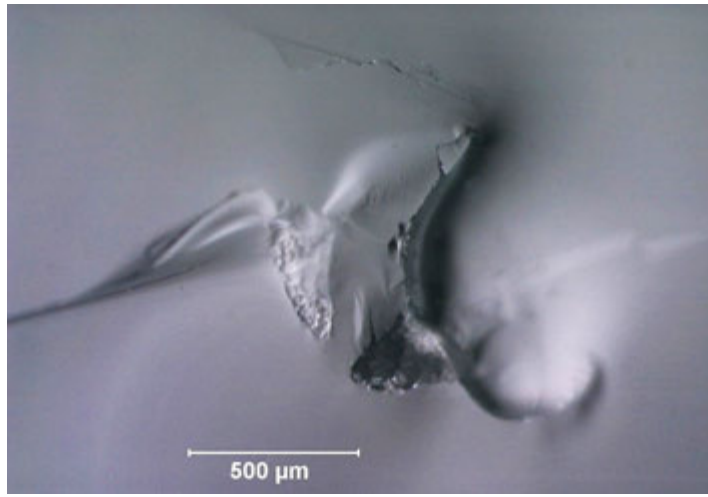

Figure 6.55 *Stone origins exposed on glass fracture surfaces. (a) is an example in a large-screen television picture tube and broke from transient thermal stress during manufacture. (specimen courtesy of J. Varner and V. Fréchette). (b) and (c) show a stone in the middle of the wall of a heat-strengthened consumer glassware.*

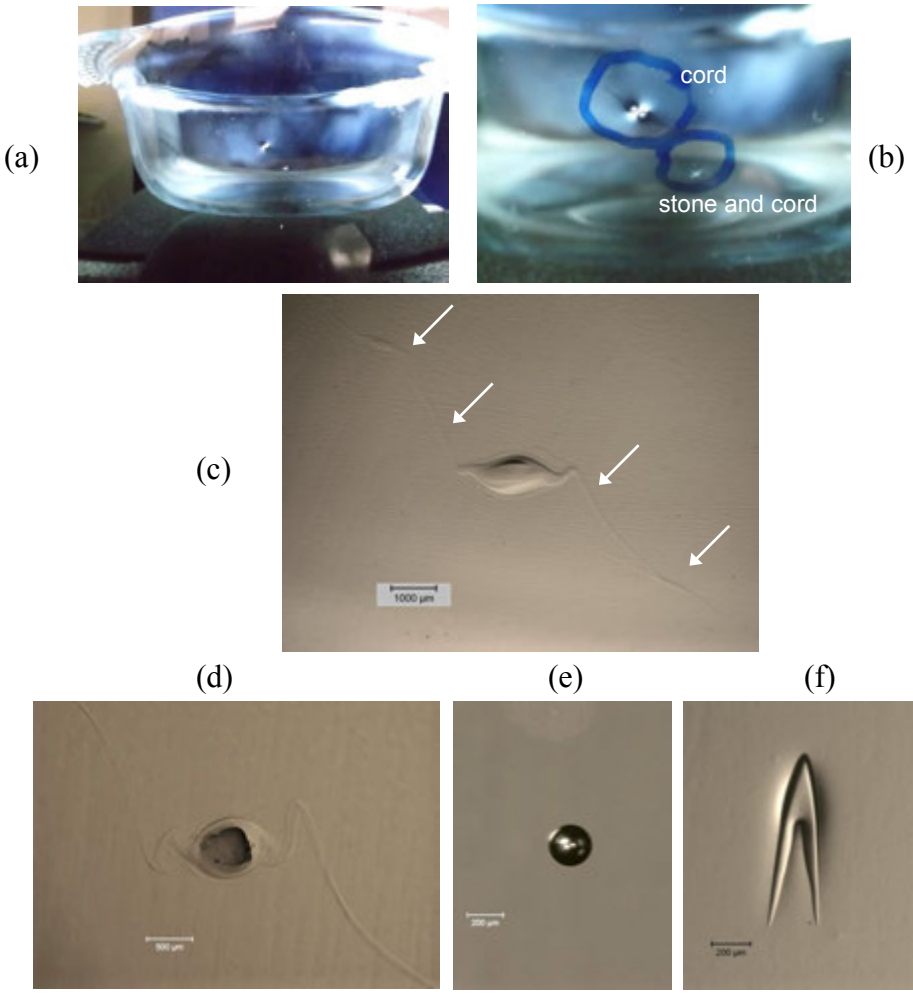

Figure 6.56 *Flaws in a borosilicate glass cookware. (a) – (c) show a chord. (crossed polarizers highlighted the internal strains in views (a) and (b). (c) is a close-up of the cord with a mix of transmitted and reflected illumination. The striae - stringers are marked by arrows. (d) shows a close-up of a stone with striae - stringers. (e) is a seed (a bubble). (f) is an odd internal hairpin flaw.*

Preston[42] described *heat sleeks*, which are burnished streaks of glass where a metallic polishing or grinding wheel makes direct rubbing contact with a glass surface if the loose abrasive and water are inadvertently squeezed out. The glass locally reaches a high temperature and develops a number of hair-like fissures entering the glass normally to the surface and penetrating only a short distance. Surface contact damage flaws were previously presented in section 6.7.4. Sharp contact damage sites are *pecks.*

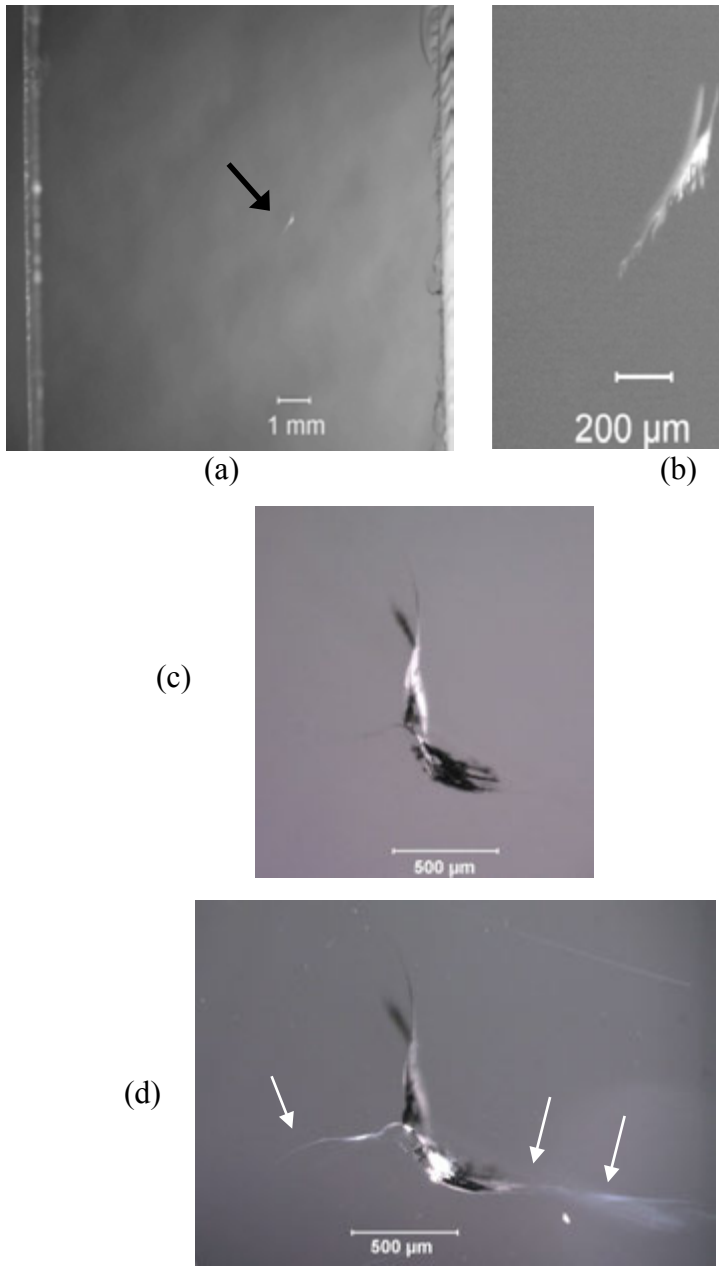

Figure 6.57 *Chill check cracks on the outer surface of unbroken glass plates. (a) and (b) show the same chill check. (c) and (d) show two close-up views of another chill check. Note how different illumination can dramatically alter the appearance and apparent extent of the flaw. Much more of the cracking is evident in (d). (Specimens courtesy V. Fréchette and J. Varner)*

Figure 6.57 shows *chill checks,* a pernicious flaw that is often very difficult to detect. A chill check is a small wavy and tight crack that is introduced into a hot glass surface by localized contact with a cooler object. Thermal stresses create the crack, but since the contact and thermal stresses are localized, the cracks are small. Glasses with high thermal expansion coefficients are most susceptible. The cracks often are difficult to detect in an unbroken component and require lighting at just at the right angle. Sometimes transmitted illumination is effective. If chill checks are suspected, then the piece or the illumination source should be manipulated a variety of ways and angles so as to try to get a momentary reflection from the crack. Chill checks form quickly and close back up very quickly. They may close so tightly (less than the wavelength of light) that they are not discernable. Nevertheless, some portions of the crack may have captured small amounts of gasses or water molecules that create slight opening pockets that are just barely detectable. These are often brightly colored, since they refract the light and may only be detectable from certain viewing angles. Once a momentary reflection is detected, the fractographer can zero in on the flaw site. Often the full extent of the crack is not visible because the crack is so tight. Fréchette[40] observed that chill checks are hard to characterize since mechanical effects can also occur at the contact site. If a glass object breaks from a chill check during subsequent use and stressing, then it is likely the origin site will be irregular and may not be recognized as a chill check without examination of the outer surface. This underscores an earlier recommendation: if an origin on a fracture surface is located at the surface of the component, then it is prudent to examine the exterior surface of the part as well as the fracture surface. Varner[44] has compared features of chill checks and impact origins. Chill checks are curved and not flat, often have no visible outer surface damage, and, once the flaw is exposed on a fracture surface, have few markings on the flaw itself other than some twist hackle. Impact cracks are semicircular and are straighter, and the outer surface has chipping and lateral cracks. Once exposed on a fracture surface, the impact flaw exhibits tertiary Wallner lines.

Polishing flaws from a loose abrasive rolled across a surface while under load can leave a variety of damage including indentations, scratches, Hertzian full or partial ring cracks and gouges according to Fréchette.[40] The crack depths are typically four to five times larger than the particle diameter. They often are very elongated along the surface. Polishing, lapping or grinding glass can create are *sleeks* which are fine, scratch like, smooth-boundary imperfections usually caused by a foreign particle during polishing.[45]

Chatter marks such as shown in Figures 6.58 and 6.59 often are clues to contact cracks underneath. The periodicity is a manifestation of vibration or a stick-

slip interaction when a contacting object slides over the surface. Fracture often starts from the first or last chatter crack in a series. Abrasion tracks, which often occur around the bottom rim or sides of a glass vessel, are also vulnerable sites for localized contact damage as shown in Figure 6.58. Polishing, lapping or grinding glass can create miniature crack patterns of chatter cracks. Preston[45] and Ghering and Turnbull[46] showed numerous examples and correlated them with the forces, the surface lubrication conditions, and the abrasive or contactor types. Preston showed that a blunt contactor or ball dragged across a surface creates small partial cones cracks behind the contactor. The cracks are created by tensile stresses behind the ball or contactor as it moves and the cracks are bowed in the direction of the contactor movement such as shown in Figure 6.36. In sharp contrast, a rolling ball creates arc cracks that bow in the opposite direction. They arch towards the direction from which the ball came.[45]

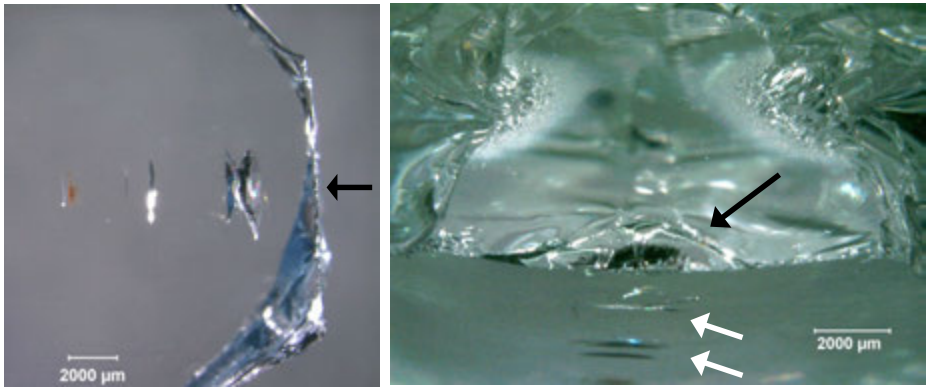

(a) (b)

Figure 6.58 *Chatter cracks from an object that contacted and slid across the surface of a heat-strengthened soda lime glass kitchenware. (a) shows the outer surface. The black arrow points to the fracture surface and the origin site. (b) shows the specimen tilted to show the origin crack on the fracture surface (large black arrow) and the other chatter cracks on the outer surface (white arrows).*

(a)

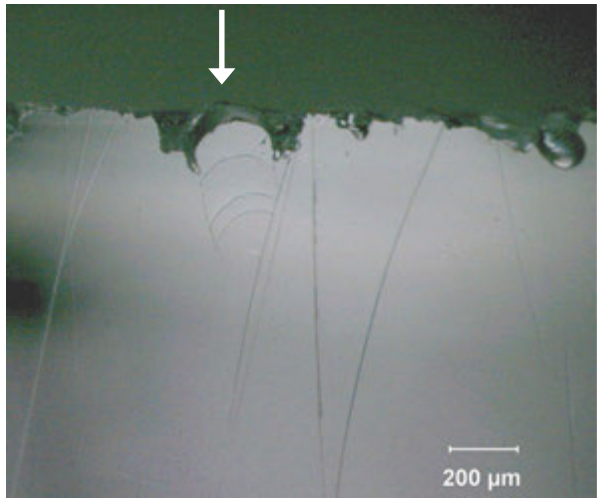

(b)

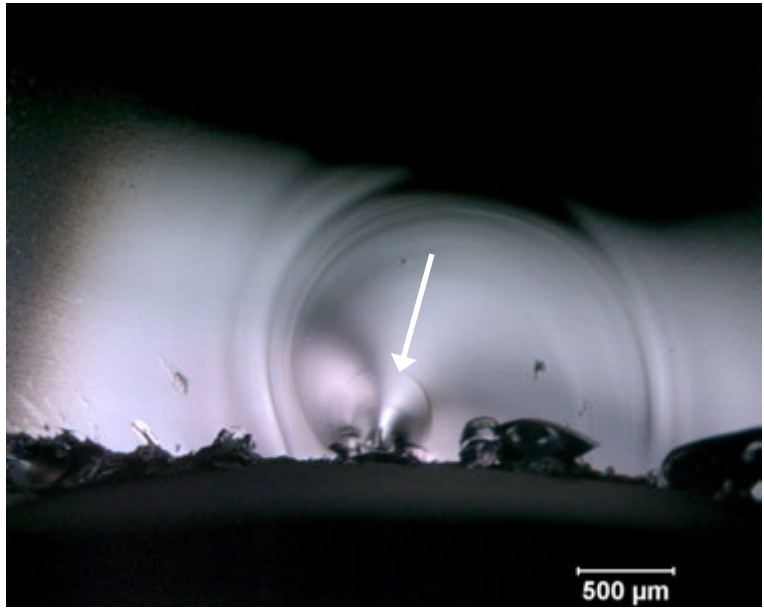

Figure 6.59 *Very tiny chatter cracks from a small object that contacted and slid across the surface of a heat-strengthened soda lime glass kitchenware. (a) shows the outer surface with an assortment of common scratches and edge chips, some of which are secondary edge chips after the main fracture. The arrow points to the exact origin site which is seen to be one of a series of curved chatter cracks. (b) shows the fracture surface. The multiple secondary edge chips may confuse interpretation, but the Wallner lines and a faint pop in arrest line are centered on the chatter crack (arrow).*

(a)

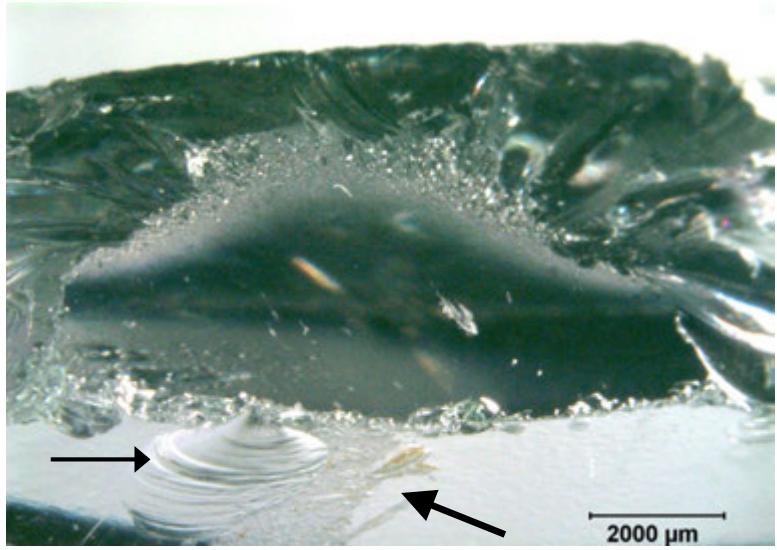

(b)

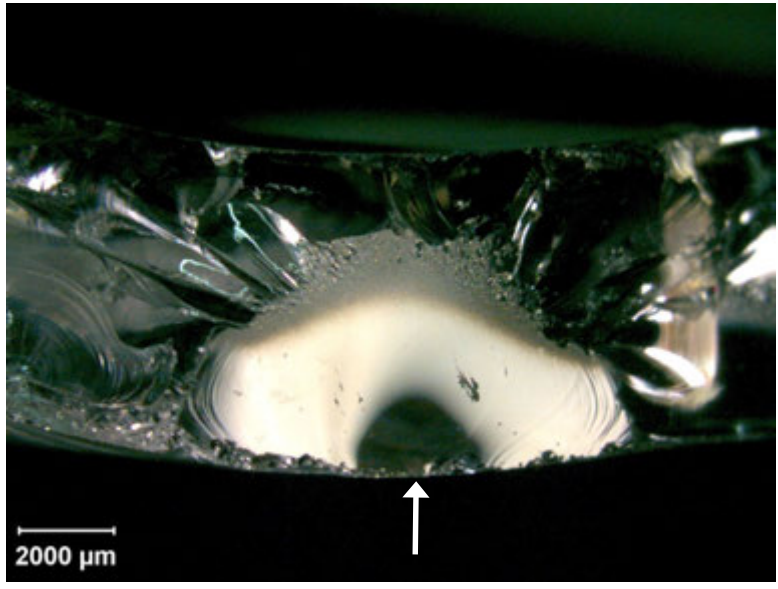

Figure 6.60 *Surface abrasion can create subsurface cracks. (a) shows a piece from a broken heat-strengthened kitchenware tilted back to show the fracture surface and the elongated mirror and the outer surface with the abrasion track (large black arrow). Incidental secondary handling edge chips on the left (smaller black arrow) came from handling after fracture. (b) is the fracture surface showing an elongated mirror and the origin (white arrow). The origin region is dark due to a slight curvature of the fracture mirror surface.*

6.9 Fracture Oddities

Innumerable other irregularities can act as strength-limiting flaws. The fractographer should expect the unexpected. Rice[47] described cases of ball mills, thermocouple beads, insect carcasses and feces, dandruff, and hair as flaws. Alcock and Riley[48] analyzed dust particles that are found in ceramic processing environments. Figure 3.19 showed a hair or piece of lint, a surprisingly common fracture origin type in laboratory-prepared cast resin composite specimens. Figure 6.61 shows some other unusual examples.

The author once had a surprising experience with very bright *retroreflective flaws* when using a stereoptical microscope with dental highly-filled resin-matrix bend bars. Slight adjustments to the lighting angle eliminated the intense reflections. Some of the fracture origins were glassy inclusions or agglomerates of glassy filler particles that strongly reflected the incoming light. This was just as disconcerting and surprising as when one shines a flashlight at the retro-reflective eyes of a cat. Retroreflective glass beads are used with roadway marker paints to improve their visibility. Regrettably, the author did not take photos at the time of examination.

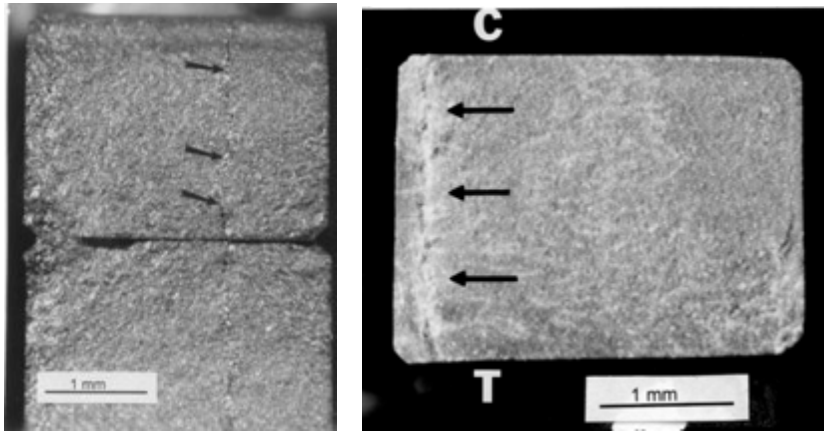

(a) (b)

Figure 6.61 *Unusual fractures. (a) shows a vein of silicon that was the strength limiting flaw in a siliconized SiC bend bar. This probably was caused by silicon infiltration of a seam or crack in the green body. (b) shows the fracture surface of a silicon nitride that had an unstable yttria silicate boundary phase. Phase changes distorted the bar shape from its original rectangular shape. Fracture occurred from the crack marked by arrows. T and C denote the tension and compression sides of the bend bar.*

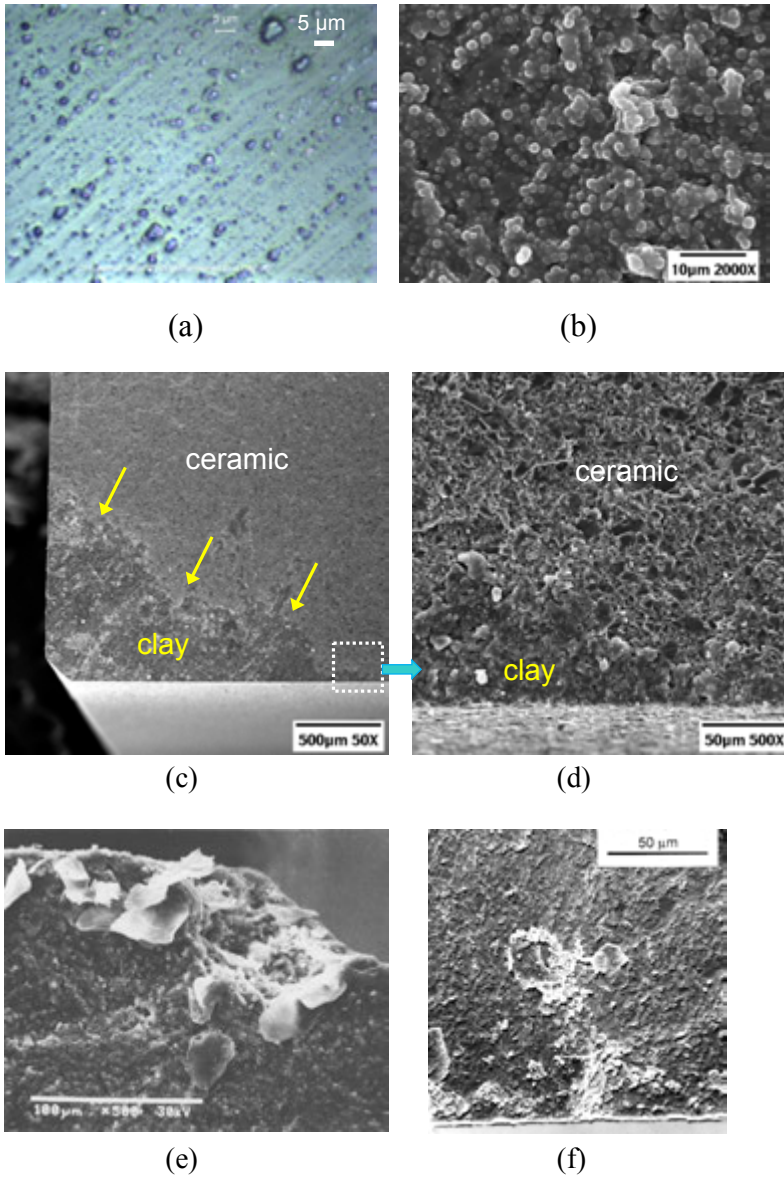

Figure 6.62 *Common contaminants. (a) shows a blue clay smeared on a glass microscope slide as photographed on an optical microscope. The tiny particles and grease smear are evident. (b) shows an SEM image of the clay. (c) shows a fracture surface of an fine-grained alumina bend bar with clay swiped across the lower left corner (arrows). The boxed area is shown enlarged in (d). (e) shows human skin (courtesy A. Pasto). (f) shows an indeterminate contamination on a sintered silicon carbide bend bar.*

6.10 Contaminants

Every care should be taken to avoid contaminating the fracture surface. This is especially true during preparation of the specimens for SEM examination. During an optical examination, cleaning is not too difficult, but it is a different story if the specimen is being examined in the SEM. Once a specimen has been gold coated and is in the SEM, it can be disappointing to realize the flaw is masked by contamination or that a photo of the origin has distracting debris in the vicinity. Extraction, recleaning, and preparation are time consuming and frustrating. Sometimes contaminants can be recognized if they appear to sit up on top of the fracture surface and are obviously not part of the material. This criterion is by no means perfect, however, as many contaminants get into the fracture surface crevices and blend in diabolically well. As noted previously in Chapter 3, modeling clays are especially pernicious since they are fine, blend in well on the fracture surface, adhere extremely well, and are next to impossible to clean off. An EDX analysis of clay contamination on a fracture surface revealed aluminum, silicon, and titanium. Figures 6.63 – 6.64 illustrates some common contaminants and how they look in the SEM.

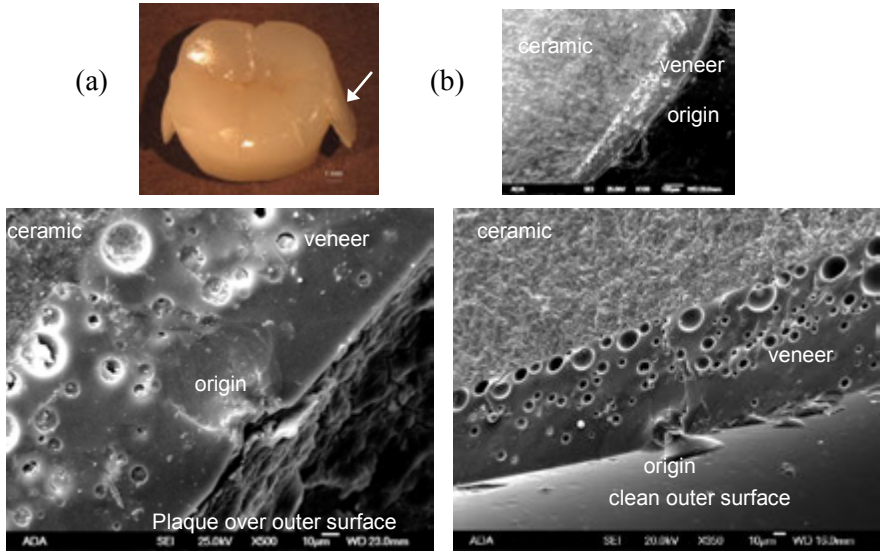

Figure 6.63 *Dental plaque is a common contaminant on ceramic restorations. (a) shows the broken middle ("pontic") piece of a lithium disilicate bridge that broke after 7 weeks in vivo. (b) shows the overall fracture surface. (c) and (d) show the origin site before and after cleaning to removal plaque. Plaque can be removed with bleach as described on page 3-6. See Figure 6.74 for additional images of this bridge.*

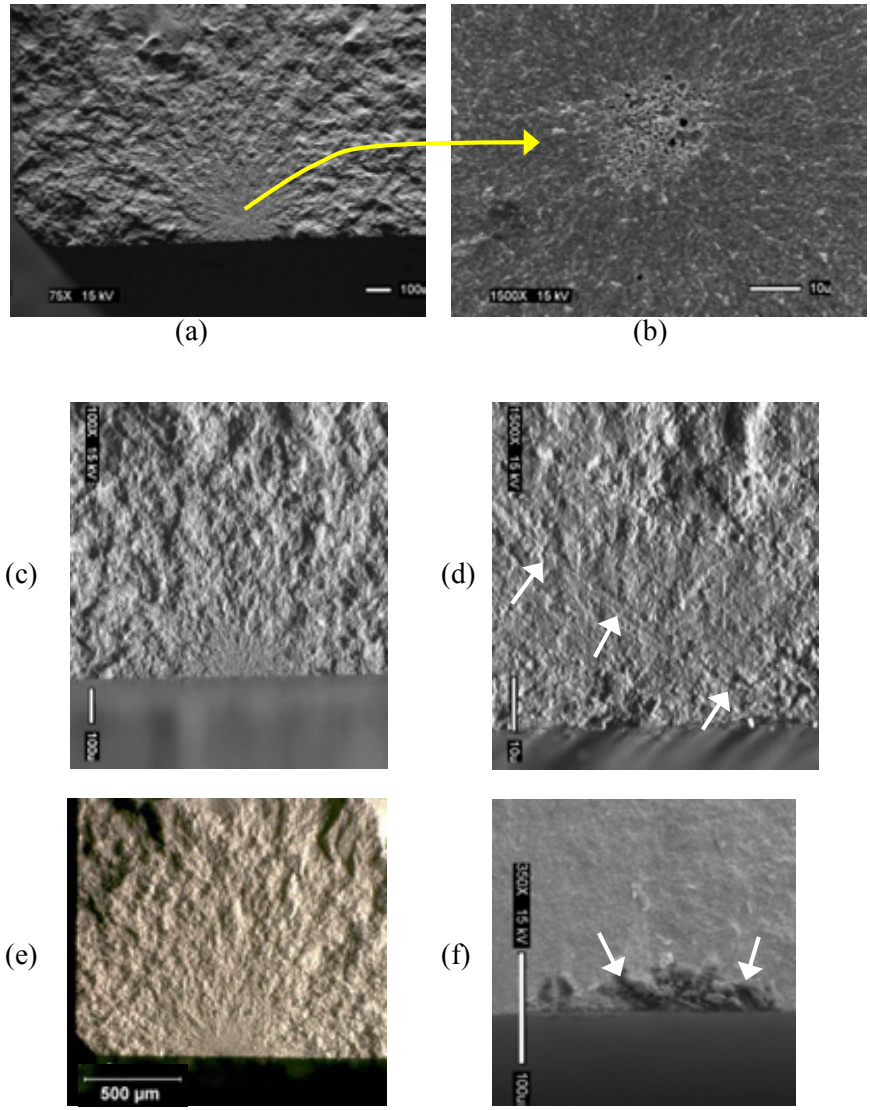

Figure 6.64 *Contaminants in 3Y-TZP bend bars. (a) and (b) show a clean fracture with a well-defined fracture mirror and the common flaw in this material: a pore or porous region origin. (c) and (d) show clay smeared over the fracture surface and fracture mirror in another specimen. Notice the parallel smear traces (arrows) from lower left to upper right in (d). The clay is not evident in the low magnification image of the mirror, but it covers the origin in (d). It is possible the wrong end of the bend bar initially was put into mounting clay! (e) and (f) show a mirror with an unknown contaminant covering the origin (arrows). (all courtesy of J. Quinn)*

6.11 Combined or Hybrid Flaws

Sometimes flaws may link up or there simply may be side-by-side flaws at a fracture origin such as shown in Figure 6.65 and 6.66. When such mixed cases arise, some judgment is required as to which origin is primary. ASTM C 1322[49] suggests several options for reporting such hybrid flaws. For example, if one origin type is primary, then a reporting code may list it first with the secondary flaw separated by an ampersand (&). For example, Figures 6.66a, b show P & LG denoting the origin is primarily a pore, but with one or more associated large grains.

In other cases two small flaws can link to form a strength limiting flaw. A plus sign may be used to indicate that these origin types linked together to limit the strength of the ceramic. For example, P + MD indicates a pore combined with machining damage. Origins can be difficult to characterize if they have mixed attributes. For example, porous *regions* often have large pores associated with them (Figure 6.66e). References 50, 51, and 52 also discuss flaw linking.

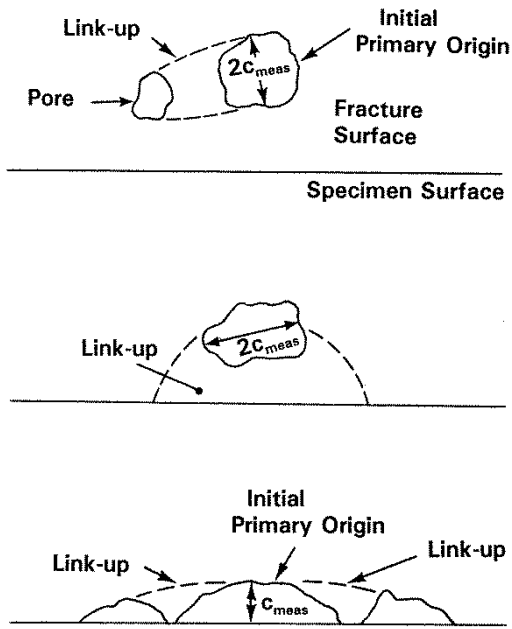

Figure 6.65 *Flaws may link up.*

(a)

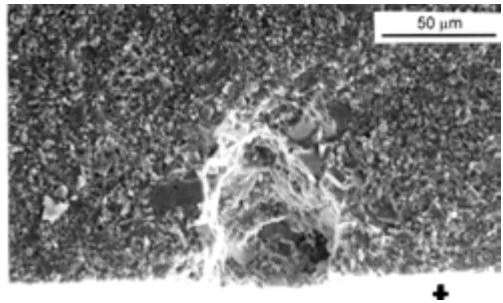

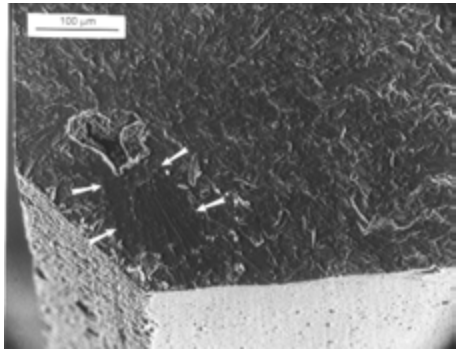

(b)

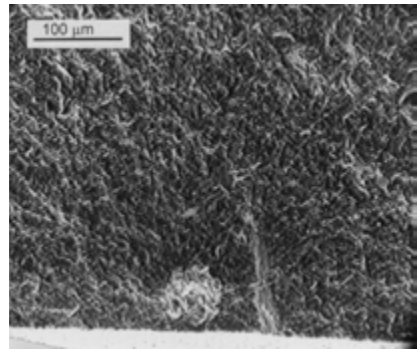

(c)

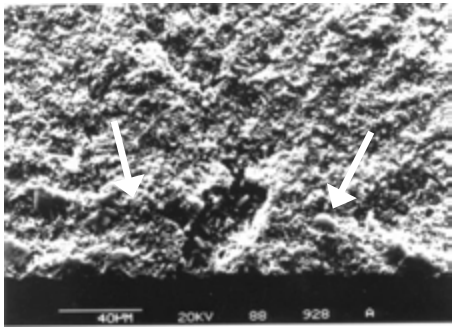

(d)

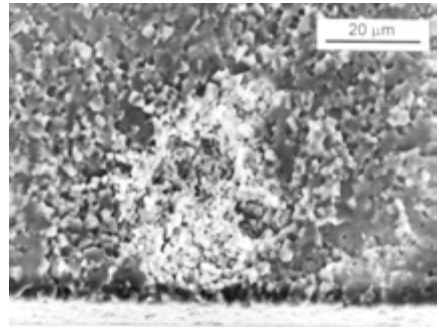

(e)

Figure 6.66 *Combined (hybrid) flaw fracture origins (a) shows a flaw in a sintered 99.9 % alumina that can be described as primarily a pore, but with some large grains (P & LG). (b) is a pore/large grain (P & LG) combination in a sintered alpha silicon carbide bend bar. Note the good quality of the chamfer. Edge damage was not a factor in this case. (c) is a combination of an agglomerate and a large grain (A & LG) in sintered silicon carbide. (d) is a surface grinding crack that linked with a pore in a sintered silicon nitride (P + MD). (e) shows a flaw in a sintered alumina could be described as either a porous region or a pore.*

6.12 Baseline Microstructure Origins

As fabricators improve materials by careful process control and eliminate large abnormal flaws, ceramics will break from origins that are part of the ordinary microstructure. Figure 6.67 illustrates the concept and Figure 6.68 shows an example. Once the inclusions are eliminated, grains from the large end of the grain size distribution become the strength-limiting flaws. The materials processor does not believe these are flaws, but the fracture mechanics expert does. Rice[47] described such origins as "mainstream microstructural features." A shorter descriptor might be "baseline microstructure" as in: "the origin flaw was a large grain from the "baseline microstructure."

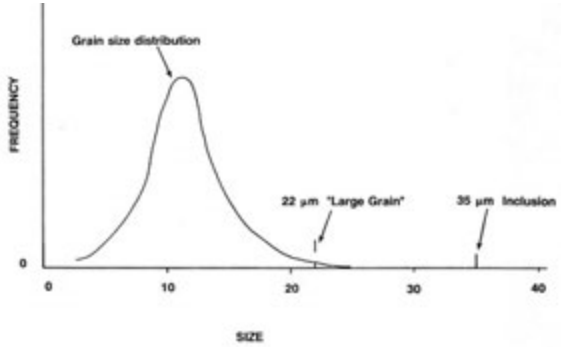

Figure 6.67 *Careful processing may eliminate severe flaws such as inclusions or gross pores. In the absence of such flaws, the material may fail from "baseline microstructure" origins.*

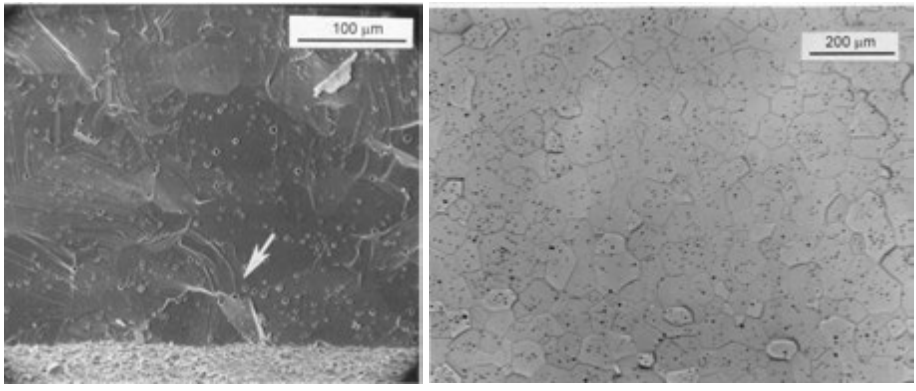

(a) (b)

Figure 6.68 *Baseline microstructure flaw in a sintered aluminum oxynitride four-point flexure bar. (a) shows a single grain that was the fracture origin. The origin in this case may actually be the grain boundary around the grain. (b) shows a polished section view of the microstructure.*

6.13 Geometric Sharp Points or Cusps

Sharp points are extremely vulnerable to crack pop-in at very low stresses during fabrication or subsequent handling. Once the part is put under stress, these pop-in cracks can propagate to fracture. There may not necessarily be a material flaw as a starter. Sometimes an arrest line will be detected at the end of the pop-in crack, but often the final plane of fracture is identical to the initial pop-in crack plane, and the latter will not stand out. Figures 6.69a-d show exceptionally thin cusps between etch pits in theta strength specimens.[53]

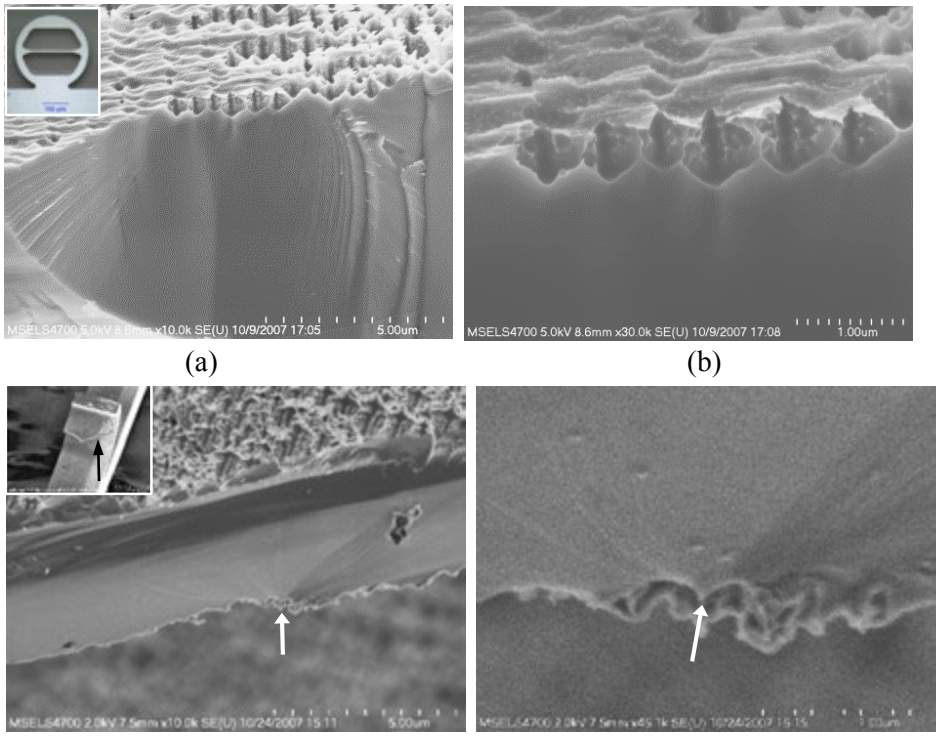

Figure 6.69 *Small cracks may pop-in from sharp points or cusps. The insert of (a) shows a miniature (300 μm) silicon theta strength-test specimen. A force applied to the top of the ring causes the middle web to stretch and break. (a) shows the fracture mirror around the surface pits fracture origin. The pits are caused by the deep reactive ion-etched (DRIE) processing. Sharp cusps between the pits are an easy path for tiny micro-cracks to pop-in and link. (c) and (d) show another theta specimen. The insert in (c) shows the fragment and the origin location. The hackle lines in (d) indicate fracture started at a single sharp cusp between two pits. The cusp is less than 50 nm in size and may be the smallest fracture origin ever recorded.*

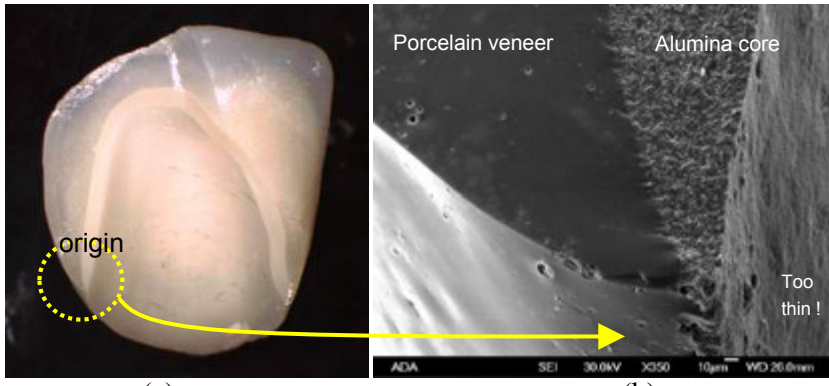

(a) (b)

Figure 6.70 *A "feather tip" margin in an alumina dental crown that broke in a patient's mouth ("clinical 22"). The margin is only 30 μm wide and was extremely vulnerable! Hoop stresses caused fracture from some of the tiny flaws at the margin tip. (crown courtesy of M. Øilo)*

Figures 6.69 shows a sharp "feather-tip margin" origin in a dental crown. The margin of this crown is much too thin. This type of margin is used by some dentists since less reduction of the tooth is needed and the crown blends into the gum line very well. Such practice is unwise for all-ceramic crowns. Figure 10.25g shows another crown with a margin pop-in crack at a feather tip.

Not all sharp point/cusp origins are in small pieces. The author once found such an origin in a ~ 1 m large SiC honeycomb structure for a space mirror.

6.14 Partially-Exposed Flaws

Flaws may not necessarily be oriented so that they are perpendicular to the principle tensile stress. Only a portion of a flaw may be exposed on a fracture surface as shown in Figure 6.71. The cone cracks of Figure 6.32 are examples.

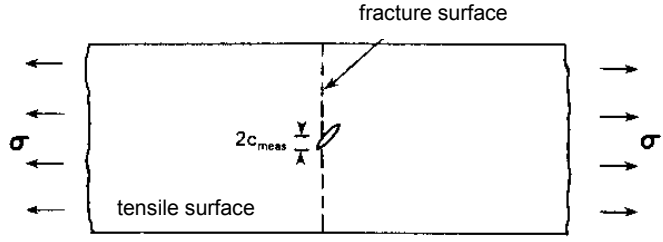

Figure 6.71 *The flaw may not be fully-exposed on the fracture surface.*

6.15 Glaze Flaws

Glazes and veneers are glassy and have low fracture toughness and resistance to fracture. A crack can form in the vulnerable glaze and then propagate into the remainder of the component. Figures 6.72 – 6.74 show some examples for three clinical dental fractures. Excessive mismatch in the thermal expansion coefficients of the glaze and the body can cause cracking, such as shown in Fig. 6.72. Glaze or veneer cracking formed by tension is called "crazing." Sometimes excessive porosity can occur at a boundary, and can be the strength-limiting flaw as shown in Figure 6.73.

(a) (b)

Figure 6.72 *Glazes can be preferred sites of fracture initiation. This was an in vivo broken three-unit zirconia bridge (courtesy T. Kosmac) with a crazed veneer probably from a mismatch of the veneer type to the ceramic. Fracture started on the plane on the left insert marked by the yellow arrow.*

(a)

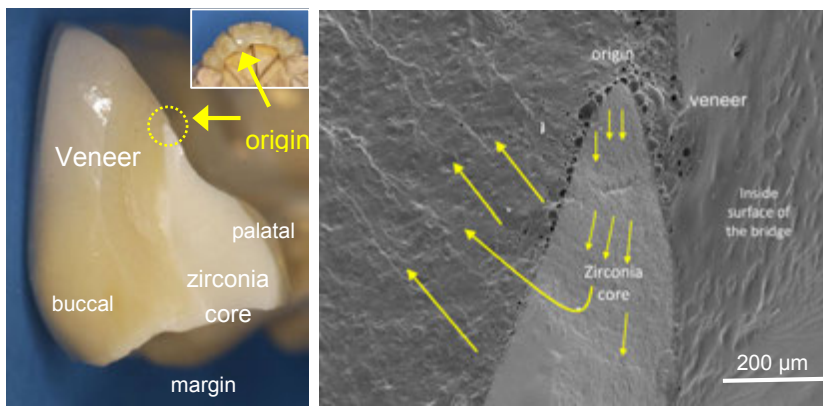

(b)

Figure 6.73 *Glaze interfaces can be preferred sites of fracture initiation. This is an in vivo broken six-unit zirconia bridge with a poor design. The origin is the pore cluster at the interface between the veneer and core apex. (images courtesy U. Lohbauer and S. Scherrer)*

Excessive compression in a glaze can cause cracking called "shivering." Buckling of the outer layer fragments, often at an edge or rim, can cause a piece to detach.

Krohn *et al.*[54] showed pore and pigment aggregate fracture origins in enamel layers that were applied to float glass. Kobayahsi *et al.*[55] showed excellent images of fracture origins that were a series of bubbles at the boundaries between an alumina porcelain and a glaze.

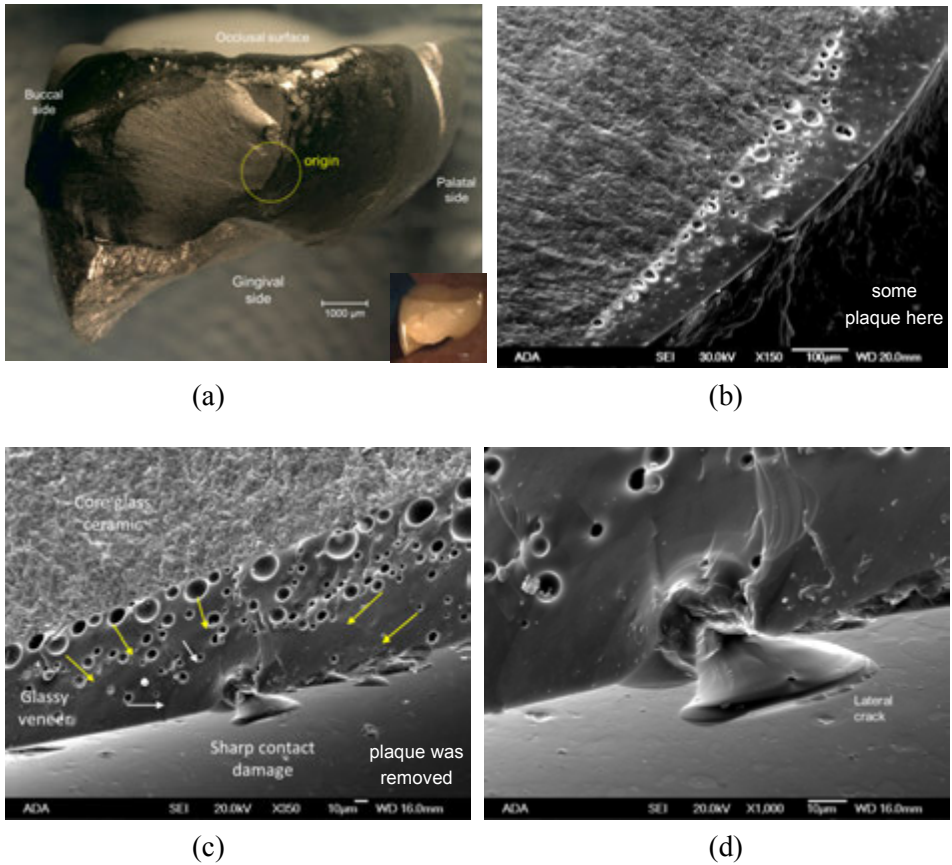

Figure 6.74 *A gold-coated lithium disilicate glass ceramic bridge pontic unit (courtesy S. Scherrer). It broke in vivo on the palatal side of a connector. The origin was a sharp contact damage crack in the vulnerable veneer. Notice the arrest lines marked by arrows in (c), the helpful wake hackle lines from the bubbles in the veneer seen in (c) and (d), and even the concentric tertiary Wallner lines typical of impact in (d). See also Figure 6.63.*

6.16 Microfault Pockets

Even if a fracture origin site can be found, there may not be an obvious flaw at the origin. Subtle porous regions or grinding damage crack at the surface can possibly be present but not detectable. This dilemma is more likely to occur with coarse-grained ceramics, porous ceramics, and heterogeneous ceramics, wherein a flaw could "hide" against the background microstructure.

There is another possibility why a discrete flaw may not be detectable at an origin site: There may not be one. Emphasis in this chapter up to this point has been on flaws that are discrete irregularities larger than the baseline microstructure. Alternatives are illustrated in Figure 6.75. Fracture origins

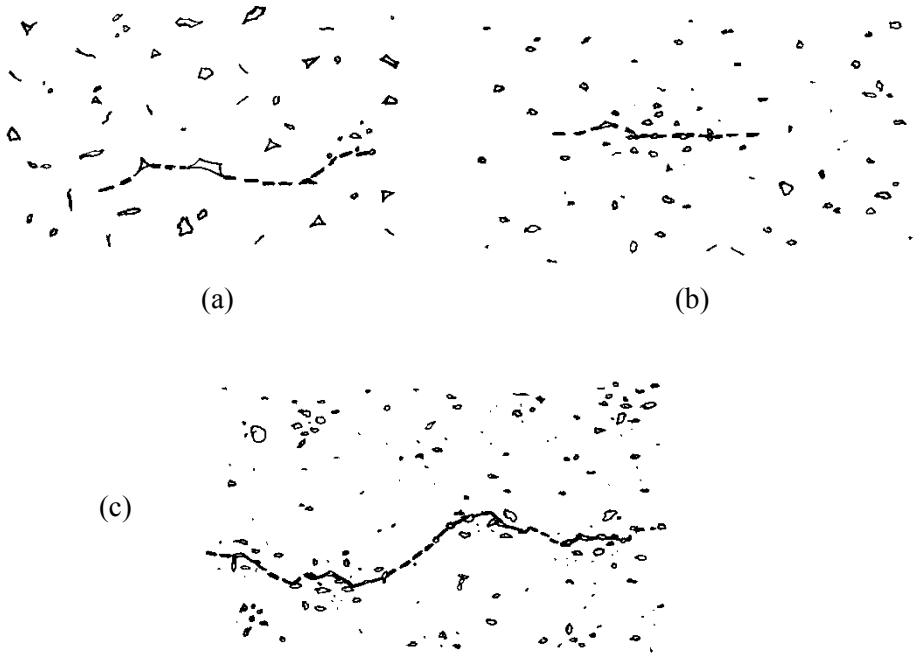

Figure 6.75 Schematics *of "microfault pockets." The fracture origin may be an array of tiny microstructural faults that are linked by microcracking. Tension stress is applied vertically. (a) is similar to a schematic by Sines and Okada.*[56,57] *(b) shows an origin site that has a greater local concentration of the irregularities. (c) shows random pockets of greater than average concentration. Fracture may entail linkage of these pockets by microcracking.*

(a)

(b)

(c)

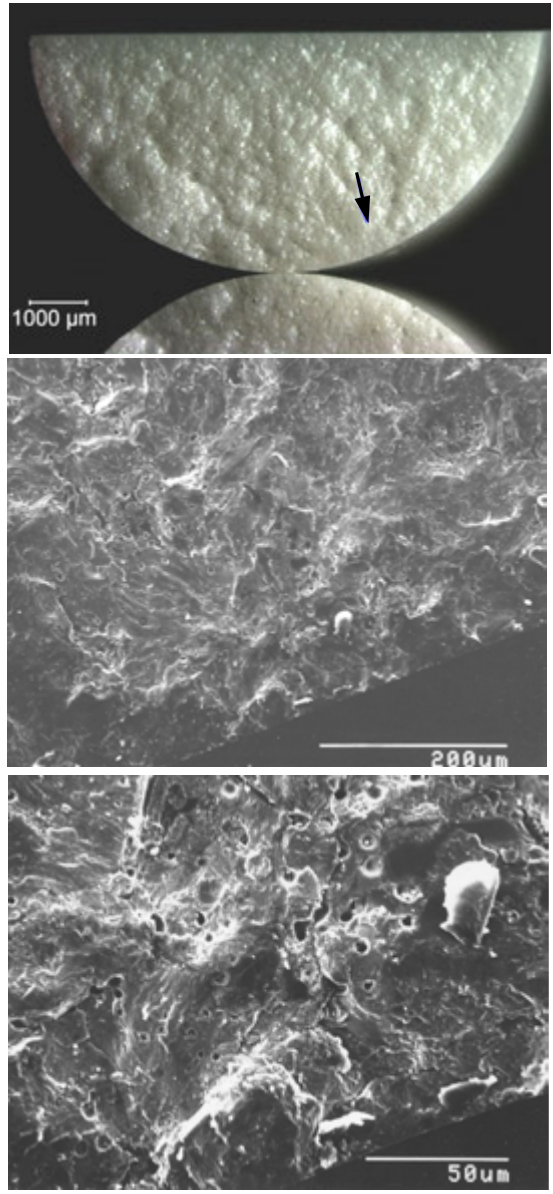

Figure 6.76 *Origin in a magnesia partially-stabilized zirconia split-rod bend specimen. Coarse hackle lines lead back to the origin. (a) shows the entire fracture surface which is very rough and undulating due to the coarse microstructure and irregularities in the microstructure. (b) and (c) show close-ups of the origin which is a pocket of micropores and grain boundary faults. Tiny wake and twist microhackle radiate away from the origin. The next figure shows a polished section of the same material.*

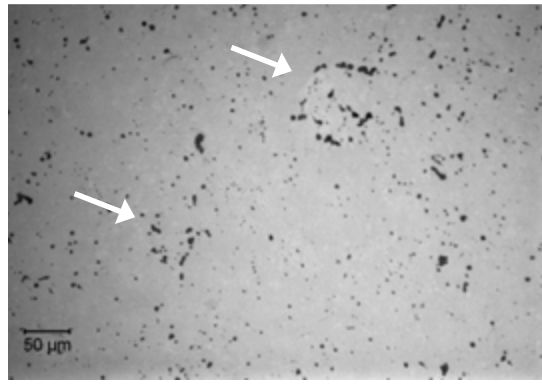

Figure 6.77 *Polished section of the magnesia partially-stabilized zirconia shown in the previous figure. Microflaw pockets are marked by the arrows.*

may be regions of slightly or moderately greater concentration of ordinary irregularities such as micropores, grain boundary cracks or other tiny faults. The regions may be termed "microfault pockets." By themselves, the tiny irregularities are insufficient to case fracture, but they can link by microcracking during loading. Sines and Okada[56,57] suggested that this could account for time-dependent fracture, but there is no reason it cannot apply to fast fracture strength as well. It should be borne in mind that a *random* distribution does not mean a *uniform* distribution. A random distribution of such tiny irregularities will have local regions of greater-than-average concentration.

Fracture origins of the types shown in Figure 6.75 are extremely difficult to diagnose on fracture surfaces, since the features at the origin look exactly like the normal microstructure. Figure 6.76 is an example. Polished specimen microstructural analysis helped with the interpretation as shown in Figure 6.77 The origin may take on the character of porous regions as shown in Figure 6.12. The literature is sparse on such flaws, no doubt because engineers and scientists are loath to show fractographs of origins that fail to show a distinct flaw!

6.17 Polished Microstructural Sections

Figure 6.78 and previous Figures 6.4, 6.67, and 6.77 show examples of how polished microstructural sections can provide complimentary information about flaw types and their distributions. Polished section preparation is a staple for metals failure analysis, usually to ensure that the microstructure is as expected and the correct phases are present.

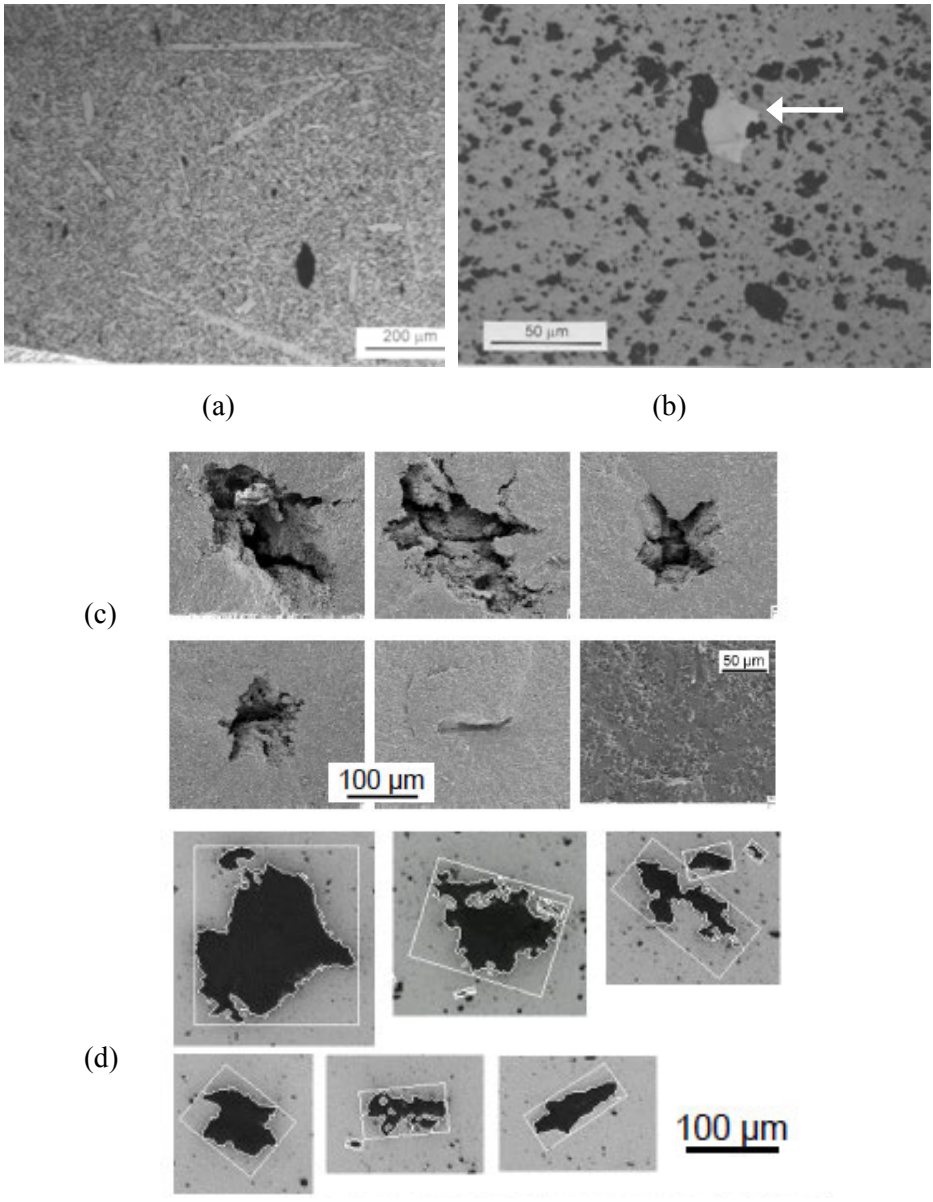

Figure 6.78 *Polished microstructural sections can aid origin interpretation. (a) Sintered alpha silicon carbide often has large grain fracture origins. The acicular or platelet shape of these and their concentration are revealed by the micrograph. (b) reaction-bonded silicon nitride sometimes fails from unreacted silicon (arrow). (c) and (d) show irregular pressing flaws on fracture surfaces and polished sections of a sintered alumina, respectively. (c and d courtesy T. Bernthaler)*

6.18 Flaw Size

It may suffice to identify the nature of the flaw, but a better characterization includes at least a rough estimate of its size. A 100 μm inclusion may not have the same source or behavior as a 20 μm inclusion. The size need not be measured precisely if the characterization is intended to describe the general nature of the origin. On the other hand, there are some instances when a good estimate is needed, such as when it is intended to do a fracture mechanics analysis of the flaw as described in the next chapter. This may be to confirm that the fractographer has found the correct flaw. So, for example, if a fractographer has tentatively identified a 2 μm feature as an origin, but fracture mechanics suggests the flaw should be 50 μm in size, then the fractographer ought to reevaluate his assessment.

Measure an approximate flaw diameter, or if the flaw is elongated, approximate it with a semi-elliptical shape and measure the minor and major axis lengths as shown in Figure 6.2. The origin's true size may not be revealed on the fracture surface. Exact fracture mechanics analyses of most origins are not possible due to their complex shape. An important exception to this is machining damage, wherein the origin size measurement may be very useful for the estimation of fracture toughness. When measuring the flaw size of surface-located flaws, measure and record the origin depth and the width. Chapter 7 and Figures 7.18 and 7.19 furnish more guidance.

6.19 What to Report

For each component, or laboratory-tested specimen, record the origin type, the location in the particular specimen, and the flaw size. If a fracture mirror is present, it may also be helpful to measure its size, especially if the fracture is in a component. Mirror size measurements in laboratory strength test specimens also may be done so that mirror constants can be estimated and published for new materials. Figure 6.79 shows images that follow the recommendations in ASTM C 1322.[49]

Organizing a wealth of fractographic images can at times be difficult. Ideally the images should be presented in a coherent fashion with some context. Section 5.10 and Figure 5.68 showed how montages can be useful in organizing a lot of local detail into a global map for a component failure analysis. Figure 6.80 shows how a montage can be constructed for laboratory strength test data.

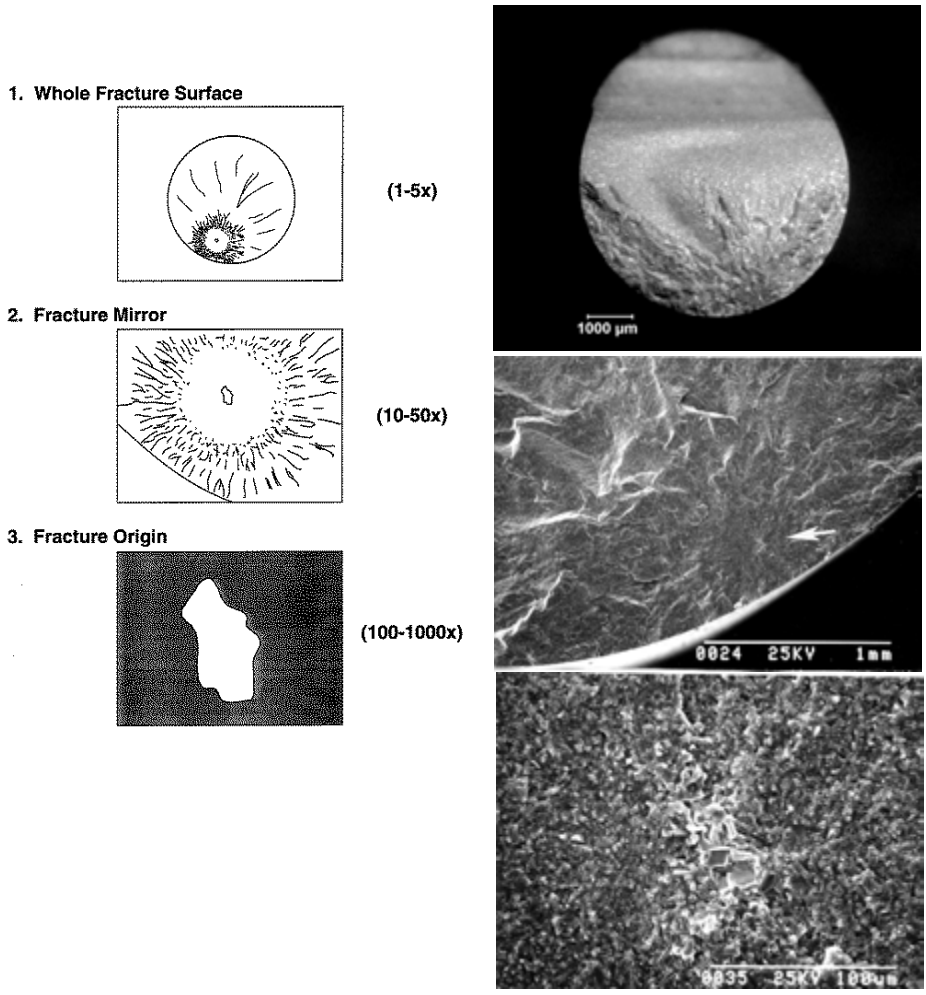

Figure 6.79 *Multiple photos should be taken showing whole fracture surface, the mirror region and the origin. The right side shows an example for an inclusion in a silicon nitride rod flexural strength specimen.*

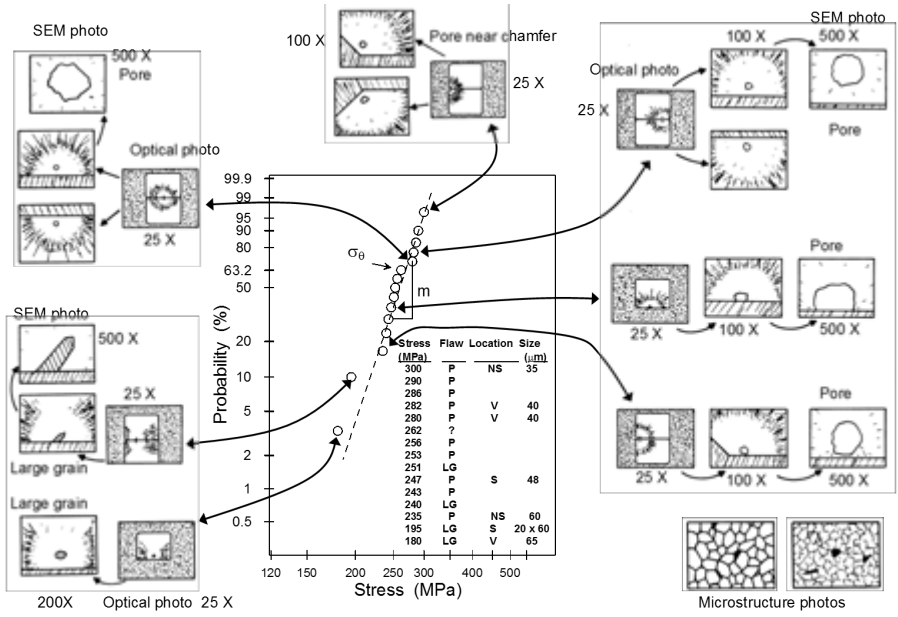

Figure 6.80 *Schematic of a fractographic montage.*

Component failure analyses often have some overall photographs of the entire structure and close-ups of various critical features. Much time and confusion can be saved if the successive images are presented in an orderly, systematic way. It is always wise to start with an overall image of the structure and then add images at progressively higher magnification at key locations.

When one jumps from one magnification to a higher magnification, later it may be difficult to correlate the two images. In the author's experience, magnification jumps of about 5 are the most one should use.

At each step the relationship of the images to each other should be clear. Figure 5-68 in the previous chapter and Figure 6-81 on the next page show good examples for two dental crown failures.

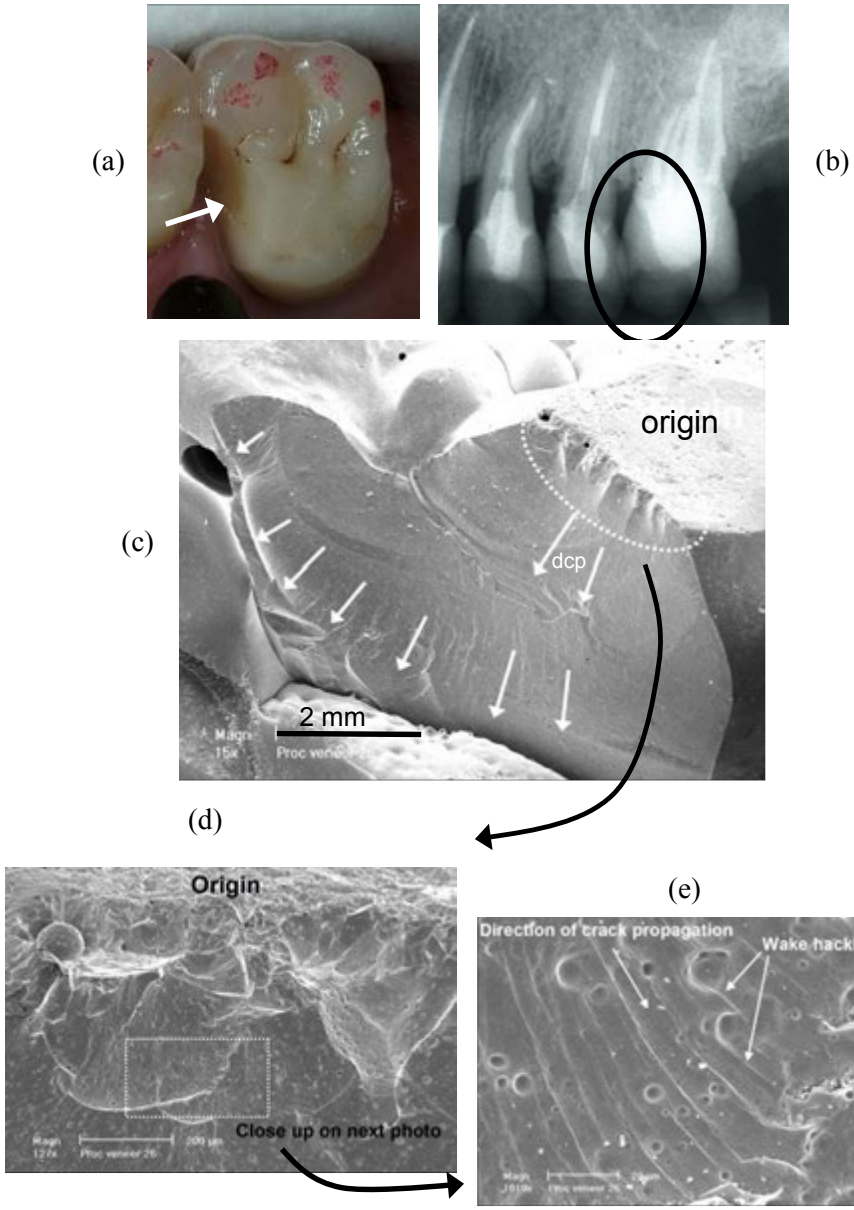

Figure 6.81 *Failure of a first upper-left molar crown. (a) shows a view onto the occlusal surface (the crown top) and the chipped porcelain veneer on the side of the crown (arrow). The porcelain veneer was inadequately supported by the alumina core as shown in the x-ray image (b). (c) – (e) show progressive close-ups of the fracture surface on an epoxy resin replica. This is the same crown as shown in Figure 3.34 on replica techniques. (All courtesy S. Scherrer, Univ. Geneva)*

Chapter 6 References

1. W. Weibull, "A Statistical Distribution Function of Wide Applicability," *J. Appl. Mech.,* **18** (1951) 293 - 297.
2. G. D. Quinn and R. Morrell, "Design Data for Engineering Ceramics: A Review of the Flexure Test," *J. Am. Ceram. Soc*., **74** [9] (1991) 2037 - 2066.
3. R. W. Davidge, *Mechanical Behavior of Ceramics*, Cambridge Univ. Press, London, 1979.
4. D. Munz and T. Fett, *Ceramics, Mechanical Properties, Failure Behavior, Materials Selection*, Springer, Berlin, 1999.
5. W. E. C. Creyke, I. E. J. Sainsbury, and R. Morrell, *Design with Non-ductile Materials,* Applied Science Publ., London, 1982.
6. R. W. Rice, "Pores as Fracture Origins in Ceramics," *J. Mat. Sci.,* **19** (1984) 895 - 914.
7. G. D. Quinn, K. Hoffman, and J. B. Quinn, "Strength and Fracture Origins of a Feldspathic Porcelain," *Dent. Mat.,* **28** [5] (2012) 502–511.
8. D. Lewis, III, "Fracture Strength and Mirror Size in a Commercial Glass-Ceramic*," J. Am. Ceram. Soc*., **64** [2] (1981) 82-86.
9 . T. Bernthaler, "Defect Imaging and Analysis for Predicting the Reliability of Ceramics," PhD thesis, School of Materials Science and Engineering, University of New South Wales, Sydney, Australia and Aalen University, Aalen, Germany, April 2011.
10. F. F. Lange, "Processing-Related Fracture Origins: I, Observations in Sintered and Isostatically Hot-Pressed Al_2O_3/ZrO_2 Composites," *J. Am. Ceram. Soc.,* **66** [6] (1983) 396-398.
11. F. F. Lange and M. Metcalf, "Processing-Related Fracture Origins: II, Agglomerate Motion and Cracklike Internal Surfaces Caused by Differential Sintering," *ibid,* 398-406.
12. F. F. Lange, B. I. Davis, and I. A. Aksay, "Processing-Related Fracture Origins: III, Differential Sintering of ZrO_2 Agglomerates in Al_2O_3/ZrO_2 Composite," *ibid*, 407-408.
13. M. Hangl, "Processing Related Defects in Green and Sintered Ceramics," pp. 133 – 143 in *Fractography of Ceramics and Glasses*, IV, eds. J. R. Varner and G. D. Quinn, Ceramic Transactions, Vol. 122, American Ceramic Society, Westerville, OH, 2001.
14. H. R. Baumgartner and D. W. Richerson, "Inclusion Effects on the Strength of Hot Pressed Si_3N_4," pp. 367 – 386 in *Fracture Mechanics of Ceramics, Vol. 1,* eds., R.C. Bradt, D. P. H. Hasselman, and F. F. Lange, Plenum, NY, 1974.
15. A. G. Evans, "Structural Reliability, A Processing Dependent Phenomenon," *J. Am. Ceram. Soc*., **65** [3] (1982) 127 - 137.
16. R. W. Rice, *Mechanical Properties of Ceramics and Composites, Grain and Particle Effects,* Marcel Dekker, NY, 2000.
17. M. G. Gee, and R. Morrell, "Fracture Mechanics and Microstructures," pp. 1 – 22 in *Fracture Mechanics of Ceramics*, Vol. 8, R. Bradt, A. Evans, D. Hasselman, and F. Lange, eds., Plenum Press, NY, 1986.

18. E. Carlstrom and R. Carlsson, "A Fractographic Study of Electrical Porcelains Containing Alumina," *J De Physique*, **47** [C-1] (1986) 563 – 567.
19. D. Southan, "The Porcelain Jacket Crown," pp. 207 -230 in *Dental Ceramics*, Proc. First International Symposium on Ceramics, ed. J. McLean, Quintessence Publ., London ,1983.
20. J. S. Banda and P. F. Messer, "Fracture-Initiating Flaws in Whitewares," pp. 363 – 375 in *Fractography of Glasses and Ceramics,* Advances in Ceramics, Vol. 22. eds, J. R. Varner and V. D. Fréchette, 1988, American Ceramic Society, Westerville, OH, 1988.
21. R. W. Davidge and G. Tappin, "The Effects of Temperature and Environment on the Strength of Two Polycrystalline Aluminas," *Proc. Br. Ceram. Soc*., **15** (1970) 47 – 60.
22. J. A. Salem, "Transparent Armor Ceramics as Spacecraft Windows," *J. Am. Ceram. Soc.,* **96** [1] (2013) 281-289.
23. J. J. Swab, R. Pavlacka, G. Gilde, S. Kilczewski, J. Wright, and D. Harris," Determining the Strength of Coarse-Grained AlON and Spinel," *J. Am. Ceram. Soc*., **97** [2] (2014) 592-600.
24. D. W. Richerson, *Modern Ceramic Engineering*, Marcel Dekker Inc., NY, 1982; and 3rd edition, CRC Press, Taylor and Francis, Boca Raton, FL, 2006.
25. C. G. Knight, M. V. Swain, and M. M. Chaudhri, "Impact of Small Steel Spheres on Glass Surfaces," *J. Mat. Sci*., **12** (1977) 1573 – 1586.
26. M. M. Chaudhri, "High-Speed Photographic Investigations of the Dynamic Localized loading of Some Oxide Glasses," pp. 87 – 113 in *Strength of Inorganic Glass*, ed. C. Kurkjian, Plenum, New York, 1985.
27. Y. Akimune, "Hertzian Cone Crack in SiC Caused by Spherical Particle Impact," *J. Mat. Sci. Lttrs.,* **9** (1990) 659 – 662.
28. H. Kirchner and R. Gruver, "Branching of Hertz Cracks," pp. 959-964 in *Fracture 1977, Vol. 3*, Proceedings of the 4th Int. Conf. on Fracture, Waterloo, Canada, ed., D. Taplin, Univ. Waterloo Press (1977).
29 B. R. Lawn, S. M. Wiederhorn, and D. E. Roberts, "Effect of Sliding Friction Forces on the Strength of Brittle Materials," *J. Mat. Sci.,* **19** (1984) 2561 - 2569.
30. M. M. Chaudhri and C. Liangyi, "The Orientation of the Hertzian Cone Crack in Soda-Lime Glass Formed by Oblique Dynamic and Quasi-static Loading with a Hard Sphere," *J. Mat. Sci.,* **24** (1989) 3441 – 3448.
31. R. W. Rice and J. J. Mecholsky, Jr., "The Nature of Strength Controlling Machining Flaws in Ceramics," pp. 351 – 378 in *The Science of Ceramic Machining and Surface Finishing II,* eds., B. J. Hockey and R. W. Rice, Special Publication 562, NBS, Gaithersburg, MD, 1979.
32. G. D. Quinn, L. K, Ives, and S. Jahanmir, "On the Nature of Machining Cracks in Ground Ceramics: Part I: SRBSN Strengths and Fractographic Analysis," *Mach. Sci. Technol.*, **9** (2005) 169 - 210.
33. G. D. Quinn, L. K, Ives, and S. Jahanmir, "On the Nature of Machining Cracks in Ground Ceramics: Part II: Comparison to Other Silicon Nitrides and Damage Maps," *Mach. Sci. Technol.*, **9** (2005) 211 - 237.

34. W. Kanematsu, "Visualization of Subsurface Damage in Silicon Nitride from Grinding by a Plasma Etching and Dye Penetration Method," *J. Amer. Ceram. Soc*., **89** [8] (2006) 2564-2570.
35. B. A. Bender, C. Kim, and C. Cm Wu, "Solid Preform Fabrication of a Piezoelectric Ceramic Torsional Actuator Motor," *Ceram. Eng. Sic., Proc*., **25** [3] (2004) 89 – 94.
36. J. R. Varner and V. D. Fréchette, "Fractography of Whitewares," pp. 305 – 315 in *Science of Whitewares*, Eds. V. Henkes, G. Y. Onoda, and W. M. Carty, American ceramic Society, Westerville, OH, 1996
37. G. D. Quinn, K. Hoffman, S. Scherrer, U. Lohbauer, G. Amberger, M. Karl, J. R. Kelly, "Fractographic Analysis of Broken Ceramic Dental Restorations, pp. 161-174 in, *Fractography of Glasses and Ceramics,* VI, *Ceramic Transactions,* Volume 230, eds., J. R. Varner, M. Wightman, Wiley, New York, 2012.
38. G. D. Quinn, "Fractographic Analysis of Broken Ceramic Dental Restorations," *Ceram. Eng. Sci. Proc.*, **35** [1] (2015) 39-51.
39. J. R. Varner, "The Practical Strength of Glass," pp. 389 – 406 in *Strength of Inorganic Glass*, ed., C. Kurkjian, Plenum, NY, 1986.
40. V. D. Fréchette, *Failure Analysis of Brittle Materials*, Advances in Ceramics, Vol. 28, American Ceramic Society, Westerville, OH, 1990.
41. H. Pfaender, *Schott Guide to Glass*, Chapman and Hall, London, 1996.
42. F. Preston, "A Study of the Rupture of Glass," *J. Soc. Glass Techn.*, **10** (1926) 234- 269.
43. ASTM C 162, Standard Terminology of Glass and Glass Products, Annual Book of Standards, Vol. 15.02, ASTM Int., West Conshohocken, PA, 1999.
44. J. Varner, private communication.
45. F. W. Preston, "The Structure of Abraded Glass Surfaces," *Trans. Opt. Soc.*, **23** [3] (1921-1922) 141 – 164.
46. L. G. Ghering and J. C. Turnbull, "Scratching of Glass by Metals," *Bull. Am. Ceram. Soc*., **19** (1940) 290 – 294.
47. R. W. Rice, "Failure Initiation in Ceramics: Challenges of NDE and Processing," pp. 1057 - 1064 in *Ceramic Developments*, eds., C. Sorrell, and B. Ben-Nissan, *Materials Science Forum*, Vol. **34–36**, Trans. Tech. Publ. Ltd., Switzerland, 1988.
48. J. R. Alcock and F.L. Riley, "A n Investigation of Dust Particles Found in a Ceramic Processing Environment," *J. Eur. Ceram. Soc*., **6** (1990) 339-350.
49. ASTM C 1322-96, "Standard Practice for Fractography and Characterization of Fracture Origins in Advanced Ceramics," *Annual Brook of Standards*, Vol. 15.01, ASTM Int., West Conshohocken, PA (1996)
50. A. G. Evans and G. Tappin, "Effects of Microstructure on the Stress to Propagate Inherent Flaws," *Proc. Brit. Cer. Soc*., **20** (1972) 275-297.
51. R. W. Davidge, *Mechanical Behavior of Ceramics*, Cambridge University Press, Cambridge, UK, 1974, pp.98-100.
52. R. W. Rice, "Machining of Ceramics," pp. 287-343 in *Ceramics for High Performance Applications*, eds., J.J. Burke, A. E. Gorum, and R. N. Katz, Brook Hill Publ., Chestnut Hill, MA, 1974.

53. G. D. Quinn, "Fractographic Analysis of Miniature Theta Specimens," *Ceram. Eng. Sci. Proc.,* **29** [3] (2008) 189 – 199.
54. M. H. Krohn, J. R. Hellmann, D. L. Shellemann, and C. Pantano, "Strength and Fatigue of Float Glass Before and After Enameling," *The Glass Researcher*, **11** [2] (2002) 24 – 27.
55. Y. Kobayashi, M. Mukai, T. Mizuno, O. Ohira, and H. Isoyama, "Effect of Cristobalite Formation and Glaze on Bending Strength of α-Alumina Reinforced Porcelain," *J. Ceram. Soc. Japan*, **113** [6] (2005) 413 – 418.
56. T. Okada, G. Sines, and D. Green, "Crack Origins and Microcracking in Delayed Fracture of Alumina," *Comm. Am. Ceram. Soc.,* May 1982, C 64 - 65.
57. G. Sines and R. Okada, "Flaws Responsible for Slow Cracking in the Delayed Fracture of Alumina*," J. Am. Ceram. Soc.,* **66** [3] (1983) 228 - 232. {correction, ibid, **66** [7] (1983) 538.}

7. Quantitative Analysis

7.1 Introduction

Quantitative analysis can aid the fractographic analysis and extend its value. It may be used to confirm that the right flaw has been identified as a fracture origin. It can make good estimates of the stresses in the part at failure. Four methods to estimate stress are shown in this chapter: fragmentation analysis, branching distance analysis, fracture mirror size analysis, and origin size analysis. Some analyses are empirical and others are based on the powerful tool of fracture mechanics. One goal of this chapter is to convey a working knowledge of fracture mechanics so that it can be used to solve practical problems. Table 1 includes some useful conversion factors.

length

1 in *	=	25.4 mm
1 micrometer (micron)	=	1 x 10^{-6} m
.001 inch *	=	25.4 micrometers

force

1 kgf (kilogram force)*	=	9.80 N (Newtons)

stress or pressure

1 ksi (1,000 psi) *	=	6.895 MPa (Megapascal)
1 Pa	=	1 N/m^2
1 MPa	=	1 MN/m^2 = 1 x 10^6 Pa
1 MPa	=	145.04 psi = 0.14504 ksi *
1 GPa	=	1000 MPa = 1 x 10^9 Pa

example: 100 ksi = 690 MPa

stress intensity

1 ksi $\sqrt{inch}$ * = 1.10 MPa$\sqrt{m}$

example: $5\ MPa\sqrt{m} \times \left(\frac{1\ ksi\sqrt{in}}{1.10\ MPa\sqrt{m}}\right) = 4.55\ ksi\sqrt{in}$

energy

1 erg	=	.0000001 (1 x 10^{-7}) J (Joule)
1 ft-lbf *(foot pound force)	=	1.355 J

energy/area

erg/cm^2	=	.001 J/m^2

Length on Photos

1 mm = 1 micrometer on a 1000X photo

* Not an official SI unit, but included here for completeness.

Table 7.1 Conversion Factors

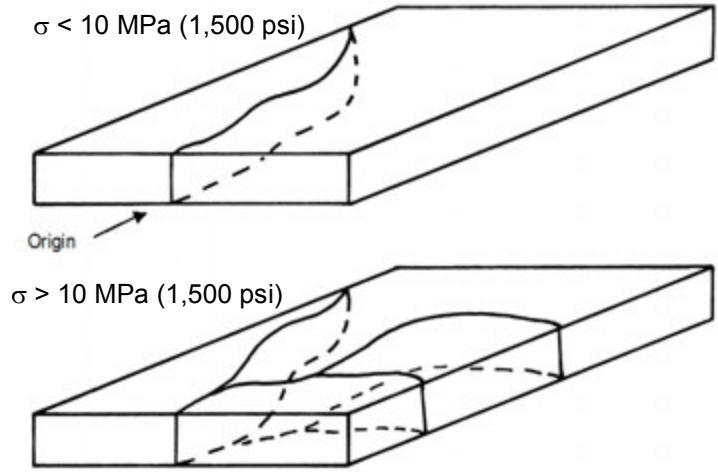

Figure 7.1 *Schematic of thermal fractures of windows. Low stress fractures (σ < 10 MPa, 1,500 psi) do not cause branching. (After Orr[2] and Fréchette[1])*

7.2 Stresses from the Extent of Fragmentation

7.2.1 Annealed parts

A general assessment of stress levels can be made from the fracture pattern. Low stressed parts break into only two pieces. Fréchette[1] and Orr[2] and have suggested that 10 MPa (1,500 psi) is a threshold stress level for branching and fragmentation in glass as illustrated in Figure 7.1**.** Additional fragmentation occurs with increasing stress in the part, or increasing stored elastic energy. Very highly-stressed parts fragment to such a degree that laypersons are apt to describe the fracture as an "explosion." Retrieval of the two fragments with the fracture origin may be problematic.

Fréchette and his students[3] have shown fragmentation correlations with internal pressure of bottles as shown in Figure 7.2. They did a similar analysis for impact velocity for impacted bottles.[4] While their work may have been specific to certain bottle types and shapes, similar testing could be done with alternative shapes and sizes to aid in the failure analysis of new service failures.

Figure 7.3 shows how the fragmentation of ring-on-ring (32 mm and 64 mm diameters) tested borosilicate crown glass disks (76 mm diameter x 5.4 mm thick) can be correlated to fracture stress. This work was done as part of a reliability analysis for a pressurized aircraft window.[5] Figures 4.12 and 4.13

showed examples of such test specimens and their breakage patterns. Fragmentation in Figure 7.3 was quantified by the number of radial cracks that reached the outer rim. This was an arbitrary criterion. Morrell showed a very similar graph for the number of fragments as a function of stress in ring-on-ring tests of high purity alumina.[6] Shand presented a similar graph counting radial cracks for 6 cm square window glass plates broken by impact in the middle.[7] He pointed out that by such counting, one could obtain a stress at failure estimate even if the impacted site was lost or destroyed. More recently, Wang[8] did stress analyses and counts of the number of pieces in glass plate coupons of different sizes when pressure loaded to fracture. Graphs such as these are very specific to specimen or component size, shape, and material.

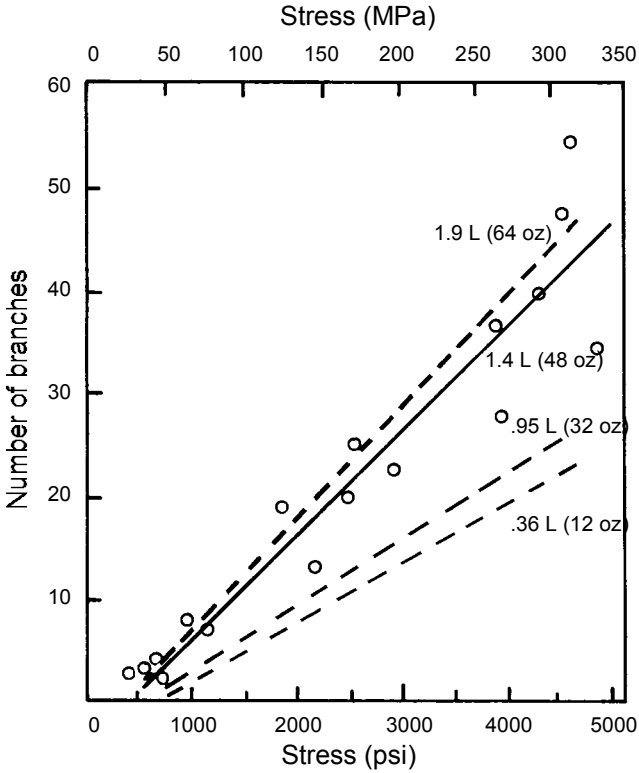

Figure 7.2 *Fragmentation of internally pressurized bottles. The number of branches (fully developed that extend more than 13 mm beyond the first fork) are shown versus the hoop stress in the glass wall for four different glass containers. Data points and a solid line are shown only for the 1.4 L (48 oz) bottles. Dotted lines show the trends for the three other sizes. Some of the scatter is due to variations in the glass wall thickness. (After Fréchette and Michalske, Ref. 3)*

Figure 7.3 was actually used to analyze an unexpected fracture. A similar glass disk was impacted by a hailstone that was intended to weaken the disk by creating surface damage that could be assessed in a subsequent strength test. The hailstone unexpectedly fractured the disk. The fragments were recovered and reassembled and the origin determined to be an ordinary polishing scratch on the surface opposite the hail impacted side. The hailstone diameter (25 mm) was similar to the inner ring diameter in the strength test set. From the number of radial cracks, the stress at failure was estimated. The estimate matched the dynamic stress estimated from an impact stress analysis, thereby confirming that the impact indeed had imparted sufficient energy to flex the disk to fracture from the ordinary surface flaw.

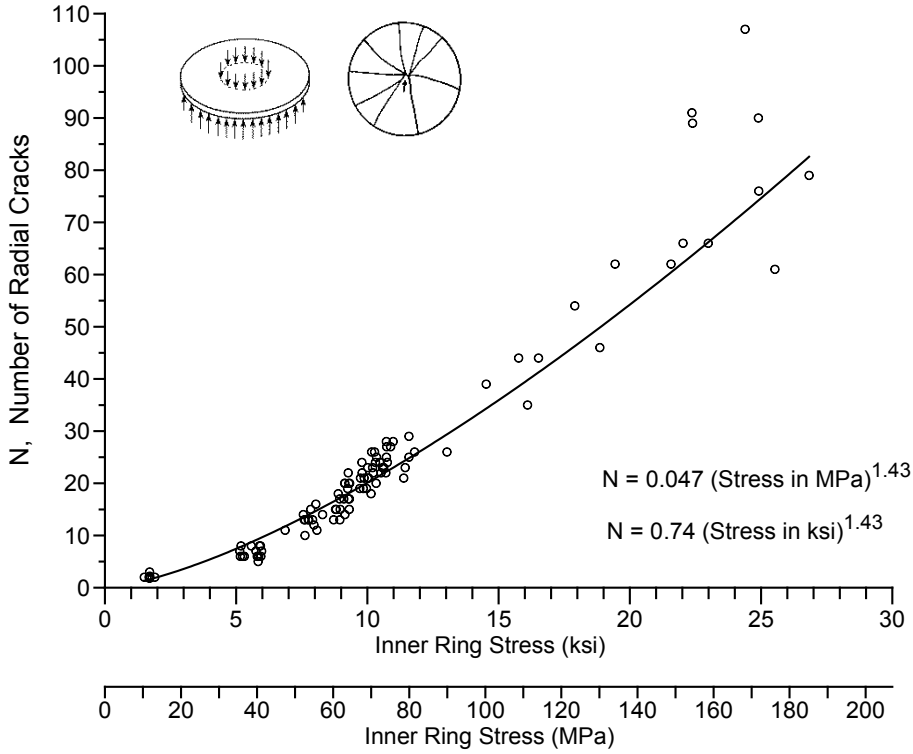

Figure 7.3 *The number of radial cracks that reach the outer rim as a function of fracture stress for 76 mm diameter by 5.4 mm thick borosilicate crown glass disk broken in ring-on-ring flexure. Data for this graph included only fractures that initiated inside the inner loading ring.*

More often, the fractographer simply makes a qualitative stress assessment with a cursory examination. This is often sufficient for a diagnosis. For example, if a fracture occurs at an unexpectedly low stress, the fractographer might search for an unexpectedly large flaw in the component or specimen. A handling or preparation flaw may have weakened it to an unexpected level.

7.2.2 Fragmentation of tempered parts

McMaster et al.[9] state that the most common method of inferring stress levels in tempered glass is by breaking it. They and Shinkai[10] cite work by Akeyoshi,[11] wherein 10 cm square tempered plates of various thickness were broken by sharp impact. The number of fragments in a 5 cm square region correlated to the internal tension temper stress as shown in Figure 7.4.

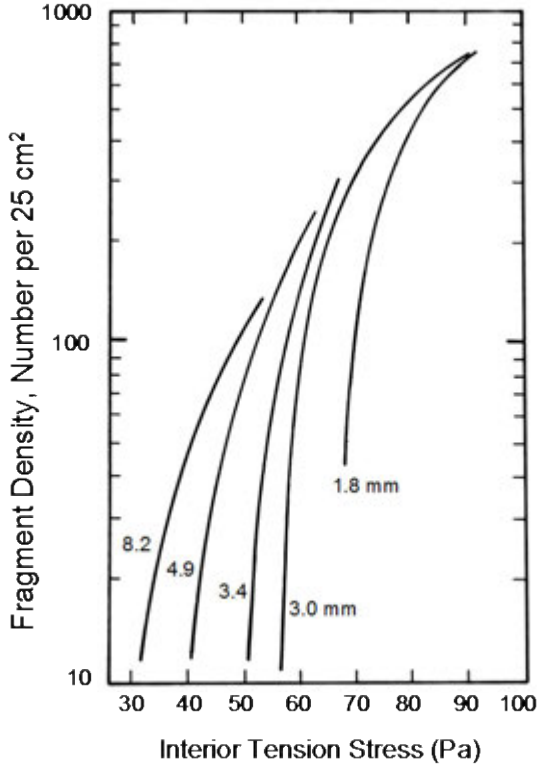

Figure 7.4 *The interior tension stress in tempered soda lime glass plates may be estimated from the fragment density when the plate is broken. Each line corresponds to the plate thickness shown. (After Akeyoshi et al., Ref. 11)*

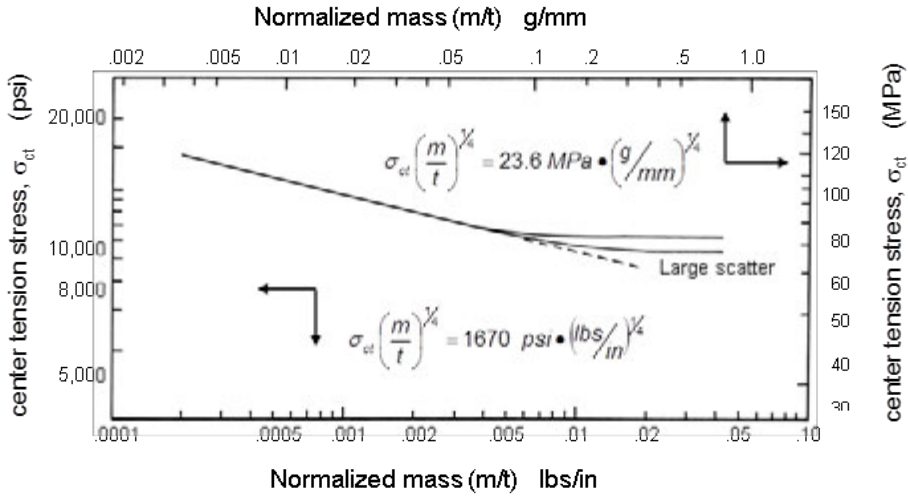

Figure 7.5 *The interior tension stress in tempered soda lime sheet and plate glass may be estimated from the average fragment mass. Center tension stress is plotted versus mass normalized by the plate thickness, t. Data for five different thickness plates and sheets from 3.2 mm to 9.5 mm (1/8 in to 3/8 in) fall on the same curve. (After Barsom, ref. 13)*

For a particular thickness plate, the data suggests there is a minimum temper stress to cause dicing. Blank[12] presented some interesting fragmentation work on tempered soda lime silica plates, 300 mm by 300 mm in size and with thicknesses varying from 3.2 to 7.2 mm. The average fragment size (area) in mm^2 dramatically decreased with increasing surface compression strengthening.

Of course, other means of assessing temper stresses are available, including polariscope inspections and use of the stress optical coefficient, but in this Guide we are concerned with fractographic techniques.

Barsom[13] showed that interior tension stress σ_{ct} was related to the fragment mass:

$$\sigma_{ct}\left(\frac{m}{t}\right)^{1/4} = \text{constant} \qquad (7.1)$$

where m is the fragment weight (mass), t is the plate thickness. The constant has units of stress • (mass/thickness)$^{1/4}$.

It should be borne in mind that these relationships and trends are altered if there are significant *externally* applied stresses superimposed on the temper stresses.

The fractographer should be on the lookout for irregular breakage patterns and fragment sizes that are signs of nonuniform temper stresses. Fréchette[1] showed two examples. In one case a glass cylinder was not tempered uniformly during the fabrication process (his case 10.18). A second case (his 10.22) featured a high-powered lamp that cracked spontaneously as a result of heating in service. The fragments were atypically large in the fracture origin area, but elsewhere the normal dicing fragmentation pattern was observed. Fréchette concluded that the intense in-service heating caused the middle of the lamp to lose its temper. Blank[12] discussed the use of tempered glass in front automobile windshields in Germany and showed a fascinating drawing of a fractured windshield that had dramatically uneven fragment sizes and crack patterns due to nonuniform heat transfer during tempering. It is commonly assumed that the residual stresses are symmetric *through the thickness* as shown in Figure 5.19, but Menčík[14] illustrated the effects of asymmetric tempering of plates on the final stress distributions. Different residual compression stresses could exist on the two plate surfaces. There may even be a net tensile stress on one surface.

7.3 Stresses from the Branching Distances

7.3.1 Annealed plates and bars

The stress at fracture is related to the branching distance away from the origin by:

$$\sigma\sqrt{R_b} = A_b \tag{7.2}$$

where σ is the stress, R_b is the branching radius, and A_b is a constant called the fracture branching constant. It has units of stress·√length. These units are the same as for stress intensity which is described in section 7.5. The relationship between A_b and fracture toughness is discussed in 7.6. A similar relationship applies to mirror sizes as will be discussed in section 7.4. Rearranging shows that the branching distance is inversely dependent upon the square of the stress:

$$R_b = \left(\frac{A_b}{\sigma}\right)^2 \tag{7.3}$$

This empirical relationship has been found to apply to uniaxially-stressed parts such as a tensile strength specimen or a component with tensile stresses primarily in one direction. The relationship also can be applied to bend bars or

components loaded in bending provided that the branching distance is measured along the surface where the tensile stresses are a maximum. The relationship also may apply to biaxially-stressed parts such as a ring-on-ring strength test disk or pressurized windows or bottles, again using matching lengths and stresses.

The term A_b may not necessarily be a material constant. It certainly does depend upon the material properties such as elastic modulus or fracture toughness, but there is evidence that stress state and component geometry affect it too. A_b is always greater than the fracture mirror constant that is described later in this chapter. Branching distances in biaxially-stressed parts may be less than the branching distances in uniaxially-stressed parts. Shetty et al. [15] showed that branching can occur just beyond the mirror in highly stressed, biaxially loaded disks. Hull[16] suggested that the cross section thickness of a component might influence when branching occurs. Despite these concerns, reported A_b values are tabulated in Appendix C. Very few values are available since most investigators have focused on fracture mirror constants instead.

The branching angle can at least be a qualitative indicator of the stress state as shown in Figure 4.4 in chapter 4. The branch angle is actually variable and curves at the exact branching location. It is recommended that the branching angle be measured close to but somewhat away from the splitting juncture, at a point where the branching angle has settled into a more or less constant value.

7.3.2 Tempered Plates

Figure 7.6 shows an interesting approach suggested by Soltesz et al.[17] to estimate temper stresses in tempered glass plates. The lengths of the first and second branches can be correlated to internal temper stresses.

(a)

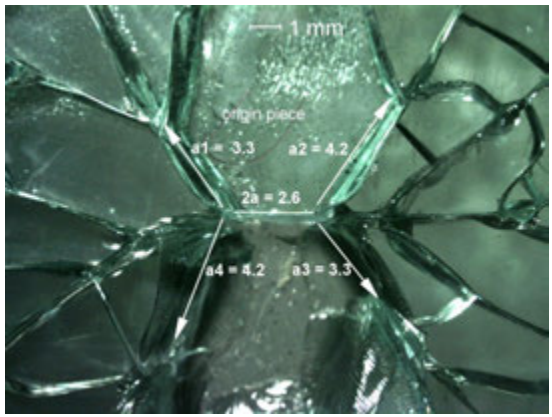

(b)

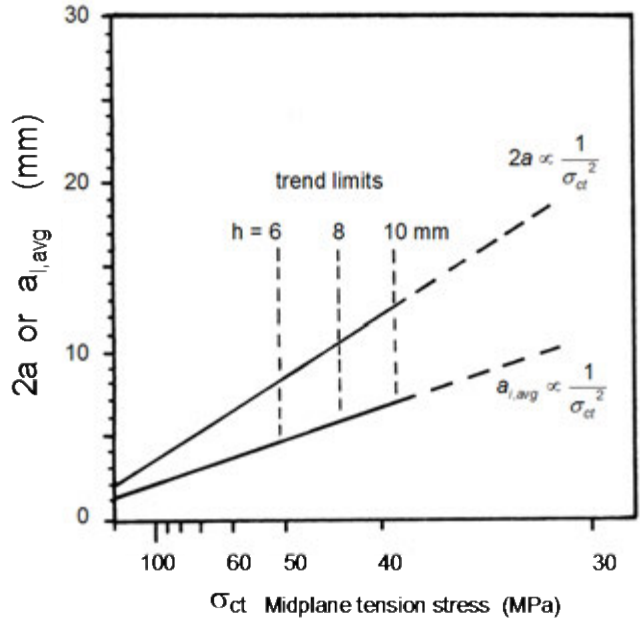

Figure 7.6 *Branch distances in tempered glass may be used to estimate internal tension stresses. (a) shows an example from a 3.3 mm thick tempered automobile window. The initial branch - crack run is 2a = 2.6 mm. The lengths of the first four branches (<u>not</u> including the segments that ran straight from the initial crack) are also labeled. (b) shows the initial branch distance 2a and the average first branch distance $a_{i,avg}$ versus the center tension stress respectively for 6 mm to 10 mm thick plates. All dimensions are in mm. Limits to the trends for different thickness plates are shown by the dashed vertical lines. Data to the right of these limits at low stresses has high scatter. (b is after Soltesz et al., Ref. 17)*

7.4 Stresses from the Mirror Size

7.4.1 Mirror analysis and constants

The fracture mirror size is related to the stress at the origin. Orr's empirical mirror size relationship is:

$$\sigma \sqrt{R} = A \tag{7.4}$$

where σ is the tensile stress at the origin at the instant of fracture, R is the mirror radius, and A is the "mirror constant" with units of stress intensity (MPa√m or ksi√in) and is considered by most as a material property. (A version of this equation with a residual stress term is discussed later in this chapter.) This relationship is similar to, but not quite the same, as that for stress intensity or fracture toughness as will be discussed in section 7.6 below. Figure 7.7 shows more details of a mirror centered on a surface flaw. This rendition also depicts the prospect that the initial flaw might grow somewhat from a to a_c before going critical.

This author reviewed the evolution of fracture mirror size analysis in a 2006 paper.[18] Leighton Orr of the Pittsburg Plate Glass (PPG) Company was the first to systematically use equation 7.4 with the square root dependence of mirror size to solve glass fracture problems as far back as the 1940s.[2,19,20]

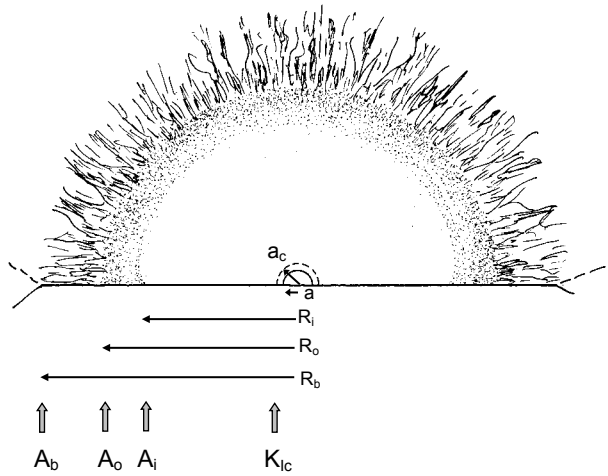

Figure 7.7 *Fracture mirror schematic. R_i is the inner or mirror-mist boundary, R_o is the mist-hackle boundary, and R_b is the branching distance. The fracture toughness K_{Ic} (discussed in section 7.5.1), the mirror constants A_i and A_o and the branching constant A_b correspond to each of these boundaries. All have units of stress √length.*

Johnson and Holloway in 1966[21] offered a physical interpretation of the relationship based on the energetics of crack propagation. Levengood,[20] Shand,[22] Kerper and Scuderi,[23,24] and later Kirchner et al.[25] gave credit to Orr for equation 7.4. Orr did not publish his findings until he retired in 1972,[2] but discussed his empirical equation at a Glass Division meeting of the American Ceramic Society in Bedford, PA in September 1955.[26] Orr told me in 2001[19] that equation 2 had been extensively used for glass fracture analysis at PPG in the 1940s. In the 1950s and 1960s, many people used a general form of equation 7.4 with the mirror size raised to an arbitrary power. Shand's 1954 and 1959 papers[22,27] presented an early argument for the 1/2 power based on stress concentrations at the tip of a sharp crack. These two papers incorporated elements of what become known later as fracture mechanics. Kerper and Scuderi[23,24] at the National Bureau of Standards in Washington performed meticulous experiments on hundreds of glass laths and rods and showed conclusive evidence that Orr's equation was applicable over a broad range of specimen and mirror sizes. (See Fig. 7.10 later in this chapter) Some have credited Terao[28] with equation 7.4, but a careful reading of his paper fails to back the claim since it shows an exponential form relating mirror size to stress instead. So, although many associate equation 7.4 with Johnson and Holloway [21] in 1966, the relationship had already been in use by Orr for 20 years.

The practical significance of equation 7.4 is that one can calculate the origin stress if a fracture mirror size is measured and a fracture mirror constant is available. The calculated stress is the net tensile stress acting on the flaw and the region around the flaw. It may include several stress sources including mechanical, thermal, and residual stresses. It is possible to discern separate mirror-mist and mist-hackle boundaries in glasses and each has a corresponding mirror constant A. The most common notation is to refer to the mirror-mist boundary as the *inner* mirror boundary and the corresponding mirror constant is designated A_i. The mist-hackle boundary is referred to as the *outer* mirror and the corresponding mirror constant is designated A_o. The mirror-mist boundary is usually not perceivable in polycrystalline ceramics and only the mirror-hackle boundary is usually measured.

Equation 7.4 is valid even for large mirrors if loading is in direct tension. If a part is in flexural loading, deviations from the trend can occur as discussed in Appendix D.

At this point it is appropriate to reiterate that equation 7.4 is empirical. In chapter 5, it was noted that there were competing models to account for the mirror formation. Kirchner and colleagues[29,30] presented compelling evidence that a fracture mechanics criterion based on a critical stress intensity, K_{IB},

(described later in section 7.5) gives the best fit to data and the exact shape of mirrors in various stress fields. A crucial observation is that the stress intensity model fully accounts for the small inward facing cusp at specimen surfaces (Figures 5.2 and 7.7), whereas the other models do not. Kirchner et al. [29,30] argued that a more fundamental material parameter might be K_{IB}, the stress intensity factor at branching, rather than the A's in equation 7.4 since the latter do not take into account the free surface, geometry factors, and non-uniform stress gradients over the crack surface. There is validity to their argument, but in practice the ease of use of 7.4 has led to its widespread adoption. (The size and shape predictions based on A or K_{IB} match very closely for the limiting cases of small mirrors in tension specimens. This is also true for most of the periphery of small semicircular mirrors centered on surface flaws in strong tension or flexure specimens.)

The accuracy of the stress estimate varies depending upon the material, the experience of the fractographer, the microscopy and illumination used, and component geometry and stress gradient effects. Stress estimates may be accurate to within ≈ 10 % with glasses if they form ideal fracture mirrors.

Kirchner and Gruver[31] also showed that the relationship holds for elevated temperature fractures in ceramics. The mirror constant was invariant from room temperature to 1400 ^{O}C for a hot-pressed alumina with a 1 μm grain size. This is a remarkable finding since the alumina was fired at 1475 ^{O}C. Kerper and Scuderi[32] also showed that mirror constants were unaffected by elevated temperature for eight glasses. Shinkai[33] showed the mirror-mist constant, A_i, varied little with temperature for three glasses. A_i varied little with temperature for the Pyrex, but for the soda lime silica float glass and the 96% silica (Vicor), the A_i values at -150^{o}C were greater (0.03 – 0.04) than at room temperature. The trends were comparable to similar increases of the fracture surface energy, γ_f, with decreasing temperature. Shinkai[33] also did experiments in various environments. There was negligible environmental effect and the A_i's measured at room temperate in air and dry N_2 gas were comparable. The lack of an environmental sensitivity is not surprising since mirror boundaries form when the crack is travelling at or near terminal velocity.

Crack branching constants A_b have sometimes been reported, but some caution is advised, however, as discussed on page 7-7. There is evidence to suggest that A_b depends upon the loading mode (uniaxial or biaxial) and the size of the mirror relative to a part thickness if the part breaks in bending. The three boundaries correspond to an expanding crack front, and hence, $A_i < A_o < A_b$. Appendix C has a comprehensive compilation of fracture mirror and branching constants. The table shows there is some variability in the published mirror

constants, even for model materials such as fused silica or soda lime silica. Some of this is due to the aforementioned metrology and judgment issues, but much of it is due to genuine material-to-material variability. Thus, one should not expect all silicon nitrides or aluminas to have the same mirror constants. Microstructural differences can change the mirror constants considerably.

The word "boundary" must be used with some caution. It is now clear from a number of studies that there probably is not a discrete or sudden transition point on the fracture surface corresponding to a mirror boundary. The mode of viewing and magnification affects the judgment of the boundaries location. The higher the magnification the smaller the mirror seems to be, since fine detail that was washed out or not resolvable at lower power can be discerned at higher power. The mirror-mist boundary probably corresponds to surface roughness features that are of the order of 0.1 μm to 0.2 μm, which is a fraction of the wavelength of light and at the threshold of observable features with an optical microscope. Section D.3 in Appendix D has a discussion of several studies that have used various surface roughness measurement methods to measure mirrors, but these methods have yielded different results.

So, although there is some variability in how different observers judge and measure fracture mirror sizes, most fractographers agree that there is a fracture mirror that can be measured. Size estimates can vary depending upon the type of microscope used, the mode of illumination, the objective power of the lens, and the judgment criteria of the fractographer.

7.4.2 How to measure mirror sizes

This section gives a brief outline of how to measure fracture mirror sizes. Very detailed guidelines are presented in Appendix D. The procedures in this Guide were adopted as an ASTM standard[34] in 2007.

In principal, a mirror size measurement is a straightforward exercise, but in practice it is not as easy as one would think, even with glasses. In addition to the boundary interpretation issue discussed above, component geometry effects, gradients in the stress fields, residual stresses, and origin flaw effects can all contribute to mirror distortions. Most investigators use simple, common sense approaches such as measuring a few mirror radii from the origin. Some have suggested more elaborate schemes. The boundary criteria are:

The mirror-mist boundary in *glasses* is the periphery where one can discern the onset of mist. This boundary corresponds to A_i, the inner mirror constant.

The mist-hackle boundary in *glasses* is the periphery where one can discern the onset of systematic hackle. This boundary corresponds to A_o, the outer mirror constant.

The mirror-hackle boundary in *polycrystalline ceramics* is the periphery where one can discern the onset of systematic new hackle, and there is an obvious roughness change relative to that inside the mirror region. This boundary corresponds to A_o, the outer mirror constant Ignore premature hackle and/or isolated steps from microstructural irregularities in the mirror or from irregularities at the origin.

Figure 7.8 shows an example in a moderately difficult-to-judge ceramic. The yttria-stabilized zirconia is a difficult to interpret since, although it has a very fine grain size (< 0.5 μm), it has a gradual progression of roughness from well within the mirror to the obvious hackle region far from the origin. Keeping in mind the criteria for polycrystalline ceramics above, the first step is to look at a region well *within* the mirror and note the typical, *inherent* roughness due to the microstructure. The next step is to observe the obvious new hackle that is greater in magnitude than anything in the relatively smooth mirror region.

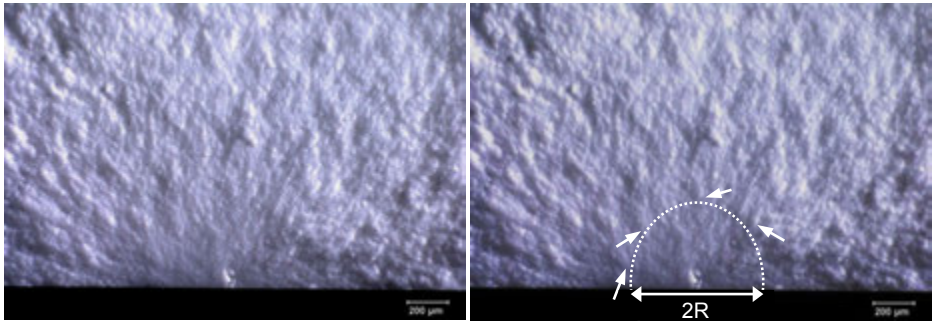

(a) (b)

Figure 7.8 *Example of a mirror in a ceramic material that is difficult to precisely measure. This is one of the specimens of the 3Y-TZP for the data in Figure 7.11 below. (a) shows the uncoated fracture surface of a 2.8 mm thick bend bar with low angle, grazing illumination (486 MPa). (b) shows an interpretation for a mirror-hackle boundary whereby new hackle is detected (small white arrows) as compared to the roughness inside the mirror. The mirror is slightly elongated into the interior due to the stress gradient. Judgments are best made while viewing the surface through a microscope.*

Figure 7.9 shows the two most common graph types that are used to show stress - mirror size data. The merits of each approach are discussed in Appendix D. This Guide recommends the use of stress versus $1/\sqrt{R}$, Fig. 7.9a.

The linear graph of stress versus $1/\sqrt{R}$ in Figure 7.9a has the advantage that the fracture mirror constant is the slope of the line, and residual stresses can be detected by non-zero intercepts as described later.

The log stress versus log R graph in Figure 7.9b facilitates plotting a broad range of stress and mirror sizes. The mirror constant corresponds to the stress necessary to create a mirror of unit size, since (from eq. 4):

$\log \sigma_a = \log A - \frac{1}{2}\log (R)$. If R = 1, then $\log \sigma_a = \log A$, and $\sigma_a = A$.

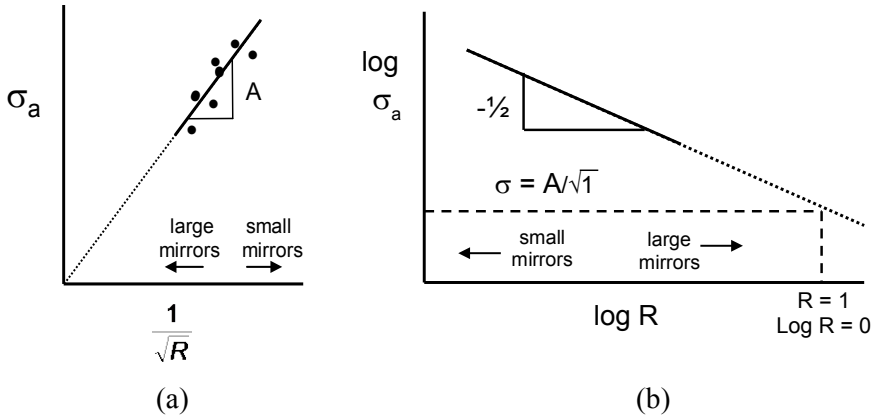

Figure 7.9 *Stress and mirror size graphs. (a) shows the preferred graph of applied stress, σ_a, versus inverse square root of mirror radius. The mirror constant is the slope of the line. (b) shows log σ_a versus log radius as commonly used in the older literature.*

Two examples of mirror data are shown in Figures 7.10 and 7.11 on the next page. The glass data in Figure 7.10 is extraordinary since the mirror size range is almost a factor of 100. The 3Y-TZP zirconia data in Figure 7.11 shows that measurements on uncoated and gold coated specimens concurred. This was gratifying since the uncoated specimens were difficult to interpret due to material translucency and difficulty in judging a boundary. Not surprisingly, the data scatter was greater for the uncoated specimens. More examples of marked fracture mirrors are shown in Appendix D which also has detail how residual stresses, stress gradients, the origin flaws, and microstructure can affect mirror sizes and shapes.

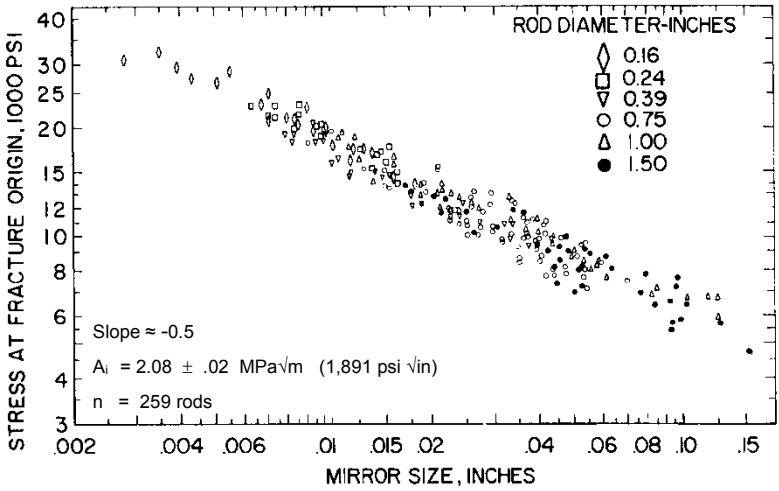

Figure 7.10 *A superb example of fracture mirror data for glass rods of many sizes and strengths. Two hundred and fifty-nine Pyrex 7740 rods varying in size by almost a factor of ten (4.1 mm to 38.1 mm) were broken in three-point flexure by Kerper and Scuderi at the National Bureau of Standards in 1964.*[32]

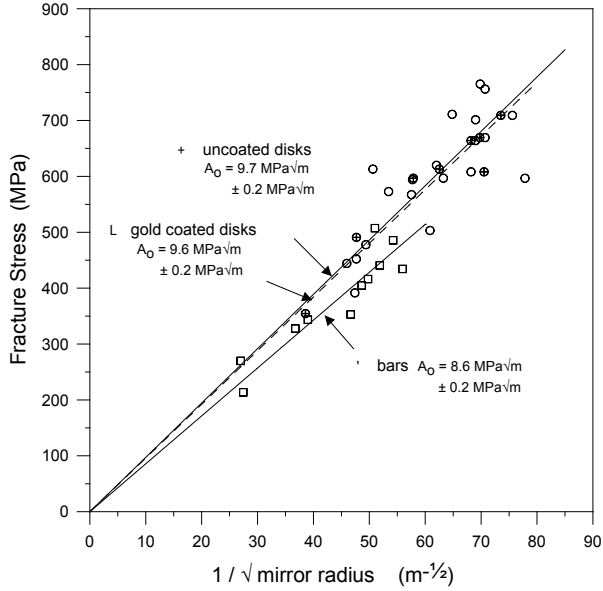

Figure 7.11 *Fracture mirror size data for a 3 mol % yttria-stabilized tetragonal zirconia (3Y-TZP) from Ref. 35. Figure 7.8 shows one of the mirrors. Figure 3.24 shows a mirror both coated and uncoated. Bend bars produced a smaller mirror constant, either due to a geometric effect or simply the scatter in the data.*

7.5 Fracture Mechanics Analysis of the Flaw Size

7.5.1 Introduction to fracture mechanics

Fracture mechanics is a powerful analytical tool to aid the fractographer. It can be used to estimate critical flaw sizes and can help determine whether a flaw the fractographer has detected is of appropriate size to cause fracture. It can also be used to estimate the stress in a fractured part. A short introduction of fracture mechanics fundamentals is presented below followed by some practical examples. Figure 7.12 shows a hypothetical "brick" loaded in tension. A force P may or may not cause breakage depending upon the size and shape of the object and the material properties. Load divided by the area carrying the load is known as stress. The stress is constant across the cross section and

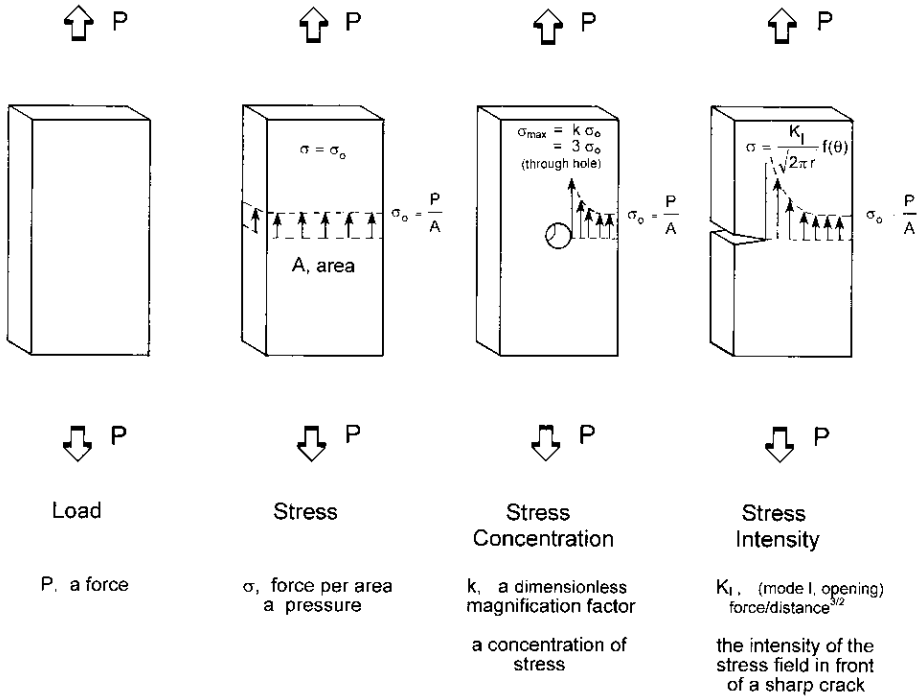

Figure 7.12 *A force P acts upon the object. Fracture occurs at a critical force that depends upon the material properties and the object's size. (b) stress is the force normalized by the cross sectional area. (c) discontinuities such as a thorough-hole concentrate stress and magnify it in the vicinity of the discontinuity. (d) sharp discontinuities such as cracks intensify the stress field in front of the discontinuity.*

throughout the brick in this simple example. Real engineering structures usually have stress variations or gradients and the stresses are magnified or concentrated in the vicinity of geometric discontinuities. So, for example, the through hole shown in the Figure 7.12c *concentrates* stresses at the side of the hole since "flow lines of stress" (described below) are diverted around the hole. Stress concentrations are dimensionless magnification factors usually designated by lower case letter k. For the case of a through hole, k = 3, meaning that in the immediate vicinity of the hole, the stress is three times the nominal stress elsewhere in the body.

Simple problems may be analyzed by the so-called "strength of materials" analysis, wherein assumptions about the structure (e.g., cross section plane sections remain plane, deflections are small, the structure remains elastic to fracture) lend themselves to simplified analysis. The maximum stress in three- or four-point beams in bending may be readily derived from "simple beam theory" a subset of the strength of materials analysis. More elaborate analyses may be solved by the "theory of elasticity" or by computer analysis using the "finite element analysis" (FEA).

The local stress conditions in the vicinity of *sharp* discontinuities such as cracks cannot be adequately modeled using the strength of materials analyses. Stress concentration analyses lead to estimates of infinite stress at crack tips. Fracture mechanics is a discipline that deals with the stresses and strains around sharp flaws and has as its roots the 1920s work of Griffith.[36,37] He showed that the strength of a brittle material with an slender elliptical flaw through crack of size 2c in a uniformly stressed plate as shown in Figure 7.13 is:

$$\sigma_f = \sqrt{\frac{2E\gamma_f}{\pi c}} \tag{7.5}$$

where σ_f is the fracture stress (the nominal stress in the plate), E is the elastic modulus, and γ_f is the fracture energy that is the energy to create unit surface area. In this Guide, flaw size is denoted as either "a" or "c" following conventional practice in the fracture mechanics literature. Usually the dimension is the radius or half width if the flaw is in the middle of a plate as shown in Figure 7.13a. If the crack is on the side of the plate, then a or c are the full crack length. The critical feature of this relationship is that strength is inversely proportional to the square root of flaw size. The larger the flaw, the weaker is the structure. Griffith's formula was derived on the premise that crack propagation occurs if the elastic strain energy release in a body is greater than the creation of surface energy due to the new surfaces if the crack were to extend. His formula sets a necessary condition for a decrease in overall energy of the system.

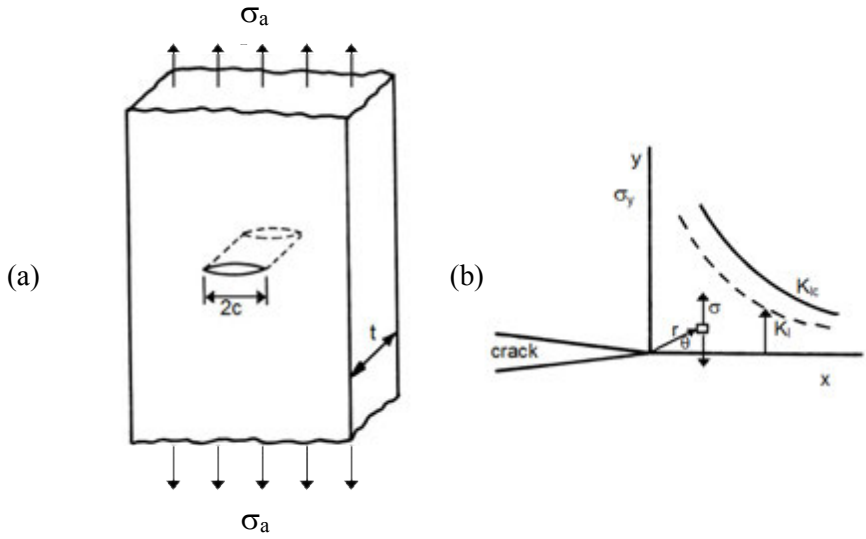

Figure 7.13 *Through crack in a plate loaded in tension. (a) Long slender elliptical cracks of this type were envisioned by Griffith as flaws. If the crack tips are atomically sharp, fracture mechanics developed by Irwin[38] in the 1950s must be used to model the stress state in the immediate vicinity for the crack tip as shown in (b). The dashed line shows σ_y as a function of x directly in front of the crack tip at y = 0. The stress intensity K_I quantifies the magnitude of the stress field acting to open up the crack tip. K_I depends upon the far field stress, σ_a and the geometry of the crack and the structure. Fracture occurs when the intensity of the stress field reaches a limiting value, K_{Ic}, known as the "critical fracture toughness, Mode I."*

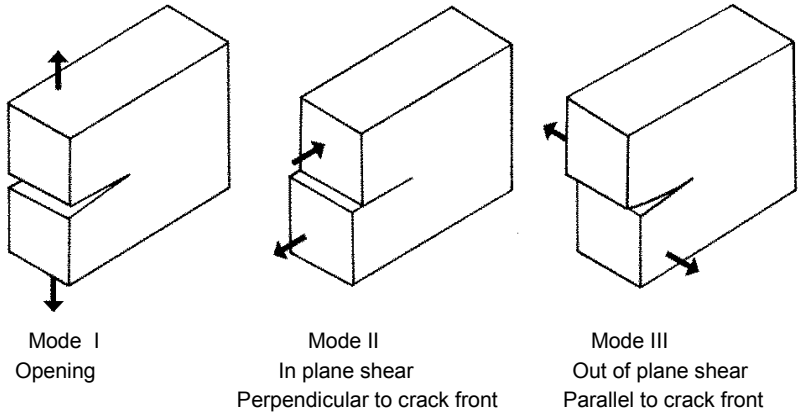

Figure 7.14 *Loading modes on a crack*

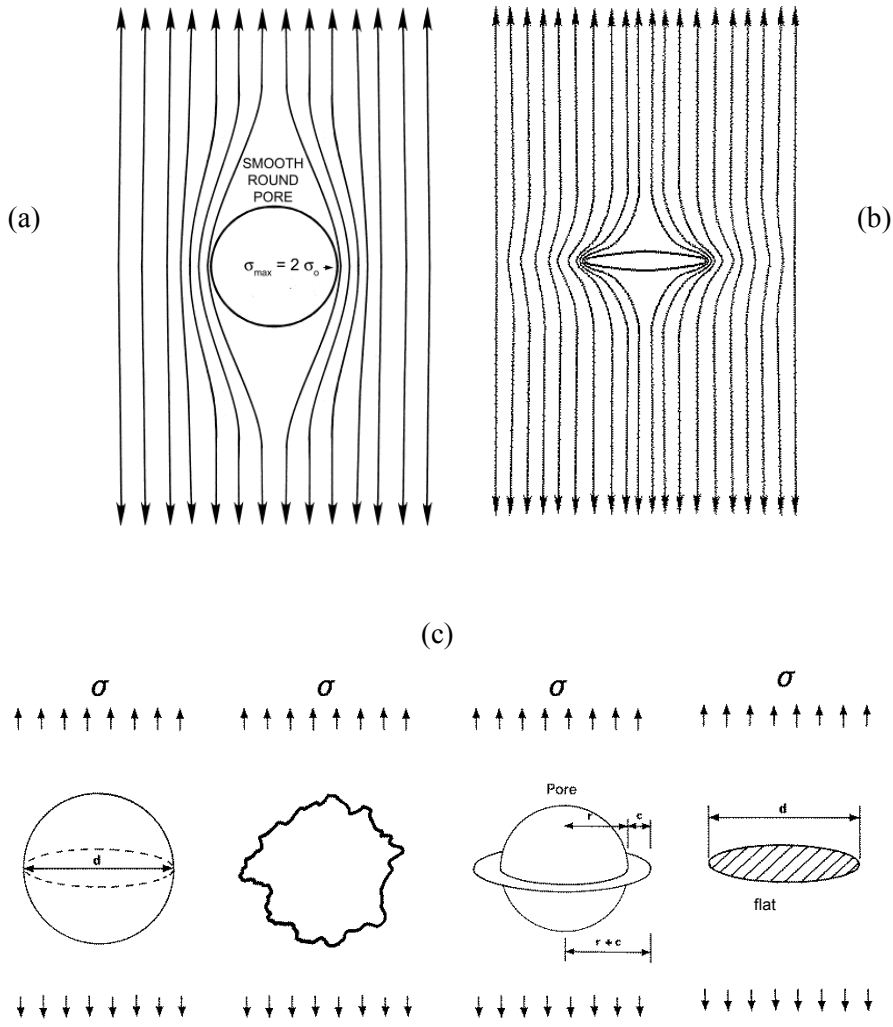

Figure 7.15 *Lines of stress or "flow lines of stress" in a body. They cannot be transmitted through the irregularity such as a bubble or a pore. The flaws create a stress concentration on the sides where the flow lines converge. Sharper irregularities, such as the flattened wide flaw on in (b) create even greater stress concentrations. In the limit, for a flat sharp crack, the flow lines of stress kink severely, and fracture mechanics must be used as opposed to a simple stress concentration factor. (c) shows four flaws that have similar size. The left two are not particularly severe flaws despite their size, but the right two are more deleterious, especially if the rim-cracked pore ("Rings of Saturn") flaw has a large rim crack, c. The flat penny-shaped flaw (shown schematically) on the right is the severest.*

Cracks may be loaded in other configurations as well, as shown in Figure 7.14. Ceramics and glasses usually break due to opening mode I loading.

Before we go any further, there is a useful concept that may aid those who are not mechanical engineers or experts in fracture mechanics. When bricks such as shown in Figure 7.12 or 7.13 are loaded by remote uniform tension, the opposing forces or stresses at either end are transmitted through the bulk by lines of stress or "*flow lines of stress*" such as shown in Figure 7.15. These flow lines kink or bend around notches, grooves, or flaws. Engineers often use this concept to qualitatively assess what would happen with notches or grooves in parts such as rotating shafts, or a step reduction in diameter in a shaft, or even the neck and gage section of a direct tension strength test specimen. The more severe the kinking, the greater the stress concentration.

Many flaws are atomically sharp and fracture mechanics analyses developed by Irwin in the 1950s are applicable.[38] This approach analyses the stress field in front of a crack tip. The intensity of the field is quantified by the term K_I, which is called the "stress intensity factor, mode I." Mode I means the opening mode, whereby the crack faces are pulled directly apart as shown in Figure 7.14. This mode is of primary concern for most ceramic and glass failures. As figures 7.12 and 7.13 show, the intensity of the stress field in front of the crack tip is proportional to K_I. The flaw will propagate when the stress intensity reaches a critical condition, K_{Ic}. For many loading configurations, once the crack begins to propagate, it will run unstably and cause fracture. K_{Ic} is called the "critical stress intensity factor, Mode I," or simply *fracture toughness*. *For a small flaw in a body loaded in tension,* σ_a, the stress intensity acting on the flaw is:

$$K_I = Y \sigma \sqrt{c} \tag{7.6}$$

and fracture occurs when:

$$K_{Ic} = Y \sigma_f \sqrt{c} \tag{7.7}$$

Y is the stress intensity shape factor, a dimensionless parameter that takes into account the shape of the crack and the loading conditions, c is the crack size, and σ_f is the stress at fracture. In this Guide, Y combines all geometric terms and π or $\sqrt{\pi}$ terms. Examples of Y are shown below. Fracture occurs when any combination of Y, σ, or c leads to the critical condition. It should be emphasized that equations 7.6 and 7.7 only apply to small flaws loaded by remote tensile stresses, also known as "far-field stresses." Most textbooks on fracture mechanics show illustrations such as Figures 7.12 and 7.13, whereby the stress field is remotely applied (not near the crack) and σ_a is the nominal stress if no crack were present. The flaws may be embedded in the bulk or may be on the specimen surface. Cracks may be loaded in other component shapes

or loading configurations that do not create far-field stresses. For example, the local stresses from the plastic deformation zone underneath a Vickers indentation (that act on a median crack) are not far-field stresses, nor are the localized contact stresses where a sphere presses on a ceramic or glass surface. Furthermore, equations 7.6 and 7.7 may be inapplicable once cracks become very large relative to a component size. For example, a bend bar with a crack that reaches half way through the bar thickness has a much more complicated equation relating force, crack size, and beam dimensions to K_I. The point here is that if one finds a fracture origin crack in a broken ceramic or glass object, and is tempted to apply equation 7.7, decide first whether the stresses really are remotely applied and are genuinely far field. Do not apply equations 7.6 or 7.7 if the stresses are localized, or if the part dimensions are so small that the flow lines of stress around the flaw are not well established as in Figure 7.15.

Note that the stress and flaw size dependencies are the same as the Griffith equation. Indeed, the energy and stress intensity approaches are consistent, and for plane strain (page 1.5) loading conditions:

$$K_{Ic} = \sqrt{\frac{2E\gamma_f}{(1-\nu^2)}} \tag{7.8}$$

where E is the elastic modulus, γ_f is the fracture energy, and ν is Poisson's ratio. (Note: sometimes the reader may find this equation without the $1-\nu^2$ term. That is the appropriate form for plane stress conditions, but nearly all practical problems for ceramics and glasses are plane stress conditions. In any case, since ν is typically between 0.15 and .25 for ceramics and glasses, ν^2 is small and the denominator is close to 1.)

Sometimes the fracture mechanics literature uses a related term, G_{Ic}, *the critical strain energy release rate.* For plane strain conditions, it is related to K_{Ic} by:

$$K_{Ic} = \sqrt{\frac{EG_{Ic}}{(1-\nu^2)}} \tag{7.9}$$

and $G_{Ic} = 2\gamma_f$. The ceramics and glass technical literature of the 1960s and early 1970s used analyses based on γ_f and the Griffith equation 7.5, but few flaws have a simple through-plate elliptical shape. Fracture mechanics analysis based upon stress intensity K_I is more versatile and can model more complex-shaped cracks. It became more common in the 1970s and is dominant today.

Fracture toughness, K_{Ic}, is an important material property that characterizes a material's intrinsic resistance to fracture. It has units of stress $\sqrt{}$length and in SI units is expressed either as MPa$\sqrt{}$m or MN/m$^{1.5}$. (The English system of units

Material	K_{Ic} MPa√m	R-curve?	SCG at room temperature?
Glasses	0.75 – 0.90	No, flat	Yes
Sintered fused silica	0.92	No	Yes
Glass ceramics	2.0 – 2.5	No	Yes
Mullite	2.2	?	?
Alumina, single crystal	2.4 to 4.5 different planes	No	Yes
Alumina (hot pressed or sintered, 99.9% pure, fine grained)	3.0 – 4.0	No	Yes
Alumina (sintered, glass bonded)	2.5 – 5.	No	Yes
Alumina (coarse grained)	3.0 – 5.0	Yes	Yes, especially if there is a glassy boundary phase
Boron carbide (hot pressed)	2.5	No, flat	No
Silicon carbide (solid state sintered)	2.5 – 3.0	No, flat	No
Silicon carbide (liquid phase sintered, elongated grains	3. – 5.	Yes	Yes
Silicon nitride (equiaxed fine grained)	4.5	No	No
Silicon nitride (elongated grains, glassy boundary phase)	5. – 8.0	Yes	Yes
Zirconia, cubic stabilized	3.	No, flat	?
Zirconia, Mg partially stabilized	3. – 18	Yes	Yes
Zirconia, Y tetragonal zirconia polycrystal	4.5. – 5.0	No	Yes
Cast iron	37. – 45.	No	No

Table 7.2 *Approximate fracture toughness, K_{Ic}, values. Fractographers should obtain a more specific value for the material being examined whenever possible. See sections 5.9.1 and 7.10 for slow crack growth (SCG). See sections 5.9.2 and 7.11 for R-curves. The larger values of K_{Ic} are usually associated with materials that have rising R-curve behavior. If R-curve behavior is suspected for a material, it is best to use a small-crack fracture toughness in a flaw size calculation rather than a plateau value.*

for fracture toughness is ksi√in and the conversion factor to the SI units is only 1.1 as listed in Table 7.1) Fracture energies are usually expressed as erg/cm^2 or as J/m^2. Table 7.2 shows some approximate K_{Ic} values. It is much better, however, to use a value for a specific material, since fracture toughness depends strongly upon composition and microstructure. Figure 7.16 shows some crack-microstructure interactions that can affect crack propagation and hence the fracture toughness.

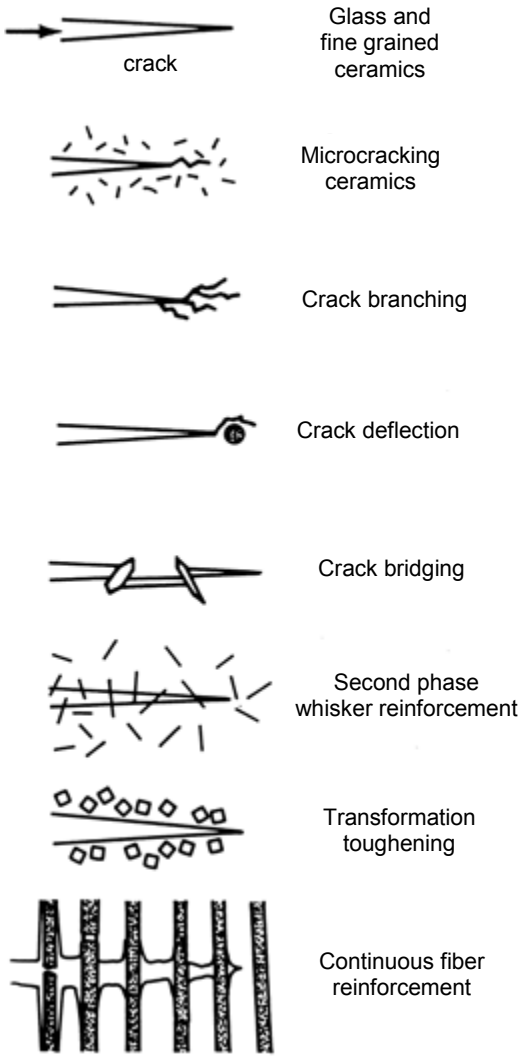

Figure 7.16 *Crack interactions with microstructure.*

Table 7.2 includes two columns that require explanation. The third column is for R-curve behavior whereby fracture resistance increases as a crack extends. This behavior is caused by several of the crack microstructure interactions shown in Figure 7.16 such as transformation toughening around a crack tip or bridging behind the crack tip. The fourth column in Table 7.2 is for "slow crack growth" which is a phenomenon whereby cracks grow stably at stress intensities less than K_{Ic}. Both of these phenomena are dependent upon the chemistry and microstructure. It is convenient to categorize materials according to Table 7.3. For now, the discussion will focus on the simplest combination in the top left box: a material that does not have slow crack growth and which has a flat R-curve. Such a material has a single value for fracture resistance, K_{Ic}. Many ceramics (e.g., solid-state sintered silicon carbide and many fine-grained materials) and all glasses if tested under inert atmosphere conditions fit this category. Slow crack growth and R-curve effects are discussed later in this chapter.

Brittle (no R-curve) no SCG K_{Ic}	Brittle (no R-curve) SCG K-V (velocity) curves
Rising R-curve no SCG K_R – a curves	Rising R-curves and SCG K_R – a curves and K-V (velocity) curves

Table 7.3 *The fracture resistance of ceramics and glasses may be categorized by whether the material does or does not exhibit slow crack growth (SCG) or rising R-curve behavior. (After Fuller, private communication.)*

Users should be cautioned that much fracture toughness data is unreliable, especially the data obtained from simple saw cut notched bend bars or Vickers indentation crack length methods. The former method almost always overestimates fracture toughness. Vickers indentation fracture toughness data are notoriously faulty. Reliable methods such as single-edged precracked beam, chevron-notched beam, or surface crack in flexure, have been refined and standardized. International round robins and reference materials such as NIST Standard Reference Materials, SRM's 2100, 2100A, and 2100B, have confirmed their reliability.[39] Slow crack growth and R-curve behavior are important phenomena that add complications to fracture analysis, but for now

we focus on a straightforward, simple application of equation 7.7 to aid fractographic analysis.

The stress intensity K_I on a flaw depends upon the flaw size and shape, the stress magnitude and distribution, and on the component size and shape. A remarkable variety of fracture crack shapes and loading configurations have been analyzed and the reference handbooks listed in Appendix A may be consulted for a specific problem. Figure 7.17 illustrates two examples. Figure 7.17a shows *a flat penny-shaped circular flaw* in uniform tension, which is a case that is commonly used to simulate internal flaws in ceramics. Equations 7.6 and 7.7 are applicable and the shape factor Y for this configuration is 1.128 as shown in the Figure.

Figure 7.17b shows a different loading configuration on the same flaw. At first glance it looks similar, but it is not. Opposing forces P pull on the center of the crack faces. This is not a far-field stress and equation 7.7 is inapplicable. K_I has a completely different form as shown in the figure. Indeed, the larger the crack size, a, the less the stress intensity! This can easily be understood by

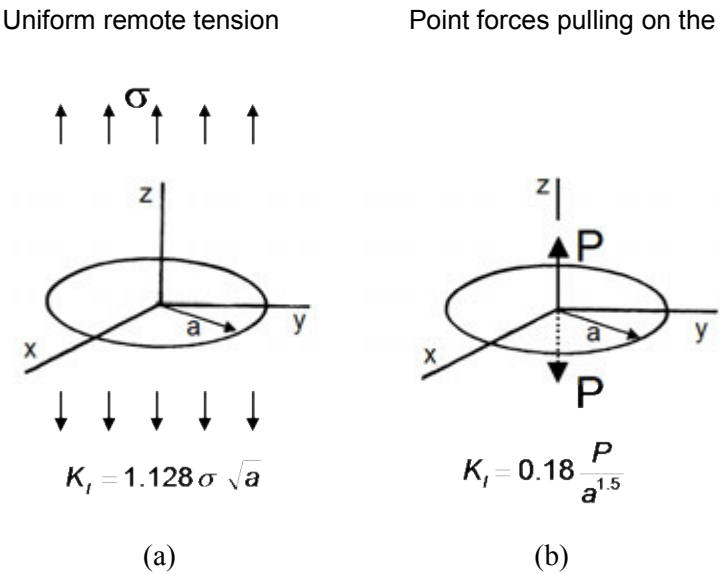

Figure 7.17 *The stress intensity K_I for penny-shaped circular cracks for two loading configurations. (The three-dimensional axes make the flaws appear elliptical in this view.) (a) shows a far-field tensile stress σ, and (b) shows opposed forces P pulling directly on the middle of the crack. K_I increases with crack size in (a), but decreases with crack size in case (b).*

considering that the effect of the force P is distributed along the flaw's perimeter. The larger the crack radius, a, the greater the perimeter and the less the force per unit length of crack perimeter. (This latter case, or more precisely the case for a semicircular surface flaw, is commonly used to represent the effect of concentrated residual indentation stresses from a Vickers indentation on a median crack flaw.)

Surface cracks can often be modeled by semielliptical flaws as shown in Figure 7.18.

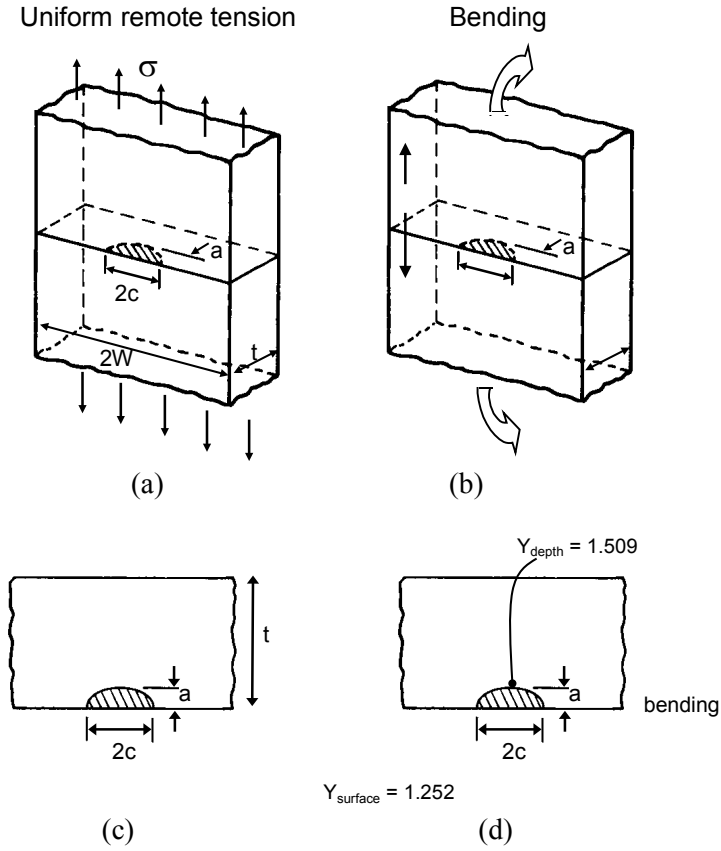

Figure 7.18 *Surface cracks in plates or bars in far-field tension (a) or bending (b). The stress intensity factor equations by Newman and Raju[40] are applicable to these configurations. The Y factors for case (a) and (b) are the same for very shallow cracks, a/t → 0. (c) is a view of the cross section. (d) shows the same but labeled with the Y factors at two locations for the flaw dimensions given in the example on page 7-31 in Section 7.5.2.1.*

The flaw shape affects the Y factor. Y varies around the flaw periphery. A flaw goes critical when one portion of the flaw reaches K_{Ic}, so the maximum Y is of primary concern. The author has seen a number of instances where localized fractographic markings confirmed that fracture indeed had started at the portion of the flaw periphery that had the maximum Y. Figure 7.19 shows maximum shape factors for a variety of elliptical and semi elliptical flaws subjected to a far field uniform tensile stress. In each instance, the flaw size for equation 7.6 is the *depth* for surface flaws, or the *half minor axis length* for internal cracks.

Note that for comparably sized internal or surface flaws, the surface flaw has a greater Y factor. This is because it has less supporting material in the vicinity to share the forces. The crack opening displacements on a surface connected flaw are also greater.

The model cracks shown in Figures 7.18 and 7.19 may be used with equation 7.7 for small flaws that cause fracture in ceramics and glasses. The equation has four variables: the far-field tensile stress at fracture, σ_f; the flaw size, a or c; the shape factor, Y; and the fracture toughness, K_{Ic}. This simple equation may be used in three different ways:

(1) Flaw size may be estimated if Y, σ_f, and K_{Ic} are known. This approach is very useful in laboratory testing, whereby specimens are broken under controlled conditions, and break loads and specimen and fixture geometries are used to compute failure stresses.
(2) The failure stress, σ_f, can be estimated if the flaw size and shape can be measured fractographically, and K_{Ic} is known. This approach is useful in estimating stresses in fractured components.
(3) Fracture toughness, K_{Ic}, may be computed if the flaw size and shape, and the failure stress are known.

Examples will be shown below, but first additional information about the flaw shape and stress gradients must be considered so that appropriate Y values may be estimated. The reader should be forewarned that there is no consistency in the fracture mechanics and materials science literatures. Crack sizes are usually described by a, b, c, 2c, or other symbol, but sometimes these same symbols are used differently and sometimes they are even used for the component dimensions. Sometimes the Y factor includes π or a $\sqrt{\pi}$ term, but often it does not. (One reference even uses Y as the inverse of how it is used everywhere else.) In this Guide, and in ASTM standards C 1322[41] for fractography and C 1421[42] for fracture toughness, all geometric terms for the stress intensity shape factor (including π or $\sqrt{\pi}$) are combined into Y.

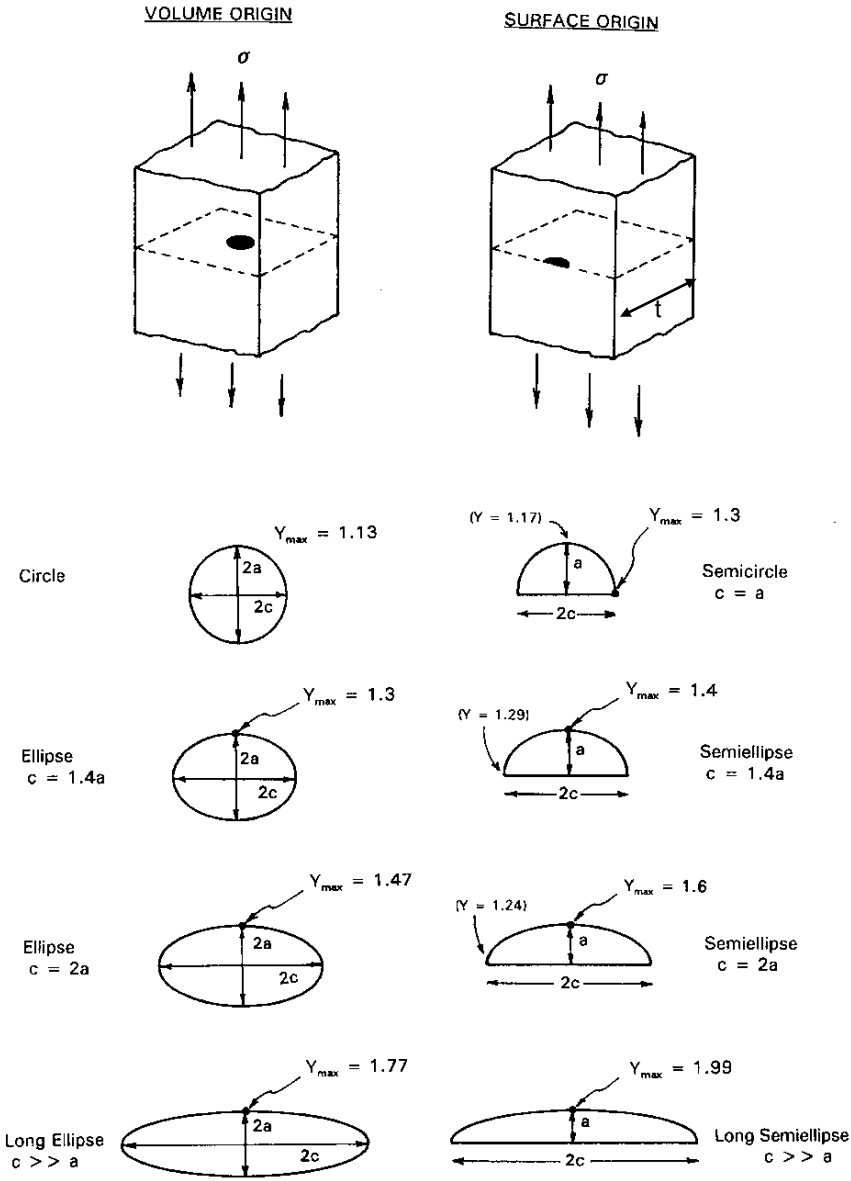

Figure 7.19 *The stress intensity shape factors Y for surface and internal round and elliptical for internal (volume) cracks and surface cracks for far-field tension stresses. Minimum Y factors for the surface cracks are shown in parenthesis. The Y factors for the surface flaws may also be used for parts loaded in bending if the flaw depth a is small relative to the specimen thickness (a/t is small).*

7.5.2 The Newman-Raju Y factors for semielliptical surface flaws in bending

7.5.2.1 The Newman-Raju formulas

Ceramics and glasses often have surface origins and the stress intensity factor solutions of Newman and Raju[40] for both tension and bending stress fields are very helpful. Their versatile solutions may be applied to tension, bend bar, and biaxial disk specimens, and indeed any component shape wherein a remote stress field causes fracture. With reference to Figure 7.18 for dimensions for surface flaws in a plate or beam in bending, the Y_{depth} and $Y_{surface}$ for locations at deepest part of the crack and at the surface are:

$$Y_{depth} = \frac{M}{\sqrt{Q}} H_2 \sqrt{\pi} \tag{7.10}$$

$$Y_{surface} = S \frac{M}{\sqrt{Q}} H_1 \sqrt{\pi} \tag{7.11}$$

where M, Q, H_2, H_1, and S are geometric terms:

$$M = \left[1.13 - 0.09\left(\frac{a}{c}\right)\right] + \left[-0.54 + \frac{0.89}{0.2 + \left(\frac{a}{c}\right)}\right]\left(\frac{a}{t}\right)^2 + \left[0.5 - \left(\frac{1.}{0.65 + \left(\frac{a}{c}\right)}\right) + 14.\left(1. - \left(\frac{a}{c}\right)\right)^{24}\right]\left(\frac{a}{t}\right)^4 \tag{7.12}$$

$$H_1 = 1. - \left(0.34 + 0.11\left(\frac{a}{c}\right)\right)\left(\frac{a}{t}\right) \tag{7.13}$$

$$H_2 = 1. - \left(1.22 + 0.12\left(\frac{a}{c}\right)\right)\left(\frac{a}{t}\right) + \left[0.55 - 1.05\left(\frac{a}{c}\right)^{0.75} + 0.47\left(\frac{a}{c}\right)^{1.5}\right]\left(\frac{a}{t}\right)^2 \tag{7.14}$$

$$\Phi = \sqrt{Q} = \sqrt{1. + 1.464\left(\frac{a}{c}\right)^{1.65}} \qquad \text{for } a/c \le 1 \tag{7.15}$$

$$S = \left(1.1 + 0.35\left(\frac{a}{t}\right)^2\right)\sqrt{\left(\frac{a}{c}\right)} \tag{7.16}$$

(Equations 7.10 and 7.11 do not include an additional term f_w in the original Newman-Raju analysis, since for nearly all cases for ceramics and glasses, the flaw width 2c is small relative to the component width, and f_w is 1.0.) These polynomials appear intimidating at first glance, but are easily programmed into hand calculators or spreadsheets. Notice how many of the dimensions appear as ratios, e.g., a/c, the flaw ellipticity ratio; or a/t, the ratio of the flaw depth to the plate thickness). The $(1-(a/c))^{24}$ term for M in eq. 7.12 is genuine and not a typographical mistake. The Newman–Raju Y factors have been widely used in many textbooks and are included in several ASTM standards including C 1421 for fracture toughness of ceramics[42] and E 740 for metals,[43] as well as ISO standard 18756.[44]

The above equations are for surface cracks in bending stress fields. Newman and Raju listed alternative formulas for direct uniform tension loadings.[40] It is not necessary to list them here. Equations 7.10 – 7.16 may be easily used for cracks in uniform tension loaded parts by the simple expedient of inputting an arbitrary large value (e.g., 1000) for the part thickness, t.

So for example, if a bend bar is broken and it has a surface crack with a depth (a) of 40. x 10^{-6} m; width (2c) of 144. x 10^{-6} m; and specimen thickness (t) of 2.998 x 10^{-3} m; then M = 1.080, H_1 = 0.995, H_2 = 0.983, $\sqrt{Q}$ = 1.247, and S = 0.820. Then, Y_{depth} = 1.509, $Y_{surface}$ = 1.252. These are shown in Figure 7.18d.

In practice, the more elliptical the flaw, the more likely the maximum Y is at the flaw depth (unless the crack penetrates deeply into the specimen interior and into the stress gradient.)

Using the larger value for Y and the flexural strength which was 453 MPa, equation 7.7 gives K_{Ic} = 1.509 x 453 MPa $\sqrt{40 \times 10^{-6}}$ = 4.32 MPa$\sqrt{m}$. In this case, the parameters are used to estimate the material's fracture toughness.

As noted on page 7.28, equation 7.7 for K_{Ic} can be used two other ways. If instead, the fracture toughness and flexural strength were known, the flaw size could have been estimated. Similarly, if the crack size had been measured and the fracture toughness was known, then the stress of 453 MPa could have been estimated.

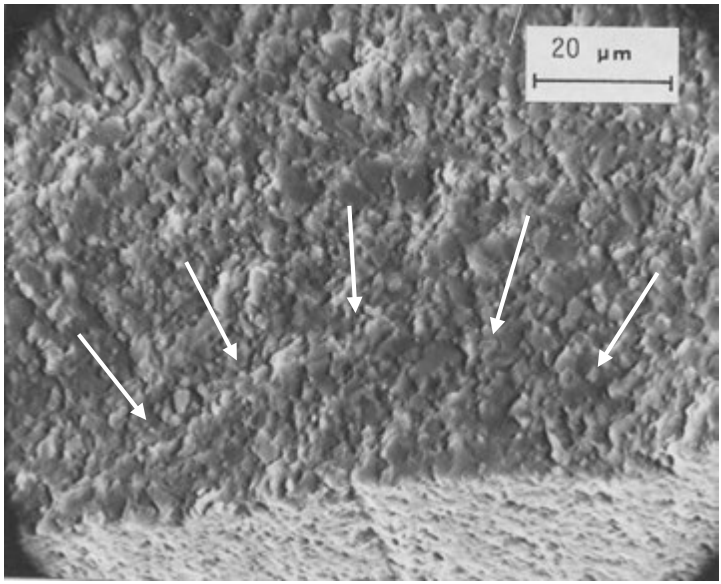

Figure 7.20 *Grinding crack in a longitudinally-ground silicon carbide bend bar at 649 MPa. This flaw was located directly in the center of a well-defined fracture mirror. The depth a is 23 µm, the width 2c is 95 µm, and the bar thickness, t, was 2.2 mm.* Y_{max} *was at the deepest point and was 1.58. The computed fracture toughness is: 1.58 * 649 MPa * √23 x* 10^{-6} *= 4.9 MPa √m, which is reasonably consistent with published average values of 4.0 to 4.5 MPa √m for the material. This orthogonal grinding crack is subtle and does not stand out clearly against the background microstructure. There may have been some doubt about its identification, but the fracture mechanics calculation shows it is about the right size.*

Figures 7.20, 7.21, and 7.21 show three examples of how the calculation can be used to confirm that the right flaw has been identified. Sometimes the calculated and measured flaw sizes agree very closely, but there are a number of reasons why they may differ as discussed below in section 7.8. ASTM standard C 1322[40] states that if the calculated and measured flaw sizes do not agree within a factor of two or three, then the origin should be reexamined to verify that the correct feature has been identified.

The surface crack in the BK-7 borosilicate crown glass disk shown in Figure 6.28a,b and 7.22 was 7.3 µm deep and the stress at fracture was 146 MPa. For a long surface crack, Y is 1.99. The calculated fracture toughness from these values is 0.78 MPa√m, which is very close to published values for this particular glass.

(a)

(b)

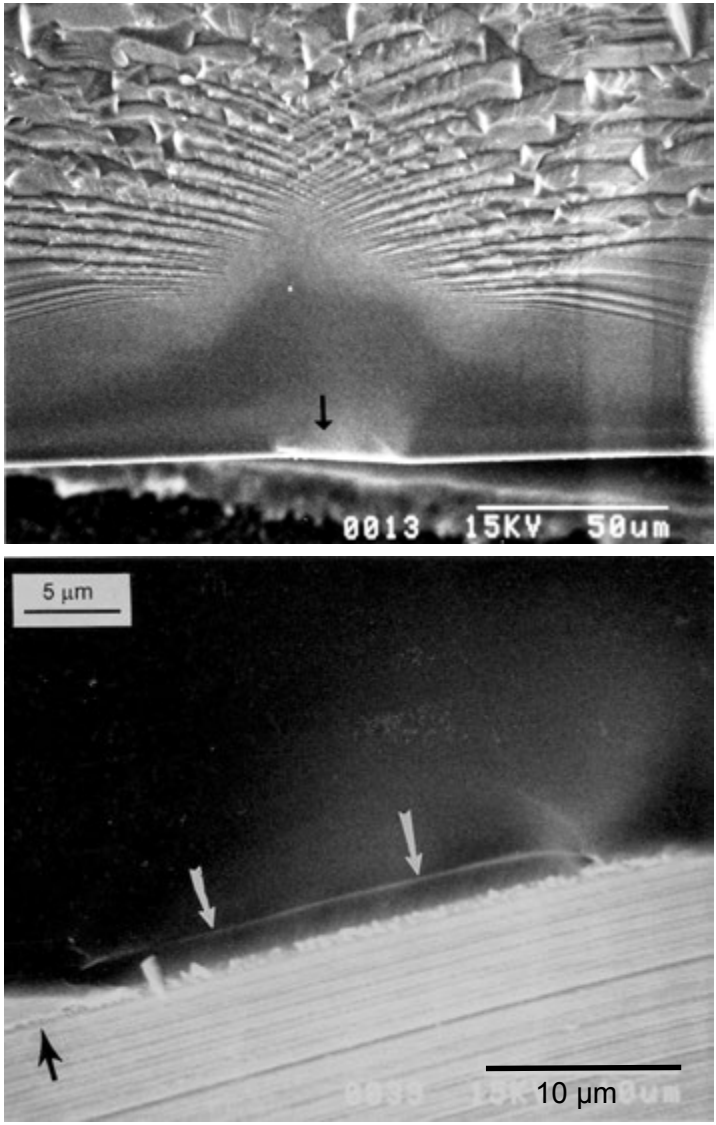

Figure 7.21 *Fracture origin in a single crystal silicon wafer. (a) shows the fracture mirror which has a very faceted shape typical of some single crystals. The origin is a grinding crack shown by the white arrows in (b). The specimen was tilted back to show both the fracture and outer ground surfaces. A 3000 X scanning electron microscope photo showed that the crack was 2 micrometers deep, and when combined with a 282 MPa fracture stress, and a Y factor of 1.99, gives* $K_{Ic} = 0.79$ *MPa* $\sqrt{m}$*, in reasonable good agreement with published values for fracture on the {110} plane.*

(a)

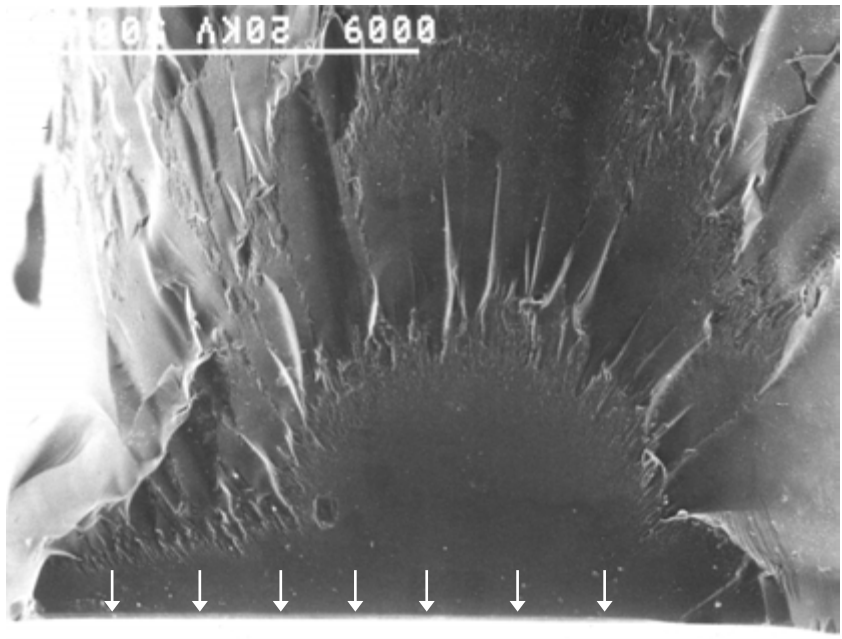

(b) (c)

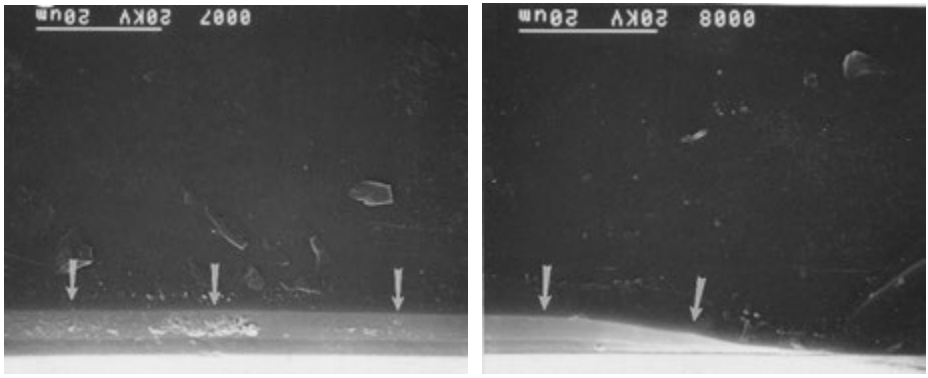

Figure 7.22 *Fracture origin crack for the borosilicate crown glass biaxial disk specimen that was broken in inert conditions as shown in Figure 5.17. (a) is an SEM photo of the distorted mirror. The arrows show the long polishing scratch. . (b) and (c) show two portions of the polishing scratch which was 7.3 mm deep (arrows). Using Y = 1.99 and the breaking stress of 146 MPa, gives* K_{Ic} *= 0.78 MPa* $\sqrt{m}$*. The optical image (see Figure 5.17) showed a slight bulge in the flaw at the center of the mirror suggesting the flaw may have grown slightly before going critical. This growth is not evident in the SEM images.*

7.5.2.1 Graphical curves for the Newman-Raju formulas

Figure 7.23 may be useful for those who do not wish to program a calculator or spreadsheet. Y values may be picked off the graph for cracks in bending problems for given a/t and a/c ratios. Notice it demonstrates how Y decreases as a flaw penetrates into the stress gradient (larger *a/t*). (Y values for small surface flaws in uniform *tension* fields may be obtained by reading the graph value for an *a/t* ratio of zero.)

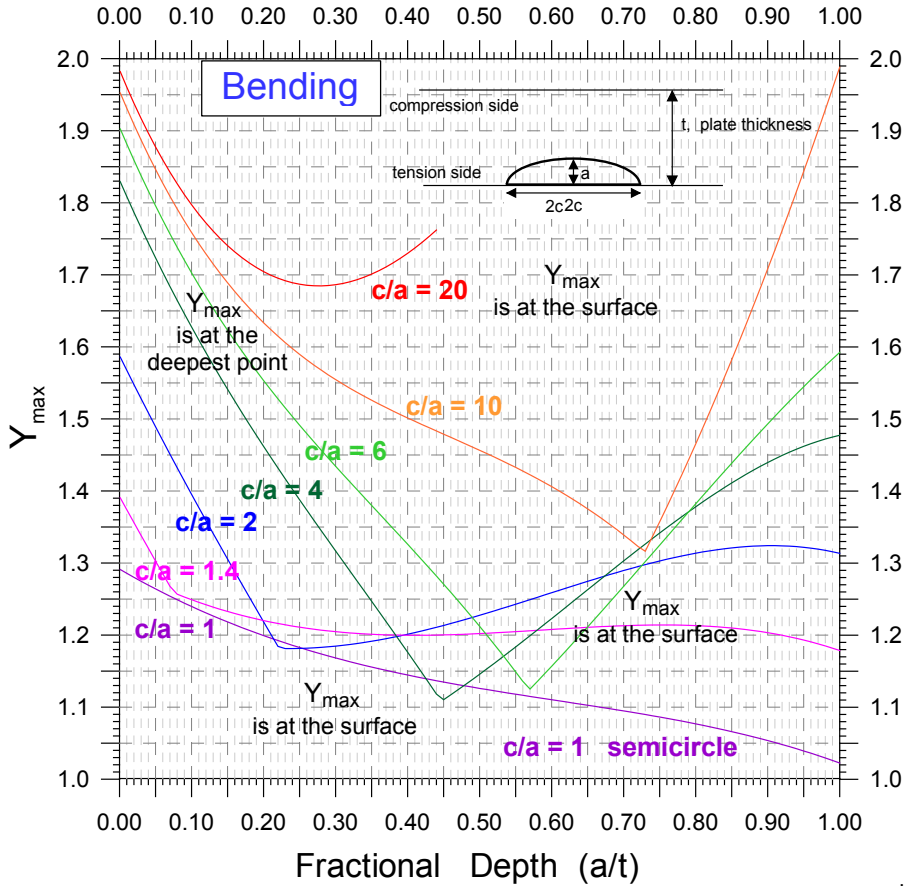

Figure 7.23 *The maximum stress intensity shape factor Y for semielliptical surface cracks in a bending stress field in a plate or bar of thickness t. In the limit as the flaw is very small relative to the plate thickness, a/t → 0, the solutions are the same as for the uniform tension case. The kink in the loci corresponds to where the maximum Y changes from the surface to the deepest point in the interior or vice versa.*

7.5.2.3 Newman-Raju formulas for deep (a/c > 1) semielliptical surface cracks

Occasionally the fractographer may find a flaw that is deeper than a semicircle, i.e., a/c > 1. Fett devised modified Newman-Raju formulas that permits one to compute the Y_d and Y_s factors in such cases for either tension or flexural loadings. The conscientious reader may consult a paper by Fett[45] for the modified formulas. Rather than listing all the revised formulas or showing charts or tables, some approximations are provided here.

In the cases with semi-ellipses that are deeper than a semicircle, the maximum Y is at the surface, Y_s. For cracks that are shallow relative to the plate thickness ($a/t \leq 0.2$) in tension or bending, the *surface* Y_s factor decreases linearly from that for a semicircle by only 10% as a/c goes from 1 (the semicircle) to 2 (a very elongated crack into the thickness).

The stress intensity shape factor Y_d for the *deepest* part of the flaw also decreases approximately linearly, but by greater amounts. Y_d decreases by 33 % in both tension and bending as a/c goes from 1 to 2. If the flaw is larger relative to the plate thickness (e.g., $a/t = 0.2$), Y_d decreases by 33% and 45% in tension and bending, respectively, as the a/c ratio goes from 1 to 2. In other words, as a very deep semi-ellipse penetrates into the stress gradient in bending ($a/t = 0.2$, or 40% of the way to the neutral axis), Y_d diminishes rapidly.

7.5.2.4 Accuracy of the Newman-Raju formulas and alternatives

A few words about the accuracy of the Newman-Raju stress intensity factors Y are in order here. For most fractographic analyses, an accuracy of a few percent is perfectly adequate. Developed by finite element analysis almost 40 years ago, the Newman-Raju factors are widely used in textbooks, fracture mechanics and fractography standards around the world. Fett has reviewed[46,47] them carefully and concluded that for most common configurations, they are accurate to within 3%. Fett noted that a solution of Isida et al.,[48] obtained by means of a modified body-force method exhibits superior accuracy with a maximum deviation of less than 1% for Y_d.

Even more accurate and versatile solutions have been developed recently by Stobl et al.[49]. For most common semi-elliptical cracks their Y_d solutions concur with Newman and Raju's within a few percent, but the newer solutions cover a broader range of Poisson's ratios and cover surface cracks that have peripheries that do not reach the specimen surface at exactly 90°. Strobl et al.'s cracks are sections of a semiellipse and in some cases they are better models.

7.5.2.5 Bansal's approximation for semielliptical surface flaws

Bansal reviewed the stress intensity shape factors for semi-elliptical surface flaws in uniform tension[50] and arrived at a simple approximation:

$$K_I = \frac{2.0}{1.68}\sigma\sqrt[4]{A} \qquad 7.17$$

where A is the area of the flaw. Since the area of a semi-ellipse is $\pi ac/2$:

$$K_I \approx 1.33\,\sigma\sqrt{\sqrt{ac}} = 1.33\sigma\sqrt[4]{ac} \qquad 7.18$$

Sometimes the expression is written as:

$$K_I = 1.33\,\sigma\sqrt{b} \qquad 7.19$$

where the effective flaw size $b = \sqrt{ac}$.

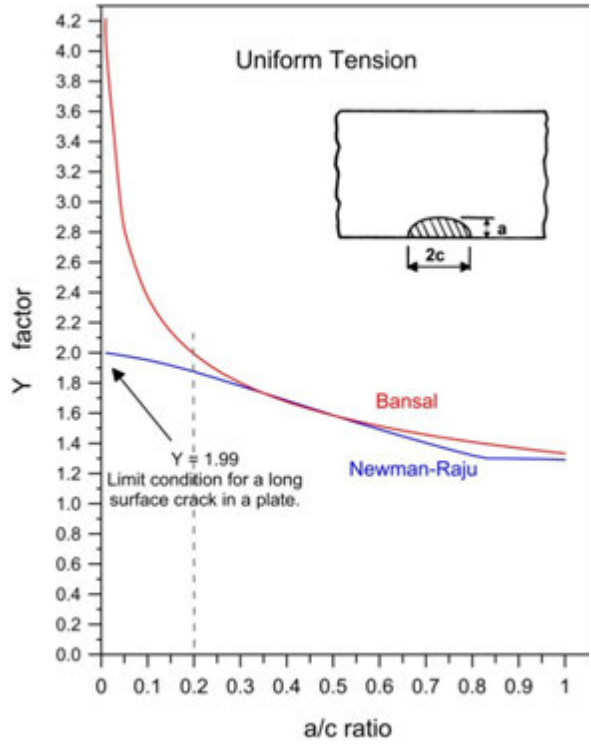

Figure 7.24 *Comparison of Bansal's approximation to the Newman-Raju solution for Y of semielliptical flaws in uniform tension. The approximation is only suitable for a/c > 0.2 .*

Figure 7.24 shows how this approximation compares to the Newman-Raju outcomes, also for the uniform tension case. Bansal's approximation is quite good for the condition of $0.2 < a/c < 1.0$. It begins to deviate for longer, shallower surface cracks, e.g., those with a/c ratios smaller than 0.2 (c/a ratios of 5 or greater). In the limit of a long surface crack in a plate in tension, Y becomes 1.99 and the Bansal approximation is in serious error. In other words, do not use Bansal's approximation for long shallow surface cracks. Furthermore, his solution is only appropriate for uniform tension, or very small flaws in bending such that the crack depth a is small relative to the plate thickness, t or h. If the flaw depth is greater, e.g. $a/t > 0.05$, then the Newman-Raju solutions should be used. (This means that the deepest part of the flaw penetrates into the bending stress gradient by no more than 10%.)

7.5.3 Irregularly-shaped surface cracks

Fracture mechanics reference books have tabulations of stress intensity formulas and shape factors for a myriad of crack shapes and loading configurations. There are even listings for multiple cracks in proximity to each other that show how the stress intensity fields interact. Real flaws in real materials often do not have convenient shapes, however. Several approximations are very helpful. Figure 7.25 shows a case of an irregular planar surface crack loaded by far-field tension. The stress intensity may be approximated, with a maximum of a 10% error (Poisson's ratio of 0.3), by a solution in Murakami's book:[51]

$$K_i = 1.15\,\sigma\sqrt[4]{A} \tag{7.20}$$

where A is the area of the flaw. For example, if the flaw is semicircular with radius a, this simplifies to

$$K_I = 1.29\,\sigma\sqrt{a} \tag{7.21}$$

that is nearly the same as equation 7.19. Numerical analysis showed that the fourth root of area equation 7.20 is an adequate approximation for stress intensity factor solution for such diverse shapes as partial circles, triangles, rectangles and semi ellipses. Equation 7.20 is also for the case of uniform tension. It may be used for small cracks in bending specimens, provided that the crack does not penetrate very deeply into the specimen, $a/t < 0.05$. The area approximation should not be used for very long shallow flaws $c/a > 5$.

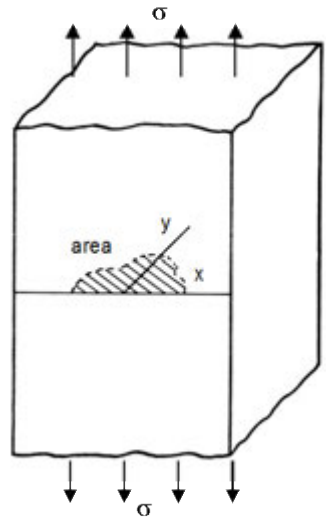

Figure 7.25 An irregular planar shaped surface crack in a tension stress field. (After Murakami, ref. 50.)

7.5.4 Three-dimensional, blunt, and inclined flaws

Real flaws are not always flat and planar. Figure 7.26a shows a sphere that is not unlike many pores in ceramics and glasses. Sometimes round pores are modeled by a penny-shaped crack, Figure 7.26c. This is a gross over-simplification. Indeed, if the pore is round and crack free, it does not act to *intensify* the stress, but simply *concentrates* stress around the flaw sides. The stress concentration factor for an interior sphere in a part in uniform tension is only k = 2. Smooth round pores require much greater force to cause fracture than the penny-shaped flaw of the same diameter. Round pores may be quite docile and not act as strength-limiting flaws. Figure 7.26b shows another variation. This rim-cracked pore ("Rings of Saturn") flaw is a combined stress concentration and fracture mechanics problem. For small rim cracks, the pore acts as a concentrator of stresses, and the rim crack size, c, may be regarded as the crack size in a fracture mechanics calculation. For a very large rim crack, the pore's effect is diminished, and the penny shaped crack is a very good approximation. In practice, it is very difficult to detect a rim crack around a pore, much less measure it. It is not unreasonable to expect that rim cracks of one or two grain diameters extend from the pore and in fact many pores in ceramics do have local microstructural irregularities or microporosity in the vicinity. Only very rarely have fractographers attempted to precisely model

such flaws and it is customary to use the penny-shaped cracks as an approx.-imation, but with full cognizance that the actual flaw is much blunter.

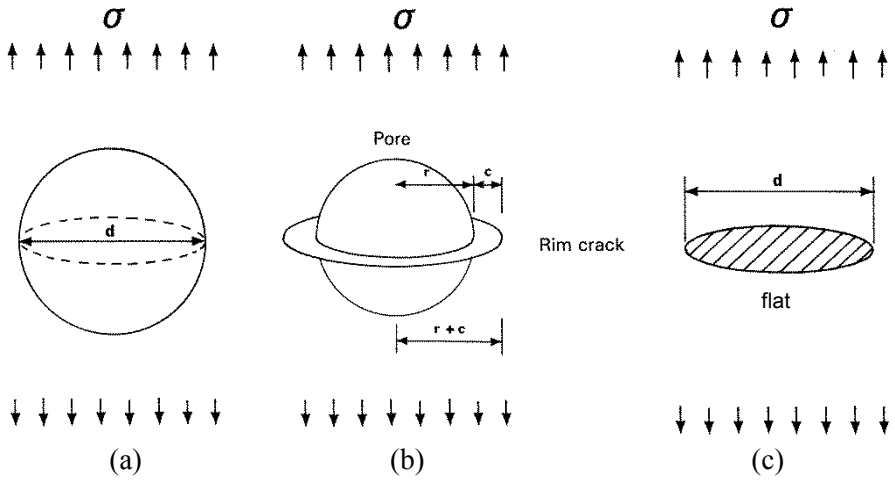

Figure 7.26 *Flaws may be three-dimensional. A flat penny shaped crack (c) is a two-dimensional approximation.*

The reader may consult fracture mechanics handbooks (e.g., Bibliography Appendix A) for more information about rim-cracked pores (also called "annular cracks around a spherical void") or flaws that are *inclined* to the stress direction. A slight inclination of 5 degrees does not affect the mode I loading very much, but beyond 10 degrees flaws experience not only mode I loading but varying degrees of modes II and III depending upon the flaw shape and inclination angle. Modes II and III are have shearing actions on a crack as shown in Figure 7.14.

7.6 Relationship of K_{Ic} and A

K_{Ic} and the fracture mirror and branching constants are related to $\sigma\sqrt{a}$ or $\sigma\sqrt{R}$ and hence have the same set of units: $MPa\sqrt{m}$ (or $ksi\cdot\sqrt{in}$). As Figure 7.7 illustrates, K_{Ic} pertains to conditions at the flaw. The A values correspond to events away from the origin as the crack propagates and reaches terminal velocity. Kirchner and Conway[30] showed that mirror shapes can be predicted on the basis of stress intensity at the crack front as it expands outwards from the origin, so it is not unreasonable to expect that K_{Ic} and the A's are related. If they are related, then in principle one can estimate K_{Ic} from A or vice versa. Mecholsky et al. [52] tabulated A's and K_{Ic}'s for over two dozen ceramics and

glasses and showed there was an approximate correlation. On average the ratio of A_o to K_{Ic} was 20/7 = 2.86, although there was considerable scatter. Bansal and Duckworth[53,54] carefully measured A_o to K_{Ic} ratios of 2.2 to 2.4 for a glass ceramic and a sintered alumina, and 2.3 for float glass and a hot-pressed alumina. Subsequent tabulations[55] on more contemporary materials, many of which have R-curve behavior, have given ratios as low as 1.5 to 2.0.

Kirchner et al.[56] showed that the branching constant A_b varied by over a factor of 2 with the degree of transformation toughening in a calcia partially-stabilized zirconia. The greater the toughening, the greater the suppression of branching to greater distances; i.e., the A_b/K_{Ic} ratio increased with increased toughness.

In a dissenting view, Bradt and colleagues[57,58] have suggested that A is not really a material constant and noted the discrepancies in A/K_{Ic} ratios. In summary, variability in the quality and accuracy of the K_{Ic} and A data, plus genuine microstructural effects, probably mean there is no unique A/K_{Ic} ratio.

7.7 Mirror to Flaw Size Ratios

A simple but very useful observation is that mirror and flaw sizes are related. Krohn and Hasselman[59] showed that the mirror size to flaw size ratio (R/c) is about 10 for glasses. Mecholsky et al. [52,60] obtained ratios of 10 to 11.6 using the mirror-mist (inner mirror) boundary in glasses. They estimated the ratio to be about 13 for the mist-hackle (outer) boundary to flaw size ratio for glasses.

Ratios for ceramics are more problematic and depend upon the microstructure and the ability to judge a specific boundary. Mecholsky et al.[51] estimated the ratio of the hackle boundary (outer mirror) to flaw size was 13 for polycrystalline ceramics and single crystals, but varied from as low as 8 to as large as 40!

Rice[61] pointed out that the bluntness of the flaw may alter the mirror to flaw size ratio. For example, pores often act as blunt flaws and it requires extra energy or stress to overcome the bluntness. The excess energy causes a mirror to form at shorter distances from the origin than if the flaw were sharp. Thus the R/c ratio is smaller.

Slow crack growth can also alter the apparent ratios.[60] If the mirror to flaw size ratio (R/c) is much greater than the values listed above, then the flaw should be checked for evidence that it grew stably prior to fracture.

Residual stresses in the vicinity of the flaw or the mirror also can change the ratios. Unexpected mirror to flaw size ratios may be evidence of residual stresses acting on the flaw or the whole mirror.

The mirror to flaw size ratio (R/c) may also be affected by the presence of mixed Mode I/II loading. Gopalakrishnan and Mecholsky[62], and Rice[63] have shown that increasing Mode II loading on a crack decreases R/c.

The R/c ratio is also affected if a material has a rising R curve. The larger the fracture toughness, the lower the R/c ratio.[61,64] In rising R-curve materials, the ratio may even depend upon how large the initial crack was and how far it might have stably grown before it went unstable. (Stable crack growth and crack instability is discussed more in sections 7.10 and 7.11 later in this chapter.) In R-curve materials, the larger the initial crack, the smaller the R/c ratio. Gopalakrishnan and Mecholsky's 2013 paper[62] even goes so far as to analyze the combined effects of R-curve and mixed Mode I/II behavior on R/c ratios. (Note, their discussions are on the ratio, c/R, unlike most other work which focuses on the R/c ratio.)

$C_{calc} < C_{meas}$	$C_{calc} > C_{meas}$	$C_{calc} > C_{meas}$ or $C_{calc} < C_{meas}$
Crack blunting	Stable crack extension -SCG	High temperature SCG
Use of 2-D model	Stable crack extension – R curve	Multiple flaws nest or interact
Stress gradients	Flaw causes a local fracture toughness degradation	Residual stresses
Crack healing	Flaw is within a single grain	Flaw is truncated on the fracture surface
	Flaw links with other flaws or the surface	Flaw shape irregularity
		Flaw elastic properties are different than the matrix
		Faulty fracture toughness data

Table 7.4 *Factors that can cause a measured flaw size c_{meas} to differ from the calculated c_{calc} size. (Quinn and Swab, Ref. 65 and 66.)*

7.8 Comparing Measured to Calculated Flaw Sizes

Differences in calculated and measured flaw sizes of 20 % to 50 % should not be considered too serious, but variations greater than a factor of 2 or 3 should prompt the fractographer to study the origin more carefully. Either the wrong feature has been identified as an origin or the origin may be more complicated than expected. Either something about the calculation is wrong or the fractographically-measured size is wrong. Table 7.4 and Figure 7.27 show some of the factors than can cause the discrepancy.[65,66] These can be appreciated if Equation 7.7 is rewritten:

$$c_{calc} = \left(\frac{K_{Ic}}{Y\sigma_f} \right)^2 \tag{7.22}$$

where c_{calc} is the calculated critical crack size at fracture, σ_f is the fracture stress, and K_{Ic} is fracture toughness.

The cases where $c_{calc} < c_{meas}$ are considered first. A blunt flaw of actual size c requires a greater stress to cause fracture than a comparably-sized sharp flaw. Some flaws are blunt to begin with. Other initially-sharp flaws may have been blunted or even partially healed by oxidation or other environmental effects. Glass cracks can partially heal in vacuum or inert atmospheres, especially if they form during dynamic events and are unloaded quickly. Inserting the greater stress to break healed or blunted cracks into equation 7.22 leads to a smaller c_{calc} than the actual flaw size c. Assuming that flaws are 2-D penny shaped or are flat ellipses when they really are 3-D flaws, usually leads to Y estimates that are too large, and this also leads to smaller c_{calc} than the actual flaw size c. Unexpected stress gradients can cause σ_f to be overestimated. That in turn will again cause c_{calc} to be too small. The stress at the origin site should be used in equation 7.22.

Next are the cases where $c_{calc} > c_{meas}$. Slow crack growth and rising R-curve behavior can cause stable crack extension. Using the actual breaking stress in equations 7.7 or 7.22 gives a correctly calculated flaw size, but if the fractographer detects and measures only the initial flaw size, then $c_{calc} > c_{meas}$. In this case it is the fractographic size measurement that is off. Alternatively, if stable crack extension due to R-curve behavior does occur, but the fractographer uses a long crack (plateau) value of fracture toughness, then the fracture toughness is overestimated and again $c_{calc} > c_{meas}$. R-curve behavior is discussed in more detail in section 7.11. Inclusions or chemical inhomogeneities can be particularly deleterious if they degrade the fracture toughness of the surrounding matrix. If the fractographer uses the baseline K_{Ic} value in

equation 7.22, this also leads to $c_{calc} > c_{meas.}$ In this case, the calculated size is wrong and the observed crack size is correct. The fracture toughness of a single crystal, or a single grain, is almost always less than that of a polycrystal. If a flaw resides within a single grain, but a polycrystalline K_{Ic} value is used in equation 7.22, then c_{calc} will be too large. Flaws may link up with other flaws or a surface weakening the specimen. If the linkage is undetected by the fractographer, then his c_{meas} will be too small compared to the calculated and actual critical flaw size.

Some factors can cause the measured size versus calculated size discrepancy to go either way. Flaws are often assumed to exist in isolation, but as Figure 7.27b shows they can interact causing either an increase or a decrease in the Y factors that act on them. It all depends upon the geometries and arrangements. This is an instance where the "flow lines of stress" concept can aid interpretation. If flaws are lined up in a row parallel to the stress, the flaws will shield each other. If they are staggered or lined up sideways, they can intensify the K_I fields and the Y factors. Flaws may be truncated and only a portion detected on the fracture surface. Undetected residual stresses can throw off the calculated flaw size as well. Faulty fracture toughness data can also throw off the correlations.

The point here is that fracture mechanics is a valuable tool to aid fractographic analysis. It can help confirm that the fractographer has found the correct origin flaw. A finding that the calculated and measured sizes are appreciably different should prompt further consideration and analysis. What factors caused the discrepancy? Is the discrepancy an isolated outcome or part of a pattern?

(a) Flaw bluntness or 2-D approximations

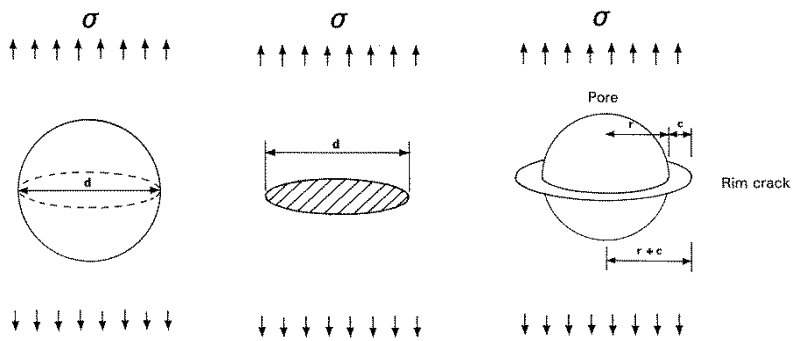

Figure 7.27 *Factors that cause calculated and measured crack sizes to differ (continued on next page)*

(b) Flaw interactions

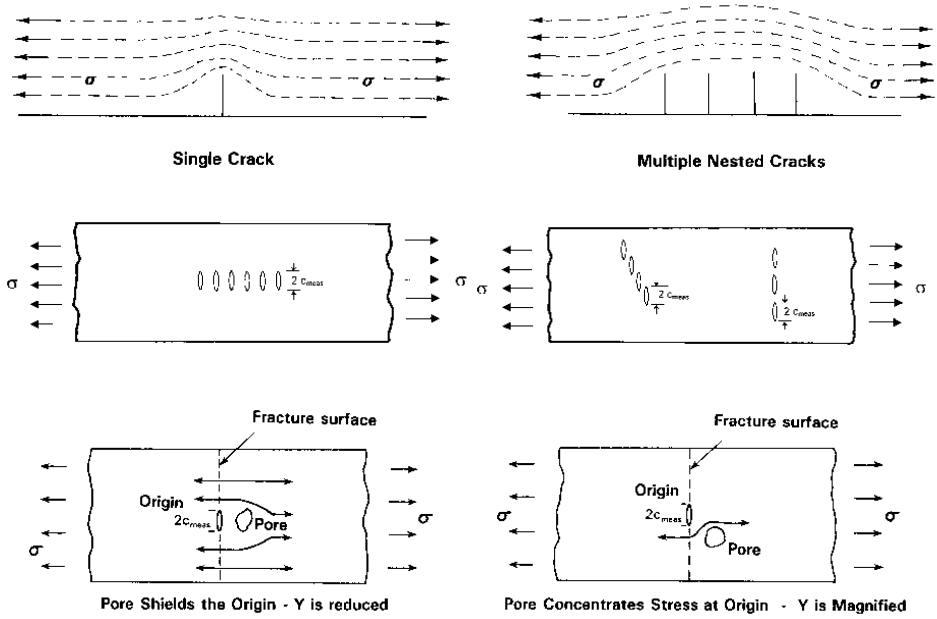

(c) Flaw linkage

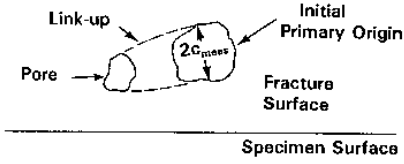

(d) Flaw slow crack growth

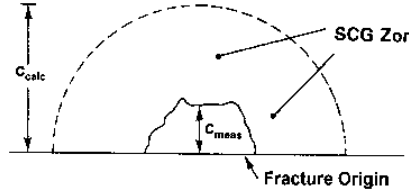

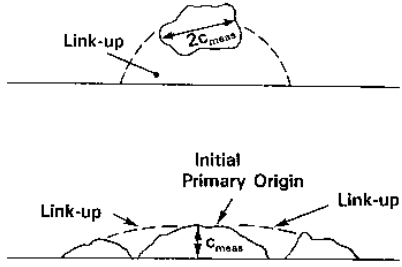

(e) Flaw truncation on the fracture surface

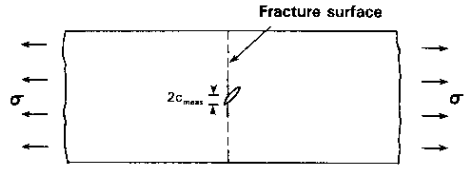

Figure 7.27 continued *Factors that cause calculated and measured crack sizes to differ.*

7.9 Crack Velocities from Wallner Line Analysis

Wallner lines can be used to estimate crack velocities, whether they are created incidentally during the fracture event or deliberately by ultrasonic fractography. Wallner lines may not be evident in very slow fractures in glass or in ceramics due to the latter's rough fracture surfaces.

Ultrasonic fractography uses a transducer to generate sonic waves that interact with the propagating crack as discussed in sections 5.4.4 (on tertiary Wallner lines) and 3.21 (on examination techniques). Usually the transducer is placed position perpendicular to the crack propagation plane. The sonic waves create tertiary Wallner lines and show the crack front shape. Velocities are easily estimated from the pulse frequency and the spacing between the Wallner lines on the fracture surface. Richter and Kerkhof[67,68] and Michalske et al.[69,70] used this technique over a broad range of crack velocities from terminal velocity down to 10^{-7} m/sec. Indeed Richter and Kerkhof[67] used this technique to show that surface cracks that grow by slow crack growth evolve in shape in accordance with the Newman-Raju stress intensity shape factors as shown in Figure 5.44. They also showed Figure 5.45a which proved a semielliptical crack could go unstable from one side as shown in Figure 5.56a,b.

Crack terminal velocities are about 50 % to 60 % of the transverse elastic wave speed and range from 1500 m/s for soda lime silica to 2500 m/s for fused silica as listed in Table 5.1. The transverse wave velocity is:

$$v_t = \sqrt{\frac{E}{2\rho(1+\nu)}} \tag{7.23}$$

where E is the elastic modulus, ρ is the density, and ν is Poisson's ratio. Richter[66,67] studied cracks running at terminal velocity at stress intensities above K_{Ic}.

Even in the absence of externally applied sonic pulses, it is possible to interpret *naturally* created Wallner lines to estimate crack velocities as shown in Figures 7.28 – 7.30. The simplest case is for a straight crack front that intersects a discontinuity such as a bubble or inclusion that creates an elastic pulse. This generates a fracture surface feature called a "gull wing." The radiating transverse elastic wave always travels faster than the crack front. Figure 7.28 shows how the radiating circular-shaped wave front catches up and intersects with other portions of the crack front. The locus of intersections generates Wallner lines that have a telltale "V" pattern centered on the elastic discontinuity. There often is a slight curl at the pulse origin. The net effect is

to produce the gull wing shape. The included angle (2β) between the wing segments may be used to calculate crack velocities. Crack velocity is quite simply:

$$v_c = v_t \cos\beta \tag{7.24}$$

where v_c and v_t are the velocities of the crack front and the transverse wave. Slowly-moving cracks do not advance very far in a time interval Δt, and the elastic pulse quickly overtakes the entire front. Thus, the "V" shape is very flat and, if it assumed that the included angle 2β is 180° – 2° = 178°, then the slowest velocity that can be measured in a glass with v_t = 3460 m/s is $v_{c,min}$ = 60 m/s. Conversely, if the crack is advancing at the terminal velocity of 60 % of the transverse wave velocity, then the minimum included angle 2β is 106°. Tsirk[71] identified hyperbolic "V" shaped Wallner lines in obsidians, created by an elastic pulse generated by secondary fracturing behind the main crack front.

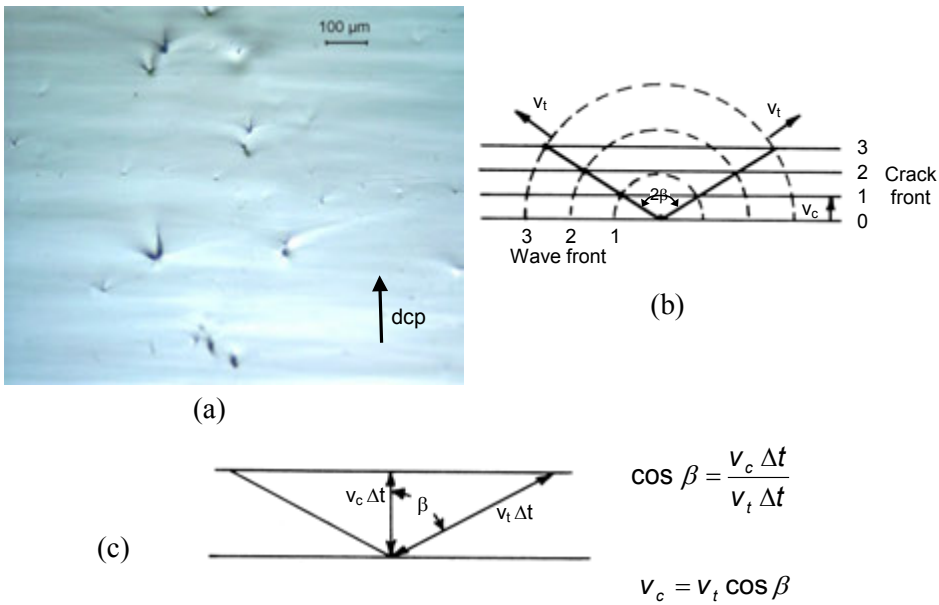

Figure 7.28 *Crack velocity may be estimated from Wallner line analysis. Gull wing lines occur when a straight crack front passes a point discontinuity such as a bubble or inclusion. (a) shows gull wings in knapped obsidian (specimen courtesy A. Tsirk). The direction of crack propagation is from bottom to top. The included angle (2β) is used to estimate crack velocity. Slow-moving cracks have flat (horizontal) wings. Fast-moving cracks create wings with a "V" shape. (b) and (c) show the geometries and simple trigonometry used to estimate crack velocity.*

Wallner lines such as those inside a mirror shown in Figure 7.29 may be analyzed as shown in Figure 7.30. [14,27,72,73]

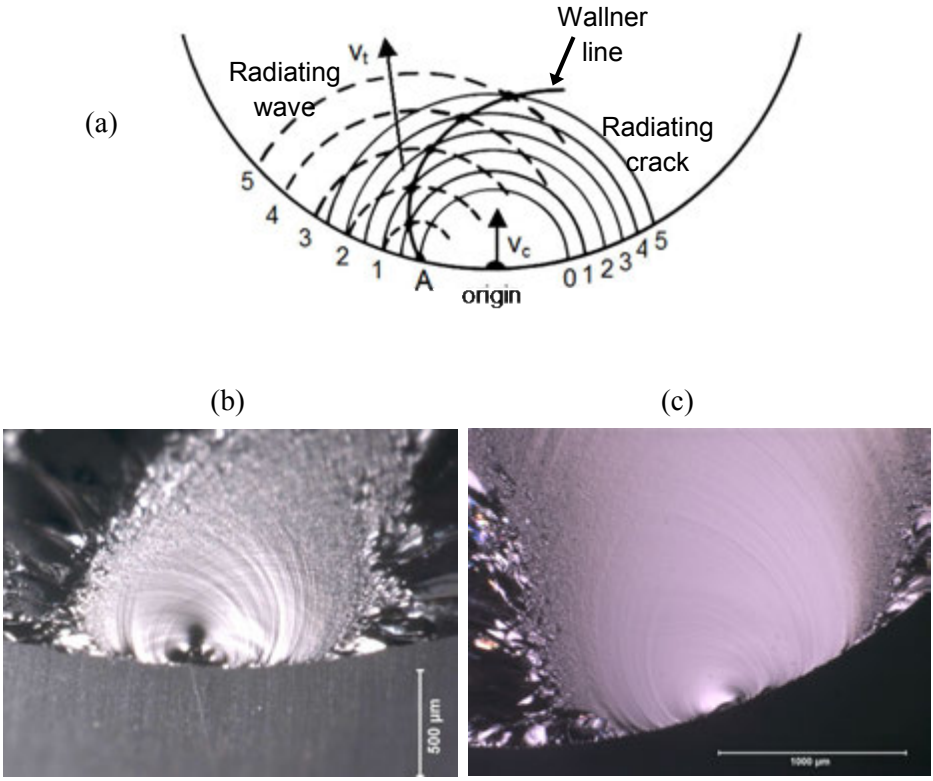

Figure 7.29 *Crack velocities can be estimated from Wallner line analysis. (a) shows a crack front that radiates outward from the origin at velocity v_c (thin circular lines) and reaches irregularity A on the left. An elastic pulse is generated at A and it radiates a transverse (shear) wave outward from A (dashed lines) with a faster speed v_t than the crack front. The numbers label the crack and elastic pulse fronts at the successive times starting at 0, the instant the crack reaches A. The intersections for the specific times are marked by dots, but of course this is a continuous process and the solid line shows the ensuing Wallner line. The crack front is assumed to be moving at constant velocity $v_c = 0.5\ v_t$ in this case. If the crack were accelerating, the Wallner line would be less hooked in the beginning and would extend more towards the upper right. (b) and (c) show Wallner lines inside mirrors in glass rods.*

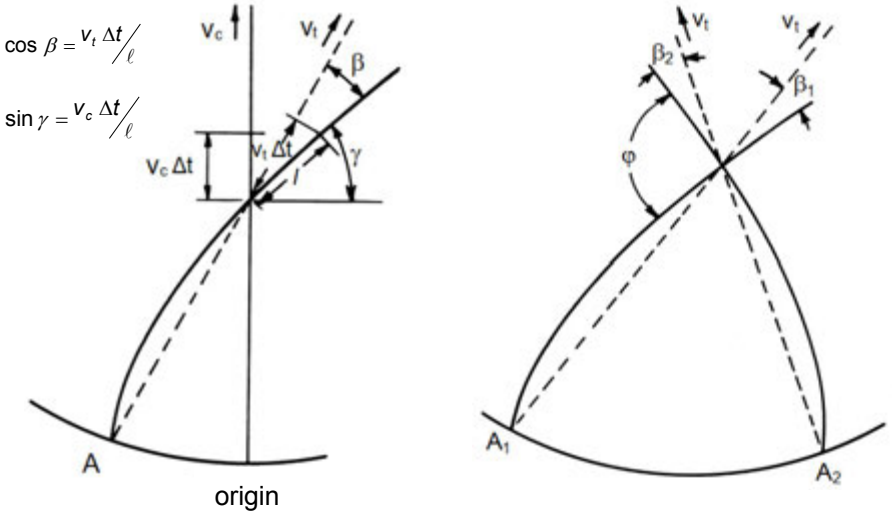

(a) (b)

Figure 7.30 *Analysis of Wallner lines to determine the crack velocity if a crack radiates outwards from an origin. (a) shows a case where the location of the Wallner line elastic wave pulse (site A) and the direction of the crack extension are known. (b) shows the case where the precise crack growth direction is not known, but the origins (A_1 and A_2) of the Wallner lines are known.*

In the case where the exact direction of crack propagation (radiating at speed v_c from the origin) and the initiation site of the Wallner line (A) are known:

$$\frac{v_c}{v_t} = \frac{\sin\gamma}{\cos\beta} \tag{7.25}$$

Crack velocity can be determined even if the crack propagation direction is not known. Two intersecting Wallner lines may be analyzed as shown in Figure 7.30b:

$$\frac{v_c}{v_t} = \frac{\sin\varphi}{\sqrt{\cos^2\beta_1 + \cos^2\beta_2 + 2\cos\beta_1\cos\beta_2\cos\varphi}} \tag{7.26}$$

and if the Wallner line intersection is symmetric ($\beta_1 = \beta_2 = \beta$), then:

$$\frac{v_c}{v_t} = \frac{\sin\left(\varphi/2\right)}{\cos\left(\beta\right)} \tag{7.27}$$

Elastic waves interactions from slowly-moving cracks run across the crack front fairly quickly and thus the Wallner line corresponds closely with the crack front shape. The *minimum* velocity that can be estimated by Wallner line analysis was estimated by Mencík as $v_c/v_t = 0.175$, using equation 7.27 with $\varphi = 2^o$, corresponding to nearly flat crossing Wallner lines. For glass with $v_t = 3460$ m/s, then $v_{c,min} = 60$ m/s. So in general, quantitative Wallner line analysis for crack velocities is most suitable for fast moving cracks.

The spacing between the legs of Wallner lambda lines, discussed in section 5.4.5 and shown in Figure 7.31, can easily be used to estimate a crack velocity. In the time that the crack advances approximately a distance a/2, the elastic wave has traveled across the thickness once. For a straight crack front:

$$V_c = V_s \frac{a}{2\sqrt{\left(a/2\right)^2 + t^2}} \tag{7.28}$$

The formula can also be used to approximate crack velocities for slightly curved crack fronts as well.

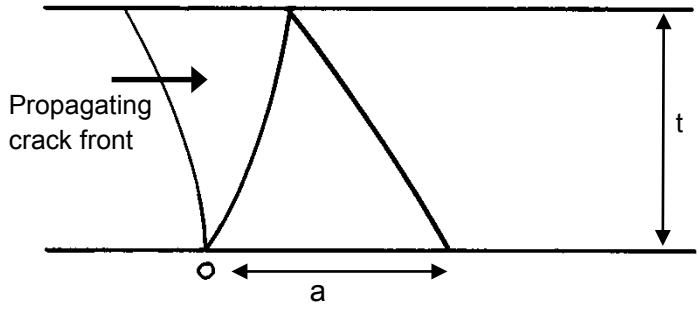

Figure 7.31 *The spacing between the lambda line legs can be used to estimate crack velocity.*

7.10 Slow Crack Growth

Cracks may grow stably when loaded at stresses and stress intensities less than that necessary for the flaw to become unstable. As discussed in sections 5.9.1 and 5.9.3, glasses, oxide ceramics, and ceramics with glassy boundary phase are susceptible. The mechanism of slow crack growth at ambient temperature is a stress corrosion phenomenon whereby stressed cracks that are open to the environment are attacked by water (or another polar molecule.) The water may be in the form of liquid or gaseous molecules. The water molecules attack the strained silicate or oxide bonds at the crack tip causing them to rupture which in turn leads to stable crack extension. Other fluids that promote slow crack growth are listed in section 5.9.1. At elevated temperature, oxidation attack, grain boundary softening, or other mechanisms can lead to slow crack growth (section 5.9.3).

Crack velocity depends strongly upon the stress intensity, K_I. The larger K_I, the faster the crack grows. Slight changes in it have dramatic effects upon crack velocity. As a crack size increases, it increases K_I in accordance with equation 7.6. If stress and the crack shape are invariant, the crack will gradually accelerate. Data are often graphed on log - log axes as shown in Figure 7.32a. Straight lines imply a power law dependence of velocity upon stress intensity:

$$V = A\, K_I^{\,N} \tag{7.29}$$

Region I crack velocity behavior often controls lifetime or rate effects on strength. (Region II occurs when insufficient amounts of the reactive element are available. Region III occurs close to K_{Ic} and does not require a reactive species. With a few exceptions, during most of the time a crack is growing it will be in Region I.) The slope of the line, N, is known as the slow crack growth exponent and is a critical parameter for reliability and rate effect analyses. Very high values of N (e.g., > 100) indicate considerable resistance to slow crack growth and hence, little rate sensitivity. Low values (e.g., 5 to 30) indicate high susceptibility. Velocity data as shown in Figure 7.32a are usually collected with laboratory specimens under controlled testing conditions.

Figure 7.32b shows how slow crack growth affects the lifetime of specimens loaded at constant stress levels below the fast fracture strength. This is referred to as “static fatigue” or “stress rupture” testing. The decrease in log strength varies with log time to the –1/N power.

Slow crack growth can even affect outcomes in ordinary strength tests as shown in Figure 7.32c. The slower the test is run, the weaker are the specimens since the crack can grow a surprising amount during the time of loading.

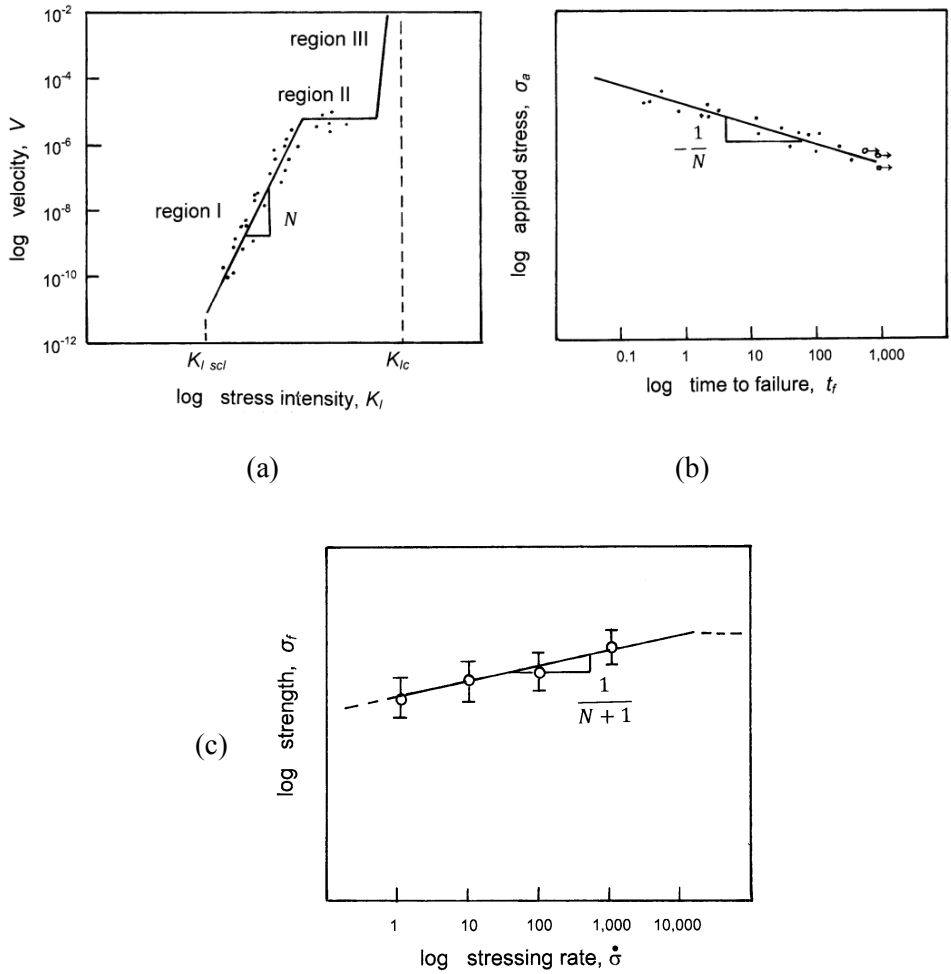

Figure 7.32 *Slow crack growth manifests itself in different ways. (a) shows a crack velocity versus stress intensity (K-V) graph showing three regions. Usually such data is plotted on log-log axes. Fracture mechanics type tests are used to collect such data. (b) shows a graph of log stress – log time to failure, also known as a "static fatigue" or "stress rupture" plot wherein a constant stress is applied until a piece breaks. (c) shows a graph of strength as a function of stressing rate also with log - log axes, also known as a "dynamic fatigue" plot. The slow crack growth exponent N plays a prominent role in each instance.*

Figure 5.56 showed an example of a flaw in glass that grew as much as 20 times its original size due to slow crack growth in water. Figure 5.55 showed a flaw in alumina that grew about twice its original size in a simple 30 second strength test.

A comprehensive theoretical justification for the power law relationship between K_I and V is lacking at the present time. There are alternatives, but the power law relationship lends itself to simple integrations and transformations and is usually adequate. It should be used with caution for any extrapolations beyond the times and velocities for which the data was collected, however.

Crack-fluid interactions can cause abrupt changes in crack growth that can create markings such as scarps on fracture surfaces as shown in section 5.6. For example, an accelerating crack may outrun the ability of a fluid to keep up with the crack tip and this may cause cavitation and a scarp. Conversely, a decelerating crack may slow down enough that water can catch up to the crack causing a scarp. Sometimes a jump in the crack from region I behavior to region II behavior creates a scarp.

The Newman-Raju stress intensity shape factors also explain one commonly observed trend: surface cracks that grow stably *evolve shape and become semielliptical.* Figure 7.33 illustrates the trend for a beam or plate in bending and Figure 5.44b an example. The stress intensity shape factor Y varies around the crack front. For a semicircular flaw, Y is greatest at the point where the crack intersects the outer surface, point B. At the internal point A, there is more material on either side of the crack front that can share the load, and hence the stress intensity shape factor is about 13 % less. Thus, the crack initially grows faster along the outer surface, but then, as the crack shape evolves into a semiellipse, the stress intensity evens itself out around the periphery. Newman and Raju[40] showed examples of this for fatigue crack growth in metals, both for bending and direct tension stress fields. The semielliptical shapes differ in the two cases, depending upon the size of the crack relative to the specimen thickness. The identical trends have also been observed in ceramics and glasses.[67,74,75,76,77,78] Small surface cracks in large, uniform, direct-tension loaded specimens or plates will assume a constant semi elliptical shape with an aspect ratio a/c of about 0.83. Cracks in bending stress fields will also gravitate to this shape if they are small relative to the thickness, but if they penetrate into the stress gradient, they will become more elongated sideways as they grow and the semiellipse ratio a/c will decrease as shown in Figures 7.33b and c.

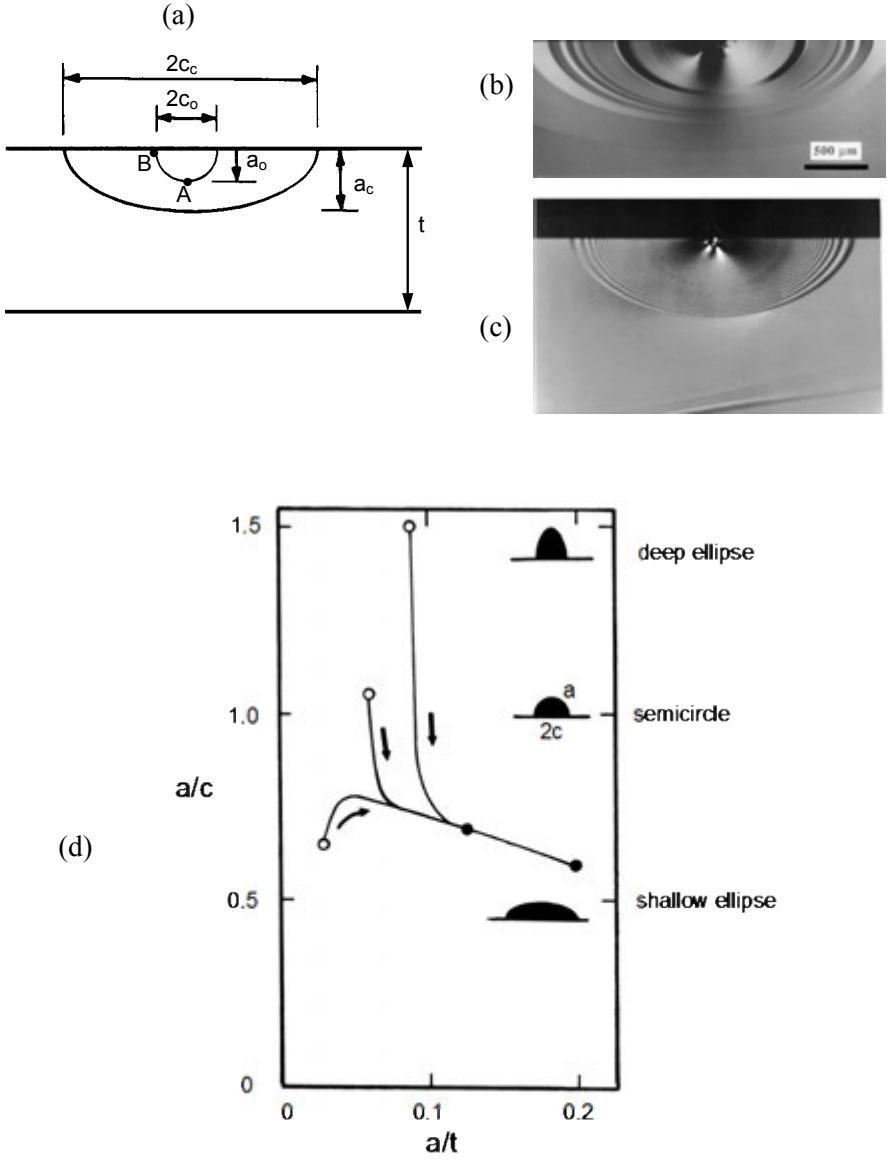

Figure 7.33 *Crack shape often changes with growth. (a) shows an initially semicircular crack of size a_o that changes to a semi elliptical shape as it grows in a bending stress field in a plate of thickness t. (b) shows concentric arrest lines from cyclic loading (same as Figure 5.47c) (c) shows tertiary Wallner lines from a rapidly moving crack (same as Figure 5.44b); and (d) shows the evolution of crack shapes in glass bend specimens converges to a shallow semiellipse, irrespective of the starting shape (hollow circles). (b courtesy D. Green. c is courtesy H. Richter. d is after Fett et al., Ref. 74)*

7.11 R-Curve Behavior

R-curve behavior, which arises from crack-microstructure interactions, is a phenomenon that may improve fracture resistance in ceramics. It can give rise to stable crack extension prior to fracture. It is not operative in glasses. Unfortunately, R-curve behavior does not leave any intrinsic telltale markings on the fracture that the fractographer can interpret.

Figure 7.34 illustrates the general concepts. Flat R-curve materials such as glasses and many fine-grained ceramics behave as shown in Figure 7.34a. Fracture toughness is independent of the crack size and has a specific value: K_{Ic}. When the combination of stress, flaw shape, and size reach the critical condition, unstable crack extension usually occurs. If there are substantial tensile stresses throughout the body, it will break. If, on the other hand, the stresses decrease either temporally as in thermal shock cases or spatially as in localized contact loading cases, the crack initially may be unstable, but then slows down and may even stop.

Rising R-curve behavior occurs when the microstructure impedes crack extension. Several crack-microstructure interactions shown in Figure 7.16 can cause this. For example, yttria-stabilized tetragonal zirconia polycrystal (Y-TZP) is carefully processed so that after firing, the microstructure is composed of metastable tetragonal grains. These can transform to the monoclinic phase when a crack tip and its stress field approaches. This martensitic phase transformation consumes some energy that might otherwise drive the crack forward. In addition, the transformed grains expand by ≈ 4% thereby putting a compressive constraint on the crack tip. The process zone may only be a few grains wide in Y-TZP. R-curves can arise from other crack-microstructure interactions. For example, with coarse-grained ceramics, large grains behind the crack tip may not necessarily be immediately cleaved. They may act as bridges across the crack faces that reduce the stress intensity field on the crack tip. They can persist for long crack propagation distances.

Phenomena such as these can lead to behavior shown in Figure 7.34b. Starting with an initial crack size, c_o, if the stress intensity K_a from an applied stress reaches the level of K_o, the crack begins to propagate. As it grows, K_a increases in proportion to $\sqrt{c}$ if the stress is held constant as per eq. 7.6. The material's fracture resistance K_R may increase at a greater rate thereby retarding or arresting further crack propagation. Further propagation requires additional applied stress to increase K_a. The R-curve typically reaches a plateau such that further toughening is not possible. Fracture may occur *before* the plateau is reached if:

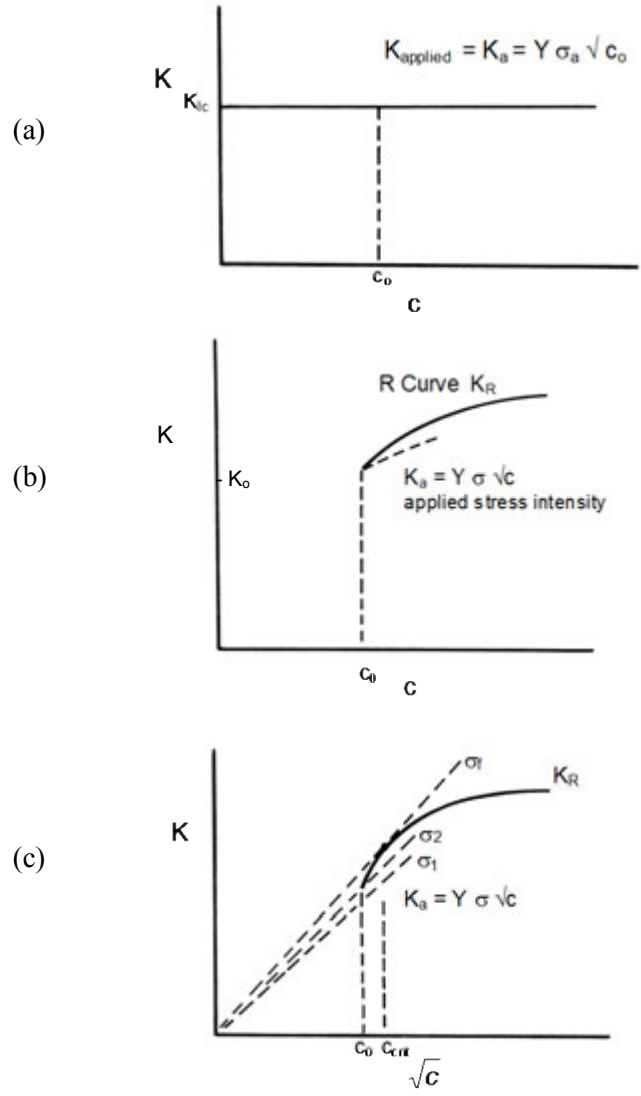

Figure 7.34 *R-curves in ceramics. (a) shows the case of a material with a constant, or flat R-curve. (b) shows a general schematic of a rising R-curve. Crack extension leads to a greater applied stress intensity K_a, but the material's fracture resistance curve K_R may also increase. (c) shows K_a versus $\sqrt{c}$, in which case the K_a plots as a straight line with slope proportional to applied stress. Fracture occurs at c_{crit} where the rate of increase of applied K_a is greater than the slope of the K_R curve. Initial flaws larger than c_{crit} may not exhibit any stable crack extension and may immediately go critical.*

$$K_a = K_R \tag{7.30}$$

and

$$\frac{dK_a}{dc} > \frac{dK_R}{dc} \tag{7.31}$$

In other words fracture occurs when the applied K_a reaches the level of the R-curve *and* the rate of increase in K_a with further extension is greater than the rate of toughening. To better show the relative increases, it is common to plot fracture resistance with K^2 versus c, or K versus $\sqrt{c}$ as shown in Figure 7.34c. In this fashion, the increase in K_a with crack size appears as a straight line with slopes that increase with σ. This K_a line can be more easily compared to the K_R trend. Instability occurs at $c = c_{crit}$, a value well before the plateau is reached, after only a small amount of crack growth has occurred.

There is no universal R-curve for a material.[79] The R-curve depends upon the starting size of the crack relative to the microstructure and its prior propagation history. It also depends upon the size, shape, and mode of loading of the specimen. R-curves for large cracks are not the same as those for small cracks. In other words, data from large crack fracture mechanics specimens are usually not applicable to natural small flaws. Large fracture mechanics specimens usually are effective in measuring plateau toughness values. A double-cantilever beam specimen has a dramatically different crack opening displacement than a notched beam or a surface flaw in a bend bar. The number of bridges behind the crack tip bridges depends upon the crack opening displacement and the greater the opening, the fewer the intact bridges. For example, a 20 μm grinding-induced crack may have already interacted with the microstructure and formed bridges or transformed some material during the crack formation. Figure 7.35 shows two possible examples. In contrast, a 20 μm round pore may not have activated any prior toughening.

It is extremely difficult to measure R-curves for small natural-sized flaws, and especially the initial K_o fracture resistance. The limited data that has been collected suggests the initial K_o may be very small, approaching single crystal or even grain boundary fracture toughness values. Some materials may have such small toughening zones that, for all practical purposes, they can be treated as having a set fracture toughness value. Many yttria-stabilized tetragonal zirconias (Y-TZPs) may be like this since the transformation zone is only a few grains large. On the other hand, magnesia partially-stabilized zirconia (Mg

(a)

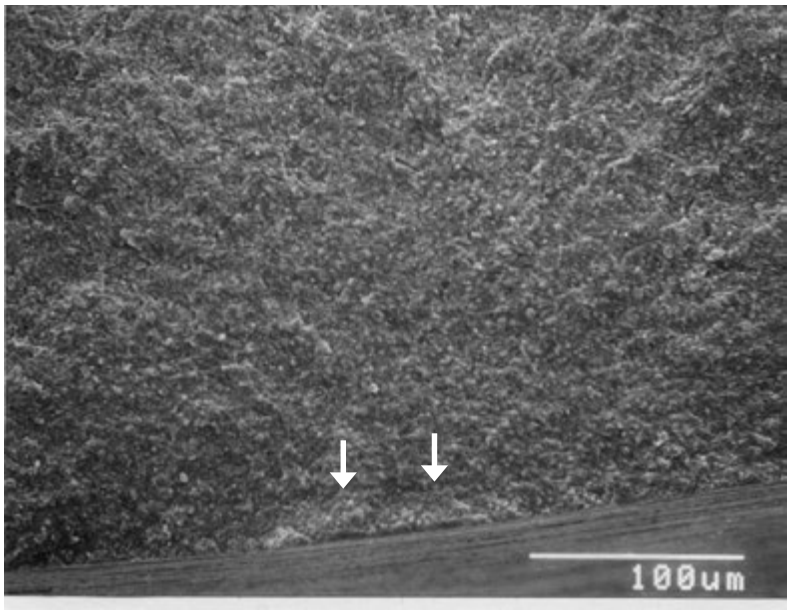

(b)

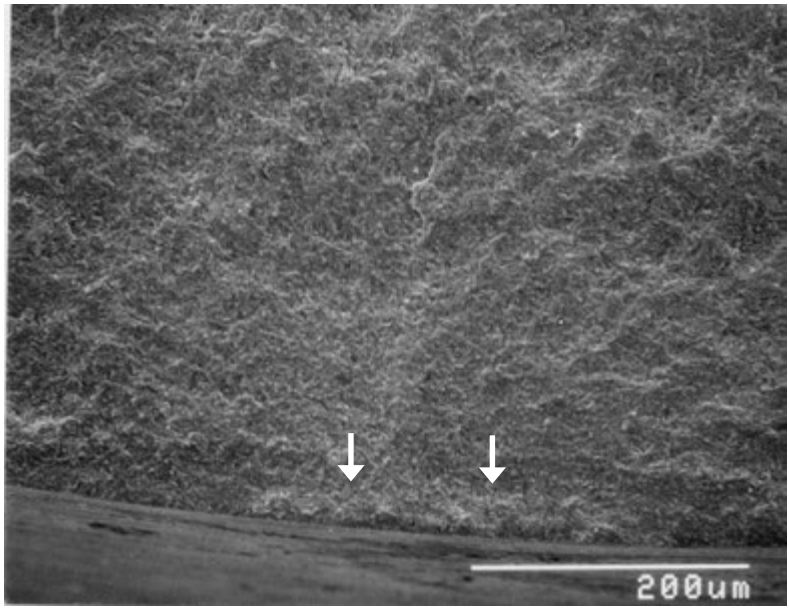

Figure 7.35 *Grinding cracks in transversely-ground rods that show evidence of stable crack extension (arrows) in a silicon nitride with rising R-curve behavior. (a) 657 MPa and (b) 641 MPa. (Ref. 80)*

PSZ) may experience considerable crack extension prior to fracture.[81]

Many studies have used Vickers indentation artificial flaws, but they often do not behave like genuine flaws as discussed in the next section. The R-curves that are generated are not relevant to natural flaws or are simply wrong. For example, one study showed that without proper care, the usual analysis with Vickers indentation flaws produced the implausible result that a soda lime silica glass has a rising R curve.[82] (The problem was that the standard indentation strength model fails to account for changes in crack shape, especially as cracks penetrate into strong flexural stress gradients.) The most credible R-curve data to date (that is applicable to strength limiting flaws) has been that collected by careful microscopic examination of crack growth from natural flaws in controlled loading experiments.[77,78,83,84]

The instability point depends upon the starting crack size and the slope of the R-curve at small crack sizes as shown in Figure 7.34c. Indeed, the overall plateau value may be inconsequential in many cases. A particular crack may grow only a small amount before going unstable[79,80,85] or it may immediately be unstable. Fett and Munz's mathematical analysis is quite revealing.[85] They showed that R-curve behavior led to negligible strength enhancements in an alumina that had bridging grains, quite simply because the natural flaws did not have a chance to grow very far before going unstable. Their analytical and experimental results may easily be understood by the simple realization that in strong aluminas the flaws are only 5 to 20 times larger than the average grain size. The stable crack extension may involve only a few grains before the flaw goes critical and it is impossible to generate many behind-the-crack tip bridges. Perceptible strengthening would only occur in very weak specimens ($\sigma < 100$ MPa) with large initial flaws. Fett and Munz also showed that the R-curve behavior in their aluminas had negligible effect on the Weibull distribution[85] contradicting predictions of dramatic improvements in Weibull modulus based on indentation mechanics analysis.[86]

Mecholsky et al.[87] and Marshall[80] suggest that a simple way to measure an effective R-curve is to measure strength and critical flaw size in strength test specimens and compute apparent K_c at fracture. Rising R-curves will be evident on a plot of K_c versus crack size. They showed evidence that the mirror to flaw size ratio changed significantly as a function of crack size.

The fractographer should keep the above factors in mind. As noted above, R-curve behavior does not leave any intrinsic telltale markings on the fracture surface. R curve behavior can throw off flaw size calculations if they are based on a single point value for fracture toughness in equations 7.7 or 7.22. In principle, the fractographer may be able to find a region of stable extension around a flaw, but in practice this may be difficult especially if the toughening phenomena and the microstructure produce a rough fracture surface. One indication of potential R-curve behavior may be a systematic $c_{calc} \neq c_{meas}$ trend. As noted previously, if the fractographer detects and measures only the initial flaw size, then $c_{calc} > c_{meas}$. In this case it is the fractographic size measurement that is off. Alternatively, if stable crack extension due to R-curve behavior does occur, but the fractographer uses a long crack (plateau) value of fracture toughness, then the fracture toughness is overestimated and the calculated crack size is wrong, and again $c_{calc} > c_{meas}$.

A rising R-curve does not necessarily translate to superior mechanical properties. Careful microstructural control is usually required. If reinforcing agents are not well dispersed and are clumped together, they can act as strength-limiting flaws. Alternatively, local regions depleted of the reinforcing elements may also have ordinary flaws. Many toughened ceramics have not shown commensurate increases in strength or Weibull moduli (which is a measure on consistency of strengths as discussed in section 7.15), contrary to expectations. The reason is simple. The very microstructural changes that enhance crack-microstructure interactions also create non-uniform microstructural regions, flaws, and microflaw concentration regions. That is why Y-TZP with a modest fracture toughness of 5 MPa√m to 6 MPa√m is stronger than Mg-PSZ. The Y-TZP has a very uniform sub-micron grain size and small ≈ 20 μm diameter pore flaws (Figure 6.6f). The Mg-PSZ has a fracture toughness of up to 10 to 20 MPa√m, but a coarse-grain microstructure loaded with grain boundary faults and concentrations of micropores (Figures 6.75, 6.76, 6.77). The flaw size may be hundreds of μm in size.

7.12 Indentation Mechanics

A substantial literature exists on the mechanics of flaws made with Vickers or Knoop indentations. Figures 7.36 illustrate some of these "controlled flaws." The indentations create not only a residual impression that is measured in a hardness test, but cracks and a concentrated damage zone directly underneath the indentation.

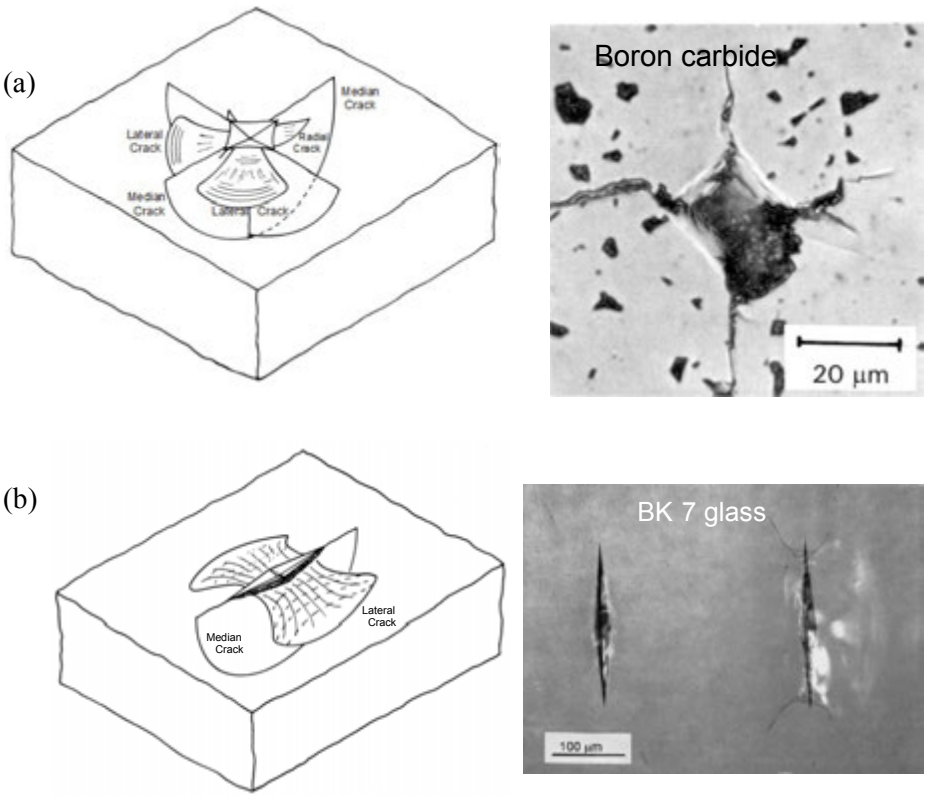

Figure 7.36 *Indentation generated damage sites. (a) and (b) show common crack patterns and examples around Vickers and Knoop indentations. The author prefers the Knoop indenter since it makes a simple crack system.*

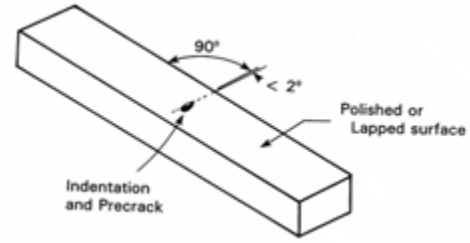

(a)

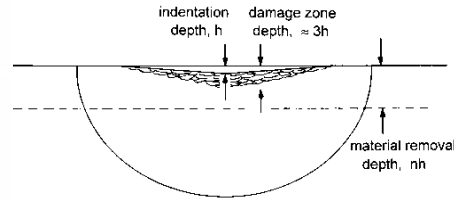

(b)

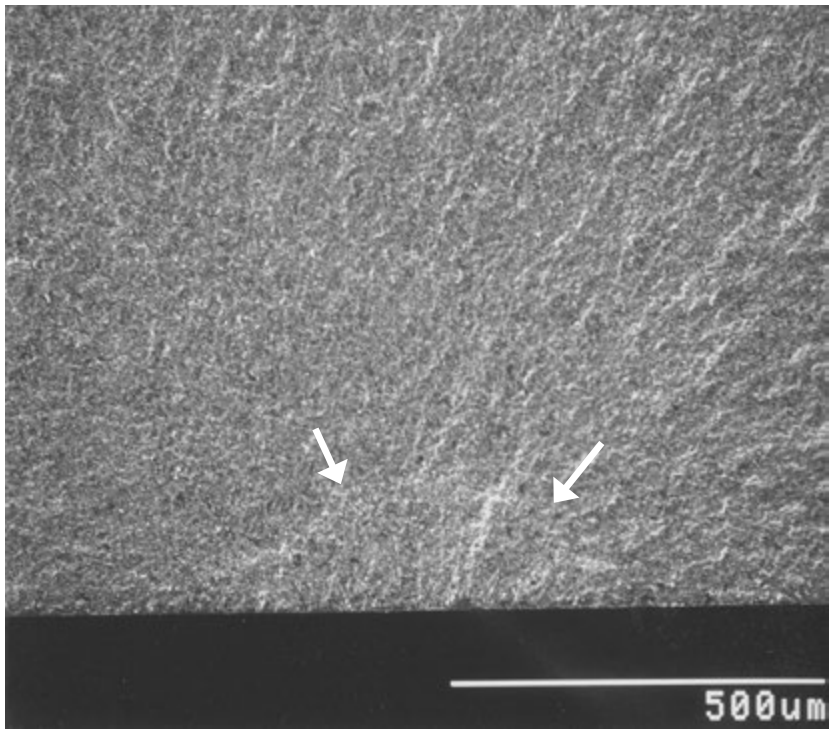

(c)

Figure 7.37 *The surface crack in flexure method uses a Knoop indenter to create a semi elliptical surface crack in a bend bar (a). (b) shows a section view of the indentation and the median crack below it. The residual stress damage zone is removed by polishing or hand grinding leaving a controlled surface flaw in the test piece. (c) shows a Knoop crack in a silicon nitride (arrows).*

Controlled flaws for fracture mechanics experiments should be made with the Knoop indenter.[88,89] The flaw geometry is simpler and more easily controlled. Loads of 19.6 N to 294 N are used to create a semi-elliptical surface cracks in ceramic bend bars (Figure 7.37). Loads of 19.6 N to 29.4 N are used for glasses. The indentation residual stress damage zone and any lateral cracks are removed by polishing and then the test piece broken in flexure. Fractographic techniques are used to find and measure the flaw size. Other precrack examples are shown in Figures 3.26, 5.55, 5.57, and 6.53.

Calculations are simple. The Newman-Raju stress intensity shape factors described in section 7.5.2 are used with equation 7.6 to compute stress intensities. The name of the method was changed from "controlled surface flaw" to the "surface crack in flexure (SCF)" method by the author in 1994 in order to avoid confusion with some Vickers indentation methods and to also use nomenclature then in use in the fracture mechanics community.[90] The SCF procedure was the primary method used to prepare the world's first standard reference material for the property fracture toughness, K_{Ic}.[39,91] It was formally standardized by the American Society for Testing and Materials[41,92] the European Committee for Standards,[93] and the International Organization for Standards.[44] The method does not work on soft, porous, or very tough materials, since median cracks will not form. Details on the SCF method are in these standards and in References 89 and 90.

Vickers indentation procedures are widely used since they usually do not require fractographic examination. This supposed advantage leads to severe drawbacks with the method, however. In 2006[94] and 2007[95] the author and Prof. R. Bradt wrote about the limitations of Vickers indentations for fracture mechanics studies. Vickers generated flaws are much more complex than Knoop median cracks, and since the Vickers flaws are tested without removal of the residual stresses and damage zones, all sorts of complications arise. Rather than a single median crack, Vickers indentations have multiple median, radial, and lateral cracks. The cracks also have a complex stress residual stress damage associated with them.[96,97] Rather than envision these Vickers indentation sites as model flaws with discrete median cracks with a modest residual stress pulling on the faces, it is actually more appropriate to regard them as Vickers *damage zones*. A semicircular median crack is typically assumed to pop in underneath the indentation, although the crack type and formation sequence is quite complicated and varies dramatically with material.[98,99,100] The residual stress damage zone is approximated by a point force acting to open the crack. The stress intensity factor K_{Ir} acting on the flaw

in this case has the relationship shown in Figure 7.17b, namely:

$$K_{Ir} = \chi \frac{P}{c^{1.5}} \tag{7.32}$$

where c is the crack size, P is the indentation load, and χ is a constant that incorporates geometry and residual stress field factors.

If a test piece with a Vickers flaw is broken, K_{Ir} combines with the stress intensity created by a far field tensile stress to produce a total K_I:

$$K_I = Y\sigma_a \sqrt{c} + \chi \frac{P}{c^{1.5}} \tag{7.33}$$

The first term on the right dominates for large cracks. The second term is significant for small crack sizes, but rapidly diminishes as the crack extends away from the residual stress damage zone. The net effect of the two terms is to cause a crack to extend stably somewhat prior to catastrophic propagation. The extent of stable propagation has been estimated to be 2.5 times the original flaw size when the testing is done in inert environment and all the assumptions in the analysis are upheld.[97]

It is clear from above that the local residual stresses dramatically alter the local stress intensity field, and that a simple application of equations 7.6 (or eq. 7.33 without the second term on the right) based on only the far-field tensile stresses, will be faulty. Typically c_{calc} will be larger than c_{meas}, if the latter is the original flaw size and stable crack extension is not detected.

By the time the crack propagates to the extent that it is forming the mirror boundary markings, the effect of the localized residual stress term is insignificant.[101] Hence, the mirror size is unaffected by the indention residual stresses and the stress-mirror size relationship equation 7.4 is unaffected. The mirror to *initial* flaw size ratio is affected, however, and can be larger than values for annealed flaws.[101] Indentation residual stresses do not affect branching distances or the fragmentation patterns.

Evidence of stable crack extension from indentation localized residual stresses may be difficult to detect on fracture surfaces. Figure 5.57 shows an example in a fine-grained silicon nitride. Stable extension is most often detected in laboratory conditions with careful microscopy on a polished outer surface, or through the material if the material is transparent.

The observant reader will note that Vickers indentation flaws do not resemble the majority of origins shown in Chapter 6. Notwithstanding claims to the contrary, it is not at all clear whether indentation damage sites simulate genuine flaws in ceramics and glasses. They may model contact damage sites and/or machining cracks, but Figure 6.30 in the previous chapter shows that actual contact damage sites are often more irregular, with significant amounts of material removed by lateral cracks and spalls. The contact-generated residual stresses are often partially or completely relieved. Service impact conditions are rarely as controlled as those in an indentation process, where an ideal diamond slowly applies load perpendicular to the surface.

The localized indentation residual stress field of a laboratory indentation has a very stabilizing influence on a flaw, allowing it to have extensive stable extension that may not be experienced by genuine flaws. The previous section on R-curve effects mentioned some examples where predictions of enhanced Weibull modulus based on indentation flaw analysis were misleading or wrong.

In summary, there has been an over reliance on Vickers indentation flaws. From some of the literature one might think that are they are more important than genuine flaws. Fractographers know otherwise.

7.13 Fractal Analysis

Fractal analysis is a tool that may be used to characterize irregular surfaces, such as fracture surfaces. It is not used to find and characterize fracture origins, but to characterize the roughness or unevenness of a surface. Fractal geometry is a non-Euclidean geometry that exhibits self-similarity and scale invariance. Self-similarity means that a geometric shape in one location is similar to a geometric shape elsewhere. Scale invariance means that the geometric shape is similar irrespective of its size. Fractal analysis is unlike classical surface roughness measurements that characterize the heights between peaks and valleys. Fractal analysis measures the extent of the "wiggliness," "tortuosity," or irregularity of the surface.[102,103]

Classical Euclidean geometry has a simple relationship between area and length. So for example, a circle of diameter D has the well-known relationships in accordance with Euclidean geometry:

$$Area = \pi D^2 / 4 \tag{7.34}$$

and

$$Perimeter = \pi D \tag{7.35}$$

so that:

$$Perimeter \propto \sqrt{Area} \tag{7.36}$$

This is the case for a perimeter line that is unwavering and follows the circle rim exactly. If on the other hand, the perimeter line had perturbations and wiggles, the perimeter length is greater. If the perimeter line is magnified and studied in greater detail, it is possible that each wiggle or perturbation itself may be seen to have yet smaller wiggles creating additional length and so on. That is the nature of fractal dimensions. The greater the magnification used, and the finer the measuring stick used to measure the lengths, the longer is the overall perimeter length. This leads to the somewhat unsatisfying outcome that the perimeter length actually varies with magnification and the size of the measuring scale. The perimeter of a fractal shape around an area can be characterized by the following relationship:

$$L = L_0 s^{1-D} \tag{7.37}$$

where L is the length of the line, L_o is a constant, s is the measuring scale or ruler size, and D is the *fractal dimension* which in this instance is between 1 and 2. If the line has no wiggles (and is a Euclidean line) then D = 1, and $L = L_o$ irrespective of the size of ruler used to measure it. On the other hand if the line is fractal, and D is between 1 and 2, then L varies with the size of the ruler. The exponent of s is negative and the smaller s is, the larger is L. The same type relationship applies if areas were to be used in equation 7.34, in which case D would be have a value between 2 and 3. The value of D-1 is often written as D^*, the fractional part of the fractal dimension.

Two ways to measure the fractal dimension of a fracture surface are the fracture profile technique and the slit island analysis.[103] The fracture profile technique simply makes a vertical cross section through a fracture surface. The profile with all its ups and downs is analyzed. In the slit island technique, a horizontal cross section is made through a fracture surface to reveal islands corresponding to the peaks of hills and ridges and their wiggly outlines. This process is repeated and measurements remade much like in a classical metallographic serial section analysis. Both procedures can be tedious, but computer analysis and image analysis software can simplify this task. Confocal

optical microscopy would seem to be an ideal tool, since it may be able to examine the fracture surface directly and section it automatically without the need for repetitive polishing.[104,105] A typical fractal analysis measures a perimeter length or roughness number with finer and finer measuring intervals. A graph of log length versus log measuring interval size is constructed and the slope used to estimate the fractal dimension.

Fractal analysis has usually been used to correlate fracture toughness with the fractal dimensions. The processes that enhance fracture toughness often increase the roughness of a fracture surface. Passoja, Mecholsky and colleagues have pioneered correlations of this type for ceramics.[102,103,106,107] For example, they have shown that:

$$K_{Ic} = K_o + A\left(D^*\right)^{1/2} \tag{7.38}$$

where K_o is a baseline toughness of the material for a smooth (Euclidean) fracture surface, D^* is the fractional part of the fractal dimension and A is a constant that can be related to the elastic modulus and the atomic dimensions of the structure of the material. The implication of this relationship is that only a small portion of a fracture surface is needed to determine the fracture toughness. In principal, this could be used in forensic analyses to determine if the material was poorly processed and had a lower than expected fracture toughness. The fractal analysis gives no information about the fracture origin, however.

Mecholsky and Freiman[107] showed that variations in the mirror to flaw size ratio correlated with the fractal dimension of the fracture surface well outside the mirror:

$$\frac{R}{c} \propto \frac{1}{D^*} \tag{7.39}$$

where R is either the mirror-mist, mist-hackle, or branching distance, and c is the flaw size. In other words, the very processes that contribute to formation of roughness at the mirror boundary are related to those that create roughness elsewhere in areas remote from the origin.

At the beginning of this section it was noted that fractal analysis is a tool to characterize fracture surfaces. Most fractal analyses have focused on using the fractal dimension as a materials science tool to study the microstructure or material properties. Additional work showing practical applications is needed.

7.14 Estimation of Residual Stresses

7.14.1 Introduction

Residual stresses may exist on many levels as discussed in section 4.19.5. They may be local to a flaw, as in a Vickers indentation or an inclusion with a mismatch in properties with the matrix. They may be distributed through the thickness, as in surface compression and internal tension in chemically- or thermally-tempered glasses. They may be global from differential shrinkage during firing. Their effects on flaws may be very difficult to analyze unless some assumptions are made about their character and distribution.

For example, residual stresses from grinding vary with direction, whether parallel to or perpendicular to the grinding direction. They are strongly compressive right at the surface, but rapidly decrease and become tensile a short distance (5 μm to 20 μm) below the surface. A grinding crack tip may be in tension or in compression depending upon how deep it is. The net effect of the stress gradient on the flaw as a whole is a complex fracture mechanics problem, but analytical attempts have been made to determine the effect on flaws with mixed success. The reader is referred to the work of Holstein et al.[108] for a good example. It is often difficult to determine whether the net effect is tensile or compressive. The weak point in these analyses is the lack of adequate quantitative information about the residual stress spatial profile.

7.14.2 Estimates of residual stresses from fragmentation

Empirical estimation of residual stresses in tempered glass plates by fragmentation patterns has been covered in sections 7.2.2 and 7.3.2.

7.14.3 Estimates of residual stresses from fracture mechanics analysis of flaws

The usual approach in dealing with residual stress problems is to rely on the principle of superposition. That is, the effect of stresses on a location or flaw in a body is additive, whether the stresses are mechanical, transient thermal, or residual. To a first approximation, residual stresses, σ_r, simply add to or subtract from the applied stresses acting on the flaw from known external sources, σ_a, so that the net stress acting on a site or a flaw is:

$$\sigma_{net} = \sigma_a + \sigma_r \tag{7.40}$$

Tensile residual stresses add to externally applied tensile stresses and

reduce the stresses or forces necessary to cause fracture from a particular flaw. Compressive residual stresses acting on a flaw must be overcome and require greater applied stresses. (The usual convention is that compressive stresses are negative.) For the case of a flaw loaded with a far-field stress σ_a with a residual stress σ_r that is constant in the vicinity of the flaw:

$$K_{Ic} = Y \sigma_{net} \sqrt{a} \tag{7.41}$$

Rearranging:

$$\sigma_r = \frac{K_{Ic}}{Y\sqrt{a}} - \sigma_a \tag{7.42}$$

If a convenient flaw is found that has a shape that is conducive to a fracture mechanics analyses and K_{Ic}, σ_a, and the flaw size, a, are known, then equation 7.42 can be used to estimate σ_r.

7.14.4 Estimates of residual stresses from fracture mirror size analysis

Residual stresses can cause systematic deviations in the stress - mirror size trends presented previously. Trend deviations are shown in Figure 7.38. The easiest interpretation is in Figure 7.38a, whereby a nonzero intercept indicates the magnitude and sign of the residual stress. A compressive residual stress shifts the line upward since a greater applied stress, σ_a, is necessary to cause fracture. If a single mirror is measured and the externally applied stress, σ_a, is

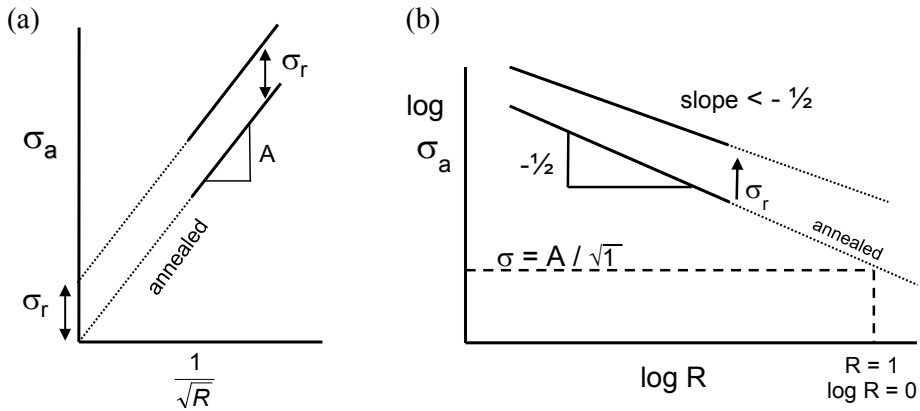

Figure 7.38 *Systematic deviations in the fracture mirror size trends for applied stress, σ_a, as a function of mirror radius are indicative of residual stresses. (a) shows that residual stresses create nonzero intercepts. (b) shows that residual stresses alter the slope.*

known, then:

$$(\sigma_a + \sigma_r)\sqrt{R} = A \tag{7.43}$$

and

$$\sigma_r = \frac{A}{\sqrt{R}} - \sigma_a \tag{7.44}$$

A good example of the application of this approach of measuring mirror-mist and mist—hackle boundaries on glass rods with cladding is in a paper by Mecholsky and Drexhage.[109] Similarly, the branching distances were used by Conway and Mecholsky [110] to estimate residual stresses in tempered glass plates. Additional details by this method are in Appendix D.

7.14.5 Estimates of residual stresses from indentation crack sizes

Surface residual stresses may be estimated by measuring the crack lengths emanating from the corners of Vickers indentations in a variation of the procedure described in section 7.12. If there are surface compression stresses, then the indentation crack lengths at a particular indentation load will be shorter than those in for an annealed piece of material.[111,112] Assuming that the indentation crack slows down and stops at $K_I = K_{Ic}$, and that slow crack growth doesn't affect its length, then:

$$K_{Ic} = \chi \frac{P}{c^{1.5}} + Y\sigma_r\sqrt{a} \tag{7.45}$$

where χ is the dimensionless contact constant which incorporates details of the indenter specimen contact conditions. Testing is usually done over a range of loads and crack lengths. This methodology is susceptible to all of the shortcomings addressed in section 7.12. If a test piece with residual stresses is indented and then broken, say in a plate or bend bar form, then the stress intensities acting on the crack sum:

$$K_{Ic} = Y(\sigma_a + \sigma_r)\sqrt{c} + \chi \frac{P}{c^{1.5}} \tag{7.46}$$

where σ_a is the applied stress from external loading, σ_r is the surface residual stresses at the location of the flaw, and the last term on the right is the stress intensity from localized indentation residual stresses. In practice, considering all the assumptions in indentation analysis, and the probable stress gradients, it may be difficult to reliably solve this equation to obtain σ_r.

7.14.6 Estimates of residual stresses by other means

Qualitative assessments can be made from mirror shapes as discussed in section 5.2.3 and also by changes in the mirror to flaw size ratio in section 7.7.

7.15 Weibull Analysis

Ceramic and glass strengths depend upon the size and shape of the specimens and the mode of loading. Specimen strengths vary due to variations in the size, severity, location, and density of flaws. Strength variability is usually analyzed in accordance with the Weibull distribution,[113] which is based on the premise that the weakest link in a body controls strength. A strength test produces two key bits of information: a strength datum and a fracture origin flaw. The flaws are just as important as the strength. "Flaw management" is an important strategy for process control and reliability improvements.

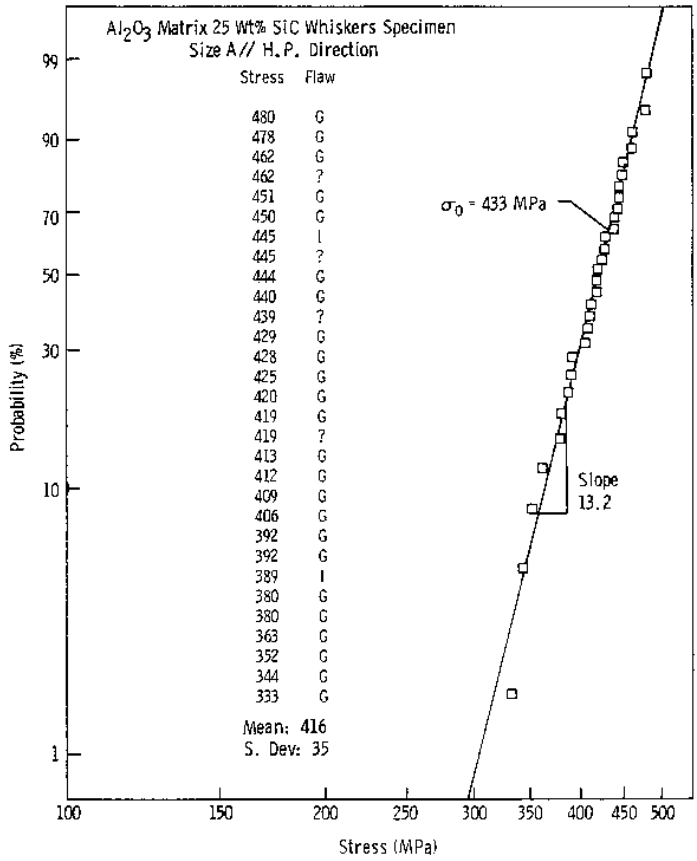

Figure 7.39 *Fractographically-labeled Weibull graph. Four-point flexural strength data for a SiC whisker-reinforced alumina. "G' is an abbreviation for a large grain origin type, "I" is for inclusion, and "?" is unknown. The slope of the fitted line is the important Weibull modulus (m) parameter. It is a measure of strength variability.*

The Weibull two-parameter distribution is:

$$P_f = 1. - \exp^{-\left(\frac{\sigma_a}{\sigma_\theta}\right)^m} \tag{7.47}$$

where P_f is the probability of fracture, σ_a is the applied stress, and m and σ_θ are constants called the Weibull modulus and the characteristic strength of the specimen, respectively. Strength data is typically ranked from weakest to strongest and then plotted on a special set of axes intended to linearize the data as shown in Figures 7.39 and 7.40.

With Weibull analyses, the maximum nominal stress in the body- is used. Stress is not adjusted for location. If the data fits the Weibull distribution, then it should fit on a line with the slope equal to the Weibull modulus, m, and the characteristic strength σ_θ corresponding to the strength of the specific test specimen configuration at the 63.2 % level. Figure 7.39 and 7.40 show two actual data sets with 100% fractographic analysis. The goodness of fit to the Weibull function can be assessed by eyeball by comparing the fitted line to the data. Both data graphs are fractographically-labeled and have not only the individual strength values, but also the flaw identities.

Figure 7.39 for the alumina with silicon carbide whisker reinforcements shows that the strength-controlling flaws were almost always large alumina grains. The whiskers that were added to enhance K_{Ic} had chemistries or impurities that caused grain growth in the matrix. The good news was that one flaw type primarily controlled strength and the Weibull distribution fit quite well.

In contrast, Figure 7.40 shows a SiAlON material that had many different concurrent flaw types and a very low Weibull modulus.[114] Brittle materials design with such a material would be problematic, since each flaw type has its own distribution. Strength scaling with size would be complicated. The tester might have wondered why the curve had so many wiggles. The fractographic analysis makes it clear why the single Weibull line does not fit very well.

Weibull originally derived his distribution on semi-empirical grounds. No assumptions about flaws or their nature were made. He simply assumed that small elements in a body had a local strength. He close a plausible distribution for the local variations in strength. He then integrated the risk of rupture for all elements to compute the failure probability for the whole specimen assuming that fracture would occur at the weakest link or element. His perceptive analysis has been theoretically verified by subsequent analyses by a number of authors, but most especially by Jayatilaka and Trustrum.[115,116] They showed

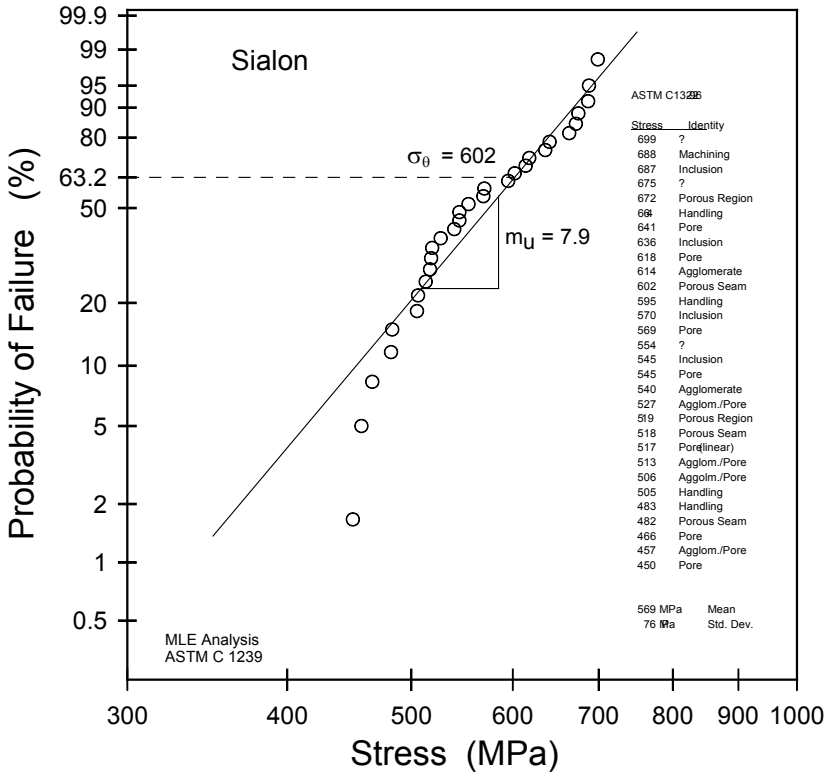

Figure 7.40 *Fractographically-labeled Weibull graph. Four-point flexural strength data for a SiAlON ceramic.*

that flaw size distributions could have the large flaw size tails matched by an inverse power law distribution as shown in Figure 7.41. Using this inverse power law distribution and applying classical fracture mechanics (equation 7.7), and weakest-link theory, they were able to mathematically derive the Weibull distribution. The Weibull modulus is directly related the flaw size distribution exponent. The Weibull distribution is now based on a solid theoretical footing. Danzer has considered more general distributions, but concluded that if the frequency of flaws follows the inverse power law, then the material may be deemed a "Weibull material.[117] In the 1990s and 2000s, a number of studies confirmed the large flaw size distribution tails can indeed be matched by the inverse power law. The reader is referred to papers by Prof. Uematsu in the Origins in Ceramics section of Appendix A for many examples. Quinn and Morrell's paper [118] has a useful review of a number of successful applications using Weibull analysis and it lists all of the assumptions necessary for Weibull strength scaling with size.

$$H'(c) = \text{constant} * \exp^{-\left(\frac{\alpha}{c}\right)} c^{-n'}$$

(a)

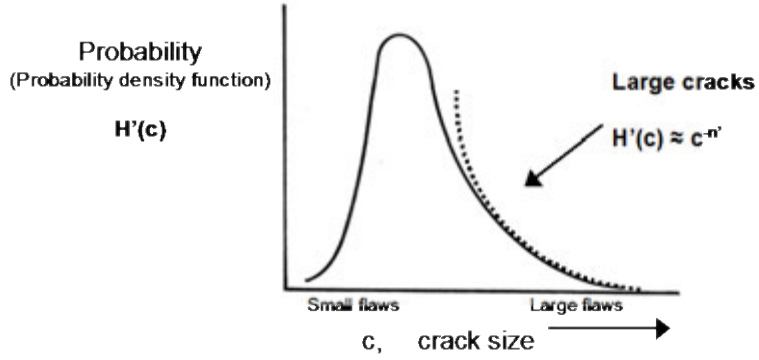

(b)

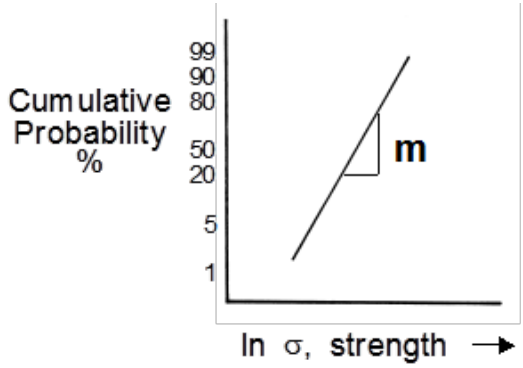

m = 2n' -2

Figure 7.41 *The Weibull distribution can be derived from the flaw size distribution shown in (a). H'(c) is the probability for occurrence of a flaw of size c. n' and α are constants. The largest flaws control strength and that portion of the distribution can be modeled by an inverse power law with exponent n'. (b) shows the Weibull distribution for strength. The Weibull modulus m is equal to 2n' –* 2.

Average bulk properties such as density, surface finish, or grain size often do not correlate with strength. Strength often depends upon infrequent or aberrant microstructural features, namely flaws, and not on the average microstructure. In some cases, the aberrant features do scale with the average microstructure, so there may be a correlation between strength and average bulk microstructure or surface finish. One important aspect of the Weibull model is that the larger the structure or test piece is, the more apt it is to contain a severe flaw. Hence, strength usually varies inversely with component size: the larger the component, the weaker it is likely to be. Strengths can be correlated or scaled by

comparing effective volumes or effective surfaces. It is beyond the scope of this Guide to delve into this topic, but suffice to say that such strength scaling analyses depend upon crucial assumptions. For example, a Weibull effective volume scaling approach is justified if fractography confirms that strength limiting flaws are volume-distributed. One often overlooked assumption in the Weibull analysis is that specimens must contain a minimum number of flaws. There must be a number of "chain links" present in the specimen for it to have strength controlled by a "weakest link." A specimen with a single flaw has only one strength controlling link. It is inappropriate to apply Weibull statistics to specimens with a single indentation flaw. It is also dangerous for engineers to ignore or discard a few specimens from the low strength tail of a Weibull distribution. These "atypical" or "non representative outcomes" may reflect a genuine flaw type that will cause trouble if the product is scaled up for mass production or if the components are designed to have very low probabilities of fracture (e.g., $P_f << 1\%$).

Strength scaling analyses become very complex if more than one flaw type (e.g., pores and inclusions; or pores, inclusions, and machining damage) controls strength such as shown in Figure 7.40. Various flaw types may suddenly appear or disappear as strength controlling flaws as component sizes are scaled up or down. See the Quinn and Morrell review[115] for more information on these fascinating topics. Sung and Nicholson published results on a good study[119] where fractography was effectively used to identify five different flaw types in a 4 mass % yttria-stabilized, tetragonal polycrystal material: fiber burn-out pores, agglomerates, iron inclusions, alumina inclusions, and pores. By careful process control and "flaw management," they were able to eliminate two flaw types, and control the remaining three. Small pores, small alumina inclusions, and small agglomerates became the primary strength-controlling flaws.

The author is often asked whether the Weibull distribution is the best for modeling strength variations, and my answer is always yes, but with some caveats. The Weibull distribution is the only one that the author knows of that permits size scaling of strength. Indeed, the ultimate proof that the Weibull distribution is valid is not whether one set of data can be plotted linearly on a Weibull graph, but whether size scaling is successful. In the dental materials community, confusion about the validity of the Weibull model prompted Dr. J. Quinn and the author to write a review article[120] on this topic. Everything in the review is applicable to other ceramics and glasses as well.

An amazing new study on *5,100* alumina flexural strength specimens by Gorjan and Ambrožič [121] that confirmed the Weibull distribution was perfectly

suitable. It was better than the log normal, the normal, or the gamma distributions. The author congratulated them on their study and offered to do some fractography. Imagine the challenge! It was learned that they broke even more and had reached *11,700* tests. The Weibull distribution still held true. Regrettably, they did not save any specimens for the author to look at. What a pity!

Chapter 7 References

1. V. D. Fréchette, *Failure Analysis of Brittle Materials,* Advances in Ceramics, Vol. 28, American Ceramic Society, Westerville, OH, 1990.
2. L. Orr, "Practical Analysis of Fractures in Glass Windows," *Materials Research and Standards*, **12** [1] (1972) 21 - 23.
3. V. D. Fréchette and T. A. Michalske, "Fragmentation in Bursting Glass Containers," *Bull. Am. Ceram. Soc.*, **57** [4] (1978) 427 – 429.
4. V. D. Fréchette and S. L. Yates, "Fragmentation of Glass Bottles by Impact," *J. Am. Ceram. Soc*., **72** [6] (1989) 1060.
5. E. R. Fuller, Jr., S. W. Freiman, G. D. Quinn, J. B. Quinn, and W. C. Carter, "Fracture Mechanics Approach to the Design of Glass Aircraft Windows: A Case Study," pp. 419 – 430 in *Proc. SPIE Symp. on Windows and Dome Technologies and Materials, IV,* 24-29 July 1994, San Diego, CA, SPIE Volume 2286.
6. R. Morrell, "Fractography of Brittle Materials," Measurement Good Practice Guide, #15, National Physical Laboratory, Teddington, Middlesex, UK, 1999.
7. E. B. Shand, "New Information on Glass Fracture," pp. 117 – 128 in *Proc. Amer. Scientific Glass Blowers Soc. Symp*., June 1969.
8. J. Wang, "Fracture and Stress Pattern Correlations in Glass Plates," Masters Thesis, Texas Tech Univ, August 1986. Avail. on-line from Texas Tech Univ.
9. R, A. McMaster, D. M. Shetterly, and A. G. Bueno, "Annealed and Tempered Glass," pp. 453 - 459 in *Engineered Materials Handbook*, Vol. 4, *Ceramics and Glasses*, S. Schneider, ed., ASM, Metals Park, OH, 1991.
10. N. Shinkai, "The Fracture and Fractography of Flat Glass," pp. 253-297 in *Fractography of Glass*, eds. R. C. Bradt and R. E. Tressler, Plenum, NY, 1994.
11. K. Akeyoshi, E. Kanai, K. Yamamoto, and S. Shima, Asahi Garasu Kenkyu Hokoku, Report of the Research Lab, Asahi Glass Co., **17** [1] (1967) 23 - 26.
12. K. Blank, "Some Practical Aspects of Thermally Strengthened Glass," pp. 485 – 499 in *Strength of Inorganic Glass*, ed. C. Kurkjian, Plenum, NY, 1985.
13. J. M. Barsom, "Fracture of Tempered Glass," *J. Am. Ceram. Soc*., **51** [2] (1968) 75 - 78.
14. J. Menčík, "*Strength and Fracture of Glass and Ceramics*," Glass Science and Technology 12, Elsevier, NY, 1992.
15. D. Shetty, A. Rosenfield, and W. Duckworth, "Crack Branching in Ceramic Disks Subjected to Biaxial Flexure," *Comm. Am. Ceram. Soc.,* Jan. 1983, C10 - C12.
16. D. Hull, "Influence of Stress Intensity and Crack Speed on the Fracture Surface Topography: Mirror to Mist to Macroscopic Bifurcation," *J. Mat. Sci.*, **31** (1996) 4483 – 4492.

17. U. Soltesz, H. Richter, and E. Sommer, "Influence of Internal Stresses on the Development of Cracks in Glasses," pp. 2303 – 2310 in *Advances in Fracture Research,* eds. D. Francois et al., Pergamon Press, NY, 1980.
18. G. D. Quinn, "Guidelines for Measuring Fracture Mirrors," pp. 163 – 190 in: *Fractography of Glasses and Ceramics,* Vol. 5, eds. J. R. Varner, G. Quinn, M. Wightman, American Ceramic Society, Westerville, OH, 2007.
19. Private Com., Letter from L. Orr to G. Quinn on December 15, 2001.
20. W. C. Levengood, "Effect of Origin Flaw Characterization on Glass Strength," *J. Appl. Phys.,* **29** [5] (1958) 820 – 826. Footnote on page 821.
21. J. W. Johnson and D. G. Holloway, "On the Shape and Size of the Fracture Zones on Glass Fracture Surfaces," *Phil. Mag.,* **14** (1966) 731 - 743.
22. E. B. Shand, "Breaking Stress of Glass Determined from Dimensions of Fracture Mirrors," *J. Am. Ceram. Soc*., **42** [10] (1959) 474 – 477.
23. M. J. Kerper and T. G. Scuderi, "Relation of Strength of Thermally Tempered Glass to Fracture Mirror Size," *Bull. Am. Ceram. Soc*., **44** [12] (1965) 953 – 955.
24. M. J. Kerper and T. G. Scuderi, "Relation of Fracture Stress to the Fracture Pattern for Glass Rods of Various Diameters," *ibid*, **45** [12] (1966) 1065 - 1066.
25. H. P. Kirchner, R. M. Gruver, and W. A. Sotter, "Fracture Stress-Mirror Size Relations for Polycrystalline Ceramics, *Phil. Mag*., **33** [5] 775 – 780 (1976).
26. *Glass Industry,* **36** [10] (1955) 523.
27. E. B. Shand, "Experimental Study of Fracture of Glass: II, Experimental Data," *J. Am. Ceram. Soc*., **37** [12] (1954) 559 – 572.
28. N. Terao, "Sur une Relation entre la Resistance a la Rupture et le Foyer d'Eclatement du Verre," *J. Phys. Soc. Japan*., **8** [4] (1953) 545 – 549.
29. H. P. Kirchner and J. W. Kirchner, "Fracture Mechanics of Fracture Mirrors," *J. Am. Ceram. Soc*., **62** [3-4] (1979) 198 – 202.
30. H. P. Kirchner and J. C. Conway, Jr., "Criteria for Crack Branching in Cylindrical Rods: I, Tension; and II, Flexure," *ibid,* **70** [6] (1987) 413 – 418 and 419 - 425.
31. H. P. Kirchner and R. M. Gruver, "Fracture Mirrors in Alumina Ceramics," *Phil Mag*., **27** (1973) 1433 – 1446.
32. M. J. Kerper and T. G. Scuderi, "Modulus of Rupture of Glass in Relation to Fracture Pattern," *Bull. Am. Ceram. Soc.,* **43** [9] (1964) 622 – 625.
33. N. Shinkai, "Fracture Mirror Constants of Silicate Glasses," *Japan J. Appl. Phys.*, **14** [1] (1975) 147-148.
34. ASTM C 1678-07, Standard Practice for Fractographic Analysis of Fracture Mirror Sizes in Ceramics and Glasses, *Annual Book of Standards*, Vol. 15.01, ASTM, West Conshohocken, PA, 2007.
35. G. D. Quinn, J. Eichler, U. Eisele, and J. Rödel, "Fracture Mirrors in a Nanoscale 3Y-TZP," *J. Am. Ceram. Soc*., **87** [3] (2004) 513-516.
36. A. A. Griffith, "The Phenomena of Rupture and Flow in Solids," *Philos. Trans. R. Soc. Lond*., **A221** (1920) 163 – 198.
37. A. A. Griffith, "The Theory of Rupture," in *Proc. 1st Int. Congress on Applied Mechanics*, eds. C. B. Biezeno and J. M. Burgers, (1924), 55.
38. G. R. Irwin, "Analysis of Stresses and Strains Near the End of a Crack Traversing a Plate," *J. Appl. Phys.*, **24** (1957) 361 – 364.

39. SRM's 2100, 2100A, and 2100B, "Fracture Toughness of Ceramics," National Institute for Standards and Technology, Gaithersburg, MD, 1999.
40. J. C. Newman and I. S. Raju, "An Empirical Stress Intensity Factor Equation for the Surface Crack," *Eng. Fract. Mech.*, **15** [1-2] (1981) 185-192.
41. ASTM C 1322-96, "Standard Practice for Fractography and Characterization of Fracture Origins in Advanced Ceramics," *Annual Book of Standards*, Vol. 15.01, ASTM, West Conshohocken, PA, 1996.
42. ASTM C1421-99, "Standard Test Method for the Determination of Fracture Toughness of Advanced Ceramics," *ibid,* 2000.
43. ASTM E 740-88, "Standard Practice for Fracture Testing with Surface-Crack Tension Specimens," *Annual Book of Standards,* Vol. 3.01, ASTM, West Conshohocken, PA, 1988.
44. ISO 18756, Fine Ceramics (Advanced Ceramics, Advanced Technical Ceramics) – Determination of Fracture Toughness of Monolithic Ceramics at Room Temperature by the Surface Crack in Flexure (SCF) Method, International Organization for Standards, Geneva, SW, 2003.
45. T. Fett, "An Extension of the Newman-Raju Formula," *Int. J. Fract*., **33** (1987) R47-R50.
46. T. Fett, "Stress Intensity Factors for Semi-elliptical Surface Cracks in a Plate Under Tension Based on the Isida's solution," *ibid,* **48** (1991) 139 – 151.
47. T. Fett and D. Munz, *Stress Intensity Factors and Weight Functions*, Computational Mechanics Publ., Southampton, UK and Boston, MA, USA, 1997.
48. M. Isida, H. Noguchi, and T. Yoshida, "Tension and Bending of Finite Thickness Plates with a Semi-elliptical Surface Crack," *Int. J. Fract*., **26** (1984) 157-188.
49. S. Strobl, P. Supancic, T. Lube, and R. Danzer," Surface Crack in Tension or Bending – A Reassessment of the Newman and Raju Formula in Respect to Fracture Toughness Measurements in Brittle Materials," *J. Eur. Cer. Soc.,* **32** (2012) 1491 – 1501.
50. G. K. Bansal, "Effect of Flaw Shape on Strength of Ceramics," *J. Am. Ceram. Soc*., **59** [1-2] (1976) 87-88.
51. Y. Murakami, *Stress Intensity Factors Handbook*, Vols. 1 and 2, ed., Pergamon Press, NY, 1986. (Case 9.49)
52. J. J. Mecholsky, Jr., S. W. Freiman, and R. W. Rice, "Fracture Surface Analysis of Ceramics," *J. Mat. Sci.*, **11** (1976) 1310–1319.
53. G. K. Bansal and W. H. Duckworth, "Fracture Stress as Related to Origin and Fracture Mirror Sizes," *J. Am. Ceram. Soc.*, **60** [7–8] (1977) 304 – 310.
54. G. K. Bansal, "On Fracture Mirror Formation in Glass and Polycrystalline Ceramics," *Phil Mag*., **35** [4] (1977) 935- 944.
55. S. R. Choi and J. P. Gyekenyesi, "Crack Branching and Fracture Mirror Data of Glasses and Advanced Ceramics," NASA Technical Report TM 1998-206536, NASA Glenn Research Center, Cleveland, OH,1998.
56. H. P. Kirchner, R. M. Gruver, M. V. Swain, and R. C. Garvie, "Crack Branching in Transformation-Toughened Zirconia," *J. Am. Ceram. Soc.*, 64 [9] (1981) 529-533.

57. A. I. A. Abdel-Latif, R. C. Bradt, and R. E. Tressler, "Dynamics of Fracture Mirror Boundary Formation in Glass," *Int. J. Fract.,* **13** [3] (1977) 349-359.
58. M. Ramulu, R. C. Bradt, A. S. Kobayashi, and K. H. Yang, "A Dynamic Fracture Mechanics Interpretation of Multiple Mist Regions on Soda-Lime-Silicate Glass Fracture Features," pp. 215 – 227 in *Fractography of Glasses and Ceramics, Advances in Ceramics*, Vol. 22, J. Varner, and V. Fréchette, eds., American Ceramic Society, Westerville, OH, 1988.
59. D. A. Krohn and D. P. H. Hasselman, "Relation of Flaw Size to Mirror in the Fracture of Glass," *J. Am. Ceram. Soc.,* **54** [8] (1971) 411.
60. J. J. Mecholsky, Jr., A. Gonzalez, and S. W. Freiman, "Fractographic Analysis of Delayed Failure in Soda-Lime Glass," *ibid*, **62** [11-12] (1979) 577 – 580.
61. R. W. Rice, "Ceramic Fracture Features, Observations, Mechanism and Uses," pp. 5 – 103 in *Fractography of Ceramic and Metal Failures,* ASTM STP 827, ASTM, 1984.
62. K. Gopalakrishnan and J. J. Mecholsky, Jr., "Quantitative Fractography of Mixed-Mode Fracture in an R-curve Material," *J. Mat. Sci.,* **48** (2013) 7081 – 7087.
63. R. W. Rice, "Ceramic Fracture Features, Observations, Mechanism and Uses," pp. 5-103 in *Fractography of Ceramic and Metal Failures*, eds., J.J. Mecholsky, Jr, S. W. Freiman, and S. R. Powell, ASTM STP 827 ASTM, Int., West Conshohocken, PA, 1984.
64. J. J. Mecholsky, Jr., T. J. Hill, and Z. Chen, "Application of Quantitative Fractography to the Characterization of R-Curve Behavior," pp.152-168 in *Fracture Resistance Testing of Monolithic and Composite Brittle Materials*, eds., J. A. Salem, G. D. Quinn, M. G. Jenkins, ASTM STP 1409, ASTM, Int., West Conshohocken, PA (2002).
65. G. D. Quinn and J. J. Swab, "Fractography and Estimates of Fracture Origin Size from Fracture Mechanics," *Cer. Eng. Sci. Proc*., **17** [3] (1996) 51 - 58.
66. G. D. Quinn and J. J. Swab, "Comparisons of Calculated and Measured Flaw Sizes," pp. 175 – 192 in *Fractography of Glasses and Ceramics IV,* Ceramic Transactions, Vol. 122 eds. J. Varner and G. Quinn, American Ceramic Society, Westerville, OH, 2001.
67. H. G. Richter and F. Kerkhof, "Stress Wave Fractography," pp. 75 – 109 in *Fractography of Glass*, eds. R. C. Bradt and R. E. Tressler, Plenum, NY, 1994.
68. H. Richter, "Crack Propagation in Glass Under Liquids in an Intermediate Range of Crack Velocities," pp. 219 – 229 in *Strength of Inorganic Glass,* ed. C. R. Kurkjian, Plenum Press, NY, 1985.
69. T. A. Michalske, M. Singh, and V. D. Fréchette, "Experimental Observation of Crack Velocity and Crack Front Shape Effects in Double-Torsion Fracture Mechanics Tests," pp. 3 - 12 in *Fracture Mechanics for Ceramics, Rocks, and Concrete*, STP 745, ASTM Int., West Conshohocken, PA, 1982.
70. T. A. Michalske and J. M. Collins, "Fractographic Determination of Crack-Tip Stress Intensity," pp. 229 – 239 in *Fractography of Glasses and Ceramics*, Advances in Ceramics, Vol. 22, eds. J. R. Varner and V. D. Fréchette, American Ceramic Society, Westerville, OH 1988.

71. A. Tsirk, "Formation and Utility of a Class of Anomalous Wallner Lines on Obsidian," *ibid,* pp. 57 – 69.
72. E. F. Poncelet, "The Markings on Fracture Surfaces," *J. Soc. Glass Technol*., **42** (1958) 279T – 288T.
73. A. Smekal, "Procedure for Measurement of Fracture Surface Propagation Velocities on Fracture Surfaces," *Glastech. Ber.,* **23** [3] (1950) 57 – 67.
74. T. Fett, D. Munz, and K. Keller, "Determination of Subcritical Crack Growth on Glass in Water from Lifetime Measurements on Knoop-Cracked Specimens," *J. Mat. Sci.,* **23** (1988) 798 - 803.
75. P. J. Dwivedi and D. J. Green, "Determination of Subcritical Crack Growth Parameters from In situ Observation of Indentation Cracks," *J. Am. Ceram. Soc*., **78** [8] (1995) 2122 - 2128.
76. V. M. Sglavo and R. Dal Maschio, "Controlled Indentation-Induced Cracks for the Determination of Fracture Toughness in Alumina," pp. 233 – 244, in *Fracture Mechanics of Ceramics, Vol. 11*, eds. R. C. Bradt et al., Plenum, NY, 1996.
77. M. Stech and J. Rödel, "Method for Measuring Short -Crack R-Curves Without Calibration Parameters: Case Studies on Alumina and Alumina-/Aluminum Composites," *J. Am. Ceram. Soc*., **79** [2] (1996) 291 - 297.
78. W. Chen, D. Lupascu, J. Rödel, and C. S. Lynch, "Short Crack R-Curves in Ferroelectric and Electrorestrictive PLZT," *ibid*, **84** [3] (2001) 393 – 397.
79. A. H. Heuer, "Transformation Toughening in ZrO_2-Containing Ceramics," *ibid,* **70** [10] (1987) 689 – 698.
80. G. D. Quinn, L. K, Ives, and S. Jahanmir, "On the Fractographic Analysis of Machining Cracks in Ground Ceramics: A Case Study on Silicon Nitride," Special Publication SP 996, NIST, Gaithersburg, MD, May, 2003.
81. D. B. Marshall, "Strength Characteristics of Transformation-Toughened Zirconia," *J. Am. Ceram. Soc.,* **69** [3] (1986) 173 – 180.
82. S. M. Smith and R. O. Scattergood, "Controlled Crack Shapes for Indentation Fracture of Soda Lime Glass," *ibid,* **75** [9] (1992) 2593 – 2596.
83. R. W. Steinbrech and O. Schmenkel, "Crack-Resistance Curves of Surface Cracks in Alumina," *ibid,* **71** [5] (1988) C271- C273.
84. T. Fett, D. Munz, J. Siedel, M. Stech, and J. Rödel, "Correlation Between Long and Short Crack R-Curves in Alumina Using the Crack Opening Displacement and Fracture Mechanical Weight Function Approach," *ibid*, **79** [5] (1996) 1189 - 1196.
85. T. Fett and D. Munz, "Evaluation of R-curve Effects in Ceramics," *J. Mat. Sci.,* **28** (1993) 742 – 752.
86. R. F. Cook and D. R. Clarke, "Fracture Stability, R-Curves and Strength Variability," *Acta Metall.,* **36** [3] (1988) 555 – 562.
87. J. J. Mecholsky, Jr., T. J. Hill and Z. Chen, "Application of Quantitative Fractography to the Characterization of R-Curve Behavior," pp. 152 – 167 in *Fracture Resistance Testing of Monolithic and Composite Brittle Materials,* ASTM STP 1409, eds., J. Salem, et al., ASTM, West Conshohocken, PA, 2002.
88. J. J. Petrovic, L. A. Jacobson, P. K. Talty, and A. Vasudevan, "Controlled Surface Flaws in Hot-Pressed Si_3N_4," *J. Am. Ceram. Soc*., **58** [3-4] (1975) 113 - 116.

89. G. D. Quinn, R. J. Gettings, and J. J. Kübler, "Fractography and the Surface Crack in Flexure (SCF) Method for Evaluating Fracture Toughness of Ceramics," pp. 107 - 144 in *Fractography of Glasses and Ceramics III*, Ceramic Transactions, Vol. 64, eds., J. R. Varner, V. D. Fréchette, and G. D. Quinn, ACS, Westerville, OH, 1996.
90. G. Quinn, R. Gettings, and J. Kübler, "Fracture Toughness by the Surface Crack in Flexure (SCF) Method: Results of the VAMAS Round Robin," *Cer. Eng. Sci. Proc.,* **15** [5] (1994) 846-855.
91. G. D. Quinn, K. Xu, J. A, Salem, and J. J. Swab, "SRM 2100: the World's First Fracture Toughness Reference Material," pp. 499 – 530 in *Fracture Mechanics of Glasses and Ceramics, Vol. 14*, eds., R. C. Bradt, D. Munz, M. Sakai, and K. W. White, Klewer/Plenum, NY, 2005.
92. I. Bar-On, G. D. Quinn, J. Salem, and M. J. Jenkins, "Fracture Toughness Standard Test Method C 1421-99 for Advanced Ceramics," pp. 315-335 in *Fatigue and Fracture Mechanics, Vol. 32*, ASTM STP 1406, ed. R. Chona, ASTM Int., West Conshohocken, PA, 2001.
93. EN ISO 18756:2005, "Advanced Ceramics, Advanced Technical Ceramics); Determination of Fracture Toughness of Monolithic Ceramics at Room Temperature by the Surface Crack in Flexure (SCF) Method," European Committee for Standards, Brussels.
94. G. D. Quinn, "Fracture Toughness of Ceramics by the Vickers Indentation Crack Length Method: A Critical Review," *Cer. Eng. Sci. Proc.,* **27** [3] (2006) 45 – 62.
95. G. D. Quinn and R. C. Bradt, "On the Vickers Indentation Fracture Toughness Test," *J. Am. Ceram. Soc*., **90** [3] (2007) 673 – 680
96. B. R. Lawn and D. B. Marshall, "Indentation Fractography," pp. 1 –36 in *Fractography of Glass*, eds., R. Bradt and R. Tressler, Plenum, NY, 1994.
97. P. Chantikul, G. R. Anstis, B. R. Lawn and D. B. Marshall, "A Critical Evaluation of Indentation Techniques for Measuring Fracture Toughness: II Strength Method," *J. Am. Ceram. Soc.,* **64** [9] (1981) 539 – 543.
98. R. F. Cook and G. M. Pharr, "Direct Observation and Analysis of Indentation Cracking in Glasses and Ceramics," *ibid*, **73** [4] (1990) 787 – 817.
99. T. Wilantewicz, "Crack Initiation Behavior of Optical Glasses from Vickers Indentations," Ph. D. Thesis, Alfred University, November, 2005.
100. T. Wilantewicz and J. R. Varner, "Vickers Indentation Fracture in Optical Glass Compositions," pp. 131 -151 in *Fractography of Glasses and Ceramics,* Vol. 5, eds. J. R. Varner, G. D. Quinn, M. Wightman, American Ceramic Society, Westerville, OH, 2007.
101. D. B. Marshall, B. R. Lawn, and J. J. Mecholsky, "Effect of Residual Stresses on Mirror/Flaw Size Relations," *J. Am. Ceram. Soc*, **63** [5-6] (1980) 358 – 360.
102. D. E. Passoja, "Fundamental Relationships Between Energy and Geometry in Fracture," pp. 101 – 126 in *Fractography of Glasses and Ceramics,* eds., J. R. Varner and V. D. Fréchette, Advances in Ceramics, Vol. 22, American Ceramic Society, Westerville, OH, 1988.
103. J. J. Mecholsky, T. J. Mackin, and D. E. Passoja, "Self-Similar Crack Propagation in Brittle Materials," *ibid*, pp. 127 – 134.

104. D. A. Lange, H. M. Jennings, and S. P. Shah, "Relationship Between Fracture Surface Roughness and Fracture Behavior of Cement Paste and Mortar," *J. Am. Ceram. Soc.,* **76** [3] (1993) 589 – 597.
105. Y. Xin, K. J. Hsia, and D. A. Lange, "Quantitative Characterization of the Fracture Surface of Si Single Crystals by Confocal Microscopy," *ibid,* **78** [12] (1995) 3201 – 3208.
106. J. J. Mecholsky, D. E. Passoja, and K. S. Feinberg-Ringel, "Quantitative Analysis of Brittle Fracture Surfaces Using Fractal Geometry," *ibid,* **72** [1] (1989) 60 – 65.
107. J. J. Mecholsky, Jr. and S. W. Freiman, "Relationship Between Fractal Geometry and Fractography," *ibid,* **74** [12] (1991) 3136 – 3138.
108. T. Hollstein, W. Pfeiffer, M. Rombach, and B. Thielicke, "Analysis of Machining Damage in Engineering Ceramics by Fracture Mechanics, Fractography, and X-ray Diffraction," pp. 145-169 in *Fractography of Glasses and Ceramics, III*, Ceramic Transactions, Vol. 64, eds., J. Varner, et al., ACS, Westerville, OH, 1996).
109. J. J. Mecholsky and M. G. Drexhage, "Comparison of Optical and Fractographic Measurements of Residual Stress in Compressively Clad Glass Rods," *J. Am. Ceram. Soc*., **63** [5-6] (1980) 347-349.
110. J. C. Conway, Jr. and J. J. Mecholsky, Jr., "Use of Crack Branching Data for Measuring Near-Surface Residual Stress in Tempered Glass," *ibid,* **72** [9] (1989) 1584-1587.
111. D. B. Marshall and B. R. Lawn, "An Indentation Technique for Measuring Stresses in Tempered Glass Surfaces," *J. Am. Ceram. Soc*., **60** [1-2] (1977) 86-87.
112. M. V. Swain, J. T. Hagan, and J. E. Field, "Determination of the Surface Residual Stresses in Tempered Glasses by Indentation Fracture Mechanics," *J. Mat Sci. Lttrs.,* **12** (1977) 1914-1917.
113. W. Weibull, "A Statistical Distribution Function of Wide Applicability," *J. Appl. Mech.,* September, (1951) 293 – 297.
114. G. D. Quinn, "Static Fatigue and Creep Resistance of a Commercial Sialon," *J. Mat. Sci*., **22** (1987) 374-380.
115. K. Trustrum and A. De S. Jayatilaka, "Application of Weibull Analysis for Brittle Materials," *J. Mat. Sci*., **18** (1983) 2765-70.
116. A. De S. Jayatilaka and K. Trustrum, "Statistical Approach to Brittle Fracture*," ibid*, **12** (1977) 1426-30.
117. R. Danzer, "A General Strength Distribution Function for Brittle Materials," *J. Eur. Ceram. Soc*., **10** (1992) 461 – 472.
118. G. D. Quinn and R. Morrell, "Design Data for Engineering Ceramics: A Review of the Flexure Test," *J. Am. Ceram. Soc*., **74** [9] (1991) 2037 - 2066.
119. J. Sung and P. S. Nicholson, "Strength Improvement of Yttria-Partially-Stabilized Zirconia by Flaw Elimination," *J. Am. Ceram. Soc*., **71** [9] (1988) 788 - 795.
120. J. B. Quinn and G. D. Quinn, "A Practical and Systematic Review of Weibull Statistics for Reporting Strengths of Dental Materials," *Dent. Mat.*, **26** [2] (2010) 135-147.
121. L. Gorjan and M. Ambrožič, "Bend Strength of Alumina Ceramics: A Comparison of Weibull Statistics with Other Statistics Based on a Very Large Experimental Data Set," *J. Eur. Ceram., Soc*., **32** (2012) 1221 -1227.

8. Single Crystals

8.1 General

Fractographic procedures for single crystals are similar to those for glasses and polycrystalline ceramics, but there are some nuances and differences. Fracture surfaces may have regions with conchoidal fracture, Wallner lines, and twist hackle. Other regions may have dramatic faceting. Fracture resistance often varies significantly between the different crystallographic planes, causing jagged fracture patterns as cracks radically change directions onto preferred cleavage planes. Fracture surfaces may be very difficult to interpret. Some examples of the unusual markings are shown in Figure 8.1.

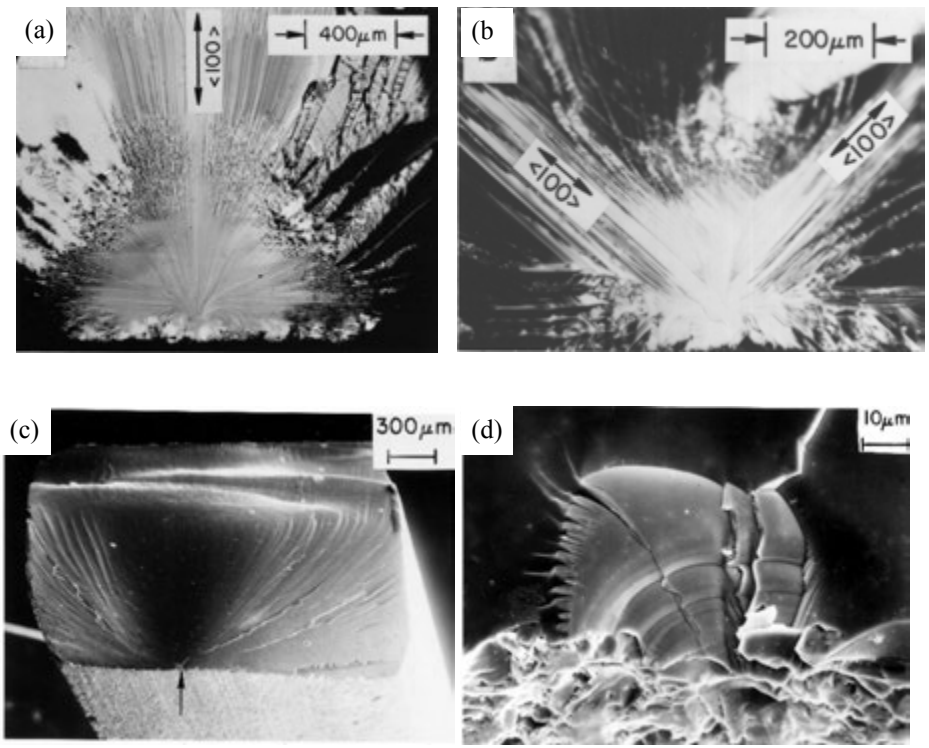

Figure 8.1 *Examples of single crystal fractures. (a) and (b) show fracture mirrors on the {100} type planes in MgO, but with two different tensile surface orientations. (c) and (d) show a cubic zirconia bend bar with curved linear lance like markings emanating from the origin area and the grinding crack origin. (courtesy R. Rice)*

The overall fracture plane may not necessarily be perpendicular to the direction of principal normal stress, since a preferred cleavage plane may be at an irregular angle to that stress. Sometimes the overall fracture extension may be approximately perpendicular to the maximum principal stresses, but local fracture proceeds in a zigzag fashion on other planes. This crack redirection is different than conventional crack branching in glasses or polycrystalline ceramics. Branching is much less common in single crystals. If the maximum principal stress is perpendicular to a preferred cleavage plane, the fracture surface may be very flat and featureless with little or no hackle, and no branching at all.

Fracture mirrors may be present, but may have odd shapes and markings. There may be no mist or hackle on preferred cleavage planes. Mirror sizes may be extremely difficult or impractical to measure. Cleavage hackle steps may be confused with Wallner lines. Twinning may cause fracture.

8.2 Preferred Cleavage Planes

Bradt et al.[1,2] have reviewed the various criteria for cleavage and concluded that fracture toughness is the best indicator of the preferred cleavage plane. The fracture toughness can vary dramatically on different planes. The energy to propagate cracks along preferred cleavage planes is less than that for less-favored planes. Nevertheless, there is contradictory information in the literature on preferred cleavage planes in some crystals, even for such well studied materials as silicon, alumina (sapphire), and magnesium aluminate spinel. Some of contradictory information surely is due to experimental error or specific aspects of the test method. The direction of crack advance on a plane is as important as the plane itself. The speed of crack advance can even determine which fracture plane is preferred.[3] Although the double cantilever beam method and the constant applied moment variation as shown in Figure 8.2 are often used, results are not strictly valid if the crack zigzags down the guiding groove or is tilted to the intended fracture plane.

Knoop indentations in bend bars may be used to generate controlled surface flaws in the surface crack in flexure (SCF) method as shown in Figure 8.2. The specimen axis and cross section and the indentation and precrack plane may be aligned with a particular cleavage plane. The local direction of crack extension may vary along the crack periphery, however. Such micro flaws, which mimic naturally occurring flaws, are valuable in demonstrating just how complex fracture resistance can be in single crystals. A good example is from the work of Chen and Leopold[4] and Xin et al.[5] on silicon as summarized in Table 8.1. Xin et al. [5] showed that the residual stresses from the indentation could change

the propagation plane. Bradt et al.[6,7,8] have used the SCF method on alumina and spinel. Figure 8.3 shows a Knoop precrack in sapphire. One unresolved issue with the SCF method for single crystals is whether or not indentation residual stresses vary with plane and orientation. Akimune and Bradt[9] showed that there is considerable hardness anisotropy even on one plane (100) in spinel, but negligible variability on the (111).

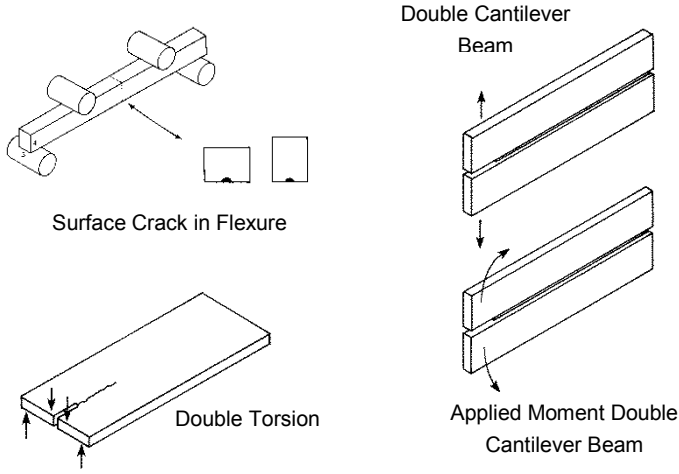

Figure 8.2 *Test methods for single crystal fracture toughness determination.*

Reference	Plane Type	K_{Ic} (MPa√m)	Fracture characteristics
Chen and Leipold (4)	{111}	0.82	Flat and smooth fractures. This is the preferred cleavage plane.
Chen and Leipold (4)	{110}	0.90	Large but asymmetric cathedral mirrors centered on the flaws. Propagation switched to {111} planes and zigzagged at the mirror boundaries.
Chen and Leipold (4)	{100}	0.95	A very rough fracture surface. Cracks switched to {111} very quickly.
Xin, Hsia, and Lange (5)	{110}	0.95	Residual indentation stresses intact: Cracks propagated on {110}.
Xin, Hsia, and Lange(5)	{110}	-	Residual indentation stresses removed by annealing. Crack switched to {111}.

Table 8.1 *Fracture toughness of single crystal silicon from Knoop SCF tests.*

(a)

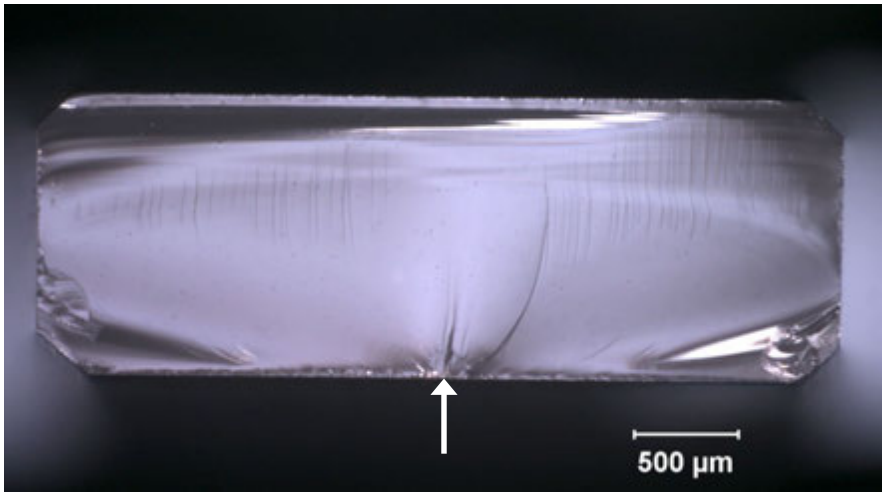

(b)

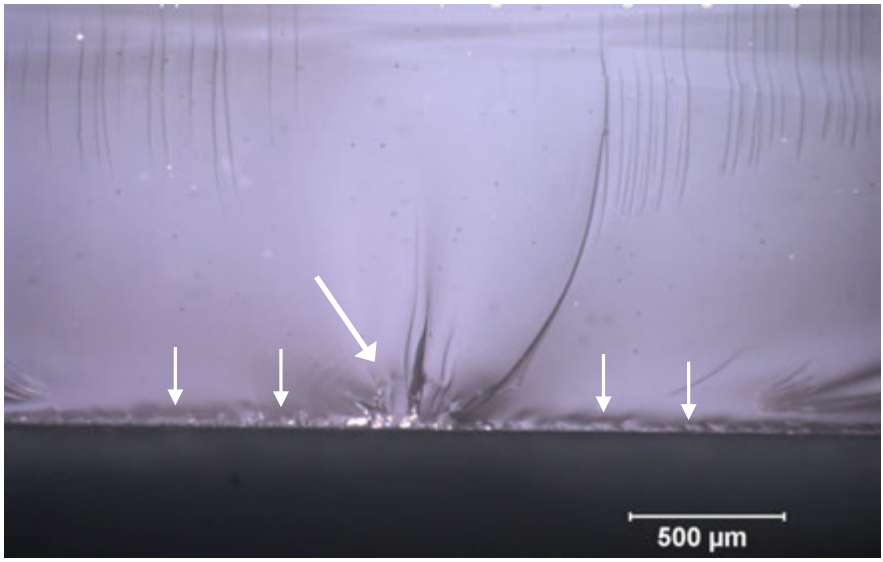

Figure 8.3 *Relatively smooth fracture surface (a) of a surface crack in flexure (SCF) sapphire test specimen with a 49 N Knoop indentation as a starter flaw (large arrow). The bar tensile surface was the a-plane. Fracture occurred on the m-plane. (b) is a close-up which shows grinding cracks along the surface (small white arrows), but the indentation crack (large white arrow) was dominant. The long curved line leading from the origin to the upper right is a "cleavage step hackle" line. (courtesy R. Krause).*

8.3 Fractographic Techniques

Reflections and translucency in some crystals make photographing single crystals difficult. Different lighting and specimen tilting are needed to bring out various details.

Low-angle grazing illumination on cleaved surfaces may be more problematic since fracture surfaces are mirror like and reflect light away from the microscope objective lens. Silicon is a good example of this and the fractographer is confronted with either getting too little or too much light reflected into the eyepieces. When using a stereomicroscope with directional illumination, it is often effective to tilt the specimen at an angle to reflect more light up into the eyepieces. The good depth of field of the stereomicroscope can accommodate the specimen tilt at low to moderate magnifications. Stopping down an aperture can increase the depth of field.

A reflected light compound microscope may be very effective with single crystals if the fracture surface is not too rough. Dark field illumination may aid finding fracture mirrors, since the symmetry of cleavage steps may be accentuated as shown in Figure 8.4.

Confocal microscopes may not be very effective due to the specular reflections.

Transmitted illumination is often useful for transparent single crystals. Polarizers are essential aids to help discern twinning, which may cause fracture in some crystals.

Gold coating of a transparent single crystal may aid in interpretation and may make the fracture surface easier to view, but if the surface is very flat, the gold coating may make it behave like a mirror, which will pose problems for inspection and photography.

X-ray topography is a unique tool for single crystals. Imperfections in the crystal and its surface produce image contrast. Figure 8.5 shows an example that reveals handling damage on the polished surface of a sapphire hemispherical dome.[10] The full extent of the handling damage was not visible with the optical or scanning electron microscopy.

(a)

(b)

(c)

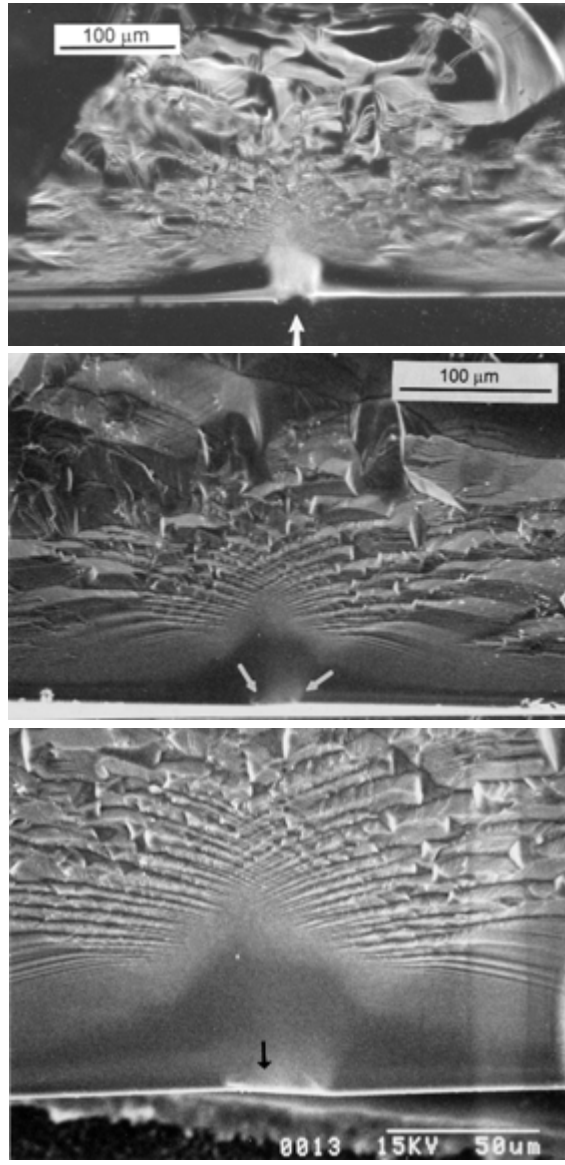

Figure 8.4 *Dark-field illumination may aid optical examination. Different views of the fracture origin in a silicon wafer tested in a biaxial ring-on-ring mode (282 MPa). Fracture initiated from the surface grinding crack (also shown later in Figure 8.17), propagated on a {110} type plane, but started to zigzag. (a) is a dark field optical image with a strange swirling appearance. It nonetheless has a symmetry that is a tip off to the existence of an origin and mirror. (b) and (c) are SEM images of the origin with arrows calling attention to the origin flaw.*

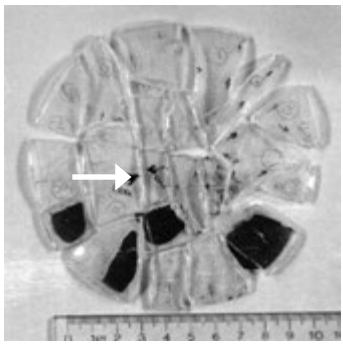

(a)

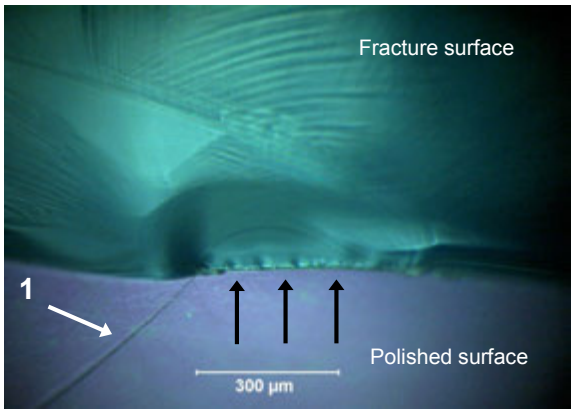

(b)

(c)

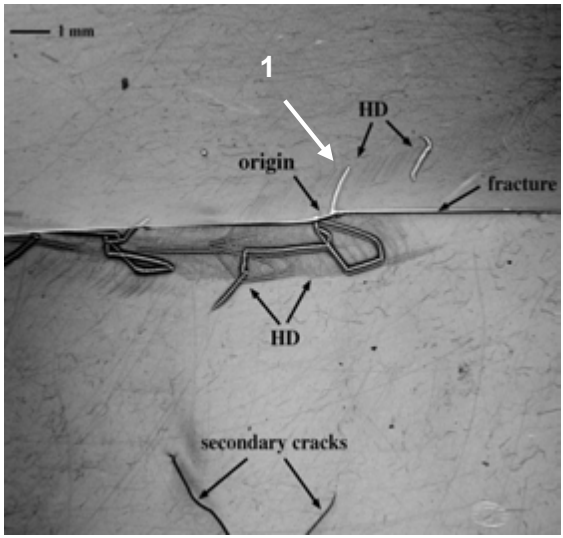

Figure 8.5 *Sapphire hemispherical dome that fractured during a thermal stress proof test. (a) shows the fractured dome and the origin (large white arrow). (b) shows an optical fractograph with the origin piece tilted back to show both the fracture surface and the polished outer surface. The cracking is marked by the black arrows. Another apparently isolated intersecting scratch is marked with the white arrow and the numeral "1." (c) is a composite of two x-ray topographs of the polished outer surface, showing the matching fracture halves where they meet at the origin. Surface and subsurface damage are exposed and the scratch labeled "1" in (b) is revealed to be part of a complex handling damage (HD) network. (c is courtesy of D. Black*)

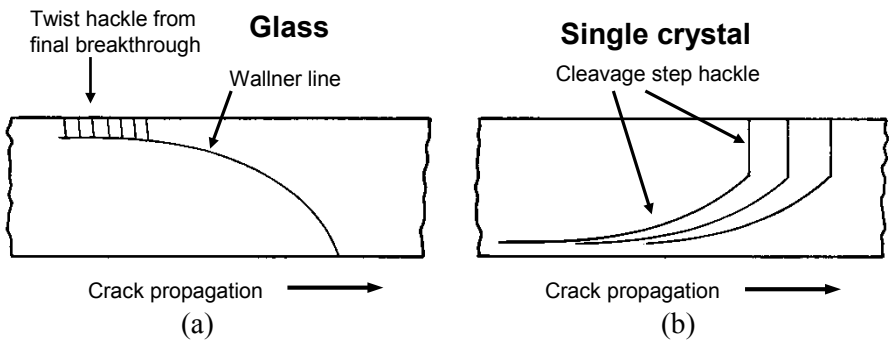

Figure 8.6 *Schematics showing (a) a Wallner line and twist hackle in a glass plate loaded in bending and (b) "cleavage step hackle" in a single crystal plate loaded in bending. In both cases the crack was leading on the bottom surface.*

8.4 Fracture Surface Markings

Single crystal fracture planes often have small *"cleavage step hackle"* that may be confused with Wallner lines. Figure 8.6 shows the differences.

Cleavage step hackle: *A form of hackle in single crystals caused by the crack running on two very close parallel planes. It is in the form of one or more single lines, parallel to the local direction of crack propagation.*

Cleavage step hackle is often generated by the origin or other surface irregularities and runs parallel to the direction of crack propagation. The hackle may suddenly change from curved lines to parallel vertical segments on the compression side of a specimen. The step may be very persistent and extend over great distances without merging, unlike twist hackle lines. Cleavage step hackle is not unlike "step hackle" in glasses as described in section 5.3.6, but here with single crystals, the step is caused by the preference of a crack to stay on two nearby parallel planes without merging. Figures 8.1c and 8.3 show good examples of cleavage step hackle in sapphire.

Fracture surfaces and fracture mirrors may have extraordinary shapes and facets, but usually have some degree of recognizable symmetry that will help the fractographer identify an origin site. Mirror shapes may vary dramatically within a crystal depending upon the fracture plane. To illustrate these fascinating variations, fracture markings for single crystal cubic spinel are shown in Figures 8.7 through 8.14. These figures follow the recommendations of this Guide and ASTM C 1322.[11] They show a picture of the whole fracture

surface, the fracture mirror, and a close up of the origin. The fractographic findings are summarized in Table 8.2. These images are from Rice and colleagues[3,12,13,14] who studied fracture in this material using double cantilever beam and flexural strength specimens. They found a remarkable variety of fracture surfaces with features such as "cathedral mirrors," "gull wing mirrors," "skewed cathedral mirrors," and "whisker lances." Cathedral and gull wing mirrors have also been observed in other cubic crystals such as silicon (Figure 8.4) and fully-stabilized zirconia. Gull wing mirrors look like cathedral mirrors that are tilted 90° on the fracture surface. Bear in mind that there may be threshold stresses or stress intensities for the formation of markings on certain planes. Thus, the flat fractures shown in figures 8.8 and 8.9 may indicate fracture on a preferred cleavage plane, or that the stresses were too low to generate mirror markings. The preferred cleavage plane in spinel is the {100} which has a fracture toughness of 0.9 to 1.2 MPa√m depending upon the method of measurement.[3,6,7,12,13,14] The fracture toughness of the {110} is not much greater at 1.0 to 1.5 MPa√m. Consequently, fracture usually runs on {100} or {110} type planes. Fracture is not preferred on the {111} and the fracture toughness is much greater (1.9 MPa√m or more). [3,6,7,12,13,14]

Intended fracture plane type	Bend bar tensile surface	Bend bar tensile axis	Fracture type	Figure
{100} (Case A)	{100}	<100>	Cathedral mirror Major crack redirection beyond the mirror sides	8.7
{100} (Case D)	{110}	<100>	No mirror Flat and featureless fracture surface	8.8
{110} (Case B)	{100}	<110>	No mirror Flat and featureless fracture surface	8.9
{110} (Cases F1 + F2) (Case C)	{110}	<110>	Skewed fracture mirror and Major crack redirection beyond the mirror sides, or Gull wing mirror and Jagged fracture surface beyond top of mirror	8.10 8.11 8.12
{110} (Cases G1 + G2)	{111}	<110>	Skewed cathedral mirror Major crack redirection beyond the mirror sides, or flat	8.13 8.14
{111} (Case E)	{110}	<111>	Gull wing mirror Jagged crack propagation beyond top of mirror	8.15

Table 8.2 *Fracture markings in $MgAl_2O_4$ spinel bend bars. The brackets {100} denote the family of (100) planes and the angles <100> denote the family of [100] directions. (After Wu, McKinney, and Rice, Ref. 3)*

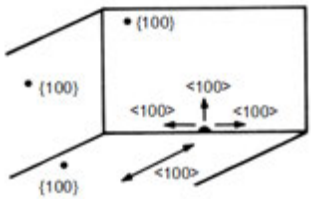

Bend bar orientation

(a)

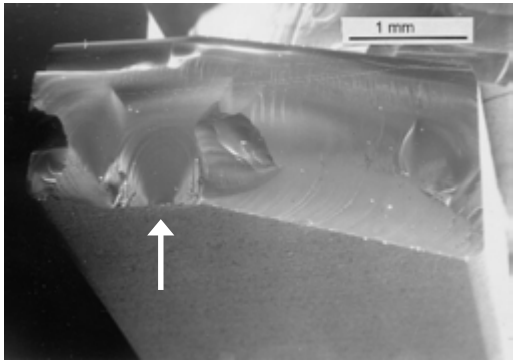

(b)

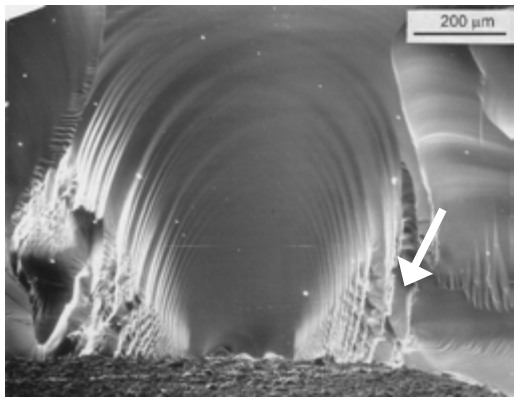

(c)

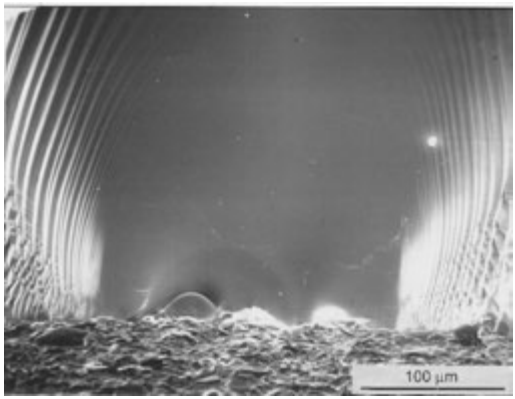

Figure 8.7 *Spinel bend bar with a {100} tensile surface and <100> tensile axis designed to cause fracture on a {100} plane. (185 MPa) (a) shows the whole fracture surface and origin (arrow). (b) shows the "**cathedral mirror**" and the arc-ribs that gradually get progressively severer until a branch or major crack redirection occurs (white arrow). (c) shows the grinding crack fracture origin. Fracture starts on the {100} but shifts or branches to the {110} just beyond the sides of the mirror. (Case A, Table 8.2) (Courtesy R. Rice)*

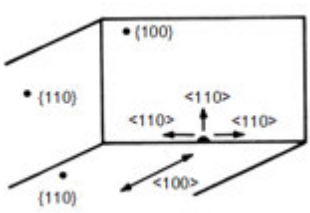

(a)

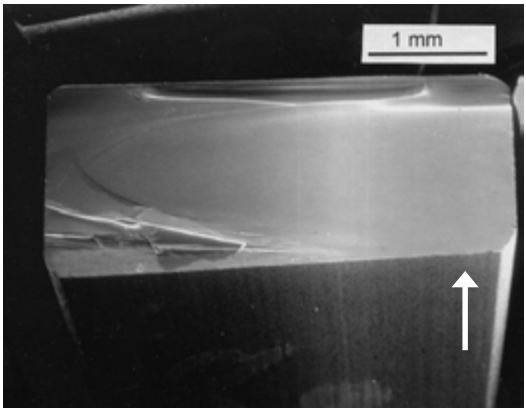

(b)

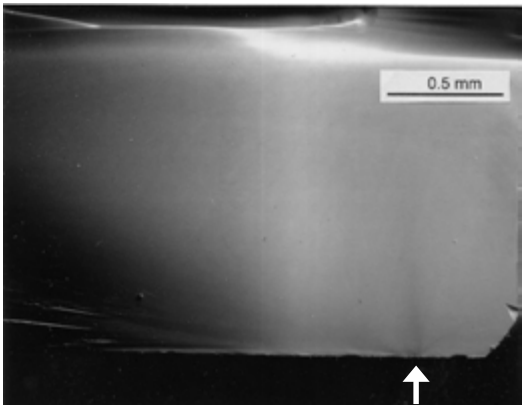

(c)

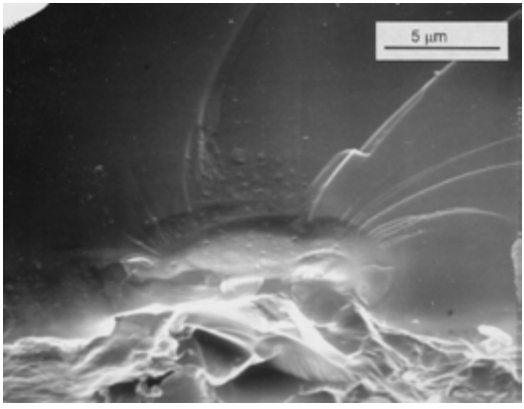

Figure 8.8 *Spinel bend bar with a {110} tensile surface and <100> tensile axis designed to cause fracture on the {100} cleavage plane. (170 MPa) (a) shows the whole fracture surface which is flat except for the cleavage steps on the side and the cantilever curl. Other similar specimens had no cleavage steps. (b) shows the origin site and (c) shows the grinding crack fracture origin. (Case D, Table 8.2) (Courtesy R. Rice*)

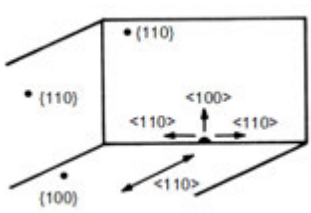

(a)

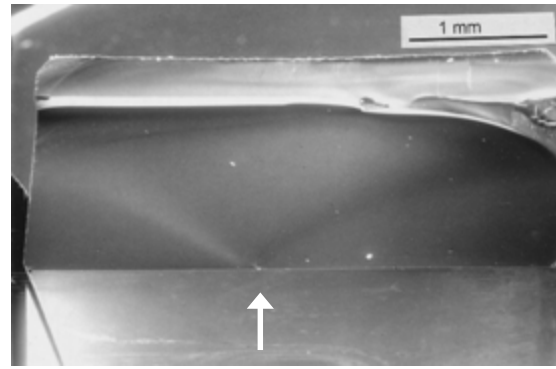

(b)

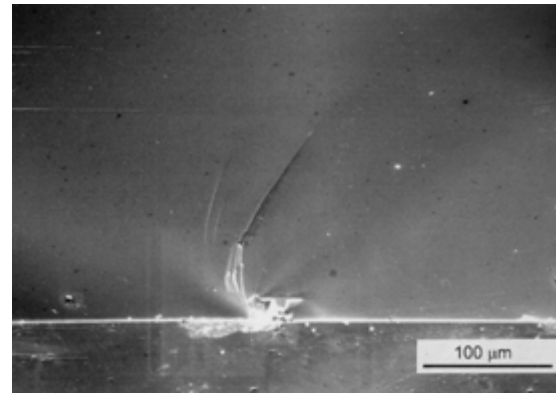

Figure 8.9 *Spinel bend bar with a {100} tensile surface and <110> tensile axis designed to cause fracture on a {110} type plane. (169 MPa) (a) shows the whole fracture surface which is flat and featureless except for the cantilever curl. The arrow shows the origin. (b) shows the grinding crack fracture origin. Fracture stays on a {110} type plane. (Case B, table 8.2) (Courtesy R. Rice)*

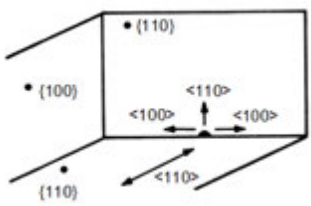

(a)

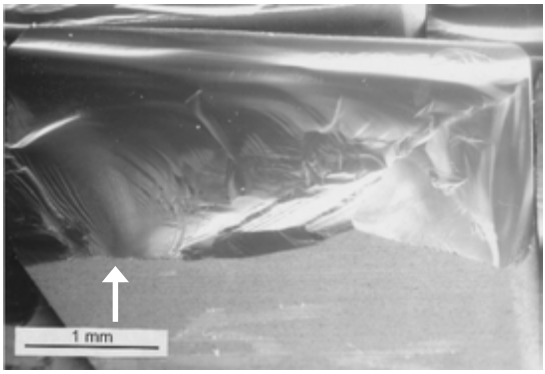

(b)

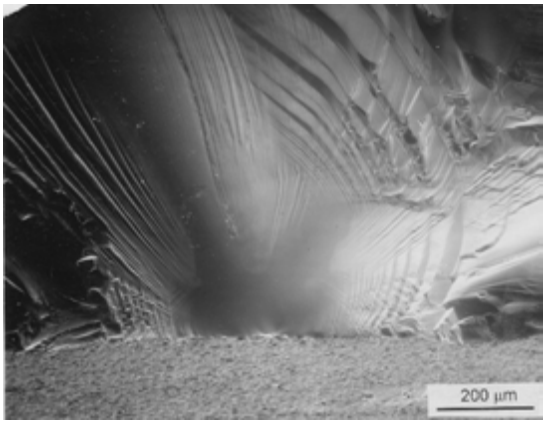

(c)

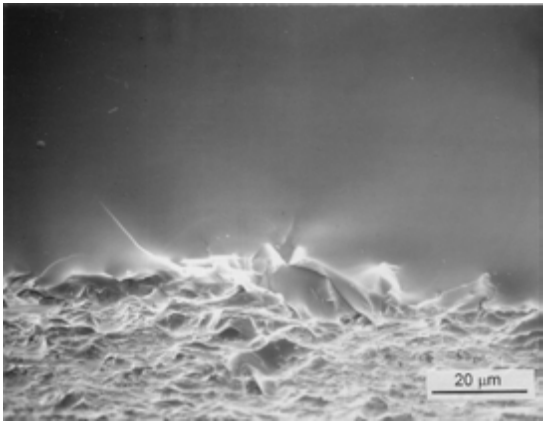

Figure 8.10 *Spinel bend bar with a {110} tensile surface and <110> tensile axis designed to cause fracture on a {110} plane. (283 MPa) (a) shows the whole fracture surface, (b) shows the mirror with "**whisker lances**" radiating outward, and (c) shows the grinding crack fracture origin. (Case F1, table 8.2) (Courtesy R. Rice)*

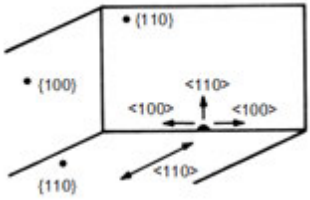

(a)

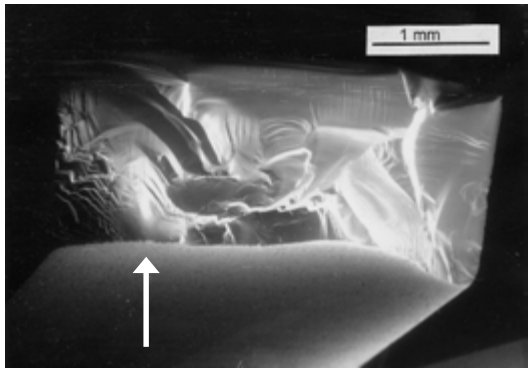

(b)

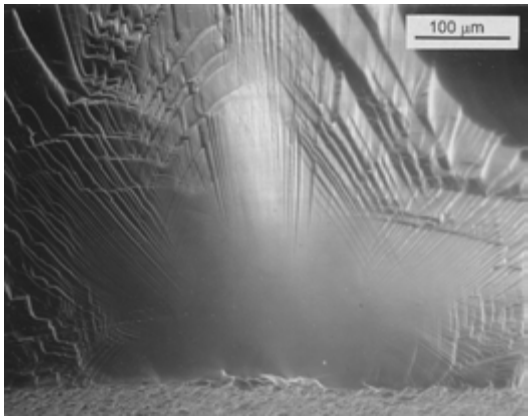

(c)

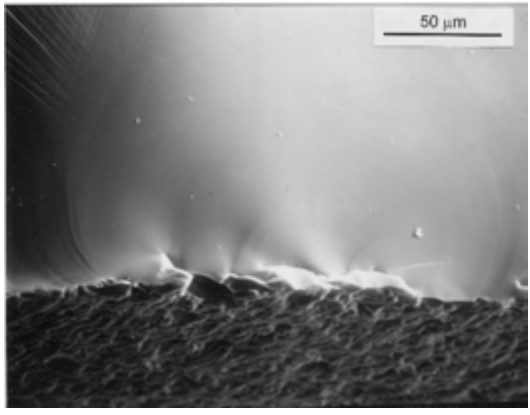

Figure 8.11 *A second example of a spinel bend bar with a {110} tensile surface and <110> tensile axis. (172 MPa) The fracture surface (a) is very rough as in the previous figure. The mirror (b) is somewhat more symmetric than in the previous figure. This mirror was shown in an earlier publication (Figure 29 of Ref. 13), but with a typographical mistake identifying it as {110}<100>. (Case F2, table 8.2). (Courtesy R. Rice)*

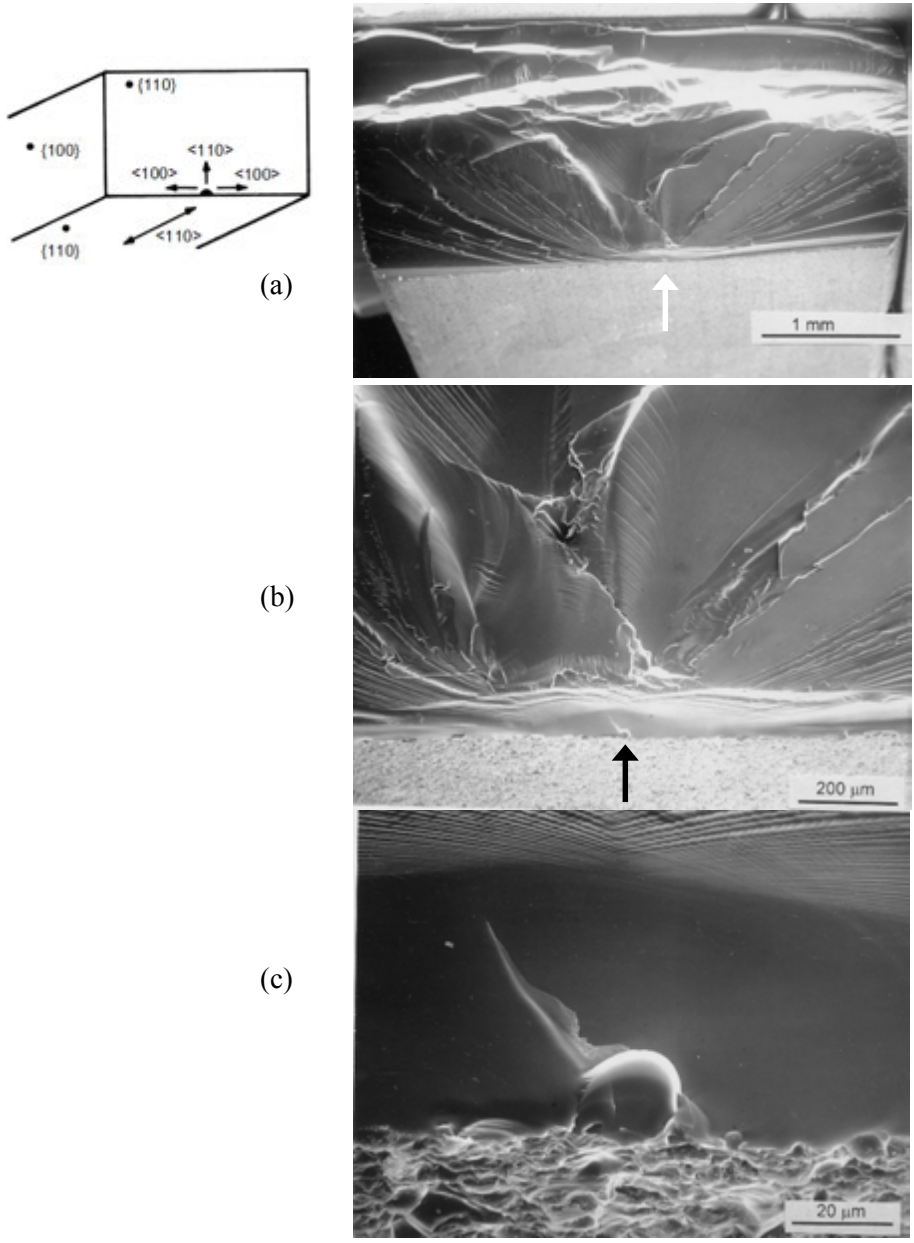

Figure 8.12 *Spinel bend bar with a {110} tensile surface and <110> tensile axis designed to cause fracture on a {110} plane. (361 MPa) (a) shows the whole fracture surface, (b) shows the "**gull wing mirror**," and (c) shows the grinding crack fracture origin. (Case C, table 8.2) (Courtesy R. Rice)*

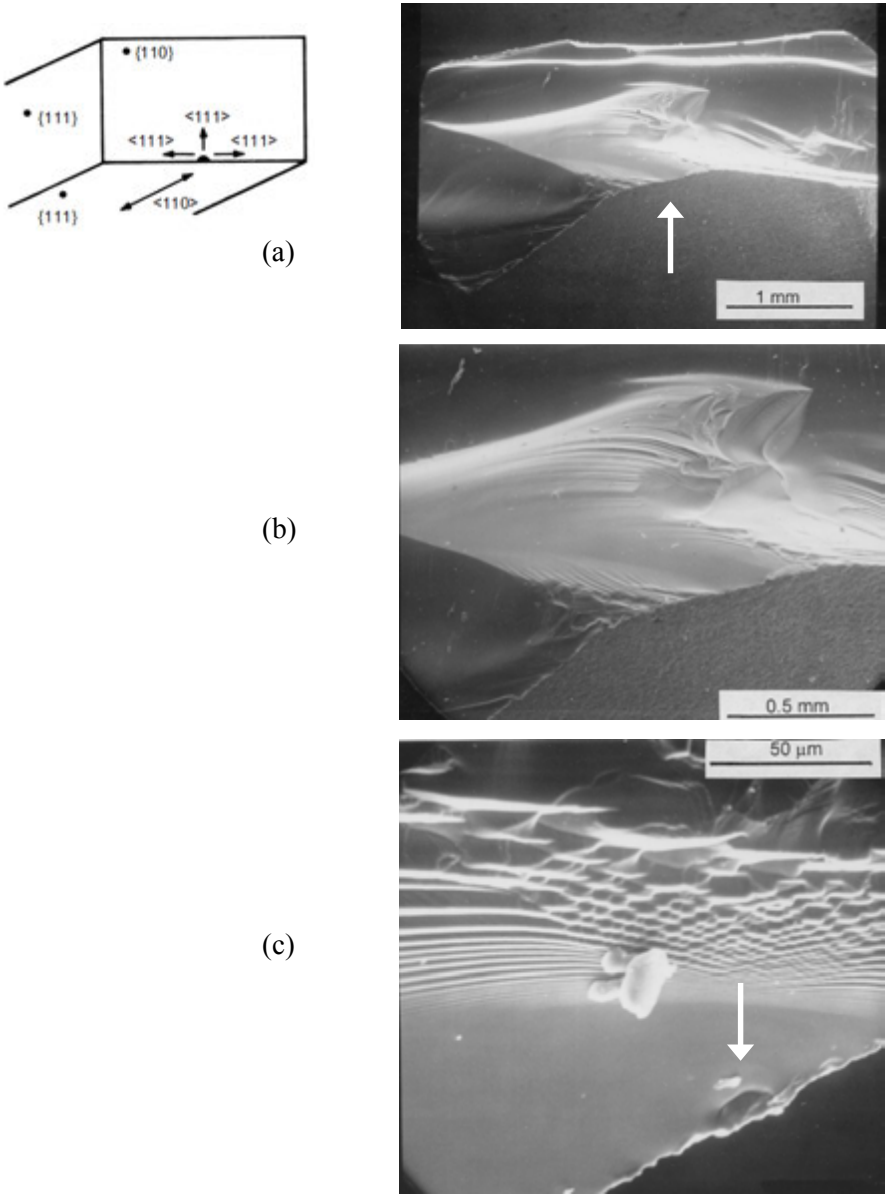

Figure 8.13 *Spinel bend bar with a {111} tensile surface and <110> tensile axis designed to cause fracture on a {110} plane. (unknown stress) (a) shows the whole fracture surface and the major crack redirection on the mirror sides. (b) shows the "**skewed cathedral mirror**," and (c) shows the grinding crack fracture origin from the matching fracture piece. (Case G1, table 8.2) (Courtesy R. Rice*)

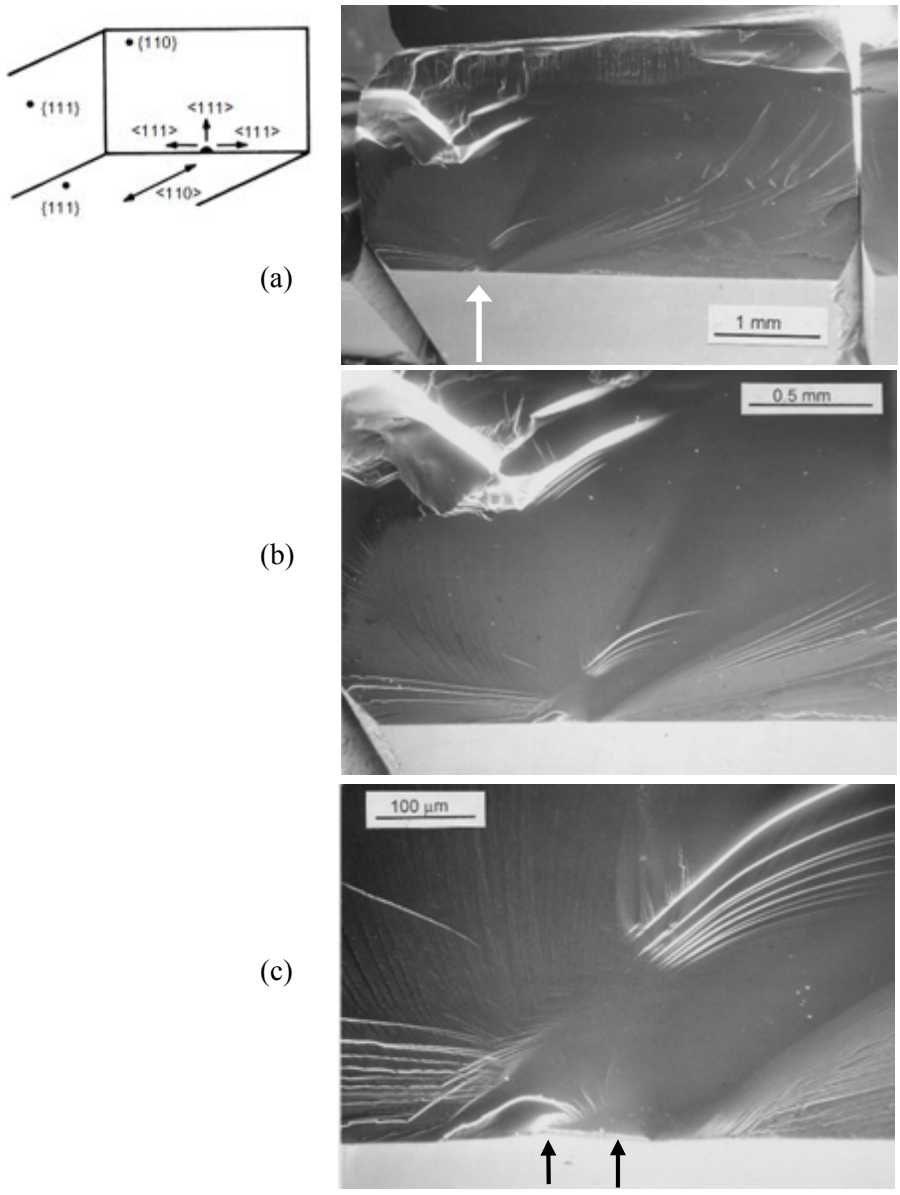

Figure 8.14 *Another example of a spinel bend bar with a {111} tensile surface and <110> tensile axis designed to cause fracture on a {110} plane. (261 MPa) (a) shows the whole fracture surface, (b) shows a "**skewed mirror**" with "**whisker lances**" and (c) shows the grinding crack fracture origin (black arrows) which is at a slight angle to the tensile stress axis and the fracture surface). (Case G2, table 8.2) (Courtesy R. Rice*)

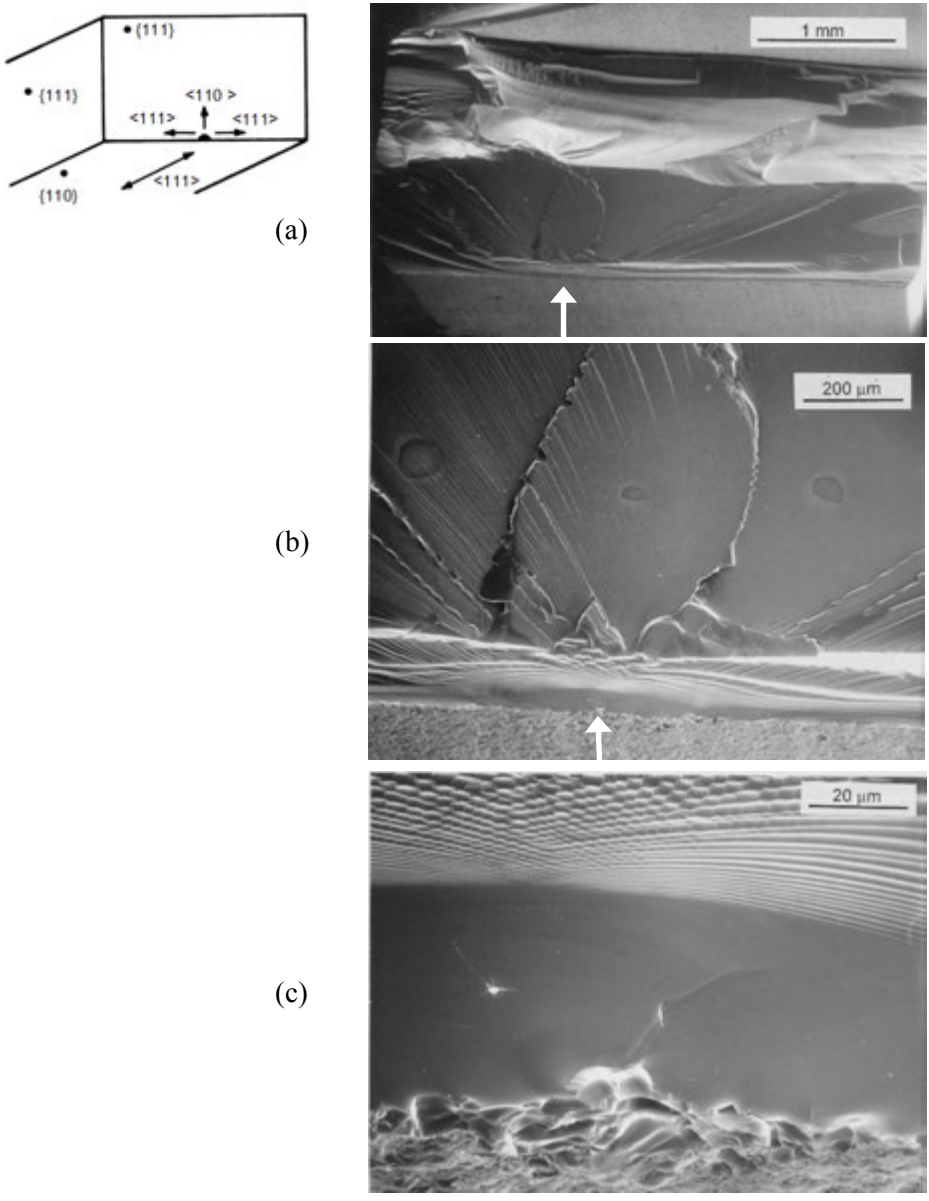

Figure 8.15 *Spinel bend bar with a {110} tensile surface and <111> tensile axis designed to cause fracture on a {111} plane. (325 MPa) (a) shows the whole fracture surface and the major crack redirection on the top half, (b) shows the "gull wing mirror," and (c) shows the grinding crack fracture origin. (Case E, table 8.2) (Courtesy R. Rice)*

Another distinctive shape seen in some crystals are long hackle lines that extend vertically from the sides of an origin suggesting a "***batman mirror***" shape as shown in Figure 8.16.

(a)

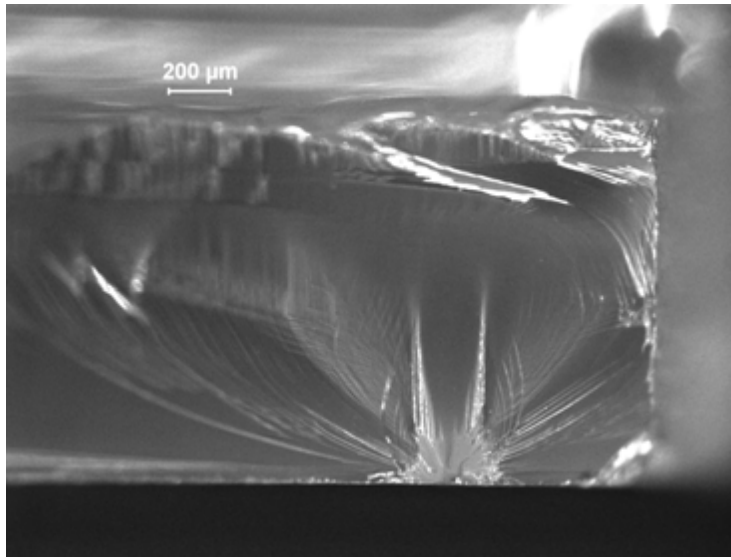

(b)

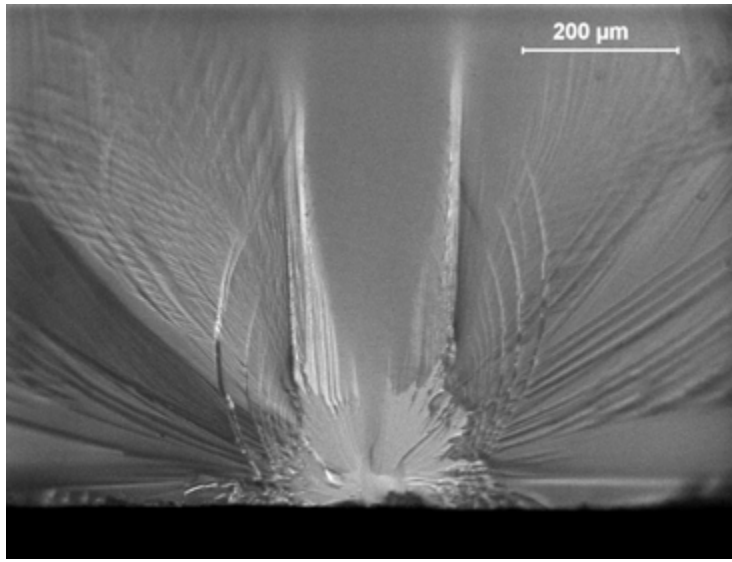

Figure 8.16 *"**Batman mirror**" in a sapphire bar. (a) shows matching halves of the bend bar with a tensile surface parallel to the a-plane and bend bar sides oriented so as to cause fracture on the r-plane. The tensile direction was the r axis. The origin was grinding damage. (Specimen courtesy R. Krause.)*

Mirror shapes seem to correlate with elastic moduli[15] or fracture surface energy[16] variations in different directions in a fracture plane. The very limited data on fracture mirror constants that have been published are listed in Appendix C. The asymmetry and diversity of fracture mirror shapes and difficulties in judging mirror sizes hamper any attempts to accurately correlate fracture stresses to mirror sizes by the methods described in chapters 7 and appendix D. Recent work by Gopalakrishnan and Mecholsky [17] provides a new explanation why mist does not appear around fracture mirrors in single crystals. The existence of any mode II loading on a crack tends to suppress mist in general and accentuates twist hackle lance lines at a mirror boundary. They argue that mixed mode I and II loading is naturally introduced in single crystals due to crystal anisotropy.

Scarps can occur in single crystals and are indicative of the presence of liquid during fracture. Figure 5.48b shows an example of scarps in sapphire.

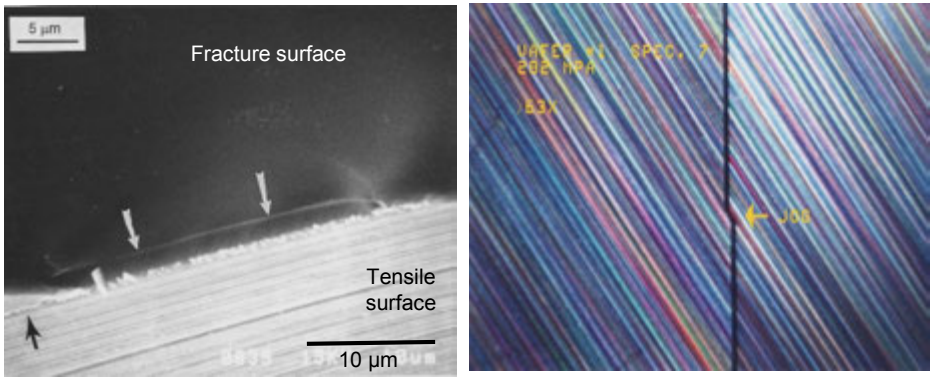

(a) (b)

Figure 8.17 *Fracture origin of the silicon wafer shown in Figure 8.4. (282 MPa) (a) shows the origin is a grinding crack that extends only 2 μm below the tensile surface and is associated with a grinding striation (groove) that seems to be deeper and has caused greater cracking than other nearby striations. The grinding direction is slightly different than the final plane of fracture, which caused the fracture surface to have a jog at the origin as shown in the optical view of the tensile surface (b). The fractographer should be alert to subtle features like the jog, since they are important clues.*

8.5 Origins

Single crystals are very sensitive to surface contact damage of any type. The low fracture toughness and high stiffness means that tiny strength-limiting cracks can easily pop into the crystal. There are no grain boundaries or other microstructural features to impede or redirect surface initiated cracks. Grinding or polishing flaws are common fracture origins. Flexure and tensile specimens are very sensitive to edge flaws and special care must be taken with the edge beveling or rounding procedures. Figure 8.17 shows the grinding crack origin of the silicon wafer shown earlier in Figure 8.4.

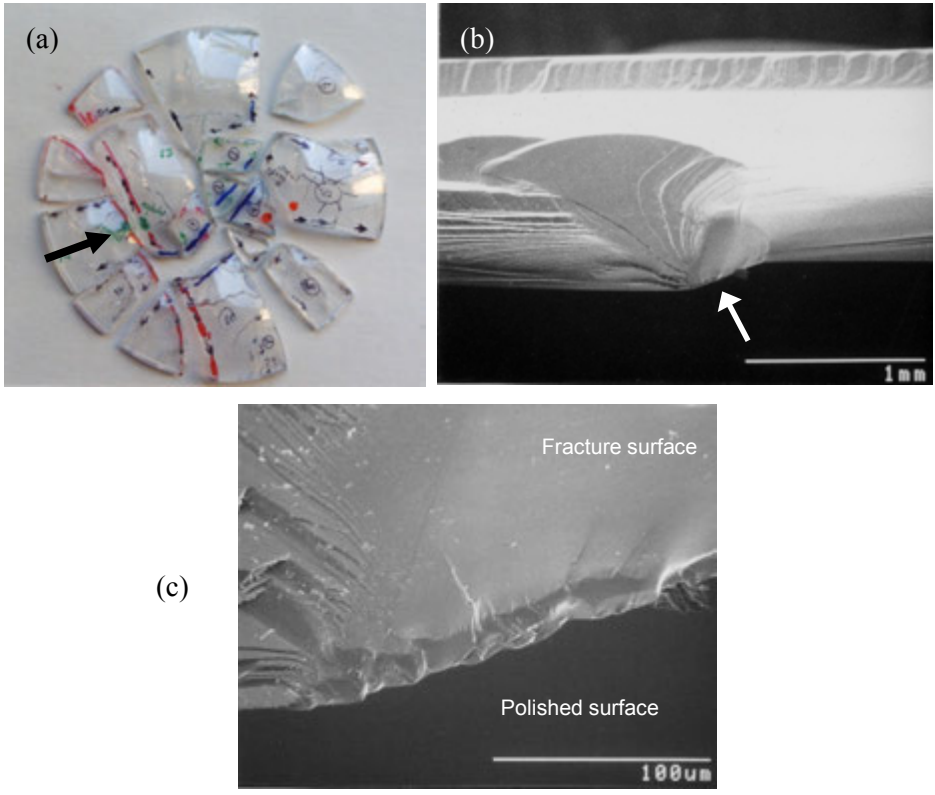

Figure 8.18 *Polishing or grinding crack origin in a sapphire dome. (a) shows the entire fractured structure. The origin is marked by the black arrow. (b) shows an SEM photo of the piece with the origin marked by the arrow. Fracture followed the axis of a polishing crack for a short distance, but then quickly shifted to a different plane. (c) is a SEM close-up of the origin. The piece has been tilted back to show both the fracture surface and the polished surface. There is no trace of damage on the polished surface.*

Single crystals are also very susceptible to polishing flaws. Subsequent polishing or finishing may eliminate any surface trace or scratch associated with the flaw, rendering optical post-finishing inspection ineffective. Figure 8.18 shows an example in a sapphire dome. Figure 8.5 is another example of a sapphire dome with subtle surface damage.

Surface impact or contact loading creates strength-limiting flaws. The contact can create cracks that may be extended by subsequent loading. Alternately, there may be stresses already present in the part that can propagate the crack. Figure 8.19 shows an example where a small high velocity particle "dinged' the surface of a sapphire dome.

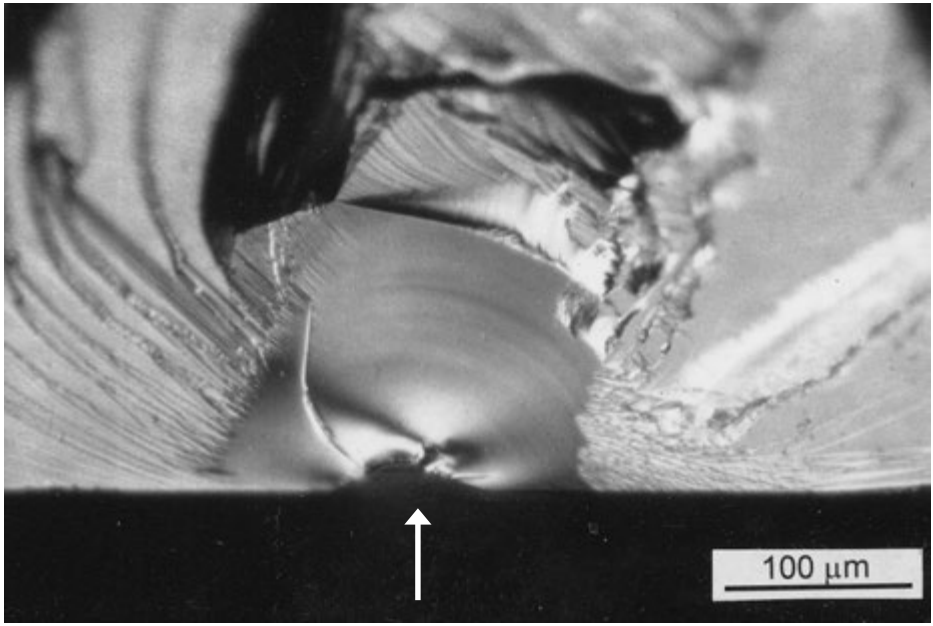

Figure 8.19 *Impact crack fracture origin in a hemispherical sapphire dome that was impacted by a small particle while the dome was under thermal stress. The impact site on the surface is missing a small divot (arrow) and the approximately 150 μm deep crack shows concentric semicircular tertiary Wallner lines that are telltale signs of impact. See Figure 4-15 on page 4-25 for views of the entire dome.*

Other surface flaws may originate as a result of processing conditions. Figures 8.20 and 8.21 show fractures in microelectromechanical (MEMS) sized single crystal silicon theta specimens.[18,19] Deep reactive ion etching (DRIE), a lithographic process used to prepare integrated circuits and small structures, was used to fabricate the specimens from a standard {100} type silicon wafer. The DRIE process created the surface damage that was strength limiting in this case. Figure 6.69 on page 6-76 shows other theta specimen origins.

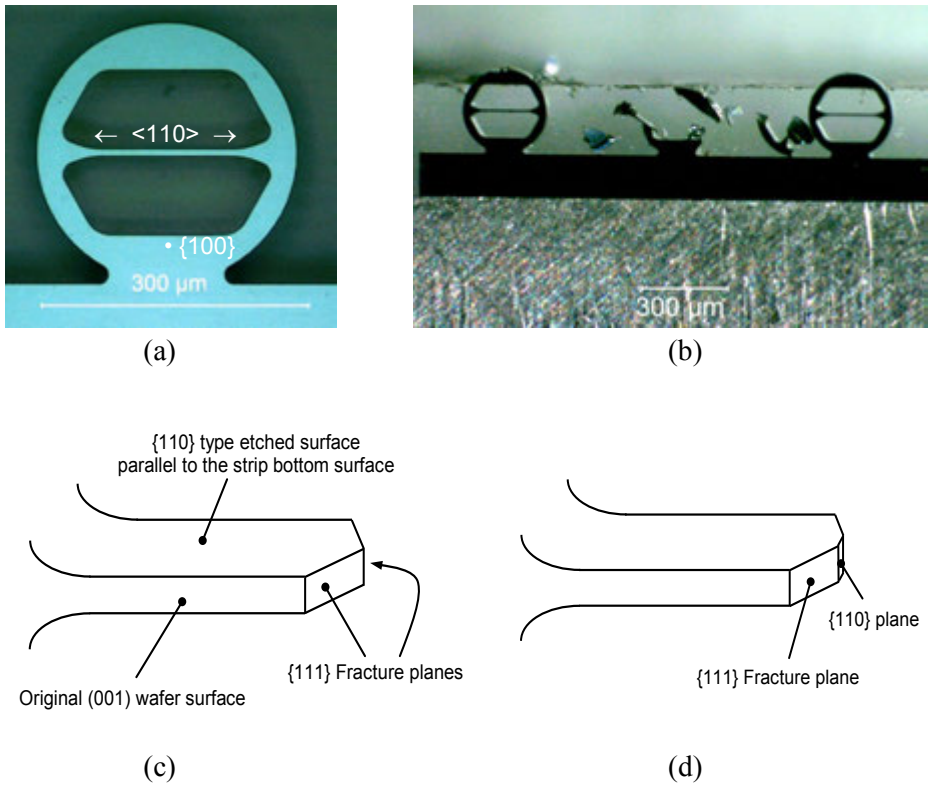

Figure 8.20 *Tiny silicon theta test specimens. The ring shown in (a) is compressed on its rim on the top and bottom in a nanoindenter causing the 7.5 µm tall by 100 µm thick web section in the middle to stretch in uniaxial tension. (b) shows a fractured specimen on a strip. (c) shows that the web fractures usually occurred on {111} planes which are the cleavage planes. A few initiated on {110} planes but then changed to {111} planes. Origin flaws are shown in the next figure.*

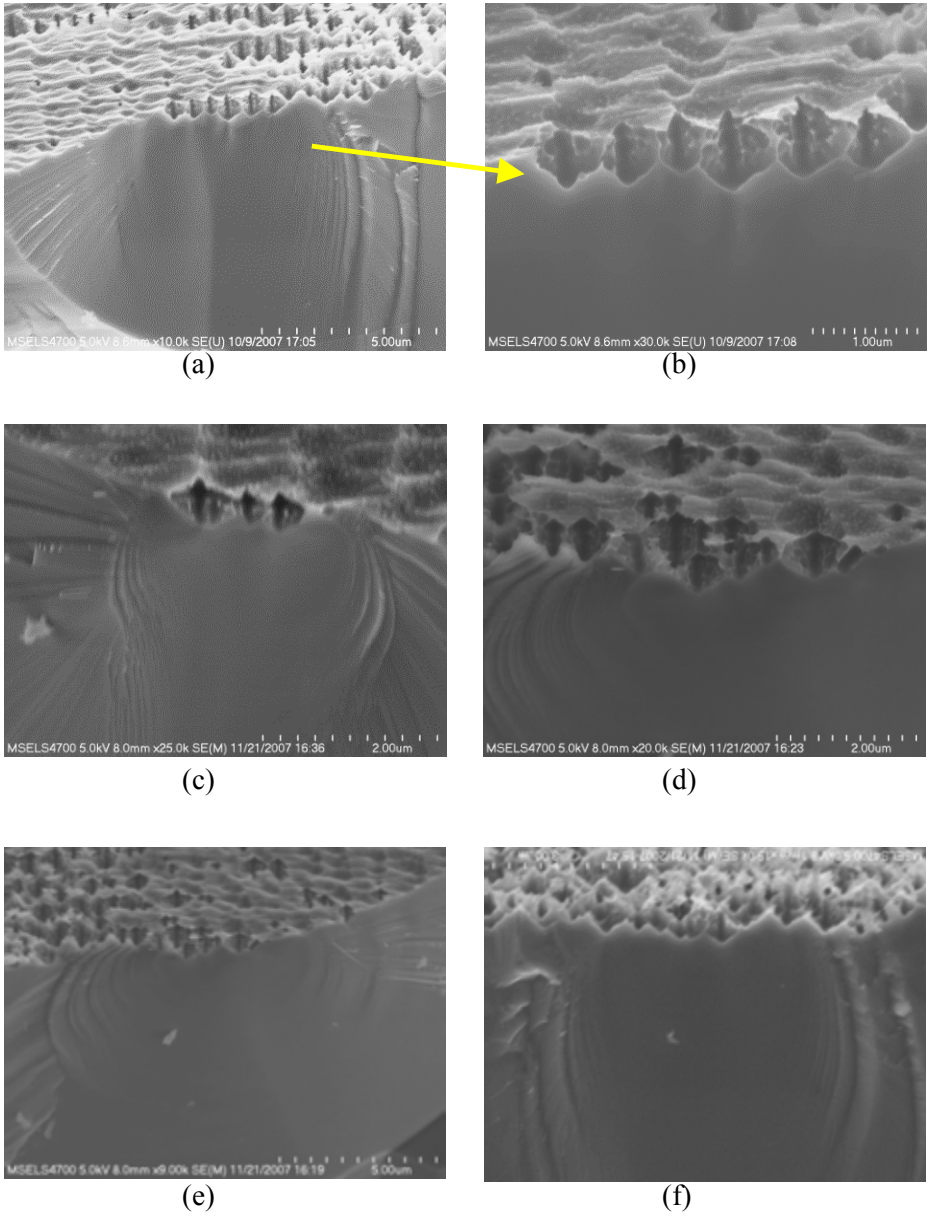

Figure 8.21 *Fracture origins in single crystal silicon theta specimens. (b) is a close-up of (a). The "cathedral mirrors" are very clear. The origins are etch pits from the DRIE processing. The cusps between them are very sharp and probably initiated cracks. Figure 6.69 shows other sharp cusp origins.*

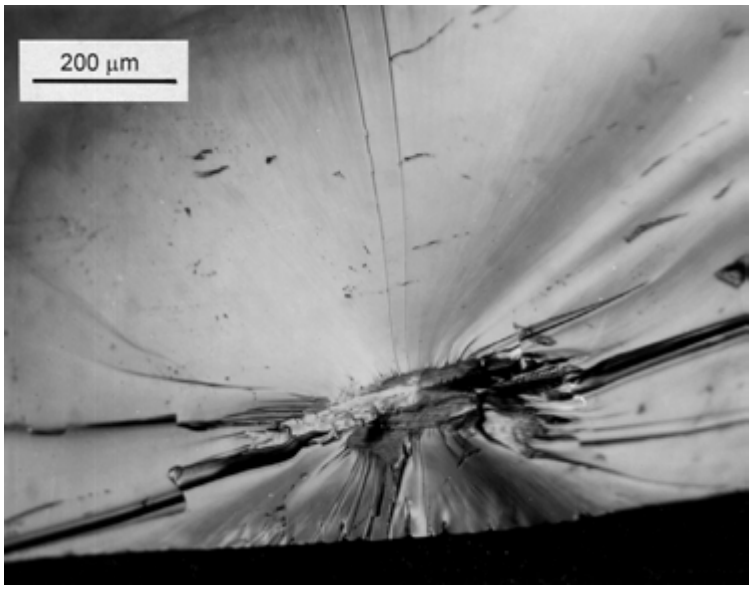

Figure 8.22 *Internal origin in a flame-polished non-stoichiometric (alumina rich) spinel single crystal. The bend bar strength was 238 MPa. (courtesy R. Rice)*

Volume-distributed flaws such as pores, inclusions or compositional inhomogeneities can also cause fracture. They usually will stand out quite clearly on the fracture surface. Newcomb and Tressler [20] and Rice[21] showed pore examples in sapphire fibers. An example of an internal origin in a nonstoichiometric spinel is shown in Figure 8.22.

Twinning can initiate fractures, especially if twins from different planes intersect and nucleate cracks. Figure 8.23 shows twins that controlled the strength in a sapphire bend bar tested at high temperature. This failure mechanism is especially a problem in sapphire since twins are easily nucleated by even small compression stresses at fairly low temperatures (300 ^{o}C to 500 ^{o}C). They cause drastic reductions of compression and flexure strengths in some orientations.[22,23] They sometimes form with an audible pop.[24] It has even been reported that twins can form in sapphire from sudden temperature changes and hydrostatic compression.[25]

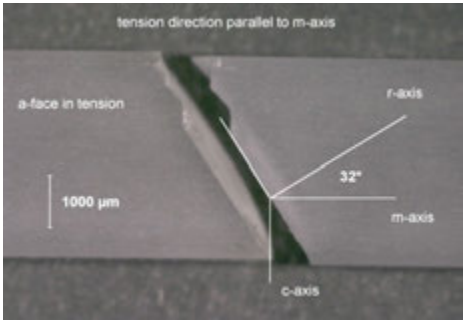

(a)

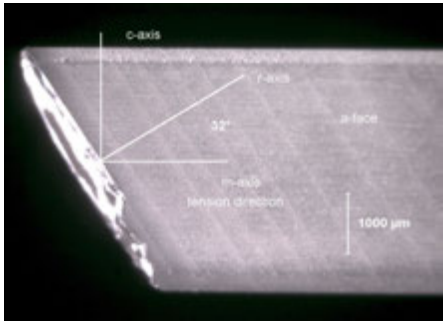

(b)

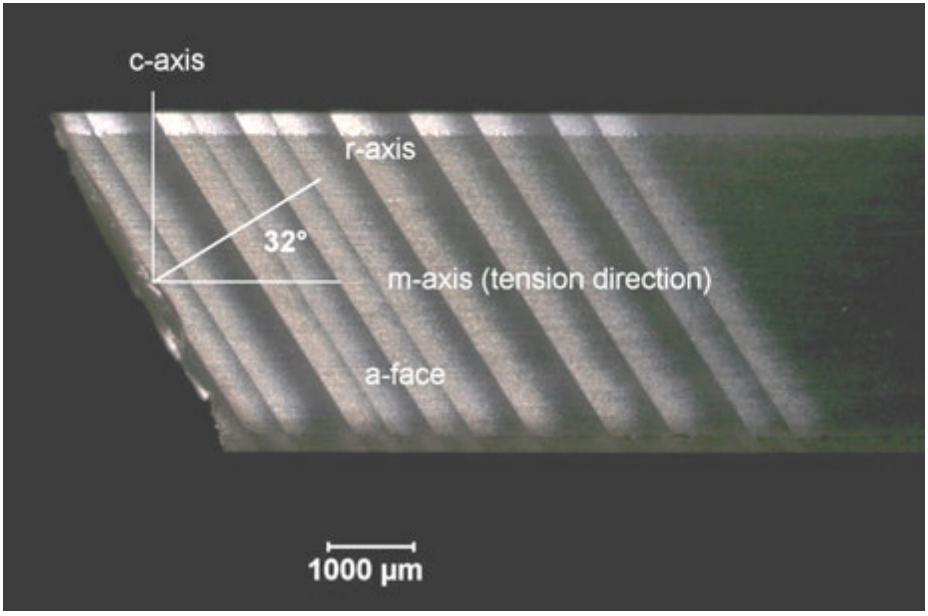

(c)

Figure 8.23 *Twinning in sapphire bend bars in an elevated temperature bend bar specimen. The bar was cut with an a-plane tensile surface and an intended m-plane fracture surface. The specimen instead broke on the r-plane from cracks initiated by twins probably from the compression side of the specimen. (a) shows the tensile face under ordinary lighting. (b) shows the same specimen, but with common reflected lighting adjusted to reflect off the twins. (c) shows the bar between crossed polarizers that make the twins much easier to detect. (courtesy R. Krause)*

Figures 8.24 and 8.25 show two fractured c-axis sapphire tubes with intersecting twins that created fracture origin cracks. The tubes were 38 mm in diameter and 400 mm long and fractured during two runs of a prototype plasma asher. This is a device used to dry-remove photoresist from large 300 mm diameter silicon wafers during manufacture of integrated circuits. The tubes contained oxygen and nitrogen gasses which were energized into a plasma state by a 2.5 kW microwave chamber which was cycled on and off in 60 s intervals. The sapphire tubes reached temperatures of 600 ºC to 700 ºC. One tube broke during a gas purge step three seconds after the shutdown of the microwave energy. The second tube broke two minutes after a shutdown. The tubes should have had lifetimes in excess of 400,000 cycles The breakage during cool down suggested thermal stresses had caused fracture. The cracks curved and wiggled at the tube ends, indicating the cracks slowed down and arrested. Some of the cracks crossed over each other, indicating that primary cracks did not run all the way through the wall thickness. During optical microscopic examination of one of the fracture surfaces, using common reflected light, a *chance reflection off one surface* revealed thin parallel reflective lines that ran counter to the fracture surface faceting as shown in Figure 8.24b. This was a sign of twinning and the next step was to view the tubes between crossed polarizers (as discussed in sections 3.8 and 3.25) with the results shown in Figure 8.25. Multiple twins in the hot region triggered crack formation at twin intersections. The twins were oriented at 32º to the sapphire tube axis corresponding to classic r-plane twinning in sapphire, which can be caused by rather low compression stresses at temperatures as low as 300 º to 500 ºC.[22]

Fracture of these tubes occurred in two stages. First, axial constraint from a new type of seal at the tube ends prevented the free expansion of the tubes during the heating portion of the operating cycle. The earlier model tubes that did not have breakages used a different seal design that allowed expansion. The constraint in the new design created compression stresses. These created the intersecting twins that generated cracks. The cracks grew in stages and propagated by cool down thermal stresses until the tube ruptured. Although initially there was some concern that the sapphire tubes were faulty, they were fine. The problem was solved when the seal design was changed to allow for expansion of the sapphire tubes.

(a)

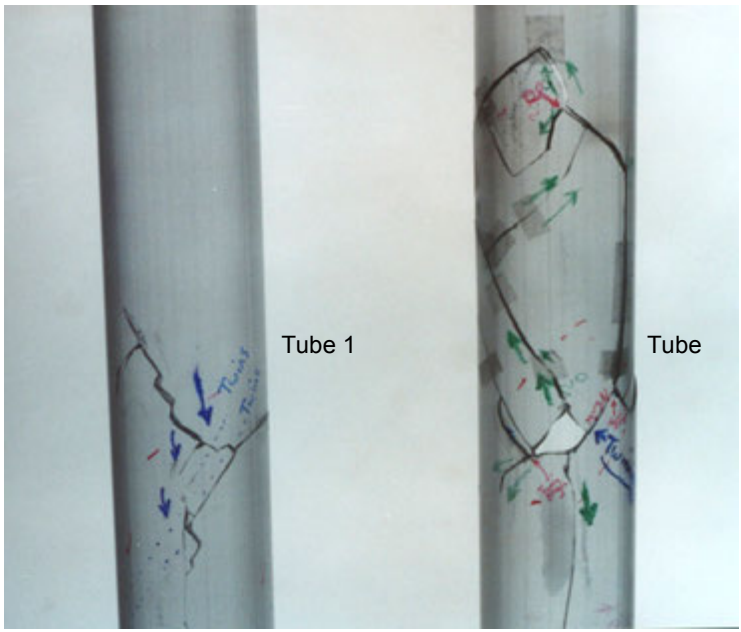

(b)

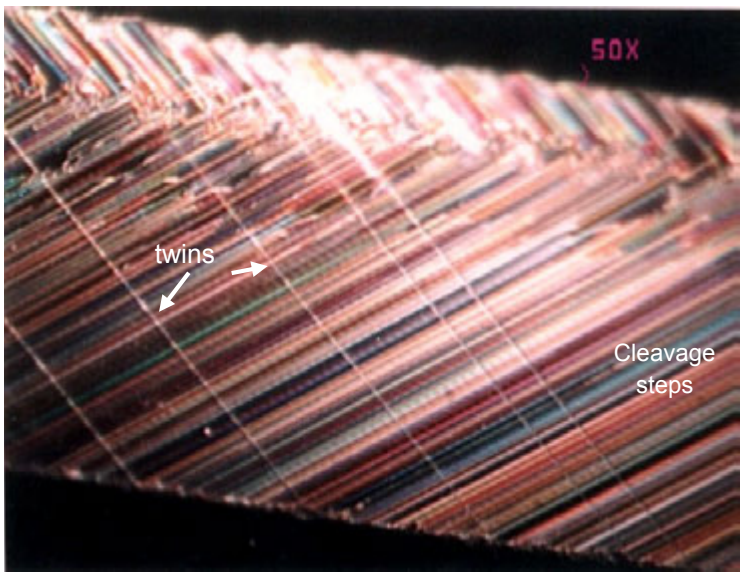

Figure 8.24 *Two broken 38 mm diameter sapphire tubes from an integrated circuit plasma asher are shown. (a) shows both tubes. Although the locations of twins are marked with a felt tip pen, the twins are not visible in this lighting. (b) shows a stereoptical microscope photo close-up of the fracture surface of a fragment from the middle of one tube in normal white light illumination at just the right angle. Five thin twin bands are visible against the very facetted fracture surface.*

(a)

(b)

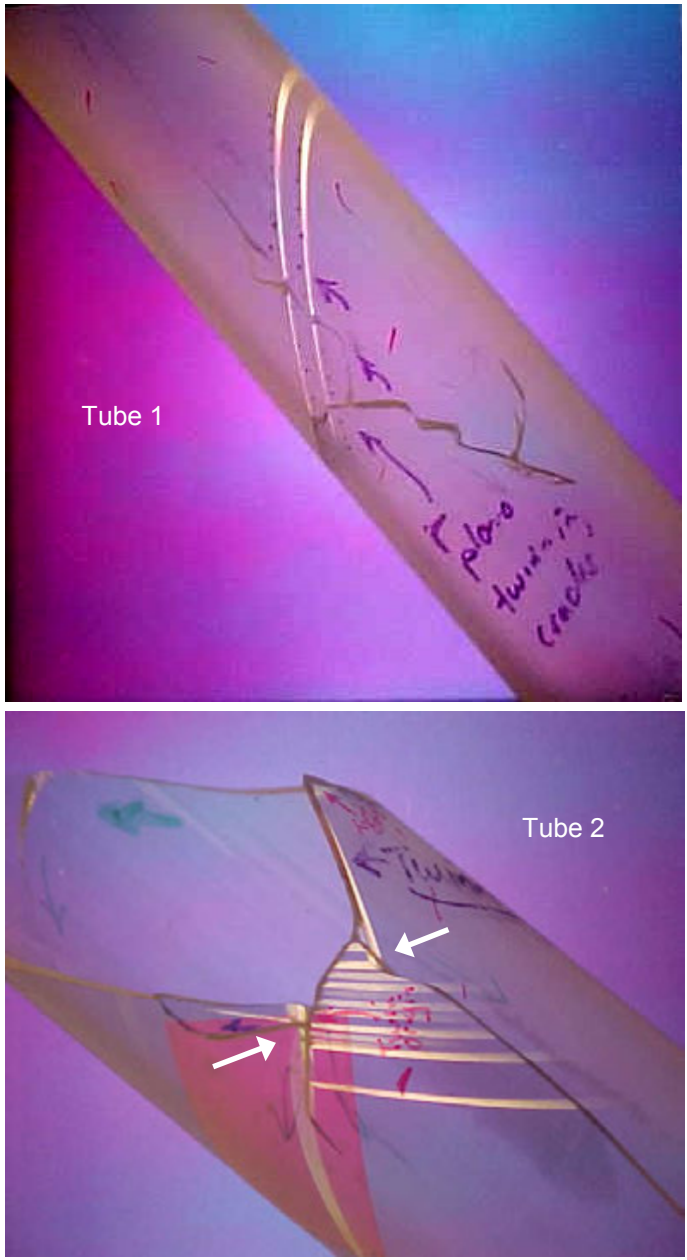

Figure 8.25 *Twin bands became very apparent when the sapphire tubes were illuminated by light from crossed polarizers. Cracks initiated at twin band intersections (white arrows) and then were propagated by cool down thermal stresses. (Photos courtesy R. Pingree)*

Case study 13 in Chapter 10 is a complex sapphire solar refractor part. It also shows twins, but they were incidental and not the cause of fracture. Very tiny "micro twins" were also detected in that part. These presumably were the nuclei of twin bands that would have grown much larger with time. The fractographer should be on the lookout for twins in materials such as sapphire, and they may be present, but not necessarily the cause of fracture.

Earlier in this chapter, it was shown in the spinel examples Figs. 8.8 and 8.9 that, if a preferred cleavage pane is perpendicular to the maximum principal tensile stress, the fracture surface will be flat and smooth and at right angles to the tensile stress. If the preferred cleavage plane is not perpendicular to the maximum principal tensile stress, then the fracture plane may be at an *inclined angle to the tensile stress*, such as in Figure 8.23 for sapphire, and the zig-zag planes of Fig. 8.10, 8.11 and 8.13 for spinel. These illustrate exceptions to the law of normal crack propagation discussed in section 4.3

In some extreme cases, the loading geometries and stresses may be such that fracture is forced to occur on an unfavorable plane, such as the basal plane in a sapphire tube shown in Figure 8.26. The fracture surface is extremely jagged with many zig-zags. Other examples of basal plane fracture in sapphire are shown in references 8, 20, and 26.

Good estimates of the fracture toughness K_{Ic} may be obtained from fracture mechanics analyses of flaws. For example, the long uniform 2 μm deep surface crack in the silicon wafer shown in Figure 8.17a combined with a breaking stress of 282 MPa and a shape factor Y = 1.99 produced an estimate of K_{Ic} = 1.99 (282) $\sqrt{2} \times 10^{-6}$ = 0.79 MPa$\sqrt{m}$ in good agreement with values in table 8.1. Rice showed several good examples[13,21] and Newcomb and Tressler[20] were able to measure fracture toughness on the basal plane of sapphire by this approach, when other methods usually fail due to the difficulty of controlling fracture on this plane. Many groups have effectively used Knoop indentation surface crack in flexure tests to study fracture behavior and measure fracture toughness of single crystals since the small semi-elliptical flaws mimic the behavior of other flaws.

(a)

(b)

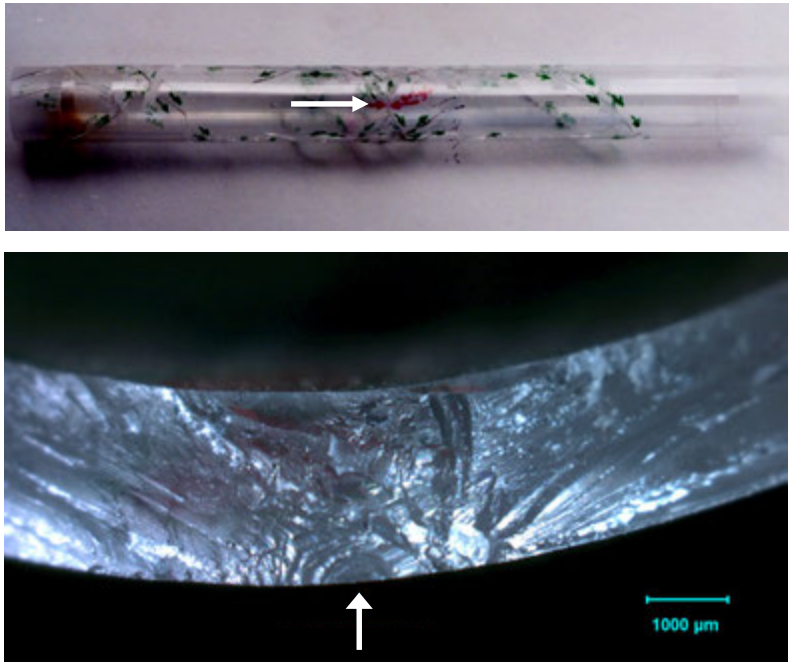

(c)

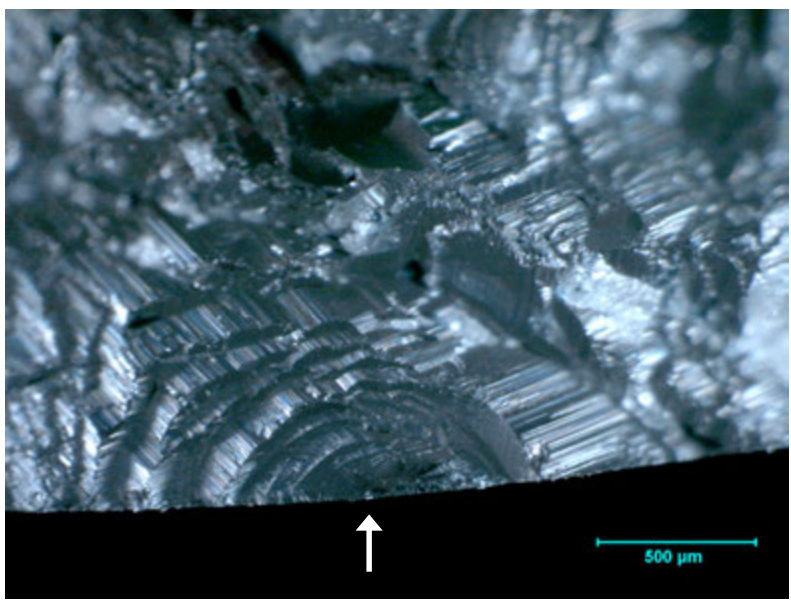

Figure 8.26 *Example of basal plane fracture in a c-axis sapphire tube that fractured from severe thermal shock (a). The origin is at the tube mid length (large arrow) and is perpendicular to the tube axis. The thermal stresses acted in the axial direction. (b) and (c) show the mirror and origin on the outer tube surface.*

8.6 Other Sources

Rice has written several outstanding, richly illustrated papers on single crystal fracture and fractography. Reference 13 is a book length article with over thirty figures showing single crystal fracture surfaces in MgO, $MgAl_2O_4$, Si, SiC, Al_2O_3, ZrO_2, CaF_2, and W. Reference 14 has six pages of illustrations and a discussion of fracture markings in various single crystal ceramics.

Chapter 8 References

1. R. A. Schultz, M. C. Jensen, and R. C. Bradt, "Single Crystal Cleavage of Brittle Materials," *Int. J. Fract.,* **65** (1994) 291- 312.
2. R. C. Bradt, "Cleavage of Ceramic and Mineral Single Crystals," pp. 355 – 365 in *Cleavage Fracture*, Proceedings of a Symposium at the 1997 TMS Fall meeting, Indianapolis, IN, Sept. 15- 17, 1997, ed. K. S. Chan, The Minerals, Metals, and Materials Society, Warrendale, PA, 1997.
3. C. C. M. Wu, K. R. McKinney, and R. W. Rice, "Zig-zag Crack Propagation in $MgAl_2O_4$ Crystals," *J. Mat. Sci. Lttrs.,* **14** (1995) 474 – 477.
4. C. P. Chen and M. H. Leipold**,** "Fracture Toughness of Silicon," *Bull. Am. Cer. Soc.*, **59** [4] (1980) 469-472.
5. Y-B. Xin, K. J. Hsia, and D. A. Lange, "Quantitative Characterization of the Fracture Surfaces of Silicon Single Crystals by Confocal Microscopy," *J. Am. Cer. Soc.,* **78** [12] (1995) 3210 – 3208.
6. R. L. Stewart, M. Iwasa, and R. C. Bradt, "Room Temperature K_{Ic} Values for Single-Crystal and Polycrystalline $MgAl_2O_4$," *Comm. Am. Cer. Soc.,* Feb. 1981, C22-23.
7. R. L. Stewart and R. C. Bradt, "Fracture of Single Crystal $MgAl_2O_4$," *J. Mat. Sci.,* **15** (1980) 67-72.
8. M. Iwasa and R. C. Bradt, "Fracture Toughness of Single-Crystal Alumina," pp. 767 – 779 in *Advances in Ceramics,* Vol. 10, ed. W. Kingery, American Ceramic Society, Westerville, OH, 1984.
9. Y. Akimune and R. C. Bradt, "Knoop Microhardness Anisotropy of Single-Crystal Stoichiometric $MgAl_2O_4$ Spinel," *J. Amer. Cer. Soc*., **70** [4] (1987) C84 – C86.
10. D. Black and G. D. Quinn, "X-ray Topography for Fractography of Single-Crystal Components," *J. Fail. Anal. Prev.*, **6** [3] (2006) 79 - 86.
11. ASTM C 1322-96, "Standard Practice for Fractography and Characterization of Fracture Origins in Advanced Ceramics," *Annual Brook of Standards*, Vol. 15.01, ASTM int., West Conshohocken, PA (1996).
12. R. W. Rice, "Fractographic Determination of K_{Ic} and Effects of Microstructural Stresses in Ceramics," pp. 509 – 545 in *Fractography of Glasses and Ceramics II,* eds. V. Fréchette and J. Varner, 1991.
13. R. W. Rice, "Ceramic Fracture Features, Observations, Mechanisms and Uses," pp. 5 –102 in *Fractography of Ceramic and Metal Failures,* ASTM STP 827, eds. J. Mecholsky and Powell, 1984, American Society for Testing and Materials, West Conshohocken, PA, 1984.

14. R. W. Rice, "Perspectives in Fractography," pp. 3-56 in *Fractography of Glasses and Ceramics,* Advances in Ceramics, Vol. 22, eds. J. Varner and V. Fréchette, American Ceramic Society, Westerville, OH, (1988).
15. S. W. Freiman, J. J. Mecholsky, and P. Becher, "Fractography: A Quantitative Measure of the Fracture Process," pp. 55 - 78 in *Fractography of Glasses and Ceramics, II* , eds. V. Fréchette and J. Varner, American Ceramic Society, Westerville, OH, 1991.
16. Y. L. Tsai and J. J. Mecholsky, Jr., "Fracture Mechanics Description of Fracture Mirror Formation in Single Crystals," *Int. J. Fract*., **57** (1992) 167-182.
17. K. Gopalakrishnan and J. J. Mecholsky, Jr., "Quantitative Fractography of Mixed-Mode Fracture in Soda Lime Silica Glass," *J. Am. Cer. Soc*., **95** [11] (2012) 3622-3627.
18. G. D. Quinn, E. Fuller, D. Xiang, A. Jillavenkatessa, L. Ma, D. Smith, and J. Beall, "A Novel Test Method for Measuring Mechanical Properties at the Small -Scale: The Theta Specimen," *Cer. Eng. Sci. Proc*., **26** [2] (2005) 117 – 126.
19. G. D. Quinn, "Fractographic Analysis of Miniature Theta Specimens," *Cer. Eng. Sci. Proc.,* **29** [3] (2008) 189 – 199.
20. S. A. Newcomb and R. E. Tressler, "High-Temperature Fracture Toughness of Sapphire," *J. Am. Cer. Soc*., **77** [11] (1994) 3030 – 3032.
21. R. W. Rice, "Corroboration and Extension of Analysis of c-Axis Sapphire Filament Fractures from Pores," *J. Mat. Sci. Lttrs*., **16** (1997) 202 – 205.
22. F. Schmid and D. C. Harris, "Effects of Crystal Orientation and Temperature on the Strength of Sapphire," *J. Am. Cer. Soc.,* **81** [4] (1998) 885 – 93.
23. P. F. Becher, "Fracture Strength Anisotropy of Sapphire," *J. Am. Cer. Soc.*, **59** [1-2] (1976) 59 –61.
24. J. A. Salem, "Slow Crack Growth and Fracture Toughness of Sapphire for the International Space Station Fluids and Combustion Facility," NASA TM 214023, NASA Glenn Center, Cleveland, OH, 2006.
25. L. M. Belyaev, *Ruby and Sapphire*, Translated from Russian, Amerind Publ. Co., New Delhi, 1980, pp. 286.
26. R. W. Rice and P. F. Becher, "Comment on Creep Deformation of 0^{o} Sapphire," *J. Am. Cer. Soc.,* **60** [3-4] (1977) 186 – 188.

9 Ceramic and Glass Composites

9.1 Particulate, Whisker, or Self-Reinforced Ceramic Composites

Ceramics or glasses that are reinforced by second phases, whiskers, or particulates may be examined using the same equipment and techniques as used for monolithic materials. The reinforcing agents act to deflect or bridge cracks and create very rough fractures surfaces that may mask classical fracture surface features such as Wallner or hackle lines.

The composite ideally should have a controlled microstructure such that the reinforcing phase is uniformly distributed. This is routinely achieved with glass ceramics, but is more problematic with fiber or particulate-reinforced ceramics. Sometimes the reinforcing agent forms clumps or aggregates that can act as strength-limiting flaws as shown in Figure 9.1. Flaws of this type may be broadly described as compositional inhomogeneities using the logic in chapter 6, but more specific descriptors are probably better (fiber clump, fiber tangle, platelet cluster, etc.).

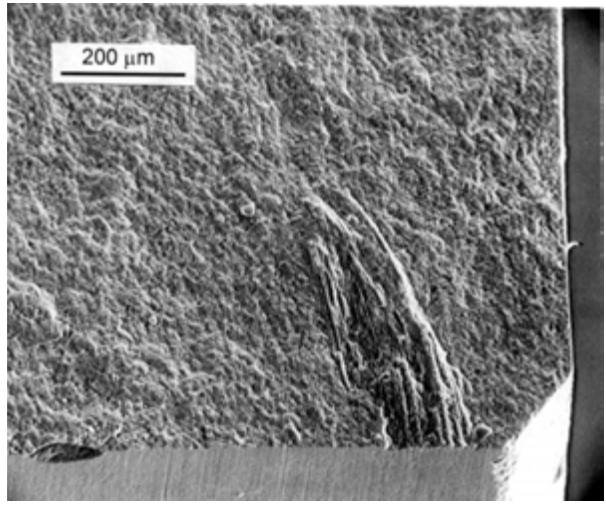

Figure 9.1 *Nonuniform dispersal of toughening agents often causes strength-limiting flaws in ceramic composites. This figure shows a whisker clump that was the strength-limiting flaw in a siliconized SiC bend bar. The material was made by mixing chopped carbon fibers with SiC starting powders and then infiltrating with silicon. The carbon fibers were intended to react with the silicon to form dispersed silicon carbide fibers that would toughen the matrix.*

Second phase aggregates can also inhibit local sintering causing pockets of porosity that also act as strength limiting flaws. Self-reinforced materials that rely on interconnected elongated-grain microstructures may develop excessively large grains that control strength as shown in Figures 6.22c and d. Very often reinforcing agents such as SiC whiskers can create local chemistry imbalances in the matrix leading to exaggerated grain growth. SiC whisker-reinforced alumina for cutting tools is an example. These large grains then can act as flaws. Although few would argue against reinforcing ceramics to enhance fracture toughness, this approach sometimes comes with a price. The very agents used to reinforce the material can create flaws that limit the material's strength.

9.2 Fiber-Reinforced Composites

Fiber-reinforced ceramics and glasses may have much greater resistance to fracture if stressed in the same direction as the fiber reinforcements. Usually the fibers have greater strength and elastic modulus than the matrix. Optimum bonding does not necessarily mean perfect bonding, however, since the latter would lead to cleavage through the reinforcing fibers. Optimum bonding is such that the fiber-matrix interface is able to transmit some load, but then fractures or debonds along the interface. The fibers pull out of the matrix with additional loading. While pulling out they exert frictional or mechanical interlocking resistance so that more energy is consumed. The microstructure is designed to shed load from the matrix to the strong fibers and to divert cracks in the matrix to run along the matrix fiber interface. The processing must be done carefully so that the interface strength is controlled and that the fiber does not deteriorate too much from microstructural changes, surface pitting, or interactions with the matrix.

Fractography of fiber-reinforced ceramics and glasses is different than that for monolithic materials. Fracture surfaces are often very rough and there often is no point looking for a specific fracture origin. There are exceptions. Figures 9.2 and 9.3 shows a silicon carbide filament-reinforced silicon nitride that did have discrete fracture origins.

Fracture typically entails damage accumulation and coalescence leading to rupture. Often the objective is to observe the general fracture mode and to ascertain whether it was due to tensile fiber pull out and fiber rupture, shear delamination in the matrix parallel to the fibers, compression buckling of fibers, or buckling of a protective coating in compression. The failure mode depends upon whether the structure is one-, two, - or three-dimensionally

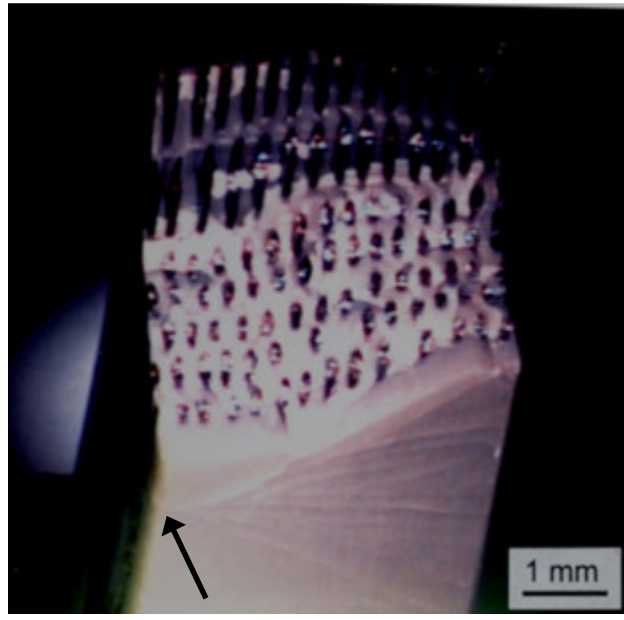

Figure 9.2 *A CVD SiC (SCS-6) filament-reinforced Si_3N_4 bend bar tilted back at an angle so as to view the fracture and tensile surfaces. A series of branching cracks radiate outwards from one origin site (arrow).*

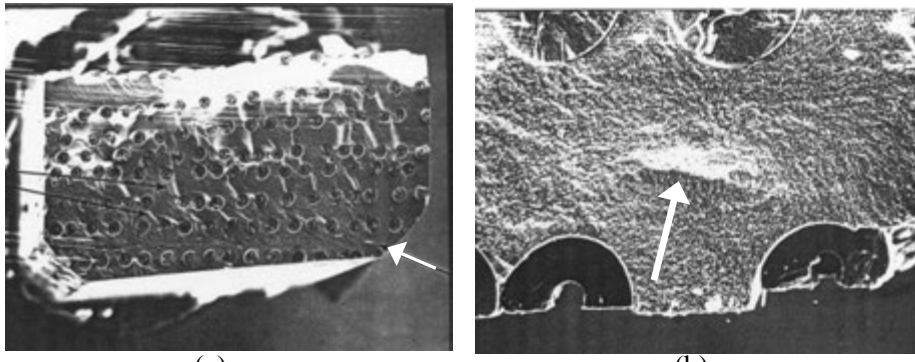

(a) (b)

Figure 9.3 *Fracture surface of CVD SiC filament reinforced Si_3N_4 bend bar. (Ref. 1) (a) shows that there was not very much fiber pullout in this case. Wake hackle in the matrix behind the filaments are telltale indicators of the local direction of crack propagation through the matrix and lead back to the origin, which is a porous seam in the matrix shown by the white arrows in (a) and (b).*

reinforced and the size and shape of the component and the loading conditions. Although bend testing is reliable for creating tensile fractures in monolithic ceramics and glasses, composites are more susceptible to alternative failure modes when loaded in bending. Figures 9.4 and 9.5 shows tensile stress fractures with good pull-out in a fiber-reinforced epoxy and a ceramic, respectively.

(a)

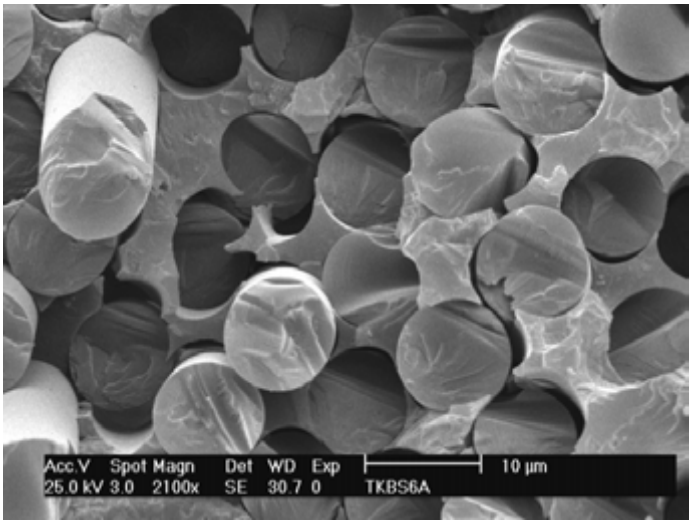

(b)

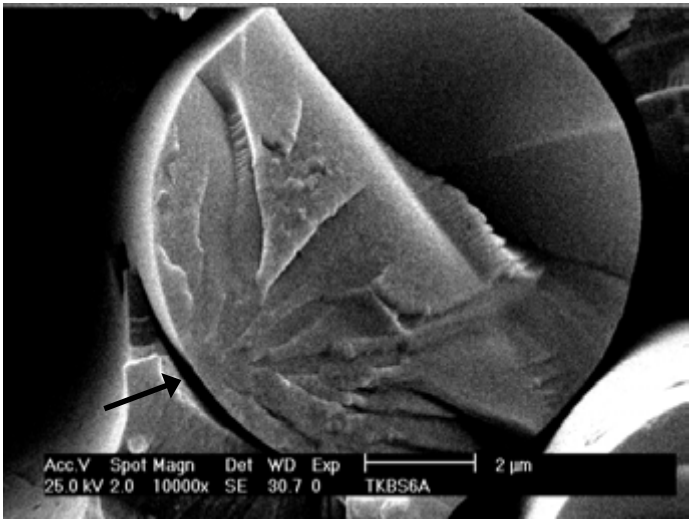

Figure 9.4 *Fracture surface of an E-glass fiber reinforced epoxy matrix one-dimensional composite. The arrow marks the origin in (b). (courtesy of S. Scherrer)*

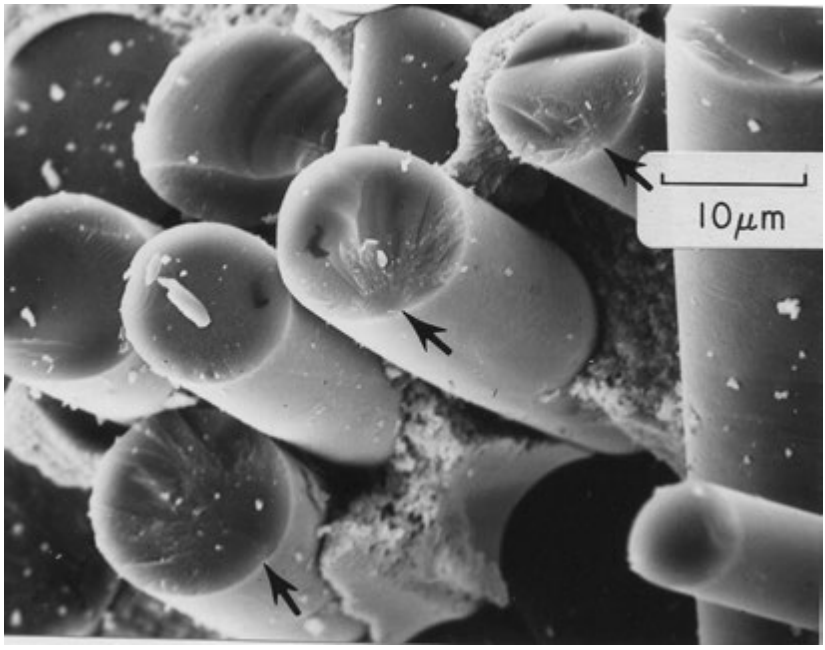

Figure 9.5 *SEM image of the fracture surface of a SiC (Nicalon) ceramic fiber – zirconia matrix composite. The arrows mark fracture origins and mirrors in several fibers. (Ref. 2, courtesy of R. Rice)*

Images such as these can be used to qualitatively assess the fiber-matrix interface bonding and also if any damage has been done to the fibers during processing. Very often the fibers have fracture mirrors and it is instructive to ascertain whether the fibers have fractured from surface or internal flaws. Furthermore, the fracture mirror sizes in the fibers may be analyzed and used to obtain good estimates of the stress at fracture in the fibers. This strength can be compared to analytical predictions for the composite behavior to determine whether the load redistribution to the fibers was as expected. The strength of the fibers in the matrix may be compared to the strength of virgin fibers tested alone. Processing interactions with the matrix or with a fiber coating often weakens the fibers. [3,4,5,6,7,8]

Some material science or material development investigations focus on crack interactions with the structure. The scanning electron microscope is the preferred tool. Emphasis is placed on cracking in the fibers, the fiber pullout lengths, cracking in and around the fiber-matrix interface, or the microcrack

density in the matrix. Micro-analytical chemical analyses are often used to study the chemistry of the fibers and the interfaces.

The usual desired mode of fracture is one with a very rough fracture surface with ample fiber pullout. Observation that portions of a composite structure have fractured in a planar fashion with minimal pull out is often a sign that some deterioration in the composite has occurred or that the fiber-matrix bond is too strong. For example, Glass et al.[9] analyzed a spectacular rupture of a large fiberglass–epoxy tank that stored pressurized sulphuric acid. Large portions of the tank had the classic rough fracture fractures with extensive fiber pullout, but the origin region had flat planar fracture zones. The cause was traced to spilled acid on the exterior surface that penetrated matrix microcracks and reached and degraded the reinforcing E-glass fibers. Fracture mirror analysis showed the fibers broke at only 20 % to 40 % of the baseline fiber strengths. Progressive fracture from the exterior occurred over a period of time as outer fibers broke, matrix microcracks opened up, and more acid penetrated and damaged more fibers until the vessel ruptured.

Composites that are exposed to elevated temperature sometimes fracture with planar fracture regions near the surface surrounding a core of rough fibrous fracture in the core.[10,11,12] Oxidation, corrosion, or surface reactions can alter the fiber–matrix bonding or fiber strength causing composite degradation.

Composites that are tested transversely, that is with tensile stresses perpendicular to the fiber directions, are usually very weak. Fractography in such cases often is focused on the crack propagation paths around or through the fiber and the fiber-matrix interface. Hull shows several examples in section 7.2 in his book on fractography.[13]

9.3 Dental composites

Although resin-matrix composite materials might seem to be outside the scope of this Guide, they are in fact brittle. Many dentists use dental composites as an alternative to ceramics, glass ceramics, or conventional porcelain fused to metal crowns. Crowns fractures are a serious problem. Fractographic analysis is underutilized by the dental materials community, but that is now changing in large part due to the leadership of Drs. S. Scherrer, Janet Quinn, K. Anusavice, J. Mecholsky, M. Øilo, and J. Robert Kelly as well as the widespread distribution of the first edition of this Guide.

Dental composites in the form of *"direct"* restoration monomers with ceramic or glass fillers can be applied to cavities in a patient's tooth in a dentist's office

They are cured in situ with a "blue" ultraviolet light to polymerize the material.

Alternatively, larger *"indirect"* restorations such as crowns (for more damaged teeth) can be made by first making an impression. An outside laboratory then fabricates a custom shaped tooth restoration that is cemented onto the reduced and prepared tooth. These indirect restoration materials are typically prepared as blanks by a manufacturer and then are custom ground to shape. (In some instances, an alternative procedure is taken whereby the dentist digitally scans a tooth and uses a CAD/CAM machine to mill crowns in his own office.) The blanks have a resin matrix with a very high glass or ceramic filler content, and are designed to have good strength, wear and fracture resistance, and good aesthetics. They behave as brittle materials and are usually linear to fracture when strength tested in a laboratory. A simple rule of thumb is that the more the filler, the more the material will fractographically resemble glasses and ceramics. Filler contents of as much as 70% by volume are not uncommon.

There are some similarities, but many important differences in the fractography of dental composites versus glass ceramics and ceramics. The lower elastic modulus of resin composites and often lower strengths mean they have much less stored elastic energy when fracture occurs. Thus, there will be less fragmentation and branching. Fracture surfaces will have some of the same markings described in this book, but sometimes are described in the polymer literature with different nomenclature. The reader is referred to Anne Roulin-Moloney's excellent book[14] on the fractography of polymers and composites for more information about resin-matrix composites in general. Much of the fractography is aimed at observing filler-matrix interfaces and what cracks do at the interfaces as opposed to finding origin flaws.

Fracture mirrors may exist, and are described as smooth areas on the fracture surface at the origin. With highly-filled composites, the interpretation is the same as described in this book: the mirror is a smooth zone surrounding the fracture origin flaw. By the time the rough hackle lines form, the crack has reached terminal velocities (e.g., 800 m/sec) that are much slower than in glasses and ceramics. Figure 9.6 shows fracture surfaces of one such highly-filled resin matrix composite from Reference15. It has a mean strength of 145 MPa, a Weibull modulus of about 10, and a fracture resistance of 0.9 MPa$\sqrt{m}$. to 1.3 MPa$\sqrt{m}$ indicative of a material with a slight R-curve. These materials have very small glass filler particles and are translucent. Inclusions and agglomerates are easy to detect in uncoated bend bars, either with reflected illumination or sometimes more effectively with transmitted illumination. Once the specimens have been examined in the natural state, they can be gold coated. The fracture surfaces will be much easier to interpret.

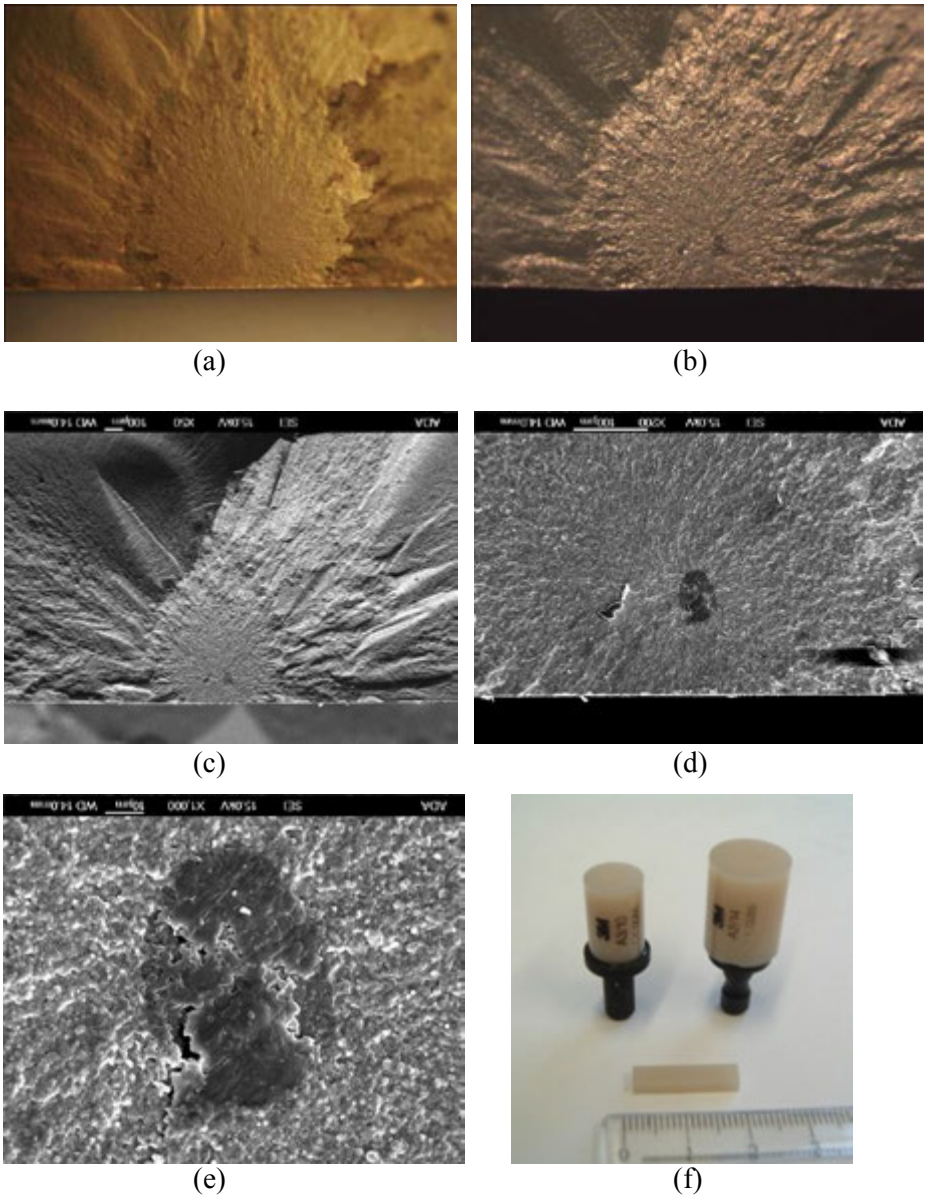

Figure 9.6 *Filled resin-matrix composite fractography. (a) shows the fracture mirror in an uncoated Paradigm MZ 100 bend bar, with transmitted light from under the bar, (b) shows the same view, but with reflected light after gold coating. (c) - (e) show SEM images of the mirror and the flaw, a calcium-rich inclusion. (f) shows the original blanks and a machined bend bar. (a-e courtesy J. Quinn)*

On the other hand, mirrors in *unfilled* resins[14,16] might look similar, but they are in fact a region of slow crack extension that occurs prior to the crack going critical. The "mirror" is in fact the critical crack. So one must be careful in interpreting "fracture mirror constants" in the polymers field. They may not be the same as those in the ceramic and glass field.

Chapter 9 References

1. J. J. Swab, G. D. Quinn, and D. J. Snoha, "Mechanical Behavior of a SiC-Fiber/Si_3N_4 Composite," U. S. Army MTL Technical Note TN 90-2, Watertown, MA, Sept. 1990.
2. R. W. Rice and D. Lewis, III, "Ceramic Fiber Composite Based Upon Refractory Polycrystalline Ceramic Matrices," pp. 117 – 142 in *Reference Book for Composite Technologies, Vol. 1*, ed S. N. Lee, Technomic Publ. Co., Lancaster, PA, 1989.
3. M. D. Thouless, O. Sbaizero, L. S. Sigl, and A. G. Evans, "Effect of Interface Mechanical Properties on Pullout in a SiC-Fiber-Reinforced Lithium Alumino Silicate Glass-Ceramic," *J. Am. Ceram. Soc*., **72** [4] (1989) 525 - 532.
4. W. A. Curtin, "*In situ* Fiber Strengths in Ceramic-Matrix Composites from Fracture Mirrors," *J. Am. Ceram. Soc*., **77** [1] (1994) 1075 –1078.
5. I. J. Davies and T. Ishikawa, "Mirror Constant for Tyranno Silicon-Titanium-Carbon-Oxygen Fibers Measured *In Situ* in a Three Dimensional Woven Silicon Carbide/Silicon Carbide Composite," *J. Am. Ceram. Soc.,* **85** [3] (2002) 691-693.
6. A. J. Eckel and R. C. Bradt, "Strength Distribution of Reinforcing Fibers in a Nicalon Fiber/Chemically Vapor Infiltrated Silicon Carbide Matrix Composite," *J. Am. Ceram. Soc.,* **72** [3] (1989) 455-458.
7. J. F. Jamet, D. Lewis, and E. Y. Luh, "Characterization of Mechanical Behavior and Fractographic Observations on Compglas SiC/LAS Composites," *Cer. Eng. Sci. Proc.,* **5** [7] (1984) 625 – 642.
8. A. C. Jaras, B. J. Norman, and S. C. Simmens, "The Measurement of Glass Fibre Strength in Composites from Studies of their Fracture Surfaces," *J. Mat. Sci*., **18** (1983) 2459 – 2465.
9. S. J. Glass, E. K. Beauchamp, M. J. Carr, T. R. Guess, S. L. Munroe, R. J. Moore, A. Slavin, and N. R. Sorenson, "Failure Analysis of A Fiberglass-Reinforced Plastic Pressure Vessel," pp. 527 – 541 in *Fractography of Glasses and Ceramics, III, Ceramic Transactions,* Vol. 64, J. Varner, Fréchette, V., and G. Quinn, eds., American Ceramic Society, Westerville, OH, 1996.
10. K. M. Prewo, "Tension and Flexural Strength of Silicon Carbide Fibre-Reinforced Glass Ceramics," *J. Mat. Sci.,* **21** (1986) 3590 – 3600.
11. T. Mah, M. G. Mendiratta, A. P. Katz, R. Ruh, and K. S. Mazdiyasni, "High-Temperature Mechanical Behavior of Fiber-reinforced Glass-Ceramic Matrix Composites," *Comm. Am. Ceram. Soc.,* **68** [9] (1985) C 248-251.
12. T. Mah, M. Mendiratta, A. Katz, and K. Mazdiyasni, "Recent Developments in Fiber-Reinforced High Temperature Ceramic Composites," *Bull Am. Ceram. Soc.,* **66** [2] (1987) 304 – 308, 317.
13. D. Hull, Fractography, Observing, Measuring and Interpreting Fracture Surface Topography, Cambridge University Press, Cambridge, 1999.

14. A. C. Roulin-Moloney, *Fractography and Failure Mechanisms of Polymers and Composites*, Elsevier, London and New York, 1989.
15. J. B. Quinn and G. D. Quinn, "Material Properties and Fractography of an Indirect Dental Resin Composite," *Dent. Mat.*, **26** [6] (2010) 589 – 599.
16. E. H. Andrews, *Fracture in Polymers*, Elsevier, NY, 1968.

10. Case Studies

The following case studies illustrate the application of fractographic techniques for failure analysis. Many additional cases are tabulated in Appendix B and can be found in the books listed in Appendix A.

Case 1 Ruptured Rotor (Ceramic gas turbine rotor)
Case 2 Busted Barrel (Silicon carbide gun liner)
Case 3 Conflicting Carbide Data (Silicon carbide flaws and slow crack growth)
Case 4 Vulnerable Vials (Broken medicinal vials)
Case 5 Damaged Dome (Coarse-grained aluminum oxynitride IR dome)
Case 6 Suffering Setter Plate (Silicon carbide furnace plate)
Case 7 Ruptured Radomes (Fused silica missile nosecones)
Case 8 Maligned machinists (Bend bars made by different machine shops)
Case 9 Modeler's Match (Fracture origins in MEMS scale micro tensile specimens)
Case 10 Fractious Fractographers (A VAMAS fractography round robin)
Case 11 Perilous Prostheses (Four ceramic dental crowns)
Case 12 Mangled Margins (Twenty alumina dental crowns)
Case 13 Ruined Refractors (Single crystal sapphire solar lenses)

Case 1: Ruptured Rotor (Ceramic Gas Turbine Rotor)

Figure 10.1 shows a model gas turbine rotor made of hot-pressed silicon nitride that was designed to fail. It was one of twelve such model structures made by the Ford Motor Company's scientific research laboratory in the late 1970s to mid-1980s.[1,2] It was part of an ambitious endeavor to incorporate advanced ceramics into automotive gas turbine engines. Considerable effort was expended on improving ceramic materials, developing reliability codes, generating data bases, fabricating parts, and running them in test rigs. Full scale engine testing was expensive and risky, so a small project was set up to verify the ceramic design and reliability codes by using a realistic model rotor. This simulated rotor was mounted in a hot-spin rig shown in Figure 10.2 and rotated at 50,000 rpm while heated by hot gasses to a peak rim temperature of 1260 ^{o}C (2300 ^{o}F). These conditions were representative of the gas turbine operating conditions and the speed, mass, and shape of the part were designed so that some of the rotors would fracture in a time-dependent manner, from slow crack growth of preexisting flaws. The goal was to correlate failure times to predictions based on life prediction computer models.

Twelve model rotors were fabricated and tested. The rotors were designed to have a high probability of survival on loading (> 95 %), but to probably fail within 25 h. The design analysis assumed that failure would occur due to slow crack growth of preexisting volume-distributed flaws. The rotors were intended to break in the thin web where the maximum principal steady state stress was 131 MPa (19 ksi) and the peak temperature was 1240 ^{o}C (2260 ^{o}F).

Figure 10.1. *A Ford silicon nitride 95 mm diameter model gas turbine rotor that survived 25 h intact. The outer rim is thicker than a real rotor in order to simulate the mass of the vanes that would be attached in a real rotor.*

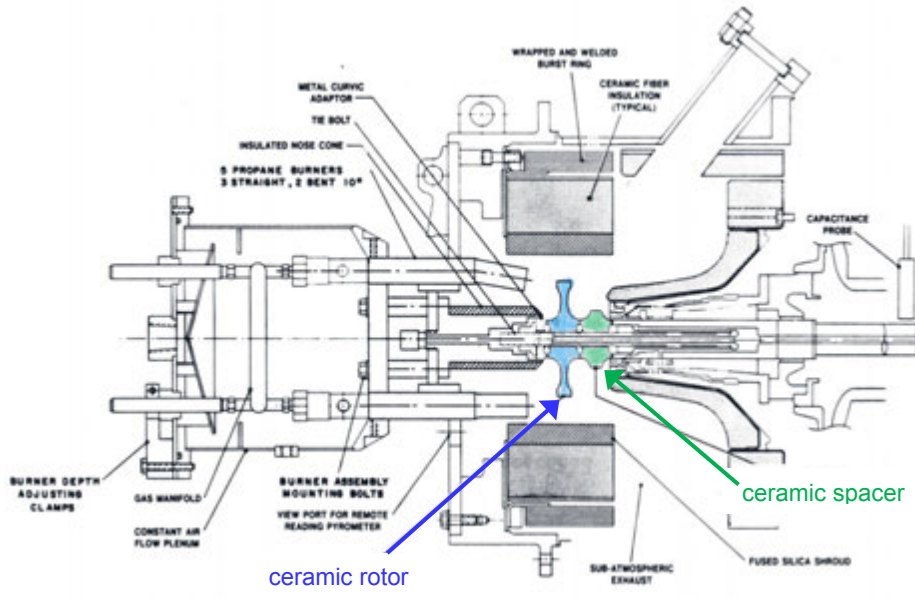

Figure 10.2 *The Ford hot spin test rig (Ref. 2).*

Six broke in a time dependent manner as intended. Two rotors broke on initial startup. Four were run outs and did not fail in the allotted 25 hour times and were treated as censored outcomes.

The rotors were made of a state-of-the-art hot-pressed silicon nitride[a] that was carefully machined to final dimensions. The particular grade was one of the most thoroughly-analyzed structural ceramics of all time and was eventually used as the world's first reference material for the property fracture toughness.[3] Eventually enough data was available that a comprehensive fracture mechanism map was constructed,[4] but that was after the conclusion of the Ford study. The finite element and heat transfer models used the best data available and temperature-dependent material properties. A substantial amount of laboratory test coupon data were available including flexural and tensile strengths, elastic properties, and slow crack growth parameters from three types of tests: variable stressing rate strength tests (dynamic fatigue), crack velocity - fracture mechanics tests (double torsion), and stress rupture (flexural and tensile).

Figure 10.3 shows the reliability as a function of time. The three types of slow crack growth data gave very divergent predictions. The six data points show the six rotors that failed at times from 0.2 h to 18.6 h. The predictions made

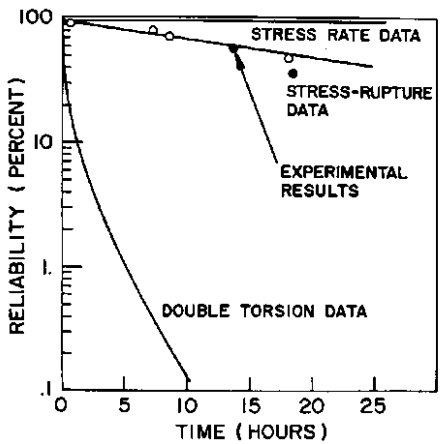

Figure 10.3 *Reliability versus time showing reliability predictions based on three different types of laboratory test data (solid lines) versus the actual outcomes for six rotors that failed.(Refs. 1,2) The actual failure times matched the predictions based on stress rupture data. The two solid points correspond to rotors that were fractographically analyzed by the author.*

[a] Grade NC 132, Norton Co., now St. Gobain Advanced Ceramics, Worcester, Ma.

with the laboratory stress rupture data gave the best correlation to the actual lifetimes. The Ford authors concluded that stress rupture data was the best for predicting reliability versus time.[1,2]

Fractographic analysis revealed that fracture did not occur quite as anticipated. The test rig was constructed in such a manner that most of the fragments were retrievable. The longest (18.6 h) and third longest (13.8 h) rotors were sent to the author for fractographic evaluation. It was felt that these would have large slow crack growth zones that would be easy to find. One virtue of NC 132 is that it was a very fine-grained fully-dense material with minimal second phase.

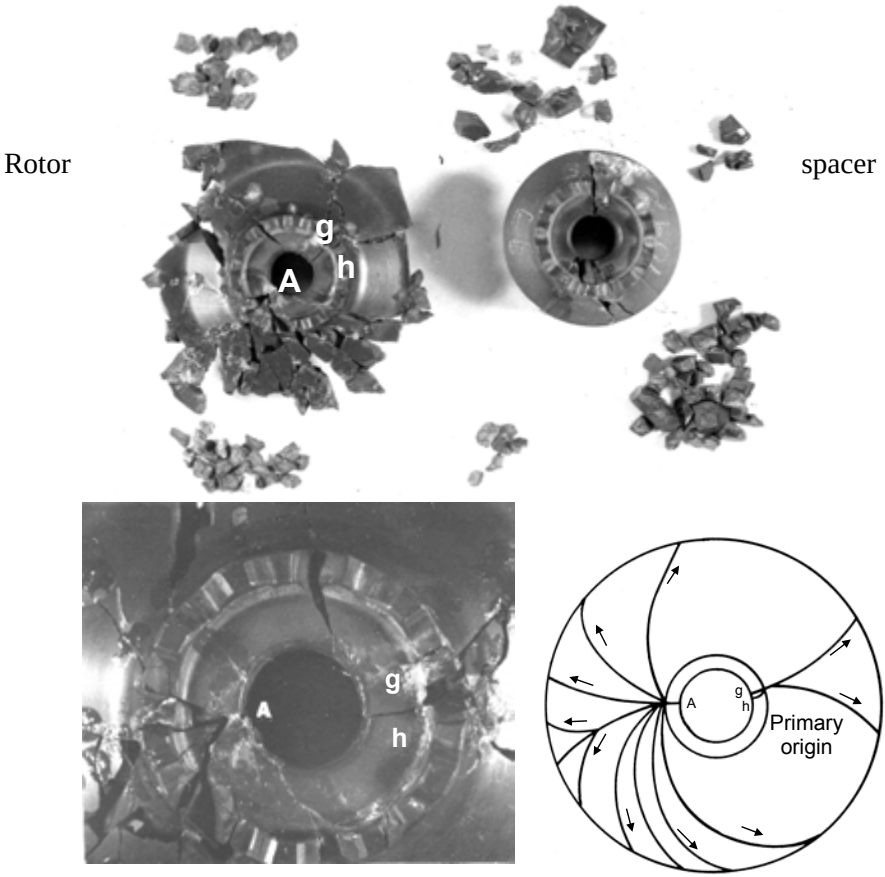

Figure 10.4 *Reconstructed model rotor and spacer. Fracture initiated either at location "A" on the left side of the bore of the rotor or at two locations "g" or "h" on the opposite side. Fracture started at "h." Fracture "g" occurred later. The lower schematic shows the overall fracture pattern in the rotor.*

Fracture markings were quite clear and the local direction of crack propagation could be assessed in every single piece. One rotor (18.6 h) was reconstructed piece-by-piece over the course of *one week* culminating in the assembly shown in Figure 10.4. It was very much a puzzle-solving exercise. Many fragments from the rim were missing, but they did not matter. The figure also shows that the ceramic spacer part had also fractured and its pieces were commingled with the rotor, thereby complicating the matter. Nevertheless, the central and web portions of the primary rotor were almost completely reassembled. After completion, the rotor was taken apart again and a map of crack propagation directions was made. The interpretation was clear. Primary fracture commenced at the bore or the curvic coupling teeth and cracks branched and ran out to the rim as shown in the schematic in Figure 10.4. Every single fragment was examined in a futile search for a web origin with a slow crack growth zone, but none were found. All primary fractures started from the bore or coupling area. There were three origins from the inner part of the rotor. Origin "A" was at the exact edge of the bore, which although chamfered, nonetheless had surface grinding cracks (Figure 10.5a-c). It could not be determined whether slow crack growth had enlarged the grinding cracks. The other two origins "g" and "h" were located on the other side of the bore and were from the curvic coupling teeth machined into the rotor (figure 10.5d,e. These were part of the attachment scheme. One origin, "g", was a parallel machining crack (aligned parallel to the axis of grinding) in the tooth, and the other, "h", was an impact – contact crack also on a tooth.

Thus, fracture started on one side of the rotor in the bore area at either "g" or "h," then branched into two main crack(s) that ran out to the rim. This opened up the disk on that side. The unbalanced forces triggered a rupture on the opposite side at site "A." Origin "A" had a well-defined small fracture mirror allowing a stress estimate of a 630 MPa (92 ksi) which is much greater than the model estimated bore stress of ≈172 MPa (25 ksi). This, plus the violent branching at that site, confirms that site "A" was a *secondary* fracture. *Primary fracture* occurred on the other side of the bore at site "g" or site "h," causing the rotor to go completely out of balance. Origin "h" was determined to be the first break based on crack intersection patterns. The flaw was a large contact damage crack with a large fracture mirror. The local stress was estimated to be 500 MPa (72 ksi) from the flaw size and approximately 580 MPa (84 ksi) from the fracture mirror. Origin "g" was determined to have fractured after site "h", since the crack from "g" stopped when it encountered the prior crack from "h." At these locations the computer models indicated there were modest bore stresses (≈138 MPa, 20 ksi) and temperatures (1150 ^{o}C, 2200 ^{o}F). These did not match the fractographic estimates.

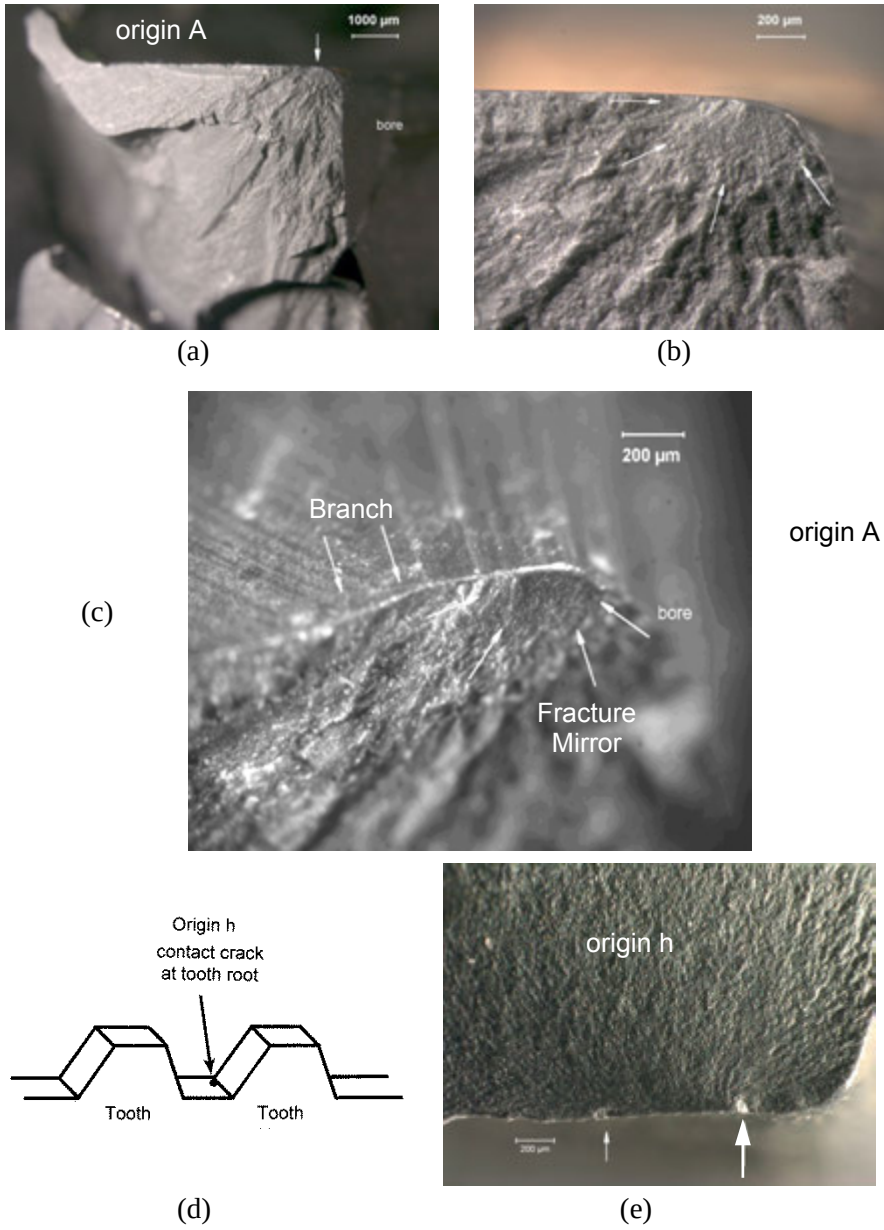

Figure 10.5 *Fracture surfaces showing a fracture mirror and the origin site A, which is a surface crack from grinding. (b) and (c) highlight the fracture mirror and grinding crack origin at site "A." The primary fracture origin was contact crack damage at site "h" on the curvic coupling teeth as shown in (d) and (e). Origin "h" is marked by the larger arrow on the right. Notice how the radiating hackle lines converge on it.*

An important fractographic observation helps explain the fracture. When the rotor and spacer were assembled in the hot test rig, it was customary to separate them with a thin platinum foil to prevent direct ceramic-to-ceramic contact. The fractographic examination showed uneven platinum wear traces and even some bare spots. Could it be that the foil deformed or crept with time such that ceramic-to-ceramic contact eventually occurred? If so, then the rotor stress distribution may have become unbalanced or local stress concentrations or contact stresses may have contributed to cause an initial contact crack and fracture at site "h."

This exercise was a good example of one of the author's laws of fractography: "The first one is the hardest." While at first glance, reassembly of a burst rotor may appear to be a formidable task, it was merely time consuming. The second rotor took less time to analyze. It also had fracture initiation sites at the bore or at the teeth. Years later, the author became aware of comparable work done on model silicon nitride rotors at Daimler-Benz's research center in Stuttgart.[5] They also reconstructed burst silicon nitride rotors and used fractography to find that grinding cracks in the bores sometimes were fracture origins.

Some lessons learned from this case study were:

a. Fracture occurred from a different cause than expected and modeled.
b. Stress rupture data may have been the best for reliability estimation, but the correlation of failure times was fortuitous.
c. Volume flaws were not found in the two fractured rotors. Surface machining cracks and contact cracks were found and Weibull area scaling should also have been included in the reliability model.

Case 2: Busted Barrel (Silicon Carbide Machine Gun Liner)

The U. S. Army has off and on over the past twenty-five years investigated ceramic liners to improve gun barrel life and reduce mass. The low density, high compression strength, refractoriness, and erosion and wear resistance of ceramics could be advantageous. Figures 10.6 and 10.7 show drawings for a 50-caliber machine gun breech with a ceramic liner from a project conducted for the U. S. Army in the 1980s.[6] One design placed the ceramic into compression by shrink fitting a steel sleeve around the ceramic. The steel sleeve was heated and placed over the cool ceramic tube. As the steel cooled, it contracted and put the ceramic liner into axial, radial, and hoop compression. The dimensions and temperature differentials were chosen so that the ceramic liner was always in compression, even when firing a projectile. Several ceramics were tried, but most testing was on a sintered α-SiC. Figure 10.7 shows the maximum *axial* stresses, σ_x, in the three components

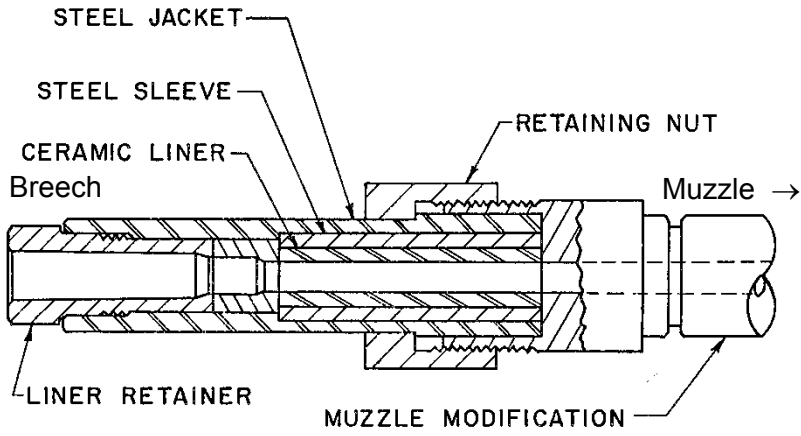

Figure 10.6 *Schematic of the breech end of the 50 caliber (12.7 mm) gun barrel (Ref. 6).*

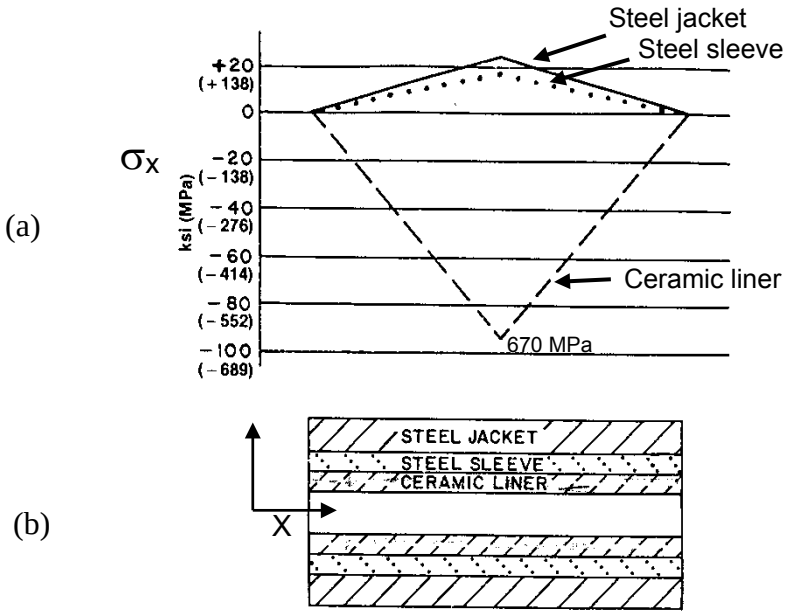

Figure 10.7 *Axial stress distribution, σ_x, as a function of position x in the assembly along the bore (a). The stresses correspond to the three parts shown in a sectional view in (b) which is a simplified version of the assembly shown in the previous figure. The stresses included those from shrink fitting and projectile firing. (Figure from Ref. 6)*

of the assembly from combining the residual shrink fit and projectile firing stresses. The maximum axial stress σ_x was 670 MPa in compression in the ceramic liner mid-portion. This stress tapered to zero at each end. The axial stress maximums were only 112 MPa tensile in the steel sleeve and 154 MPa tensile in the steel jacket. The maximum *radial* stress in the ceramic sleeve was 345 MPa compression, and the maximum *hoop* stress, σ_θ, was 590 MPa compression during projectile firing. The environment is severe, but if the ceramic was always under compression, perhaps it would not fracture.

Some assemblies survived as many as a thousand single-shot firings, confounding skeptics who felt that the assembly would not survive one shot. One assembly that did develop ceramic cracking after a few hundred shots had circumferential fractures as shown in Figure 10.8a. The steel sleeve and jacket were machined away to allow extraction of the ceramic as shown in Figure 10.8b. The fracture planes were perpendicular to the axial direction, suggesting that hoop stresses from internal pressure during projectile firing were not the cause of failure. The latter would have created radial cracking. Fractographic analyses showed that every fragment fractured from one or more contact cracks that were periodically spaced on the *outer rim* of the ceramic where it contacted the steel sleeve.

So if the shrink fitting created compressive stresses, where did the tensile stresses come from? The plane of the fractured surfaces and also of the initial semi-elliptical contact cracks indicated that the tensile stresses were *axial:* σ_x. Figure 10.7 shows that the axial residual compressive stresses did taper off towards the tube ends. The most likely sources of tensile stresses are dynamic stress waves generated during the firing. Even if these are initially compressive, they can change phase and become tensile when the stress wave reflects off of the end faces. Furthermore, the elastic wave velocity and impedance of the silicon carbide and the steel sleeve are not matched, and stress waves propagated axially at different rates. Hence, a dynamic tensile stress could develop at the steel/ceramic interface due to mismatch of the transient elastic strains.

The contact stress cracks often were periodic around the rim. Although the parts were machined to tight tolerances, it is likely that slight variations in the mating surfaces led to an uneven fit and stress concentration sites that triggered the contact cracks.

So, in this case, the ceramic was designed to always be in compression, but fractography showed otherwise. Some design and modeling improvements were suggested. The tolerances and surface specifications for the mating parts

could be changed. The elastic properties of the ceramic and the confining sleeve could be matched better. More sophisticated stress models could examine the transient stress states in the assembly.

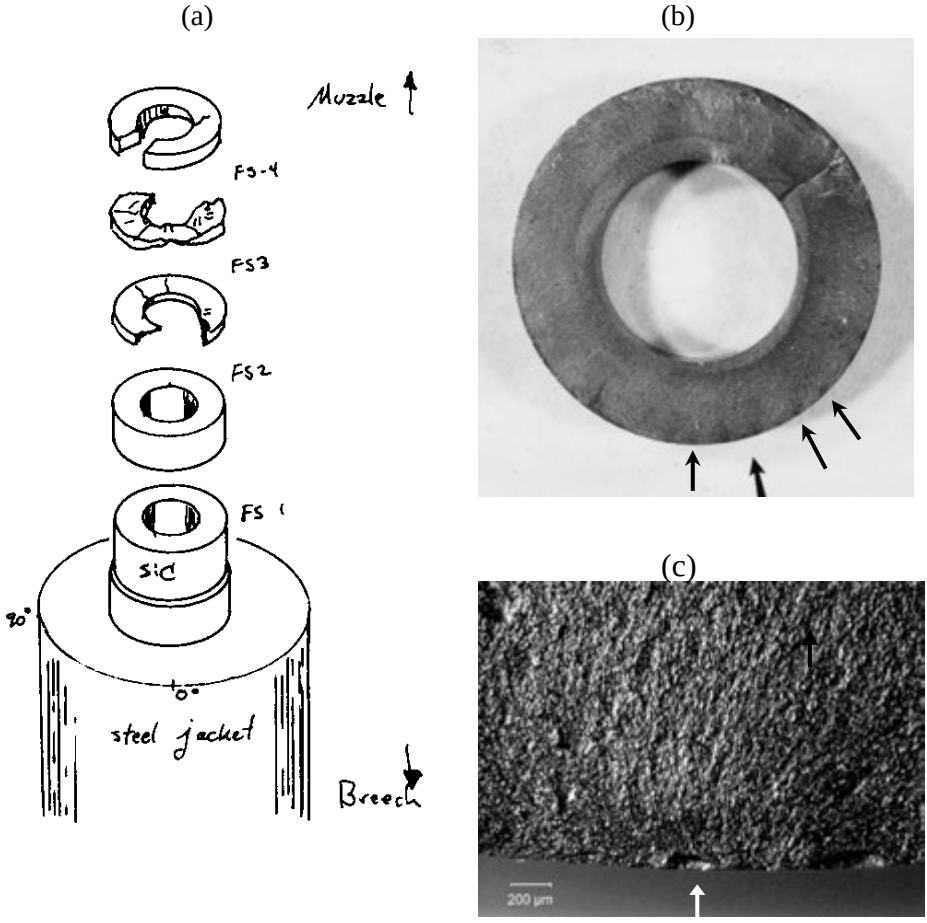

Figure 10.8 *Fractured α-SiC gun barrel. (a) is a schematic sketch. (b) shows the fracture surface of one of the ring shaped fragments. Contact cracks are spaced periodically around the outer rim and appear as shadows in this view (arrows). The bore diameter is 12.7 mm. (c) shows a close-up of one of the contact cracks.*

Case 3: Conflicting Carbide Data (Silicon carbide flaws and slow crack growth)

This case is not about a specific component, but about the risk of treating all flaws as if they behave the same. As part of a program on characterization of structural ceramics for heat engine ceramics in the 1980s, the author conducted extensive stress rupture testing of pressureless-sintered α-SiC.[b] [7,8,9] Stress rupture testing entails applying a constant stress to a specimen, at a level below that needed to cause fast fracture, and measuring the time to failure. Slow crack growth can cause flaw enlargement and time-dependent fracture. Sometimes such tests are termed creep rupture if the loading conditions are such that bulk creep deformation leads to accumulated damage and fracture.

The author's data[7,8,9] at 1300 °C in air was consistent with data published by another team.[10] Both teams detected time-dependent fractures due to intergranular slow crack growth of preexisting flaws as shown in Figure 10.9.

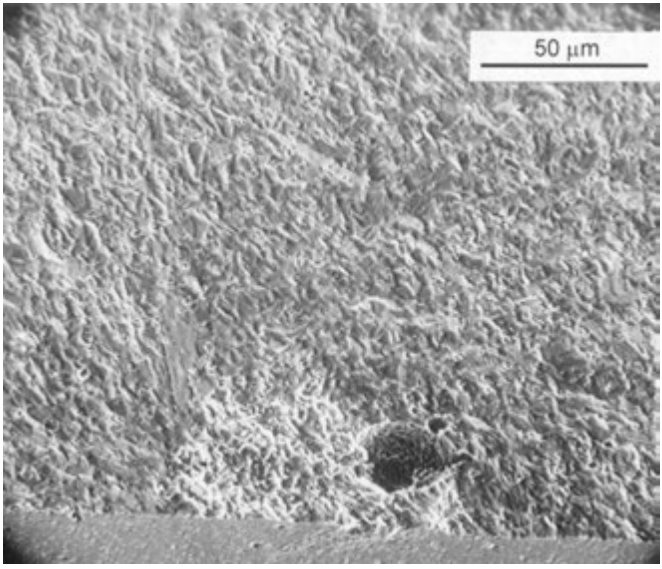

Figure 10.9 *Fracture origin in a 1300 °C stress rupture SiC specimen. The origin is a large intergranular slow crack growth region that may have started from the side of or beneath the large pore.*

[b] Hexoloy SA, Carborundum, Co., Niagara Falls, NY. Now St. Gobain Advanced Ceramics.

A much different story emerged at 1200 °C. This author recorded time-dependent fractures such as shown in Figure 10.10 with origin flaws as shown in Figure 10.11. The other team did not observe a single time-dependent fractures at all in their experiments. Why did the two groups have such contrasting outcomes at 1200 °C? The answer was that they used Knoop indented, artificially-flawed specimens, whereas the author used as-machined specimens that allowed the material to fail from whichever of its flaws it "chose."

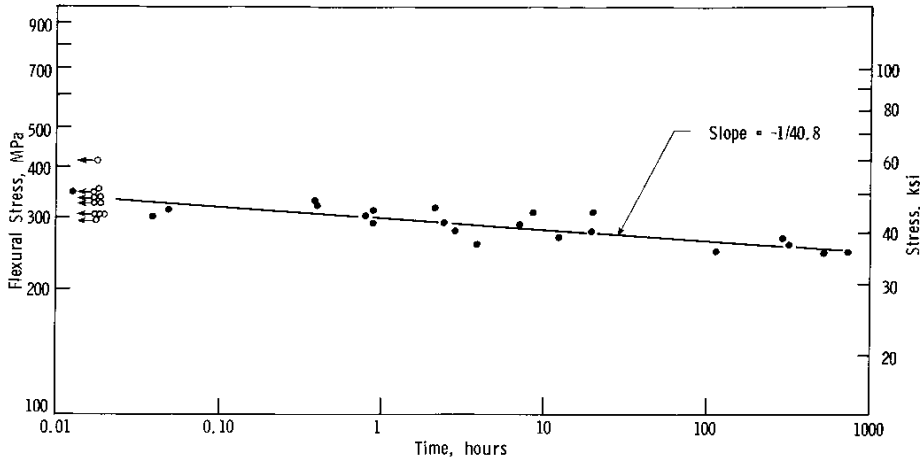

Figure 10.10 *Stress rupture curve at 1200 °C in air for sintered α-SiC.*[7-9] *Every time-dependent fracture was from a pore or porous zone and only if it was surface connected. The hollow points with arrows to the left are breaks on loading and are consistent with the fast fracture strength which was about 350 MPa. The slow crack growth exponent N was 40.8.*

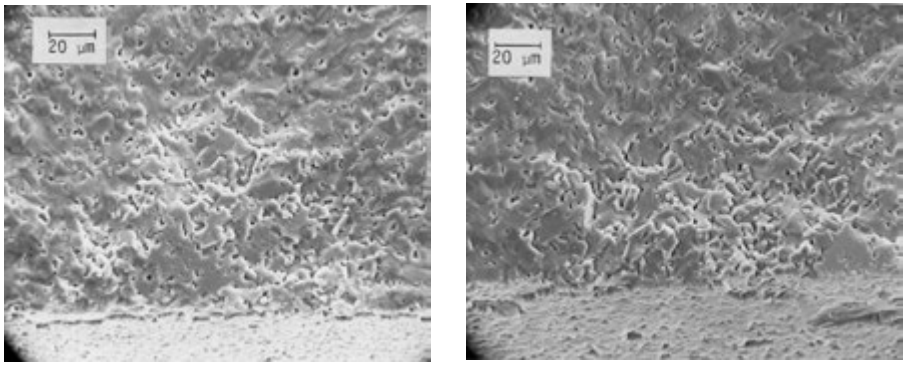

(a) (b)

Figure 10.11 *Fracture origins in 1200 °C α-SiC specimens that fractured at 863 h (a) and 1460 h (b) from surface-connected porous regions.*

At 1300 °C and above, easily-detected intergranular slow crack growth caused fracture from volume-distributed flaws such as large grains, pores, or agglomerates as shown in Figure 10.9. Some of these volume origins were located in the bulk. Both teams detected this behavior.

On the other hand, every one of the 1200 °C time-dependent fracture origins was a pore or porous region *connected to the outer surface* as shown in Figure 10.11. These flaws did not have slow crack growth markings. Evidently these flaws were susceptible to very localized stress-corrosion crack extension (from oxidation) that sharpened or locally extended tiny microcracks on the pore periphery. These flaws did not need much change in flaw size or severity for them to go critical, since the failures occurred at stresses (250 to 350 MPa) very close to the fast fracture strength (350 MPa). Figure 10.12 summarizes the fractographic findings.

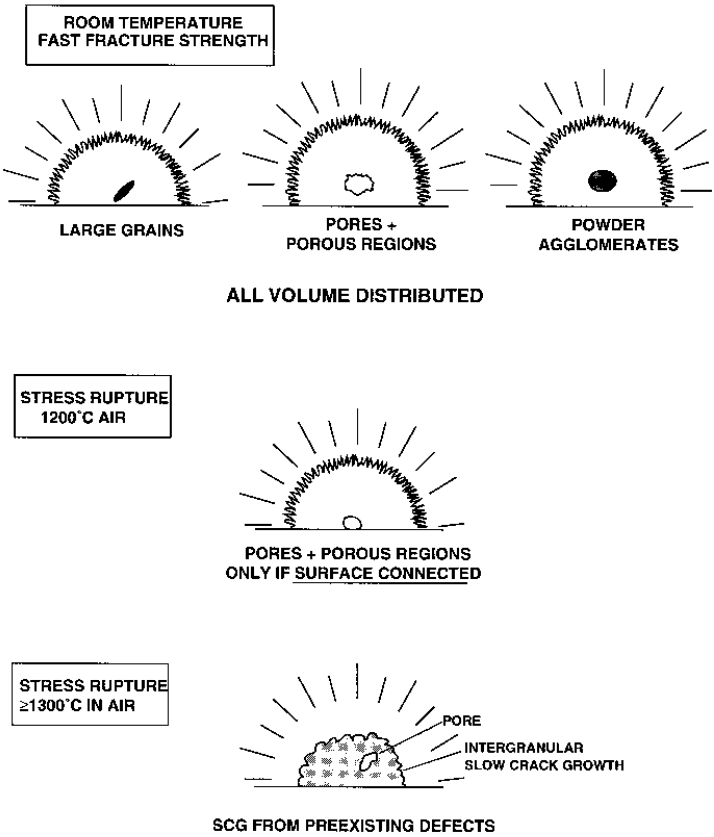

Figure 10.12 *Fracture origins in α-SiC.*

The other testing team did not detect the 1200 °C stress corrosion mechanism since they used Knoop artificial flaws in all of their bend specimens.[10] Artificial flaws often are effective tools for studying fracture, but in this instance they produced misleading results. At 1300 °C and above, the Knoop flaws did grow by slow crack growth. They did not grow by slow crack growth or by stress corrosion at 1200 °C. The Knoop flaws were not susceptible to the same failure mechanism as the pores and porous zones in the as-machined specimens. The Knoop flaws reduced the fast fracture strength of the specimens to less than 200 MPa. Their stress rupture specimens were loaded at stresses from 100 to 200 MPa, a stress well below that necessary to activate the pore flaw stress corrosion mechanism.

This case demonstrates that it is often best to let a material reveal what type of flaws it is apt to fail from, rather than rely on artificial indentation flaws.

Case 4: Vulnerable Vials (Broken Medicinal Bottles)

A pharmaceutical company had a problem with neck rim cracking in 17 mm diameter medicinal vials. The cracking rarely caused the vials to break, but trace leakage and loss of the airtight seal due to through-cracks in the rim caused great concern. Loss of seal carries a risk of contamination with potential fatal consequences (e.g., see case 10.8 in Fréchette, Ref. 11).

Optical stereomicroscope examination of vials with either intact or severed caps revealed a circumferential damage zone in the glass just under the aluminum cap seal (Figure 10.13 a,b). Focusing through the glass revealed that some cracks had penetrated deep beneath the surface although the full extent of the penetration was difficult to assess. Examination of a vial with a severed cap confirmed the contact cracks could reach all the way to the interior. No defects in the glass were detected. The concentricity of the neck with the vial body was within specifications. The source of the fractures was traced to a misalignment of the cap crimping machine star-wheel assembly. An incidental finding was the beautiful example of scarps, shown previously as Figure 5.48a, on one of the fracture surfaces of a severed cap. The scarps were consistent with the outer surface cracks having reached the vial interior and the interior medicinal fluid, therein aiding the final fracture of the glass neck.

(a)

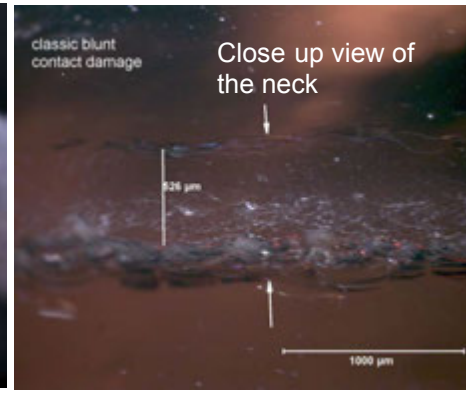

(b)

(c)

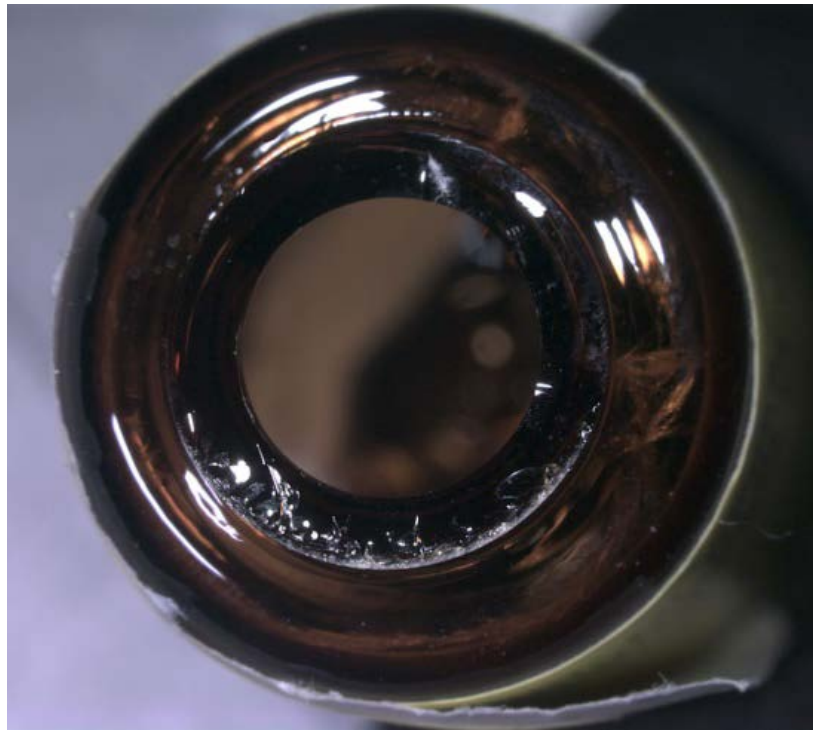

Figure 10.13 *Rim cracking in glass medicinal vials. (a) and (b) show blunt contact cracking damage (arrows). (c) shows a top view of the fracture surface of a vial with a severed cap.*

Case 5: Damaged Dome (AlON IR dome)

This case illustrates what can be accomplished with optical microscopy alone, even on very difficult ceramics. A coarse-grained aluminum oxynitride missile sensor dome broke during a thermal stress proof test. It broke into several pieces, and the branching patterns directed attention to an area near the base as shown in Figure 10.14a. One might expect the origin to be at the dome rim, possibly at a bevel, but that was not the case.

The roughness of the microstructure hid nearly all fracture markings as shown in 10.14b. Careful adjustment of low-angle grazing lighting at higher magnifications revealed local hackle lines and twist hackle within the transgranularly-fractured grains as shown in Figure 10.14c and d. It was possible to read these lines back to the inside surface of the dome to a location well away from the rim. Close-up examination in Figure 10.15 revealed the origin site had zipper machining crack hackle lines within one or two grains, indicating the origin was grinding or scratch damage that was not completely removed by polishing.

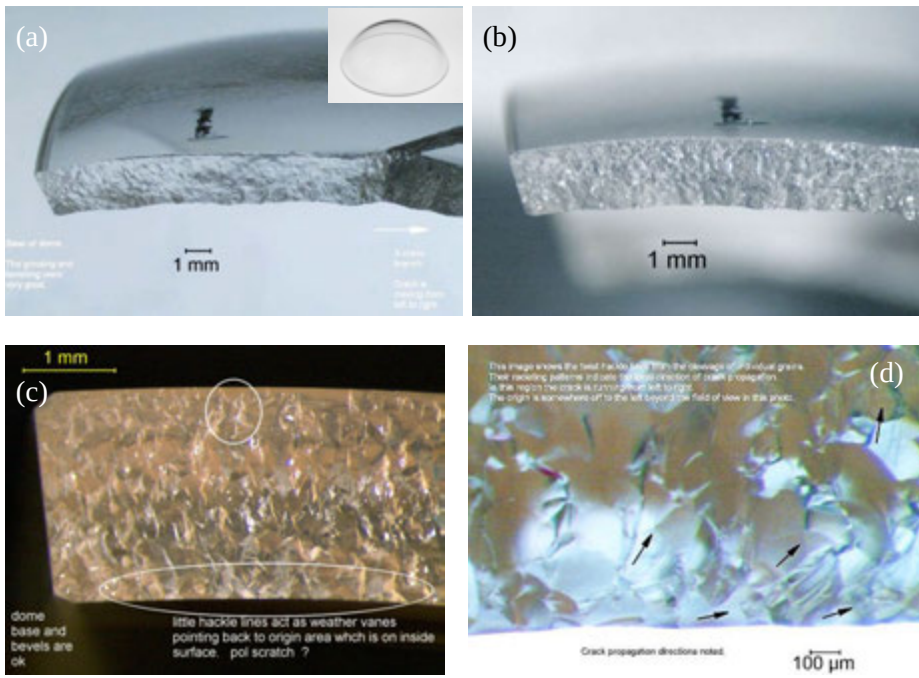

Figure 10.14. *AlON infrared missile dome. (a) shows how the branch on the right leads away from the origin area. (b) shows the fracture surface with the coarse microstructure.*

Unfortunately, the dome was not available for SEM confirmation or further examination of the inside surface for traces of a scratch at the origin site. The polished surfaces in general did have an assortment of polishing flaws as shown in the insert. Similar grinding/polishing flaws inside single grains of aluminum oxynitride have been reported by Swab et al. [12] A similar approach may be used to find origins in coarse-grained polycrystalline alumina (PCA) lamps.

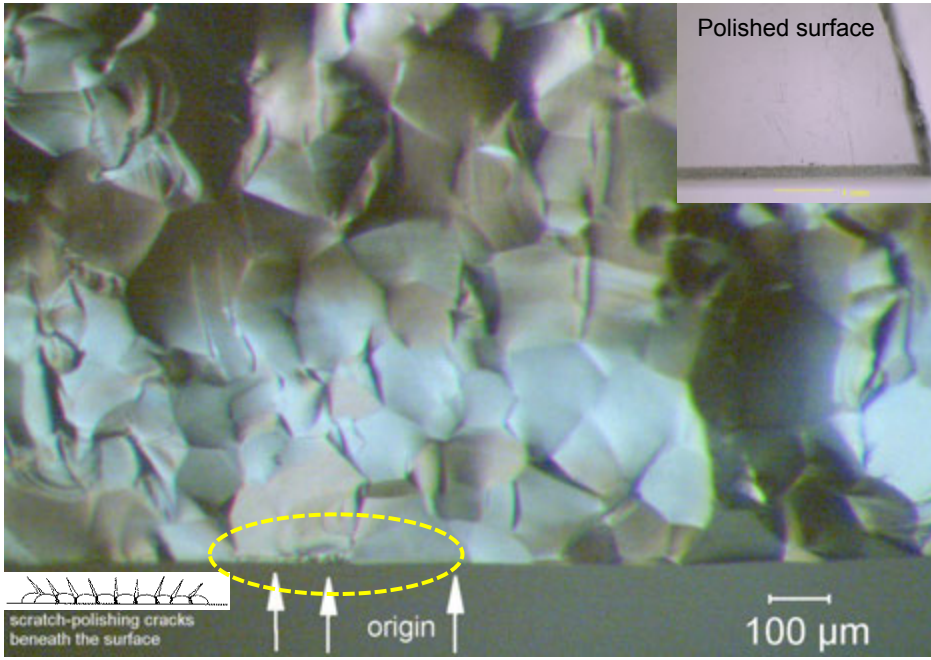

Figure 10.15 *Wake and twist hackle within cleaved AlON grains lead back to the inside surface and to tiny zipper machining crack hackle lines within one or two large grains. This image was taken at the maximum magnification (125X) of the stereoptical microscope that was used for the examination. The insert shows the outer polished surface with polishing scratches and a well-ground bevel-chamfer.*

Case 6: Suffering Setter Plate (Silicon Carbide Furnace Plate)

A large silicon carbide furnace setter plate fractured during a furnace run. Was the material faulty or was there some other cause? Figure 10.16 shows one half of the broken plate. It has the wavy fracture that is a telltale sign of a center-heated plate fracture as shown in Section 4.12. Figure 10.17 shows the fracture surface revealing that fracture initiated from grinding damage at a hole near the rim. No material flaws of consequence were detected. The mirror size was about 9.3 mm. Using an A_o value of 11 MPa$\sqrt{m}$ for a dense hot-pressed SiC (from Appendix C), the stress at fracture was estimated to be only 115 MPa. The material was completely satisfactory, but the machining, grinding, and attachments were not. This failure analysis required only a one minute visual inspection.

(a)

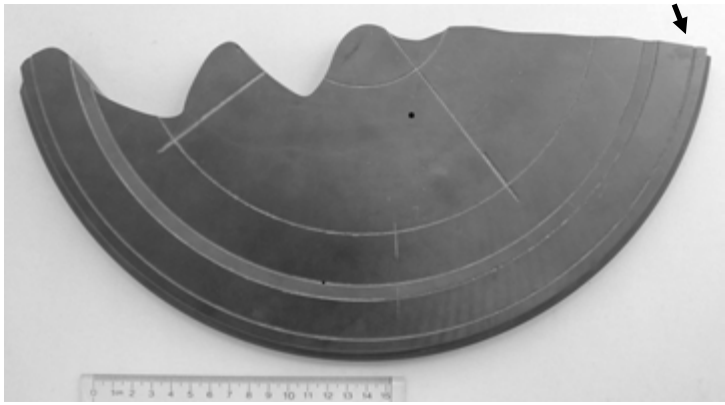

(b)

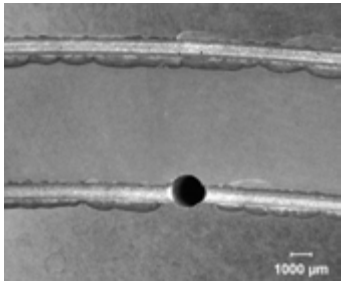

(c)

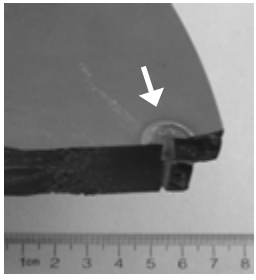

Figure 10.16 *Fractured SiC furnace setter plate (a). The curvy pattern is typical of a center-heated plate fracture as shown in Chapter 4. The arrow marks the origin which is a hole through the plate. The machined grooves were chipped and had ragged edges as shown in (b). The plate was 36 cm round and 1.9 cm thick. (c) shows the origin hole from the bottom surface. There is spall and evidence of a chemical reaction with a mounting bolt or washer. (plate courtesy of B. Mikijelj)*

(a)

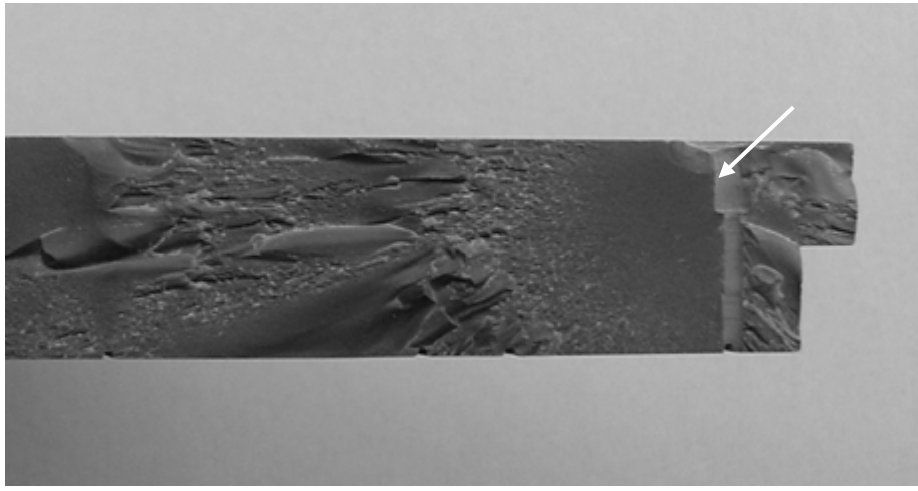

(b)

Figure 10.17 *Fracture surface of the SiC setter plate. A fracture mirror at the origin (arrow in (a)) attests to a moderate stress level. Hoop tensile stresses on the rim were generated by thermal strains. Thermal expansion of the hot plate center was resisted by the cooler rim. As the crack propagated towards the plate middle it slowed since it reached hot regions that were originally in compression. The fracture surface became relatively featureless and the crack meandered. The hole through the plate at the origin (b) had chipping and grinding damage that weakened the plate.*

Case 7: Ruptured Radomes (Fused Silica Missile Nosecones)

First generation U. S. Army Patriot air defense missiles in the early 1980's utilized fused-silica radomes (Figure 10.18). Radomes are nosecones that are radar transmissive. The radome was prepared by slip casting and then sintering silica particles to greater than 85% density. This porous structure had a low but acceptable strength and, like an insulating firebrick, was more effective in arresting cracks than if the radome were a fully-dense glassy body. Although sintered fused silica is weak, it was selected since it had a low coefficient of thermal expansion and thus would be less susceptible to thermal stresses from aerodynamic heating. Selected radomes were deliberately loaded to fracture or proof tested as part of the engineering development program. This was done by attaching a sling to the side of the radome and pulling it laterally several times in different directions. Unexpected fractures occasionally occurred. Most fractures occurred in the ceramic where it was joined to a threaded fiber-epoxy thread ring attachment part (Figure 10.19a,b). Fractography was difficult in the porous weak ceramic since it had a rough fracture surface, but a number of fractures were successfully diagnosed. Figure 10.19 shows an instance where atypical grinding damage created strength limiting cracks. Better control of the surface grinding eliminated the problem. Figure 10.20 shows a different example wherein excessive shrinkage of the epoxy bond caused debonding. This created a stress concentration site in the ceramic that initiated fracture. The remedy in this case was to adjust the bond-cure thermal cycle.

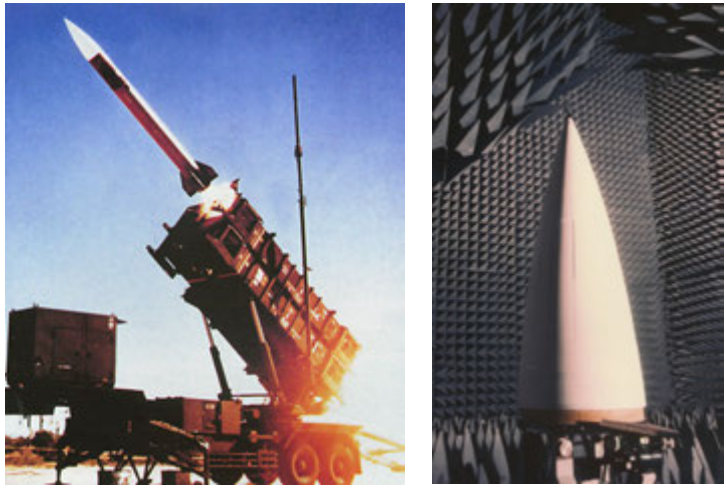

(a) (b)

Figure 10.18 *U. S. Army first generation Patriot air defense missile. The radome was 1.1 m tall with a 40 cm diameter. (b is courtesy Raytheon)*

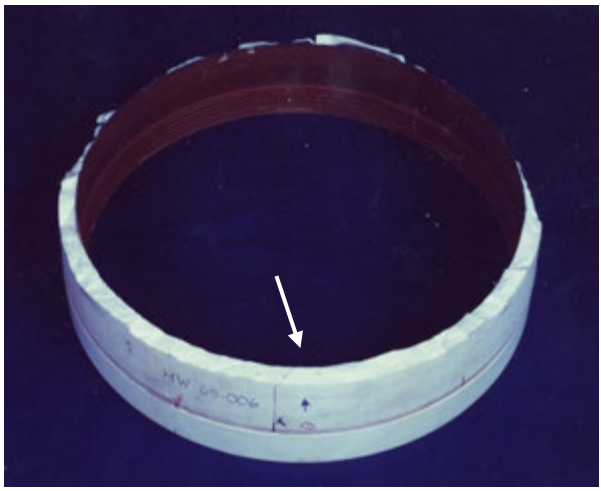

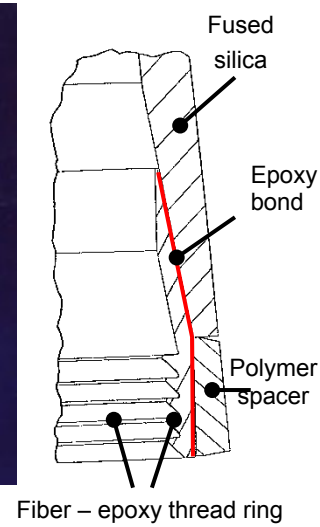

(a) (b)

(c)

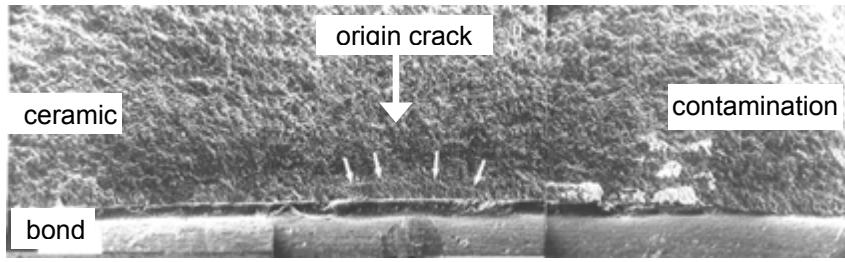

(d)

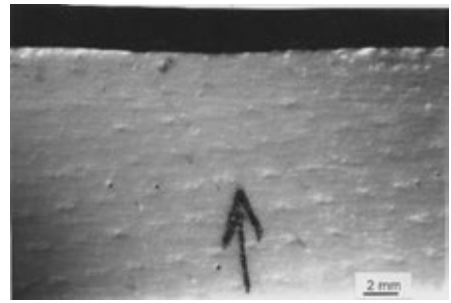

Figure 10.19 *Sintered fused silica radome that fractured during a proof test. (a) is a top view with the origin region marked by the arrow. The ceramic is bonded on the inside to a fiber epoxy attachment ring. (b) is a schematic showing the bottom of the radome where it was attached to the thread ring. Fractures in the ceramic typically occurred near the top of the thread ring. (c) shows a grinding crack at the origin area (arrows). (d) shows a grinding pattern on the inside ceramic surface.*

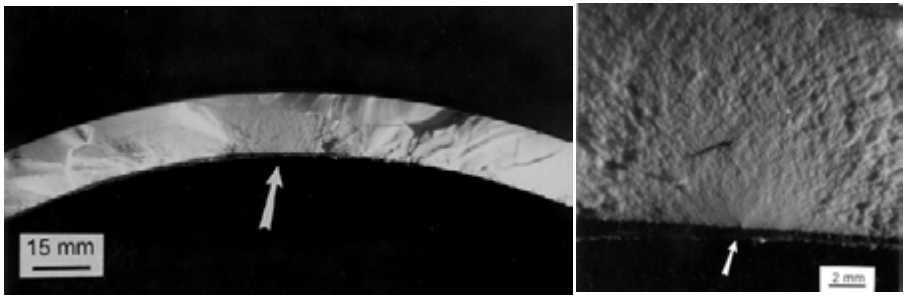

(a) (b)

(c)

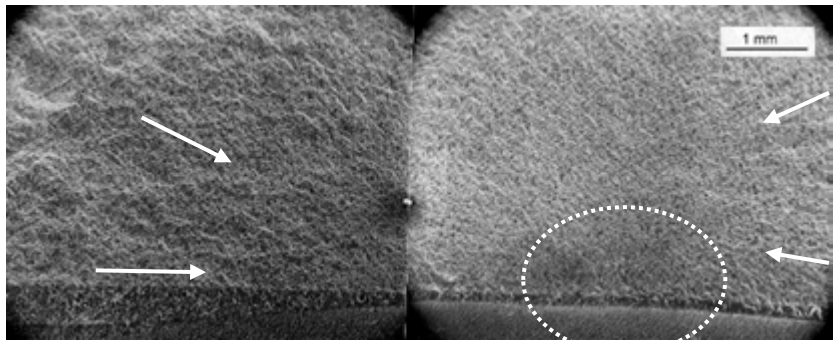

(d)

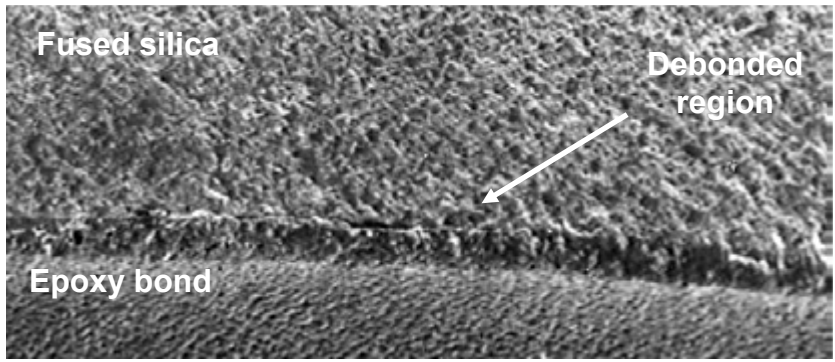

Figure 10.20 *Sintered fused silica radome fracture. (a) shows the origin site on the inside wall. (b) is a close-up showing a fracture mirror centered on a feature on the inside wall of the ceramic at the top of the bond line. (c) is a composite of two SEM photos of the origin area. The origin is less obvious, but hackle lines point back (white arrows) to the circled area. (d) shows there is no significant material flaw at the origin, but the ceramic and the epoxy are debonded at the origin.*

Case 8: Maligned Machinists (Bend Bars from Machine Shops)

This case was part of an investigation whether different machine shops could prepare common bend bars to a set of specifications, with minimal damage and at a reasonable cost. The work described here was done in the 1980s in support of the first standard test method for flexural strength of high performance ceramics in the United States, MIL STD 1942(MR).[13] The standard, which was adopted by the U.S. Army in 1983, served as a basis for American Society for Testing and Materials standard C 1161 in 1990[14] and (along with elements from analogous European and Japanese standards) was used as the basis for Inter-national Organization for Standards ISO 14704 in 2000.[15] Standardization has led to dramatic improvements in the quality of data and significant cost savings. Bend bar costs decreased as machine shops prepared specimens to a common, reliable procedure.

As part of the standardization work, a major international round robin on flexural strength with 11 labs around the world was conducted in 1984 and 1985.[16,17] Several thousand specimens of 99.9 % pressureless-sintered alumina and reaction bonded silicon nitride were tested. The round robin showed that consistent flexural strength results could be obtained if the standard procedure with defined test fixtures and alignments were used.

It has long been known that grinding may introduce strength-limiting damage. A side topic investigated in the round robin was whether different machine shops could meet the grinding specifications and prepare damage-free B type bend bars (3 mm x 4 mm x 50 mm). Requests for price quotations were sent to eight machine shops to prepare 20 specimens from the sintered alumina according to the MIL STD 1942. The specifications were for a multi-step grinding process ranging from coarse initial grinding to final finishing. Finer grinding wheels with reduced depths of cut were used at each step with the objective of removing prior damage and minimizing final residual damage. One shop did not bid. Two others bid $101 and $112 per bar and were not contracted since these prices were exorbitant. In 1984 – 1985 the typical price for bend bars from experienced shops were in the $12 to $25 range. Plates from the common batch were sent to each of the remaining five shops which bid from $15 to $50 per bar. The bars that they machined were then broken in four-point flexure on 20 mm x 40 mm spans. The surfaces and edges of all bars were inspected beforehand to ascertain whether the bars met specifications or if there were any signs of machining damage. The results are shown in Table 10.1. The initial visual examination showed that the five venders met all of the specifications for the most part. Deviations were usually on isolated

specimens. Machining damage can be hidden, however, and the strength testing was intended to reveal the damage.

A comparison of the average strength values suggested that venders B, C, and D damaged their specimens since the strengths of their specimens were much lower than those from shops A and E. It would have been tempting to reject venders B, C, and D for further jobs on the basis of the strength outcomes, but the fractographic analysis revealed a surprising explanation for the outcomes.

Optical examination of the fracture surfaces revealed that machining damage was not the prime factor in any of the five samples sets. Machining cracks did cause fracture in a few specimens, but the primary strength-limiting flaws were volume-distributed sintering flaws such as pores, porous zones, porous seams, agglomerates, and occasional inclusions. Figures 6.6a, 6.13, and 6.66a,e show some of these. The crucial difference was that the *flaws varied between the plates.*

Shop	Bar Price $	Were the specifications met?	alumina plate	Avg. MPa	Std. Dev. MPa	Char. Str. MPa	Weibull Modulus	Fracture Origins
A	15	Yes	P	372	42	391	10.3	Round pores Porous zones Porous seams 2 machining
B	19	Yes, a, b	2	315	22	325	17.1	Porous zones Porous seams Agglomerates 4 machining
C	20	Yes, c	1	301	30	314	11.5	Porous seams Pores Agglomerates
D	41	Yes, b	3	335	32	350	12.0	Porous seams Porous zones Agglomerates
E	50	Yes, b	4	373	36	389	11.9	Pores Agglomerates 2 machining

a Minor edge chips on some
b Some skip marks or deep striations
c Chamfers a bit uneven

Table 10.1 *Flexural strengths of sintered 99.9% alumina from test sets prepared by different machine shops. The flaws that were strength limiting are listed in their order of frequency in each set.*

Porosity was the most common flaw type, but it manifested itself differently in the plates. In some plates the flaws were primarily round discrete pores. In other plates, the flaws were equiaxed regions of microporosity, porous seams, or porosity associated with inclusions. The plates were prepared from the same powder lot by the identical procedure and to all external appearances were identical. Only when the specimens were fractured was the true flaw character revealed.

This case illustrates the hazards of interpreting strength results without supportive fractographic analysis. The variability in flaw character between billets and its effect on strength also underscores a serious problem for structural ceramic designers. If the flaws in a material vary between nominally identical ceramics pieces, this does not bode well for the success of reliability analyses.

Case 9: Modeler's Match (Fracture Origins in MEMS Scale SiC Micro Tension Specimens)

Testing methodologies must keep pace with emerging technologies for miniature devices and structures for microelectromechanical systems (MEMS) and even smaller devices. Sharpe et al.[18] investigated the strength of miniature silicon carbide specimens shown in Figure 10.21. These had cross section sizes of ≈ 200 μm or less and were prepared by Beheim at NASA-Glenn by chemical vapor deposition (CVD) followed by deep reactive ion etching (DRIE) to final shape.[19] Specimens with straight, curved, and notched gage sections were tested in direct tension and fractured in a special miniature tensile tester. Weibull statistics were applied to scale the strengths and to determine whether surface or volume flaw scaling gave better correlation. The Weibull analysis using area scaling worked reasonably well for the curved and straight specimens, but gave a poor correlation for the notched specimens, which were much weaker than expected.

Fractographic analysis was difficult, but productive.[19,20] The CVD SiC had a coarse microstructure that created a very rough fracture surface that masked common fracture markings. Large SiC grains affected the crack propagation across the fracture surface, causing significant crack redirection and severe roughness as the propagating crack sought out preferred cleavage planes. The most helpful features for pinpointing the origin were twist hackle lines on cleaved grains and occasional large hackle lines that showed the local direction of crack propagation. These markings led back to the origins.

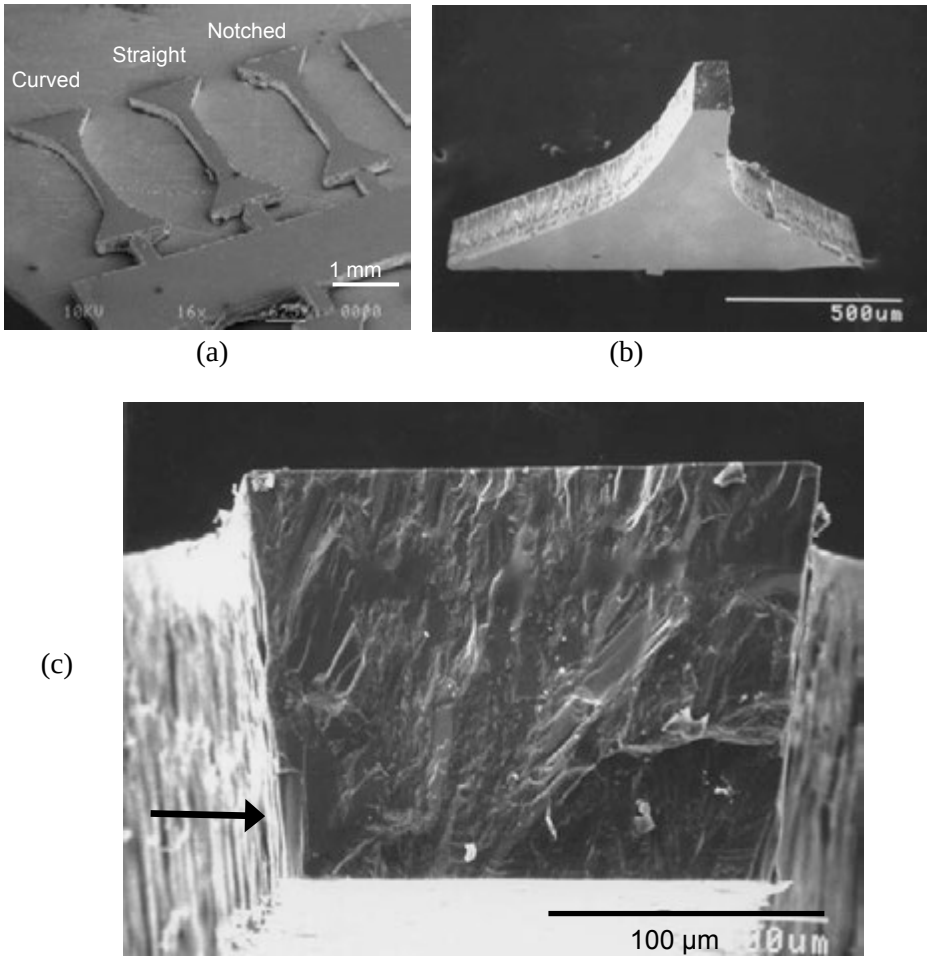

Figure 10.21 *Miniature 3.1 mm long SiC tensile test specimens. (a) shows curved, straight and small notched gage sections. The notch is too small to see in this view. (b) shows a fractured curved gage length specimen (c) shows the fracture surface of a straight section specimen. The arrow shows the origin is a 25 μm x 50 μm large grain at the root of an etch groove. (photos a and b, courtesy of W. Sharpe)*

The fracture origins in all three specimen types usually were a combination of a deep etch groove that combined with a large, favorably-oriented columnar grain. Cracks popped-in on a preferred cleavage plane in such grains. Thus, most critical flaws were a hybrid surface-volume type flaw: a sidewall groove and a large grain as shown in Figure 10.21c. The fractographic results supported the Weibull area scaling for comparing the straight and curved

specimens, and the best correlation was obtained if only the etched *sidewall areas* were used in the calculation.

The reason the Weibull strength scaling did not work for the intentionally-notched specimens became obvious as shown in Figure 10.22. The notches were quite small (15μm to 25 μm radius). They concentrated stress to a very small region around the notches. Hence, the Weibull effective volumes or areas were tiny, and comparable to the size of some of the single grains. Hence, one cannot assume there is a well-distributed set of flaws scattered throughout the stressed volume, as is assumed in conventional Weibull analysis. Furthermore, an analysis based on continuum mechanics assuming the material was isotropic and homogeneous is questionable.

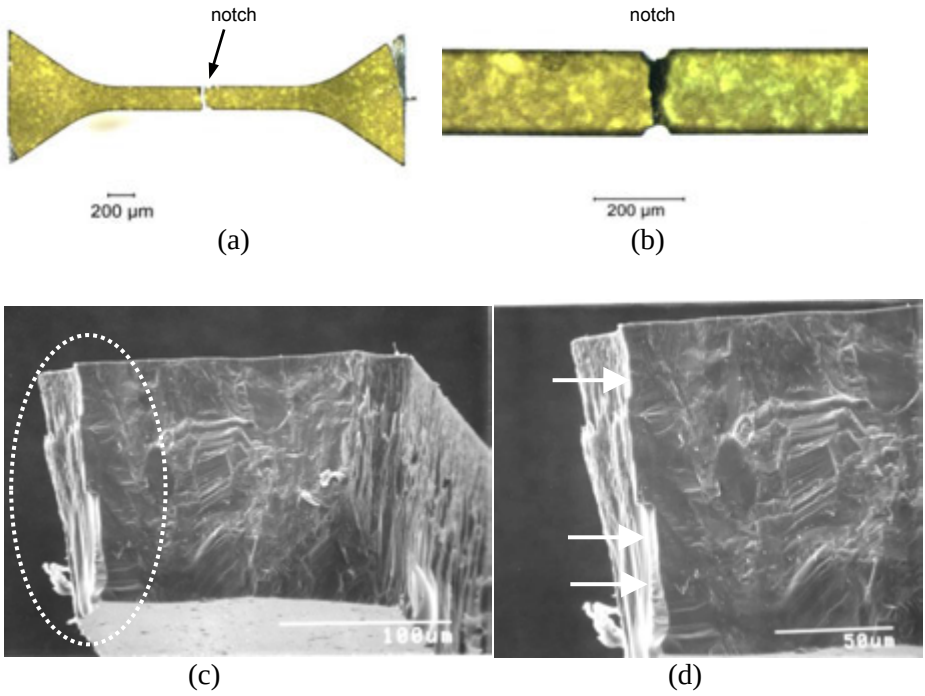

Figure 10.22 *A broken notched miniature SiC tensile specimen. (a) shows the whole specimen. (b) shows a close-up of the gage section notches. Trans-illumination through the green single crystal SiC grains created the light patches. They are individual grains. (c) and (d) show the fracture surface. Fracture started at the bottom of the round notch (arrows), from a etch groove linked with a single long and large columnar SiC grain that ran from the top to the bottom.*

Case 10: Fractious Fractographers (A Fractography Round Robin)

Can different fractographers agree on fracture origin analysis? Can they reach similar conclusions? How do they exercise their craft?

These were questions addressed in an international round robin conducted in the mid-1990s.[21] Round robins are interlaboratory exercises using a common procedure. There are many reasons for conducting a round robin, but usually the goals are to evaluate whether different laboratories can apply a prescribed procedure and obtain consistent results, or to generate test method uncertainty data such as repeatability or reproducibility precision estimates.

This author and Dr. J. Swab of the U.S. Army Materials Technology Laboratory (now with U. S. Army Research Lab, Aberdeen, MD) conducted a major international round robin on characterization of fracture origins of advanced ceramics in 1994 - 1995. Seventeen laboratories participated. The participants had experience that ranged from zero to thirty-five years. The project was coordinated under the auspices of the Versailles Advanced Materials and Standards (VAMAS) program. This work evaluated a new (1992) set of guidelines for finding and characterizing fracture origins in ceramics: "Fractography and Characterization of Fracture Origins in Advanced Structural Ceramics," Military Handbook MIL HDBK 790[22] which was a predecessor to ASTM Standard Practice C 1322,[23] the world's first fractography standard for characterizing fracture origins.

Topic 1 of the VAMAS round robin was a photo interpretation exercise with focus on detection and characterization of grinding damage in bend bars. Photos of one specimen each of silicon nitride, a zirconia-alumina composite, and an alumina were furnished. Six photos of each specimen were provided showing for each half, a low magnification overall shot, a picture of the fracture mirror area, and a close-up of the origin area. Results were mixed. There was consensus that the origins were machining cracks, but there was considerable variability in how they were marked and measured. Some participants disagreed and felt the origins were not grinding damage. Although a short paragraph on each specimen with strength and fracture toughness information was furnished along with the photos, very few of the participants used this information to estimate a critical crack size. Participants were also asked to mark and measure the fracture mirror sizes on the photos. The organizers were surprised at the scatter in mirror size estimates. Evidently many participants were not familiar with measuring fracture mirrors.

Topic 2 was an actual examination of six bend bar strength specimens. Each participant received one example of the specimens listed in Table 10.2. Most were carefully prepared (no small feat) by Dr. Swab. Again, results varied. Most participants had no trouble identifying the pore as the fracture origin in specimen #3. Many had difficulty with the others. For example, the scratch that caused cracking damage in specimen #2 was sometimes identified as machining damage or even a pore or large grain. Figure 6.25c shows one of these scratched specimens. The scratch should have been obvious. Dr. Swab had made it with a diamond indenter and it stood out very clearly on the tension surface of the bend bar. Evidently some participants *did not bother looking at the external surface* and only looked at the fracture surface.

In the other specimens, participants looked at only one half. Sometimes this was satisfactory, but in just as many cases observers looked at the less clear piece.

Many participants evidently did not read the brief four to six sentences of information furnished with each specimen, including treatments if any and the breaking stress and fracture toughness. For example, the surface pit origin specimens #4 had been exposed to an oxidizing environment at high temperatures. Some labeled the origin a pore and ignored the surface condition and reaction zones around the pits. Only a few participants estimated flaw sizes from fracture mechanics and compared them to their fractographically-measured sizes for verification.

Specimen type	Material	Origin Flaw
1	Hot-pressed alumina with silicon carbide whiskers	Large grain
2	Sintered 99.9% alumina	Handling damage (scratch)
3	Sintered 3 mol% yttria stabilized zirconia (Y-TZP)	Pore
4	Reaction bonded silicon carbide	Surface Pit
5	Hot isopressed silicon nitride	Machining damage
6	Sintered titanium diboride	Porous seam or porous region

Table 10.2 *Bend bar specimen types distributed in Topic 2 of the VAMAS round robin.*

The entire exercise was a learning experience for the organizers. Some participants did very well, but many had difficulty. Much was learned by studying the causes of the misinterpretations. Even for such mundane objects as bend bars, there was considerable variability in how the participants analyzed the photos, the specimens, and the ancillary information provided. Some simply looked at the fracture surfaces and ignored everything else. The organizers came to realize that fractographic analysis (and failure analysis in general) is a process whereby an expert integrates all information including, but not limited to, fracture surface examination. This realization led the author and Dr. Swab to prepare Figures 1.1 (the fractographer as detective) and 1.2 (the fractographic analysis puzzle) of this Guide. The organizers also came to the realization that they had a huge advantage compared to the participants. The organizers could look at many specimens of a type, and were not limited to a solitary example. The participants only had one. Furthermore, there is no substitute for actually looking at the actual specimen under a microscope, as opposed to looking at two-dimensional photographs as in Topic 1. Several of the author's fractographic Rules of Thumb listed in the next chapter stem from this exercise.

Case 11: Perilous Prostheses (Four Ceramic Dental Crowns)

All-ceramic dental crowns are increasingly being used as alternatives to gold or porcelain fused-to-metal restorations (Figure 10.23). A variety of ceramic materials have been used including feldspathic or leucite porcelains, glass ceramics, alumina, and zirconia. These ceramics function as the main load bearing and structural elements of the crown, and are called the "core" or the

Figure 10.23 *A fractured Dicor[c] glass ceramic molar crown. (courtesy of S. Scherrer)*

[c] Dentsply Int., York, PA.

"foundation." The crowns also have a glassy exterior veneer layer added for cosmetic purposes. Brittle, highly-filled resin matrix composites with ceramic or glass fillers are common crown materials as well, but do not need a veneer layer. The fracture resistance and durability of the new ceramic and composite crowns are a primary concern. Despite the sanguine claims of the manufacturers, premature fractures do occur, much to the consternation of the patient and his or her dentist.

Progress in the field has been typified by a trial and error approach. The usual approach has been to statistically analyze the rates of failures and infer or guess causes of failures. There are conflicting explanations as to why the crowns do or do not fail. It is not even clear what properties are desired and what are the best laboratory-scale tests to evaluate these properties. Until the late 1990s, postmortem failure analyses were quite rare.

One key reason for this was that dental ceramic crown fractures are in fact among the most challenging problems to solve. Many dental ceramics have coarse-grained and/or porous microstructures. They often fracture at low stress and classic fractographic markings are often masked by the roughness of the fracture surface. High-density aluminas and 3Y-TZP zirconias are exceptions and are easier to interpret. Another complication is that stress states in the crowns are transient and uneven. Fracture mirrors are almost never observed in a clinical fracture since fracture stresses are low, or they are larger than the crown wall sizes. Another difficulty is that key fragments are often missing, either due to loss in the mouth or damage during crown extraction. Crowns usually accumulate damage from multiple events at multiple sites, creating complex, conflicting fracture networks. For example, the author has often detected Hertzian cone crack damage sites on crown occlusal and facial surfaces, but has only seen a few instances where the cone acted as an actual crown fracture origin. The Hertzian cones crack damage sites usually are dormant. Contact damage does occur and cause clinical failures, but it almost always in due to *edge chipping*.

Fractographic analysis of all-ceramic dental prostheses is a field where recent fractographic analyses have been very productive.[24,25,26,27,28,29] Additional references are listed in the Appendix B, Case Studies. The following four crown fracture case studies illustrate the progress that has been made. Figure 10.24 shows a Cerestore[d] alumina-magnesia spinel fractured molar crown that was documented by J. Quinn et al., in Ref. 24. In this and the

[d] Originally developed by Coors Biomedical, Lakewood, Co.. Available later from Ceramco Inc., East Windsor, NJ.

following three examples, gold coating has made the veneer look dark in the optical images and the core material lighter. The origin was located at the margin (or bottom) of the crown and the vertical-split nature of the fracture suggests that hoop stresses around the bottom of the crown, where the crown

(a)

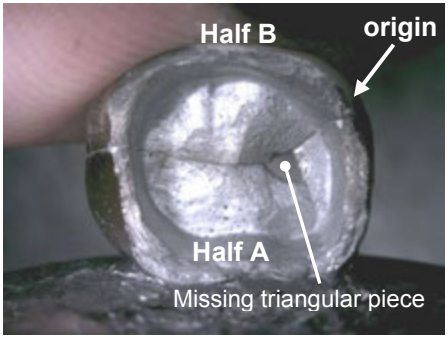

(b)

(c)

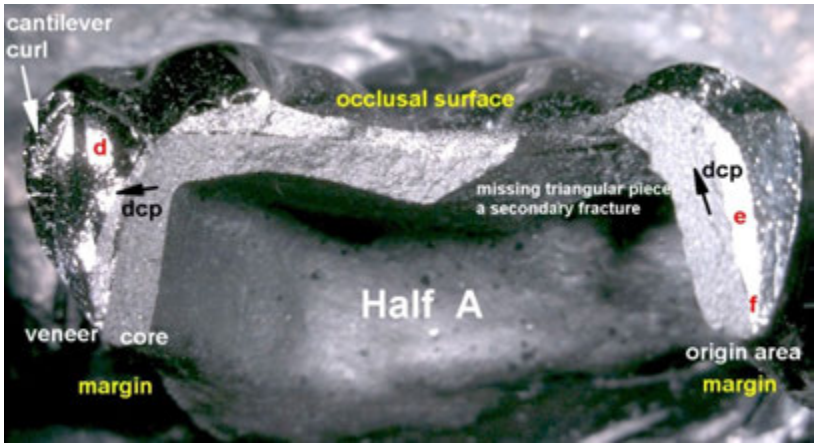

Figure 10.24 a-c *Fractured alumina-spinel molar crown. (a) is a top occlusal surface view showing the two halves held together. Half A is fully- and half B is partially-gold coated. (b) shows the interior looking up into the crown. The missing triangular piece was caused by secondary breakage. The origin was on the margin, at the bottom of the crown. (c) shows an optical photo of the fracture surface with arrows showing the local crack propagation direction. The dark outer regions are the gold-coated glassy veneer. The lighter gray portions are the gold-coated core ceramic material. The letters d, e, f identify regions shown in images (d) – (f) on the next page. (images courtesy J. Quinn)*

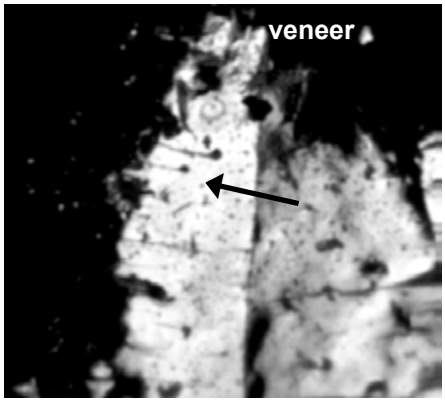

(d)

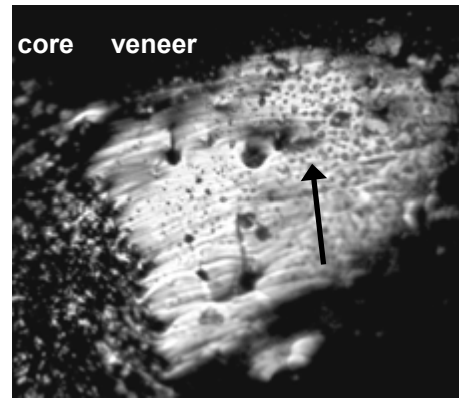

(e)

(f)

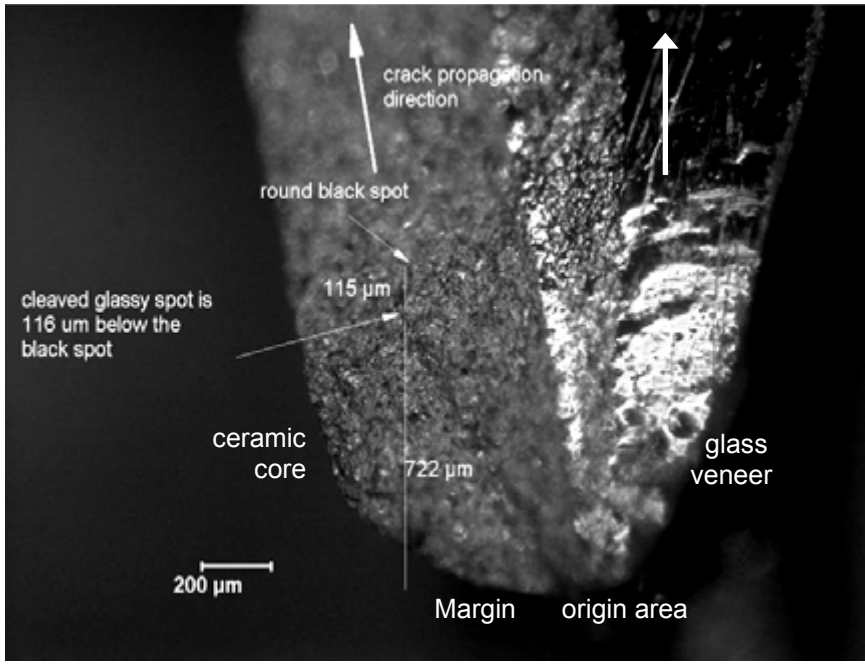

Figure 10.24 d-f (continued). *(d) wake hackle from tiny bubbles in the veneer glass. This location is marked on the left of view (c) and indicates the crack moved right to left (arrow). (e) shows wake hackle and gull wings from bubbles in the veneer on the right side of the crown. At this location the crack was running upwards from the margin. Careful scrutiny of the adjacent core ceramic material showed that it also had wake hackle generated by pores in the ceramic pointing in the same direction. (f) is an optical image from the origin area at the margin. There is no obvious flaw.*

was the thinnest, caused the breakage. A specific material flaw could not be identified. This is not unusual with dental crown fractures: an exact site is identified, but a specific flaw is not obvious. It is very likely that an initial radial crack has popped-in at some point, and then final fracture occurred on the same plane. Sometimes the final fracture will be on a slightly different plane, and an arrest line from the pop-in will be apparent as evident in the next example given below. By the time the crack propagated over to the opposite side of the crown, the two halves hinged apart in bending, creating the compression curl.

Figure 10.25 shows a second example, a similar case from Ref. 24, but for a Procera 99.9% purity alumina.[e] It also split vertically, evidently in response to a hoop stress. The fractographic markings again lead to a margin origin site. A specific single material flaw is not evident. In the first edition of this Guide, the author stated that the origin site coincided with the end of the cement bond to the core material, on the inside of the crown. The author reevaluated the crown and now believes the origin was in fact a barely-discernable semicircular crack in the core material at the end of the margin as shown in Figure 10.28f+g. The origin crack was on almost exactly the same plane as the final fracture. It was not discernable in SEM photos. From its size (179 μm radius), and using

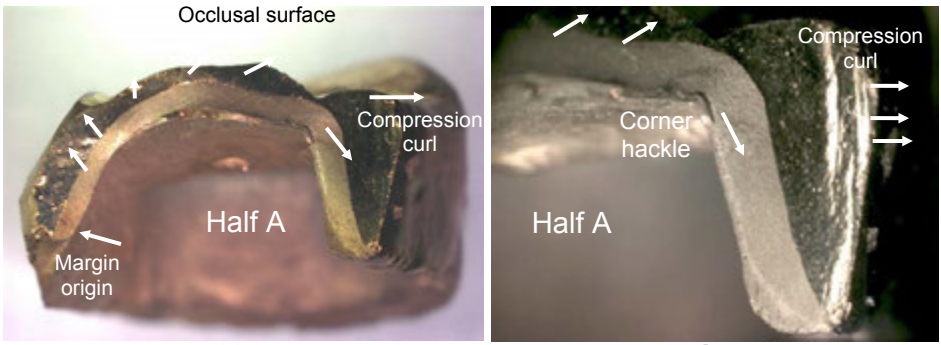

(a) (b)

Figure 10.25 *Procera alumina molar crown. The crown split vertically into two halves. The fracture surfaces have been gold coated. (b) is a close-up of the compression curl on the side away from the origin site. The veneer glass is dark and the core ceramic is a lighter shade. The arrows show the dcp from: corner hackle around the inside corner, the compression curl, and from veneer wake hackle. (c) – (g) are on the next page.*

[e] Nobel Biocare, Stockholm, Sweden.

K_{Ic} of 4.0 MPa√m for dense fine-grained alumina, and a Y of 1.4, the hoop stress at fracture was estimated to be 213 MPa. The margin in this example was well-prepared and over 1 mm thick.

(c)

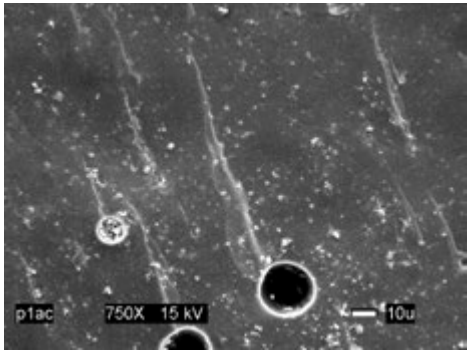

(d)

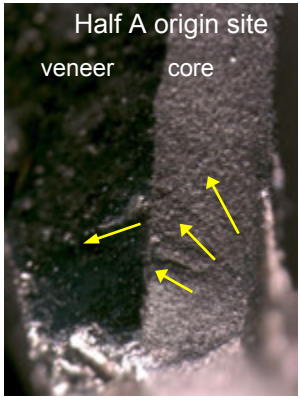

(e)

(f)

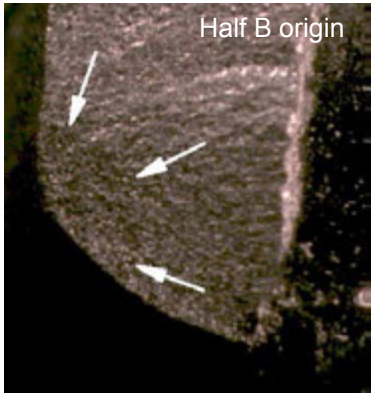

(g)

Figure 10-25 continued. *(c) and (d) are examples of wake hackle from pores in the veneer. (c) is an optical image, and (d) is an SEM image. (e)-(g) show optical images of the margin. The origin is a subtle margin crack as marked clearly in (f) and (g). This origin crack was so flat and coplanar with the final fracture surface, that it did not stand out well in SEM images. (all images courtesy of J. Quinn and S. Scherrer)*

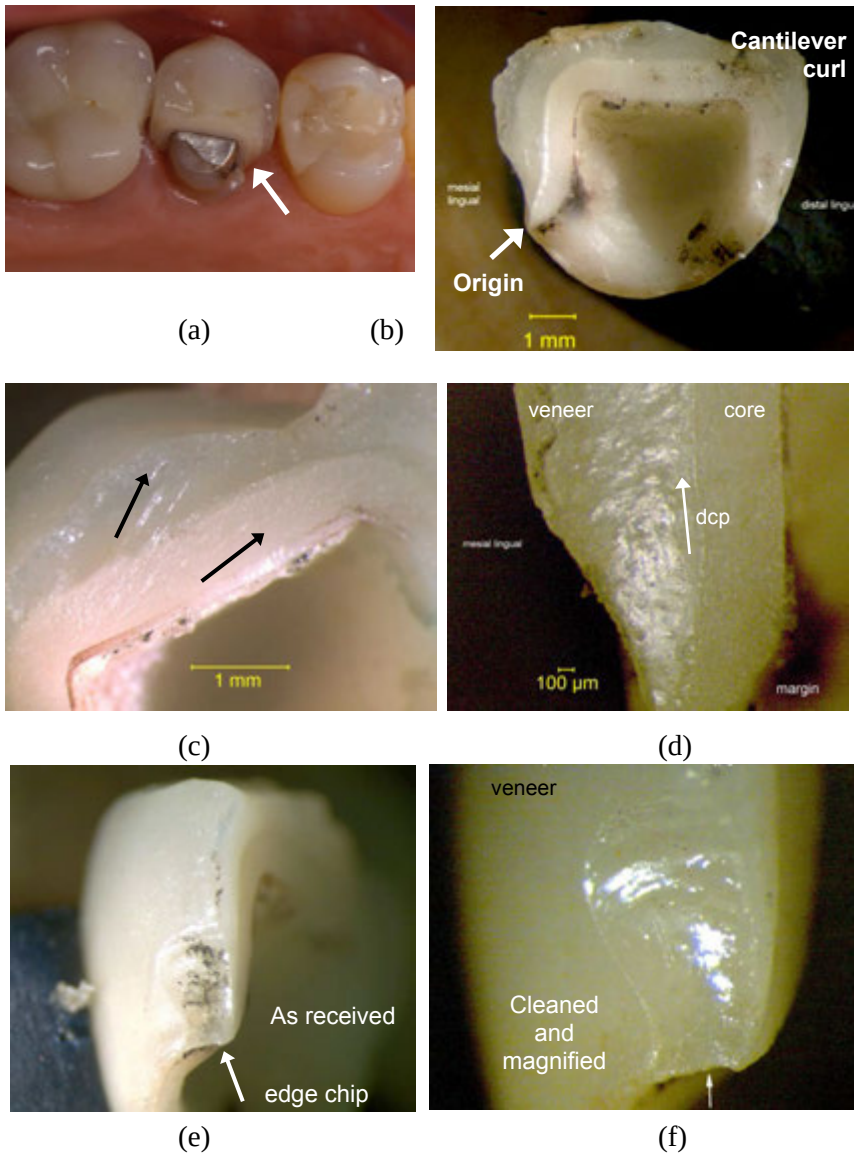

Figure 10.26 *Procera alumina molar crown that broke from a margin chip. (a-f) are optical images without any coatings. (a) is a clinical view with the origin marked. (b) is one half of the fractured crown. (c) shows a fanlike array of corner hackle (between the two arrows which show the propagation direction) in both the veneer and core emanating from the top inside corner. (d) is from near the margin on the left side and shows tiny wake hackle from veneer pores. The crack ran from bottom to top. (e) and (f) show the origin was an edge chip from a force applied on the bottom of the margin aimed upwards (image a courtesy of S. Scherrer).*

The third crown, also a Procera alumina, is shown in Figures 10.26 and 10.27. It also has a margin origin site that led to crack propagation by hoop stresses. Images 10.26 a-f are all optical images of the crown without coatings. As such, some of the details were "washed out" and did not photograph well due to the material's translucency and light scattering. Nevertheless, this crown failure was diagnosed solely on the basis of an optical examination with a stereo optical microscope. Subsequent SEM examination produced the sharper images shown in Figures 10.27. A full fractographic montage for this crown was shown previously as Figure 5.68.

Corner hackle around the inside corners of the core, a compression curl, and wake hackle again led back to a margin initiated fracture origin. A well-defined edge chip on the veneer was the origin. The edge chip was discolored suggesting that it had been present for quite some time. The direction of the edge chip was puzzling as well. It appeared to have been from a force directed upwards on the crown. Such a loading is not likely in the mouth since the margin is protected by the gum line and jaw. The chip was probably created during fabrication or installation.

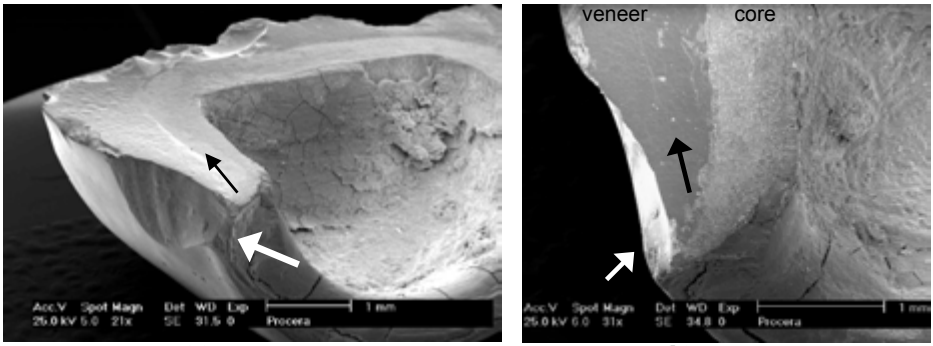

(a) (b)

Figure 10.27 *SEM images for the Figure 10.26 Procera crown that broke from a margin chip (arrows). The final fracture that split the crown started at the bottom at the margin, from part of the margin chip, and ran as shown by the black arrows. (images courtesy of S. Scherrer)*

The fourth crown shown in Figures 10.28 -10.31 is an Empress II lithium disilicate glass ceramic incisor.[f] The crown had been in service only 4 months when it split into two pieces. No information was furnished on how the fracture event occurred or on the installation or fabrication of the crown. The

[f] Ivoclar, Schaan, Liechtenstein.

fracture plane was vertical and perpendicular to the dental arch. The two halves fitted closely together. A few small chips were missing, probably from secondary fracture, and were inconsequential to the analysis. The lingual surface (the side that faces the tongue) had some surface damage and also an unusually thick veneer. There were several shallow depressions (≈ 1 mm^2 square area) as well as numerous conchoidal chip fractures, small pits and gouges at mid crown height. The shallow depressions had tool marks indicating they were from adjustments to the lingual surface by the dentist once the crown had been cemented in place and opposing tooth contact checked. This adjustment was only partially successful in relieving contact from the opposing tooth as evidenced by the numerous pits, chips and gouges. This location was eventually determined to be near the fracture origin region.

The facial surface (the surface that faces outwards) was in good condition and had little damage or evidence of abuse. The unusually thin veneer had a few secondary spall chips and one harmless Hertzian cone crack that did not penetrate into the core material. The chips were noted on one fragment but not on the other, indicating that they were secondary fractures that occurred after the crown had broken.

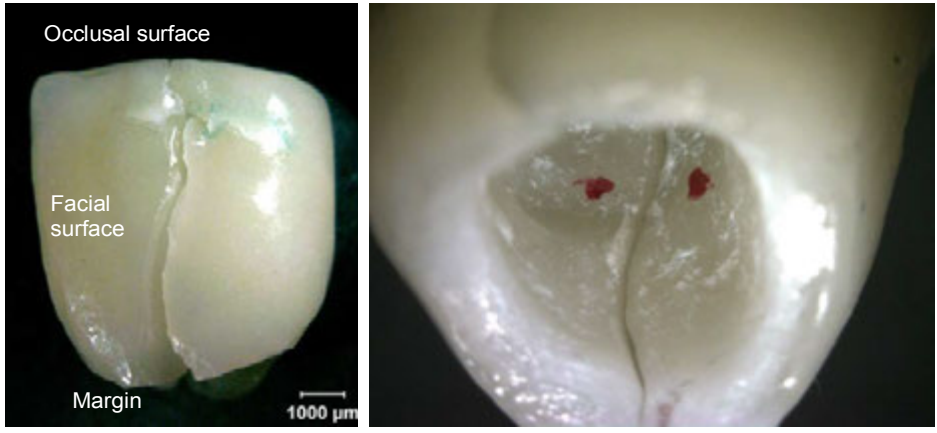

(a) (b)

Figure 10.28 *Fractured Empress II glass ceramic anterior (#7) incisor crown. The insert (a) shows a facial view of the cleaved crown. (b) is a view looking up into the interior with the two halves together. The origin is located between the two red dots on the inside surface.*

(a)

(b)

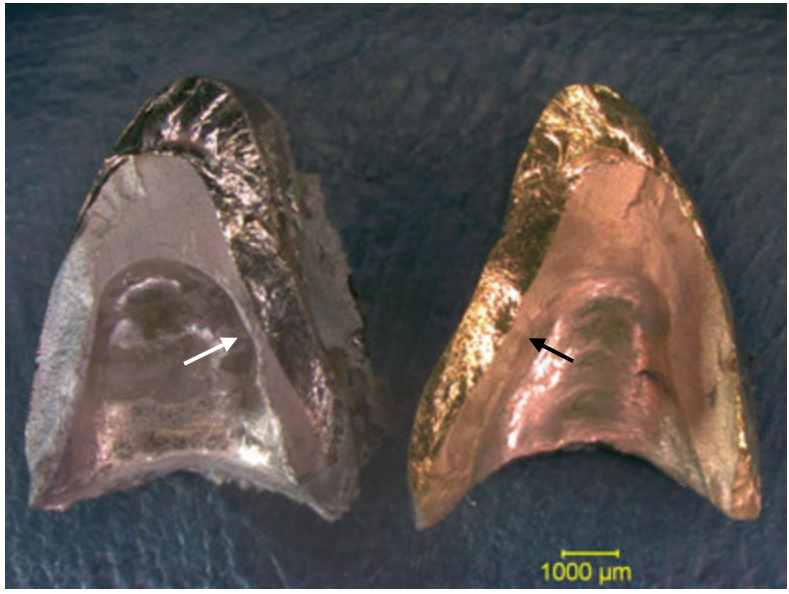

Figure 10.29 *The fracture surfaces of the two halves. (a) shows an optical photo of the uncoated halves. (b) shows gold-coated surfaces. Two different coaters were used causing the different coloration. The gold coating of the glassy veneer reflects more. The veneer thickness is very uneven and out of normal guidelines. It is very thick on the lingual side and very thin on the facial side. The arrows mark the origin site located at the thinnest part of the core glass ceramic material.*

(a)

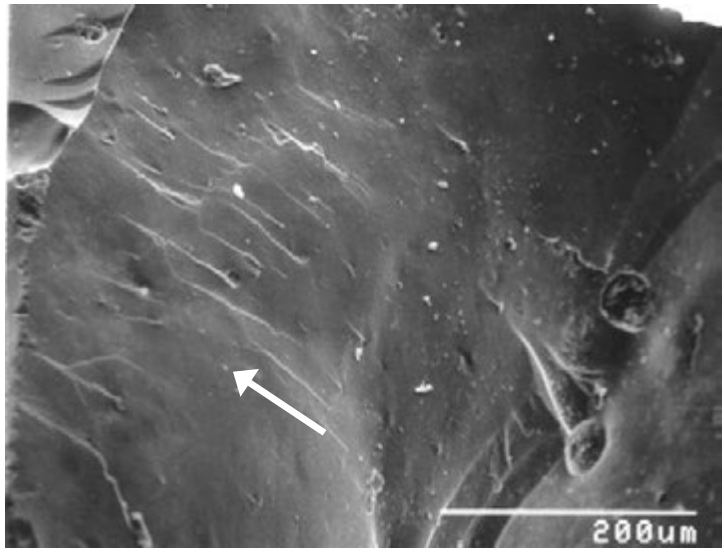

(b)

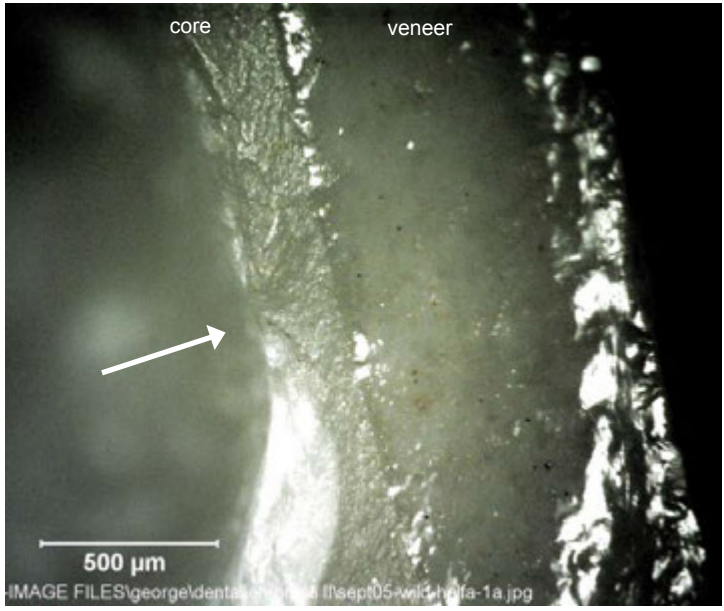

Figure 10.30 *Details of the incisor crown fracture. (a) is an SEM image wake hackle in the glassy veneer from a region near the top (occlusal) surface of the A half. The wake hackle shows that the crack was running in the direction of the arrow in this region. All the wake hackle in the entire crown showed fracture ran from the inside to the outside. (b) is an optical image of the origin which originated from a contact crack on the inside of the crown at the thinnest point of the core.*

(a)

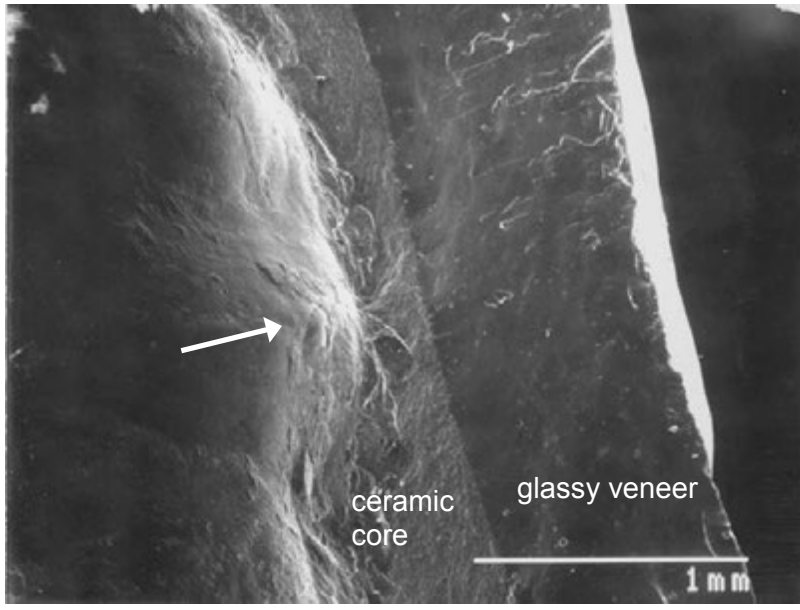

(b)

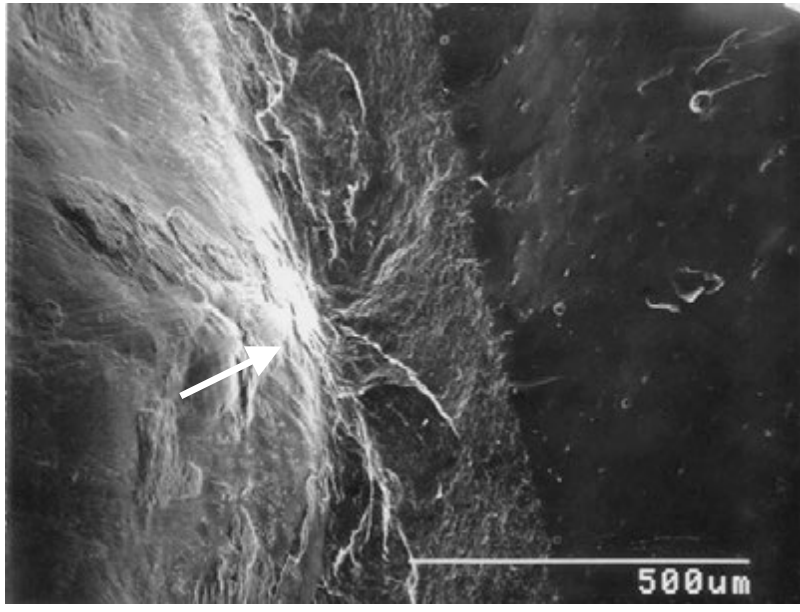

Figure 10.31 *SEM images of the origin. Notice all the wake hackle in the veneer aiming away from the interior. The crack ran from the inside to the outside. The inside surface is uneven and there are mold or tool marks in the vicinity. This region is directly opposite a region of extensive localized contact damage on the outer veneer surface.*

There was negligible damage on the occlusal (top) surface. Some residual porous powdery material was detected on the inside surface of the crown and was the remnants of the cement. Tool grinding marks and/or casting impression marks were detected on the inside of the crown.

Green dye staining for an optical examination and subsequent SEM examination brought out a number of telltale brittle material fracture features. Fractographic markings in the glass ceramic core material were difficult to detect, but subtle hackle markings were similar to features observed on bend strength test specimens of the same material. Extensive wake hackle was detected from bubbles in portions of the glassy veneer as shown in Figure 10.30a and 10.31,a,b. Seven or eight crack arrest lines were also detected.

This was a difficult analysis. Initial examinations had only limited success, but with repeated careful scrutiny of the fragments using different examination techniques (optical, optical green dye coated, optical gold coated, and SEM) enabled the author and J. Quinn to find the origin region. Maps of crack propagation direction were constructed, primarily through observations of the wake hackle markings in the veneer. Fracture initiated in the core material (where it was very thin) from an *internal* surface Hertzian cone crack. This location was in the same vicinity where *external* lingual surface damage has also been detected. Fracture then radiated upwards and downwards in response to hoop stresses causing the crown to split into two halves.

Only after repeated examination was it realized that both fracture halves showed matching damage features characteristic of blunt contact damage at the exact same location on the inside (cementatious) surface of the crown. The critical observation occurred when stereo SEM paired images were viewed of this area, and the arc-shaped crack that is typical of blunt contact damage was revealed. It was further observed that the inside crown surface was uneven and had raised hills, ridges, and depressions.

In summary, the Empress II incisor crown had uneven veneer and core wall thickness. Fracture initiated from contact damage on the *inside* of the crown, probably due to an uneven fit or improper placement. Opposing tooth contact in the same vicinity on the crown exterior surface (as evidenced by shallow pit and chip damage) created the stresses in the origin area. Surface grinding adjustments made to the same area suggested a fitting problem.

These four crowns broke from hoop stresses and split vertically, perpendicular to the dental arch. Specific gross material flaws were not be detected in any of the four.

Case 12: Case of the Mangled Margins (Twenty dental crowns)

Recent work that typifies progress in the dental fractography field is presented here. The failures shown above in Case 11 were *isolated cases.* Most failure analyses have been on such isolated examples or on batches of laboratory-tested (*in vitro*) crowns, which may or may not be accurate representations of *in vivo* failures. Indeed, many "crunch the crown" tests with loading by steel or tungsten carbide balls on the occlusal surfaces are ridiculous and clinically irrelevant.

The cases presented here are the first study to identify a single leading cause of fracture, with high specificity, for a large number of cases in one particular restoration system. Prof. M. Oilo at the University of Bergen, Norway has collected dozens of clinical fractures and is organizing them by type. As discussed in Chapter 4, she has also devised a laboratory set-up that causes crowns to fracture into the same patterns as clinical fractures.[30,31] The author and she identified the fracture origins in twenty-two crowns of a set of twenty-seven retrieved crowns, all from one material system.[32] The crowns were all high-alumina crowns prepared by CAD/CAM machining. They fractured *in vivo* from times as short as days to years. Twenty-one of the twenty-two crowns (95%) broke from one cause: hoop stresses on the margins that split the crowns, usually at the area of shortest wall length in the approximal area, with the fracture origins being irregularities in the margin including chips, grinding cracks and veneer irregularities. Figures 10.32 - 10.34, show several of the fractured crowns.

One common element in all these crowns was irregular grinding damage on feather margins that were as thin as 100 μm (0.1 mm). Compare these margins to the nice, thicker ones in Figures 10.24 and 10.25. It is unwise to make thin ceramic margins since they are vulnerable to all sorts of machining and handling damage and chipping.

Dental material fractography is making progress. We now can analyze clinical fractures by the dozens. Patterns are emerging. Analysis in this alumina crown project was still time consuming, but it went quicker the more that we did. Over two thousand images were taken and organized and assembled into one gigantic PowerPoint file, which served as our record-keeping and organization tool. Of note is that the origin area was identified in all crowns by light microscopy. We learned that gold coating the specimens dramatically speeded up the process. Green dye worked, but gold coating was better. It was then not too difficult to get the appropriate piece and area in the SEM and focus on the origin itself.

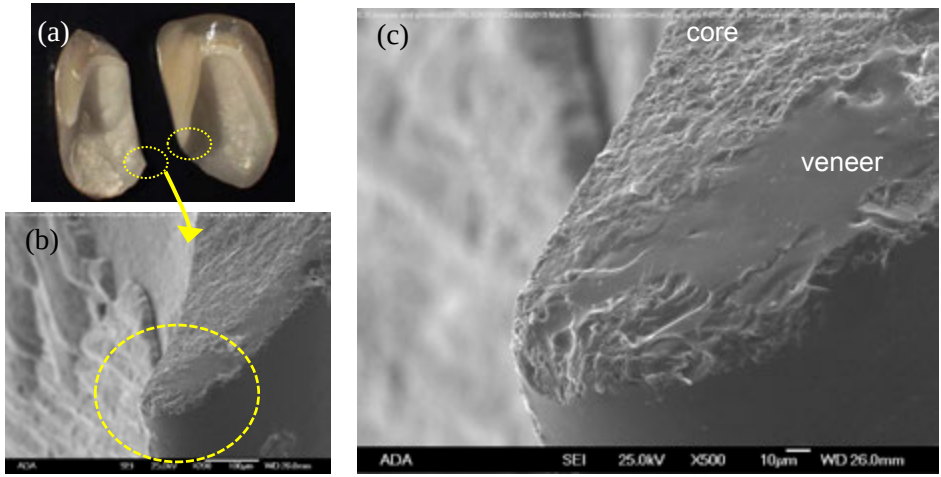

Figure 10.32 *Alumina central incisor that broke in vivo after 1 year. Fracture started at the margin from cracking in both the veneer and core. The margin is too thin, and even worse, the core portion is exceptionally thin. The origin is chipping damage at the margin. (clinical case 2)*

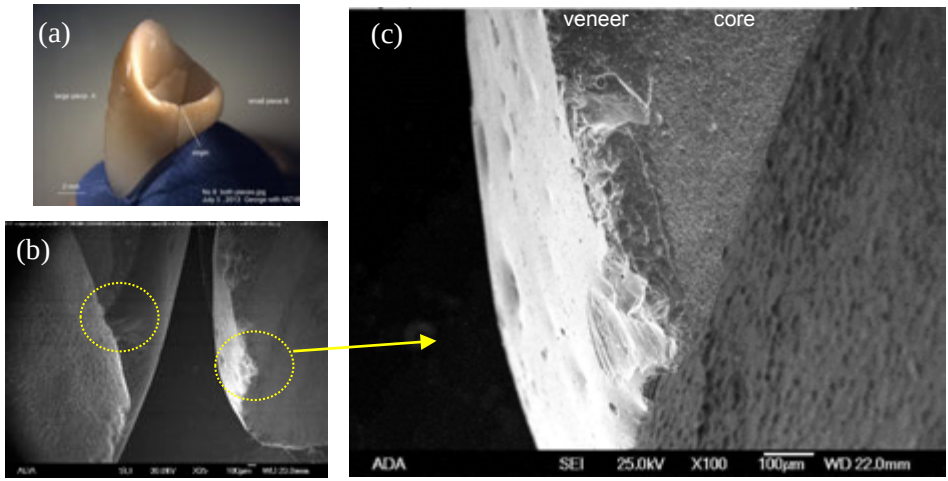

Figure 10.33 *Alumina incisor that broke in vivo at an unreported time. Fracture started at the margin from cracks and chipping in both the veneer and core. The crown split in half from the mesial to distal side. The margin is too thin and the core portion is exceptionally thin. (clinical case 8).*

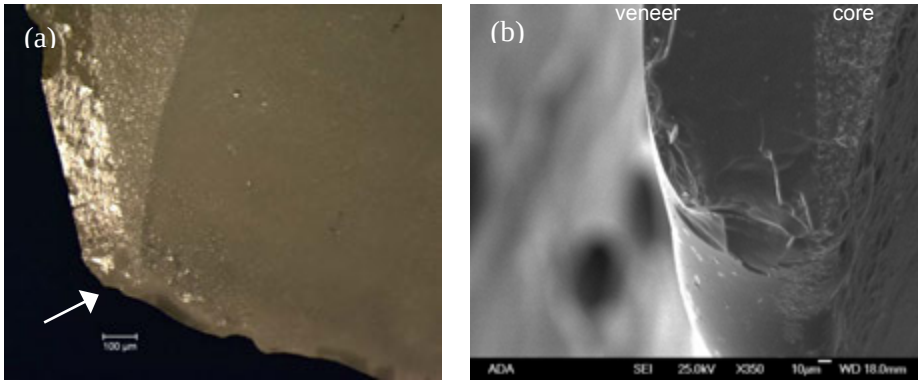

Figure 10.34 *Alumina molar #37 that broke in vivo at 7 months in vivo. It split in half from the mesial to distal side. Fracture started at the margin from cracks and chipping in the veneer which extends to the very tip and even onto the inside surface as evident in (a) Notice the tiny wake hackle lines in the veneer in (a) that show the origin was at the margin. (a) also shows chipping elsewhere on the margin. (clinical case 9).*

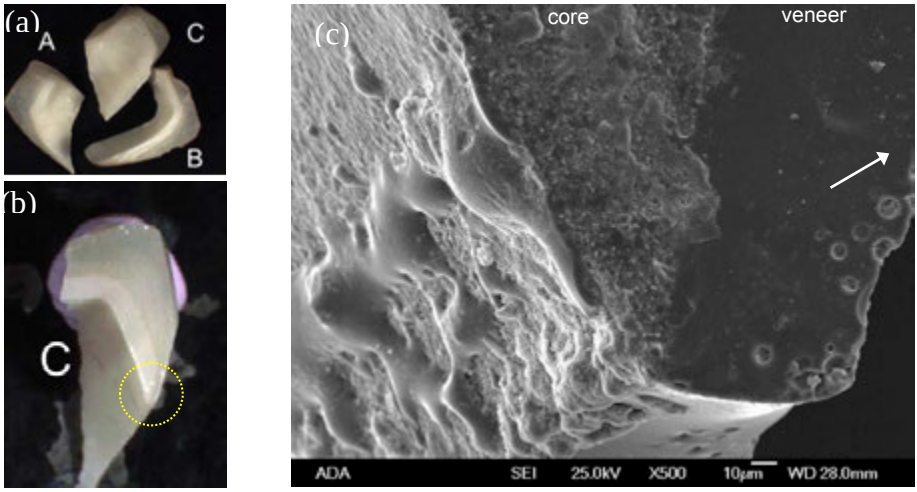

Figure 10.35 *Alumina molar that broke in vivo at 5.5 year in vivo. It split into two pieces, but additional fractures were made during extraction. The initial split was from mesial to distal side. The origin is at the margin of piece C. The SEM image in (c) shows excess veneer that has come into the inside surface and tiny wake hackle lines from the veneer bubbles(marked by the arrow showing the dcp, and the exceedingly small core thickness at the margin tip. Ceramic margins should never be made this thin. (clinical case 12).*

Case 13 Case of the Ruined Refractors (Sapphire Lenses)

This case is of two large elaborate components made of single crystal sapphire. Sapphire is a harsh mistress. She has alluring physical and mechanical properties such as good transmission of optical and infrared light, strengths of 1000 MPa or more, and good high temperature properties. She also has vulnerabilities, such as high variability in strength, sensitivity to contact and machining damage, and a shocking weakness at 300 ^{o}C - 500 ^{o}C due to compression-induced twinning.

NASA is laying the groundwork for spacecraft of the future that could harness solar energy. One concept is to use a large primary mirror solar collector that focuses light to a secondary lens collector. The collector focuses and concentrates energy by total internal reflection into a heat exchanger.[33] Two of these full-scale (30 cm long by 9.5 mm diameter) c-axis sapphire lenses were tested in the giant solar thermal vacuum facility that simulates outer space at the Glenn Research Center. They fractured during high-temperature trials. This fractographic analysis was done by Dr. J. Salem and myself.[33]

Figure 10.36 shows one of the fractured lenses, which has changed to a rose-brown color from solarization at the 1300^{o} C peak temperature of the test. The fracture surface had a mix of cleavage and conchoidal fracture and some crack bifurcations. The fracture origin was on the lens face. The origin shown in Figure 10.37 was a large, partial Hertzian cone crack that extended from one of two partially polished impact divots or “bruises” on the polished surface. From the size of the ring crack, it was deduced that the impact object had a diameter greater than 0.5 mm. Thermal stresses subsequently caused the lens to fracture. This structure also had twins, but they were incidental and not a cause of fracture. Figure 3.59b in the chapter on equipment shows one twin in a polariscope.

Figure 10.38 shows the origin in the second broken refractor. It also broke from an origin on the curved incident surface, again from thermal stresses, but the origin was a scratch. Unusual “micro twins” were found near the origin site, but they were not associated with the fracture.

Both of these refractors, and some of the earlier IR domes shown in this Guide typify the vulnerability of sapphire to residual grinding cracks, polishing and handling damage. The thermal gradients created both tensile and compression stresses, and it is very likely that with additional high-temperature exposure and cycling, more twins would have formed with the possibility they would have intersected at some point leading to crack formation and eventually fracture.

(a)

(b)

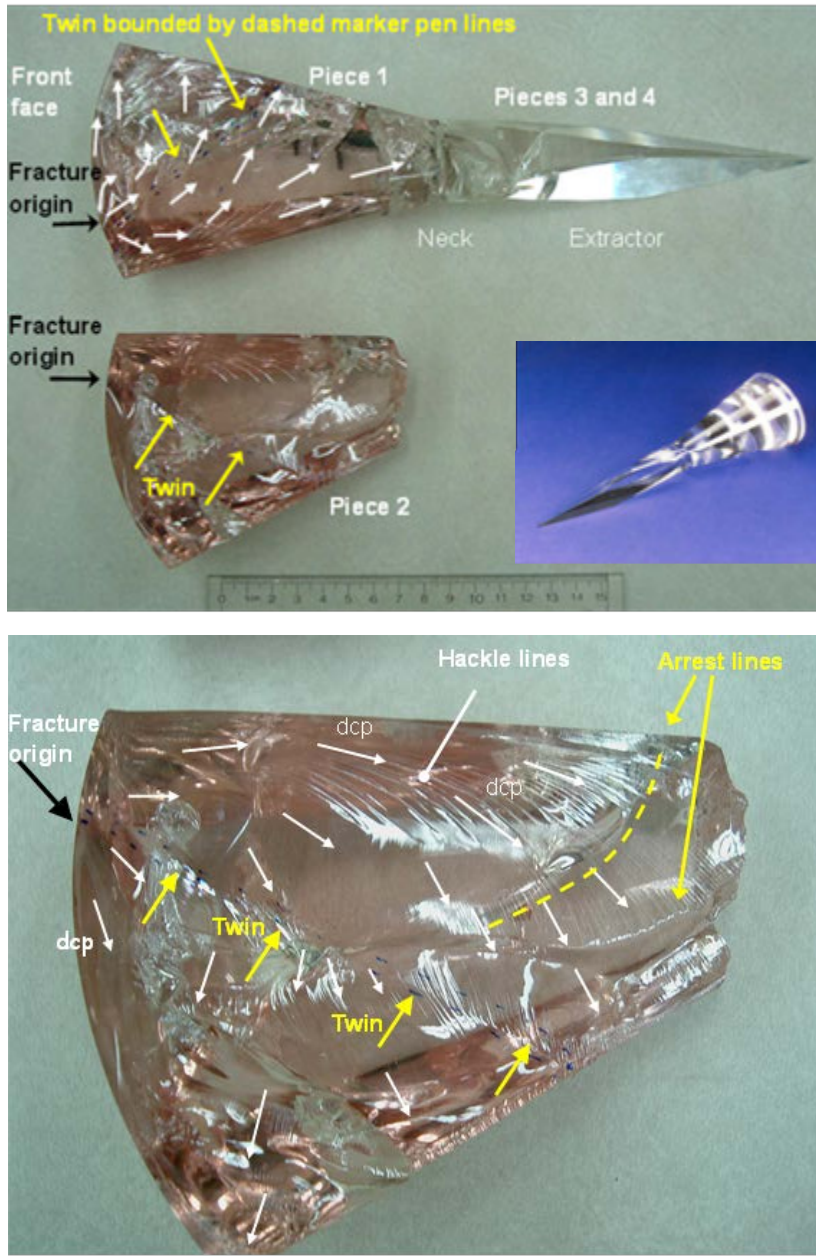

Figure 10.36 *Fractured sapphire solar light secondary concentrator which broke into four pieces. The origin was on the rounded surface where incoming light is focused into the body. The blue insert in (a) shows an intact lens prior to testing. It is a complex but beautiful piece.*

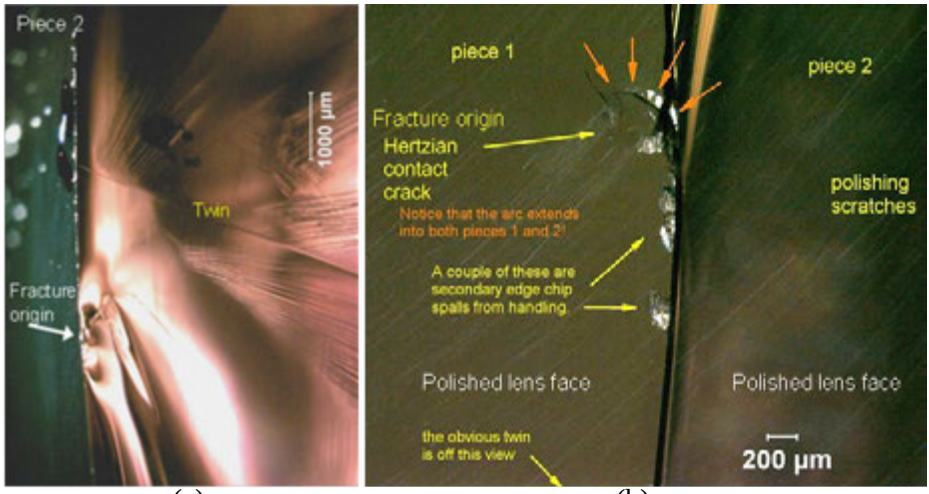

(a) (b)

Figure 10.37 *The origin of the first refractor was a blunt contact damage crack shown on the fracture surface (a) and on the lens face in (b).*

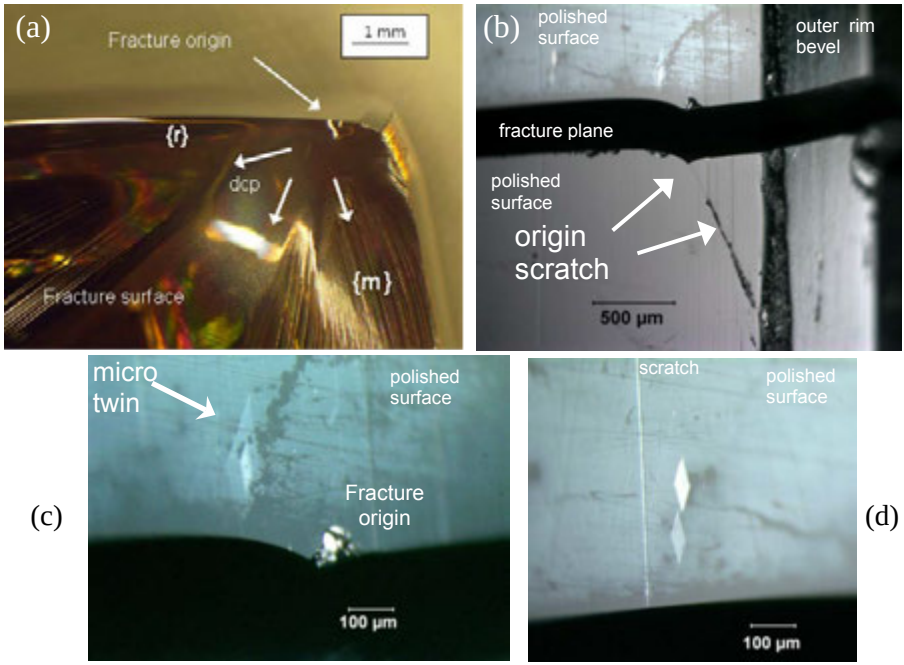

Figure 10.38 *The second refractor lens also broke from damage on the rounded surface, but from a scratch. (a) shows the fracture surface. (b) shows the scratch on the outer polished surface. It curves at the origin site. With careful lighting in (c) and (d), "micro-twins" near the origin site are revealed.*

Chapter 10 References

1. R. R. Baker, L. R. Swank, and J. C. Caverly, "Ceramic Life Prediction Methodology - Hot Spin Disk Life Program," AMMRC TR 83-44, Army Materials and Mechanics Research Center, Watertown, MA, August, 1983.
2. L. R. Swank, R. R. Baker, and E. M. Lenoe, "Ceramic Life Prediction Methodology," pp. 323 - 330 in *Proc. of the 21st Automotive Technology Development Contractors Coordination Meeting*, SAE, Warrendale, PA, 1984.
3. G. D. Quinn, K. Xu, R. J. Gettings, J. A. Salem, and J. J. Swab, "Does Anyone Know the Real Fracture Toughness? SRM 2100: The World's First Ceramic Fracture Toughness Reference Material," pp. 76 - 93 in *Fracture Resistance Testing of Monolithic and Composite Brittle Materials, ASTM STP 1409*, eds., J. A. Salem, G. D. Quinn, and M. G. Jenkins, ASTM Int., West Conshohocken, PA, 2002.
4. G. D. Quinn, "Fracture Mechanism Maps for Advanced Structural Ceramics, Part I, Methodology and Hot-Pressed Silicon Nitride," *J. Mat. Sci*, **25** (1990) 4361 - 4376.
5. K. D. Mörgenthaler and E. Tiefenbacker, "Bauteile Aus Keramik Für Gasturbinen," (Ceramic Components for Gas Turbines), Final Report of Phase III, Daimler-Benz AG, Technical Report, Stuttgart, 1983.
6 E. J. Bunning, D. R. Claxton, and R. A. Giles, "Liners for Gun Tubes – A Feasibility Study," *Ceram. Eng. and Sci. Proc*., **2** [7-8] (1981) 509 -519.
7. G. D. Quinn, "Characterization of Turbine Ceramics After Long Term Environmental Exposure," AMMRC TR 80-15, Army Materials and Mechanics Research Center, Watertown, MA, May, l980.
8. G. D. Quinn, "Review of Static Fatigue in Silicon Nitride and Silicon Carbide," *Ceram. Eng. and Sci. Proc*., **3** [1-2] (1982) 77 - 98.
9. G. D. Quinn and R. N. Katz, "Time Dependent High Temperature Strength of Sintered Alpha SiC," *J. Amer. Ceram. Soc*., **63** [1-2] (1980) 117 - 119.
10. J. Coppola, M. Srinivasan, K, Faber, and R. Smoak, "High Temperature Properties of Sintered Alpha Silicon Carbide," presented at *the International Symposium on Factors in Densification and Sintering of Oxide and Non-Oxide Ceramics*, Hakone, Japan, October, 1978.
11. V. D. Fréchette, *Failure Analysis of Brittle Materials*, Advances in Ceramics, Vol. 28, American Ceramic Society, Westerville, OH, 1990.
12. J. J. Swab, R. Pavlacka, G. Gilde, S. Kilczewski, J. Wright and D. Harris," "Determining the Strength of Coarse-Grained ALON and Spinel," *J. Amer. Ceram. Soc*., **97** [2] (2014) 592-600.
13. MIL STD 1942 (MR), "Flexural Strength of High Performance Ceramics at Ambient Temperature," U. S. Army Materials Technology Laboratory, Watertown, MA, 21 Nov., 1983.
14 ASTM C 1161-90, "Standard Test Method for Flexural Strength of Advanced Ceramics at Ambient Temperature," ASTM Int., West Conshohocken, PA, 1990.
15. ISO 14704, "Fine Ceramics (Advanced Ceramics, Advanced Technical Ceramics) – Test Method for Flexural Strength of Monolithic Ceramics at Room Temperature," Int. Org. for Standards, Geneva, SW, 2000.

16. G. D. Quinn, "Fractography and the Army Flexure Standard," pp. 319 - 334 in *Fractography of Glasses and Ceramics*, eds., J. Varner and V. Fréchette, American Ceramic Society, Westerville Ohio, (1988).
17. G. D. Quinn, "Flexure Strength of Advanced Structural Ceramics: A Round Robin," *J. Am. Ceram. Soc.*, **73** [8] (1990) 2374 - 2384.
18. W. N. Sharpe, Jr., O. Jadaan, N. N. Nemeth, G. M. Beheim, and G. D. Quinn, "Fracture Strength of Silicon Carbide Microspecimens," *J. Microelectromechanical Systems*, **14** [5] (2005) 903 - 913.
19. G. D. Quinn, W. Sharpe, Jr., G. Beheim, N. Nemeth, and O. Jadaan, "Fracture Origins in Miniature Silicon Carbide Structures," pp. 62 - 69 in *Fractography of Advanced Ceramics, II*, eds., J. Dusza, R. Danzer, and R. Morrell, TransTech Publ., Zurich, 2005.
20. G. D. Quinn, "Design and Reliability of Ceramics, Do Modelers, Designers and Fractographers See the Same World?" *Ceram. Eng. and Sci. Proc.*, **26** [2] (2005) 239 - 252.
21. J. J. Swab and G. D. Quinn, "The VAMAS Fractography Round Robin: A Piece of the Fractography Puzzle," pp. 55 -70 in *Fractography of Glasses and Ceramics III*, Ceramic Transactions, Vol. 64, eds., J. R. Varner, V. D. Fréchette, and G. D. Quinn, ACS, Westerville, OH, 1996.
22. MIL HBK 790, "Fractography and Characterization of Fracture Origins in Advanced Structural Ceramics," U. S. Army Materials Technology Laboratory, Watertown, MA, June, 1992.
23. ASTM C 1322-96, "Standard Practice for Fractography and Characterization of Fracture Origins in Advanced Ceramics," *Annual Book of Standards*, Vol. 15.01, ASTM Int., West Conshohocken, PA.
24. J. B. Quinn, G. D. Quinn, J. R. Kelly, and S. S. Scherrer, "Fractographic Analyses of Three Ceramic Whole Crown Restoration Failures," *Dent. Mater.*, **21** (2005) 920 - 929.
25. S. S. Scherrer, J. B. Quinn, G. D. Quinn, and J. R. Kelly, "Failure Analysis of Ceramic Clinical Cases Using Qualitative Fractography," *Int. J. Prosthodont.*, **19** [2] (2006) 151 - 158.
26. J. B. Quinn, G. D. Quinn, J. R. Kelly, and S. S. Scherrer, "Useful Tools for Dental Failure Investigation," pp. 36 - 53 in *Proc. Conf. on Scientific Insights and Dental Ceramics and Photopolymer Networks*, ed. D. C. Starrett, Trans. Academy of Dental Materials, Vol. 16, 2004.
27. J. R. Kelly, "Fractography of Dental Ceramics," pp. 241 – 251 in *Fractography of Glasses and Ceramics*, IV, eds., J. R. Varner and G. D. Quinn, American Ceramic Society, Westerville, OH, 2001.
28. J. B. Quinn, "Failure Analysis of a Broken Tooth," *J. Fail. Anal. Prev.*, **4** [1] (2004) 41 - 46.
29. J. Y. Thompson, K. J. Anusavice, A. Naman, and H. F. Morris," Fracture Surface Characterization of Clinically Failed All-Ceramic Crowns," *J. Dent. Res*., **73** [12] (1994) 1824 – 1832.
30. M. Øilo, A. K. Kvam, J. E. Tibballs, and N. Gjerdet, "Clinically Relevant Fracture Testing of All-Ceramic Crowns," *Dent. Mater.*, **29** (2013) 815-823.

31. M. Øilo, N. R. Gjerdet, “Fractographic Analysis of All-Ceramic Crowns: A Study of 27 Clinically-Fractured Crowns,” *Dent. Mater*., **29** (2013) e78-e84
32. M. Øilo and G. D. Quinn, “Fracture Origins in Twenty-two Dental Alumina Crowns,” *J. Mech. Beh. Biomed. Mater*., **53** (2016) 93 – 103.
33. J. A. Salem and G. D. Quinn, “Fractographic Analysis of Large Single Crystal Sapphire Refractive Secondary Concentrators,” *J. Eur. Cer. Soc.*,**34** (2014) 3271-3281.

11. Conclusions

This Guide is intended to introduce engineers and scientists to the science of fractographic analysis of brittle materials as a tool to solve fracture problems. This tool may be applied to a broad range of practical problems including component failure analyses, materials processing refinements, routine materials characterization, laboratory scale mechanical testing, and reliability and design. Fractography is the examination of fracture surfaces, the examination of the general crack patterns, other part surfaces, other specimens, and a review of processing, exposure, and testing conditions. Much like the master detective, the fractographer starts with an open mind, integrates and analyzes the available information and relates it to similar episodes from his own experience and to what is published in the literature. The fractographer applies deductive logic to arrive at a conclusion.

Figure 11.1
The fractographer as a detective.

We are in the midst of microscopy revolution, as the marriage of computers with digital cameras and glass lenses expands the fractographer's tool box dramatically. Quantitative, virtual, three-dimensional imaging is already available. Nonetheless, no matter how powerful these tools become, they will never supplant the fractographer as an expert system. No computer or artificial intelligence is likely to ever replace the skill of a fractographer who knows how to tilt a specimen or light source under a stereoptical microscope and recognize a fleeting reflection that unlocks a fractographic puzzle. No computer will know how to improvise how to look at something differently or how to stain a specimen on a hunch.

My fractographic experiences over forty-seven years have been distilled into the following rules of thumb for fractography:

1. The first one is the hardest.
The more examples of a particular fracture problem that are examined the better. This is true for both experienced and novice fractographers. Patterns may be recognized that are not apparent in a single example. An unfamiliar or subtle feature may be overlooked in one example. When the fractographer sees a curious or unfamiliar marking in multiple examples, he is less likely to dismiss it as a random artifact. One of the most gratifying experiences a

fractographer has is when he or she first recognizes and understands a new marking and adds it to his or her experience base.

2. The more experience the fractographer has the better.
Fractography is a cumulative learning experience. The more one learns, the easier and faster fractography becomes. The fractographer should look at as many different test specimens, components, and materials as possible.

3. Photos almost never show all there is to see.
Photos are two-dimensional representations of a three-dimensional world and perspective is inevitably lost.

4. Good equipment makes the job easier or even possible, but is no substitute for skill and experience.
One must know where to look and great pictures of the wrong things are worthless. Many published close-up SEM images fit this category.

5. Good fractography under laboratory testing situations begins even before the specimen is broken.
The specimen should be tested in clean conditions to minimize contamination and secondary fractures of the fracture surfaces.

6. Fractography is more than looking at fracture surfaces.

7. A good fractographer is patient.
Don't be afraid to reexamine the pieces. Look at all the pieces, even the ones that may not seem to be relevant. Sometimes, in a group of laboratory-tested specimens, a key feature is discerned or recognized on the very last specimen. Fractographers in a rush often overlook important details.

8. It's better to let the material tell you why it failed than the other way around. Theoretical modelers cause the most trouble. They already know why something should fail since it is in their computer model. Indentation mechanics people come next. They have more interest in indentations than in the real flaws in a material.

9. A good fractographer does not overreach, guess, or force an interpretation. Don't let other people put words in your month.
The good fractographer is not afraid to say: "I don't know." It is often a good idea to say up front: "I'll take a look, but I make no promises." The credibility of the fractographer is a precious commodity.

10. Fractography may seem subjective to the uninitiated, but it is very objective.

One last metaphor to summarize the fractographic craft is offered. When a fractographer first sees broken fragments, he or she sees pieces that are trying to tell a tale. With the tools of the trade and with the fractographic skills summarized in this Guide, a fractographer can listen to the pieces, interpret their story, and unlock the secrets of the fracture.

Finally, the astute reader will have noted that fracture surfaces can be objects of beauty. Figure 11.2 is one such example. This figure, from an unpublished study by Dr. J. Quinn of dental porcelains with varying amounts of crystallization and leucite content, illustrates many of the features described in this book.

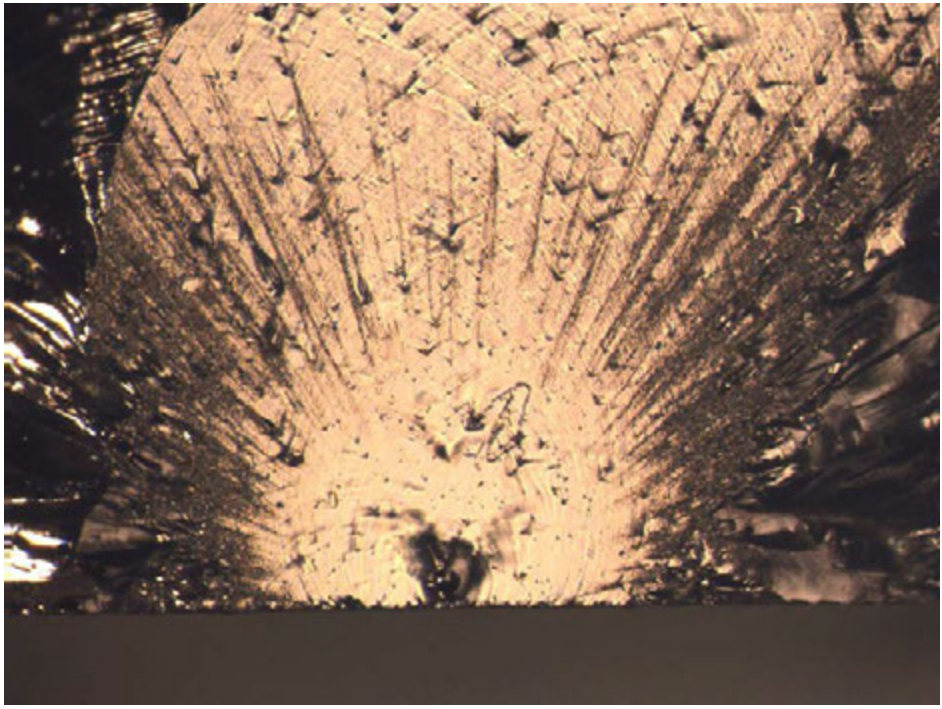

Figure 11.2 *Fracture surface of a dental glass-porcelain, flexural strength bar. One can see an origin that is a row of grinding cracks that interacted with a near-surface bubble. One also sees the fracture mirror, Wallner lines, gull wings, wake hackle, mist, and velocity hackle. (unpublished, found in Dr. J. Quinn's computer after her death.)*

APPENDIX A BIBLIOGRAPHY

Books on Glass and Ceramic Fractography

V. D. Fréchette, *Failure Analysis of Brittle Materials, Advances in Ceramics*, Vol.28, American Ceramic Society, Westerville, OH, 1990.

A must for the serious fractographer. This book covers all aspects of the fractography of glasses including fundamental markings on crack surfaces (Wallner lines, hackle, and so forth), crack forking, failure origins, and estimates of stress at fracture and fractographic techniques. Superbly illustrated with a number of service failures and amazing case histories.

Fractography of Glass, Ed. R. C. Bradt and R. E. Tressler, Plenum, NY, 1994.

Eight technical articles on glass fractography.

Fractography, D. Hull, Cambridge University Press,1999.

A superbly illustrated and laid out textbook on the fractography of metals, ceramics, and polymers. Strong on the physics underlying the fracture markings, but weak on practical applications.

Fractography, Vol. 12 ASM Handbook, ASM Int., Materials Park, OH, 1987.

The seminal work for metals fractography. Expensive. Includes a large atlas of metal failures, but only a few examples for ceramics or glasses. Includes excellent chapters on the history of fractography, metal models of fracture, photographic equipment and techniques, optical and electron microscopy that are directly relevant to ceramics and glasses. **Caution:** Some cleaning and preparation techniques such as surface coatings, replicating tapes, replicating tape stripping, and aggressive detergent cleaning prescribed for metals are *not recommended* for ceramic fracture surfaces.

Failure Analysis and Prevention, Vol. 11, ASM Handbook, ASM Int., Materials Park, OH, 2002.

Includes sections on fractography, and fractographic equipment and techniques, but deals more with the broader issues of failure analysis: why a component fails to perform its intended function. Fracture is but one of many failure modes. Includes sections on failure analysis philosophies and approaches. Has one brief chapter on ceramics. The fracture mechanics chapter is tailored towards metals fracture and not ceramic or glass fracture. The quantitate fractography chapter by Gokahle is excellent and has good information about quantitative microcopy and fractals and their limitations.

Fractography and Failure Mechanisms of Polymers and Composites, ed. A. Roulin-Moloney, Elsevier, 1989.

This is by far the best book on fractography of polymeric materials and composites. There are chapters on microscopy, analytical techniques, the materials including unfilled and filled composites, and failure mechanisms. Some of the more brittle composites and polymers have similar fracture markings to those on glasses and ceramics, and this book is a very complementary tool to this Guide. Out of print, this is an excellent book on fractography of polymers and polymeric composites that has value to dental restoration researchers.

Conference Series Books on Fractography of Glasses and Ceramics

Fractography of Glasses and Ceramics, Advances in Ceramics, Vol. 22, J. Varner, and V. Fréchette, eds., American Ceramic Society, Westerville, OH, 1988.

Proceedings of the first of a quadrennial-quinquennial conference series by the same name held at Alfred University in 1986. Sections on: fundamental phenomena, high-temperature fracture, fractography and fracture mechanics, fractography in materials development and testing, and component failures.

Fractography of Glasses and Ceramics, II, Ceramic Transactions, Vol. 17, V. Fréchette, and J. Varner, eds., American Ceramic Society, Westerville, OH, 1991.

Twenty-six papers from the second Alfred University conference, held on campus in 1990.

Fractography of Glasses and Ceramics, III, Ceramic Transactions, Vol. 64, J. Varner, V. Fréchette, and G. D. Quinn, eds., American Ceramic Society, Westerville, OH, 1996.

Twenty-five papers from the third Alfred University conference, held on campus in 1995.

Fractography of Glasses and Ceramics, IV, Ceramic Transactions, Vol. 122, J. Varner, and G. D. Quinn, eds., American Ceramic Society, Westerville, OH, 2001.

Thirty-two papers from the fourth Alfred University conference, held on campus in 2000. Special session on edge chipping.

Fractography of Glasses and Ceramics, V, Ceramic Transactions, Vol. 199, J. Varner, G. D. Quinn, and M. Wightman, eds., American Ceramic Society, Westerville, OH, 2007.

Thirty-six papers from the fifth Alfred University conference, held in 2006 but this time in Rochester, NY. Papers by Quinn on fracture mirror size measurements; Wilantewicz and Varner on indentation damage evolution under Vickers indentations in glass and the importance of the ratio of G/K; by Hecht-Mijic and Richter on fractography of hip joint balls; Morrell on component fractures including SiC seal rings, CaF_2 windows, and alumina hip balls; Cleary and Nichols on automotive windows; and Engelder about controversies in interpreting mesoscopic cracks in rock fractures in the earth.

Fractography of Glasses and Ceramics, VI, Ceramic Transactions, Vol. 230, J. Varner and M. Wightman, eds., American Ceramic Society and Wiley, Westerville, OH, 2012.
Twenty-five papers from the sixth Alfred university conference, held in 2011 this time in Jacksonville, FL. Notable papers by Quinn on the history of fractography; Glaesemann et al., on fractography in the development of ion-exchanged cover glasses (e.g., Gorilla glass); Gross on crack evolution in alkali aluminosilicate glasses for cover glass; Bradt on an energy criterion for mirror formation; Hecht-Mijic on dental implants; Maurer on a glass pharmaceutical syringe fracture.

Fractography of Advanced Ceramics, ed., J. Dusza, Trans Tech Publ., Zurich, 2002.
First (2001) of a new conference series in Stará Lesná, Slovakia. Thirty-six papers, many of which are on mechanical testing and have no fractography. Excellent papers including a bioceramics fracture paper by H. Richter and a paper by R. Morrell and J. Kübler on the background of the then new CEN prEN 843-6 fractography standard.

Fractography of Advanced Ceramics II, eds. J. Dusza, R. Danzer, and R. Morrell, Trans Tech Publ. Zurich, 2005.
Second (2004) of the Stará Lesná, Slovakia conference series. Sixty one short papers. Papers by Quinn et al. on machining damage detection and characterization, Wang et al. on ZnO varistor failures, Supanic et al., on fractures in stacked PZT piezoceramic actuators, and Tatami et al. on nanofractography of alumina by scanning probe microscopy. Many of the papers have negligible fractography, however, and deal more with mechanical properties, processing, and indentation.

Fractography of Advanced Ceramics III, eds. J. Dusza, R. Danzer, R. Morrell, and G. D. Quinn, Trans Tech Publ. Zurich, 2009.
Third (2008) of the Stará Lesná, Slovakia conference series. Sixty-three short papers. Papers by Quinn on the history of fractography of brittle materials; Bradt on some legal aspects and challenges; Varner on use of replicas. (The fourth conference in this series was held in 2013, in Smolenice castle outside Bratislava in Slovakia. Dozens of papers were presented, but only 23 were included in a special edition of the Journal of the European Ceramic Society in November, 2014.)

Fractography of Ceramic and Metal Failures, J. Mecholsky, Jr., and S. Powell, Jr., eds., *ASTM STP 827*, ASTM, Philadelphia, PA, 1984.
Eight papers on ceramics from a 1982 symposium at ASTM headquarters in Philadelphia. Includes an outstanding, comprehensive, and well-illustrated review paper by Rice, and papers by Pantano and Kelso, and Healy and Mecholsky (cited below).

Fracture Mechanics of Ceramics, Vol. 1, R. Bradt, D. Hasselman, and F. Lange, eds., Plenum Press, NY, 1974.
Proceedings of a conference at Pennsylvania State University in 1973 with twenty-three papers on fracture mechanics applied to origin detection and fractography in ceramics. The later volumes of this quadrennial series also have some fractography papers.

Microscopy Techniques

C. G. Pantano, and J. F. Kelso, "Chemical Analysis of Fracture Surfaces," *Fractography of Ceramic and Metal Failures, ASTM STP 827*, ASTM, 1984, pp. 139–156.

The applicability of various instrumental techniques for chemical analysis of fracture surfaces is reviewed. The relative merits and spatial and depth resolutions of Auger microscopy and energy or wavelength dispersive electron microscopy are given.

J. T. Healy, and J. J. Mecholsky, Jr., "Scanning Electron Microscopy Techniques and Their Application to Failure Analysis of Brittle Materials," *Fractography of Ceramic and Metal Failures, ASTM STP 827*, ASTM, 1984, pp. 157–181.

Discusses cleaning, coating, and other procedures for SEM specimens. The merits of secondary and backscattered electron imaging are presented.

C. R. Brooks and B. L. McGill, "The Application of Scanning Electron Microscopy to Fractography," *Mater. Char.*, **33** (1994) 195-243.

An excellent, well-illustrated review of the application of scanning electron microscopy for topographical and chemical analysis of fracture surfaces of ceramics, metals, and polymers. Includes a good discussion of stereo SEM fractography.

Fractography of Ceramics and Glasses - Overview Papers

J. J. Mecholsky, Jr., and S. W. Freiman, "Determination of Fracture Mechanics Parameters Through Fractographic Analysis of Ceramics," pp. 136 – 150 in *Fracture Mechanics of Ceramics Applied to Brittle Materials*, S. Freiman, ed., *ASTM STP 678*, ASTM, 1979.

A short but useful overview of the utility of fractography as a quantitative tool to determine strength-limiting origins, the stress at failure, and critical fracture toughness.

R. W. Rice, "Fractographic Identification of Strength Controlling Flaws and Microstructure," pp. 323 – 345 in *Fracture Mechanics of Ceramics*, Vol. 1, R. Bradt, D. Hasselman, and F. Lange, eds., Plenum Press, NY, 1974.

A short but valuable discussion of several key origins (pores, pore groups, and large grains) and their relationship to fracture energy. The fracture energy can either be a single-crystal or polycrystalline value depending upon the relative sizes of origin and microstructure.

G. D. Quinn, J. J. Swab, and M. J. Slavin, "A Proposed Standard Practice for Fractographic Analysis of Monolithic Advanced Ceramics," MTL TR 90-57, November 1990, NTIS Access No. ADA-231989.

Discusses MIL HDBK 790 the predecessor of ASTM C 1322 in 1996. Discusses essential background information and the rationale for consistency in characterization. A standard nomenclature and origin characterization scheme were proposed.

R. W. Rice, "Topography of Ceramics," pp. 439 – 472 in *Surfaces and Interfaces of Glass and Ceramics*, V. Fréchette, W. LaCourse, and V. Burdick, eds., Plenum Press, NY, 1974 .

A very helpful introduction describes the role of unaided eye, hand lens, optical, scanning, and transmission electron microscopy. Fracture surface features such as transgranular and intergranular fracture, crack microstructure interactions, crack branching, mirrors, and single crystal fractography are discussed.

R. W. Rice, "Ceramic Fracture Features, Observations, Mechanism and Uses," *Fractography of Ceramic and Metal Failures, ASTM STP 827*, ASTM, 1984, pp. 5–103.

An extraordinary book-length article with many useful tips and analyses. Many single crystal examples.

T. A. Michalske, "Quantitative Fracture Surface Analysis," pp. 653 – 662 in *Ceramics and Glasses, Engineered Materials Handbook*, Vol. 4, ed. S. Schneider, ASM, Metals Park, OH, 1991.

J. R. Varner, "Descriptive Fractography," pp. 635 - 644 in *Ceramics and Glasses, Engineered Materials Handbook*, Vol. 4, ed. S. Schneider, ASM, Metals Park, OH, 1991.

J. S. Wasylyk, "Special Terminology Used in Fractography," pp. 632 – 634 in *Ceramics and Glasses, Engineered Materials Handbook*, Vol. 4, ed. S. Schneider, ASM, Metals Park, OH, 1991.

R. C. Bradt, "The Fractography and Crack Patterns of Broken Glass," *J. Fail. Anal. Prev*., **11** (2011) 79-96.

R. J. Parrington, "Fractography of Metals and Plastics," *J. Fail. Anal. Prev*., **2** [5] (2002) 16-19, 44-46.

A short article with some interesting history of fractography. Metals and plastic fracture modes and patterns are compared.

Fractography Round Robins

J. J. Swab and G. D. Quinn, "Fractography of Advanced Structural Ceramics, Results from the VAMAS Round Robin Exercise," U.S. Army Technical Report, ARL-TR-656, U.S. Army Research Laboratory, Aberdeen, MD, Dec. 1994.

An international Versailles Advanced Materials and Standards (VAMAS) Round Robin for identification of fracture origins in test coupons and photographs. Lessons learned.

J. J. Swab and G. D. Quinn, "Fractography of Advanced Structural Ceramics: Results From Topic #2 of the VAMAS Round Robin Exercise"" *Ceram. Eng. Sci. Proc.*, **16** [5] (1995) 929-938.

A short summary of part of the 1994 VAMAS round robin on ceramic fractography.

J. J. Swab and G. D. Quinn, "Results of a Round Robin Exercise on the Fractography of Advanced Structural Ceramics," *Cer. Eng. Sci. Proc.*, **15** [5] (1994) 867-876.
A short summary of findings from the 1994 VAMAS fractography round robin.

J. J. Swab and G. D. Quinn, "The VAMAS Fractography Round Robin: A Piece of the Fractography Puzzle," pp. 55 - 70 in *Fractography of Glasses and Ceramics III*, eds. J. Varner and G. D. Quinn, American Ceramic Society, Westerville, OH, Ceramic Transactions, Vol. 64, (1996).
Seventeen laboratories analyzed photos of grinding cracks. They also analyzed actual specimens with different flaws. Results varied. Much was learned by the organizers from this exercise. How do fractographers sift through and use the clues?

Origins in Ceramics

H. Kirchner, R. Gruver, and W. Sotter, "Characteristics of Flaws at Fracture Origins and Fracture Stress—Flaw Size Relations in Various Ceramics," *Mater. Sci. Eng.*, **22** (1976) 147–156.
A concise but useful report on strength-limiting origins in alumina, silicon nitride, and silicon carbide with a detailed tabulation of different types of origins. Emphasis is on porosity, large grains, and machining origins. An important observation (Fig. 1b) is that origins in the center of fracture mirrors may intersect the fracture surface at an angle and a true view of the origin may not be seen.

H. Baumgartner and D. Richerson, "Inclusion Effects on the Strength of Hot Pressed Si_3N_4," *Fracture Mechanics of Ceramics*, Vol. 1, 1974, pp. 367–386.
Good characterization of machining damage and inclusions in silicon nitride. The inclusions are much smaller than expected due to local-degradation of the matrix K_{Ic}.

M. G. Gee and R. Morrell, "Fracture Mechanics and Microstructures," pp. 1 – 22 in *Fracture Mechanics of Ceramics*, Vol. 8, R. Bradt, A. Evans, D. Hasselman, and F. Lange, eds., Plenum Press, NY, 1986.
Principally a discussion of the application of fracture mechanics theories to strength. Microstructural influences significantly complicate matters and may limit utility to qualitative issues. The nature of strength-limiting origins and their severity is discussed. In some instances, sharp cracks will not form until the stress is applied.

A. G. Evans, "Structural Reliability, A Processing Dependent Phenomenon," *J. Amer. Ceram. Soc,* **65** No. [3] (1982) 127–139.
Evans didn't spend much time looking through microscopes, but he was the preeminent mathematic modeler of mechanical behavior in ceramics and glasses in the 1970s - 2000s. This paper and the two below were important contributions pertaining to flaws and their effect upon strength and reliability. This paper has an emphasis on the micromechanics of fracture with a good discussion of the effect of thermal and mechanical property mismatches between an origin and the matrix. Graph of stress versus origin size for silicon nitride showing the relative severity of different origins (WC, Fe, Si, C inclusions, porosity, and machining damage).

A. G. Evans, “Non-Destructive Failure Prediction in Ceramics,” pp. 595-626 in *Progress in Nitrogen Ceramics,* ed. F. L. Riley, Matirnus Nijhoff Publ., The Hague, 1983.

Includes the graph of stress versus origin size for silicon nitride showing the relative severity of different origins (WC, Fe, Si, C inclusions, porosity, and machining damage).

A. G. Evans, M. E. Meyer, K. W. Fertig, B. I. Davis, and H. R. Baumgartner, “Probabilistic Models for Defect Initiated Fracture in Ceramics,” *J. Nondest. Eval.*, **1** [2] (1980) 111 – 122.

Includes some of the actual data used to construct the strength versus flaw size graph for different flaws. Many of the flaws were intentionally seeded into hot-pressed silicon nitride. Additional data were obtained from work done at the U.S. Army Materials and Mechanics Research Center at Watertown, MA and documented in U.S. Army Technical Report TR78-11 by Brockelman and Hansen in 1978.

G. D. Quinn, L. K. Ives, and S. Jahanmir, “On the Fractographic Analysis of Machining Cracks in Ground Ceramics: A Case Study on Silicon Nitride,” Special Publication SP 996, NIST, Gaithersburg, MD, May, 2003.

An exhaustive, well-illustrated treatment of the nature of machining flaws in ground ceramics and how to find them. Photos and many schematics.

G. D. Quinn, L. K. Ives, and. S. Jahanmir, “On the Nature of Machining Cracks in Ground Ceramics: Part I: SRBSN Strengths and Fractographic Analysis,” *Mach. Sci. Technol.*, **9** (2005) 169 - 210.

G. D. Quinn, L. K. Ives, and S. Jahanmir, “On the Nature of Machining Cracks in Ground Ceramics: Part II: Comparison to Other Silicon Nitrides and Damage Maps,” *Mach. Sci. Technol.*, **9** (2005) 211 - 237.

G. D. Quinn, L. K. Ives, and S. Jahanmir, “Machining Damage Cracks: How to Find and Characterize Them by Fractography,” *Ceram. Eng. Sci. Proc*., *24* [4] (2003) 383-394.

A short summary of the work in the previous three references.

G., D. Quinn, L. K. Ives, and S. Jahanmir, “Machining Cracks in Finished Ceramics,” pp. 1-14 in *Fractography of Advanced Ceramics, II*, eds. J. Dusza, R. Danzer, and R. Morrell, TransTech Publ., Zurich, 2005.

A short summary of the work in the previous three references.

R. W. Rice and J. J. Mecholsky, “The Nature of Strength Controlling Machining Flaws in Ceramics,” pp. 351-378 in *The Science of Ceramic Machining and Surface Finishing II*, eds. B. Hockey and R. Rice, National Bureau of Standards, Gaithersburg, MD, Special Publication SP562. 1979.

R. W. Rice, "Failure Initiation in Ceramics: Challenges of NDE and Processing," and "Ceramic Developments," C. Sorrell, and B. Ben-Nissan, eds., *Materials Science Forum*, Vol. 34–36, Trans. Tech. Publ. Ltd. Switzerland, 1988, pp. 1057–1064.
A comprehensive, well-illustrated review of failure-initiating origins. Nearly an encyclopedia of flaws. Origins include: agglomerates, pores, large grains, inclusions, machining damage, handling damage, thermocouple beads, ball mills, dandruff, insects, feces, inadequate mixing of constituents, etc.

R. W. Rice, "Processing Induced Sources of Mechanical Failure in Ceramics," pp. 303–319 in *Processing of Crystalline Ceramics*, eds., H. Palmour, R. Davis, and T. Hare, Plenum Press, NY, 1978.
A short, well-illustrated review of origins. A good starting point.

R. W. Rice, J. J. Mecholsky, Jr., and P. F. Becher, "The Effect of Grinding Direction on Flaw Character and Strength of Single Crystal and Polycrystalline Ceramics," *J. Mat. Sci.*, **16** (1981) 853–862.
Machining damage in a variety of ceramics is well illustrated by nine figures.

J. J. Mecholsky, Jr., S. W. Freiman, and R. W. Rice, "Effects of Grinding on Flaw Geometry and Fracture of Glass," *J. Amer. Ceram. Soc.*, **60** [3–4] (1977) 114–117.
Two primary sets of cracks result from surface grinding. These are schematically shown and complemented by SEM photos and related to fracture mechanics parameters.

R. W. Rice, "Pores as Fracture Origins in Ceramics," *J. Mat. Sci.*, **19** (1984) 895–914.
A well-illustrated examination of pores in glassy and polycrystalline materials. Pores tend to be "sharper" in the latter than in the former.

R. W. Rice, S. W. Freiman, and J. J. Mecholsky, Jr., "The Dependence of Strength-Controlling Fracture Energy on the Flaw Size to Grain Size Ratio," *J. Am. Ceram. Soc.*, **63** [3-4] (1980) 129-136.
The flaw-size to grain-size ratio determined whether the relevant fracture toughness is that for a polycrystalline material or that for a single crystal. Small flaws within very large grains are ruled by single crystal fracture toughness values which are much less than for polycrystals. Large grains are susceptible to machining cracks.

D. Munz, O. Rosenfelder, K. Goebells, and H. Reiter, "Assessment of Flaws in Ceramic Materials on the Basis of Non-Destructive Evaluation," pp. 265–283 in *Fracture Mechanics of Ceramics*, Vol. 1, eds. R. Bradt, D. Hasselman, and F. Lange, F., Plenum Press, NY, 1986 .
Six different flaw types were characterized in reaction bonded and sintered silicon nitrides. Some flaws were artificially created to support a fracture mechanics analysis. Pores have a different effect upon strength than inclusions.

J. E. Ritter, Jr., and R. W. Davidge, "Strength and Its Variability in Ceramics with Particular Reference to Alumina," *J. Am. Ceram. Soc*., **67** [6] (1984) 432-437.
A good study of strength variability in alumina with flaws deliberately introduced by adding glucose or corn starch to starting powders, or by grit blasting surfaces. Flaw linking was observed.

F. F. Lange, "Processing-Related Fracture Origins: I, Observations in Sintered and Isostatically Hot-Pressed Al_2O_3/ZrO_2 Composites," *J. Am. Ceram. Soc.*, **66** [6] (1983) 396-398.
Four companion articles about flaws generated during processing one system. Differential shrinkage of agglomerates created cracking.

F. F. Lange and M. Metcalf, "Processing-Related Fracture Origins: II, Agglomerate Motion and Cracklike Internal Surfaces Caused by Differential Sintering," *ibid*, 398-406.

F. F. Lange, B. I. Davis, and I. A. Aksay, "Processing-Related Fracture Origins: III, Differential Sintering of ZrO_2 Agglomerates in Al_2O_3/ZrO_2 Composite," *ibid*, 407-408.

F. F. Lange, B. I. Davis, and E. Wright, "Processing-Related Fracture Origins: IV, Elimination of Voids Produced by Organic Inclusions," *J. Am. Ceram. Soc.*, **69** [1] (1986) 66-609.

M. Hangl, "Processing Related Defects in Green and Sintered Ceramics," pp. 133-156 in *Fractography of Glasses and Ceramics, IV, Ceramic Transactions*, Vol. 122, J. Varner, and G. D. Quinn, eds., American Ceramic Society, Westerville, OH, 2001.
An excellent article about spray-dried agglomerates in varistor grade sintered zinc oxide. Many photographs show the agglomerates from their initial state through green body and final sintered stages. Agglomerates can be hollow or donut shaped. The final fracture surface will reveal the spray-dried pattern if one looks carefully.

S. Nakamura, S. Tanaka, R. Furushima, K. Sato, and K. Uematsu, "Estimation of Weibull Modulus from Coarser Defect Distribution in Dry-pressed Alumina Ceramics," *J. Ceram. Soc. Japan*, **117** [6] (2009) 742-747.
Starting in the 1990s, Profs. Keizo Uematsu and Satoshi Tanaka at Nagaoka University did exceptional work characterizing flaws in ceramics, starting from the earliest processing stages and monitoring their evolution during subsequent processing. Innovative microscopy techniques were devised to see the flaw population in ceramic bodies, as well as the flaws exposed by conventional polished section work and fractographic analysis of test specimens. The flaws were closely coupled to the final strength distribution. Their work confirmed analytical predictions by Jayatilaka and Trustrum in 1977 and 1983. The latter work plus the Nagaoka University work established beyond any doubt that the Weibull distribution is appropriate for brittle materials. There are dozens of good papers by this group, and only a few are listed here.

H. Abe, M. Naito, T. Hotta, N. Shinohara, and K. Uematsu, "Flaw Size Distribution in High-Quality Alumina," *J. Am. Ceram. Soc*., **86** [6] (2003) 1019-1021.

Y. Saito, S. Tanaka, N. Uchida, and K. Uematsu, "Direct Observation of Three-Dimensional Structure in Powder Compact,' pp. 657-660 in *Key Engineering Materials*, Vols. 206-213, Proceedings of the 7th European Ceramic Society, Brugge, Belgium, 2001, Transtech Publ., Zurich, Switzerland, 2002.

Confocal laser scanning fluorescence microscopy with a special immersion fluid was used to see the three dimensional flaw distribution in alumina.

Y. Saito, S. Tanaka, N. Uchida, and K. Uematsu, "Direct Evidence for Low-Density Regions in Compacted Spray-Dried Powders," *J. Am. Ceram. Soc*., **84** [10] (2001) 2454-2456.

K. Sato, S. Tanaka, N. Uchida, and K. Uematsu, "Characterization of Large Defects in Alumina," *Bull. Am. Ceram. Soc.*, **82** [4] (2003) 39-42.

Transmission optical microscopy was used to study the flaw population through a thin 200 µm piece of alumina.

K. Sato, S. Tanaka, N. Uchida, and K. Uematsu, "Morphological Change of Large Pores in Alumina Ceramics in the Final Stage of Densification," *J. Ceram. Soc. Japan*, **111** [7] (2003) 525-527.

Transmission optical microscopy was used to study the flaw population through a thin 200 µm piece of alumina.

K. Sato, S. Tanaka, N. Uchida, and K. Uematsu, "Direct Study on the Formation of Large Defects in Final Stages of Sintering in Alumina Ceramics," pp. 225 – 228 in Key Engineering materials, Vols. 264-268, Proceedings of the 8th European Ceramic Society conference, Trans Tech Publ., Zurich, 2004.

The formation and development of defects in sintered alumina was studied with transmission optical microscopy and the SEM.

N. Shinohara, M. Okumiya, T. Hotta, K. Nakahira, M. Naito, and K. Uematsu, "Morphological Changes in Process-Related large Pores of Granular Comp-acted and Sintered Alumina," *J. Am. Ceram. Soc*., **83** [7] (2000) 1633-1640.

Exceptional pictures and characterization of pores of different shapes formed as a result of power agglomerate collapse during processing. Compacts sintered at different temperatures had different flaws.

H. Takahasi, N. Shinohara, K. Uematsu, and T. Junichiro, "Influence of Granule Character and Compaction on the Mechanical Properties of Sintered Silicon Nitride," *J. Am. Ceram. Soc*., **79** [4] (1996) 843-858.

N. Shinohara, M. Okumiya, T. Hotta, K. Nakahira, M. Naito, and K. Uematsu, "Seasonal Variation of Microstructure and Sintered Strength of Dry-Pressed Alumina," *J. Am. Ceram. Soc*., **82** [12] (1999) 3441 – 3446.

An exceptional study that showed strength varied with the season of the year. The variation was traced to subtle flaw variations in the powder compacts that were caused by differences in the flowability of the spray-dried powders and their deformability in winter and summer due to temperature and humidity differences in the processing environment!

H. Abe, M. Naito, T. Hotta, N. Shinohara, and K. Uematsu, "Flaw Size Distribution in High-Quality Alumina," *J. Am. Ceram. Soc*., **86** [6] (2003) 1019 -1021.

Transmission optical microscopy characterized the flaws in three-dimensional pieces of three aluminas. The exponents of the flaw size distributions did not correlate well to the actual four–point strength distributions in this case, probably since only flaws in a small 0.5 mm^3 slice were measured by transmission optical examination. In contrast, the bend bars had Weibull effective volumes of 1.9 – 2.5 mm^3. The flaws were also round pores and not penny-shaped cracks.

Y. Zhang, M. Inoue, N. Uchida, and K. Uematsu, "Characterization of Processing Pores and Their Relevance to the Strength in Alumina Ceramics," *J. Mater. Res.*, **14** [8] (1999) 3370-3374.

T. Bernthaler, "Defect Imaging and Analysis for Predicting the Reliability of Ceramics," PhD Thesis, School of Materials Science and Engineering, University of New South Wales, Sydney, Australia, and the University of Aalen, Germany, April 2011

A remarkable study under the guidance of Profs. Mark Hoffman and Gerhard Schneider, comparing flaw size distributions measured with automated image analysis on polished sections and strength distributions and fractographic analysis in alumina, alumina with seeded defects, dense and porous silicon carbide, and an alumina-zirconia composite. A variety of flaw types were identified and characterized. The size distributions matched an inverse power law function.

Origins in Glass

J. R. Varner, "The Practical Strength of Glass," pp. 389 – 406 in *Strength of Inorganic Glass*, ed. C. Kurkjian, Plenum, NY, 1986.

V. D. Fréchette, *Failure Analysis of Brittle Materials, Advances in Ceramics*, Vol.28, American Ceramic Society, Westerville, OH, 1990.

Fracture Mirrors

J. J. Mecholsky, Jr., S. W. Freiman, and R. W. Rice, "Fracture Surface Analysis of Ceramics," *J. Mat. Sci.*, **11** (1976) 1310–1319.

A detailed correlation of origin size, fracture mirror sizes and characterization, and fracture mechanics parameters for single and polycrystalline ceramics. A table of mirror constants is given for a range of ceramics, and it is demonstrated that the outer

mirror (hackle) to origin size ratio is about 13 to 1. The inner mirror (mist) ratio is between 6 to 1 and 10 to 1.

J. J. Mecholsky, Jr., R. W. Rice, and S. W. Freiman, "Prediction of Fracture Energy and Flaw Sizes in Glasses from Measurements of Mirror Size," *J. Amer. Ceram. Soc.*, **57** [10] (1974) 440–443.
Details of fracture mirror features are discussed and related to fracture mechanics parameters for glasses. A table of mirror constants for glasses.

H. P. Kirchner, R. M. Gruver, and W. A. Sotter, "Fracture Stress—Mirror Size Relations for Polycrystalline Ceramics," *Phil. Mag.*, **33 [5]** (1976) 775–780.
Many mirror constants for a range of ceramics.

H. P. Kirchner, and J. C. Conway, Jr., "Fracture Mechanics of Crack Branching in Ceramics," pp. 187–213 in *Fractography of Glass and Ceramics, Advances in Ceramics*, Vol. 22, American Ceramic Society, Westerville, OH, 1988.
Analysis that fracture mirror features are controlled by stress intensity.

J. J. Mecholsky, Jr., and S. W. Freiman, "Determination of Fracture Mechanics Parameters Through Fractographic Analysis of Ceramics," pp. 136 – 150 in *Fracture Mechanics Applied to Brittle Materials, ASTM STP 678*, S. Freiman, ed., ASTM, 1979.
A short discussion of fracture mirrors and mirror constants with a comparative table of mirror constants. Comments on useful techniques to measure mirror parameters.

Fracture Mechanics—Estimates of Flaw Size

D. W. Richerson, *Modern Ceramic Engineering*, Marcel Dekker Inc., NY, 1982.
Chapter 3 is a good primer on strength and fracture toughness measurements and their applicability to fractographic analysis. Several numerical examples are given for estimating the strength of a specimen on the basis of a fracture mechanics calculation using the measured flaw size.

H. K. Baumgartner and D. W. Richerson, "Inclusion Effects on the Strength of Hot Pressed Si_3N_4," *Fracture Mechanics of Ceramics*, Vol. 1, eds. R. Bradt, D. Hasselman, and F. Lange, Plenum Press, NY, 1974, pp. 367–386.
Applies fracture mechanics to one class of flaws with several numerical examples. The strength-limiting inclusions are smaller than expected from fracture mechanics, suggesting that the fracture toughness is altered in the vicinity of the inclusions.

J. J. Mecholsky, Jr., S. W. Freiman, and R. W. Rice, "Fracture Surface Analysis of Ceramics," *J. Mat. Sci.*, **11** (1976) 1310–1319.
Compares measured flaw sizes to fracture mechanics estimates for a range of ceramics and glasses.

H. P. Kirchner, R. M. Gruver, and W. A. Sotter, "Characteristics of Flaws at Fracture Origins and Fracture Stress-Flaw Size Relations in Various Ceramics," *Mater. Sci. Eng.*, **22** (1976) 147–156.

Measured flaw sizes were compared to fracture mechanics estimates for several different types of flaws in alumina, silicon nitride, and silicon carbide.

A. G. Evans, and G. Tappin, "Effects of Microstructure on the Stress to Propagate Inherent Flaws," *Proc. Brit. Ceram. Soc.*, **20** (1972) 275–297.

Discusses flaws in alumina ceramics and compares the stress actually needed to cause fracture to estimates based on fracture mechanics. Microstructural factors such as flaw linking prior to catastrophic fracture are discussed.

D. Munz, O. Rosenfelder, K. Goebells, and H. Reiter, "Assessment of Flaws in Ceramic Materials on the Basis of Non-Destructive Evaluation," pp. 265–283 in *Fracture Mechanics of Ceramics*, Vol. 1, eds. R. Bradt, D. Hasselman, and F. Lange, Plenum Press, NY, 1986.

A superb, comprehensive fracture mechanics analysis of six different flaw types in two silicon nitrides. Fractographic size measurements agreed with fracture mechanics estimates for some flaw types, but not others. Over 100 specimens. Discusses the different crack models that can be used to simulate real flaws as well as the shortcomings of such models. Includes Raju-Newman and elliptical integral flaw stress intensity factor solutions.

G. D. Quinn and J. J. Swab, "Fractography and Estimates of Fracture Origin Size from Fracture Mechanics," *Ceram. Eng. Sci. Proc.*, **17** [3] (1996) 51–58.

Fracture mechanics should be used routinely in fractographic analyses to verify that the correct feature has been identified as the fracture origin. This paper reviews the factors that may cause calculated and measured flaw sizes to differ.

Fracture Mechanics—Stress Intensity Factors

Y. Murakami, *Stress Intensity Factors Handbook*, Vols. 1 and 2, Pergamon Press, NY, 1986.

A collection of stress intensity factors for various cracks under different loading conditions.

H. Tada, P. C. Paris, and G. R. Irwin, *The Stress Analysis of Cracks Handbook*, 3rd edition, ASM International, Metals Park, OH, 2000.

An update of their 1973 collection of stress intensity factors for various cracks under different loading conditions.

T. Fett, and D. Munz, *Stress Intensity Factors and Weight Functions*, Wessex Institute of Technology, Southhampton, UK, 1997.

A collection of stress intensity factors for various cracks under different loading conditions.

D. P. Rooke, and D. J. Cartwright, *Compendium of Stress Intensity Factors*, Her Majesty's Stationary Office, London, 1976.

A collection of stress intensity factors for various cracks under different loading conditions.

G. C. Sih, Handbook of Stress Intensity Factors, Lehigh University, Bethlehem, PA, 1973.

An older but still useful collection of stress intensity factors for various cracks under different loading conditions.

I. Bar-on, "Applied Fracture Mechanics," *Engineered Materials Handbook*, Vol. 4, *Ceramics and Glasses*, S. Schneider, ed., ASM, Metals Park, OH, 1991, pp. 645–651.

A good introduction to the application of fracture mechanics analysis to idealized crack configurations. Stress intensity shape factors are given for through slits, surface cracks, and pores with rim cracks.

J. C. Newman, Jr., and I. S. Raju, "An Experimental Stress-Intensity Factor Equation for the Surface Crack," *Eng. Fract. Mech.*, **15** [1–2] (1981)185–192.

Presents an widely used equation for the calculation of the stress intensity shape factors (*Y*) for surface semicircular or semielliptical cracks. Y is given for the location where the origin meets the surface and at the deepest point of the origin. Both direct tension and flexural solutions are presented.

S. Strobl, P. Supancic, T. Lube, and R. Danzer, "Surface Crack in Tension or Bending – A Reassessment of the Newman and Raju Formula in Respect to Fracture Toughness Measurements in Brittle Materials," *J. Eur. Cer. Soc*., **32** (2012) 1491–1501.

Also presents shape factor (*Y*) for surface semicircular or semielliptical cracks, but for more general cases than the Newman-Raju solutions. The Strobl et al. solutions can be considered refined solutions. They allow different values of Poisson's ratio and crack intersection angles at the tensile surface to be input. For most surface cracks the new solutions are only a few percent different than Newman and Raju's. The solutions match Newman and Raju's for $\nu = 0.3$ and for semielliptical surface cracks (where the crack surface angle is 90^{o}).

F. Baratta, "Stress Intensity Factor Estimates for a Peripherally Cracked Spherical Void and a Hemispherical Surface Pit," *J. Am. Ceram. Soc*., **61** [11-12] (1978) 490-492.

F. Baratta." Refinement of Stress Intensity Factor Estimates for a Peripherally Cracked Spherical Void and a Hemispherical Surface Pit," *J. Am. Ceram. Soc*., **64** [1] (1981) C3-C4.

D. J. Green, "Stress Intensity Factor Estimates for Annular Cracks at Spherical Voids," *J. Am. Ceram. Soc.*, **63** [5-6] (1980) 342-344.

T. Fett, "Stress Intensity Factors and Weight Functions for a Void with an Annular Crack," *Int. J. Fract*., **67** (1994) R41-R47.

APPENDIX B FRACTOGRAPHIC CASE STUDIES

Case studies for components and structures are organized by topic. Glass cases come first, followed by ceramics and glass ceramics, fibers, single crystals, gemstones, and rocks and lithics.

Glass Windows and Plates of All Sizes

Automotive and building windows

N. Shinkai, "The Fracture and Fractography of Flat Glass," pp. 253 – 297 in *Fractography of Glass*, eds. R. C. Bradt and R. E. Tressler, Plenum Press, NY, 1994.

A superb practical article on annealed, tempered, and laminated glass for automobiles or building windows.

V. D. Fréchette and M. Donovan, "Some Effects of the Glue Chipping Process on Strength," pp. 407 – 411 in *Fractography of Glasses and Ceramics II, Ceramic Transactions Vol. 17,* eds. V. D. Fréchette and J. R. Varner, American Ceramic Society, Westerville, OH, 1991.

Fractures of hundreds of very large float glass windows in a Boston skyscraper.

V. D. Fréchette, *Failure Analysis of Brittle Materials,* Advances in Ceramics, Vol. 28, American Ceramic Society, Westerville, OH, 1990, pp. 119 -120.

Fractures in large float glass windows in a skyscraper. Glue chips.

T. Sakai, M. Ramulu, A. Ghosh, and R. C. Bradt, "A Fractal Approach to Crack Branching (bifurcation) in Glass," pp. 131 –146 in *Fractography of Glasses and Ceramics II,* eds., V. D. Fréchette and J. R. Varner, *Ceramic Transactions,* Vol. 17, American Ceramic Society, Westerville, OH, 1991.

Fracture patterns in laminated safety glass for bus passenger shelters.

S. T. Gulati, R. Akcakaya, and J. Varner, "Fracture Behavior of Tin vs. Air Side of Glass," pp. 317 – 325 in *Fractography of Glasses and Ceramics,* IV, eds., J. R. Varner and G. D. Quinn, American Ceramic Society, Westerville, OH, 2001.

S. T. Gulati, J. D. Helfinstine, T. A. Roe, "Strength Degradation of Automotive Windshield from Manufacturing to On-Road Service," *Glass Technol.,* **43C** (2002) 303 – 308.

Testing of singlets and windshield coupons. Edging, scoring, solder tabs.

T. Cleary and S. Gulati, "Influence of Glass Score and Seam Orientation on Edge Strength of Multi-Layered Glass Articles," pp. 327 – 341 in *Fractography of Glasses and Ceramics,* IV, eds. J. R. Varner and G. D. Quinn, American Ceramic Society, Westerville, OH, 2001.

Fracture patterns in laminated safety glass (sandwich of two glass plates and a central plastic sheet).

R. A. Allaire and T. Ono, "Fracture Analysis of the Glass Scoring Process," pp. 467 – 471 in *Fractography of Glasses and Ceramics,* IV, eds. J. R. Varner and G. D. Quinn, American Ceramic Society, Westerville, OH, 2001.

Fracture patterns on scored glass plates.

T. M. Cleary and R. T. Nichols, " Adhesive Induced Fracture of Automotive Glass," pp. 369-380 in *Fractography of Glasses and Ceramics V*, eds. J. R. Varner, G.D. Quinn, M. Wightman, *Ceramic Transactions*, Vol. 199, American Ceramic Society, Westerville, OH, 2007.

Glue chips and adhesive and thermally-induced fractures in both front laminated and tempered rear windows.

R. Huet, J. M. Wolf, P. D. Moncarz, "Delayed Fracture of Tempered Glass Panels Due to Nickel Sulfide inclusions," pp. 431-433 in Handbook of Case Studies in Failure Analysis, Vol. 1, ed. K. A. Esakul, ASTM Int. Materials park, OH, 1992.

C. C. Hsiao, "Spontaneous Fracture of Tempered Glass, " pp. 985 -992 in Fracture 1977, Vol. 3, ed. D. Taplin, International Congress on Fracture 4, Waterloo, Canada, 1977.

S. A. Batzer, "Failure Mechanisms of Automotive Side Glazing in Rollover Collisions," *J. Fail. Anal. Prev*., **6 [**3] (2006) 6-11, 33,34.

R. C. Bradt, M. E. Barkey, S. E. Jones, M. E. Stevenson, "Projectile Impact – A Major Cause for Fracture of Flat Glass," *J. Fail. Anal. Prev*., **3** [1] (2003) 5-11.

R. C. Bradt, "Macro- and Microfracture Patterns of Thermally Tempered Plate Glass Falling from Nickel Sulfide Inclusions," pp. 417 – 426 in *Fractography of Glasses and Ceramics,* eds. J. D. Varner and V. D. Fréchette, Advances in Ceramics, Vol. 22, American Ceramic Society, Westerville, OH, 1988.

Cell phone cover glass

G. S. Glaesemann, T. M. Gross, J. F. Bayne, and J. J. Price, "Fractography on Ion-Exchanged Cover Glass," pp. 85 – 93 in *Fractography of Glasses and Ceramics VI,* eds. J. Varner and M. Wightman, *Ceramic Transactions*, Vol. 230, American Ceramic Society, Wiley, Westerville, OH, 2012.

T. M. Gross, "Scratch Damage in Ion-Exchanged Alkali Aluminosilicate Glass: Crack Evolution and the Dependence of Lateral Cracking Threshold on Contact Geometry," pp. 113-122 in *Fractography of Glasses and Ceramics VI,* eds. J. Varner and M. Wightman, *Ceramic Transactions* ,Vol. 230, American Ceramic Society, Wiley, Westerville, OH, 2012.

Sight glass windows, water hammer

V. D. Fréchette, *Failure Analysis of Brittle Materials,* Advances in Ceramics, Vol. 28, American Ceramic Society, Westerville, OH, 1990, p. 112.

Tempered glass spontaneous failure

R. C. Bradt, "Macro- and Microfracture Patterns of Thermally Tempered Plate Glass Falling from Nickel Sulfide Inclusions," pp. 417 – 426 in *Fractography of Glasses and Ceramics,* Advances in Ceramics, Vol. 22, ed. J. D. Varner and V. D. Fréchette, American Ceramic Society, Westerville, OH, 1988.

C. C. Hsiao, "Spontaneous Fracture of Tempered Glass," pp. 985 – 992 in *Fracture 1977*, Vol. 3, International Congress on Fracture 4, Waterloo, Canada, 1977.

Plate glass mirrors for solar cells

V. D. Fréchette, *Failure Analysis of Brittle Materials,* Advances in Ceramics, Vol. 28, American Ceramic Society, Westerville, OH, 1990, p. 117.

Hail stones, thermal stresses, and edge cracks.

Laser glass slabs

J. E. Marion, "Fracture Mechanisms of Solid Sate Slab Lasers," pp. 307 – 318 in *Fractography of Glasses and Ceramics,* eds. J. D. Varner and V. D. Fréchette, Advances in Ceramics, Vol. 22, American Ceramic Society, Westerville, OH, 1988.

J. E. Marion, "Fracture of Solid State Laser Slabs," *J. Appl. Phys.,* **60** [1] (1986) 69 – 77.

Borosilicate Glass Flowmeter

J. Kübler, "Failure Analysis on a Flowmeter," pp. 65-71 in *Fractography of Advanced Ceramics III*, eds. J. Dusza, R. Danzer, R. Morrell, and G. D. Quinn, Trans Tech Publ. Zurich, 2009.

Home cocktail table

A. A. Johnson and R. J. Storey, "A Fatal Accident Involving a Glass-Topped Cocktail Table," *J. Fail. Anal. Prev*., **14** (2014) 267-271.

A college-graduating student fell over a glass-topped cocktail table which shattered. A long sharp shard pierced his heart and killed him. The untempered glass was supported by eight tabs, only four of which had plastic inserts.

Glass Containers, Lamps, and Pressure Vessels

Pharmaceutical Glass Vials and Syringes

F. Maurer, "Application of Fractography in Pharmaceutical Industry," pp. 289 – 298 in *Fractography of Glasses and Ceramics,* VI, eds. J. R. Varner, M. Wightman, *Ceramic Transactions,* Vol. 230, Wiley, New York, 2012.

Glass syringe compliant specimen.

G. D. Quinn, This Guide, Chapter 10. Medicinal Glass Vials

Neck cracking from the cap sealing operation.

Bottles and flasks

V. D. Fréchette, *Failure Analysis of Brittle Materials,* Advances in Ceramics, Vol. 28, American Ceramic Society, Westerville, OH, 1990, pp. 94 – 101, 112, 118, 123.

Internal pressure, water hammer, thermal shock, and impact fractures. Various bottles including intravenous medical bottles, wine bottles, frozen citrus fruit concentrate bottles, malformed bottles.

F. W. Preston, "Bottle Breakage – Causes and Types of Fractures," *Am. Ceram. Soc. Bull.,* **18** [2] (1939) 35 – 60.

An early paper, but with an exceptional treatment of a variety of failure causes.

V. D. Fréchette and T. A. Michalske, "Fragmentation in Bursting Glass Containers*,"* *Bull. Amer. Ceram. Soc.*, **57** [4] (1978) 427 – 429.

Four different sizes of internally-pressurized, water-filled bottles.

V. D. Fréchette and S. L. Yates, "Fragmentation of Glass Bottles by Impact," *J. Am. Ceram. Soc*., **72** [6] (1989) 1060.

Three different sizes of water-filled bottles were swung at different velocities against a stationary steel rod.

J. B. Kepple, and J. S. Wasylyk, "Fracture of Glass Containers," pp. 207 –252 in *Fractography of Glass*, eds. R. C. Bradt and R. E. Tressler, Plenum Press, NY, 1994.

An excellent, multifaceted treatment. Shows fracture causes and patterns.

R. E. Mould, "The Behavior of Glass bottles Under Impact," *J. Amer. Ceram. Soc.,* **35** [9] (1952) 230 – 235.

A well illustrated paper on controlled breakages of bottles. This article (and Dimmick's that followed it) proved that hinge origins away from the impact site were sources of breakage in some cases.

C. Colin and J. L. Heitz, "Failure Analysis: Glass Bottle Breakage," *Verre,* **16** [4] (2010) 33-36.

Sparkling wine bottle broke spontaneously in boxes in a warehouse. Glass-to-glass contact damage from improper packing caused cracks that grew to failure.

D. D. Cannon, C. S. Musso, J. C. Williams, and T. W. Eagar, "Analysis of Brittle Fracture of Soda Glass Bottles Under Hydrostatic Pressure," *J. Fail. Anal. Prev.,* **45** [5] (2004) 72-77.

Soda glass bottles were fractured in the lab by increasing pressure after a scratch had been made. Other bottles were impacted in various manners.

Fluorescent lamps

D. Johnson, "Arc Induced Fractures from Lampmaking Test Equipment," pp. 517 – 525 in *Fractography of Glasses and Ceramics, III, Ceramic Transactions,* Vol. 64, J. R. Varner, V. D., Fréchette, and G. D. Quinn, eds., American Ceramic Society, Westerville, OH, 1996.

Cathode Ray Tube

A. Ghosh, C. Y. Cha, Vaidyanathan, and R. C. Bradt, "Finite Element Stress Analysis and Crack Path Prediction of Imploding CRT," pp. 1- 24 in *Fractography of Glasses and Ceramics II,* eds. V. D. Fréchette and J. R. Varner, *Ceramic Transactions,* Vol. 17, American Ceramic Society, Westerville, OH, 1991.

Glass cooking thermometer

V. D. Fréchette, *Failure Analysis of Brittle Materials,* Advances in Ceramics, Vol. 28, American Ceramic Society, Westerville, OH, 1990, p. 120.

Tempered glass cylinders

V. D. Fréchette, *Failure Analysis of Brittle Materials,* Advances in Ceramics, Vol. 28, American Ceramic Society, Westerville, OH, 1990, pp. 120 –121, 123 –124.

Uneven thermal temper in a structural cylinder and also a high power gymnasium lamp that lost its temper due to heating.

Glass neutron beam guideline

G. D. Quinn, O. Zilcha, J. M. Rowe, and D. J. Pierce, "Failure Analysis of a 41 Meter Long Neutron Beam Line Guide," 4th International Conference on Fractography of Advanced Ceramics," Smolenice Castle, Oct. 2013, *J. Eur. Cer. Soc.,* **34** (2014) 3263-3270.

Glass Bulletproof or Impact Resistant Windows

M. E. Stevenson, S. E. Jones, and R. C. Bradt, "Fracture Patterns of a Composite Safety Glass Panel During High Velocity Projectile Impacts," pp. 473 – 488 in Fractography *of Glasses and Ceramics,* IV, eds. J. R. Varner and G. D. Quinn, American Ceramic Society, Westerville, OH, 2001.

D. L. Ahearn, J. L. Ladner, S. E. Jones, R. E. Wright and R. C. Bradt, "Fracture Patterns of Impact Resistant Glass Panel Laminates with Annealed and Heat Strengthened Glass Plates," pp. 383 – 395 in *Fractography of Glasses and Ceramics V*, eds. J. R. Varner, G.D. Quinn, M. Wightman, Ceramic Transactions, Vol. 199, American Ceramic Society, Westerville, OH, 2007.

H. Yoshimura and R. G. Morrone, "Analysis of Projectile Impact Damage in Bulletproof Glasses," pp. 397 – 406 in *Fractography of Glasses and Ceramics V*, eds. J. R. Varner, G.D. Quinn, M. Wightman, *Ceramic Transactions* ,Vol. 199, American Ceramic Society, Westerville, OH, 2007.

J. LK. Ladner, D. L. Ahearn, and R. C. Bradt, "Laminate Design Effects on the Fracture Patterns of Impact Resistance Glass Panels," pp. 281-287 in in *Fractography of Glasses and Ceramics,* VI, eds. J. R. Varner, M. Wightman, *Ceramic Transactions,* Vol. 230, Wiley, New York, 2012.

Ceramic Windows, IR Domes, Radomes

Magnesium Fluoride (MgF_2) IR window test coupons
R. W. Rice, " Failure Analysis of Ceramics," pp. 369 – 388 in *Fractography of Glasses and Ceramics,* IV, eds. J. R. Varner and G. D. Quinn, American Ceramic Society, Westerville, OH, 2001.

Calcium Fluoride (CaF_2) windows in a laser flash diffusivity apparatus
R. Morrell, "Dealing with Component Failures," pp. 353 -368 in Fractography of Glasses and Ceramics V, eds. J. R. Varner, G.D. Quinn, M. Wightman, *Ceramic Transactions,* Vol. 199, American Ceramic Society, Westerville, OH, 2007.

48 mm diameter single crystal disks that broke from thermal stresses activating edge damage or impact damage.

Glass ceramic missile radome, thermal shock
R. W. Rice, "Failure Analysis of Ceramics," pp. 369 – 388 in *Fractography of Glasses and Ceramics,* IV, eds. J. R. Varner and G. D. Quinn, American Ceramic Society, Westerville, OH, 2001.

Fused silica Missile radome
This Guide. Chapter 10, case 7.

Grinding flaws and joint debonding.

Polycrystalline Alumina (PCA) Lamp Tubes
F. Lofaj, V. Ivančo, and P.P Varga, "Fracture of Thin walled Translucent Polycrystalline (PCA) Tubes," pp. 223 – 230 in *Fractography of Advanced Ceramics III*, eds. J. Dusza, R. Danzer, R. Morrell, and G. D. Quinn, Trans Tech. Zurich, 2009.

Microwave tube (alumina)
R. W. Rice, "Failure Analysis of Ceramics," pp. 369 – 388 in *Fractography of Glasses and Ceramics,* IV, eds. J. R. Varner and G. D. Quinn, American Ceramic Society, Westerville, OH, 2001.

Ceramic Seals

Tetragonal zirconia polycrystalline (TZP) hydraulic seal disks
R. W. Rice, "Failure Analysis of Ceramics," pp. 369 – 388 in *Fractography of Glasses and Ceramics,* IV, eds. J. R. Varner and G. D. Quinn, American Ceramic Society, Westerville, OH, 2001.

Mechanical seal rings – silicon carbide
R. Morrell, "Fractography of Brittle Materials," R. Morrell, Measurement Good Practice Guide 15, National Physical Laboratory, Teddington, Middlesex, United Kingdom, 1999, pp. 76 – 85.

Large open rotating rings with shoulders and notches. Impact damage - chipping, preexisting cracks, grinding cracks, handling damage.

Large (300 mm) silicon carbide seal rings

R. Morrell, "Dealing with Component Failures," pp. 353 -368 in *Fractography of Glasses and Ceramics V,* eds. J. R. Varner, G.D. Quinn, M. Wightman, *Ceramic Transactions*, Vol. 199, American Ceramic Society, Westerville, OH, 2007.

Fractures during over-speed poof testing by spinning the disks. Good sketches of 5 disk fractures, illustrating how multiple crack patterns can be deciphered to find the primary fracture. Origins were edge chamfer damage, contact damage cracks, and machining cracks.

Ceramic Containers and Pressure Vessels

Large porcelain tubes

V. D. Fréchette, *Failure Analysis of Brittle Materials,* Advances in Ceramics, Vol. 28, American Ceramic Society, Westerville, OH, 1990, pp. 125 – 126.

"Spontaneous" fracture during end-face machining. Internal residual stresses.

Beta alumina hollow cylinders, burst pressure loading

B. J. McEntire, R. H. Snow, J. L. Huang, L. Viswanathan, and A. V. Virkar, "Characterization of Processing Flaws in Beta Alumina," pp 335 – 349 in *Fractography of Glasses and Ceramics,* eds. J. D. Varner and V. D. Fréchette, Advances in Ceramics, Vol. 22, American Ceramic Society, Westerville, OH, 1988.

Beta alumina electrolyte tubes, service failures

E. K. Beauchamp, "Beta Alumina failures in Sodium/Sulfur Batteries," pp. 377 – 387 in *Fractography of Glasses and Ceramics,* eds. J. D. Varner and V. D. Fréchette, Advances in Ceramics, Vol. 22, American Ceramic Society, Westerville, OH, 1988.

Ceramic Armor Plates

S. Winkler, H. Senf, and H. Rothenhäusler, "High Velocity Fracture Investigation in Alumina," pp. 165 – 183 in *Fractography of Glasses and Ceramics II,* eds. V. D. Fréchette and J. R. Varner, *Ceramic Transactions,* Vol. 17*,* American Ceramic Society, Westerville, OH, 1991.

High-speed photography of alumina and glass plates hit on end.

M. E. Stevenson, S. E. Jones, and R. C. Bradt, "Fracture Patterns of a Composite Safety Glass Panel During High Velocity Projectile Impacts," pp. 473 – 488 in *Fractography of Glasses and Ceramics, IV*, eds. J. R. Varner and G. D. Quinn, American Ceramic Society, Westerville, OH, 2001.

J. J. Swab, G. A., Glide, P. J. Patel, A. A Wereszczak, J. W. McCauley, and J. D. Risner, "Fracture Analysis of Transparent Armor Ceramics," pp. 489 – 508 in *Fractography of Glasses and Ceramics, IV,* eds. J. R. Varner and G. D. Quinn, American Ceramic Society, Westerville, OH, 2001.

Biaxial strength tests on sapphire, aluminum oxynitride, and magnesium alumina spinel.

R. L. Woodward, R. G. O'Donnell, B. J. Baxter, B. Nicol, and S. D. Pattie, "Energy Absorption in the Failure of Ceramic Composite Armors," *Mater. Forum*, **13** (1989) 174 – 181.

M. J. Slavin, "Fractographic Analysis of Long Rod Penetrator-Armor Ceramics Interactions," U. S. Army Technical Report, TR 89-93, U.S. Army Materials Technology Laboratory, Watertown, MA, Oct. 1989.

C. Tracy, M. Slavin, and D. Viechnicki, "Ceramic Fracture During Ballistic Impact," pp. 295 – 306 in *Fractography of Glasses and Ceramics,* eds. J. D. Varner and V. D. Fréchette, Advances in Ceramics, Vol. 22, American Ceramic Society, Westerville, OH, 1988.

S. Rodriguez, V. B. Munoz, E. V. Esquivel, L. E. Muir, and N. L. Rupert, "Microstructural Characterization of TiB_2 Armor Targets," *J. Mat. Sci. Lttrs*., **21** (2002) 1161 – 1666.

V. D. Fréchette and C. F. Cline, "Fractography of Ballistically Tested Ceramics," *J. Am. Ceram. Soc.,* **49** [11] (1970) pp. 994 – 997.

V. D. Fréchette, "Fractography and Quality Assurance of Glass and Ceramics," pp. 227 236 in *Quality Assurance in Ceramic Industries*, eds. V. D. Fréchette, L. D. Pye, and D. E. Rase, Plenum, NY, 1978.

Hot-pressed boron carbide blanks fractured during machining. Internal residual stresses were created by too rapid a cool down from the firing temperature.

R. N. Katz and W. A. Brantley, "Fractography of High Boron Ceramics Subjected to Ballistic Loading," pp. 271 – 282 in *Materials Science Research*, Vol. 5, ed. W. W. Kriegel, Plenum, NY, 1971.

D. G. Christie and H. Kolsky, "The Fractures Produced in Glass and Plastics by the Passage of Stress Waves," *J. Soc. Glass Technol.,* **36** (1952) 65 - 73.

Ceramic Ball Bearings

J. J. Swab and M. P. Sweeney, "Fracture Analysis of An All-Ceramic Bearing System," U. S. Army Research Laboratory Technical Report, ARL TR 512, September 1994.

Y. Wang and M. Hadfield, "Rolling Contact Fatigue Failure Modes of Lubricated Silicon Nitride in Relation to Ring Crack Defects," *Wear*, **225-229** (1999) 1284 – 1292.

Y. Wang and M. Hadfield, "The Influence of Ring Crack Location on the Rolling Contact Fatigue Failure of Lubricated Silicon Nitride: Experimental Studies," *Wear*, **243** (2000) 157 – 166.

T. Lube, S. Witsching, P. Supancic, R. Danzer, O. Schöppl, "The Notched Ball Test – Characterization of Surface Defects and Their Influence on Strength," pp. 225 – 234 in *Fractography of Glasses and Ceramics, VI*, eds. J. R. Varner, M. Wightman, *Ceramic Transactions,* Vol. 230, Wiley, New York, 2012.

P. Supancic, R. Danzer, W. Harrer, Z. Wang, S. Witschnig, and O. Schöppl, "Strength Tests on Silicon Nitride Balls," pp. 193 – 200 in *Fractography of Advanced Ceramics III*, eds. J. Dusza, R. Danzer, R. Morrell, and G. D. Quinn, Trans Tech Publ. Zurich, 2009.

Cellular Ceramics, Catalytic Converters, Filters

D. J. Green and R. Brezny, "Fractographic Determination of Strut Strength in Cellular Ceramics," pp. 199 – 129 in *Fractography of Glasses and Ceramics II,* eds. V. D. Fréchette and J. R. Varner, *Ceramic Transactions,* Vol. 17, American Ceramic Society, Westerville, OH, 1991.

J. Kübler, R. Baechtold, G. Blugan, L. Lemster, and S. Fuso, "Failure Analysis on a De-No_x Catalyst of a Large Waste Burner," pp. 78 - 85 in *Fractography of Advanced Ceramics II,* eds. J. Dusza, R. Danzer and R. Morrell, Transtech, Zurich, 2005.

Special Ceramic Components

MEMS structures

S. J. Glass, D. A. LaVan, T. E. Buchheit, and K. Jackson, "Strength Testing and Fractography of MEMS Materials," pp. 227 –240 in *Fractography of Glasses and Ceramics,* IV, eds. J. R. Varner and G. D. Quinn, American Ceramic Society, Westerville, OH, 2001.

G. Quinn, W. Sharpe, G. M Beheim, N. Nemeth and O. Jadaan, "Fracture Origins in Miniature Silicon Carbide Structures," pp. 62 –69 in *Fractography of Advanced Ceramics II,* eds. J. Dusza, R. Danzer and R. Morrell, Transtech, Zurich, 2005.

Theta Specimens

G. D. Quinn, "Fractographic Analysis of Very Small Theta Specimens," pp. 201-208 in *Fractography of Advanced Ceramics III*, eds. J. Dusza, R. Danzer, R. Morrell, and G. D. Quinn, Trans Tech Publ., Zurich, 2009.

Ceramic automotive valves

R. Danzer, M. Hangl, and R. Paar, "Edge Chipping of Brittle Materials," pp. 43 – 55 in *Fractography of Glasses and Ceramics,* IV, eds. J. R. Varner and G. D. Quinn, American Ceramic Society, Westerville, OH, 2001.

M. J. Andrews, A. A. Wereszczak, K. Breder, and T. P. Kirkland, "Fractographic Analysis Applied to Ceramic Component Life Prediction," pp. 301 – 315 in

Fractography of Glasses and Ceramics, IV, eds. J. R. Varner and G. D. Quinn, American Ceramic Society, Westerville, OH, 2001.

Ceramic gas turbine model rotor

G. D. Quinn, This Guide, Chapter 10, and
G. D. Quinn, "Design and Reliability of Ceramics, Do Modelers, Designers and Fractographers See the Same World?" *Ceram. Eng. Sci. Proc.,* **26** [8] (2005) 239 - 252.

α - silicon carbide heat exchanger tube

K. Breder and J. R. Kaiser, "Failure Analysis of an α-SiC Tube Subjected to Thermal Cycling in and Oxygen-Steam Atmosphere," pp. 301 –315 in *Fractography of Glasses and Ceramics, III,* eds. J. R. Varner, V. D. Fréchette, and G. D. Quinn, *Ceramic Transactions,* Vol. 64, American Ceramic Society, Westerville, OH, 1996.

Silicon carbide machine gun barrel

G. D. Quinn, This Guide, Chapter 10, and
G. D. Quinn, "Design and Reliability of Ceramics, Do Modelers, Designers and Fractographers See the Same World?" *Ceram. Eng. and Sci. Proc.,* 26 [8] (2005) 239 - 252.

Contact cracks from shrink fitting and stress reverberations

Silicon nitride rolling mill rollers

M. Lengauer, R. Danzer, D. Rubesa, W. Harrer, and W. Zleppnig, "Failure Analysis of Si_3N_4 Rolls for Wire Hot Rolling by Numerical Simulation of Thermal and Mechanical Stresses," pp. 94 -101 in *Fractography of Advanced Ceramics II,* eds. J. Dusza, R. Danzer and R. Morrell, Transtech, Zurich, 2005.

R. Danzer, M. Lengauer, D. Rubesa, and W. Harrer, "Silicon Nitride Tools for Hot Rolling of High-alloyed Steel and Superalloy Wires," pp. 43 – 54 in *Fractography of Advanced Ceramics III*, eds. J. Dusza, R. Danzer, R. Morrell, and G. D. Quinn, Trans Tech Publ. Zurich, 2009.

Lead zirconate titanate (PZT) sonar rings

R. W. Rice, "Failure Analysis of Ceramics," pp. 369 – 388 in *Fractography of Glasses and Ceramics,* IV, eds. J. R. Varner and G. D. Quinn, American Ceramic Society, Westerville, OH, 2001.

Epoxy bonding stresses

Silicon Nitride foundry tubes and rolls

W. Harrer, R. Danzer, K. Berroth, "Thermal Shock Behavior of Si_3N_4 Specimens – Influence of Annealing and Edges," pp. 245 – 254 in *Fractography of Glasses and Ceramics,* VI, eds. J. R. Varner, M. Wightman, *Ceramic Transactions,* Vol. 230, Wiley, New York, 2012.

Beryllium oxide hollow cylinder

J. R. Varner and V. D. Frechette, "Fractography of Whitewares," pp. 305 – 315 in *Science of Whitewares,* eds. V. Henkes, G. Onoda, and W. Carty, American Ceramic Society, Westerville, OH, 1996.

Hollow cylinder loaded at high temperature under laboratory conditions.

Electronic Ceramics

Porcelain railroad electrical insulator

J. Woodtli, K. Beroth, and T. Luthi, "Combination of Fractography and Computed Tomography for the Determination of the Cause of Fracture," pp. 257 – 271 in *Fractography of Glasses and Ceramics, III,* eds. J. R. Varner, V. D. Fréchette, and G. D. Quinn, *Ceramic Transactions,* Vol. 64, American Ceramic Society, Westerville, OH, 1996.

Porcelain insulator, high tension power line

J. R. Varner and V. D. Frechette, "Fractography of Whitewares," pp. 305 – 315 in *Science of Whitewares,* eds. V. Henkes, G. Onoda, and W. Carty, American Ceramic Society, Westerville, OH, 1996.

Material fault, a clump of feldspar grains

Silicon wafers

R. E. Moore, P. G. Hansen, W. Carty, and J. W. Ha, "Fracture of Thermally Shocked Silicon Disks," pp. 351 – 361 in *Fractography of Glasses and Ceramics,* eds. J. D. Varner and V. D. Fréchette, Advances in Ceramics, Vol. 22, American Ceramic Society, Westerville, OH, 1988.

Stacked PZT piezoelectric actuator material

P. Supancic, Z. Wang, W. Harrer, K. Reichmann, and R. Danzer, "Strength and Fractography of Piezoceramic Multilayer Stacks," pp. 46 –53 in *Fractography of Advanced Ceramics II,* eds. J. Dusza, R. Danzer and R. Morrell, Transtech, Zurich, 2005.

PTC (Positive Temperature Coefficient) thermistors – barium titanate

A. Platzer, P. Supancic, C. Lembacher, U. Theiszi, and R. Danzer, " Thermography and Simulation as a Combined Method for Failure Analysis of PTCs," pp. 54 - 61 in *Fractography of Advanced Ceramics II,* eds. J. Dusza, R. Danzer and R. Morrell, Transtech, Zurich, 2005.

R. Danzer, A. Platzer, P. Supoancic, Z. Wang, "Fractography of Thermistors," pp. 231 – 241 in *Fractography of Glasses and Ceramics V,* ,eds. J. R. Varner, G.D. Quinn, M. Wightman, *Ceramic Transactions*, Vol. 199, American Ceramic Society, Westerville, OH, 2007.

ZnO varistors

Z. Wang, P. Supancic, F. Aldrian, A. Schriener and R Danzer, "Strength and Fractography of High Power Varistors," pp. 358 - 365 in *Fractography of Advanced Ceramics II,* eds. J. Dusza, R. Danzer and R. Morrell, Transtech, Zurich, 2005.

R. W. Rice, "Failure Analyses of Ceramics," pp. 369 - 388 in *Fractography of Glasses and Ceramics,* IV, eds. J. R. Varner and G. D. Quinn, American Ceramic Society, Westerville, OH, 2001.

Components suffer dielectric breakdown.

Sold Oxide Fuel Cells

J. Malzbender, R. W. Steinbrech, E. Wessel, "Brittle Fracture Studies of Solid Oxide Fuel Cells," pp. 81-93 in *Fractography of Advanced Ceramics III*, eds. J. Dusza, R. Danzer, R. Morrell, and G. D. Quinn, Trans Tech Publ. Zurich, 2009.

L. Blanco, S. Taylor, and K. Wiggins, "Unexpected Thermal Fracture of a Ceramic Sensor," *J. Fail. Anal. Prev*., **11** (2011) 478-480.

A ceramic substrate, to which an electronic infrared sensor was bonded, fractured when thermally cycled due to excessive force from a polymer pad used to clamp the assembly together.

Bioceramics

Ceramic hip joint ball heads

H. G. Richter, "Fractography of Bioceramics," pp. 157 - 180 in *Fractography of Advanced Ceramics,* ed. J. Dusza, Trans Tech Publ., Zurich, 2002.

S. Hecht-Mijic and H. G. Richter, "Fractography of Bioceramic Components for Hip Joint Replacement," pp 313 – 328 in *Fractography of Glasses and Ceramics V,* ,eds. J. R. Varner, G.D. Quinn, M. Wightman, *Ceramic Transactions*, Vol. 199, American Ceramic Society, Westerville, OH, 2007.

R. Morrell, L. Byrne, and M. Murray, "Fractography of Ceramic Femoral Heads," pp. 253 – 266 in *Fractography of Glasses and Ceramics,* IV, eds. J. R. Varner and G. D. Quinn, American Ceramic Society, Westerville, OH, 2001.

A. Walter, "Fracture Phenomena in Orthopedic Alumina," pp. 403 – 414 in *Fractography of Glasses and Ceramics,* eds. J. R. Varner and V. D. Fréchette, Advances in Ceramics, Vol. 22, American Ceramic Society, Westerville, OH, 1988.

R. Morrell, "Dealing with Component Failures," pp. 353 -368 in *Fractography of Glasses and Ceramics V*, eds. J. R. Varner, G.D. Quinn, M. Wightman, *Ceramic Transactions,* Vol. 199, American Ceramic Society, Westerville, OH, 2007.

Includes general observations of femoral head fractures, plus two specific alumina cases. One *in-vivo* ball fracture had an unusual, circular, shiny region of slow

crack growth. The second case was an *in vitro* fracture that broke from cracks in the bore created by contact with a Co-Cr stem.

R. Morrell, R. Danzer, I. Milošev, R. Trebše, "An Assessment of in vivo Failures of Alumina Ceramic Total Hip Joint Replacements*," J. Eur. Cer. Soc.,* **32** (2012) 3073-3084.

Four *in vivo* cases. Femoral heads may be damaged by the surgeon, or contaminated during or prior to installation.

Dental Ceramics and Glass Ceramics

J. R. Kelly, "Fractography of Dental Ceramics," pp. 241 –251 in *Fractography of Glasses and Ceramics, IV*, eds. J. R. Varner and G. D. Quinn, American Ceramic Society, Westerville, OH, 2001.

J. B. Quinn, "Failure Analysis of a Broken Tooth," *J. Fail. Anal. Prev.*, **4** [1] (2004) 41 – 46.

A patient's natural tooth fractured days after open-heart surgery. Was the laryngoscopy by the anesthesiologist done correctly?

S. S. Scherrer, J. B. Quinn, G. D. Quinn, and J. R. Kelly, "Failure Analysis of Ceramic Clinical Cases Using Qualitative Fractography," *Int. J. Prosthodont.,* **19** [2] (2006) 151 – 158.

Five dental crown restorations that failed in service were analyzed. The materials were: Procera alumina, Cerestore alumina-spinel, In-ceram glass in-fused alumina, and porcelain fused to metal. Fractography identified the failure causes. These were correlated to clinical observations and crown design.

J. B. Quinn, G. D. Quinn, J. R. Kelly, and S. S. Scherrer, "Fractographic Analyses of Three Ceramic Whole Crown Restorations," *Dent. Mat.*, **21** (2005) 920 – 929.

Three dental crown restorations that failed in service were analyzed. The materials were Procera alumina, Cerestore alumina-spinel, and Empress II lithium disilicate. Origin sites were found in each case.

S. S. Scherrer, J. B. Quinn, G. D. Quinn, and H. W. A. Wiskott, "Fractographic Ceramic Failure Analysis Using the Replica Technique: Two Case Studies," *Dental Materials*, **23** [11] (2007) 1397-1404.

S. S. Scherrer, J. B. Quinn, G. D. Quinn, and H. W. A. Wiskott, "Descriptive Fractography on All Ceramic Dental Crown Failures," pp. 339 – 352 in *Fractography of Glasses and Ceramics, V*, eds., J. R. Varner, G. D. Quinn, M. Wightman, *Ceramic Transactions,* Vol. 199, American Ceramic Society, Westerville, OH, 2007.

S. S. Scherrer, G. D. Quinn, and J. B. Quinn, "Fractographic Failure Analysis of a Procera AllCeram Crown Using Stereo and Scanning Electron Microscopy," *Dent. Mater.*, **24** (2008) 1107 – 1113.

J. B. Quinn, S. S. Scherrer, and G. D. Quinn, "The Increasing Role of Fractography in the Dental Community," pp. 253 - 270, *Fractography of Glasses and Ceramics, V*, eds, J. R. Varner, G. D. Quinn, M. Wightman, *Ceramic Transactions,* Vol. 199, American Ceramic Society, Westerville, OH, 2007.

J. B. Quinn, G. D. Quinn, J. R. Kelly, and S. S. Scherrer, "Useful Tools for Dental Failure Investigation," pp. 36 - 53 in *Proc. Conference on Scientific Insights and Dental Ceramics and Photopolymer Networks*, ed. D. C. Starrett, Transactions of the Academy of Dental Materials, Vol. 16, 2004.

S. S. Scherrer, J. B. Quinn, and G. D. Quinn, "Fractography of Dental Restorations," in *Fractography of Advanced Ceramics, III*, ed. J. Dusza, R. Danzer, R. Morrell and G. Quinn, TransTech Publ., Zurich, 2009. *Key Engineering Materials,* **413** (2009) 72-80.

B. Taskonak, J. J. Mecholsky, Jr., and K. J. Anusavice, "Fracture Surface Analysis of Clinically Failed Fixed Partial Dentures," *J. Dent. Res.,* **3** (2006) 277 – 281.

J. Y. Thompson, K. J. Anusavice, A. Naman, and. H. F. Morris, "Fracture Surface Characterization of Clinically Failed All-Ceramics Crowns, *J. Dent. Res.,* **73** [12] (1994) 1824 - 1832.

Ten Dicor crown were fractographically analyzed in accordance with MIL HDBK 790 and the principles outline by Fréchette. Fracture initiated on the inside surfaces from abrasive damage or failure of the cement at the restoration/cement interface. Twelve Cerestore crowns were more difficult and appeared to break from the porcelain/core interface or inside the core material. Biaxial disk specimens furnished valuable property and fractographic information.

G. D. Quinn, K. Hoffman, S. Scherrer, U. Lohbauer, G. Amberger, M. Karl, J. R. Kelly, "Fractographic Analysis of Broken Ceramic Dental Restorations, pp. 161-174 in *Fractography of Glasses and Ceramics, VI*, eds. J. R. Varner, M. Wightman, *Ceramic Transactions,* Vol. 230, Wiley, New York, 2012.

Three case studies: an alumina 3-unit bridge; a 6-unit zirconia bridge; a 5-unit zirconia telescoping-denture.

G. D. Quinn, "Fractographic Analysis of Broken Ceramic Dental Restorations," *Ceramic Engineering and Science Proceedings*, **35** [1] (2015) 39-51.

S. Hecht-Mijic, "Fractography of Ceramic Dental Implants," pp 175 – 191 in *Fractography of Glasses and Ceramics, VI*, eds. J. R. Varner, M. Wightman, *Ceramic Transactions,* Vol. 230, Wiley, New York, 2012.

Fractures in ceramic dental implants.

M. Borba, H. N. Yoshimura, J. A. Griggs, P. F. Cesar, A. Della Bona, "Qualitative and Quantitative Fractographic Analysis of All-Ceramic Fixed Partial Dentures," pp. 205 – 212 in in *Fractography of Glasses and Ceramics, VI,* eds. J. R. Varner, M. Wightman, *Ceramic Transactions,* Vol. 230, Wiley, New York, 2012.

U. Lohbauer, R. Belli, G. Arnetzl, S. Scherrer, and G. D. Quinn, "Fracture of a Veneered-ZrO2 Dental Prosthesis from an Inner Thermal Crack," *Case Studies in Engineering Fracture Analysis*, **2** (2014) 100-106.

U. Lohbauer, G. Amberger, G. D. Quinn, S. S. Scherrer, "Fractographic Analysis of a Dental Zirconia Framework: A Case Study on Design Issues, *J. Mech. Behav. Biom. Mat*., **3** (2010) 623-629.

M. Øilo, A. K. Kvam, J. E. Tibballs, and N. Gjerdet, "Clinically Relevant Fracture Testing of All-Ceramic Crowns," *Dent. Mater.*, **29** (2013) 815-823.

M. Øilo, N. R. Gjerdet, "Fractographic Analysis of All-ceramic Crowns: A Study of 27 Clinically-fractured Crowns," *Dent. Mater*., **29** (2013) e78-e84.

M. Øilo, G. D. Quinn, "Fracture Origins in Twenty-two Dental Alumina Crowns," *J. Mech. Beh. Biomed. Mater.,* 53 (2016) 93 – 103.

Whitewares and Kitchenware

J. S. Banda and P. F. Messer, "Fracture-Initiating Flaws in Whitewares," pp. 363 - 375 in *Fractography of Glasses and Ceramics,* eds. J. D. Varner and V. D. Fréchette, Advances in Ceramics, Vol. 22, American Ceramic Society, Westerville, OH, 1988.

P. B. Adams and S. E. DeMartino, "Glass-Ceramic Cookware Failure Analysis," pp. 669 – 673 in *Ceramics and Glasses, Engineered Materials Handbook*, Vol. 4, ed. S. Schneider, ASM, Metals Park, OH, 1991.

V. D. Fréchette, *Failure Analysis of Brittle Materials,* Advances in Ceramics, Vol. 28, American Ceramic Society, Westerville, OH, 1990, pp. 113 - 114.

Teapots on stoves – thermal stresses.

V. D. Fréchette, *Failure Analysis of Brittle Materials,* Advances in Ceramics, Vol. 28, American Ceramic Society, Westerville, OH, 1990, pp. 114 - 115.

Lasagna dish, cone crack – impact origin crack, subsequently propagated by thermal stresses.

J. R. Varner and V. D. Frechette, "Fractography of Whitewares," pp. 305 – 315 in *Science of Whitewares,* eds. V. Henkes, G. Onoda, and W. Carty, American Ceramic Society, Westerville, OH, 1996.

Porcelain Coffee Storage Jars – contact damage from a metal band cover seal
Porcelain Bushing, 2.7 m long by 0.9 m diameter – residual stresses from firing
Porcelain Bushing, small - screw holes acted as origins

V. D. Fréchette, *Failure Analysis of Brittle Materials,* Advances in Ceramics, Vol. 28, American Ceramic Society, Westerville, OH, 1990, p. 113.

Porcelain faucet handles

M. D. Hayes and D. L. Ahearn, "Thermomechanical Analysis of a Ceramic Cooker," *J. Fail. Anal. Prev*., **13** (2013) 383-388.

Escape of hot gasses through a crack in a ceramic cooker/grill caused a house fire. The cause of the crack was not determined.

R.C. Bradt and R. L. Martens, "Shattering Glassware," *Bull. Amer. Ceram. Soc*., **91** [7] (2012) 33-38.

Consumerwares. Thermal shock fractures of heat-strengthened soda lime silica versus borosilicate glass.

Porcelain Toilet Bowls

D. L. Ahearn, "Residual Failure Due to Incomplete Sintering of Vitreous China Plumbing Fixtures, pp 273 – 279 in *Fractography of Glasses and Ceramics, VI*, eds. J. R. Varner, M. Wightman*, Ceramic Transactions,* Vol. 230, Wiley, New York, 2012.

J. R. Varner and V. D. Frechette, "Fractography of Whitewares," pp. 305 – 315 in *Science of Whitewares,* eds. V. Henkes, G. Onoda, and W. Carty, American Ceramic Society, Westerville, OH, 1996.

Toilet Bowl – water hammer

Toilet Tank – mounting-bolt hole failure from mechanical overload

Other Ceramic Components

Porcelain faucet handles

V. D. Fréchette, *Failure Analysis of Brittle Materials,* Advances in Ceramics, Vol. 28, American Ceramic Society, Westerville, OH, 1990, p. 113.

Earthenware sewer pipe

V. D. Fréchette, *Failure Analysis of Brittle Materials,* Advances in Ceramics, Vol. 28, American Ceramic Society, Westerville, OH, 1990, p. 116.

Uranium dioxide fuel element – bushing

V. D. Fréchette, *Failure Analysis of Brittle Materials,* Advances in Ceramics, Vol. 28, American Ceramic Society, Westerville, OH, 1990, pp. 120-121.

Thermal fracture.

Beryllium oxide hollow cylinder

J. R. Varner and V. D. Frechette, "Fractography of Whitewares," pp. 305 – 315 in *Science of Whitewares,* eds. V. Henkes, G. Onoda, and W. Carty, American Ceramic Society, Westerville, OH, 1996.

Hollow cylinder loaded at high temperature under laboratory conditions.

Ceramic machine base (Electrically insulating base)
R. Morrell, "Fractography of Brittle Materials," R. Morrell, *Measurement Good Practice Guide 15,* National Physical Laboratory, Teddington, Middlesex, United Kingdom, 1999, pp. 67 – 69.
Bending failure from bolt holes.

Ceramic ball valve – alumina
R. Morrell, "Fractography of Brittle Materials," R. Morrell, *Measurement Good Practice Guide 15,* National Physical Laboratory, Teddington, Middlesex, United Kingdom, 1999, pp. 70- 71.
150 mm alumina ball with slots and large hole, internal pressure.

Gas valve plate - alumina
R. Morrell, "Fractography of Brittle Materials," R. Morrell, *Measurement Good Practice Guide 15,* National Physical Laboratory, Teddington, Middlesex, United Kingdom, 1999, pp. 72 -74.
Possible grinding or lapping damage near a complex hole.

Steel continuous casting nozzles – Carbon-bonded alumina, zirconia, magnesia, graphite.
A. Mašelejová and A. Leško, "Fracture Characteristics of Isostatic Pressed Submerged Entry Nozzle," pp. 370 – 373 in *Fractography of Advanced Ceramics II,* eds. J. Dusza, R. Danzer and R. Morrell, Transtech, Zurich, 2005.

Fibers - Glass - Optical

H. C. Chandan, R. D. Parker, and D. Kalish, "Fractography of Optical Fibers," pp. 143 – 184 in *Fractography of Glass*, Ed. R. C. Bradt and R. E. Tressler, Plenum Press, NY, 1994.

W. R. Wagner, "Failure Analysis of Fiber Optic Connectors," pp. 389 – 402 in *Fractography of Glasses and Ceramics,* Advances in Ceramics, Vol. 22, ed. J. D. Varner and V. D. Fréchette, American Ceramic Society, Westerville, OH, 1988.

J. J. Mecholsky, "Fracture Surface Analysis of Optical Fibers," pp. 663 – 668 in *Ceramics and Glasses, Engineered Materials Handbook*, Vol. 4, ed. S. Schneider, ASM, Metals Park, OH, 1991.

P. G. Simpkins and J. T. Krause, "Dynamic Response of Glass Fibers During Tensile Fracture," *Proc. R. Soc. London A,* **350** (1976) 253-265.
High-speed photos of strong (> 2.8 GPa) glass fibers tested in tension reveal that secondary fractures occur as the result of fiber whipping and flexural and longitudinal wave interactions. Fibers disintegrate into a particulate cloud.

Fibers – Nonoptical

P. K. Gupta, "Fractography of Fiberglass," pp. 185 – 206 in *Fractography of Glass*, Ed. R. C. Bradt and R. E. Tressler, Plenum Press, NY, 1994.

G. V. Srinivasan and V. Venkateswaren, "Fractographic Investigation of Flaws in Sintered SiC Fiber," pp 317 –337 in *Fractography of Glasses and Ceramics, III,* eds. J. R. Varner, V. D. Fréchette, and G. D. Quinn, *Ceramic Transactions,* Vol. 64, American Ceramic Society, Westerville, OH, 1996.

C-T. Li and N. R. Langley, "Development of a Fractographic Method for the Study of High-Temperature Failure of Ceramic Fibers," pp. 177 – 184 in *Fractography of Glasses and Ceramics,* eds. J. D. Varner and V. D. Fréchette, Advances in Ceramics, Vol. 22, American Ceramic Society, Westerville, OH, 1988.

T. Clark, "Fracture Properties of Thermally Aged Ceramic Fiber Produced by Polymer Pyrolysis," pp. 279 – 305 in *Fractography of Glasses and Ceramics,* eds. J. D. Varner and V. D. Fréchette, Advances in Ceramics, Vol. 22, American Ceramic Society, Westerville, OH, 1988.

Fiber Composites

Silicon carbide fibers in a glass matrix

A. S. Fareed, M. J. Koczak, F. Ko, and G. Layden, "Fracture of SiC/LAS Ceramic Composites," pp. 261 – 293 in *Fractography of Glasses and Ceramics,* eds. J. D. Varner and V. D. Fréchette, Advances in Ceramics, Vol. 22, American Ceramic Society, Westerville, OH, 1988.

Glass fibers in a fiberglass-reinforced plastic pressure vessel

S. J. Glass, E. K. Beauchamp, M. J. Carr, T. R. Guess, S. L. Munroe, R. J. Moore, A. Slavin, and N. R. Sorenson, "Failure Analysis of A Fiberglass-Reinforced Plastic Pressure Vessel," pp. 527 – 541 in *Fractography of Glasses and Ceramics, III,* eds. J. R. Varner, V. D. Fréchette, and G. D. Quinn, *Ceramic Transactions,* Vol. 64, American Ceramic Society, Westerville, OH, 1996.

Violent rupture of a pressurized tank holding sulphuric acid. Occasional and incidental spillage penetrated microcracks in the matrix and caused progressive degradation in glass fibers.

Single crystal ceramic components

Sapphire secondary refractor lens for spacecraft

J. A. Salem and G. D. Quinn, "Failure Analysis of Sapphire Refractive Secondary Concentrators," NASA Technical Report: TM-2009-215802, NASA Glenn Research Center, Cleveland, OH, Dec. 2009. Also in this Guide, chapter 10.

J. A. Salem, G. D. Quinn, "Fractographic Analysis of Large Single Crystal Sapphire Refractive Secondary Concentrators," second keynote presentation and paper, 4th International Conference on Fractography of Advanced Ceramics," Smolenice Castle, Oct. 2013, *J. Eur. Cer. Soc.,* **34** (2014) 3271-3281.

Large single crystal lens designed to concentrate sunlight in space. Fracture occurred from thermal stresses that propagated cracks from polishing and impact flaws from handling. Although strong and hard, sapphire is vulnerable to surface damage. Also this Guide, chapter 10.

Sapphire Tubes, Plasma Asher

This Guide, chapter 8.

Calcium Fluoride (CaF_2) windows in a laser flash diffusivity apparatus

R. Morrell, "Dealing with Component Failures," pp. 353 -368 in *Fractography of Glasses and Ceramics V,* eds. J. R. Varner, G.D. Quinn, M. Wightman, *Ceramic Transactions,* Vol. 199, American Ceramic Society, Westerville, OH, 2007.

48 mm diameter single crystal disks that broke from thermal stresses activating edge damage or impact damage.

Coatings and Glazes

Diamond coatings

H. A. Hoff, K. A. Snail, A. A. Morrish, and J. E. Butler, "Fractography and Fracture Mechanics of Combustion Grown Diamond Thin Films," pp. 25 – 54 *in Fractography of Glasses and Ceramics II*, eds. V. D. Fréchette and J. R. Varner, *Ceramic Transactions,* Vol. 17, American Ceramic Society, Westerville, OH, 1991.

Whiteware glazes

V. D. Fréchette, *Failure Analysis of Brittle Materials,* Advances in Ceramics, Vol. 28, American Ceramic Society, Westerville, OH, 1990, pp. 94 – 101.

Internal pressure, water hammer, thermal shock, and impact fractures.

Stoneware reactor catalyst media balls

R. W. Rice, "Failure Analysis of Ceramics," pp. 369 – 388 in *Fractography of Glasses and Ceramics*, *IV*, eds. J. R. Varner and G. D. Quinn, American Ceramic Society, Westerville, OH, 2001.

Gemstones and Jade

Emerald gemstone (3.66 carat)

R. W. Rice, " Failure Analysis of Ceramics," pp. 369 – 388 in *Fractography of Glasses and Ceramics*, IV, eds. J. R. Varner and G. D. Quinn, American Ceramic Society, Westerville, OH, 2001.

Impact on ceramic kitchen tile countertop caused cracking.

Jade

D. J. Rowcliffe and V. Frühauf, "The Fracture of Jade," *J. Mat. Sci.,* **12** (1977) 35 – 42.

Gemstones

J. E. Field, "Brittle Fracture: Its Study and Application," *Contemp. Phys.,* **12** [1] (1971) 1 - 31.

Rocks, Lithic Materials

J. B. Quinn, J. W. Hatch, and R. C. Bradt, "The Edge Flaking Test as an Assessment of the Thermal Alteration of Lithic Materials, Bald Eagle Jasper," pp. 73 – 85 in *Fractography of Glasses and Ceramics, IV,* eds. J. R. Varner and G. D. Quinn, American Ceramic Society, Westerville, OH, 2001.

A. Tsirk, "An Exploration of Liquid-Induced Fracture Markings," pp. 87 – 101 in *Fractography of Glasses and Ceramics, IV*, eds. J. R. Varner and G. D. Quinn, American Ceramic Society, Westerville, OH, 2001.

Obsidian tools.

A. Tsirk, "Fractographic Evidence for Liquid on Obsidian Tools," *J. Archeol. Sci.*, **27** (2000) 987 – 991.

A. Tsirk, "Formation and Utility of a Class of Anomalous Wallner Lines on Obsidian," pp. 57 - 69 in *Fractography of Glasses and Ceramics,* eds., J. D. Varner and V. D. Fréchette, Advances in Ceramics, Vol. 22, Amer. Ceram. Society, Westerville, OH, 1988.

A. Tsirk, "*Fractures in Knapping*," Archaeopress, Oxford, UK, 2014.

A comprehensive compilation of the author's lifelong work in fractures of rocks and glasses. This book was published very shortly before the author's death. Well illustrated and with links to modern fracture mechanics.

Geological, Tectonic Structures

D. Bahat, *Tectono-fractography,* Springer-Verlag, Berlin, 1991.

Bahat's book is a good starting point, but readers should be warned that some of the interpretations are controversial and are not settled.

B. R. Kulander, "Hackle Plume Geometry and Joint Propagation Dynamics," pp. 85 – 94 in *Proceedings of the International Symposium on Fundamentals of Rock Joints*, Björkilden, 15-20 September 1985.

O. H. Muller, "Fractography Applied to Large Scale (m to km) Cracks in the Earth," pp. 427 – 438 in *Fractography of Glasses and Ceramics,* eds. J. D. Varner and V. D. Fréchette, Advances in Ceramics, Vol. 22, American Ceramic Society, Westerville, OH, 1988.

Similar features observed over nine orders of magnitude of size.

A. I. Younes and T. Engelder, "Fringe Cracks: Key Structures for the Interpretation of the Progressive Alleghanian Deformation of the Appalachian Plateau," *Geolog. Soc. of Amer. Bull.,* **111** [2] (1999) 219 – 239.

D. Bahat, T. Bankwitz, and E. Bankwitz, "Preuplift Joints in Granites: Evidence for Subcritical and Postcritical Fracture Growth," *Geolog. Soc. of Amer. Bull.,* **115** [2] (2003) 148 – 165.

D. T. McConaughy and T. Engelder, "Joint Initiation in Bedded Clastic Rocks," *J. Struct. Geol.,* **23** (2001) 203 – 221.

T. Engelder, "Tectonic Implication Drawn from Differences in the Surface Morphology on Two Joint Sets in the Appalachian Valley and Ridge, Virginia," *Geology,* **32** (2004) 413 - 416.

T. Engeleder, "Propagation Velocity of Joints: A Debate Over Stable vs. Unstable Growth of Cracks in the Earth," pp.457-482 in *Fractography of Glasses and Ceramics V*, eds. G. D. Quinn, M. Wightman, and J. R. Varner, *Ceram. Trans*., Vol. 199, American Ceramic Society, Westerville, OH, 2007.

APPENDIX C FRACTURE MIRROR AND BRANCH CONSTANTS

The following table includes all the published values of mirror and branching constants that the author could find up to late 2015 when the second edition of this Guide was in preparation. The original reference is listed for each entry.

The mirror and branching constants were analyzed assuming:

$$\sigma \sqrt{R} = A \qquad \text{(C.1)}$$

Mirror-mist (or inner mirror) A_i and mist-hackle (or outer mirror) A_o constants are listed for glass and glass ceramics. Mist is difficult or impossible to discern in most ceramics and the mirror constant A_o that is listed corresponds to the mirror-hackle boundary.

Entries where a modified version of equation C.1 was used are noted by a footnote.

No judgment is made of the veracity of the listed values. Some of the values may be inaccurate. Even for ideal materials such as fused silica and soda lime silica there are unsettling variations in reported values. The variations probably are caused by:

1. Differences in viewing mode, including type of microscope, magnifycations, illumination techniques, and magnification accuracy and precision.
2. Differences in observer judgment.
3. Differences in the radii measured (e.g., along the surface, into the depth, or other) and the accuracy and precision of the length measurements.
4. Differences in test method (e.g., flexure, tension, biaxial plate) and accuracy and precision of the strength data.
5. Differences in whether or not corrections were made for stress gradients and the stress at the origin location.
6. Unaccounted for residual stresses.
7. Differences in the analysis used including whether data were plotted and regressed as log stress versus log mirror radius, or linear stress versus inverse square root of radius.
8. Variations in density, microstructure, or fracture toughness between nominally identical materials.
9. Variations in the number of specimens tested.

One is tempted to conclude that most of the discrepancies are due to viewer judgment, but this cannot account for the all of the variability. The mirror

constant is only sensitive to the square root of the measured radii. In other words, a 10% systematic error in radii measurements causes only a 5% error in the mirror constant.

All values in the table are listed with the same number of significant figures as in the original reference, but only up to a limit of three significant figures. Uncertainties (± one standard deviation) are listed when available from the original reference. Multiple entries in a cell denote estimates by different microscopy techniques or analysis. For polycrystalline ceramics, the mirror constants taken from the reference sources are assumed to be for the mist-hackle boundary unless otherwise stated.

If the user cannot find the mirror constant for a particular material, he or she may consider values for comparable materials within the same class. For example, if a particular glass is not listed, then use the value for a glass of similar composition. For polycrystalline ceramics, microstructure plays an important role in determining a mirror constant. Conscientious readers should check the references listed for more details on a particular material.

As discussed in chapter 7, the fracture mirror constants do not vary significantly with temperature or environment. Any variability with temperature usually follows trends in fracture surface energy, γ_f, or fracture toughness, K_{Ic}.

It is hoped that the adoption of the Guidelines in Appendix D, and the adoption of ASTM C 1678, Standard Practice for Fractographic Analysis of Fracture Mirror Sizes in Ceramics and Glasses in 2007, will lead to improved consistency and accuracy in future mirror size constant determinations.

Material	Technique	*Mirror-Mist* A_i (MPa·$\sqrt{m}$)	*Mist-Hackle or Mirror-Hackle* A_o (MPa·$\sqrt{m}$)	Branching A_b (MPa·$\sqrt{m}$)	Reference
Glasses					
Flint (Kimble R6 soda lime)	Flexure (Rods)		2.0		Kirchner, 8
Flint (Kimble R6 soda lime)	Flexure (Rods)		1.9		Kirchner, 9
Flint (Kimble R6 soda lime)	Flexure (Rods)		2.3		Kirchner, 10
Soda-Lime Silicate – window glass	Flexure (biaxial ring-on ring, large)	2.09			Orr, 5
Soda-Lime Silica (window, sheet, and plate)	Flexure (Bars or laths)	2.05			Shand, 4
Soda-Lime Silicate – float, plate, sheet	Flexure (biaxial ring-on-ring and bend bars)		2.09		Barsom, 62
Soda-Lime Silicate – window glass	Pressurized windows, large	1.96			Reed, 39
Soda-Lime Silicate	Flexure (Bars, 3-point)	1.74			Bansal, 14
Soda-Lime Silicate A – plate glass Soda-Lime Silicate B – plate glass	Flexure (Bars – large) Room Temperature to Strain Point	1.86 ± 0.66 1.82 ± 0.91			Kerper, Scuderi 6
Soda-Lime Silica Float	Flexure (Bars)	1.80 ± 0.15 * 1.81 ± 0.25	2.42 ± 0.16 * 2.29 ± 0.24		Ball, 40
Soda-Lime Silica Float (G.E.C. – X8)	Tension (Rods) Flexure (Bars)	1.89 ± 0.06	2.04 ± 0.06 2.09		Johnson, Holloway, 1
Soda-Lime Silica Float	Flexure (Bars) Flexure–Delayed failure (Bars)	1.92 2.0 ± 0.1	2.21 2.2 ± 0.1		Mecholsky, 18,21 Mecholsky, 21
Soda-Lime Silica	Flexure	1.8	2.0	2.3	Mecholsky, 22
Soda Lime Silica Float	Flexure (Bars, large and small, 3-point and 4-point)	2.06 ± 0.07	2.29 ± 0.19		Duckworth, 16
Soda-Lime Silica	Tension (Plates)			1.2 – 1.6	Congleton, Petch, 2
Soda-Lime Silica	Flexure (Bars) Flexure (Biaxial ring-on-ring plates)	1.81 ± 0.28		3.54 ± 0.64	Choi, 33
Soda-Lime Silica	Tension			1.9	Clark, 34
Soda-Lime Silica	Pressurized Tube			2.0	Aoki, 35
Soda-Lime Silica	Flexure (Biaxial ring-on-ring disks) 3 environments, Vickers indented	1.82 - 1.94	2.03 – 2.13	2.28 – 2.42	Marshall, 19
Soda-Lime Silica	Flexure (Biaxial, pressure on ring disks)			2.1 ± 0.1 $^{NZ}(10 \pm 4)$	Shetty, 15
Soda-Lime Silica	Flexure (rods)	1.8			Terao, 63
Soda-Lime Silica	Flexure (rods)	1.85 ± 0.21 3.20 ⊕ 2.82 ⊕			Varner, 68, 70
Soda-Lime Silica	Flexure (3-point rods) Flexure (4-point rods) Tension (Fibers)	3.15 ± 0.11 2.74 ± 0.15 1.72 ± 0.28			Abdel-Latif, 49
Soda-Lime Silica	Flexure (3-point, laths)	(2.9 ***)			Levengood, 64
Soda-Lime Silica	Flexure, plates, 2 sizes	1.47 $^{NZ\ (19.5)}$ 1.92 $^{NZ\ (7.0)}$		2.88 $^{NZ\ (18.)}$ 3.1 $^{NZ\ (5.7)}$	Gaume. 73

Material	Technique	*Mirror-Mist* A_i (MPa·$\sqrt{m}$)	*Mist-Hackle or Mirror-Hackle* A_o (MPa·$\sqrt{m}$)	Branching A_b (MPa·$\sqrt{m}$)	Reference
Soda-Lime Silica	Flexure (4-point, laths)	1.80 ± 0.07 (air, 20°C) 2.08 ± 0.04 (air, -150°C) 1.89 ± 0.05 (water, 17°C) 1.92 ± 0.04 (dry N_2,24°C)			Shinkai, 69
Borosilicate A (P 3235) Borosilicate B (C 7740)	Flexure (Bars – large; Room Temperature to Strain Point)	1.98 ± 0.46 2.04 ± 0.75			Kerper, Scuderi, 6
Borosilicate (C 7740)	Flexure (Rods, many diameters)	2.08 ± 0.02			Kerper, Scuderi, 7
Borosilicate (C 7740)	Flexure (Bars)	1.87 ± 0.3	2.10		Mecholsky, 17,18
Borosilicate (C 7740)	Flexure (Bars) and Biaxial disks	1.9 ± 0.3			Mecholsky, 20
Borosilicate (C 7740)	Flexure (Rods)	2.2, 2.35			Shand, 3
Borosilicate Pyrex	Flexure (4-point, laths)	1.98 ± 0.09 (air, 20°C) 2.08 ± 0.11 (air, -150°C) 2.02 ± 0.08 (water, 17°C) 1.98 ± 0.12 (dry N_2,24°C)			Shinkai, 69
Borosilicate	Flexure and Tension (Rods)	1.9*			Alarcón et al. 56
Borosilicate crown (Schott BK-7)	Flexure (Biaxial, ring on ring disks)*	1.98 ± 0.02 NZ	2.11 ±0.03 NZ 2.3	2.28 ±0.03 NZ	Quinn, 25
Aluminosilicate (C 1723)	Flexure (Bars)	2.14	2.40		Mecholsky, 18
Aluminosilicate A (P 6695) Aluminosilicate B (C 1723)	Flexure (Bars –large) Room Temperature to Strain Point	2.31 ± 0.76 2.34 ± 0.97			Kerper, Scuderi, 6
Alkali-borosilicate	Tension (Fibers)	1.33 *			Jaras et al., 12
Alkaline-earth boro aluminosilicate (C1737)	Flexure (Biaxial ring-on-ring)	2.07 ± 0.01			Gulati et al., 57
Barium silicate $3BaO\text{-}5SiO_2$	NR (Flexure Bars?)	1.3	1.5		Mecholsky, 22
E glass $CaO\text{-}Al_2O_3\text{-}B_2O_3$ alumina borosilicate	Tension (Fibers)	1.47 *			Jaras et al., 12
Lead silicate (G.E.C. L1)	Tension (Rods)	1.71 ± 0.06			Johnson, Holloway, 1
Lead silicate	Flexure (Bars)	1.61	1.78		Mecholsky, 18
Leaded silicate, 6.7 g/cm^3	Flexure (Rods)	1.4 ± 0.1	1.6 ± (0,1)		Salem et al., 77
Lithium silicate $Li_2O\text{-}2SiO_2$	Flexure Bars (3-point)	2.2	2.6		Mecholsky, 22
Zinc silicate	Flexure Bars	2.1	2.6	3.2	Mecholsky, 22
Zirconia silicate (Cem-FIL AR)	Tension (Fibers)	2.37 *			Jaras et al., 12
Yttrium-Alumino-Silica Oxyntride (2Y-Al-Si-O-N)	Flexure (Bars)	1.5 ± 0.2			Coon, 48
Fused Silica (C 7940)	Flexure (Bars)	2.23	2.42	2.7	Mecholsky, 18, 22

Material	Technique	*Mirror-Mist* A_i (MPa·$\sqrt{m}$)	*Mist-Hackle or Mirror-Hackle* A_o (MPa·$\sqrt{m}$)	Branching A_b (MPa·$\sqrt{m}$)	Reference
Fused Silica (C 7940)	Flexure (Bars – large; Room Temperature to Strain Point)	1.89 ± 0.51			Kerper, Scuderi, 6
Fused silica (Vitreosil)	Tension (Rods)	2.33 ± 0.06			Johnson, Holloway, 1
Fused silica	Flexure (Rods)	2.20 ± 0.33			Choi, 33
Fused silica	Flexure and Tension (Rods)	1.2 [NZ]			Alarcón et al. 56
Fused silica fibers	Tension	2.10			Choi, 33
Fused silica clad fibers	Tension	1.96 ± 0.13			Baker, 29
Fused silica fibers	Tension	1.83			Castilone, 30
Fused silica fibers, bars, disks	Tension (Fibers) Flexure (Bars) Flexure (Biaxial, piston on 3 balls)	2.2 ± 0.5 2.3 ± 0.5 2.4 ± 0.3			Mecholsky, 20
Fused silica fibers	Tension	2.224			Chandan, 37
Leached High Silica (C 7930)	Flexure (Bars)	0.91	1.19		Mecholsky, 18
96% Silica (C 7900)	Flexure (Bars – large; Room Temperature to Strain Point)	1.84 ± 0.65			Kerper, Scuderi, 6
96% Silica Vycor	Flexure (4-point, laths)	1.77 ± 0.06 (air, 20°C) 2.14 ± 0.06 (air, -150°C) 1.80 ± 0.05 (water, 17°C) 1.83 ± 0.07 (dry N_2, 24°C)			Shinkai, 69
Glassy Carbon	Flexure (Bars)	1.17	1.67		Mecholsky, 17,18
Glassy Carbon	Flexure (Bars)			2.1	Bullock, Kaae, 61
Chalcogenide As-S-Se and Ge-AS-Se-Te	Flexure (Fibers, 2 point bending)	1.58 1.77 ± 0.14 [NZ] (- 66.4 ± 45.5)			Quinn et al., 75
As_2Se_3 chalcogenide glass, untreated As_2Se_3 chalcogenide glass, UV irradiated	Tension (Fibers)	0.69 0.35 irradiated	0.77 0.38 irradiated		Hulderman, 45
As_2S_3	Flexure (Bars)	0.56	0.65		Mecholsky, 18
$Ge_{33}As_{12}Se_{55}$	Flexure (Bars)	0.55	0.65		Mecholsky, 18
0.3PbSe - $0.7Ge_{1.5}As_{0.5}Se_3$	Flexure (Bars)	0.48	0.55		Mecholsky, 18
ZBLA (halide glass)	Flexure (Bars)	0.8			Mecholsky, 22
Lead Borate glass $30PbO-70B_2O_3$ (mol) $40PbO-60B_2O_3$ $50PbO-50B_2O_3$ $60PbO-40B_2O_3$ $70PbO-30B_2O_3$	Flexure (Bars)	1.7 ± .05 1.45 ± .05 1.15 ± .05 0.85 ± .01 0.65 ±.01			Shinkai, Ishikawa, 60 **
Glass Ceramics					
Pyroceram 9608 (Li, Mg, Al silicate)	NR		2.8		Adams + DeMartino, 27
Pyroceram 9607 (Li, Mg, Zn, Al silicate)	NR		2.1 [NZ]		Adams + DeMartino, 27
Pyroceram 9606 (Cordierite, Mg, Al silicate)	Flexure	3.6	6.5		Mecholsky, 17

Material	Technique	*Mirror-Mist* A_i (MPa·$\sqrt{m}$)	*Mist-Hackle or Mirror-Hackle* A_o (MPa·$\sqrt{m}$)	Branching A_b (MPa·$\sqrt{m}$)	Reference
Pyroceram 9606 (Cordierite, Mg, Al silicate)	Flexure (Bars)		6.5		Lewis, 44
Pyroceram 9606 (Cordierite, Mg, Al silicate)	Flexure (Bars, 3-point and 4-point)		5.7		Bansal, 13,14
Pyroceram 9606 (Cordierite, Mg, Al silicate)	Flexure (Bars) and Flexure (Biaxial, piston on 3 balls)		6.3		Mecholsky, 20
Pyroceram 9606 (Cordierite, Mg, Al silicate)	Flexure (Biaxial, pressure on ring, and ball on ring)			3.1 ± 0.2 [NZ] (84 ± 6)	Shetty, 15
Pyroceram 9606 (Cordierite, Mg, Al silicate)	Flexure (Rods)		4.8		Shand, 3
Li_2O-SiO_2 (NPL glass ceramic, 2 grades)	Flexure (Bars)	3.3, 3.8	4.5, 5.4		Mecholsky, 17
Dental Ceramics and Filled Composites					
Dicor (dental, tetra silica fluoromica) glass ceramic	Flexure (Bars)		0.97		Kelly, 47
Feldspathic Porcelain (alumina filled, Vitadur N 338)	Flexure (Bars)		2.82		Kelly, 47
Feldspathic Leucite Porcelain, Optec OPC,	Flexure (Bars)		2.1		Fischer, 52
Empress I Leucite glass ceramic	Flexure (Bars)		1.7		Fischer, 52
Empress II Lithium disilicate glass ceramic	Flexure (Bars)		3.9		Fischer, 52
Omega - Opaker	Flexure (Bars)		1.3		Fischer, 52
Cerec Mark II Porcelain	Flexure (Bars)		1.6		Fischer, 52
Glass infused Alumina, In-Ceram	Flexure (Bars)		6.6		Fischer, 52
Dental resin, 85 wt% zirconia-silica filler in bisGMA-TEGDMA Paradigm MZ100	Flexure (Bars, 4-point)		2.6		Quinn, 59
3Y-ZTP, Lava	Flexure (Bars, 4-point)		10.7		Quinn, 58
Alumina					
β-Al_2O_3	Flexure		~ 6.5		Mecholsky, 17
Hot-pressed (1 μm, Cer. Fin.))	Flexure (Rods, 4-point) 25 C to 1400 C		10.4		Kirchner, 11
Hot-pressed (99+% pure, Cer. Fin.)	Flexure (Rods, 4-point) Flexure-Delayed Fracture (Rods)		10.3 9.9		Kirchner, 8,9 Kirchner, 8
Hot-pressed (99+% pure,Cer. Fin.)	Flexure (Rods-3-point)		9.1		Kirchner, 10
Hot-pressed (99+% pure)	Flexure	5.2	12		Mecholsky, 17
Hot pressed	Flexure (Rods)		10.4		Mecholsky, 11
Hot-pressed (Avco, 1-2 μm)	Flexure (4-point, 2 sizes)		9.8		Bansal, 14
Sintered (Lucalox)	Tension (Plates)			7.3	Congleton, Petch, 2

Material	Technique	*Mirror-Mist* A_i (MPa·$\sqrt{m}$)	*Mist-Hackle or Mirror-Hackle* A_o (MPa·$\sqrt{m}$)	Branching A_b (MPa·$\sqrt{m}$)	Reference
Sintered (96%) (Alsimag 614)	Flexure (Rods)		8.5		Kirchner, 9
Sintered (96%) (Alsimag 614)	Flexure (Rods) Flexure-Delayed Fracture (Rods)		8.3 8.9		Kirchner, 8
Sintered (96%) (Alsimag 614)	Flexure (Bars, 3-point and 4-point, 2 sizes)		9.0		Bansal, 13,14
Sintered (96%) (Alsimag 614)	Flexure (Rods)		9.1		Kirchner, 10
Sintered (96%) (Alsimag 614)	Flexure (Bars)		13.1		Mecholsky, 17
Sintered (96%) (Alsimag 614)	Flexure (Bars), Flexure (Biaxial ball on ring), Flexure (Biaxial ring on ring)		7.6 ± 0.5	7.4 ± 0.6? 7.2 ± 0.7?	Choi, 33
Sintered 96% (Alsimag 614)	Flexure (Biaxial, pressure on ring disks)			4.0 ± 0.3 NZ (164 ± 11)	Shetty, 15
Hot isopressed Biolox forte	Flexure (Bars, 4-point)		7.7		Hecht-Mijic, 76
Hot isopressed Biolox delta ZTA	Flexure (Bars, 4-point)		9.5		Hecht-Mijic, 76
Silicon Carbide					
Sintered SiC (Hexoloy SA)	Flexure (Bars)		5.39		Quinn, 23
Sintered SiC (Hexoloy SA)	Flexure (Biaxial, ring on ring plates)			6.3 ± 0.5	Salem, 31
Sintered SiC (Hexoloy SA)	Flexure (Biaxial, ring-on-ring plates)			5.5 ± 0.3	Choi, 33
Sintered SiC (Hexoloy SA)	C-ring	5.50 ± 0.94	8.20 ± 0.54	10.5 ± 1.0	Conway et al. 67
Sintered SiC toughened (Hexoloy SX)	Tension (Rods) and Flexure (Bars)		7.0	7.0?	Srinivasan, 42
Sintered with Al (Rioceram SiC)	C-ring	5.67 ± 0.60	8.16 ± 0.54	11.6 ± 0.8	Conway et al. 67
Sintered (Carolt S)	Flexure (Bars, optical, SEM)		6.1, 6.8		Woodtli, 36
Hot-pressed SiC (NC-203)	Flexure (Rods) Flexure-Delayed Fracture (Rods)		11.4 11.9		Kirchner, 8
Hot-pressed SiC (NC-203)	Flexure (Rods)		11.5		Kirchner, 9
Hot-pressed SiC (ACE)	Flexure (Rods)		10.8		Kirchner, 10
Siliconized SiC (KT)	Flexure		10.7		Mecholsky, 17
Reaction bonded SiC (Coors SCRB205)	C-ring	4.11 ± 0.31	5.22 ± 0.23	6.4 ± 0.4	Conway et al. 67
Silicon Nitride					
Sintered Reaction Bonded (Ceralloy 147-31N)	Flexure (Rods) Flexure (Bars)		8.47 ± 0.07 7.79 ± 0.02		Quinn, 26
Sintered (SSN-500 yttria/alumina)	Flexure (Bars)		5.8		Quinn, 23
Sintered (SN 220)	Flexure (Biaxial, ring on ring disks)			8.1 ± 2.4	Choi, 33

Material	Technique	*Mirror-Mist* A_i (MPa·$\sqrt{m}$)	*Mist-Hackle or Mirror-Hackle* A_o (MPa·$\sqrt{m}$)	Branching A_b (MPa·$\sqrt{m}$)	Reference
Sintered (AS 44)	Flexure (Biaxial, ring on ring disks)			10.9 ± 2.7	Choi, 33
Hot-pressed (Ceralloy 147A)	Flexure (Bars)		7.83		Quinn, 23
Hot-pressed (NC-132)	Flexure (Rods)		9.2		Kirchner, 9
Hot pressed (NC-132)	Flexure (Rods) Flexure-Delayed Fracture (Rods)		8.9 9.2		Kirchner, 8
Hot-pressed (NC-132)	Flexure (Rods)		14.3		Kirchner, 10
Hot-pressed (NC-132)	Flexure (Bars, 1100°C) Flexure (Biaxial ring on ring, 1100°C)		9.4 ± 1.2	7.9 ± 2.1?	Choi, 33
Hot-pressed (HS-130)	Flexure		18.1		Mecholsky, 17
Hot-pressed (HS-130)	Flexure (Rods)		9.1		Kirchner, 8
Hot-isopressed (NT 154)	Flexure (Bars)		5.9 ± 0.14		Choi, 32,33
Hot-isopressed + 30vol% SiC whiskers	Flexure (Bars)		6.6 ± 0.11		Choi, 32,33
Hot-isopressed (GN-10)	Flexure (Biaxial ring-on-ring) Tension (Rods)		 11.8 ± 1.4	10.3?	Choi, 33
Reaction Bonded (NC 350)	Flexure (Bars)		3.89		Messier, 24
Reaction Bonded (NC 350)	Flexure (Bars)		3.19		Larsen, 28
Reaction Bonded (AME A25B)	Flexure (Rods)		4.2		Kirchner, 8
Zirconia					
Ytttria stabilized (3Y-TZP)	Flexure (Bars)		9.95		Morrell, 43
Ytttria stabilized (3Y-TZP)	Flexure (Bars) Flexure (Biaxial piston on 3 ball)		8.6 ± 0.23 9.6 ± 0.23		Quinn, 50
Yttria stabilized (3Y-TZP, Lava)	Flexure (Bars)		10.7		Quinn, 58
Yttria stabilized (3.5Y-TZP)	Flexure (Biaxial, ring on ring disks)			11.5 ± 1.5	Choi, 33
Calcia partially stabilized PSZ As fired - quenched As fired Under aged, 1300°C Peak aged Peak aged Over aged	Flexure (Bars, 3-point)			 9.9 15.5 19.2 22.1 25.3 -	Kirchner et al, 80
Zircar (Alfred-Union Carbide, 0.4 μm, 5-6 mol% Y TZP)	Flexure (Bars)		15.2		Mecholsky, 17
Zyttrite (AFML, 10 μm, cubic)	Flexure (Bars)		7.4		Mecholsky, 17
Single crystals					
Ammonium diphosphate, single crystal	Flexure (Bars)		0.5		Mecholsky, 17

Material	Technique	*Mirror-Mist* A_i (MPa·$\sqrt{m}$)	*Mist-Hackle or Mirror-Hackle* A_o (MPa·$\sqrt{m}$)	Branching A_b (MPa·$\sqrt{m}$)	Reference
$MgAl_2AlO_4$ Spinel, single crystal	Flexure (Bars)		2.6		Mecholsky, 17
Quartz ($11\bar{2}0$) plane with tension in [0001] direction	Tension (Plates)			1.64	Ball, Payne, 78
MgO	?			4.3	Ball, Payne, 78
Sapphire (average of several planes)	Flexure		6.1		Mecholsky 17
Sapphire (Tyco filaments, c-axis parallel to fiber axis)	Tension Flexure		5.5 10.0		Abdel-Latif, 38
Sapphire (Ruby rods, c axis ~60° off rod axis)	Flexure (Rods)		3.3		Abdel-Latif, 38
Sapphire Filament, c-axis parallel to fiber axis	Tension, 800 to 1000°C	2.4	3.2		Rice, 51
Sapphire, a plane	Flexure (Bars, 4-point)			7.3 ± 0.6 7.1 ± 0.3 NZ (11)	Salem, 70
Sapphire	?			7.3	Ball, Payne 78
Sapphire filament, c-axis parallel to fiber axis	Tension, 800 to 1000°C	2.4	3.2		Rice, 51
Silicon, single crystal	Flexure (Bars)		$2.01 \pm .14$ {110} plane <110> dir. $1.61 \pm .14$ {110} plane <100> dir.		Tsai and Mecholsky, 72
Silicon, single crystal	?			5.8	Ball, Payne, 78
Other					
$3BaO\text{-}SiO_2$	Flexure (Bars)	3.9	6.0		Mecholsky, 17
B_4C hot-pressed	Flexure (bars)	4.8	9.27		Mecholsky, 17
$BaTiO_2$ (2 grades)	Flexure (Bars)		5.0, 5.4		Mecholsky, 17
Chromium	?			4.5	Ball, Payne, 78
Mullite	Flexure		6.1		Mecholsky, 17
MgO	Flexure		9.6		Mecholsky, 17
MgO	Tension (Plates)			4.3	Congleton, Petch, 2
MgO, single crystal	Flexure (Bars)		5		Mecholsky, 17
MgF_2 (Kodak)	Flexure (Bars)	1.8	3.1		Mecholsky, 17
MgF_2 (Kodak, IRTRAN 1)	Flexure (Bars) and Biaxial Disks			4.4	Mecholsky, 20
$MgAl_2AlO_4$ Spinel	Flexure (Bars)	4.0	7.8		Mecholsky, 17
$MgAl_2AlO_4$ Spinel, single crystal	Flexure (Bars)		2.6		Mecholsky, 17
PMMA	?		8.5 *	8.5 *	Ball, Payne, 78
Porcelain, aluminous, electrical insulator grades	Flexure, (Rods, 3-point)		~ 3.5		Carlström, 74
PZT	Flexure	1.7	3.7		Mecholsky, 17
Graphite (POCO)	Flexure		3.32		Mecholsky, 17
$SrZrO_3$	Flexure (Bars)	4.4	6.0		Mecholsky, 17
Steatite (Mg silicate insulator, DC -144)	Flexure (Rods)		4.8 4.5		Kirchner, 8,9 Kirchner, 10

Material	Technique	*Mirror-Mist* A_i (MPa·$\sqrt{m}$)	*Mist-Hackle or Mirror-Hackle* A_o (MPa·$\sqrt{m}$)	Branching A_b (MPa·$\sqrt{m}$)	Reference
WC-Co 8 wt % (H8 grade) 12 wt % (H12) 10 wt % (G10) 15 wt % (G15) 30 wt % (E30) 10 wt % (J10) 15 wt % (WCS15) 20 wt % (WCS20) 25 wt % (WCS25)	Flexure (Bars, 4-point)		24.4 ± 5 41.0 ± 2 36.8 ± 2 51.7 ± 10 75.0 ± 3 29.6 ± 2 58.8 ± 4 71.9 ± 2 86.4 ± 1		Luyckx, 41
WC-Co 6% Ni (Kennametal)	Flexure (Biaxial, disks pressure-on-ring (POR) POR + ring-on-ring			8.2 NZ ⊗ (1154) 14. NZ ⊗ (329)	Salem, et al, 79
WC-Co 2% Ni, 1% Co (Cercom)	Flexure (Bars?- 4-point)		3.6 NZ ⊗ (493)		Salem, et al, 79
WC (no Co)	Flexure		10 ⊗		Swab, 46
Yttrium Aluminum Garnet, polycrystal. (2.2 μm)	Flexure (Bars)		2.15 ± 0.08		Mezeix and Green, 66
Yttrium Aluminum Garnet, single crystal (111)	Flexure (Bars)		2.20 ± 0.06		Mezeix and Green, 66
Zircon Porcelain (Alsimag 475)	Flexure (Rods)		4.0		Kirchner, 8,9
ZnSe	Flexure (Bars)			1.7	Mecholsky, 17
ZnSe (44 μm)	Flexure (Biaxial, ring-on-ring disks)			0.8, 1.0 #	Salem, 65
Fibers					
Alkali-borosilicate	Tension (Fibers)	1.33 NZ			Jaras et al., 12
Chalcogenide As-S-Se and Ge-AS-Se-Te	Flexure (Fibers, 2 point bending)	1.58 1.77 ± 0.14 NZ (-66.4 ± 45.5)			Quinn et al., 75
Chalcogenide As_2Se_3	Tension (Fibers)	0.69 (0.35 if UV irradiated)	0.77 (0.38 if UV irradiated)		Hulderman et al., 76
E glass CaO-Al_2O_3-B_2O_3 alumina borosilicate	Tension (Fibers)	1.47 NZ			Jaras et al., 12
Fused silica fibers	Tension	2.10			Choi, 33
Fused silica clad fibers	Tension	1.96 ± 0.13			Baker, 29
Fused silica fibers	Tension	1.83			Castilone, 30
Fused silica fibers	Tension (Fibers)	2.2 ± 0.5			Mecholsky, 20
Fused silica fibers	Tension	2.224			Chandan, 37
Si-Ti-C-O (Tyranno LoxM) fiber	Fibers in 3-D SiC matrix composite		2.50 ± 0.09		Davies, 53
Si-C-O fibers (Nicalon) Si-C-N-O fibers Si-N-C-O fibers	Tension		~2		Sawyer, 54
Si-C-O, (Nicalon)	Fibers in 2-D CVI SiC matrix composite		2.51		Eckel + Bradt, 55
Sapphire filament, c-axis parallel to fiber axis	Tension, 800 to 1000ºC	2.4	3.2		Rice, 51
Zirconia silicate (Cem-FIL AR)	Tension (Fibers)	2.37 NZ			Jaras et al., 12

NR Not reported

NZ A non-zero intercept was detected on the graph of stress versus inverse square root radius. The intercept value in MPa is listed in parenthesis. Mirror or branching constants calculated with non-zero intercepts are usually different than those calculated with intercepts through the ordinate. Consult the original reference for more information.

* It is not clear whether Ball and Payne, ref. 78 listed this as A_o for PMMA, or A_b. Their other listed glass and polycrystalline ceramic A_b values are actually A_o values from Kirchner or Johnson and Holloway.

** Additional mirror constants for the lead borate glasses are available at liquid nitrogen temperature (-196 ^oC) in the original reference.

*** Mostly likely an overestimate since stresses were not adjusted for failure location in the 3-point rod specimens.

\# Alternative analyses (besides a graph of stress versus inverse square root radius) are in the original reference.

? These values (from the original references) for A_b cannot be correct since they are less than or equal A_o.

⊗ Large internal residual stresses have been reported in WC-Co materials, often lead to large non-zero intercepts. Consult the original reference for guidance.

⊕ Tempered soda lime silica rods

REFERENCES

1. J. W. Johnson, and D. G. Holloway, "On the Shape and Size of the Fracture Zones on Glass Fracture Surfaces," *Phil. Mag.*, **14** [130] (1966) 731 - 743.
2. J. Congleton, and N. J. Petch, "Crack Branching," *Phil. Mag.,* **16** [142] (1967) 749 - 760.
3. E. B. Shand, "Breaking Stress of Glass Determined from Dimensions of Fracture Mirrors," *J. Amer. Ceram. Soc.*, **42** [10] (1959) 474 - 477.
4. E. B. Shand, "Breaking Stresses of Glass Determined from Fracture Surfaces," *The Glass Industry*, April 1967, 90-194.
5. L. Orr, "Practical Analysis of Fractures in Glass Windows," *Materials Research and Standards*, **12** [1] (1972) 21 - 23.
6. M. J. Kerper, and T. G. Scuderi, "Modulus of Rupture of Glass in Relation to Fracture Pattern," *Bull. Amer. Ceram. Soc.,* **43** [9] (1964) 622 - 625.
7. M. J. Kerper, and T. G. Scuderi, "Relation of Fracture Stress to the Fracture Pattern for Glass Rods of Various Diameters," *Bull. Am. Ceram. Soc.*, **45** [12] (1966) 1065 - 1066.
8. H. P. Kirchner, R. M. Gruver, and W. A. Sotter, "Fracture Stress-Mirror Size Relations for Polycrystalline Ceramics," *Phil. Mag.*, **33** [5] (1976) 775 - 780.
9. H. P. Kirchner, R. M. Gruver, and W. A. Sotter, "Use of Fracture Mirrors to Interpret Impact Fracture in Brittle Materials," *J. Am. Ceram. Soc.*, **58** [5–6] (1975)188 - 191.
10. H. P. Kirchner, and R. M. Gruver, "Fracture Mirrors in Polycrystalline Ceramics and Glass," pp. 309 – 321 in *Fracture Mechanics of Ceramics 1*, eds. R. C. Bradt, D. P. H. Hasselman, and F. F. Lange, Plenum, NY, 1973.
11. H. P. Kirchner, and R. M. Gruver, "Fracture Mirrors in Alumina Ceramics," *Phil. Mag.*, **27** [6] (1973)1433 - 1446.
12. A. C. Jaras, B. J. Norman, and S. C. Simmons, "The Measurement of Glass Fibre Strength in Composites from Studies of Their Fracture Surfaces," *J. Mat. Sci.*, **18** (1983) 2459 - 2465.

13. G. K. Bansal, and W. H. Duckworth, "Fracture Stress as Related to Origin and Fracture Mirror Sizes," *J. Am. Ceram. Soc.*, **60** [7–8] (1977) 304 -310.
14. G. K. Bansal, "On Fracture Mirror Formation in Glass and Polycrystalline Ceramics," *Phil. Mag.*, **35** [4] (1977) 935 - 944.
15. D. K. Shetty, A. R. Rosenfeld, and W. H. Duckworth, "Crack Branching in Ceramic Disks Subjected to Biaxial Flexure," *Comm. of the Amer. Ceram. Soc.*, Jan. 1983, C10 - C13.
16. W. H. Duckworth, D. K. Shetty, and A. R. Rosenfeld, "Influence of Stress Gradients on the Relationship Between Fracture Stress and Mirror Size for Float Glass," *Glass Technology,* **24** [5] (1983) 263 - 273.
17. J. J. Mecholsky, Jr., S. W. Freiman, and R. W. Rice, "Fracture Surface Analysis of Ceramics," *J. Mat. Sci.*, **11** (1976) 1310 - 1319.
18. J. J. Mecholsky, R. W. Rice, and S. W. Freiman, "Prediction of Fracture Energy and Flaw Size in Glasses from Measurements of Mirror Size," *J. Amer. Ceram. Soc.*, **57** [10] (1974) 440 - 443.
19. D. B. Marshall, B. R. Lawn, and J. J. Mecholsky, "Effect of Residual Contact Stresses on Mirror/Flaw Size Relations," *J. Amer. Ceram. Soc.*, **63** [5-6] (1980) 358 - 360.
20. J. J. Mecholsky, Jr., and R. W. Rice, "Fractographic Analysis of Biaxial Failure in Ceramics," in *Fractography of Ceramics and Glass Failures,* ASTM STP 827, eds. J. Mecholsky and S. Powell, ASTM, Westerville, OH, 1984 185-193.
21. J. J. Mecholsky, A. C. Gonzalez, and S. W. Freiman, "Fractographic Analysis of Delayed Failure in Soda Lime Glass," *J. Am. Ceram. Soc.*, **62** [11-12] (1979) 577 - 580.
22. J. J. Mecholsky, "Quantitative Fractographic Analysis of Fracture Origins in Glass," pp. 37 – 173 *in Fractography of Glass*, eds. R. C. Bradt and R. E. Tressler, Plenum, NY, 1994.
23. G. D. Quinn, D. R. Messier, and L. J. Schioler, "Characterization of Ceramic Vane Materials for 10 kW Turboalternator," U.S. Army Materials and Mechanics Research Center Technical Report TR 83-18, April 1983.
24. D. R. Messier, L. J. Schioler, and G. D. Quinn, "Fracture Behavior and Strength of Reaction-Bonded Si_3N_4 Turbine Shrouds," *Bull. Am. Ceram. Soc. Bulletin*, **60** [8] (1981) 812 - 817.
25. J. B. Quinn, "Extrapolation of Fracture Mirror and Crack-Branch Sizes to Large Dimensions in Biaxial Strength Tests of Glass," *J. Am. Ceram. Soc.*, **82** [8] (1999) 2126 - 2132.
26. G. D. Quinn, L. K. Ives, S. Jahanmir, and P. Koshy, "Fractographic Analysis of Machining Cracks in Silicon Nitride Rods and Bars," in *Fractography of Glasses and Ceramics, IV, Ceramic Transactions,* Vol. 122, eds., J. R. Varner and G. D. Quinn, American Ceramic Society, Westerville, OH, 2001 343 - 365.
27. P. B. Adams and S. E. DeMartino, "Glass-Ceramic Cookware Failure Analysis," in *Engineered Materials Handbook, Vol. 4, Ceramics and Glasses*, ASM, Metals Park, OH, 1991 669 – 673.
28. D. C. Larsen, and G. C. Walther, "Property Screening and evaluation of Ceramic Turbine Engine Materials," IIT Research Institute, Chicago, IL, Interim Technical Report No. 5, IITRI D 6114-ITR-30, 1978.

29. L. K. Baker, and G. S. Glaesemann, "Break Source Analysis, Alternate Mirror Measurement Method," *Proceedings of the International Wire and Cable Symposium*, Philadelphia, PA, 1998, 933-937.
30. R. J. Castilone, G. S. Glaesemann, and T. A. Hanson, "Relationship Between Mirror Dimensions and Failure Stress for Optical Fibers," pp. 11 – 20 in *Optical Fiber and Fiber Component Mechanical Reliability and Testing II,* eds. J. Matthewson and C. R. Kurkjian, Proc. of SPIE, Vol. 4639, (2002).
31. J. A. Salem, S. R. Choi, and L. M. Powers, "Toughened Ceramics Life Prediction," in Ceramic Technology Project Semiannual Progress Report for October 1992 Through March 1993, Oak Ridge National Laboratory Technical Report TM 12428, September, 1993, 307-316.
32. S. R. Choi, and J. A. Salem, "Indentation Flaw Formation and Strength Response of Silicon Nitride Ceramics at Low Indentation Loads," *J. Mat. Sci. Lettrs*, **11** (1992) 1398–1400.
33. S. R. Choi, and J. P. Gyekenyesi, "Crack Branching and Fracture Mirror Data of Glasses and Advanced Ceramics," NASA Technical Report TM 1998-206536, 1998.
34. A. B. J. Clark, and G. R. Irwin, "Crack Propagation Behaviors," *Experimental Mechanics*, **6** [6] (1966) 321 - 330.
35. S. Aoki, and M. Sakata, "Crack Bifurcation Under Hydrostatic Pressure," *Engineering Fracture Mechanics*, **13** [3] (1980) 491 – 499.
36. J. Woodtli, "Quantitative Fractographie in Keramik: Auswertung von Spiegelzonen in SiC," Swiss Federal Laboratories for Materials Testing and Research, Report 157361, Dec. 1997.
37. H. C. Chandan, and R. D. Parker, "Fractography of Optical Fibers," pp. 143- 184 in *Fractography of Glass*, eds. R. C. Bradt and R. E. Tressler, Plenum Press, NY, 1994.
38. A. I. A. Abdel-Latif, R. E. Tressler, and R. C. Bradt, "Fracture Mirror Formation in Single Crystal Alumina," in *Fracture 1977*, Vol. 3, ed. D. Taplin, University of Waterloo Press, 1977, 933 - 939.
39. D. A. Reed, and R. C. Bradt, "Fracture Mirror-Failure Stress Relations in Weathered and Unweathered Window Glass Panels," *Comm. Am. Ceram. Soc.,* Nov. 1984, C 227 – C 229.
40. M. J. Ball, D. J. Landini, and R. C. Bradt, "Fracture Mist Region in a Soda-Lime Silica Float Glass," pp. 110-120 in *Fractography of Ceramic and Metal Failures, ASTM STP 827*, J. Mecholsky, Jr., and S. Powell, eds., ASTM, 1984.
41. S. Bartolucci Luyckx, and A. Sannino, "Crack Branching and Fracture Mirrors in Cemented Tungsten Carbide," *J. Mat. Sci.*, **23** (1988) 1243 - 1247.
42. G. V. Srinivasan, J. Gibson, and S. K. Lau, "The Origin of Strength Limiting Defects in a Toughened SiC (Hexoloy SX-SiC), in *Fractography of Glasses and Ceramics III*, *Ceramic Transactions* Vol. 64, eds, J. R. Varner, V. D. Fréchette, and G. D. Quinn, American Ceramic Society, Westerville, OH, 1996, 181-192.
43. R. Morrell, L. Byrne, and M. Murray, "Fractography of Ceramic Femoral Heads," in *Fractography of Glasses and Ceramics, IV,* Ceramic Transactions, Vol. 122, eds., J. R. Varner and G. D. Quinn, American Ceramic Society, Westerville, OH, 2001, 253 - 266.

44. D. Lewis, III, "Fracture Strength and Mirror Size in a Commercial Glass-Ceramic," *J. Am. Ceram. Soc.*, **64** [2] (1961) 82 - 86.
45. F. Hulderman, J. S. Sanghera, and J. D. Mackenzie, "The Effect of UV Radiation on the Mechanical Strength of As_2Se_3 Glass Fibers," *J. Non-Cryst. Sol.*, **127** (1991) 312 - 322.
46. J. J. Swab, J. C. LaSalvia, and W. A. Gooch, "Characterization of WC-Based Armor Ceramics," unpubl. priv. com., U.S. Army Research Laboratory, Aberdeen Proving Ground, MD, 21005.
47. J. R. Kelly, "Fractography of Dental Ceramics," pp. 241-251 in *Fractography of Glasses and Ceramics, IV*, eds. J. R. Varner and G. D. Quinn, Ceramic Transactions Vol. 122, American Ceramic Society, Westerville, OH 43081, 2001.
48. D. N. Coon, "Mirror/Mist Radius Constant for Y-Al-Si-O-N Glass," *J. Mat. Sci. Lettrs*., **21** (2002) 1121-1122.
49. A. I. A. Abdel-Latif, R. C. Bradt, and R. E. Tressler, "Dynamics of Fracture Mirror Boundary Formation in Glass," *Int. J. Fract.,* **13** [3] (1977) 349 - 359.
50. G. D. Quinn, J. Eichler, U. Eisele, and J. Rödel, "Fracture Mirrors in a Nanoscale 3Y-TZP," *J. Am. Ceram. Soc.*, **87** [3] (2004) 513 - 516.
51. R. W. Rice, "Corroboration and Extension of Analysis of c-Axis Sapphire Filament Fractures from Pores," *J. Mat. Sci. Lttrs*., **16** (1997) 202 - 205.
52. H. Fischer, J. Gröbel, and R. Marx, "Fraktograpische Schadensanalyse an Dentalkeramik*," Deutsche Zahnarztl. Zeitschrifft*, **55** [10] (2000) 667 - 670.
53. I. J. Davies, and T. Ishikawa, "Mirror Constant for Tyranno Silicon-Titanium-Carbon-Oxygen Fibers Measured in Situ in a Three-Dimensional Woven Silicon Carbide/Silicon Carbide Composite," *J. Am. Ceram. Soc.,* **85** [3] (2002) 691 -693.
54. L. C. Sawyer, M. Jamieson, D. Brikowski, M. I. Haider, and R. T. Chen, "Strength, Structure, and Fracture Properties of Ceramic Fibers Produced from Polymeric Precursors: I: Base-Line Studies," *J. Amer. Ceram. Soc*., **70** [11] (1987) 798 - 810.
55. A. J. Eckel, and R. C. Bradt, "Strength Distribution of Reinforcing Fibers in a Nicalon Fiber/Chemically Vapor Infiltrated Silicon Carbide Matrix Composite," *J. Am. Ceram. Soc.,* **72** [3] (1989) 455 - 458.
56. O. E. Alarcón, R. E. Medrano, and P. P. Gillis, "Fracture of Glass in Tensile and Bending Tests," *Metall. Mat. Trans A,,* **25A**, May (1994) 961 - 967.
57. S. T. Gulati, J. F. Bayne, W. R. Powell, and J. D. Helfinstine, "Mirror Constant for AMLCD Glass," *Bull. Am. Ceram. Soc.*, **83** [5] (2004) 14 - 15.
58. J. B. Quinn, D. Cheng, R. Rusin, and D. Suttor, "Fractographic Analysis and Material Properties of a Dental Zirconia," International Association for Dental Research (IADR) paper, 0560, Baltimore, MD, March, 2005.
59. J. B. Quinn and G. D. Quinn, "Materials Properties and Fractography of an Indirect Dental Resin Composite," *Dent. Mater*., **26** (2010) 589-599.
60. N. Shinkai, and H. Ishikawa, "Crack Branching of Binary PbO-B_2O_3 Glasses," *J. Noncryst. Solids*., **52** [1-3] (1982) 385 - 394.
61. R. E. Bullock, and J. L. Kaae, "Size Effect on the Strength of Glassy Carbon," *J. Mat. Sci.,* **14** (1979) 920 - 930.
62. J. M. Barsom, "Fracture of Tempered Glass," *J. Am. Ceram. Soc*., **51** [2] (1968) 75 - 78.

63. N. Terao, "Sur ene Relation entre la Résistance à la Rupture et le Foyer d'Eclatement du Verre*," J. Phys. Soc. Jap.,* **8** [4] (1953) 545 - 549.
64. W. C. Levengood, "Effect of Origin Flaw Characteristics on Glass Strength," *J. Appl. Phys.*, **29** [1] (1958) 820 - 826.
65. J. A. Salem, "Mechanical Characterization of ZnSe Windows for Use With the Flow Enclosure Accommodating Novel Investigations in Combustion of Solids (FEANICS) Module," NASA Technical Report TM-2006-214100, NASA-Glenn Center, Cleveland, OH, 2006.
66. L. Mezeix and D. J. Green, "Comparison of the Mechanical Properties of Single Crystal and Polycrystalline Yttrium Aluminum Garnet*," Int. J. Appl. Cer. Technol.,* **3** [2] (2006) 166 - 176.
67. J. C. Conway, Jr., J. J. Mecholsky, O. M. Jadaan, and D. L. Shelleman, "Test Methodology for Ceramic Tubular Components," Center for Advanced Materials Research Report, Pennsylvania State University, 1989.
68. J. R. Varner and H. J. Oel, "Einfluss von Oberflächenbeschädigungen auf die Festigkeit von Glasstäben, " *Grastechn. Ber*., **48** [5] (1975) 73 – 78.
69. N. Shinkai, "Fracture Mirror Constants of Silicate Glasses," *Japan J. Appl. Phys.*, **14** [1] (1975) 147-148.
70. J. A. Salem, Private communication, March, 2008.
71. J. R. Varner and H. J. Oel, "Surface Defects:Their Origin, Charcaterization and effects on Strength, *"J. Non-Cryst. Sol*., **19** (1975) 321-333.
72. Y. L. Tsai and J. J. Mecholsky, Jr, "Fractal Fracture of Single Crystal Silicon," *J. Mater. Res.,* **6** [6] (1991) 1248-1263.
73. O. Gaume and S. Pelletier, "Analysis of Fracture Featrures for Uni-axial Bent Glass Plates,*"* in *2002 Glass Odyssey*, proc. 6th ESG conf., June 26, 2002, Montpellier, France.
74. E. Carlström and R. Carlsson, "A Fractoraphic Study of Electrical Porcelains Containing Alumina," *J. De Physique*, **47** (C-1) (1986) 563-567.
75. J. B. Quinn, V. Q. Nguyen, J. S. Sanghera, I. K. Lloyd, P. C. Puzera, R. E. Miklos, and I. D. Aggarwal, "Strength and Fractographic Analysis of Chalcogenide AS-S-Se and Ge-As-Se-Te Glass Fibers," *J. Non-Cryst. Sol*., **325** (2003) 150-157.
76, S. Hecht-Mijic, "Fracture Mirror Constants of Bioceramics for Hip Joint Replacement: Determination and Application, " pp. 303 -312 in *Fractography of Glasses and Ceramics V*, eds. J. R. Varner, G.D. Quinn, M. Wightman, Ceramic Transactions Vol. **199**, American Ceramic Society, Westerville, OH, 2007.
77. J. A. Salem, N. Smith, and A. Ersahin, "Mechanical Properties of a High Lead Glass Used in the Mars Organic Molecule Analyzer," NASA Glenn Research Center, Cleveland, OH, Technical Report, TM 2015-218847, August 2015.
78. A. Ball and B. W. Payne, "The Propagation and Bifurcation of Cracks in Quartz," pp. 971 – 978 in *Fracture 1977, Vol. 3,* Waterloo, Canada, 1977.
79. J. A. Salem, S. Slingluff, R. Rogers, and J. J. Swab, "Stress Gradients and Crack Branching in Tungsten Carbide," *to be publ.* 2015
80. H. P. Kirchner, R. M. Gruver, M. V. Swain, and R. C. Garvie, "Crack Branching in Transformation-Toughened Zirconia," *J. Am. Ceram. Soc.*, **64** [9] (1981) 529-533.

APPENDIX D GUIDELINES FOR MEASURING FRACTURE MIRRORS

D.1 Introduction

This appendix presents a set of guidelines for measurement of fracture mirrors in glasses and ceramics. These guidelines were originally presented by the author at the Fifth Conference on the Fractography of Glasses and Ceramics in Rochester New York in 2006. [1] That paper reviewed the historical development (going back as far as 1894) of fracture mirror analysis as a quantitative tool for glasses and ceramics. These guidelines also were included in the first edition of this NIST Guide in 2007. They were adopted as an ASTM standard C 1678 [2] in 2007.

Fracture mirror measurements are a powerful diagnostic tool for quantitative analysis. Mirrors are circular in ideal loading conditions such as uniform tension specimens. Otherwise, they can be elongated or distorted due to stress gradients or geometrical effects. There is a strong subjective element to estimating the location of the mirror boundary. Johnson and Holloway[3] said:

> "The position assigned to the boundary between mirror and mist zones depends upon the illumination and the magnification at which the fracture is examined, even within the range of the optical microscope. …. However, under given conditions a reproducible position for the boundary can be assigned."

Since many of the early mirror measurements were made while viewing through the optical microscope, it is safe to say that the first perception of a mirror boundary was where the surface roughness was a fraction of the wavelength of light (0.39 μm - 0.80 μm). Threshold levels of detectability have been estimated to be as small as a few tens of nanometers to as much as 0.25 μm. Attempts to make objective determinations of the mirror boundary by quantitative surface roughness characterization are discussed in section D.3 below, but a single threshold roughness value cannot be specified.

The following Guidelines are intended to bring some consistency to measurement procedures. Some of the following recommendations are based on common sense. Others are based upon the experiences of the author and other experts. The empirical mirror relationship for a residual stress free part is:

$$\sigma \sqrt{R} = A \qquad \text{(D.1)}$$

where σ is the stress at the origin, R is the mirror radius, and A is the appropriate mirror constant as described below. Leighton Orr recognized as early as 1945 that stress varied inversely with the square-root dependence of the mirror radius, so the author now refers to equation D.1 as "Orr's equation."

The boundary criteria are:

The mirror-mist boundary in *glasses* is the periphery where one can discern the onset of mist. This boundary corresponds to A_i, the inner mirror constant.

The mist-hackle boundary in *glasses* is the periphery where one can discern the onset of systematic hackle. This boundary corresponds to A_o, the outer mirror constant.

The mirror-hackle boundary in *polycrystalline ceramics* is the periphery where one can discern the onset of systematic new hackle and there is an obvious roughness change relative to that inside the mirror region. This boundary corresponds to A_o, the outer mirror constant. Ignore premature hackle and/or isolated steps from microstructural irregularities in the mirror or irregularities at the origin.

In coarse-grained or porous materials, it may be impossible to identify a mirror boundary. In polycrystalline ceramics, it is highly unlikely that a mirror-mist boundary can be detected due to the inherent roughness created by the crack-microstructure interactions even within the mirror. Another reason a boundary may not be evident is that in very weak materials, the mirror may be larger than the specimen or component.

If the mirror is being measured for a component failure analysis, and if the mirror constant A is known, follow steps 1 through 9 in the next section and compute the stress *at the origin* in accordance with equation D.1. Note that this origin stress may or may not necessarily be the *maximum* stress in the part.

On the other hand, if the fracture mirror constant A is being evaluated by means of testing laboratory specimens and the origin stresses are known, follow steps 1 through 12.

Examples of how to judge the boundaries are shown in Figures D.1 through D.6. Low power images provide an overview. Matching unmarked and marked images are shown so that the reader can make a judgment for comparison. The boundaries were assessed while looking through a microscope and the digital images in Figures D.1 to D.6 were marked. Mirrors

should be evaluated while looking in a microscope. Although some of the mirrors are approximately circular or semicircular, examples of common alternative shapes are presented. Kirchner et al.[4,5] presented compelling evidence that fracture mechanics analyses account for stress gradient and geometric effects upon mirror shapes.

(a)

(b)

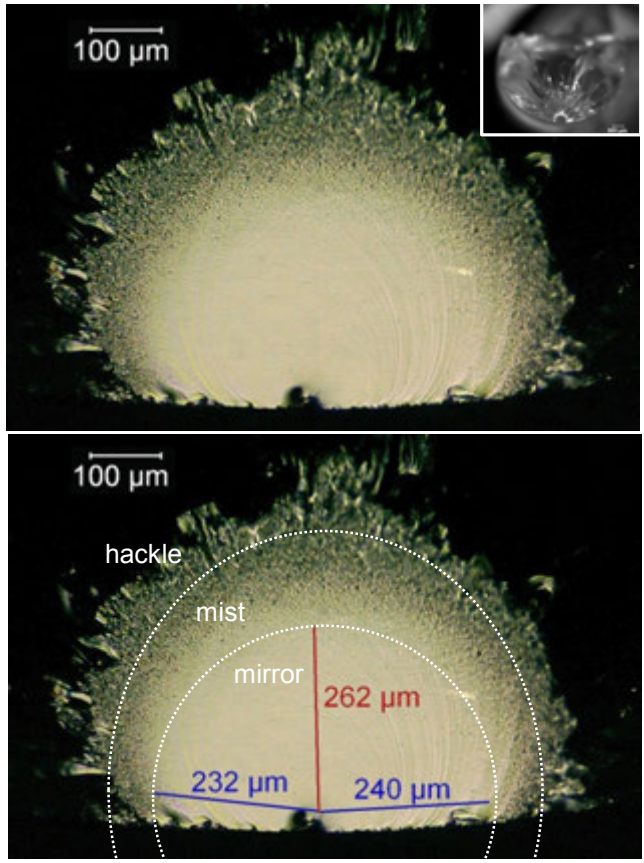

Figure D.1 *Fused silica rod broken in flexure (122 MPa). The origin is a surface flaw located at the bottom of the specimen (the insert in a) where the stress was a maximum. A stress correction is unnecessary. The mirror-mist boundary is small relative to the cross section size and is approximated by a circle in (b). The inward cusps at the surface are ignored as discussed in section D.3. The mist – hackle boundary is slightly elongated towards the top. Close examination of the fracture surface in the vicinity of the flaw (not shown) showed that fracture started from the deepest part of the flaw. (c) and (d) on the next page show SEM images of the same mirror.*

(c)

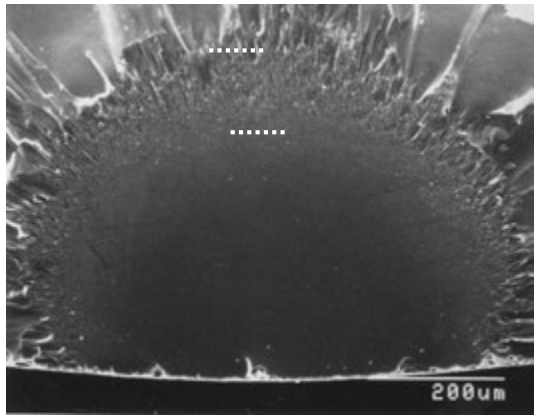

(d)

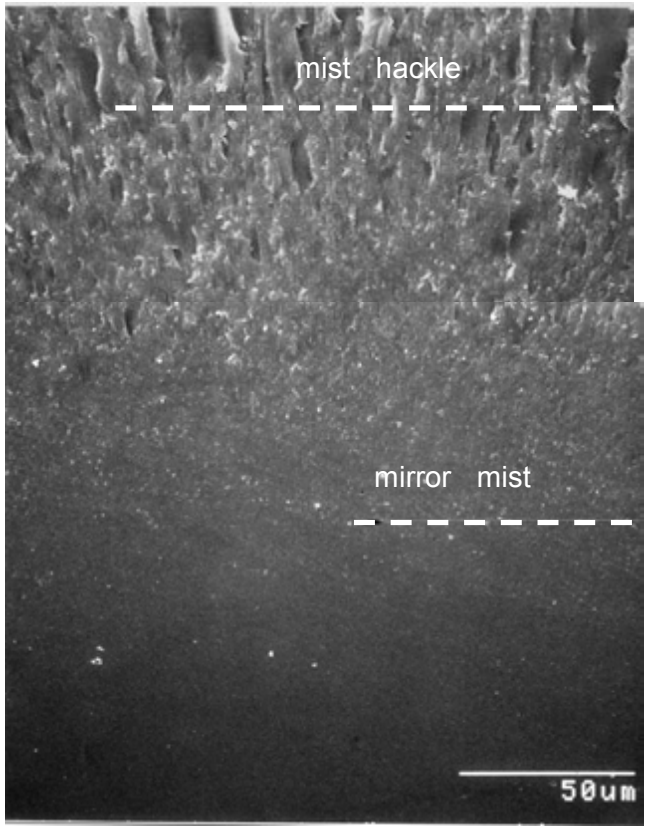

Figure D.1 continued *(c) is an SEM image of the same mirror and at the same magnification as (a) and (b). The mist is indistinct in the SEM image. (d) is a composite of two SEM images showing the transition from mirror to mist to hackle. The locations of the boundaries as assessed by optical microscopy (as shown in (b))are marked by dashed lines on the SEM images.*

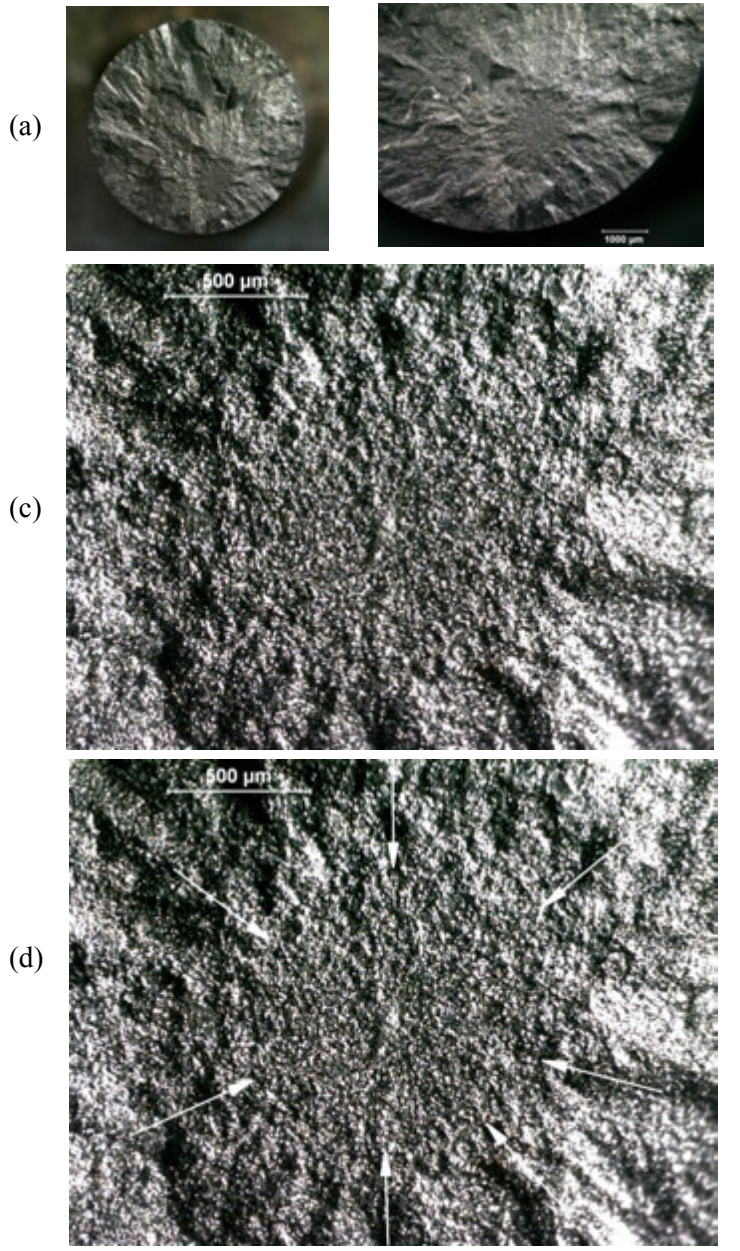

Figure D.2 *Silicon carbide tension strength specimen (371 MPa) with a mirror centered on a compositional inhomogeneity flaw shown in Figure 6.20a,b. Note how clear the mirror is in the low power images. The mirror boundary (arrows in d) is where systematic new hackle forms and there is an obvious difference compared to the roughness inside the mirror region.*

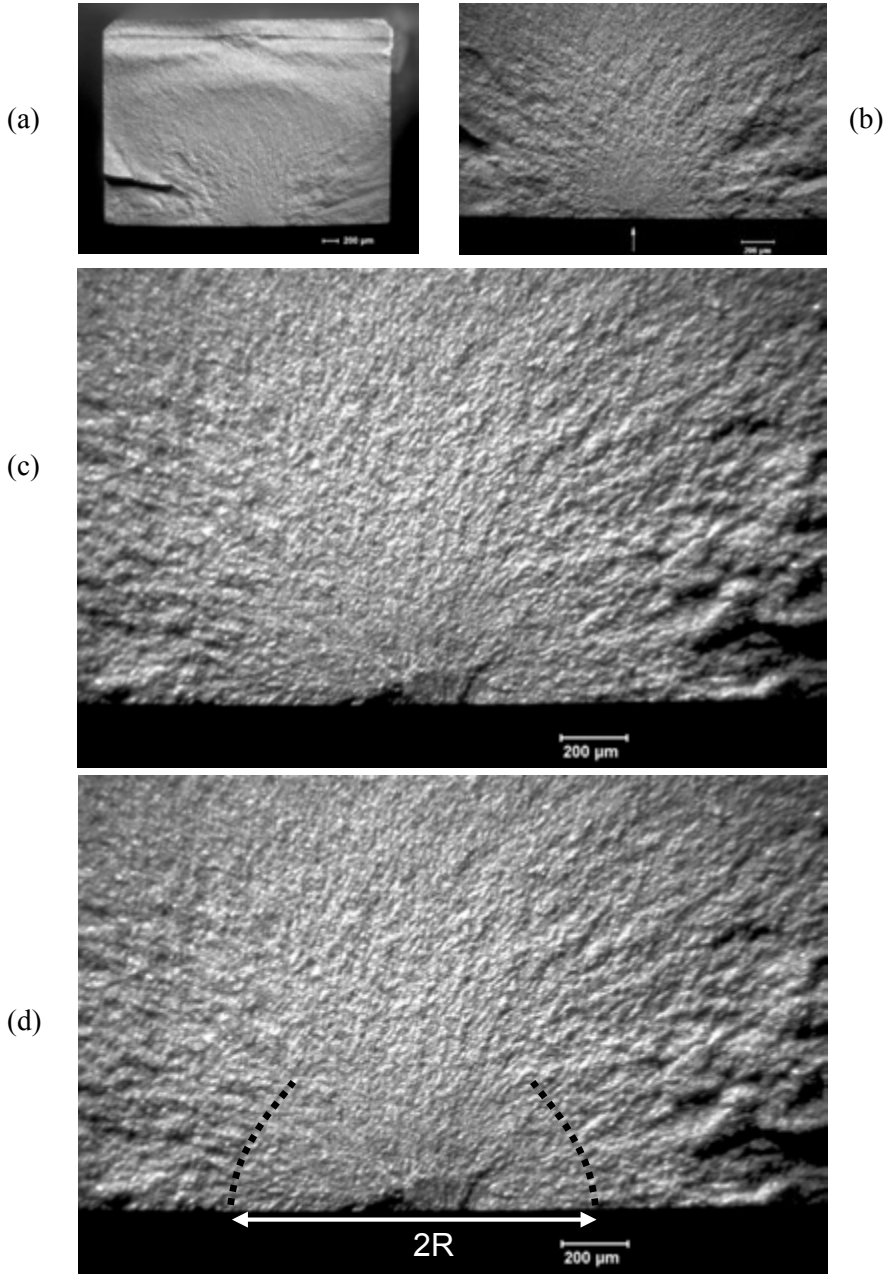

Figure D.3 *Silicon nitride bend bar with a Knoop surface crack (449 MPa, Ceralloy 147-31N, Refs. 6,7). The mirror is incomplete into the stress gradient, but the mirror sides can be used to construct boundary arcs in (d). Radii are measured in the direction of constant stress along the bottom.*

(a)

(b)

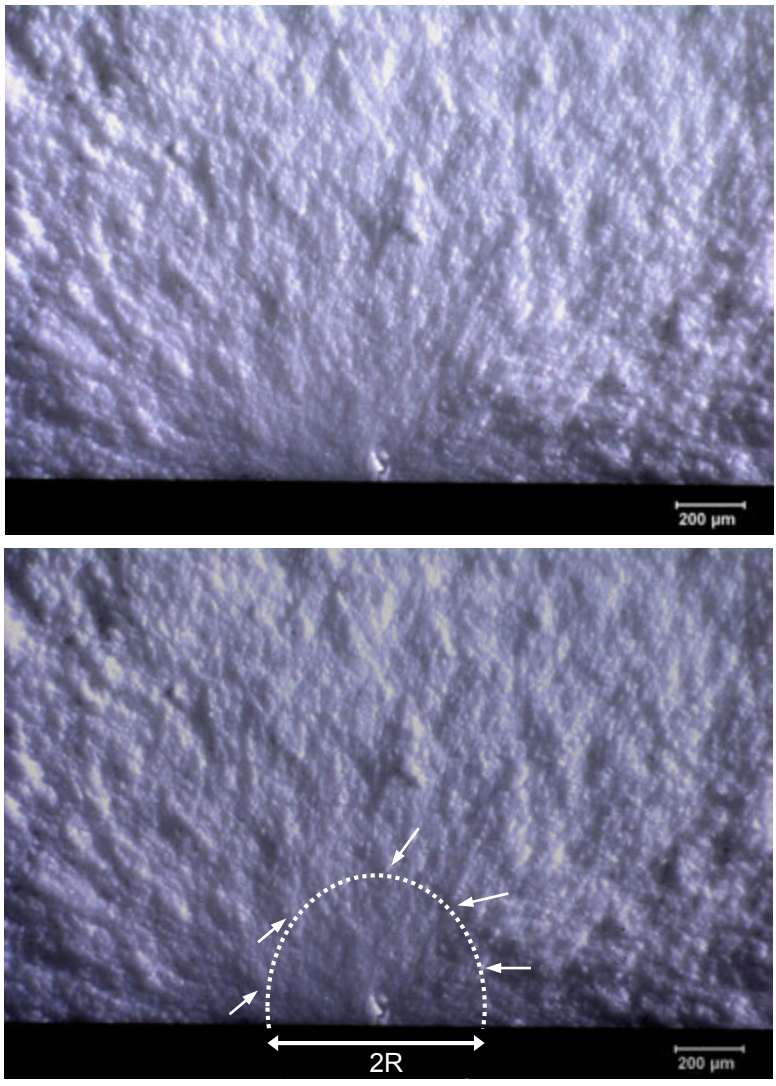

Figure D.4 *Example of a mirror in a fine-grained 3 mol % yttria-stabilized tetragonal zirconia (3Y-TZP) polycrystal (Bosch, Ref. 8). The mirror is difficult to mark in this material. (a) shows the uncoated fracture surface of a 2.8 mm thick flexural strength specimen (486 MPa) with low-angle grazing illumination. (b) shows an interpretation for a mirror-hackle boundary where systematic new hackle is detected (small white arrows) as compared to the roughness inside the mirror. The marked circle is elongated somewhat into the depth due to the stress gradient. The radius was 345 µm.*

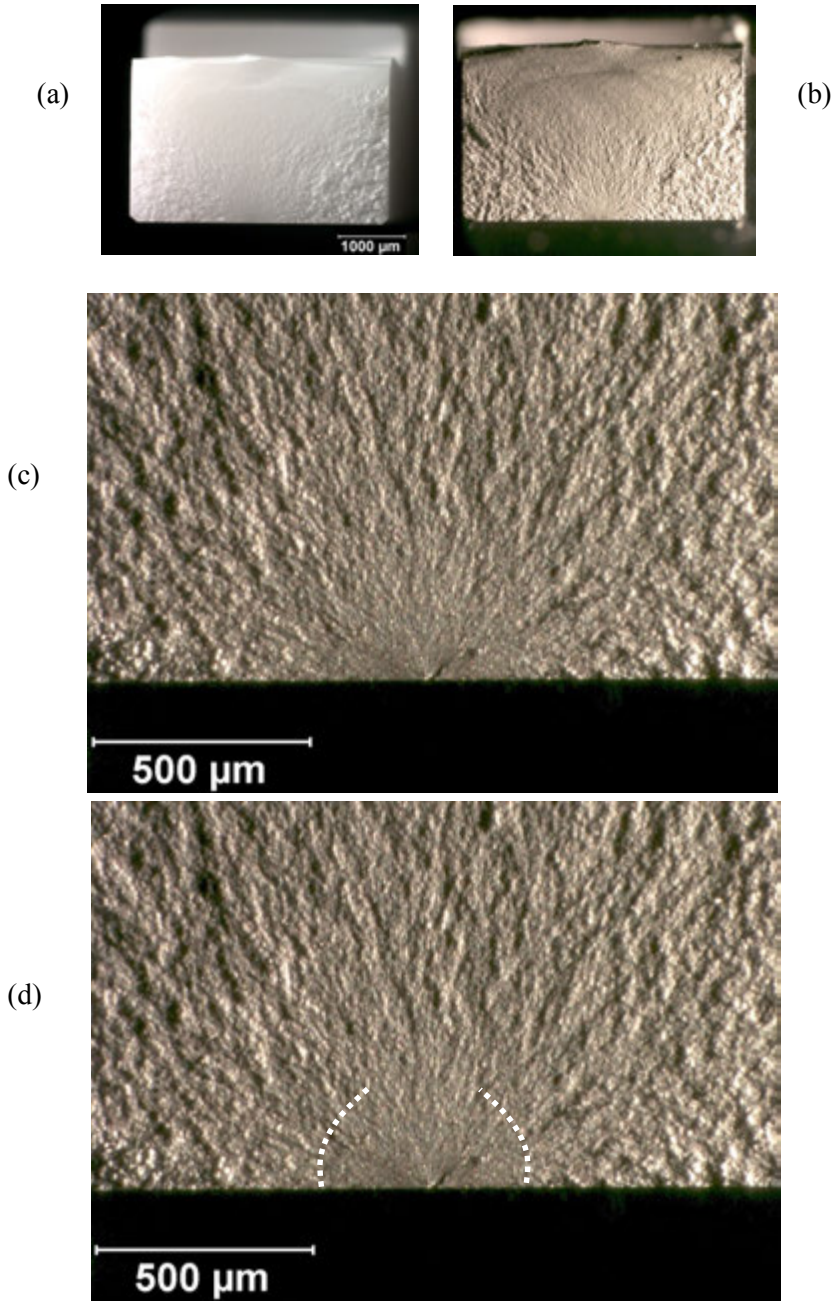

Figure D.5 *Fracture mirror in a 3Y-TZP zirconia flexural strength specimen (3M-ESPE Lava, 798 MPa). (a) and (b) are uncoated and gold coated images of the whole fracture surface, respectively. (Images courtesy J. Quinn)*

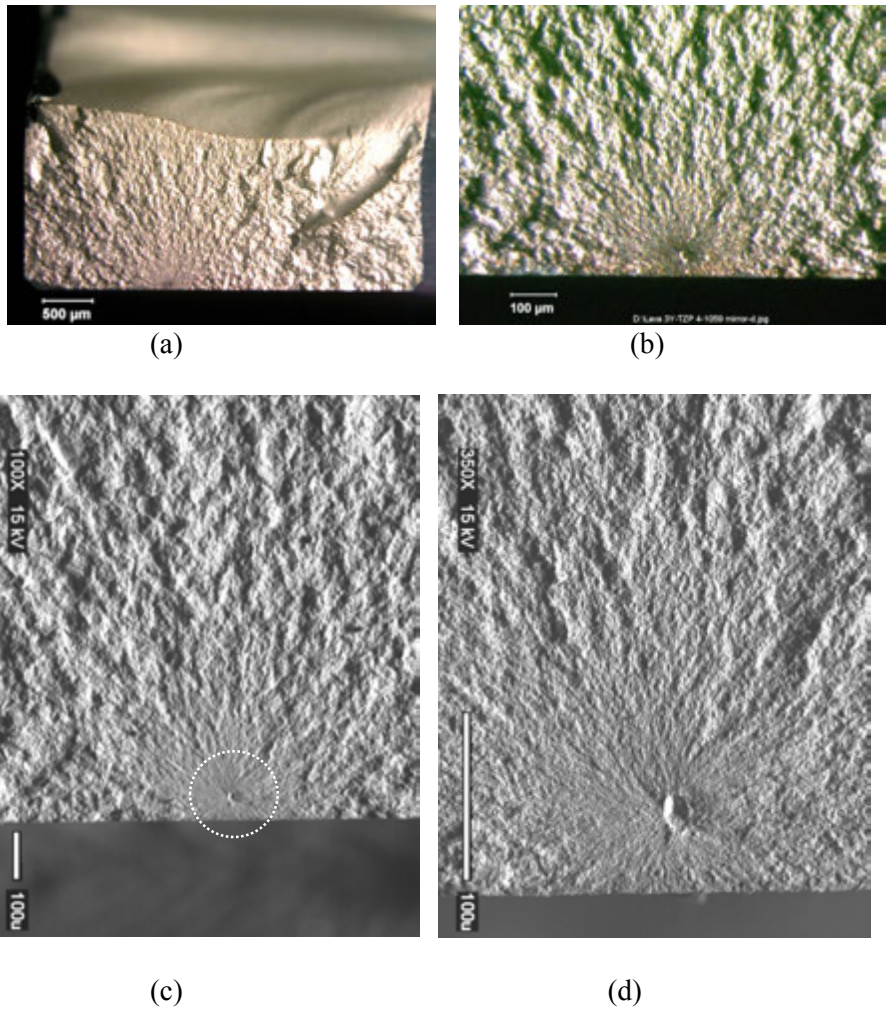

Figure D.6 *Fracture mirror in another 3Y-TZP bend bar. (3M ESPE Lava, 1059 MPa maximum stress, 1024 MPa at the origin). (a) and (b) are stereo optical microscope images. (c) and (d) are SEM images. Images (b) and (c) are at the same magnifications. The flaw is a pore. Fine hackle lines in the mirror run right to the origin. They are created by the flaw itself and the microstructure. The mirror boundary is where systematic new hackle forms and there is an obvious difference compared to the roughness inside the mirror region. This is a very difficult example. One interpretation is shown in the lower magnification SEM image. (SEM images (c) and (d) courtesy J. Quinn)*

D.2 Measure the Mirror Size

Use the following steps to measure mirror sizes. These steps are repeated, but with detailed notes, clarifications, and illustrations in section D.3.

1. **Use an optical microscope whenever possible.** A compound optical microscope is best for glasses. A stereoptical microscope is best for ceramics. A thin coating may be applied to translucent or transparent ceramics. A scanning electron microscope may be used if optical microscopy is not feasible.

2. **The fracture surface should be approximately perpendicular to the microscope optical path or camera.**

3. **Optimize the illumination to accentuate topographical detail.** Ceramics may be coated with gold or carbon.

4. **Use a magnification such that the fracture mirror area occupies about 75 % to 90 % of the width of the field of view for glasses, and approximately 33 % to 67 % of the width of the field of view for ceramics.** An additional, lower-power image may be helpful for ceramics.

5. **Measure the mirror size while viewing the fracture surface with an optical microscope whenever possible.**
   Use either calibrated reticules in the eyepieces or traversing stages with micrometer-positioning heads. Alternatively, measurements may be made on digital images on a high-resolution computer monitor, preferably while the fracture surface can be simultaneously viewed through the microscope eyepieces in order to aid judgment.

   Measurements from photos may be used as a last resort if the steps above cannot be followed. This may be necessary for very small specimens or very strong specimens with tiny mirrors and a scanning electron microscope must be used to photograph the mirror.
   Measurements from other devices may be used provided that the criterion used for identifying the mirror boundary is carefully documented.

6. **Measure radii in directions of approximately constant stress whenever possible.** A mirror diameter may be measured and halved to estimate the radius if the origin site is indistinct or complex.

7. **Exercise caution when mirrors are large relative to the specimen cross-section size.**

8. **Show at least one photo with arrows or lines marking the mirror size.**

9. **Report how the mirrors were measured.**

Additional steps for the determination of fracture mirror constants:

10. **Use the stress *at the origin site*.**
Correct the stress for location in specimens with stress gradients.

11. **Evaluate the fracture mirror constants by regressing stress on inverse square root of mirror radius. (Preferred method)**
Use linear regression methods to obtain A in accordance with equation D.2 with a forced zero intercept as shown in Figure D.7 Use units of MPa for stress and $1/\sqrt{m}$ for the graph axes. (It is a major nuisance to have to correct the numerical value of the slope if the x axis is in units of mm.) The mirror constant A is the slope of the regression line.

$$\sigma_a = \frac{A}{\sqrt{R}} \tag{D.2}$$

where σ_a is the stress at the origin site, computed from the known applied stresses. R is the mirror radius in the direction of constant stress.

Use some judgment in the regression analysis since fracture mirror data frequently has moderate scatter. If the data does not appear to fit a trend that has a zero intercept, regress the data with a non-zero intercept and equation D.3. Report the intercept if it deviates significantly (> 10 MPa) from zero. Investigate possible residual stresses or specimen size or shape issues if the intercept deviates significantly from zero.

$$\sigma_a = \frac{A}{\sqrt{R}} - \sigma_r \tag{D.3}$$

where σ_a is the stress at the origin from known applied stresses, σ_r is the residual stress at the origin location. A negative σ_r is a compressive residual stress and a positive σ_r is tensile, i.e., a positive intercept on the graph corresponds to a compressive residual stress and a negative intercept corresponds to a residual tensile stress.

12. **Mirrors sizes should be collected over a broad range of sizes and fracture stresses if possible.** Data from different specimen types and sizes may be combined.

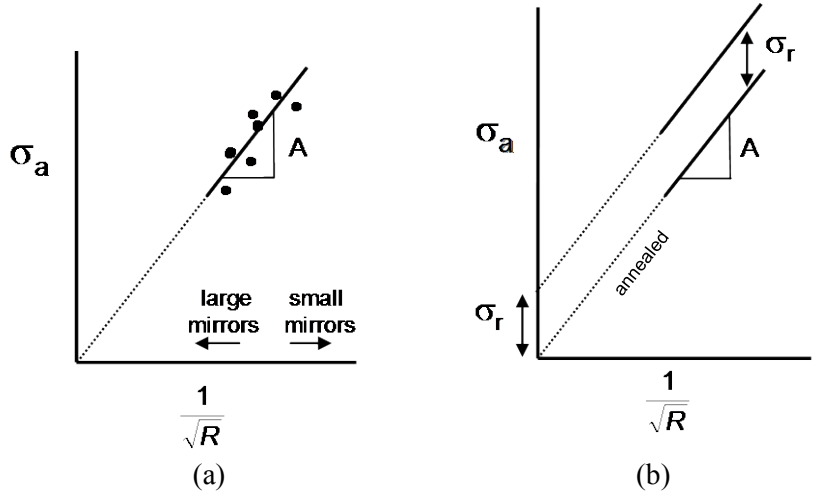

Figure D.7 *Plot of applied stress σ_a (at the origin) versus $1/\sqrt{R}$. (a) shows the trend for residual stress-free parts. (b) shows it for parts with residual stresses. Compressive residual stresses move the locus up with a positive intercept σ_r, but with the same slope. Tensile residual stresses shift the data downwards with a negative intercept (not shown).*

D.3 Clarifications, Additional Notes, and Illustrations

1. Use an optical microscope whenever possible. A compound optical microscope with bright field illumination is best for glasses. A stereo optical microscope is best for ceramics. A thin coating may be applied to translucent or transparent ceramics. A scanning electron microscope may be used if optical microscopy is not feasible.

Differential interference contrast (DIC, also known as Nomarski) mode viewing with a research compound microscope *originally was not recommended* by this Guide. It is only suitable for glasses. It is not suitable for rough ceramic fracture surfaces. There are complications with glass fracture surfaces. There is no question that DIC mode viewing can discern very subtle mist features in glasses, but the threshold of mist detectability is highly dependent upon how the polarizing sliders are positioned. Hence, DIC measured radii are quite variable. DIC measured radii can be substantially

smaller than those obtained with conventional viewing modes. During a review process in 2010, paragraph 6.1.3 of standard ASTM C 1678[2] was revised to allow DIC mode for glasses, provided that the polarizing elements are used in a consistent manner in the grey mode (with the lambda plate for color control removed).

Dark-field illumination may be used with glasses, but dark-field images may lose a little resolution with glasses and radii may be slightly larger as a result. It is very effective with highly-reflective mirror surfaces in single crystals.

Confocal optical microscopes and optical interferometers have been occasionally used to examine fracture mirrors, but I am unaware of any published systematic study to correlate apparent mirror sizes from these tools to those measured with conventional optical microscopes. The quantitative surface roughness capabilities of these instruments in principle could be used to correlate an average or root mean square roughness to the mist or hackle boundaries.

Scanning electron microscope images of mirrors are not recommended for measuring the mirror-mist boundary in glasses since the boundary is usually indiscernible at the magnifications needed to see the overall mirror. SEM images often appear flat and do not have adequate contrast to see the fine mist detail. SEM images may be used to measure mirror hackle boundaries with very small mirrors that would be difficult to see with optical microscopy, e.g., as in high strength optical fibers.

Scanning electron microscope images may be used for ceramics if necessary, but steps should be taken to enhance contrast and shadowing to produce images such as shown in Figures D-6c and d.

Attempts to correlate the mirror boundaries with a simple surface roughness parameter have produced mixed results. The work has been limited to glasses. Duckworth et al.[9] carefully studied mirror sizes in float glass using optical photographs and a conventional surface profilometer. They obtained a good correlation with optical boundary estimates when the surface roughness reached a level of 0.25 μm for the mirror- mist A_i boundary, and 5 μm for the mist-hackle A_o boundary. Kuluwansa et al.[10] used scanning tunneling microscopy (STM) to study mirror features and suggested the transition from a nano-mist region to the mist-hackle region with its rougher features (that were observable in the SEM) may be sharp. The characteristic scale of crack branching in the mirror to mist-hackle transition region ranged from 50 nm (the size of typical nano-mist features) to about 50 μm (the size of typical hackle

features. Hull[11,12] and Wünsche et al.[13] used atomic force microscopy to show that the mist region in glass or brittle epoxy has a roughness of as small as a few tens of nanometers, which is much less than the wavelength of visible light (390 nm to 800 nm). The scanned regions were quite small, however, and both groups noted that if the AFM scans a small region between hackle or river line steps, then the measured roughness is much less than if the latter are included. Hull pointed out that the greater undulations from Wallner lines need to be factored out when evaluating the intrinsic mist roughness. His study showed that roughness increased continuously and there were no dramatic jumps in roughness at the boundaries, but the *rate of change* of roughness did change significantly at the mirror-mist boundary. Surface roughness measurements should be taken perpendicular to the direction of crack propagation since high-resolution transmission microscope images[14,15,16] of the mist and hackle show the surface features are elongated in the direction of crack propagation.

Hull[12] pointed out that different surface roughness characterization devices such as atomic force microscopes (AFMs), mechanical profilometers, and laser optical profilometers all have different advantages, disadvantages, sensitivities and scanning zone sizes. AFM's can measure tiny regions with very high sensitivities, but may miss large hackle steps in a mist or hackle zone. These latter features can dramatically alter the average or root mean square roughness. A mechanical stylus profilometer or laser profilometer with a 1 μm spot size may miss the small undulations and be more sensitive to larger hackle steps on the fracture surface. Mist and hackle regions may have different roughness at different scales. Hull discuses these various scales of roughness in some detail in his book.[12]

The author is not aware of any systematic studies comparing fracture mirror sizes as a function of the viewing mode or microscope type.

2. The fracture surface should be approximately perpendicular to the microscope optical path or camera.
This simple and fairly obvious requirement is intended to avoid the foreshortening that can occur if the specimen is tilted. A small amount of tilting is acceptable in order to get a favorable reflection in a glass piece. A compound optical microscope is best for glasses. A stereo optical microscope is best for ceramics.

The requirement poses a small problem if the mirrors are examined with stereo binocular microscopes. These have two different tilted optical paths. If viewing with *both* eyes in a stereomicroscope, the specimen should be flat and

facing directly upwards. The observer's brain will interpret the image as though he is facing it directly.

Alternatively, if a camera is mounted on one light path of the stereomicroscope and it is used to capture or display the mirror, then the specimen should be tilted so that the camera axis is normal to the fracture surface. For example, tilt the specimen to the right if the camera is attached to the right optical path.

3. Optimize the illumination to accentuate topographical detail.
The mist and hackle features should be accentuated. Glasses may either be illuminated from directly down onto a fracture surface or by low-angle grazing illumination. Ceramics should not be directly illuminated since the light will reduce contrast, especially in translucent or transparent materials. Ceramics should be illuminated with low-angle grazing illumination. Stereoptical microscopes are strongly preferred for ceramics. Low-angle illumination is less convenient with compound light microscopes. The observer should experiment with whatever illumination options are available to accentuate subtle surface roughness and topography features. Contrast and topographic detail should be emphasized with the SEM if it is necessary to use this mode of examination because the mirror is too small to be measured optically.

4. Use a magnification such that the fracture mirror area occupies about 75 % to 90 % of the width of the field of view for glasses, and approx.-imately 33 % to 67 % of the width of the field of view for ceramics. An additional, lower-power image may be helpful for ceramics.

Observers usually mark the mirror boundaries closer to the origin at greater magnifications than they would at lower magnifications. This is because mist or micro hackle markings are easier to see at distances closer to the origin at high magnification. This is particularly the case with glasses. Conversely, at very low magnifications, much detail is lost and observers typically overestimate the mirror size.

Fracture mirrors are reasonably easy to see in glasses and magnifications should be used such that they nearly fill the field of view.

Mirror interpretation is more problematic with polycrystalline ceramics. Excessive magnification often leads to confusion as to where the boundary is located. Even though a mirror may be obvious at low or moderate magnifications, at higher magnifications it may be impossible to judge a boundary. It is more practical to view the mirror region (and the natural microstructural roughness therein) relative to the hackle roughness in the

regions outside the mirror. "Stepping back" and using the 33 % to 67 % rule should help an observer better detect the topography differences. Images recorded at these magnifications are also more convincing when shown to other fractographers or engineers. Even lower magnification images may also be made to aid interpretation such as shown in Figures D-2b, D-3b, and D-6b. The images should not be more than 5 times different in magnification; otherwise it is difficult to correlate features in one image to another.

Sometimes the microstructure of polycrystalline ceramics creates even worse judgment problems in ceramic matrix composites (particulate, whicker or platelet) or self-reinforced ceramics whereby elongated and interlocking grains impart greater fracture resistance. These difficulties were experienced in studies of the fracture surfaces of a self-reinforced silicon nitride[6,7] and also a yttria-stabilized tetragonal zirconia polycrystal.[8] Mirrors were plainly evident at low magnifications, but accurate assessment of their size was difficult. The mirror region itself was somewhat bumpy in the self-reinforced silicon nitride, so some judgment as to what was the mirror boundary was necessary. The zirconia had intrinsic micro hackle lines well within the mirror. The criterion for the mirror boundaries was as follows: *The mirror boundary was judged to be the point where systematic new radiating hackle commenced and there was an obvious roughness change relative to the inside-mirror region.*

The word systematic requires some elaboration. Mirror boundary hackle lines are velocity hackle lines created after the radiating crack reaches terminal velocity. Premature, isolated hackle can in some instances be generated well within a mirror, however. It should be disregarded when judging the mirror boundary. Wake hackle from an isolated obstacle inside the mirror (such as a large grain or agglomerate) can trigger early "premature" hackle lines such as shown in Figure 5.5 in the main text. Steps in scratches or grinding flaws can trigger hackle lines that emanate from the origin itself.

5. Measure the mirror size while viewing the fracture surface with an optical microscope whenever possible.
A compound optical microscope is best for glasses. A stereoptical microscope is best for ceramics. Use either calibrated reticules in the eyepieces or traversing stages with micrometer-positioning heads. For routine measurements for ceramics, the author uses a stereoptical binocular microscope with a traversing X-Y stage with digital micrometer heads that read out to 0.001 mm (1 μm). Alternatively, measurements may be made on digital images projected onto a high resolution computer monitor preferably while the fracture surface can be simultaneously viewed through the microscope eyepieces in order to aid judgment.

Measurements from photos may be necessary for very small specimens or very strong specimens with tiny mirrors, such as in fibers or microelectro-mechanical system (MEMS) devices. Scanning electron microscope images may be used. Again, the fractographer should take an overall framing photograph or image shot in accordance with the 75 % to 90 % rule for glasses and 33 % to 67 % rule for ceramics. Higher and lower magnification images may be used to help aid in interpretation.

Mirror size measurements from photographs are usually less accurate. They frequently overestimate mirror sizes unless conditions are carefully optimized to accentuate contrast and topographic detail. Two-dimensional photographic renditions of a three-dimensional fracture surface usually lose much of the topographic detail discernable by the eye with a compound optical or stereomicroscope.

Mirror size measurements made on computer monitor screens are also subject to inaccuracies, also because they are two-dimensional renditions of a three-dimensional fracture surface. Video cameras should not be used to capture mirror images since they lack adequate resolution. High-resolution cameras and monitors are beginning to match the capabilities and accuracy of an observer peering through the optical microscope.

6. Measure radii in directions of approximately constant stress whenever possible. A mirror diameter may be measured and halved to estimate the radius if the origin site is indistinct or complex.

There is no consensus on how many mirror radii measurements should be taken and in how many directions. Ideally, measurements should be taken from the center of the mirror region, but some judgment may be necessary. A common practice is to make a judgment whether a mirror is indeed approximately semicircular or circular. If it is, then multiple radii measurements may be made in different directions and averaged to obtain the mirror size estimate.

The center of the mirror may not necessarily be the center of the flaw at the origin. Careful inspection of tiny localized fracture surface markings (Wallner lines and micro hackle lines) right around the origin may reveal that fracture started at one spot on a flaw periphery. For example, fracture from grinding or impact surface cracks in glass often starts from the deepest point of the flaw and not at the specimen outer surface. Figure D.1 shows an example. Large pores often trigger unstable fracture from one side. An example is the pore in Figure D.6d, where fracture seems to have started on the left side of this

internal flaw. If an exact mirror center cannot be determined, it is adequate to measure a mirror diameter and halve the measurement. This is commonly done for semicircular mirrors centered on irregular surface-located flaws whereby the mirror center may be difficult to judge.

Circular embedded mirrors are easiest to interpret (such as in Figure 5.7). Small semicircular mirrors on the surface of a part, such as in a bend bar or a flexurally loaded plate, are also not too difficult to interpret. The mirror relationship holds up remarkably well in glass optical fibers tested in tension for mirror radii almost as large as the fiber diameter.[17] The mirror radius should simply be measured from the origin to the mirror-mist or mist-hackle boundary on the opposite side of the fiber, R_d as shown in Figure D.8.

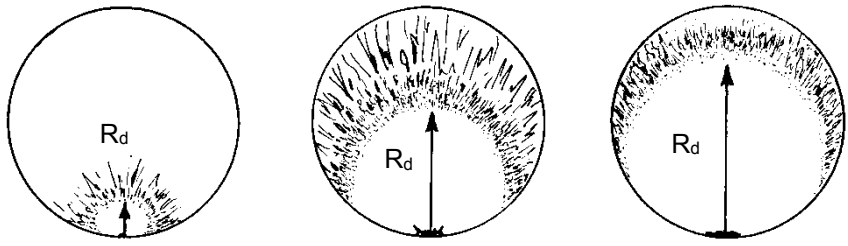

Figure D.8 *Mirrors surrounding surface origins in rods or fibers loaded in direct tension. (after Ref. 17) Measure both the mirror-mist radius (shown) and mist hackle radii into the depth as shown.*

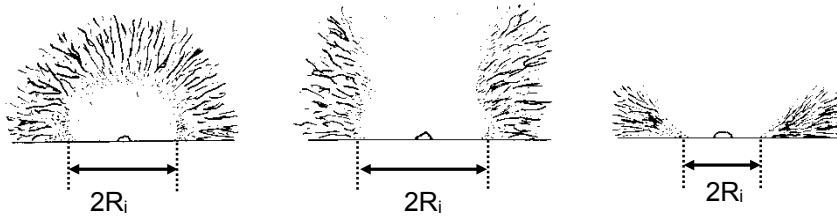

Figure D.9 *Elongated mirrors in bending stress fields. If the mirror is small relative to the part size (i.e., a strong part), then the mirror may be semicircular as shown in (a). Weaker parts have larger mirrors that flare into the interior and are incomplete as shown in (b) and (c). Measure the mirror size (R_i or $2R_i$ for the mirror-mist in the illustrations here) in the direction of constant stress. (Note: special guidance on how to deal with small inward bending cusps at the surface is shown in Figure D.12 below.)*

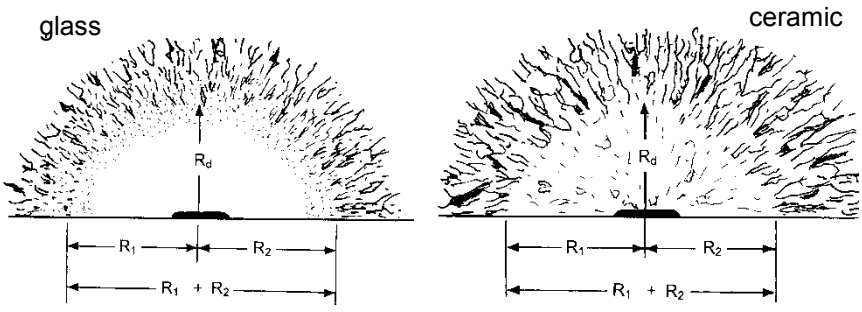

Figure D.10 *Grinding cracks and scratches can cause mirror elongations along the surface, even in bend bars with stress gradients. (a) shows a schematic of such a mirror with the mist-hackle boundary marked in glass, and (b) shows a comparable image in a polycrystalline ceramic. It has some intrinsic microstructural roughness inside the mirror and the mirror-hackle boundary is marked. Use an average radius:* $R_{avg} = \{(R_1 + R_2 + R_d\}/3$.

Quarter circular mirrors centered on an edge or chamfer should be measured from the origin.

On the other hand, mirror shapes are commonly affected by stress gradients in a plate or a beam. Mirror radii are elongated in the direction of decreasing stress. Examples are shown in Figure D.9b and c. In such cases, measure the mirror radius along the tensile surface where the stress is constant. Do not measure the mirror radii into the gradient. Even with this precaution, there is considerable evidence that the data begins to depart from the stress-mirror size curves and the relationship in equation D.1 when the sizes approach the plate, beam, or rod thickness. For mirrors radii larger than the plate thickness, data points fall above the trend on a log stress – log mirror size plot which means that mirrors are larger than they would otherwise be if the part were loaded in uniform tension.

A trend for mirrors to elongate the opposite way, along the external surface of a specimen, was detected by the author in recent work on the fractographic analysis of grinding flaws in structural ceramics.[6,7] Long surface cracks often caused mirrors to have perceptible deviations from a semicircular shape as shown in Figure D.10. In such cases, measure an average radius:

$$R_{avg} = (R_1 + R_2 + R_d) / 3. \qquad \text{(D-4)}$$

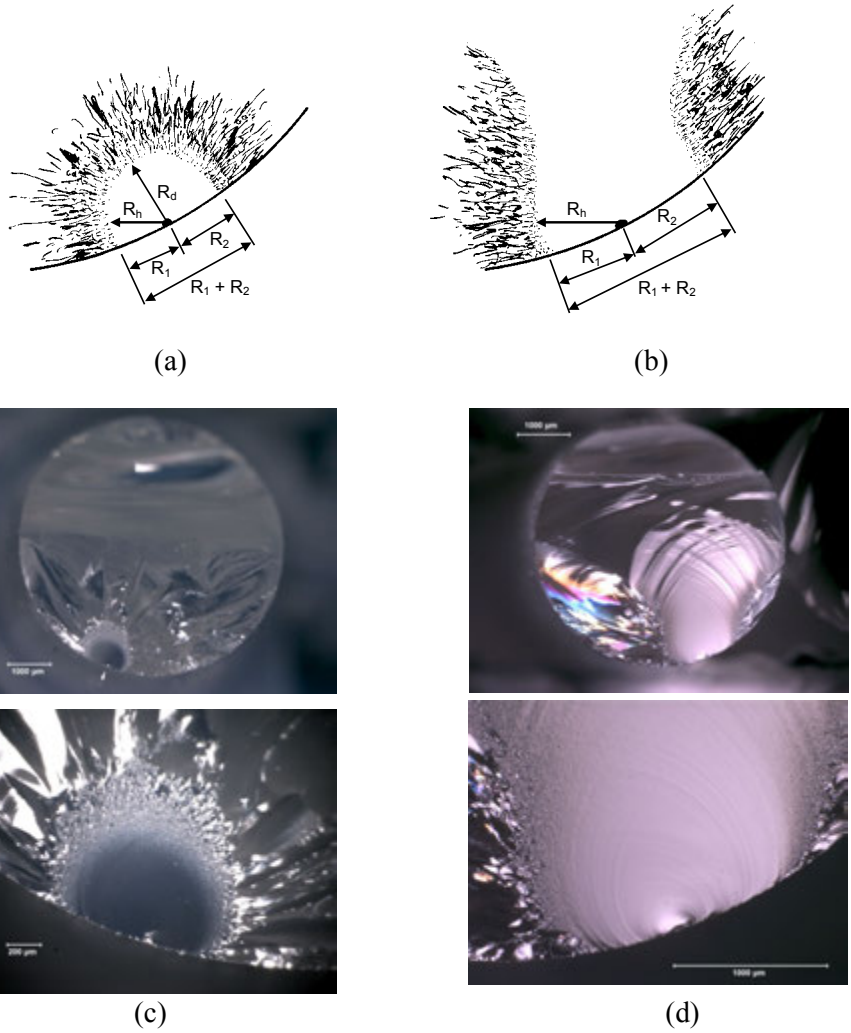

Figure D.11 *Fracture mirrors in rods tested in flexure. The load was applied in a vertical direction and the maximum tensile stresses are at the bottom center. Fractures started at flaws part way up the sides of the rods causing the mirrors to have unequal radii. Schematics (a and b) are similar to two glass rods (c and d). The rod shown in (c) was sufficiently strong that a nearly semicircular mirror formed, but with unequal radii due to the stress gradient. Use* $R = R_h$ *if the origin and mirror center is distinct. Otherwise use* $R_{avg} = (R_1 + R_2 + R_d) / 3$ *if the mirror is nearly semicircular. Use* $R_{avg} = (R_1 + R_2) / 2$ *if the mirror is elongated into the interior and* R_d *is large. (d) shows a weaker glass rod. Use* $R = R_h$ *if the origin and mirror center are distinct, otherwise use* $R_{avg} = (R_1 + R_2) / 2$.

In some cases, it may be difficult to measure mirrors in directions of constant stress. The two sides of a mirror may have unequal lengths since the stresses are different on either side of the mirror. Figure D.11 shows examples from the author's research of round rods broken in flexure. Many origins were not at the rod bottom where the stresses were a maximum, but part way up the side of the specimen. The specimen orientation was easily determined from observation of the compression curl. The maximum tensile stress on the bottom of the specimen was on the rod directly opposite the cantilever curl. It was a simple task (see section 9 below) to compute the actual stress at the origin location. The mirror radii had obviously different lengths due to the stress gradient. *Use a radius in the direction of constant stress, R_h, as shown in Figure D.11, if the mirror is centered on a well-defined origin site.* If there is any doubt, then an average radius may be computed. Use $R_{avg} = (R_1 + R_2 + R_d) / 3$ if the mirror is nearly semicircular. Use $R_{avg} = (R_1 + R_2) / 2$ if the mirror is elongated into the interior and R_d is large or is incomplete.

For origins located in the interior of a rod broken in flexure, *only use the radii in the direction of constant stress*. As a check, and only if the mirror is a complete ellipse, one may measure two orthogonal mirror diameters and compute an average diameter and halve this to obtain an average radius.

There is one important detail about mirror sizes that warrants discussion. Mirrors located on a specimen external surface have *small cusps* at the intersection with the outer surface as shown in Figure D.12a. Cusps are often detected in glass mirrors, but they are rarely if ever discerned in polycrystalline ceramic mirrors. The small cusp is a consequence of fracture mechanics. A small element of material near the tip of a crack at the specimen exterior surface experiences greater stress intensity than a similar element buried in the interior whereby neighboring elements can "share the load." Kirchner et al.[4,5] discussed the shapes of fracture mirrors that intersect outer surfaces and they showed that the local enhancement of the stress intensity K_I accounts for the cusps. The slightly-greater stress intensity at the surface triggers the mirror markings a bit sooner than for interior elements. *The usual convention, and the one adopted in this Guide, is to truncate the cusp. Extend the semicircular (or other mirror shape) arcs as shown in Figure D.12c.* Another reason to be wary of measurements right along the surface is that surface roughness, machining damage, or other surface irregularities may trigger mist or hackle formation a bit earlier than in the interior. Others have noted that measurements taken right on an exterior surface are slightly different than those

(a)

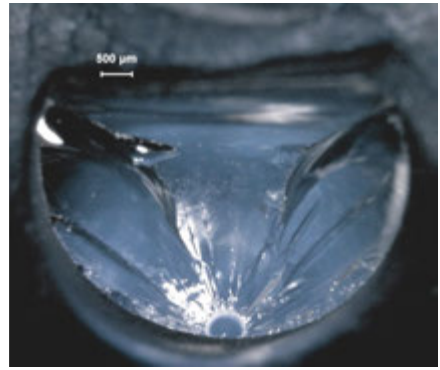

(b)

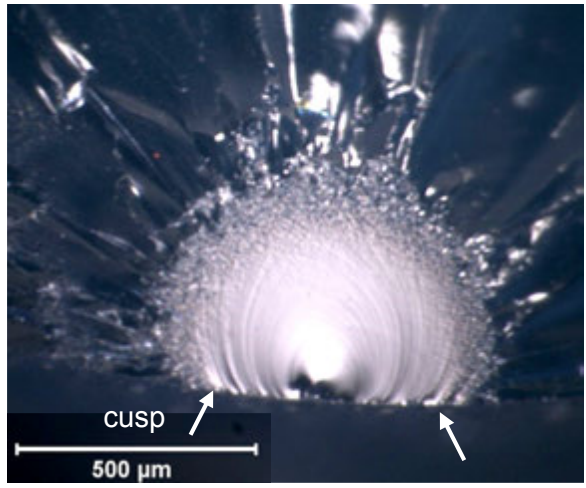

(c)

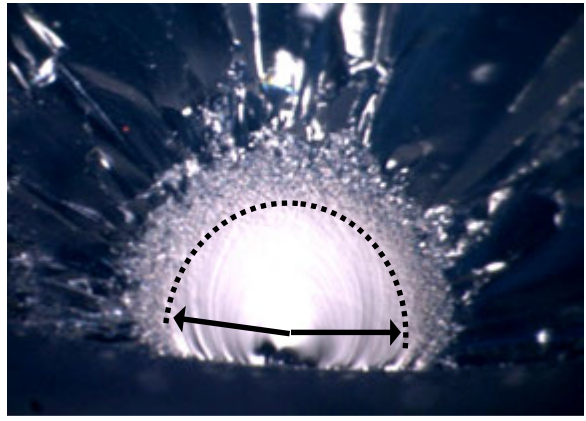

Figure D.12 *Fracture mirror in a fused silica rod (a), illustrating the cusps in the mirror near the outer surface (b). Mirror measurements should not include the inward bend of the mirror and may be made as shown in (c).*

taken into the interior. Even Shand[18] recommended in 1959 that size measurements be taken 0.1 mm (.004 in) beneath the exterior surface. Mecholsky and Freiman[19] in 1979 recommended ignoring the cusp at the surface on the basis of fracture mechanics considerations: "In measuring the mirror-mist and mist-hackle boundaries, these should be projected to the tensile surface to compete a circular arc, since there is curvature at the surface due to free surface effects."

A dilemma occurs when mirrors are large in plates or beams broken in flexure as shown in Figure D.9c. Cusps cannot be detected. In this case the only plausible way to measure a mirror radius is directly along the surface. In such cases, the general warning of step 7 applies.

It is worth reiterating that equations D.1 and D.2 are empirical. Kirchner and colleagues[4,5] showed a more rigorous fracture mechanics analysis (based on a critical stress intensity for branching) completely explained the mirror shapes and distortions including the cusp mirrors in various stress fields. Despite the merits of their rigorous fracture mechanics analysis, there is significant practical advantage to using the simpler mirror size - stress relationships D.1 and D.2 even if some rigorousness is sacrificed. In addition, for small mirror sizes relative to the specimen dimensions, the simpler approach is almost as rigorous.

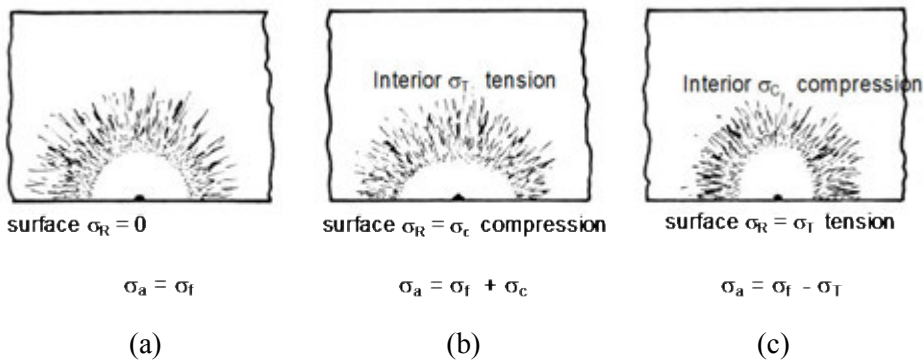

Figure D.13 *Surface residual stresses also may alter a mirror shape. σ_a is the applied stress to cause fracture and σ_f is the fracture stress in an annealed plate. (a) shows a surface mirror in an annealed plate. (b) shows the mirror shape in a plate with surface compression stresses that decrease into the interior and become tensile. (c) shows a mirror in a plate with surface tensile stresses that diminish into the interior and become compressive.*

Residual stresses alter mirror shapes. If the mirror is very small relative to the stress gradient, the mirror shape may remain circular or semicircular if along the surface. On the other hand, if the mirror is larger or the stress gradient is steep, then the gradient alters the mirror shape as shown in Figure D.13. Figure D.13a shows an annealed plate that requires an applied stress of $\sigma_a = \sigma_f$ to cause fracture. Figure D.13b shows the case where the same plate has residual surface compression stress $\sigma_r = \sigma_c$ from ion exchange or thermal tempering, so that an applied stress to cause fracture is $\sigma_a = \sigma_f + \sigma_c$. In other words, the applied stress must be increased to overcome the residual surface stress. Nevertheless, the net stress at the surface at the moment of fracture is $\sigma = \sigma_a - \sigma_c = (\sigma_f + \sigma_c) - \sigma_c = \sigma_f$, the same stress as in the annealed plate. Hence the mirror radii along the surface are *unchanged* compared to the annealed plate. In contrast, in the direction into the interior, tensile stresses combine with the applied tensile stress to cause the mirror markings to form sooner, at a shorter radius into the interior than in the annealed plate. In this example, the mirror shape is flattened to a semiellipse. Mirror radii should be measured *only along the surface* (or just beneath the surface if there is a cusp) in these cases.

Figure D.13c shows that surface residual tensile stresses have the opposite effect: mirror radii are elongated into the interior. Mirror radii again should only be measured along the surface, since again the net stress to cause fracture is $\sigma = \sigma_f$.

There are two possible paths for data analysis if there are residual stresses:

(a) The mirror is measured on a component. The applied stress and the residual stresses are unknown. In this instance the net stress σ at the origin can be evaluated from R_{avg} and equation D.1.

(b) The mirrors are collected in laboratory conditions with multiple specimens such that the apparent origin stresses σ_a, from applied external stresses are known. In this instance, one or more matched pairs of σ_a and R are obtained. Graphical analysis as shown in Figures D.1 or D.2 reveals the existence and magnitude of the residual stresses.

7. Exercise caution when mirrors are large relative to the specimen cross-section size.

At some point, one can expect departures from of the stress - mirror size relationship. The point where the departure occurs depends upon the loading geometry and the stress state.

Pronounced deviations occur once the mirror size approaches or is greater than the component thickness in plate or beam *bending* fractures. Experimentally measured radii are much greater than predicted by equation D.1. Shand recommended that the maximum mirror size should be no more than 15% of the rod diameter (or 30% of the distance to the centroid) for *flexure* tests.[18,20] Kirchner and Conway[5] warned about limitations in the fracture mechanics models for mirror radii exceeding 20 % of a rod diameter tested in flexure. On the other hand, Castilone et al.[17] had success with mirrors that were almost as large as the fiber diameters for fibers tested in *tension*.

There is merit to measuring and recording mirrors even if they are large relative to a cross section size. The data may have value for use with analyzing genuine component fractures.

Mecholsky and Freiman[19] warned that systematic deviations from the mirror size relationship occur at large mirror sizes but also at very small sizes, the latter due to internal stress effects, e.g., from thermal expansion anisotropy of grains in ceramics.

8 Show at least one photo with arrows or lines marking the mirror size.
This simple step will help clear up a lot of the doubt and confusion about what an investigator has actually measured.

9. Report how the mirrors were measured.
This simple last step is often overlooked or ignored, and the reader is left wondering exactly what had been done. The fractographer should report the microscope used, whether interpretation was made while looking through the microscope or from photos, and approximately what magnifications were used. The direction the mirror radii were measured should be documented. The approximate shape of the mirrors (semicircular, circular, or elliptical) should be noted. It should also be noted whether the mirrors were an appreciable fraction of the size of the cross section or not. Lastly, and most importantly, the judgment criterion used should be reported.

10. Use the stress at the origin site (additional steps to determine A).
If the specimen was broken in controlled conditions where the stress distribution was known (e.g., beams, rods, or plates in flexural loadings) correct the stress for location in specimens with stress gradients.

No correction is needed if a part was stressed in uniform tension. On the other hand, many parts or laboratory specimens do have stress gradients. The general principal that should be followed is that the mirror formation is guided by the

stresses that acted on and in the immediate vicinity of the flaw origin. While this may seem obvious, it is probable that some analysts in the past have erroneously used *nominal stresses* in a specimen or component rather than the *actual stress* that was acting upon the mirror region in a body. In contrast, some researchers have correlated the stress at every site along the mirror periphery with the mirror radius at that periphery site, but this complex process is not practical on a routine basis.

Example 1: Flexural strength test specimens

The nominal flexural strength is the maximum stress at the outer fiber or tensile surface of the bar. The stress correction for locations beneath the surface is

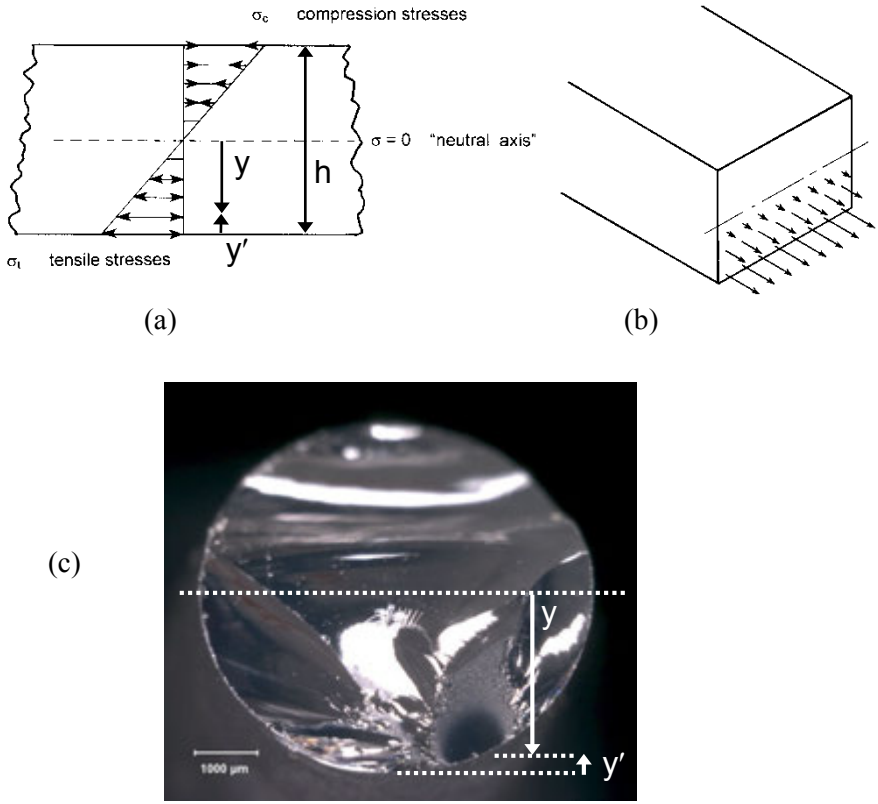

Figure D.14 *The flexural stress gradient is shown in (a) and (b) for a rectangular beam. (c) shows how the origin location may be measured from a rod neutral axis.*

simple if the material is linearly elastic. The stress decreases from a maximum at the outer tensile surface to zero at the middle "neutral axis" which corresponds to the centroid in a square, rectangular, or circular cross-section beam specimen as shown in Figure D.14. At the origin,

$$\sigma = (2y/h)\ \sigma_{max} \qquad (D.5)$$

where y is the distance from the centroid and h is the beam thickness or rod diameter. Alternatively, in terms of the distance from the tensile surface, y':

$$\sigma = (1 - 2y'/h)\ \sigma_{max}. \qquad (D.6)$$

In similar fashion, if a fracture origin is not directly under the middle loading point in three-point bending, or if the origin is outside the inner gage length in four-point bending, then the stress should be correspondingly adjusted to the stress that actually acted on the origin site. Corrections for breaks outside the gage section or away from the middle loading point are also linear. The stress is reduced in proportion to the distance from the fracture plane to the outer loading points. This correction requires knowledge of the loading point locations. This is an important reason why loading points should be marked on any test piece prior to its fracture. For three-point loading:

$$\sigma = (2x/L)\ \sigma_{max} \qquad (D.7)$$

where x is the distance from the outer loading point to the fracture plane and L is the total three-point span. For four-point flexure,

$$\sigma = (x/a)\ \sigma_{max} \qquad (D\text{-}8)$$

where x is the distance from an outer loading point to the fracture plane, and a is the distance from the outer loading point to an inner loading point. If an origin in a flexural beam is subsurface and outside the inner span, then both corrections should be applied. If the origin is on the tensile surface, within the inner span length, and the mirror size is small and semicircular, then no stress correction is needed.

Example 2: Ring-on-ring biaxial strength test specimens.

If the origin is on the tensile surface in the inner loading circle, and the mirror size is small and semicircular, then no stress correction is needed. Fracture mirrors from volume flaws located beneath the tensile surface should be corrected in the same manner as above for the uniaxial bend test methods.

Corrections for mirrors located outside the inner loading ring also should be corrected for location. The corrections are not as simple in this case, however. In the annulus outside the inner loading ring, the radial and circumferential (hoop) stresses decrease out to the specimen rim but at different rates.[21],[22] Radial stresses decrease faster, and are zero at the outer rim, and are therefore less likely to induce fracture. Fracture planes and mirrors will usually be perpendicular to the hoop stresses outside the inner ring, so use the hoop stress in the analysis.

On the other hand, hoop stresses decrease more slowly and *are non-zero at the outer circumference* of the specimen. So although the outer hoop stresses are only 10 % to 50 % of the maximum stress in the inner circle (depending upon the disk and fixture geometries, and especially the disk thickness), large grinding or handling flaws on the specimen rim can cause fracture.

The same comments apply to piston on three-balls, ball on three balls, or even pressure loaded plates in bending. Consult appropriate references as needed for the stress distributions in these configurations.

Example 3: Component failure analyses

If the mirror constant for the material is known and a mirror size is measured, the stress at the origin site can be calculated. The peak stress or the nominal stress in the part may be different, however. So as a rudimentary example, imagine a bend bar that broke from an internal origin site, but at an unknown stress. The fractographer uses the mirror size and the mirror constant to estimate the stress at the origin site. The nominal strength of the beam (the maximum outer fiber stress) or the "flexural strength" is greater, however. In this case, the stress adjustment should use σ, A, h, x, y or y' to compute the greater nominal stress, σ_{max}.

11. Evaluate the Fracture Mirror Constants

Once a set of matching mirror radii and fracture stresses is compiled, it is customary to plot the data on either a graph of log stress versus log mirror size (Figure D-7a) or linear stress versus inverse square root of mirror size (Figure D.7b). A linear regression analysis is then performed and a mirror constant calculated from the regressed line. The mirror constants should be reported as either MPa$\sqrt{m}$ (or ksi$\sqrt{in}$ if the older units are in use). Both are widely found in the literature. Each is discussed in turn and it is this author's conclusion that the *stress versus inverse square root of size procedure is better.*

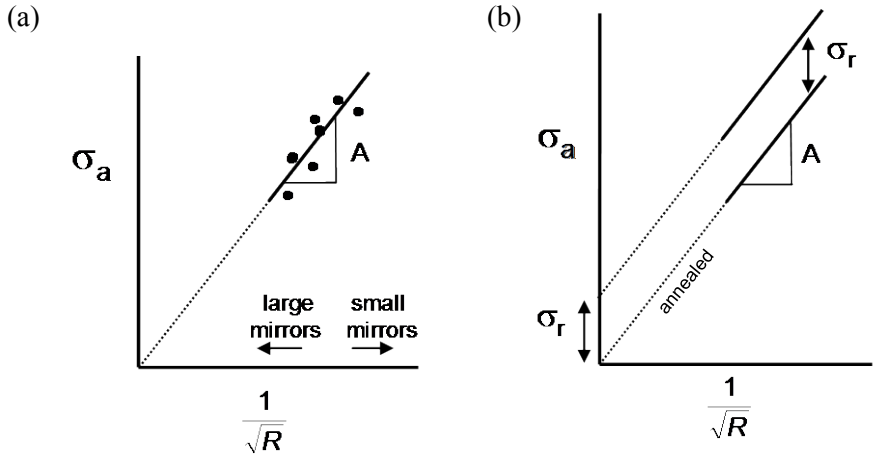

Figure D.7 *(duplicate) Plot of applied stress, σ_a, versus $1/\sqrt{R}$, the preferred regression method. (a) shows the trend for parts with no residual stress. (b) shows the effects of residual stresses. Compressive residual stresses move the line up with a positive intercept σ_r, but with the same slope. Tensile residual stresses shift the data downwards.*

11a. Plot σ versus 1/√R. (Preferred)

Use linear regression methods to obtain A in accordance with equation D.9 (same as D.2) with a zero intercept. Use units of MPa for stress and $1/\sqrt{m}$ for the graph axes. In a typical strength test experiment in a laboratory, applied stress, σ_a, and mirror radius, R, are independently measured. It is customary to regress σ_a on R and this procedure shall be followed in this Guide. A is the slope of the regression line:

$$\sigma_a = \frac{A}{\sqrt{R}} \qquad \text{(D-9)}$$

Use some judgment in the regression analysis since fracture mirror data usually has moderate scatter. If the data does not appear to fit a trend that has a zero intercept, regress the data with a non-zero intercept as shown in Figure D.7b. Again use some judgment in the interpretation, since a strict linear regression fit may produce implausible outcomes, particularly if the data is collected over a limited range of mirror sizes and stresses. Report the intercept if it deviates significantly (> 10 MPa) from zero. Investigate possible residual stresses or specimen size or shape issues in such cases.

Consistent units should be used. That is to say, if the stress axis is MN/m^2 or MPa, then the abscissa (horizontal axis) should be $1/\sqrt{R}$ where radius is in units

of *meters*. If the mirror is measured in mm or μm, then appropriate conversion factors should be added, but this is not trivial and can cause confusion, since the square root of a conversion factor of 1000 (e.g., meters to mm) is an odd value. (If the stress units are psi or ksi, the mirror radii should be measured in inches.)

The mirror constant as a slope is easily visualized. Deviations from the trend usually cause a nonzero intercept, which may be conveniently interpreted as an effective residual stress. If residual stresses σ_r are present in addition to the externally applied stress, σ_a, then the net stress acting on the origin site is: $\sigma_a + \sigma_r$. The fracture and the mirror markings respond to the actual net stress, σ_{net}:

$$\sigma_{net} = (\sigma_a + \sigma_r) = \frac{A}{\sqrt{R}} \tag{D.10}$$

$$\sigma_a = \frac{A}{\sqrt{R}} - \sigma_r \tag{D.11}$$

An intercept below the origin corresponds to a net tensile residual stress. A positive intercept corresponds to residual compressive stress since the usual sign convention is for compressive stresses to have a negative sign.

Some caution is advised since residual stresses are often nonuniform. The residual stress estimated from the intercept is an effective residual stress, which in reality may vary in magnitude through the mirror region. If the mirror is in a heat-strengthened or tempered piece (where stress may be constant along the surface, but change dramatically through the thickness) the mirrors should only be measured along the surface or just underneath to avoid the cusp. Residual stresses from an indentation or impact site are very local to the origin and may have very little effect on a mirror size.

Although most researchers have felt that the regressed lines should go through the origin in *annealed* test pieces, there is evidence by J. Quinn[23] that a small but measurable intercept may exist in even annealed materials. The intrinsic intercept was evaluated as 10 MPa (1,500 psi) for glass, a value that interestingly concurs with Orr's[24] estimate of the minimum stress necessary for branching in glass.

b. Plot log σ versus log R. (Alternative method)

Use linear regression methods to fit the data in accordance with equation D.12 (slope set at – ½) as shown in Figure D.15a. Use units of MPa for stress and meters for the graph axes. This will simplify the computation of the mirror

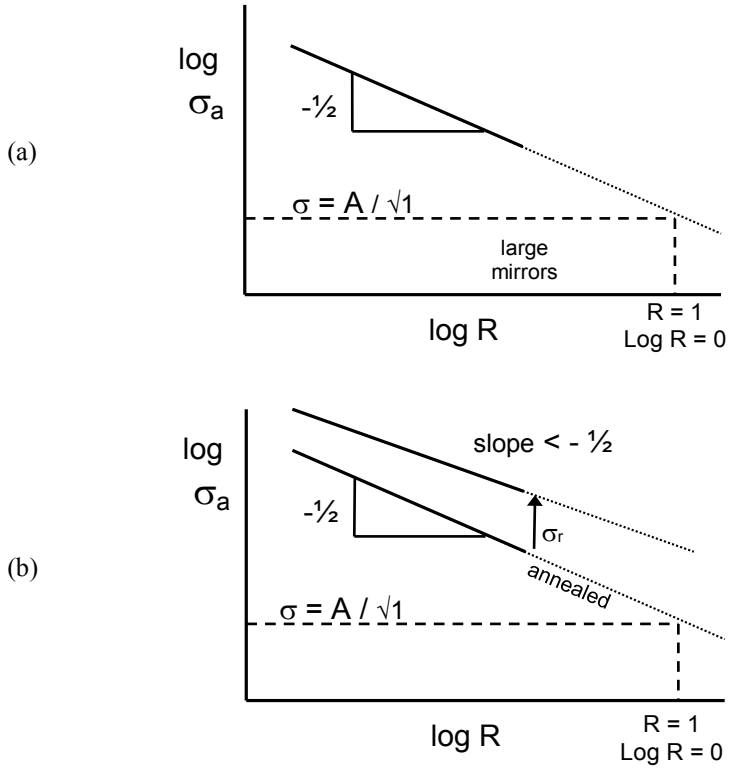

Figure D.15 *Plot of log σ_a versus log R for residual stress-free parts (a) and parts with residual stress (b). Compressive residual stresses move the locus upwards, but with a different slope and intercept. Tensile residual stresses move the loci below the baseline curve (not shown).*

constants in units of MPa√m. The mirror constant A corresponds to the stress that would create a mirror of size = 1 meter.

$$\log \sigma_a = -\frac{1}{2} \log R + \log A \qquad \text{(D.12)}$$

where σ_a is the stress at the origin site, A is the mirror constant and R is the mirror radius in the direction of constant stress. Use some judgment in the regression analysis since fracture mirror data frequently has moderate scatter. If the data does not appear to fit a trend with slope -½, then regress the data with equation D.13:

$$\log \sigma_a = m \log R + \log A' \qquad \text{(D.13)}$$

where σ_a is the stress at the origin estimated from known applied stresses. R is the mirror radius in the direction of constant stress. A' is a modified mirror constant. Report the slope m and the alternative constant A'. Again use some judgment in the interpretation, since a strict linear regression fit may produce implausible outcomes, particularly if the data is collected over a limited range of mirror sizes and stresses. Investigate possible residual stresses or specimen size or shape issues if m deviates significantly from the value –½.

If stresses are in units of MN/m^2 (MPa) and the mirror size is measured in meters, then the mirror constant A has units of $MN/m^{1.5}$ or $MPa\sqrt{m}$. If the mirror size is 1 m, then log R = 0. Then log σ = log A and hence, σ = A. Thus, the mirror constant A corresponds to the value of stress that would create a mirror of size 1 m.

Use consistent units with this approach for the same reasons mentioned in section 11a. If the stresses are in MPa, then the abscissa (horizontal axis) should be with radii in units of *meters or micrometers.* (If the stress units are psi or ksi, the mirror radii should be in inches.)

Since most actual mirrors that are measured are usually much smaller than unit size, it is apparent from Figure D.15 that the mirror constant (or the stress at R = 1) lies somewhat beyond the range of data usually collected. This method of showing the results and calculating a mirror constant was common in the older technical literature and is occasionally still found today. Deviations from the linear relationship on a log - log plot occur when residual stresses are present but unaccounted for (since the plotted stress may not be the true stress at the origin), or when the mirror size becomes large relative to the component size, or when there are stress gradients. The residual stress deviations cause the line to have a slope other than -½ as shown in Figure D.15b. Attempts to compute the residual stresses may then be made by guessing values of the residual stresses σ_r, replotting the data with a vertical axis of $(\sigma_a - \sigma_r)$, and checking the goodness of fit of a line of slope -½. This is a fairly cumbersome process and the alternative procedure in section 11a and Figure D.7b may be simpler and more effective.

If a single mirror is measured, and the externally applied stress, σ_a, and the mirror constant A are both known, then:

$$(\sigma_a + \sigma_r)\sqrt{R} = A \tag{D.14}$$

and

$$\sigma_r = \frac{A}{\sqrt{R}} - \sigma_a \tag{D.15}$$

Mecholsky and colleagues[25,26] have shown excellent examples how residual surface stresses in tempered or clad glasses may be estimated from equation D.8 and fracture mechanics analysis.

11c. Comparison of the two curve fitting and regression approaches

The merits of the two plotting - regression schemes vary. They put different weights on large and small mirror measurements. In one case, the mirror constant is a slope of a line, in the other it is an intercept at R = 1, a rather large mirror size not likely to be realized in practice.

Some researchers may have evaluated test pieces with residual stresses, and then force-fitted regression lines through the data with zero intercepts in the former scheme, or lines of slope -½ through the data in the latter scheme. This probably contributed to variability in published mirror constants.

Figure D-16 shows both graph types for a common set of data from the author's work on the effects of machining on the strength of silicon nitride.[6,7] A large number of rod- or bar-shaped specimens were tested. They had various grinding treatments. The mirror constants from the two analyses are quite similar, although there is a small difference (9%) between the constants for the rods and bars.

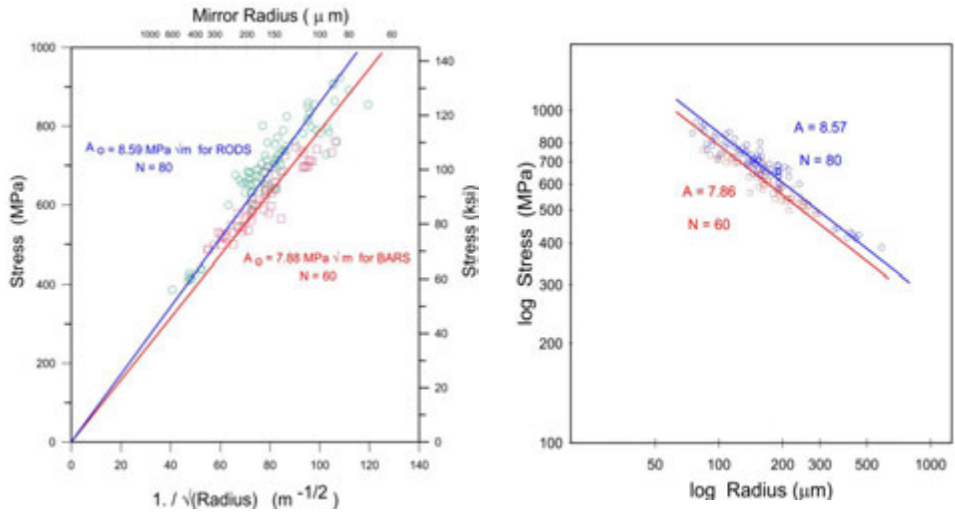

Figure D-16 *Fracture minor data for silicon nitride.[6,7] The round blue symbols are for 60 rods and the square red symbols are for 80 bars.*

Data from flexurally-loaded specimens frequently deviate from the trends when mirror sizes are large and are a significant fraction (50 % or greater) of the cross section size. Upward deviations from the log stress - log radius graphs have been noted in a number of studies (e.g., Shand,[20,27] Orr[24]). The experimentally measured mirrors are larger than they otherwise would be in a uniform tension stress field. Regression lines chase the upward deviations from the trend and dramatically alter the estimate of the mirror constant. On the other hand, with the σ versus $1/\sqrt{R}$ graph, large or oversized mirror data points are closer to the origin and have less influence on the regression line, and hence have less effect upon the slope.

Regression analysis with the σ versus $1/\sqrt{R}$ approach minimizes the deviations of σ from the fitted line. Regression analysis for the log σ versus log R approach minimizes deviations of log σ from the fitted line.

In the 1950s and 1960s many researchers plotted log stress versus log radius probably because they were not confident of the theoretical justification for the -½ slope. They let the exponent vary on the log-log plots and discussed the differences, if any, relative to -½ power. Differences were usually due to residual stresses or overly-large mirrors relative to the specimen size. Gradually the case for the $\sigma\sqrt{R}$ relationship solidified and more researchers began to plot stress versus $1/\sqrt{R}$.

In summary, *the linear stress versus inverse square root radius approach is superior and is recommended by this Guide.* Analyses are simple and intuitive. The mirror constant is the slope of the regressed line. Residual stresses may be interpreted from non-zero intercepts. The uncertainty of the slope can be estimated from routine analyses available in many statistical software packages. Data deviations due to large mirrors in flexure specimens have less effect upon the regression process and the mirror constant estimates. The alternative method (log stress – log radius) may be useful in some cases for displaying data with an unusually large range of mirror sizes and stresses.[28]

12. Mirrors sizes should be collected over a broad range of sizes and fracture stresses if possible. Data from different specimen types and sizes may be combined.

This is a fairly obvious conclusion in light of the discussion in the previous paragraph. Superb examples are shown by Kerper and Scuderi[28,] for borosilicate glass rods with diameters that varied by a factor of ten, and by Mecholsky and Rice[29] for various sized fused silica rods, disks, and fibers.

Ideally, data from many small specimens could be complemented by testing of a few large specimens. Another common procedure is to anneal or fine grind/polish some specimens to obtain high strengths, but abrade or damage others to obtain low strengths. Sometimes the mode of loading can be changed to alter the fracture stress. For example, some studies have used mirrors with large four-point and small three-point flexure specimens. Some specimens may be tested in inert conditions and others tested in conditions conducive to slow crack growth.

D.4 Some Final thoughts

The goal of these guidelines is to bring some consistency to procedures used to measure fracture mirrors. They were adopted as ASTM Standard C1678 in 2007. This should facilitate improved data bases and better estimates of failure stresses. These Guidelines were prepared on the basis of the author's own experiences as well as a careful review of sixty years of literature as summarized in reference 1. One is struck by the conclusion, which nearly all writers have reached, that measurement of the mirror sizes requires subjective interpretation. The perception of the observer and the type of equipment are important factors. Although advanced microscopy and software tools hold considerable promise in the future, it is unlikely that a simple definitive criterion (such as a set level of surface roughness) will emerge. Despite this, most students of the technique have concluded that consistent readings are possible between observers. The quotation from Johnson and Holloway[3] at the start of this Appendix is one example. Another is from Mecholsky and Freiman[19] who said:

> "While one might think initially that the measurements of a mirror boundary using a microscope is quite a qualitative operation and would vary from observer to observer; in fact, experiments performed over a number of years by a large number of investigators have shown that the values of mirror constants obtained in different laboratories are quite nearly the same."

They then listed some values for a few glasses and ceramics that did in fact vary as much as 20 % to 30 %. For example, the soda-lime glass values varied by 23 %. Hopefully, adoption of the guidelines in this Guide and ASTM C 1678 will improve the consistency of future data to within 10%.

One positive conclusion is that fracture mechanics principles do seem to account for the observed shape variations in mirrors.[4,5] (A caveat is that the fracture mechanics analyses have been based on static loading, whereas the

mirror boundaries are formed by a very dynamic crack traveling at or near terminal velocity.) A logical conclusion of this finding is that equation 1 is over simplistic, since it does not account for stress gradients or geometric effects. Nevertheless, it *does have the proper functional form* for the stress intensity of a crack in a far-field tension stress. For a small mirror in a uniform tensile stress field, equation 1 is completely justifiable.

Another interesting finding from the literature review is how few authors have shown good fracture mirror photos. Even fewer have marked them. Perhaps the authors were not sure or were hesitant to show an interpretation for fear of criticism. Hopefully, step 8 of this Guide (which requires marked photos) and the examples shown in this Guide will help future authors improve their reporting. One is also struck by the fact that nearly all the mirrors shown in the literature, even in the classical papers, are not exactly semicircular or circular, despite all the schematics that imply that they are. Fractographers should not be alarmed if their mirrors are not perfect.

Many of the steps in this Guide have already been proposed. Shand recommended that stresses be corrected for the origin location,[20] that radii be measured beneath the surface to avoid surface effects,[18] that low-angle grazing illumination be used.[20] He also warned about deviations from the trends if the mirror sizes were too large relative to the component thickness.[20] Shand also said that mist could not be discerned in glass ceramics.[20] Morrell et al. [30] agonized over the interpretation of mirrors in Y-TZP zirconia (such as shown in Figures D.4 – D.6), but settled on a set of specific criteria. Optical microscopy with a stereo optical microscope at a fixed magnification was used, with grazing incidence illumination. No reflective coating was applied to the surface. The specimen sides were masked to block transmitted-light scatter. Matching fracture halves were mounted together to aid the interpretation. The best set of recommendations predating this Guide were crafted by Mecholsky and Freiman.[19] Six of their recommendations match steps in this Guide: (a) optical microscopy is preferred over scanning electron microscopy whenever possible, (b) suitable magnifications should be used, (c) mirror boundary arcs should be projected to the outer surface to complete a circular arc to eliminate the surface cusps, (d) lighting should be varied to obtain optimum contrast, (e) radii should be measured in directions of constant stress and not into gradients, and (f) trend deviations occur for mirrors that are large relative to part thickness.

Appendix D References

1. G. D. Quinn, "Guidelines for Measuring Fracture Mirrors," pp. 163 – 190 in: *Fractography of Glasses and Ceramics, V*, eds., J. R. Varner, G. D. Quinn, M. Wightman, American Ceramic Society, Westerville, OH, 2007.
2. ASTM C 1678, "Standard Practice for Fractographic Analysis of Fracture Mirror Sizes in Ceramics and Glasses," Annual Book of Standards, Vol. 15.01 ASTM Int. West Conshohocken, PA, 2007.
3. J. W. Johnson and D. G. Holloway, "On the Shape and Size of the Fracture Zones on Glass Fracture Surfaces," *Phil. Mag.,* **14** (1966) 731 - 743.
4. H. P. Kirchner and J. W. Kirchner, "Fracture Mechanics of Fracture Mirrors," *J. Am. Ceram. Soc.,* **62** [3-4] (1979) 198 - 202.
5. H. P. Kirchner and J. C. Conway, Jr., "Criteria for Crack Branching in Cylindrical Rods: I, Tension and II, Flexure," *J. Am. Ceram. Soc*., **70** [6] (1987) 413 - 425.
6. G. D. Quinn, L. K, Ives, and S. Jahanmir, "On the Fractographic Analysis of Machining Cracks in Ground Ceramics: A Case Study on Silicon Nitride," SP 996, NIST, Gaithersburg, MD, May, 2003.
7. G. D. Quinn, L. K. Ives, S. Jahanmir, and P. Koshy, "Fractographic Analysis of Machining Cracks in Silicon Nitride Rods and Bars," pp. 343 - 365 in *Fractography of Glasses and Ceramics IV,* Ceramic Transactions, Vol. 122, eds., J. R. Varner and G. D. Quinn, American Ceramic Society, Westerville, OH, 2001.
8. G. D. Quinn, J. Eichler, U. Eisele, and J. Rödel, "Fracture Mirrors in a Nanoscale 3Y-TZP," *J. Am. Ceram. Soc*., **87** [3] (2004) 513 - 516.
9. W. H. Duckworth, D. K. Shetty, and A. R. Rosenfeld, "Influence of Stress Gradients on the Relationship Between Fracture Stress and Mirror Size for Float Glass," *Glass Technol.,* **24** [5] (1983) 263 - 273.
10. D. M. Kuluwansa, L. C. Jensen, S. C. Langford, and J. T. Dickinson, "Scanning Tunneling Microscope Observations of the Mirror Region of Silicate Glass Fracture Surfaces," *J. Mater. Res*., **9** [2] (1994) 476 – 485.
11. D. Hull, "Influence of Stress Intensity and Crack Speed on Fracture Surface Topography: Mirror to Mist Transition," *J. Mat. Sci*., **31** (1996) 1829 - 1841.
12. D. Hull, Chapter 5, in *Fractography, Observing, Measuring and Interpreting Fracture Surface Topography*, Cambridge Univ. Press., Cambridge, 1999.
13. C. Wünsche, E. Rädlein, and G.H. Frischat, "Morphology of Silica and Borosilicate Glass Fracture Surfaces by Atomic Force Microscopy," *Glastech. Ber. Glass Sci. Technol.,* **72** (1999) [2] 9 - 54.
14. E. Gölz, "Übermikroskopische Feinstructuren an Glasbruchflächen," *Zeitschrift für Physik*, **120** (1943) 773 - 777.
15. E. K. Beauchamp, "Mechanisms of Hackle Formation and Crack Branching," pp. 409 - 446 in *Fractography of Glasses and Ceramics III,* eds., Varner, Fréchette, Quinn, *Cer. Trans*., Vol. 64, 1996, American Ceramic Society, Westerville, OH.
16. E. K. Beauchamp, "Fracture Branching and Dicing in Stressed Glass," Sandia Research Report SC-RR-70-766, January 1971, Sandia National Laboratory, Albuquerque, NM.

17. R. J. Castilone, G. S. Glaesemann, and T. A. Hanson, "Relationship Between Mirror Dimensions and Failure Stress for Optical Fibers," pp. 11 - 20 in *Optical Fiber and Fiber Component Mechanical Reliability and Testing II*, eds., M. J. Matthewson and C. R. Kurkjian, Proc. SPIE, 4639 (2002).
18. E. B. Shand, "Strength of Glass – The Griffith Method Revised," *J. Amer. Ceram. Soc.,* **48** [1] (1965) 43 - 48.
19. J. J. Mecholsky and S. W. Freiman, "Determination of Fracture Mechanics Parameters Through Fractographic Analysis of Ceramics," pp. 136 -150 in *Fracture Mechanics Applied to Brittle Materials*, ASTM STP 678, ed., S. W. Freiman, ASTM Int., West Conshohocken, PA, 1979.
20. E. B. Shand, "Breaking Stress of Glass Determined from Dimensions of Fracture Mirrors," *J. Am. Ceram. Soc.,* **42** [10] (1959) 474 - 477.
21. H. Fessler and D. C. Fricker, "A Theoretical Analysis of the Ring-On-Ring Loading Disk Test," *J. Am. Ceram. Soc*., **67** [9] (1984) 582 - 588.
22. J. A. Salem and L. Powers, "Guidelines for the Testing of Plates," *Cer. Eng. Sci. Proc.,* 24 [4] (2003) 357-364.
23. J. B. Quinn, "Extrapolation of Fracture Mirror and Crack-Branch Sizes to Large Dimensions in Biaxial Strength Tests of Glass," *J. Am. Ceram. Soc.*, **82** [8] (1999) 2126 - 2132.
24. L. Orr, "Practical Analysis of Fractures in Glass Windows," *Materials Research and Standards*, **12** [1] (1972) 21 - 23, 47.
25. J. C. Conway, Jr. and J. J. Mecholsky, Jr., "Use of Crack Branching Data for Measuring Near-Surface Residual Stresses in Tempered Glass," *J. Am. Ceram. Soc.,* **72** [9] (1989) 1584 - 87.
26. J. J. Mecholsky and M. G. Drexhage, "Comparisons of Optical and Fractographic Measurements of Residual Stress in Compressively Clad Glass Rods," *J. Am. Ceram. Soc.,* **63** [5-6] (1980) 347 - 349.
27. E. B. Shand, "Breaking Stresses of Glass Determined from Fracture Surfaces," *The Glass Industry*, April (1967) 190 - 194.
28. M. J. Kerper and T. G. Scuderi, "Relation of Fracture Stress to the Fracture Pattern for Glass Rods of Various Diameters," *Bull. Am. Ceram. Soc.,* **45** [12] (1966) 1065 - 1066.
29. J. J. Mecholsky, Jr. and R. W. Rice, "Fractographic Analysis of Biaxial Failure in Ceramics," pp. 185 - 193 in *Fractography of Ceramic and Metal Failures*, eds., J. J. Mecholsky, Jr. and S. R. Powell, ASTM STP 827 American Society for Testing and Materials, West Conshohocken, PA, 1984.
30. R. Morrell, L. Byrne, and M. Murray, "Fractography of Ceramic Femoral Heads," pp. 253 - 266 in *Fractography of Glasses and Ceramics, IV, Ceramic Transactions,* Vol. 122, eds., J. R. Varner and G. D. Quinn, American Ceramic Society, Westerville, OH, 2001.

INDEX

A

Abrasion	6-39, 6-66 – 6.69
Acid, aqua regia	3-26
Acid storage tank	9-6
Agglomerate, see origins	
Alumina	4-18, 4-32, 4-45, 5-19, 5-68, 5-71, 6-7, 6-8, 6-11, 6-12, 6-14, 6-23, 6-30, 6-70, 6-77 10-30 –10-37, 10-43 – 10-45
Alumina, β	6-16
Alumina furnace plate	4-32
Alumina crown	4-45, 10-30 – 10-37, 10-43 – 10-45
Alumina single crystal, see sapphire	
Alumina, whisker reinforced	7-71
Aluminum oxynitride	5-34, 5-67, 5-74, 6-8, 6-13, 6-75, 10-16 – 10-17
Aqua regia	3-26
Arrest lines	5-58 - 5-60
Atomic Force Microscope	3-60
Automobile window	4-31, 4-50, 7-7

B

Ball bearings	3-68, 6-39
Ball mill	6-60
Baseline microstructural flaws	6-75
Batman mirror	8-19
Bend bar	4-14 – 4-18, 10-19 – 10-25
Bevels, see chamfers	
Biaxial disk	3-23, 4-5, 4-9, 4-19 – 4-21, 5-72, 6-29, 6-31, 7-4
Biaxial stress	1-3, 1-4, 4-19 – 4-21
Bifurcation	
Black light	3-55
Blanchard grinding	6-40
Bleach	3-6
Blisters, see origins	
Blood	5-63
Boron carbide	4-50, 7-61
Bottles	4-7, 4-38, 7-3, 10-14, 10-15
Boundary phases, ceramics	5-78, 5-79

Branching 4-3 – 4-10, 7-7 – 7-9
Branching angles 4-6 – 4-9
Branching constant 4-9, 7-8, C-1
Branching distance 4-9, 7-7 - 7-9
Branching constants 4-9, Appendix C
Brick, Roman 4-41
Bubbles 6-7 – 6-11, 6-78, 6-79

C
C crack 3-68, 6-35
Camera 3-7 – 3-11, 3-14 – 3-16
Camera, single lens reflex 3-8
Camera stand 3-7
Camera mount, F-mount or C-mount 3-14
Cantilever curl 4-15 – 4-17, 5-2
Capacitor, multilayer 3-23
Cathedral mirror 8-9, 8-10, 8-16, 8-24
Cavitation, scarp 5-61, 5-62 7-53
Cell phone 3-10, 3-11
Cellulose acetate 3-36 - 3-38, 3-42
Center heated plate 4-32, 4-33
Chain of events 1-10
Chamfers 6-16, 6-23, 6-40, 6-53
Characteristic strength 7-72
Chatter marks, see origins
Chill checks, see origins
Chips, chipping, see edge chips
Clay 3-5, 6-70, 6-71
Cleaning coatings off 3-26, 3-71
Cleaning specimens 3-5, 3-6, 3-71, 5-1
Cleaning, dental plaque 3-6
Cleaning, green dye 3-29
Cleaning, removal of gold coatings 3-26
Cleaner, ultrasonic 3-71
Cleavage 5-3, 8-1, 8-2, 8-5
Cleavage step hackle 8-8
Coatings 3-26 – 3.29
Combination flaw 6-73, 6-74
Component fracture patterns 4-22, 4-44, 4-45
Composites 6-20, 7-24, 7-72, 9-1 – 9-11
Compositional inhomogeneity, see origins
Compound optical microscope 3-32 – 3-35

Compression curl 4-15 – 4-18
Compression fracture 4-51 – 4-54
Conchoidal fracture 5-3
Cone cracks, see Hertzian cone crack
Confocal microscope 3-62, 3-63
Contact cracks 3-68, 4-30, 4-37, 6-34– 6-39, 10-6, 10-9, 10-10, 10-31, 10-46 - 10-48
Contaminants, see also clay 6-70 - 6-72
Conversion factors 7-1
Cooking ware 6-63, 6-66, 6-68
Cords, see origins
Corner hackle 10-36
Corrosion flaws 4-49, 6-28
Crack branching 4-3 – 4-10, 7-7 – 7-9, 7-24
Crack bridging 7-24, 7-55
Crack front shape 5-46
Crack healing 4-28, 7-43
Crack, processing 4-10, 6-54 - 6-58
Cracks, intersecting 4-26, 4-27
Crack velocity 7-46 – 7-53
Crack velocity, terminal 5-6, 5-7, 7-46 – 7-49
Crazing 6-78
Creep fracture 5-77 – 5-81
Critical strain energy release rate, G_{Ic} 7-22
Crossing cracks 4-27
Crowns, see dental
Cusps 6-76

D

Damage wave 5-6
Dandruff 6-69
Dark field illumination 3-20, 3-24, 3-32, 8-5, 8-6
Debonding 10-20, 10-21
Debris on fracture surface 5-83, 5-84
Deep Reactive Ion Etching (DRIE) 6-76, 8-23, 8-24, 10-25 – 10-27
Deer 4-23
Defect, see also flaws and origins 6-1
Delaminations 6-57
Delta markings 5-3, 5-36
Dental ceramics, crowns, bridges 3-38, 3-40, 3-41, 10-30 – 10-45
  Alumina 3-41, 4-45, 6-55, 6-58, 6-87, 10-30–10-37, 10-43 – 10-45

Bovine dentin	4-15
Bridge, lithium disilicate	6-79
Bridge, zirconia	6-55, 6-78
Cerestore alumina-magnesia spinel	10-31 – 10.33
Composites, filled and unfilled	6-20, 6-61, 6-69, 9-6 – 9-8
Denture material	4-43
Dicor	10-30
Empress II glass ceramic	5-34 10-37 – 10-42
Human enamel	4-4
Lithium disilicate glass ceramic	4-41, 6-60, 6-71, 6-79, 10-37 – 10-42
Porcelain	4-3, 4-43, 6-10
Resin, PEG with ACP filler	3-23
Resin infiltrated ceramic, Enamic	6-60
Replicas	3-38 – 3-41
Veneers, glazes	5-33, 5-34, 6-78, 6-79
Zirconia, see also zirconia	4-43, 6-55, 6-58
Dental plaque	3-6, 6-71, 6-78
Devitrification stones, see origins	
Differential Interference Contrast	D-12, D-13
Digital camera, photos	3-3 – 3-11, 3-14 – 3-16
Digital image formats	3-8, 3-9
Digital image processing	3-17
Digital microscope	3-19, 3-20
Digs	6-31, 6-33, 6-34
Discussion stereo microscope	3-18, 3-19
Disk specimen, see biaxial disk	
Dome, IR	8-7, 8-21, 10-16 – 10-17
Dome, see sapphire domes	
Double cantilever beam specimen	8-3
Double torsion specimen	5-36, 5-49, 8-3
Drawings	4-24 – 4-26
Dunt crack	6-58
Dust	6-69
Dye staining	3-28, 3-29, 4-48
Dye penetration	3-66 – 3-70, 4-48, 6-51
Dynamic fatigue (variable rate strength test)	7-52

E

E-glass composite	9-4, 9-6
Edges	6-1, 6-2, 6-40, 6-53
Edge chips	4-40 – 4-44, 10-36, 10-37, 10-43 – 10-45
Elastic waves	5-6, 5-47 – 5-58, 7-46 – 7-50

Electrical insulators 3-37, 6-8, 6-37
Electronic part, multilayer capacitor 3-23
Electronic part, thick film resistor 5-65
Electronic part, varistor 6-16
Epoxy, replica 3-40, 3-42, 3-45
Electron backscatter diffraction 3-55
Extrinsic flaws 6-4

F
Failure analysis 1-6 – 1-8
Far field stress 7-21
Fatigue crack 3-24, 5-81 – 5-84
Fiber composite 9-1 – 9-6
Fiberglass- epoxy composite 9-4, 9-5
Fiber reinforcement 7-24, 9-1, 9-2
File formats, digital images 3-8, 3-9
Finite element analysis 1-5, 4-46, 7-18
Firing cracks 4-10, 6-54 – 6-56, 6-58
Flaw 6-1
Flaw bluntness 7-20, 7-39 – 7-41
Flaw linkage 6-50, 6-73, 6-74, 6-80 – 6-82, 7-44, 7-45
Flaw management 6-75, 7-75
Flaw shielding 7-44, 7-45
Flaw size 6-3, 6-75, 7-18, 7-19
Flaw size distribution 7-73, 7-74
Flaw truncation 6-77, 7-42, 7-44, 7-45
Flexural strength 4-14 – 4-18, 5-20
Flexural stress gradient D-18, D-19, D-26, D-27
Flow lines of stress 7-20, 7-21, 7-44
Fluorescent dye penetration 3-67 – 3-68
Focus stacking 3-17
Ford Rotor 10-1 – 10-7
Ford Turbocharger 6-56
Fractal analysis 7-65 – 7-67
Fractography, definition 1-1
Fractography, Laws of 11-1 – 11-3
Fracture, conchoidal 5-3
Fracture energy 7-18, 7-22
Fracture map 5-80, 5-81
Fracture mirror, definition 5-3
Fracture mirror 5-3 – 5-30, Appendices C and D, see also mirror

Fractographic montages 5-84, 5-85, 6-84 – 6-86
Fracture origin, definition 4-1
Fracture origins, see origins
Fracture toughness 7-21 – 7-25, 7-40
Fracture toughness, single crystal 8-2, 8-3
Fragmentation 4-10 – 4-12, 4-19, 7-2 – 7-7
Furnace plate 4-32, 10-18, 10-19

G
Gas turbine rotor 10-1 – 10-7
Glass
    Borosilicate, Pyrex 7-16
    Borosilicate crown 4-5, 4-21, 6-31, 6-59, 7-4, 7-34, 7-61
    Fused silica 5-2, 5-4, 5-5, 6-6, D-3, D-22
    Fused silica, sintered 10-20 – 10-22
    Soda lime 4-23, 6-18, 6-57 – 6-64, 7-3, 7-5, 7-6, 7-9
Glass bottles, see bottles
Glass ceramic 6-7, 6-11, 6-60
Glass ceramic, dental 3-29, 6-60
Glass disk, see biaxial disk
Glass rod, flexure 1-1, 4-15, D-3, D-20, D-22, D-26
Glass tube 4-36
Glass windows, see windows
Glazes, veneers 5-33, 5-34
Gloves, cotton 3-2
Glue, specimen reconstruction 4-2, 4-3
Glue chips 5-63 - 5-66
Grazing illumination 3-12, 3-22
Green pen, dyes 3-28, 3-29, 10-42
Griffith flaw 6-1, 7-18, 7-19
Griffith criterion, equation 7-18, 7-19
Grinding cracks, see origins, grinding cracks
Grinding damage, glass disks 4-20, 4-21
Gull wings 5-14, 5-49, 5-50, 7-46, 7-47
Gull wing mirrors 8-9, 8-15, 8-18
Gun Barrel 10-7 – 10-10

H
Hackle 5-10 – 5-16, 5-31 - 5-44
    cleavage step 8-8
    corner 5-43

definition	5-12
coarse microstructural	5-31, 5-32
grinding crack	6-40 – 6-52
fine microstructural	5-36, 5-41
mist hackle	5-12
shear hackle	5-42
step hackle	5-43, 5-44
twist hackle	5-36 – 5-41
velocity hackle, definition	5-12
wake hackle	5-33 – 5-36, 5-49
Hailstone	7-4
Hair	3-23, 6-69
Halo, slow crack growth	5-71
Hand magnifier	3-2
Handling damage	6-29, 6-36, 6-39, 8-7
Healed cracks	4-28
Heat sleeks	6-63
Hertzian cone cracks	6-34 – 6-40, 10-10, 10-31, 10-47, 10-48
High speed photography	3-64
Hinge fracture	4-34 – 4-36
History of brittle materials fractography	1-8, 1-9
Holders	3-4, 3-5
Hoop stress	4-33, 4-37 – 4-38
Hopf bifurcation	4-32
Human enamel	4-4, 4-46
Human skin contamination	6-70
Hybrid flaws	6-73, 6-74
Hydrogen peroxide	3-29

I

Illumination	3-12, 3-20 – 3-26
Impact	4-29, 4-35, 4-49
Impact origins, see origins impact	
Impact, tertiary Wallner lines	5-53
Inclusion, see origins-inclusion	
Incomplete bonding	6-16
Indentation fracture mechanics	7-25, 7-61 – 7-65
Insect	3-37, 6-69
Insulator, electric	6-8
Intrinsic flaws	6-3, 6-4
Intergranular fracture	5-17, 5-66 - 5-70, 5-75, 5-79
Intersecting cracks	4-26, 4-27

Invisible cracks 4-28
IR dome 8-7, 8-21, 10-16, 10-17

J
Jeweler's Loupe 3-3, 3-4
Joint 5-3
JPEG format 3-8, 3-9

K
Kitchenware 6-63, 6-66, 6-68
Knoop indentation crack, see origins
K-V diagram (slow crack growth) 7-51 – 7-53

L
Laboratory fractures 4-11, 4-44
Lambda lines 5-58
Lamp fracture 4-11, 7-7
Lances, see also hackle 5-16, 5-36, 8-13, 8-17
Law of normal crack propagation 4-3
Lead zirconium titanate (PZT) 5-35, 6-57
Leader crack 4-35, 4-36
Lint 6-8, 6-69
Lithic fractures 5-3, 5-62
Lithic fractures - Obsidian 5-35, 5-49, 5-62
Litigation 1-8
Longitudinal grinding 6-40, 6-41
Loupes 3-3, 3-4
Low-angle grazing illumination 3-12, 3-22, 5-19, 6-45, 8-5

M
Machine gun barrel 10-7 – 10-10
Machine shops 10-23 – 10-25
Machining cracks, see origins
Machinist loupe 3-3, 3-4
Macrofractography camera stand 3-7
Magnesium fluoride 5-71
Magnesium oxide 8-1
Magnesium aluminate spinel, see spinel
Magnifying glass 3-2
Mandelbrot relationship 7-66
Margin damage, dental crowns 10-32 – 10-37, 10-43 – 10-45
Maximum distortion energy criterion 1-5

Mechanical engineers 1-4
Mechanical overload 4-47
Medicinal vial 4-37, 6-39, 10-14, 10-16
Microcracking 7-24
Microelectromechanical structures (MEMS) 8-23 – 8-24, 10-25 – 10-27
Microflaw pocket 6-80 – 6-82
Micrometer, damage from 6-36
Micrometer, stage 3-30
Microscope
  Atomic force 3-60
  Compound optical 3-32 – 3-35
  Confocal 3-62
  Discussion stereo optical 3-19
  Environmental scanning electron 3-59
  Field emission scanning electron 3-58
  Scanning electron 3-43 – 3-57
  Stereo optical 3-11 – 3-16
  Transmission electron 3-59
Mirror, fracture
  Alumina bend bar 5-19
  Borosilicate crown glass 5-22, 5-26
  Bent 5-22
  Glass rod 1-1, 3-61, 3-63, 5-2, 5-4, 5-6, 5-24
  Medicinal vial 4-37
  Multiple 5-20, 5-21
  Silicon carbide 5-18
  Silicon nitride 5-20, 5-27
  Tempered glass 5-29, 5-30
  Zirconia 3-27, 5-17, 5-19
Mirrors, single crystals 8-2, 8-6, 8-8, 8-9
  Batman 8-19
  Cathedral 8-9, 8-10, 8-16
  Gull wings 8-9, 8-15, 8-18
Mirror constants 5-13, 7-10–7-16, 7-40, 7-41, Appendices C and D
Mirror cusp D-21 – D-24
Mirror, fibers 9-5
Mirror size, radius 7-10 – 7-16, Appendix D
Mirror size, residual stresses 7-69, 7-70, D-20 – D-23
Missile domes
Missile radomes 10-20 – 10-23
Mist 5-9 – 5-16

Mist hackle, definition 5-12
Mohr's circle 1-5
Montages 5-84, 5-85, 6-84 – 6-87

N
Near surface 6-3
Neutral axis, bending 4-14 – 4-16
Nickel sulfide 6-18
Nomarski illumination 5.62, D-12, D-13
Nomenclature 1-8, 1-9, 5-1, 5-3, 6-1

O
Obsidian 5-14, 5-35, 5-49, 5-62
Optical comparator 3-3
Optical profilometer 3-60 – 3-62
Origin 6-1
- Abrasion tracks 6-66 – 6-48
- Agglomerate 3-51, 6-6, 6-13, 9-1
- Ball mills 6-5, 6-69
- Baseline microstructure 6-75
- Blank pressing flaws 6-11
- Blisters, glass 6-61
- Bubbles 6-7, 6-9, 6-10, 6-11
- Chatter marks, cracks 5-29, 6-65 – 6-68
- Chill checks 4-28, 4-48, 6-64, 6-65
- Chips 6-53
- Contact cracks 3-42, 3-68, 6-34 – 6-39
- Cords, glass 6-61
- Compositional inhomogeneity 3-51, 6-21, 6-22
- Cusps, geometric irregularities 6-76
- Dandruff 6-69
- Delaminations 6-58
- Devitrification stones, inclusions 6-61
- Dunt cracks 6-57
- Etch groove 10-26, 10-27
- Etch pits 8-24
- Fatigue crack 3-24
- Feces 6-69
- Fiber 6-8
- Fiber clump 9-1
- Firing cracks 6-54 – 6-56, 6-58
- Geometric sharp points 6-76

Grain boundary	6-25, 6-26, 6-75
Grinding cracks, see origins, machining	
Hair	3-23, 6-8
Handling damage	6-29, 6-36, 6-39, 8-7
Heat sleeks	6-63
Hybrid	6-73, 6-74
Impact, blunt	4-29, 4-30, 6-34 - 6-39
Impact, sharp	4-29, 4-30, 6-33, 8-22
Inclusion	3-52 – 3-54, 6-17 – 6-20, 6-61, 9-8
Insect	6-69
Knoop indentation crack	3-29, 3-68, 5-32, 5-71, 5-73, 6-59, 6-60, 7-61, 7-63, 8-2 – 8-4, 10-12 – 10-14, D-3
Large grain	6-22 – 6-24
Lint	6-8, 6-69
Machining cracks	6-6, 6-28 – 6-36, 10-5, 10-6, 10-16–10-18, 10-20, 10-21, 10-23
Herring bone	6-51
Orthogonal cracks	6-41 – 6-43
Parallel cracks	6-41 – 6-46, 6-48
V-grinding cracks	6-42, 6-46, 6-47
Zipper cracks	6-44 – 6-46
Machining crack skin zone	6-46
Microflaw pockets	6-80 – 6-82
Nickel sulfide, glass	6-18
Pecks	6-33, 6-63
Pits	6-28
Polishing surface flaws	3-65, 5-72, 6-29 – 6-32, 8-21, 10-48
Pore	6-4, 6-8, 6-13
Porous region	6-13, 6-14, 10-12, 10-13
Porous seam	6-14, 9-3
Pressing flaws	6-11
Processing cracks	4-10, 6-14, 6-54 – 6-58, 6-83
Quartz grains, Quartz inversion	6-24, 6-57
Scratch	6-6, 6-29 – 6-32, 8-7
Seeds, glass	6-61
Silicon vein	6-69
Skin	6-70
Sleeks	6-65
Stones, glass	6-61
Striae, glass	6-61
Surface void	6-27

Vickers indentation crack 5-22, 6-59, 6-33, 7-25, 7-25, 7-59, 7-61 – 7-65
Whisker clump 9-1
Origin, fracture definition 4-1
Orthogonal machining crack, see origins
Oxidation 4-49, 6-28

P
Parallel machining crack, see origins
Parfocal 3-12, 3-20
Parting 5-3
Patriot missile 10-20
Pattern recognition 1-3
Pecks 6-33, 6-63
Penny shape cracks 7-26, 7-29, 7-40
Pharmaceutical vials and syringes 4-37, 5-62, 6-39, 10-14, 10-15
Phase instability 6-69
Photos, Photography 3-7 – 3-11
Pits, see origins
Plaque, dental 3-6
Plasma asher 8-27 – 8-29
Plane strain 1-5
Plane stress 1-5
Plaque, dental 3-6, 6-71
Plate fracture patterns 4-28 – 4-30
Plate fracture patterns, thermal 4-32, 4-33
Plate, whiteware 3-42
Polariscope 3-70, 3-71
Polarizer 3-25, 3-26, 8-5, 8-26 – 8-29,
Polished microstructural section 6-5, 6-75, 6-82, 6-83
Polishing surface flaws, see origins
Polycrystalline alumina (PCA) 10-17
Porcelain 3-37, 3-42, 3-66, 4-41, 6-8, 6-10, 6-24, 6-37, 6-52
Porcelain electrical insulator 3-37, 6-8, 6-37
Polyvinylchloride (PVC), replicas 3-38
Polyvinylsiloxane (PVS) replicas 3-38, 3-41
Pore, see origins
Porous region, see origins
Porous seam, see origins
Pressing flaws 6-11
Pressure flaking 5-63

Pressure vessel 4-7, 4-33 – 4-38
Processing cracks, see origins
Proof test, radome 10-20
PZT, see Lead zirconium titanate

Q
Quartz grains, Quartz inversion 6-24, 6-57
Quasi static loading 6-35

R
R-curve 5-73, 6-48, 7-23, 7-25, 7-55 – 7-60
Radome, fused silica 10-20 – 10-22
Rayleigh wave velocity 5-5
RAW format 3-8
Reliability 10-1 – 10-7
Renegade abrasive grit 6-48, 6-49
Replicas 3-35 – 3-42, 6-82
Residual stress 4-49 – 4-50
  Compression induced cracking 5-63
  Estimates of magnitude 7-68– 7-70, D-30 – D-34
  Grinding 6-40, 7-68
  Heat strengthened glass 5-28, 5-29
  Indentation 6-59, 6-60, 7-63 – 7-65, 7-70
  Mirror shapes, effect on 5-28, D-18 – D-24
  Stable crack extension from 5-73
  Tempered glass 4-28 – 4-31, 4-49, 5-30
Resin-matrix composite, dental 6-20, 6-21, 6-69, 9-6 – 9-8
Retroreflective flaws 6-69
Rib marks 5-45, 5-58
Rings of Saturn 6-7, 7-20, 7-39, 7-40
Ripples 5-45, 5-56
River deltas 5-3, 5-36
Rock fracture, see lithic fracture
Roman brick 4-41
Rotor, gas turbine 10-1 – 10-7
Round robin, flexural strength 10-23 – 10-25
Round robin, fractography 10-28 – 10-30
Round robin, machining 10-23 – 10-25

S
Saliva 5-63
Sapphire, single crystal alumina 3-65, 6-31, 8-4, 8-7, 8-19, 8-21, 8-22,

	8-25 - 8-29, 10-46 – 10-48
Sapphire dome	3-65, 4-25, 5-62, 6-31, 8-7, 8-21, 8-22
Sapphire scarp	5-62
Sapphire tubes	8-27 – 8-29
Scanner	3-71
Scanning electron microscope	3-43 – 3-57
Scarps	5-61, 5-62, 7-53, 8-20, 10-14
Scratch, see also origin	6-6, 6-30 – 6-32
Scratch/Dig specification	6-31, 6-33
Secondary fracture, edge chips	4-44
Secondary origins	4-3, 4-18, 4-44
Secondary Wallner line	5-50, 5-53
Seeds, see origins	
Self-toughened ceramics	9-2
Shark's teeth	6-42 – 6-46
Shear hackle	5-42
Shrink fit	10-7 – 10-9
Sialon	6-18, 6-30, 7-72, 7-73
Side wall damage	6-52
Sierra scarp	5-61, 5-62
Silica, fused	5-2, 5-4, 5-5, 6-6, 10-20 – 10-22, D-3, D-22
Silicon	6-76, 7-33, 8-2, 8-3, 8-6, 8-20, 8-23, 8-27
Silicon carbide	4-4, 5-18, 5-40, 5-62, 5-75, 6-5, 6-8, 6-13, 6-16, 6-21, 6-23, 6-37, 6-53, 6-59, 6-69, 6-70, 6-83, 7-32, 9-2, 9-3, 10-9 – 10-15, 10-18, 10-19, D-5
Silicon carbide, CVD	5-40, 9-3, 10-25 – 10-27
Silicon carbide, fibers	9-1 – 9-3, 9-6
Silicon carbide machine gun barrel	10-7 – 10-10
Silicon carbide furnace plate	10-18, 10-19
Silicon nitride	3-51, 3-52, 3-53, 4-9, 4-15, 5-17, 5-21, 5-27, 5-32, 5-68, 5-73, 5-76, 5-77, 5-79, 5-80, 5-81, 6-6, 6-8, 6-13, 6-16 – 6-18, 6-21 – 6-23, 6-27, 6-28, 6-30, 6-32, 6-36, 6-47 – 6-49, 6-51, 6-53, 6-54, 6-56, 6-60, 7-58, 9-2, 9-3, 10-1 – 10-7, D-6, D-33
Single crystals	8-1 – 8-32
Alumina, see sapphire	
Spinel	8-9 - 8-18, 8-25
Silicon	6-76, 7-33, 8-2, 8-3, 8-6, 8-20, 8-24

Zirconia	8-1
Sketches	4-24 – 4.26
Sleeks	6-65
Slow crack growth	4-51, 5-69 – 5-76, 7-23, 7-25, 7-51 – 7-54, 10-1 – 10-5, 10-11 – 10-14
Slow crack growth exponent, N	7-51, 7-52
Soda Lime silica, see glass	
Spinel, magnesium aluminum oxide	6-25, 6-26, 8-9 - 8-18, 8-25
Spray-dried particles	6-5, 6-15, 6-16, 6-55
Stable crack extension	5-69 - 5-76, 7-42, 7-43, 7-51 – 7-60, 10-11
Staining	3-26– 3-29, 3-66 – 3-70
Standards	
ASTM C 1322, fractography	6-73, 6-84, 7-28, 7-32, 8-9, 10-28
ASTM C 1421, fracture toughness	7-28, 7-31
ASTM C 1678, fracture mirrors	C-2, D-1
ISO 14704, flexural strength	10-23
ISO 18756, fracture toughness	7-31
MIL STD 1942 (MR), flexural strength	10-23
MIL HDBK 790, fractography	10-28
Standard Reference Material 2100, K_{Ic}	7-25
Stage micrometer	3-30
Stage, traversing	3-31, 3-34
Static fatigue	7-51, 7-52, 10-11 – 10-14
Steel, fatigue crack	3-24
Step hackle	5-43, 5-44
Stereoptical microscope	3-1, 3-11 – 3-16
Stereoscope	3-57
Stones, glass, see origins	
Streaks	5-61, 5-62
Stress	1-4, 7-17 – 7-19
Stress concentration	7-17, 7-18, 7-20, 7-39
Stress, biaxial	1-4
Stress corrosion	10-13
Stress, far field	7-21
Stress, flexural	4-14 – 4-17
Stress intensity	7-17 - 7-29
Stress intensity shape factor	7-21 – 7-38
Stress intensity factors, Newman-Raju	7-30 – 7-36, 7-53
Stress rupture	7-52, 10-3, 10-11 – 10-14
Stress state	1-4
Stress, triaxial	1-4
Stress uniaxial	1-4

Stress wave fractography 3-64
Striae, see also origins 6-61
Striations, fatigue cracks 5-81, 5-82
Striations, grinding 6-6, 6-41, 6-43
Subcavitation hackle 5-61, 5-62, 5-72
Surface crack – fracture mechanics 7-27 – 7-38, 7-53, 7-54
Surface crack in flexure, see origins Knoop 6-59
Surface finish 6-40
Surface grinding 6-41 – 6-52
Surface void, see origins
Syringes 6-39

T
Teeth 4-4, 4-46
Telescoping denture 6-58
Tempered glass, heat strengthened glass 3-10, 4-11, 4-29 – 4-31, 6-18, 6-66, 6-68, 7-5 - 7-9
Tension strength 4-13, 10-25 – 10-27, D-5
Terminal velocity 5-6, 5-7
Tertiary Wallner lines 5-53 – 5-57
Thermal crack 6-57
Thermal fracture 4-32, 4-33, 4-47, 4-48, 10-18, 10-46 – 10-48
Thermal shock 4-47, 4-48, 6-58, 8-27
Thermal stresses 6-58, 8-7, 8-27, 10-18, 10-46 – 10-48
Thermocouple bead origin 6-69
Theta strength specimen 8-23, 8-24
Time dependent fracture 4-51
TIFF format 3-8, 3-9
Torsion 4-7, 4-18, 4-39
Transformation toughening 7-24, 7-25, 7-57
Transgranular fracture 5-17, 5-66, 5-67, 5-69, 5-71, 10-11, 10-12
Transillumination 3-24, 3-25, 4-3, 4-4, 8-5, 10-27
Transmission electron microscope 3-59, 5-79
Transmitted illumination 3-24, 3-25, 4-3, 4-4, 8-5, 9-8,10-27
Transverse grinding 6-41, 6-44 – 6-49, 6-52
Triaxial stress 1-4
Tube fracture 4-36, 8-27 – 8-29, 10-7– 10-9
Tungsten inclusion 6-18, 6-19
Turbocharger, silicon nitride 6-56
Twinning 3-64, 4-54, 8-5, 8-25 - 8-30, 10-46 – 10-48
Twist hackle 5-36 – 5-42

U
Ultrasonic cleaner 3-71
Ultrasonic fractography 3-64, 5-56, 5-57
Uniaxial stress 1-4
USB microscope 3-19

V
VAMAS 10-28
Vanadium inclusion 6-17
Velocity hackle 5-11, 5-12, 5-31
Velocity, terminal 5-6, 5-7
Veneer, dental 6-36, 6-71, 6-77 – 6-79, 6-87
Vials, medicinal 4-37, 5-62, 6-39,10-14, 10-15
Vicinal illumination 3-22, 3-23
Vickers indentation flaws, see origins
Video camera 3-15
V machining crack, see origins
Von Mises failure criterion 1-5

W
Wake hackle 5-33 – 5-36, 5-49, 9-3, 10-16, 10-17, 10-33
10-35, 10-36, 10-45
Wallner lines 5-39– 5-58, 7-46 – 7-50, 8-8
Gull wings 5-14, 5-49, 5-50
Lambda 5-58
Primary 5-45 – 5-47
Secondary 5-50 – 5-52
Tertiary 5-53 – 5-55, 8.22
Watch bracelet 6-56
Watchmaker's loupe 3-3
Water hammer 4-34, 4-35
Wave velocity, see elastic waves
Weibull distribution 6-86, 7-71 – 7.76
Weibull modulus 7-59, 7-71 – 7-76
Whisker lances, single crystal 8-9, 8-13, 8-17
Whisker reinforcement 7-24, 9-1, 9-2
Wing cracks 4-53
Window failure 4-23 – 4-33
Window failure, glue chips 5-66
Window patterns 4-28 – 4-33

Window, thermal fracture 4-32, 7-2
Witness marks 4-22, 4-49, 6-33, 6-34, 6-39

X
X-ray topography 3-65, 8-5, 8-7
X-Y stage, traversing 3-31, 3-34

Z
Zinc oxide, varistor 6-16
Zipper crack, see origins, machining
Zirconia, cubic single crystal 8-1
Zirconia, magnesia stabilized 5-31, 6-25, 6-26, 6-81, 6-82, 7-23, 7-57, 7-58
Zirconia, yttria stabilized 5-17, 5-19, 6-8, 6-13, 6-18, 6-56, 6-58, 6-72, 7-14, 7-15, 7-16, 7-60, D-7 – D-9